frontiers | Research Topics

Advanced application technology for plant protection: Sensing, modelling, spraying system and equipment

Edited by
Changyuan Zhai, Wei Qiu, Paul Weckler, Xiongkui He and Khawar Jabran

Published in
Frontiers in Plant Science

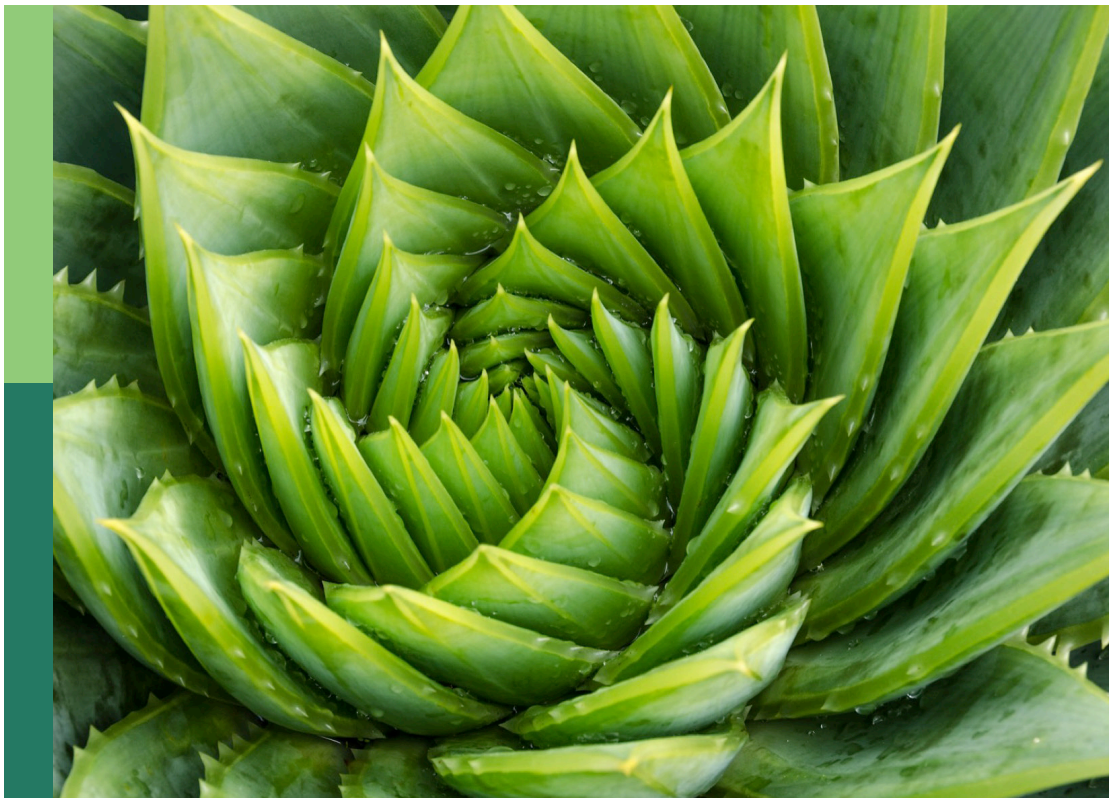

ISSN 1664-8714
ISBN 978-2-83251-863-2
DOI 10.3389/978-2-83251-863-2

About Frontiers

Frontiers is more than just an open access publisher of scholarly articles: it is a pioneering approach to the world of academia, radically improving the way scholarly research is managed. The grand vision of Frontiers is a world where all people have an equal opportunity to seek, share and generate knowledge. Frontiers provides immediate and permanent online open access to all its publications, but this alone is not enough to realize our grand goals.

Frontiers journal series

The Frontiers journal series is a multi-tier and interdisciplinary set of open-access, online journals, promising a paradigm shift from the current review, selection and dissemination processes in academic publishing. All Frontiers journals are driven by researchers for researchers; therefore, they constitute a service to the scholarly community. At the same time, the *Frontiers journal series* operates on a revolutionary invention, the tiered publishing system, initially addressing specific communities of scholars, and gradually climbing up to broader public understanding, thus serving the interests of the lay society, too.

Dedication to quality

Each Frontiers article is a landmark of the highest quality, thanks to genuinely collaborative interactions between authors and review editors, who include some of the world's best academicians. Research must be certified by peers before entering a stream of knowledge that may eventually reach the public - and shape society; therefore, Frontiers only applies the most rigorous and unbiased reviews. Frontiers revolutionizes research publishing by freely delivering the most outstanding research, evaluated with no bias from both the academic and social point of view. By applying the most advanced information technologies, Frontiers is catapulting scholarly publishing into a new generation.

What are Frontiers Research Topics?

Frontiers Research Topics are very popular trademarks of the *Frontiers journals series*: they are collections of at least ten articles, all centered on a particular subject. With their unique mix of varied contributions from Original Research to Review Articles, Frontiers Research Topics unify the most influential researchers, the latest key findings and historical advances in a hot research area.

Find out more on how to host your own Frontiers Research Topic or contribute to one as an author by contacting the Frontiers editorial office: frontiersin.org/about/contact

Advanced application technology for plant protection: Sensing, modelling, spraying system and equipment

Topic editors

Changyuan Zhai — Beijing Academy of Agricultural and Forestry Sciences, China
Wei Qiu — Nanjing Agricultural University, China
Paul Weckler — Oklahoma State University, United States
Xiongkui He — China Agricultural University, China
Khawar Jabran — Niğde Ömer Halisdemir University, Türkiye

Citation

Zhai, C., Qiu, W., Weckler, P., He, X., Jabran, K., eds. (2023). *Advanced application technology for plant protection: Sensing, modelling, spraying system and equipment*. Lausanne: Frontiers Media SA. doi: 10.3389/978-2-83251-863-2

Table of contents

frontiers | Frontiers in Plant Science

TYPE Editorial
PUBLISHED 23 February 2023
DOI 10.3389/fpls.2023.1113359

OPEN ACCESS

EDITED AND REVIEWED BY
Jucheng Yang,
Tianjin University of Science and Technology, China

*CORRESPONDENCE
Changyuan Zhai
zhaicy@nercita.org.cn

SPECIALTY SECTION
This article was submitted to Sustainable and Intelligent Phytoprotection, a section of the journal Frontiers in Plant Science

RECEIVED 01 December 2022
ACCEPTED 09 January 2023
PUBLISHED 23 February 2023

CITATION
Zhai C, Qiu W, Weckler P, He X and Jabran K (2023) Editorial: Advanced application technology for plant protection: Sensing, modelling, spraying system and equipment.
Front. Plant Sci. 14:1113359.
doi: 10.3389/fpls.2023.1113359

Editorial: Advanced application technology for plant protection: Sensing, modelling, spraying system and equipment

Changyuan Zhai[1]*, Wei Qiu[2], Paul Weckler[3], Xiongkui He[4] and Khawar Jabran[5]

[1]Intelligent Equipment Research Center, Beijing Academy of Agricultural and Forestry Sciences, Beijing, China, [2]College of Engineering, Nanjing Agricultural University, Nanjing, China, [3]Department of Biosystems & Agricultural Engineering, Oklahoma State University, Stillwater, OK, United States, [4]Centre for Chemicals Application Technology (CCAT), China Agricultural University, Beijing, China, [5]Department of Plant Production and Technologies, Niğde Ömer Halisdemir University, Niğde, Türkiye

KEYWORDS

unmanned aerial vehicles, drift characteristics, deep learning, pests and diseases, airflow velocity loss characteristics, air-assisted spray

Editorial on the Research Topic
Advanced application technology for plant protection: Sensing, modelling, spraying system and equipment

As editors of this Research Topic, we summarized the contributions of 20 articles accepted in this topic. The research contents mainly focused on the following sections: drift characteristics of unmanned equipment and development of autonomous navigation spray system, identification and classification of pests and diseases based on deep learning, and airflow velocity loss characteristics of air-assisted spray in orchard.

Drift characteristics of unmanned equipment and development of autonomous navigation spray system

In recent ten years, agricultural unmanned aerial vehicles (UAV), also known as Unmanned Aerial Spraying Systems (UASS), as a new method for the application of plant protection products, has developed rapidly in the world. Compared with ground equipment, UAV spray is more likely to cause spray drift and environmental pollution to non-target areas. Therefore, it is important to study the spray drift characteristics of UASS.

Chen et al. reviewed the drift characteristics of UAV spray system and the factors affecting UAV system drift, and put forward suggestions on the optimization of spray system and structure layout, modeling of drift test, and standardization of measurement methods. Jiang et al. compared the performance of UAV, unmanned ground vehicle (UGV) and spray gun pesticide application technology of spray target coverage, off-target coverage, time efficiency and gasoline consumption in the pear orchard. The results showed that compared with UGV, UAV has the advantages of high working efficiency, less environmental pollution

and consumption of natural resources. Although the traditional spray gun technology showed good spraying performance, it is not conducive to the protection of environment and resources. The achievement was helpful to the research and development of intelligent pesticide application technology. Shan et al. carried out research on corn fertilization method based on UAV. The difference of the effectiveness between the water sprayed on the sampling rod and leaves was studied. They found that sampling methods have a significant effect on deposition results and determined the optimum spraying concentration. Qi et al. compared the effects of multi-functional unmanned aerial vehicle (mUAV) planter, mechanical rice seeder and mechanical rice transplanter on rice cultivation. The results showed that there was no significant difference in rice yield among the three regions. In terms of labor cost and seeding efficiency, UAV was more effective than mechanical planter and transplanter. Li et al. studied the influence of UAV flight velocity on deposition distribution and droplet size, especially the usage of compound pesticides as spray solution. The results demonstrated that increasing flight velocity is helpful for pesticide droplets to spread and penetrate the canopy. However, it also led to uneven deposition of pesticides, reduced deposition volume, and reduced effective coverage and effective density ratio.

Jiang et al. developed a greenhouse autonomous navigation system based on Simultaneous Localization and Mapping (SLAM) algorithm. In this paper, three-dimensional Lidar data was filtered and fused into two-dimensional Lidar data containing the environment information in the range of robot motion height. They used Dijkstra algorithm for global planning and DWA algorithm for local navigation path planning of robot. This method not only ensured the accuracy of greenhouse environment map but also reduced the accuracy of greenhouse environment map and the performance requirements of industrial computers. According to the three perception decision control modules of unmanned system, Wang et al. constructed the environment perception and map building strategy based on 3D Lidar under the complex environment background of orchard. They pointed out two difficulties in developing automatic orchard sprayer: one is to realize efficient penetration of pesticides in low-density canopy and reduce losses, and the other is to make the machine automatically pass through orchard without manual control. They also provided a basis for the development of technology for independent and precise spraying of pesticides in the orchard environment based on automatic navigation.

Identification and classification of pests and diseases based on deep learning

At present, researches have carried out extensive research in the fields of pest image recognition, segmentation and feature extraction based on deep learning. The purpose of most researches was to improve the running speed and recognition accuracy of the system by optimizing or building the models.

Zhao et al. proposed an improved deep convolution neural network to identify crop pests. They also developed a new attention module, which includes parallel attention mechanism module and residual blocks. This module was integrated into ResNet-50 CNN, which is used to classify 10 different types of crop pests. This network had significant advantages in terms of accuracy and real-time performance compared with other models. Yao et al. studied the segmentation and recognition of peach disease based on Mask R-CNN and Mask Scoring R-CNN to provide evidence for disease control and treatment. This work was valuable in engineering applications, such as the classification of plant diseases and the location and segmentation of lesion areas. Li et al. proposed an imaging model for detecting corpuscle insects such as whitefly and thrips in greenhouse. The author used an automatic detection method to reduce pest detection. This method could satisfy the needs of continuous monitoring of pests in greenhouse, and estimate the total population density. Lin et al. proposed a few-shot learning method for plant disease recognition based on multi-scale feature fusion and attention. The results showed that plant disease identification technology based on a few-shot learning method is feasible in the future application.

Airflow velocity loss characteristics of air-assisted spray in orchard

Air-assisted spray technology has been widely used in the high-efficiency application of pesticides in orchards. In this section, the authors mainly studied the influence characteristics of canopy airflow velocity loss on air-assisted spray performance.

Zhang et al. established a theoretical model of airflow velocity attenuation in a pear canopy by selecting the velocity attenuation factor k and incoming velocity as model inputs. It was demonstrated that high-speed airflow will disturb the outer branches and leaves and thus affecting the accuracy of the model. The research results could provide theoretical basis for the adjustment of air flow parameters of air-assisted spray in the pear orchard. Wu et al. discussed the feasibility of using the resistance characteristics of crop canopy to evaluate its droplet deposition effect through theoretical analysis and wind tunnel test. The results could provide theoretical basis for rapid and low-cost research and development of crop protection technology and equipment. Yang et al. proposed a new three-dimensional airflow velocity and direction synchronous measurement method, and established a new sensor system and calculation model. This method could be used as a solution to measure and evaluate the airflow velocity field characteristics of sprayers. Gu et al. studied the airflow velocity loss model for a canopy. They built a three-dimensional airflow velocity measurement platform for fruit tree canopy, and obtained the point cloud data by Lidar scanning. Classical regression, partial least squares regression (PLSR) and back propagation (BP) neural network algorithms were adopted. This study could provide a basis for airflow velocity control of precise variable spray and promote the development of airflow velocity control technologies.

In addition to these three main sections, the authors also conducted the following researches. Zhang et al. proposed a method to evaluate the adjuvant efficacy of herbicides under different temperature conditions by using chlorophyll fluorescence of herbaceous plants. The experiment was carried out under the control of greenhouse environment by using two-factor block experiment scheme. The results distinguished the differences

among treatments and determined the optimum solution to improve the efficacy of topramzone against weeds at different temperatures. Electrochemical fingerprinting technology can collect the electrochemical behavior of electrochemically active molecules in plant tissues, which is considered as a new plant analysis technology. Hu et al. found that electrochemical fingerprint signals are positively correlated with the number and type of electrochemical active molecules in plant tissues, and can also be used to reflect the genetic differences among different species. Liu et al. established the numerical model of plant-soil-machine system, and introduced the details on the construction and calibration method of plant mechanics model based on the discrete element method (DEM). The discrete element model of taro plant established in this paper was reliable. In order to solve the issues of low weeding rate and severe seedling damage of rice weeding machinery, Zhang et al. optimized the key components of rice weeding. Through the analysis of the motion trajectory and DEM simulation analysis of the weeding wheel, the structural parameters of the weeding wheel were determined. This study provided a technical reference for the improvement of paddy-field weeding equipment. Xie et al. proposed a new method to predict the waterlogging tolerance of poplar. They used different feature selection algorithms to analyze the waterlogging tolerance of different parameters such as photosynthesis and chlorophyll fluorescence. Machine learning algorithm was used to study and analyze different parameters of poplar waterlogging resistance. This research provided new information for the selection of poplar seedlings with waterlogging tolerance.

Author contributions

All authors listed have made a substantial, direct, and intellectual contribution to the work and approved it for publication.

Acknowledgments

We thank the authors and reviewers for their valuable contributions on this topic.

Conflict of interest

The authors declare that the research was conducted in the absence of any commercial or financial relationships that could be construed as a potential conflict of interest.

Publisher's note

All claims expressed in this article are solely those of the authors and do not necessarily represent those of their affiliated organizations, or those of the publisher, the editors and the reviewers. Any product that may be evaluated in this article, or claim that may be made by its manufacturer, is not guaranteed or endorsed by the publisher.

frontiers in Plant Science

ORIGINAL RESEARCH
published: 11 February 2022
doi: 10.3389/fpls.2022.821365

Poplar's Waterlogging Resistance Modeling and Evaluating: Exploring and Perfecting the Feasibility of Machine Learning Methods in Plant Science

Xuelin Xie[1†], Xinye Zhang[2†], Jingfang Shen[1] and Kebing Du[3*]*

[1] College of Sciences, Huazhong Agricultural University, Wuhan, China, [2] Hubei Academy of Forestry, Wuhan, China, [3] College of Horticulture and Forestry Sciences, Hubei Engineering Technology Research Center for Forestry Information, Huazhong Agricultural University, Wuhan, China

OPEN ACCESS

Edited by:
Khawar Jabran, Niğde Ömer Halisdemir University, Turkey

Reviewed by:
Milind Ratnaparkhe, ICAR Indian Institute of Soybean Research, India
Shixiong Zhang, Xidian University, China

****Correspondence:***
Jingfang Shen
sjf_712@mail.hzau.edu.cn
Kebing Du
kebingdu@mail.hzau.edu.cn

[†] These authors have contributed equally to this work

Specialty section:
This article was submitted to Sustainable and Intelligent Phytoprotection, a section of the journal Frontiers in Plant Science

Received: *01 December 2021*
Accepted: *20 January 2022*
Published: *11 February 2022*

Citation:
Xie X, Zhang X, Shen J and Du K (2022) Poplar's Waterlogging Resistance Modeling and Evaluating: Exploring and Perfecting the Feasibility of Machine Learning Methods in Plant Science. Front. Plant Sci. 13:821365. doi: 10.3389/fpls.2022.821365

Floods, as one of the most common disasters in the natural environment, have caused huge losses to human life and property. Predicting the flood resistance of poplar can effectively help researchers select seedlings scientifically and resist floods precisely. Using machine learning algorithms, models of poplar's waterlogging tolerance were established and evaluated. First of all, the evaluation indexes of poplar's waterlogging tolerance were analyzed and determined. Then, significance testing, correlation analysis, and three feature selection algorithms (Hierarchical clustering, Lasso, and Stepwise regression) were used to screen photosynthesis, chlorophyll fluorescence, and environmental parameters. Based on this, four machine learning methods, BP neural network regression (BPR), extreme learning machine regression (ELMR), support vector regression (SVR), and random forest regression (RFR) were used to predict the flood resistance of poplar. The results show that random forest regression (RFR) and support vector regression (SVR) have high precision. On the test set, the coefficient of determination (R^2) is 0.8351 and 0.6864, the root mean square error (RMSE) is 0.2016 and 0.2780, and the mean absolute error (MAE) is 0.1782 and 0.2031, respectively. Therefore, random forest regression (RFR) and support vector regression (SVR) can be given priority to predict poplar flood resistance.

Keywords: flood disaster, prediction of waterlogging tolerance, machine learning, feature selection, model establishment and evaluation

INTRODUCTION

Natural disasters are inherently a phenomenon that has adverse consequences for society (Paprotny et al., 2018). It damages the living environment and life of human beings. Flood disasters, as one of the most common and expensive natural disasters, have caused huge losses to human lives and property (Hu et al., 2018; Ao et al., 2020). With the development of social industry and economy, the warming of the atmosphere caused by greenhouse gas emissions may increase the risk of river flooding (Hallegatte et al., 2013; Hirabayashi et al., 2013; Willner et al., 2018;

Bloeschl et al., 2019). Therefore, many studies want to build a system for predicting flood risk (Alfieri et al., 2017; Shafizadeh-Moghadam et al., 2018; Choubin et al., 2019; Khosravi et al., 2019), and a variety of machine learning methods are used in these studies. Choubin et al. (2019) used multivariate discriminant analysis (MDA), classification and regression trees (CART), and support vector machine (SVM) algorithms to predict flood risk in Iran's Khiyav Chai drainage basin. The results show that the residential areas at the outlet of the drainage basin are very susceptible to floods. Khosravi et al. (2019) adopted three Multi-Criteria Decision-Making techniques (VIKOR, TOPSIS, and SAW) and two Machine Learning methods (NBT and NB) to test the flood sensitivity modeling of the Ningdu River Basin in China. Finally, their research shows that the NBT model is a powerful tool for evaluating flood-prone areas, and can properly plan and manage flood disasters. Nevertheless, predicting flood risk cannot substantially reduce the life and economic losses of human society. Afforestation can strengthen the stability of water, soil, and carbon sinks in the forest ecosystem, thereby effectively coordinating the relationship between humans and the natural environment. A considerable number of studies have shown that afforestation can weaken the impact of global warming and effectively reduce the risk of river flooding (Hong et al., 2018, 2020; Liu X. et al., 2018; Forster et al., 2021). Thus, afforestation is widely used to resist flood disasters.

Plants have evolved numerous resistance mechanisms to resist flood disasters, including plant morphological Screening of Candidate Genesristics, metabolic responses, and molecular transcriptional regulation (Loreti et al., 2016; Du et al., 2017; Yin et al., 2017; Zeng et al., 2019; Lukic et al., 2020; Lee et al., 2021). Among the diverse plant populations, poplar has become the main flood-resistant tree varieties in flood-prone areas due to its rapid growth and flood resistance features. Many studies have shown that the root system is the key organ of poplar responding to Flooding stress (Coleman et al., 2000; Major and Constabel, 2007; Berhongaray et al., 2013; Ye et al., 2018; Gerjets et al., 2021). Flooding stress affects the diffusion of oxygen in plant root tissues. At the same time, it limits the mitochondrial respiration of root cells and accumulates toxic substances, which seriously affects its normal physiological activities (Arbona et al., 2008; Voesenek and Bailey-Serres, 2013; Tian et al., 2019). In addition, flooding stress will destroy the photosynthesis performance of plants, which will inhibit plant growth and biomass accumulation (Du et al., 2012; Zhu et al., 2016; Zheng et al., 2017; Xiong et al., 2019; Zhou et al., 2020). Flooding stress not only reduces the chlorophyll content of plants, but also reduces the carotenoid content (Zhou et al., 2017). Kreuzwieser et al. (2009) found that the metabolite changes occurred in leaves and roots of submerged poplar. Du et al. (2012) compared the physiological and morphological adaptability of two poplar clones (hypoxia-resistant and hypoxia-sensitive) to flooding, and Peng et al. (2018) monitored the different response mechanisms of these two clones of poplar to flooding stress. These studies have greatly promoted people's understanding of the waterlogging resistance mechanism, and to a considerable extent, strengthened people's resistance to flood risks. Thus far, there are still few studies on the influence of poplar on the waterlogging resistance factors. These factors include the intrinsic features of poplar trees (photosynthesis and chlorophyll fluorescence, etc.) and external environmental features (ambient temperature, humidity, etc.). As a popular research direction, machine learning has recently been gradually introduced into the field of plant science. For the research on the resistance of poplar to waterlogging, Xie and Shen (2021) used poplar photosynthesis features and external environmental factors to predict the waterlogging tolerance of poplar. By using the SVR method in machine learning, they confirmed the feasibility of applying photosynthesis and other characteristic parameters to predict poplar flood resistance. However, previous prediction studies did not consider important parameters such as chlorophyll fluorescence. Additionally, the related forecasting research is not systematic enough, and the corresponding investigation and research are still lacking.

Based on the above considerations, the main purpose of this article is to consider more comprehensive feature parameters and use a variety of machine learning methods to predict the flood resistance of poplar. At the same time, it aims to supplement and improve the key content and procedures of poplar flood resistance prediction. First of all, the evaluation indicators of waterlogging tolerance were well defined and explained. Then, 26 internal characteristics and external environmental factors of poplars were screened by using feature selection algorithms such as significance test and stepwise regression. Finally, four machine learning methods were used to establish the flood resistance models of poplar, and the results were comprehensively evaluated in detail. Compared with previous studies, this study supplements the evaluation index and prediction system of poplar waterlogging tolerance. The main contribution is that the definition and analysis of evaluation indicators for waterlogging tolerance have been improved, and more comprehensive characteristic parameters have been considered. Moreover, the feature selection, prediction methods, and evaluation indicators were adjusted, and more machine learning methods and results have been considered and analyzed. This research has enriched the prediction of poplar's flood resistance, which is of great significance to poplar's accurate flood resistance, intelligent selection of seedlings, and cultivation of high-quality saplings. Furthermore, to a considerable extent, it promotes the research of flood resistance mechanisms, which have great theoretical and practical value.

MATERIALS AND METHODS

Experimental Area and Materials

Research area: Huazhong Agricultural University, Wuhan, China (114°35′E, 30°49′E), subtropical humid monsoon climate. This area has four distinct seasons, with plenty of sunshine and plenty of rainfall. The annual average temperature is 15.8–17.5°C, rainfall is 1,269 mm, and total sunshine hours are between 1,810 h to 2,100 h.

Experimental objects: There were 20 poplar varieties in total. The scientific names corresponding to the 20 poplar varieties are shown in **Table 1**.

TABLE 1 | Scientific names of 20 poplar varieties.

Varieties	Scientific names
LS68	*Populus deltoides "Lux" × P. simonii (LS68)*
LS81	*P. deltoides "Lux" × P. simonii (LS81)*
NL895	*P. × euramericana "Nanlin 895"*
I-63	*P. deltoides "Harvard"*
I-69	*P. deltoides "Lux"*
I-72	*P. euramaricana "an Martino"*
I-214	*P. × euramericana "I-214"*
I-45-51	*P. × euramaricana "I-45/51"*
Flevo	*P. euramericana "Flevo"*
Juba	*P. deltoides "55/56" × P. deltoides "2KEN8"*
LH04-13	*P. deltoides "Lux" × P. deltoides "Harvard" (LH04-13)*
LH04-17	*P. deltoides "Lux" × P. deltoides "Harvard" (LH04-17)*
Triplo	*P. euramericana "Triplo"*
DD102-4	*P. deltoides "DD102-4"*
Raspalje	*P. deltoides "Raspalje"*
Danhong	*P. deltoides "Danhong"*
Canadensis	*P. canadensis Moench.*
2L2025	*P. deltoides "Lux" × P. deltoides "Shanhaiguan"*
Ningshanica	*P. ningshanica*
Lushan	*P. × liaoningensis*

Experimental Process and Parameter Measurement

The 1-year-old branches of 20 poplar clones were cut into about 15 cm cuttings with 3–4 buds. There were 4 experimental groups and 4 control groups for each variety, with a total of 160 experimental materials. After being soaked in water for 24 h, the cuttings were planted in mixed soil. The container was seedling pots (150 mm × 100 mm × 130 mm), and the soil was 1:1 substrate soil and peat soil (The soil consisted of 2–5% N, P_2O_5 and K_2O, pH = 6.2, total organic matter of nutrient soil was ≥ 28%, and the total nutrient was ≥ 2%). The morphological changes of the plants were observed every day, including the chlorosis and shedding of leaves. We measured the height, biomass, photosynthesis, and chlorophyll fluorescence parameters of poplar seedlings on the 0th and 60th days. The characteristic parameters were measured by the LI-6400 photosynthesis analyzer (LI-COR, Lincoln, NE, United States), and the time was concentrated between 9:00 am and 11:30 am. In the experiment, a standard LI-COR leaf chamber and red and blue light sources (6400-02 LED light sources) were used. The light intensity was 1,000 $\mu mol \cdot m^{-2} \cdot s^{-1}$, and the air velocity was 500 $\mu mol \cdot s^{-1}$. 26 characteristic parameters of poplar samples were measured, including photosynthesis, chlorophyll fluorescence features, and environmental variables. The specific information of these features is shown in **Appendix Table A1**, and the treatment process of the experimental group and the control group is as follows.

- Control group: Watered normally (CK). There were drainage holes at the bottom of the flower pots in the Control group. Watered the plants according to the needs of normal plant growth, and the soil moisture was maintained at about 75% of the maximum water holding capacity in the field.
- Experimental group: Shallow flooded (FL). The waterlogging test was started 5–6 weeks after cuttings, and the water surface was 10 cm higher than the soil surface. The experiment lasted for 60 days, of which, the flooding time was 45 days, and the drainage recovery time was 15 days.

Programming Environment

In this article, R 4.0.5 was used to perform data Processing and Feature selection process, and MATLAB R2018a was used to implement the Model building and evaluation.

METHODOLOGY

The methodology is divided into data processing, feature selection, model establishment and evaluation. The main procedures are shown in **Figure 1**, and the specific implementation steps will be introduced one by one below.

Data Processing

Evaluation Index of Waterlogging Tolerance

The changes in biomass and seedling height can reflect the waterlogging tolerance of plants. In previous studies, Xie and Shen (2021) proposed the waterlogging tolerance evaluation index Zscore. This article supplemented the definition of the other two waterlogging tolerance evaluation indicators, and used the three waterlogging tolerance evaluation indicators for outlier analysis. Finally, the most suitable evaluation index for waterlogging tolerance was selected. The definitions of the three evaluation indicators are given below.

The first evaluation index for waterlogging tolerance is Zbio, which is obtained based on changes in biomass. This indicator is based on the change in biomass of the test group within 60 days to judge the flood resistance of poplar, and it is dimensionless. The stronger the waterlogging resistance performance, the larger the corresponding Zbio. The calculation method is shown in Formula (1):

$$Zbio = \frac{bio(x_i) - E(bio)}{Std(bio)} \tag{1}$$

The second waterlogging tolerance evaluation index is Zsap, which is similar to the definition of Zbio. This index only considers the change of poplar seedling height, and its calculation method is shown in Formula (2):

$$Zsap = \frac{sap(x_i) - E(sap)}{Std(sap)} \tag{2}$$

The third evaluation index of waterlogging tolerance is Zscore. This indicator takes into account the changes in biomass, as well as changes in seedling height. Compared with Zbio and Zsap, this index can more comprehensively reflect the flood resistance of poplar, and its calculation formula is shown in Formula (3):

$$Zscore(x_i) = \omega_{bio} \times Zbio + \omega_{sap} \times Zsap \tag{3}$$

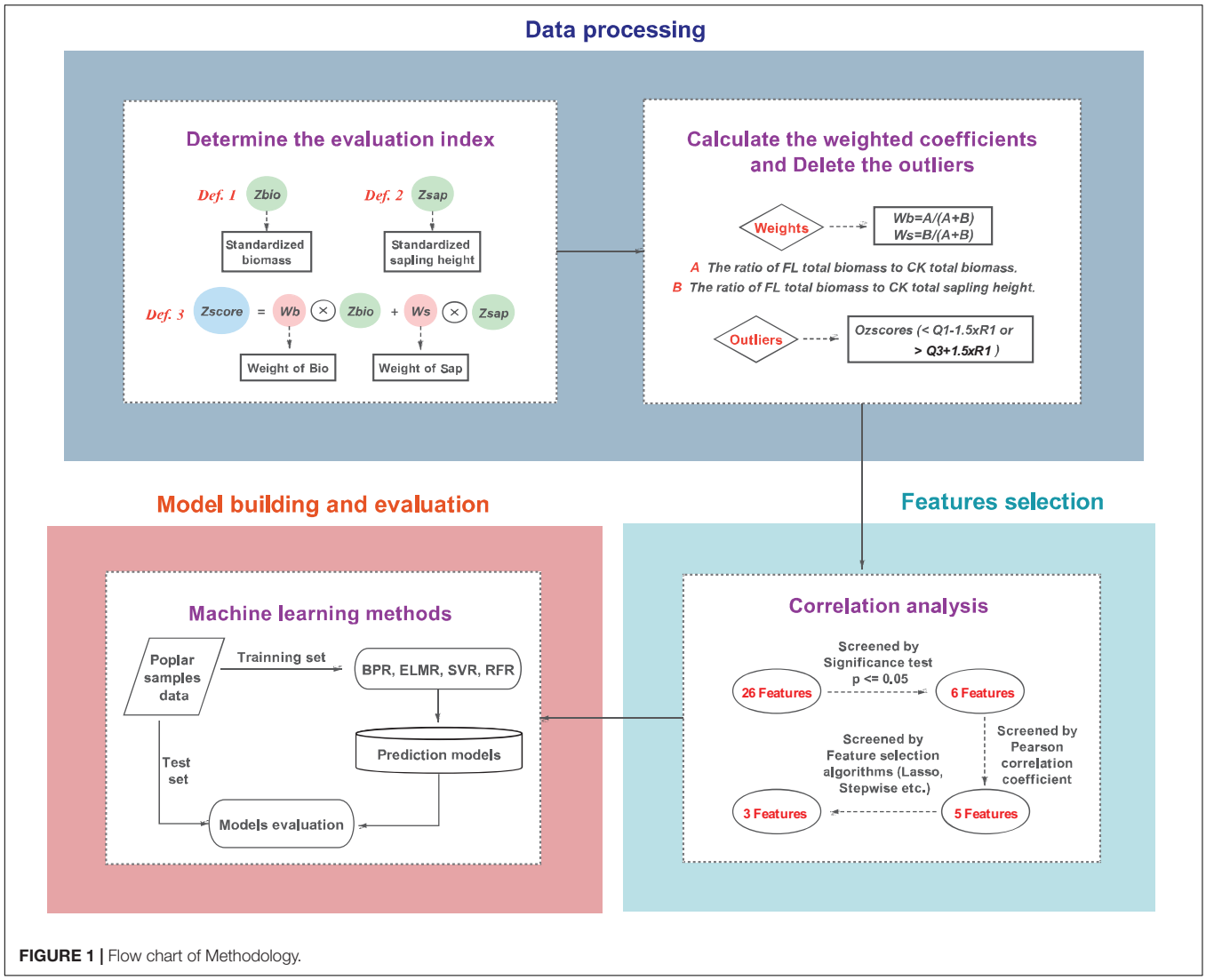

FIGURE 1 | Flow chart of Methodology.

where ω_{bio} and ω_{sap} are the weight coefficients, which satisfy the condition $\omega_{bio}\omega_{sap} = 1$. The calculation method of the weight is shown in equation (4). Zbio and Zsap are the two evaluation indicators mentioned in above.

$$\omega_{bio} = \frac{A}{A+B},\ \omega_{sap} = \frac{B}{A+B} \tag{4}$$

where $A = \frac{FL(Sum(bio(x_i)))}{CK(Sum(bio(x_i)))}$, $B = \frac{FL(Sum(sap(x_i)))}{CK(Sum(sap(x_i)))}$.

Treatment of Outliers

Extremely different from other observations, the outliers often cause anomalies (Aggarwal and Yu, 2005). Outliers may affect the accuracy of the final model (Domingues et al., 2018; Zhao et al., 2020). Consequently, before feature selection and models establishment, outliers in the data should be eliminated. The outlier Ozscore is defined in formula (5):

$$\text{Ozscore} > Q_3 + 1.5 \times R_1 \ or \ \text{Ozscore} < Q_1 - 1.5 \times R_1 \tag{5}$$

where Q_3 and Q_1 are the upper and lower quartiles, and the quartile range $R_1 = Q_3 - Q_1$.

Feature Selection

Feature selection is to effectively remove irrelevant and redundant features (Arora and Anand, 2019; Sayed et al., 2019). It can improve the performance of the model and reduce the cost of calculation (Li et al., 2018; Angulo and Shin, 2019). The 26 characteristic parameters considered in this study meet the conditions of multi-dimensional data. Therefore, these features need to be selected.

Hierarchical Clustering

Hierarchical clustering is a clustering method used to describe the hierarchical structure of samples in a group (Wu et al., 2009). The result of hierarchical clustering is usually represented by a dendrogram. The tree diagram shows the organization and relationship of the sample in the form of a tree, which is convenient for people to divide intuitively (Granato et al., 2018).

For related clustering research work, refer to Xu and Wunsch (2005) and Murtagh and Contreras (2012). A hierarchical clustering method was adopted to cluster the poplar varieties and the five features selected by correlation analysis, and the measurement method was Euclidean distance.

Lasso and Stepwise Regression

The Lasso method is proposed by Tibshirani (1996) by combining the advantages of both ridge regression and subset selection meth. It not only has the interpretability of subset selection, but also has the stability of ridge regression. To achieve the purpose of feature selection, this method compresses the coefficients of insignificant variables to 0 (Zou and Hastie, 2005; Cui and Gong, 2018). Stepwise regression uses collinearity and variance contribution tests to gradually find all the significant features, thereby obtaining the optimal model. The basic idea of stepwise regression is to add new variables one by one, each time a new variable is added, consider whether to eliminate the selected variable until no more variables are introduced. Stepwise regression is mainly used to solve the problem of multicollinearity. For related research, refer to Guidolin and Pedio (2021), Ou et al. (2016), and Yang et al. (2019).

Establishment and Evaluation of Regression Model

Machine Learning Methods

BP Neural Network

BP neural network is a multi-layer network structure composed of an input layer, an output layer, and one or more hidden layers (Yang et al., 2018), which can effectively deal with linear and non-linear relationships between data (Moghadassi et al., 2010). BP is called the error back propagation algorithm. In essence, the BP algorithm takes the error square as the objective function, and uses the gradient descent method to calculate the minimum value of the objective function. BP neural network can systematically solve the hidden layer connection weight learning problem of multilayer neural network, and it is one of the most widely used neural networks at present.

Extreme Learning Machine

The extreme learning machine is a new single hidden layer feedforward neural network (Ding et al., 2015). This algorithm can produce good generalization performance in most cases, and its learning speed is thousands of times faster than the traditional feedforward neural network algorithm. Therefore, many studies apply extreme learning machines for regression and prediction (Miche et al., 2010; Huang et al., 2011; Yao and Ge, 2018; Yaseen et al., 2018).

Support Vector Regression

Support vector machine (SVM) is a supervised machine learning method proposed by Cortes and Vapnik (1995) in the mid-1990s, which is used to deal with binary classification problems. The core idea of SVM is to find a hyperplane or hypersurface to segment the sample points to maximize the interval between the segmentation points. Support vector regression (SVR) is an application model of support vector machine (SVM) on regression problems (Demir and Bruzzone, 2014). As a classic regression algorithm in machine learning, support vector regression has been widely used in many fields, such as plant science, data mining, and biomedicine (Khosravi et al., 2018; Moazenzadeh et al., 2018; Zhuo et al., 2018; Han et al., 2019; Mishra and Padhy, 2019).

Random Forest Regression

Random forests produce reliable classifications by using predictions from a set of decision trees (Breiman, 2001). It is composed of multiple decision trees, and there is no correlation between each decision tree. The final output of the model is jointly determined by each decision tree in the forest. When dealing with regression problems, random forest uses the mean value of each decision tree as the final result. Due to the excellent regression results and the relatively fast processing speed, the use of random forest regression has also received extensive attention (Du et al., 2015; Chen et al., 2018; Dou et al., 2019).

The relationship between variables is often non-linear. Thus, compared with traditional linear regression, machine learning algorithms may have higher accuracy. There may be a non-linear relationship between poplar resistance to flooding and features. Consequently, the four machine learning methods mentioned above will be used to predict the waterlogging resistance of poplar.

Model Parameters

Manual tuning is the traditional method of adjusting the hyperparameters of machine learning models (Yang and Shami, 2020). With the improvement of automatic optimization methods, grid search (GS), particle swarm optimization (PSO), genetic algorithm (GA), and other optimization methods were proposed to find the optimal hyperparameters. to find the optimal hyperparameters. However, there are still problems such as complex optimization processes and slow convergence speed. Based on experience, we have selected the parameters of the four machine learning methods. The parameter sensitivity and parameter selection of each method will be analyzed below.

There are many kinds of training functions for the BPR algorithm, and most of the data sets are very sensitive to the training function. In the experiment, a variety of training functions were selected. Compared with other training functions such as trainlm function (based on Levenberg-Marquardt algorithm), the trainbr function based on Bayes rule has better network generalization ability and higher accuracy. Hence, the trainbr function was finally used in the BPR method. In addition, previous studies have shown that the number of hidden layer nodes is a key factor affecting the accuracy of BPR and ELMR models (Liu Z. T. et al., 2018; Zhang et al., 2018). For the number of hidden layer nodes, 3, 5, 7, 9, and 11 hidden layer nodes were used to train the BPR model, 2, 3, 4, 5, and 6 hidden layer nodes were used to train the ELMR model. The root mean square error (RMSE) of the training is shown in **Table 2**. When the hidden layer nodes of the BPR and ELMR methods were 9 and 5, respectively, the RMSE was considered to be the smallest. Therefore, the number of hidden layer nodes of BPR was set to 9, and the number of hidden layer nodes of ELMR was set to 5.

TABLE 2 | RMSE of models with different Nodes or *Mtry*.

BPR		ELMR		RFR	
Nodes	**RMSE**	**Nodes**	**RMSE**	**Mtry**	**RMSE**
3	0.5654	2	0.3836	1	0.1940
5	0.4221	3	0.3785	2	0.2654
7	0.3703	4	0.3591	3	0.3210
9	0.3680	5	0.3426	4	0.3558
11	0.3939	6	0.3438	5	0.3982

TABLE 3 | Machine learning model parameters.

Methods	Model parameter
BPR	Training function: trainbr
	Number of input layers: 3
	Number of hidden layers: 9
	Number of output layers: 1
	Transfer function: logsig, purelin (Input-Hidden, Hidden-Output)
	net.trainparam.goal: 0.0001
	net.trainparam.lr: 0.01
	net.trainparam.epochs: 1000
ELMR	Training function: elmtrain
	Number of input layers: 3
	Number of hidden layers: 5
	Number of output layers: 1
	Activation function: sigmoid
SVR	Training function: svmtrain
	Model: ε-SVR
	Kernel function: RBF
	Regularization parameter C: 65
	Gamma: 0.001
	p: 0.01
RFR	Training function: TreeBagger
	Number of decision trees: 200
	Minimum number of leaves: 1
	Fraction of in-bag observations (FBoot): 1

For the SVR method, two SVR models (nu-SVR and epsilon-SVR) and four kernel functions (linear, polynomial, sigmoid, and radial basis functions) of the LibSVM toolbox were selected. Due to the higher precision of the model on the training set, the epsilon-SVR model (ε-SVR, a model that minimizes the RMSE) based on the RBF kernel function was finally selected. The regularization parameter C and the penalty coefficient gamma were determined by fivefold cross validation. The minimum number of leaves (*Mtry*) is the sensitive parameter of the RFR model, and the value of *Mtry* is generally set to 2 (Probst et al., 2018). In the experiment, we set the value of *Mtry* to 1, 2, 3, 4, and 5. The RMSE of the training function is shown in **Table 2**. When the value of *Mtry* was 1, RMSE was considered to be the smallest. Therefore, the value of *Mtry* was set to 1. Other parameters of the machine learning method were set as common parameters. The specific values of the parameters are shown in **Table 3**.

Evaluation of Model Performance

The three evaluation indexes of coefficient of determination (R^2), root mean square error (RMSE) and mean absolute error (MAE) were used to evaluate the performance of the model. The corresponding calculation formulas are shown in (6)-(8):

$$R^2 = 1 - \frac{\sum_{i=1}^{n} (y_i - \widehat{y_i})^2}{\sum_{i=1}^{n} (y_i - \overline{y_i})^2} \tag{6}$$

$$RMSE = \sqrt{\frac{\sum_{i=1}^{n} (y_i - \widehat{y_i})^2}{n}} \tag{7}$$

$$MAE = \frac{1}{n} \sum_{i=1}^{n} \left| y_i - \widehat{y_i} \right| \tag{8}$$

where n is the number of varieties, y_i is the actual value, $\widehat{y_i}$ is the predicted value, and $\overline{y_i}$ is the mean of the true y_i.

RESULTS

Treatment of Outliers and Selection of Evaluation Index

Three evaluation indicators are used to deal with outliers in the data. The calculated descriptive statistics are shown in **Table 4**, where Max and Min are the maximum and minimum values, and Med is the median. The results of deleting outliers are shown in **Figure 2**.

As shown in **Figure 2**, the points outside the red dotted line in the figure are outliers. It can be observed that for all samples, the defined Zscore roughly ranges from [−2, 2], while the ranges of Zbio and Zsap are larger than Zscore, and only Zscore has outliers. In addition, from the definition of the waterlogging tolerance evaluation index, we know that Zscore not only considers the biomass but also the change of seedling height, which can more comprehensively reflect the flood resistance of poplar. Thus, based on the above viewpoints, Zscore was finally selected as the waterlogging tolerance evaluation index in this article.

Screening of Features

Significance Test and Correlation Analysis

According to the significance level of the correlation between the features and the poplar waterlogging tolerance score Zscores, 6 features were selected from 26 features, and these 6 features were all established under the condition that the significance level $p = 0.05$. We calculated the Pearson correlation coefficient, and

TABLE 4 | Descriptive statistics of the three evaluation indicators.

Methods	Min	Q_1	Med	Q_3	Max
Zbio	−2.409917	−0.748933	−0.095463	0.615642	2.614667
Zsap	−1.984857	−0.799594	−0.033385	0.722554	2.419308
Zscore	−2.076712	−0.554362	−0.039611	0.466923	2.257776

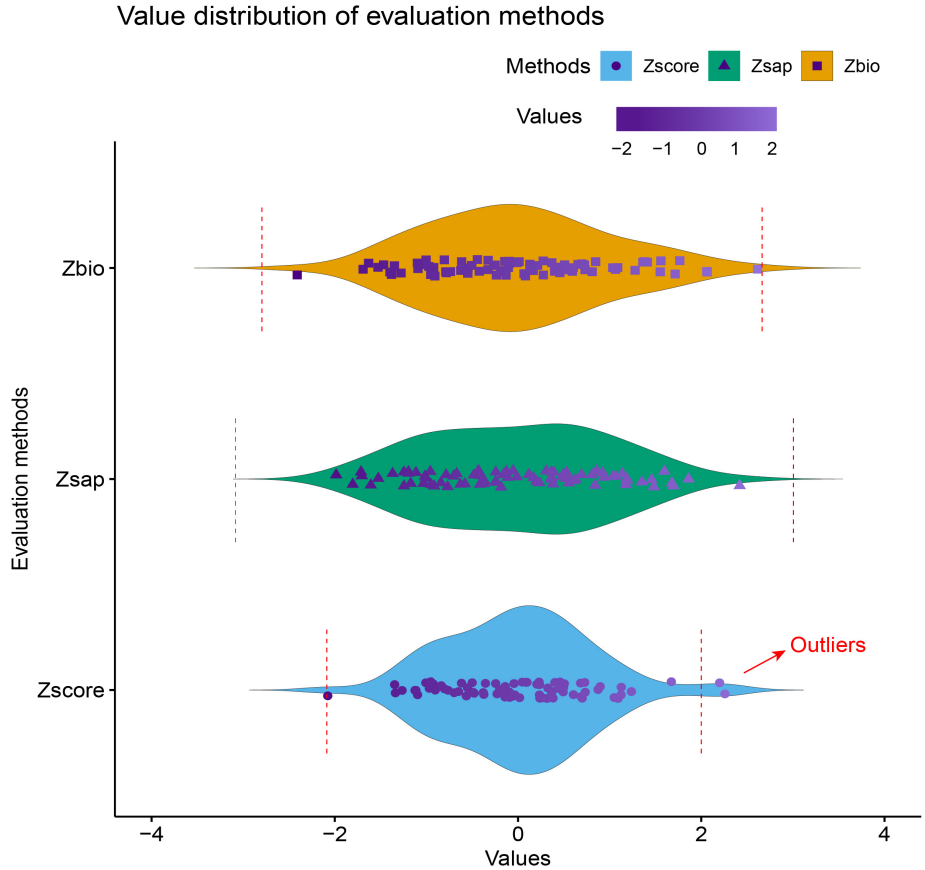

FIGURE 2 | Distribution of three evaluation indexes.

the results are shown in **Figure 3**. **Figure 3A** is the heat map of 26 features, the blank part is the case of $p = 0.05$, that is, it is not significant. **Figure 3B** is a heat map of the correlation coefficient that satisfies the condition of $p = 0.05$, and **Figure 3C** is the exact value of Pearson's correlation coefficient between 6 significant features. The specific meanings corresponding to the 6 significant features are shown in **Appendix Table A1**.

From **Figure 3C**, it can be found that the correlation between qN_Fo and H_2OS is particularly strong. The correlation coefficient between them exceeds 0.8. Thus, the feature with the largest coefficient is selected from these related features, and the highly related features are excluded. After this operation, the retained features are Fv, qN_Fo, Fm, H_2OS/H_2OR, and RH_S/RH_R.

Before establishing the regression model, univariate regression prediction was carried out on the features of significance test and correlation screening, and the result is shown in **Figure 4**. It can be observed that the five variables all meet the significance level of $p = 0.05$, and there is a considerable proportional relationship between them. Nevertheless, the results of univariate regression were general, and the highest coefficient of determination (R^2) is 0.57. For this reason, other methods should be chosen for regression analysis, such as multiple linear regression and machine learning regression methods.

It is undeniable that the 5 features of significance testing and correlation screening may still have multicollinearity. To implement machine learning modeling more reasonably and accurately, three methods of hierarchical clustering, Lasso, and Stepwise regression were adopted for further feature selection. Before predicting the waterlogging tolerance of different poplar varieties and further feature screening, the characteristic parameters and Zscore of each sample were averaged according to the variety.

Clustering Results

The results of hierarchical clustering are shown in **Figure 5**. **Figure 5A** is the total clustering heat map, **Figure 5B** is the poplar varieties clustering, and **Figure 5C** is the poplar characteristic clustering.According to the clustering results in **Figure 5**, we can divide poplar varieties and features into 3 groups. The classification of poplar varieties is marked as A, B, and C, and the classification of characteristic parameters is marked as F1, F2, and F3.

Results of Lasso and Stepwise Regression

Lasso regression and backward stepwise regression are used to screen the 5 features (Fv, qN_Fo, Fm, H_2OS/H_2OR, and RH_S/RH_R) obtained by significance and correlation. The

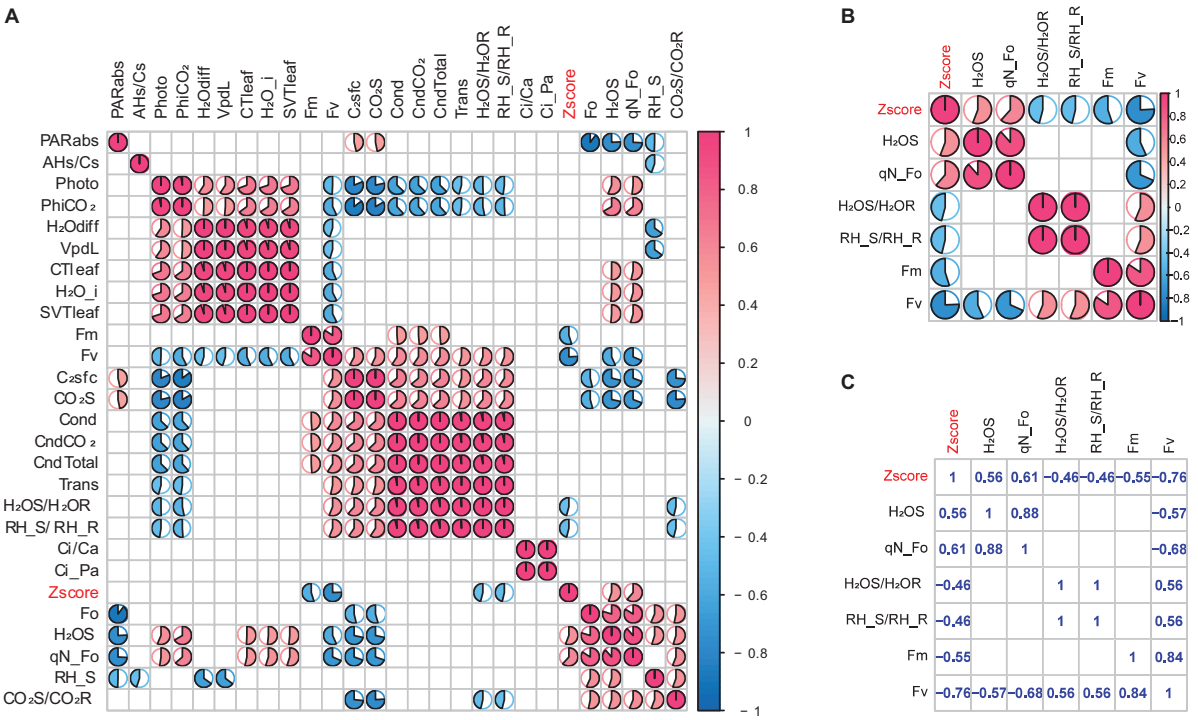

FIGURE 3 | Heat map of Pearson's correlation coefficient. **(A)** Heat map of 26 features. **(B)** Heat map of 6 features. **(C)** Specific values of 6 features.

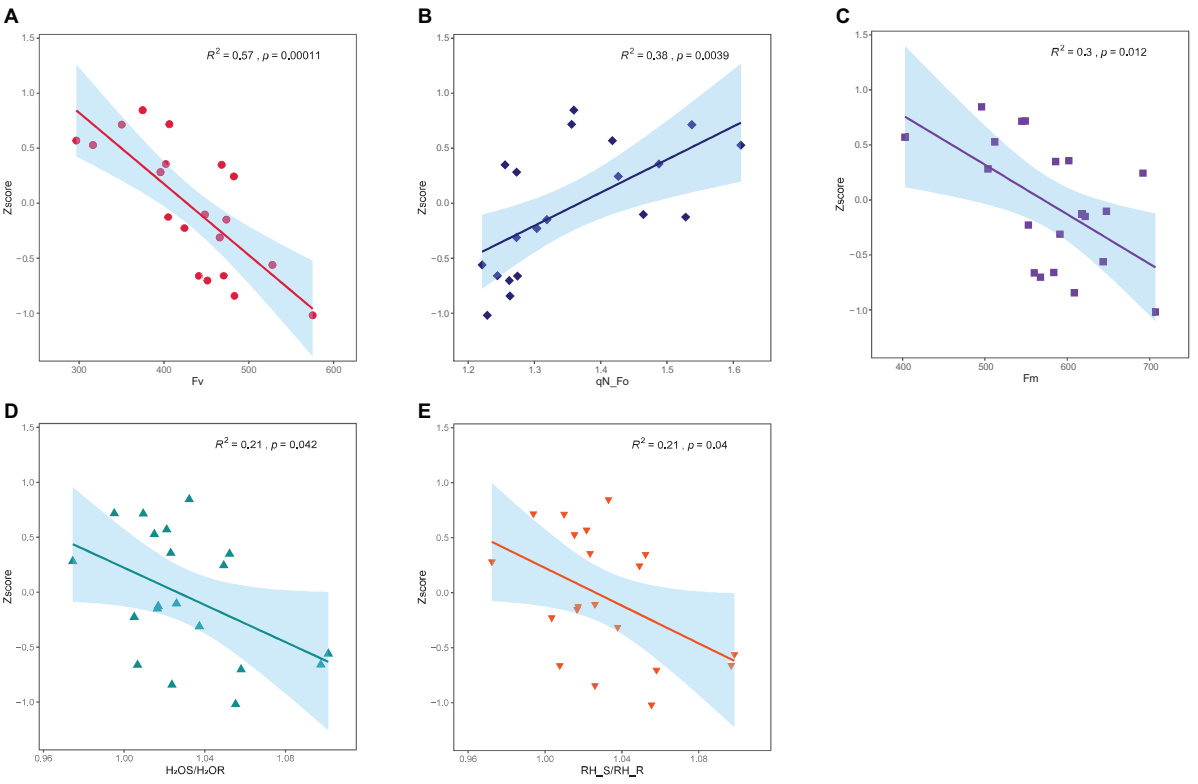

FIGURE 4 | Regression prediction of single feature. **(A)** Fv. **(B)** qN_Fo. **(C)** Fm. **(D)** H_2OS/H_2OR. **(E)** RH_S/RH_R.

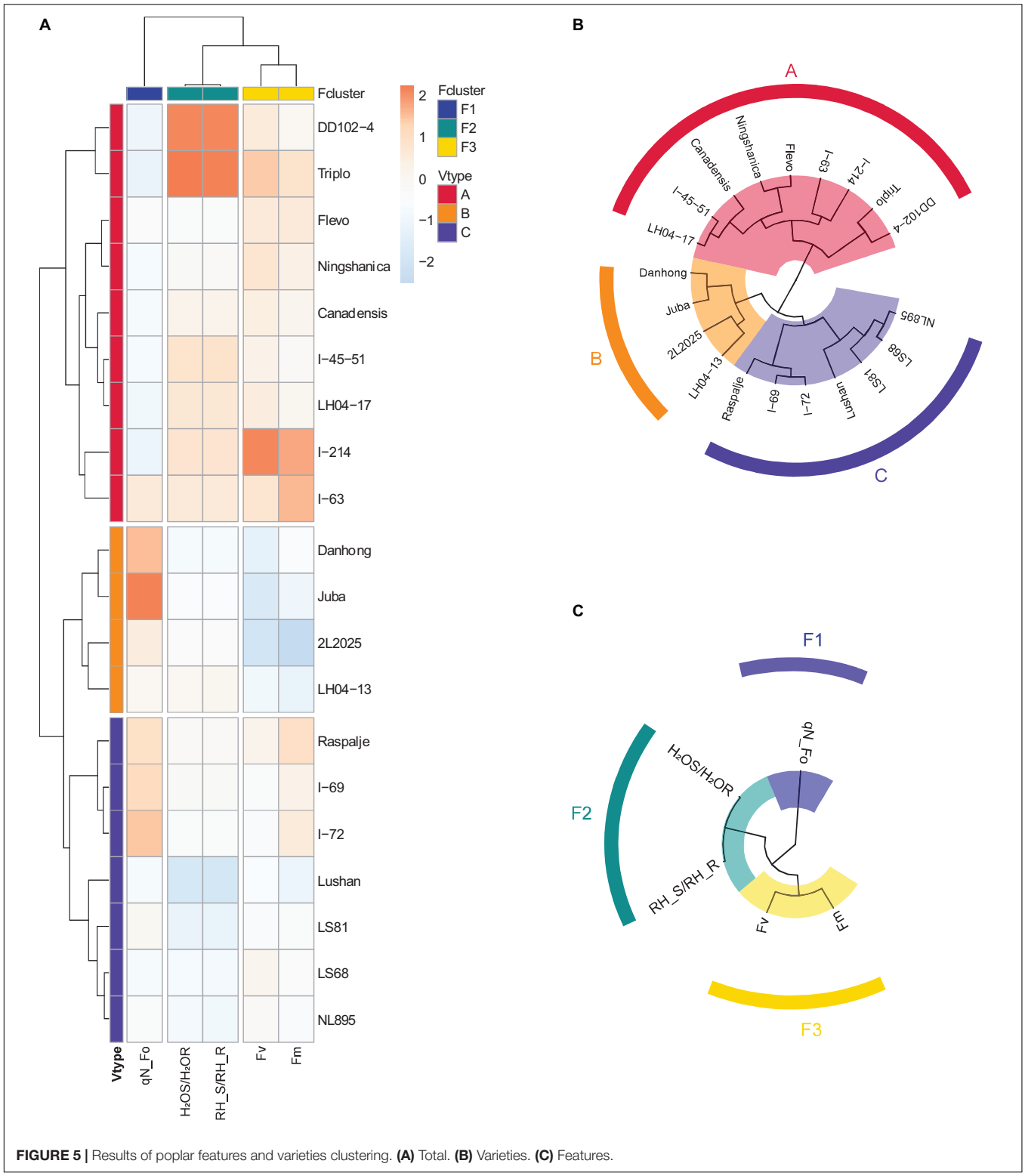

FIGURE 5 | Results of poplar features and varieties clustering. **(A)** Total. **(B)** Varieties. **(C)** Features.

results of the Lasso method are Fv, qN_Fo, and RH_S/RH_R. However, the screening result of stepwise regression only has the variable Fv. From the univariate regression analysis results in **Figure 4**, we know that the coefficient of determination (R^2) of Fv is 0.57. A single feature used for regression may lack interpretability and may affect the accuracy of the final model. In addition, according to the results of hierarchical clustering in **Figure 5**, a feature with the largest correlation coefficient was

selected from each of the three groups (F1, F2, and F3), and the results obtained are consistent with the Lasso method. Therefore, combining the results of hierarchical clustering and univariate analysis, in the final machine learning modeling, we used the three characteristic parameters of Fv, qN_Fo and RH_S/RH_R.

Regression Results of Machine Learning Models

The Division of Test Set and Training Set

Before establishing the machine learning regression model, the poplar varieties were divided into training set and test set according to the ratio of 4:1 (the training set had 16 varieties, and the test set was 4 varieties). The four poplar varieties in the test set were selected from the three groups of A, B, C by stratified sampling based on the poplar hierarchical clustering results. The poplar varieties used and their corresponding Zscore and Vtype are shown in **Table 5**.

TABLE 5 | Main information of poplar varieties.

Samples	Z score	V type
Canadensis	−0.31136376	A
DD102-4	−0.659417544	A
Flevo	−0.149084082	A
I-214	−1.018704692	A
I-63	0.244020869	A
LH04-17	0.348729466	A
Ningshanica	−0.843303666	A
Danhong	0.714574083	B
Juba	0.528127585	B
LH04-13	0.845992953	B
I-69	0.356889463	C
I-72	−0.12622992	C
LS68	−0.662543236	C
LS81	0.717527146	C
Lushan	0.282405203	C
NL895	−0.227444975	C
I-45-51	−0.702652584	A
Triplo	−0.561219766	A
2L2025	0.570264018	B
Raspalje	−0.103562886	C

Training Set

Four machine learning regression methods were used to perform regression prediction on the three screened features (Fv, qN_Fo and RH_S/RH_R). The results obtained on the training set, and the corresponding R^2, RMSE, and MAE are shown in **Figure 6** and **Table 6**.**Figure 6D** is a histogram of model evaluation indexes (R^2, RMSE, and MAE) of four machine learning methods on the training set. The colored columns correspond to the four machine learning methods of BPR, ELMR, SVR, and RFR, respectively. From the first subplot of **Figure 6D**, it can be noticed that on the training set, the highest R^2 of the four machine learning methods is random forest regression (RFR). Specifically, from **Figure 6B** and **Table 6**, we can observe that the coefficient of determination (R^2) of RFR is 0.8847. Then, the second one is support vector regression (SVR), the R^2 is 0.7027. In contrast, the performance of BP neural network regression (BPR) and Extreme learning machine regression (ELMR) methods are relatively poor, and their R^2 are 0.5847 and 0.6401, respectively. In addition, from **Figure 6D**, we can get similar results from the performance of RMSE and MAE. Similarly, from **Table 6**, we can find that the RMSE of the RFR method is the smallest with a value of 0.1940, and at the same time, the MAE of RFR is also the smallest, with a value of 0.1591. Therefore, for the four machine learning methods, the RFR method has the best regression effect. Then, the second is the SVR method. Correspondingly, the prediction effects of ELMR and BPR on the training set are relatively trivial.

Test Set

Similarly, the results of the four machine learning regression methods on the test set, and the corresponding R^2, RMSE and MAE are shown in **Figure 7** and **Table 7**.

Figure 7D is a histogram of model evaluation indexes (R^2, RMSE, and MAE) of four machine learning methods on the test set. The colored columns correspond to the four machine learning methods of BPR, ELMR, SVR, and RFR, respectively. As shown in **Figure 7D**, random forest regression (RFR) has the highest R^2 for the four machine learning methods on the test set. In addition, from **Figure 7B** and **Table 7**, we can observe that the R^2 of RFR is 0.8351. Then, the second one is SVR, the R^2 is 0.6864. The third and fourth are ELMR and BPR, their performance is relatively poor, and the corresponding R^2 are 0.6207 and 0.5703, respectively. Besides, from **Figure 7D** and **Table 7**, on the test set, the smallest root mean square error (RMSE) is RFR, followed by SVR and other methods. Similar results appear on the mean absolute error (MAE). Consequently, our results show that not all machine learning algorithms can show high accuracy. The best performance on the test set is RFR, followed by SVR. Then, the third and fourth are ELMR and BPR. This result is consistent with the training set.

In summary, according to the results of the training set and the test set, for the flood resistance of poplar, the best prediction effect of the four machine learning methods is random forest regression (RFR), and the second one is support vector regression (SVR). By contrast, the performance effects of BP neural network regression (BPR) and Extreme learning machine regression (ELMR) methods are poor. The prediction accuracy from high to low is RFR > SVR > ELMR > BPR. Hence, when predicting the flood resistance of poplar, random forest regression (RFR) and support vector regression (SVR) can be used first, and RFR can be given more consideration.

DISCUSSION

Machine learning is a field of artificial intelligence (AI). Compared with traditional statistical models, machine learning has higher performance, and at the same time, its complexity is relatively lower (Mekanik et al., 2013). In fact, before establishing the regression model of machine learning, we performed multiple linear regression (MLR) on the five variables (Fv, qN_Fo, Fm, H_2OS/H_2OR, and RH_S/RH_R) selected by the significance

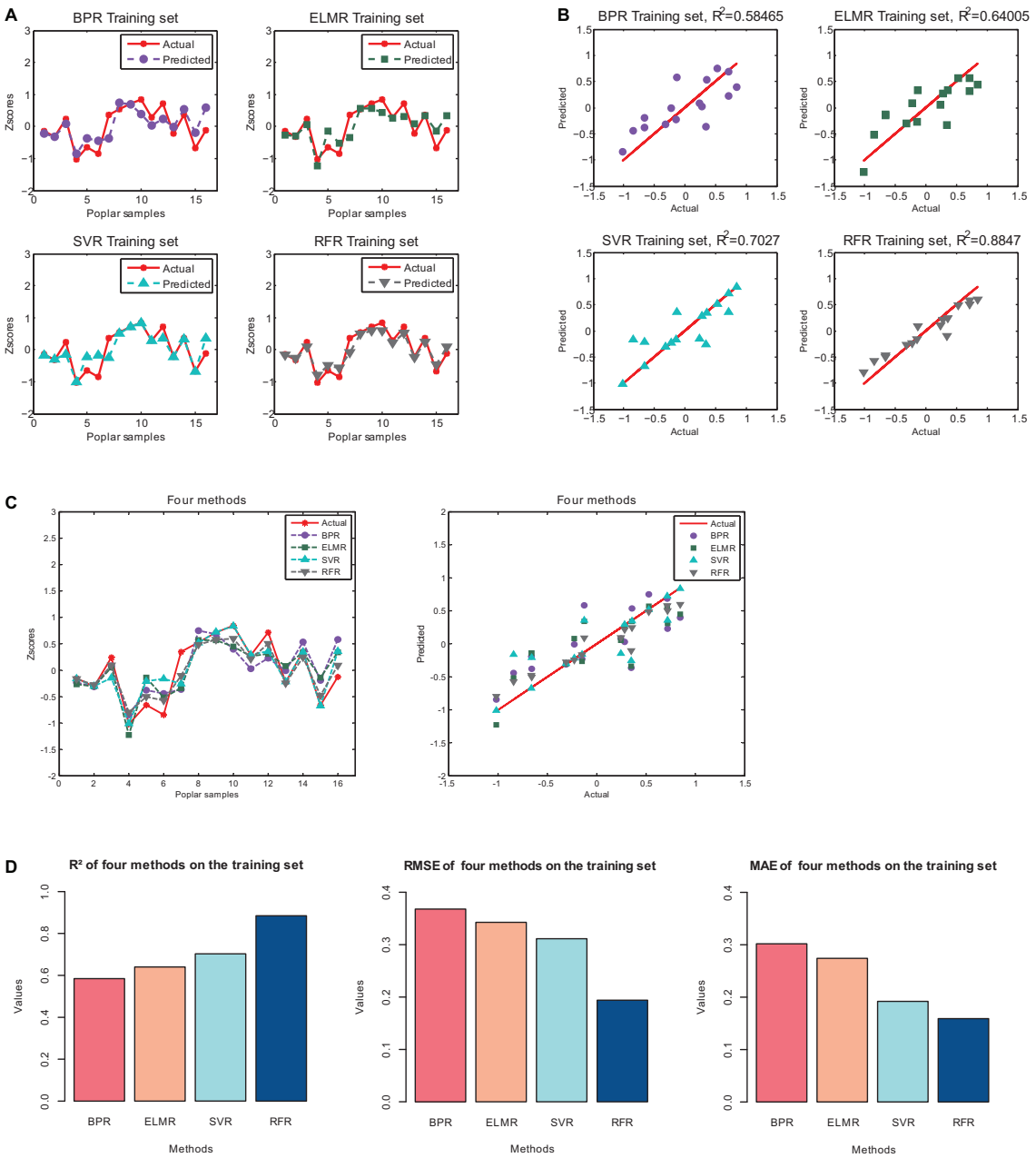

FIGURE 6 | The regression results of the four machine learning methods on the training set. **(A)** Results of Predicted. **(B)** Predicted and actual value. **(C)** Comparison of results of four methods. **(D)** The R^2, RMSE and MAE of the four machine learning methods on the training set.

TABLE 6 | The R^2, RMSE and MAE of the training set.

Methods	BPR	ELMR	SVR	RFR
R^2	0.5847	0.6401	0.7027	0.8847
RMSE	0.3680	0.3426	0.3113	0.1940
MAE	0.3019	0.2741	0.1920	0.1591

testing and correlation analysis. However, the results show that the coefficients of determination (R^2) of MLR on the training set and test set are 0.5616 and 0.5172, respectively. The regression results are shown in **Appendix Figure A1**. Many studies have compared machine learning models with traditional statistical models (Aertsen et al., 2010; Rezaeianzadeh et al., 2014; Idowu et al., 2016; Johnson et al., 2016; Wang and Srinivasan, 2017). In most cases, machine learning models are better than traditional statistical models, such as linear regression. The model and the variables are not linearly related in most situations, and the variables involved are also multivariate. Therefore, more and more fields have begun to use machine learning algorithms. Even

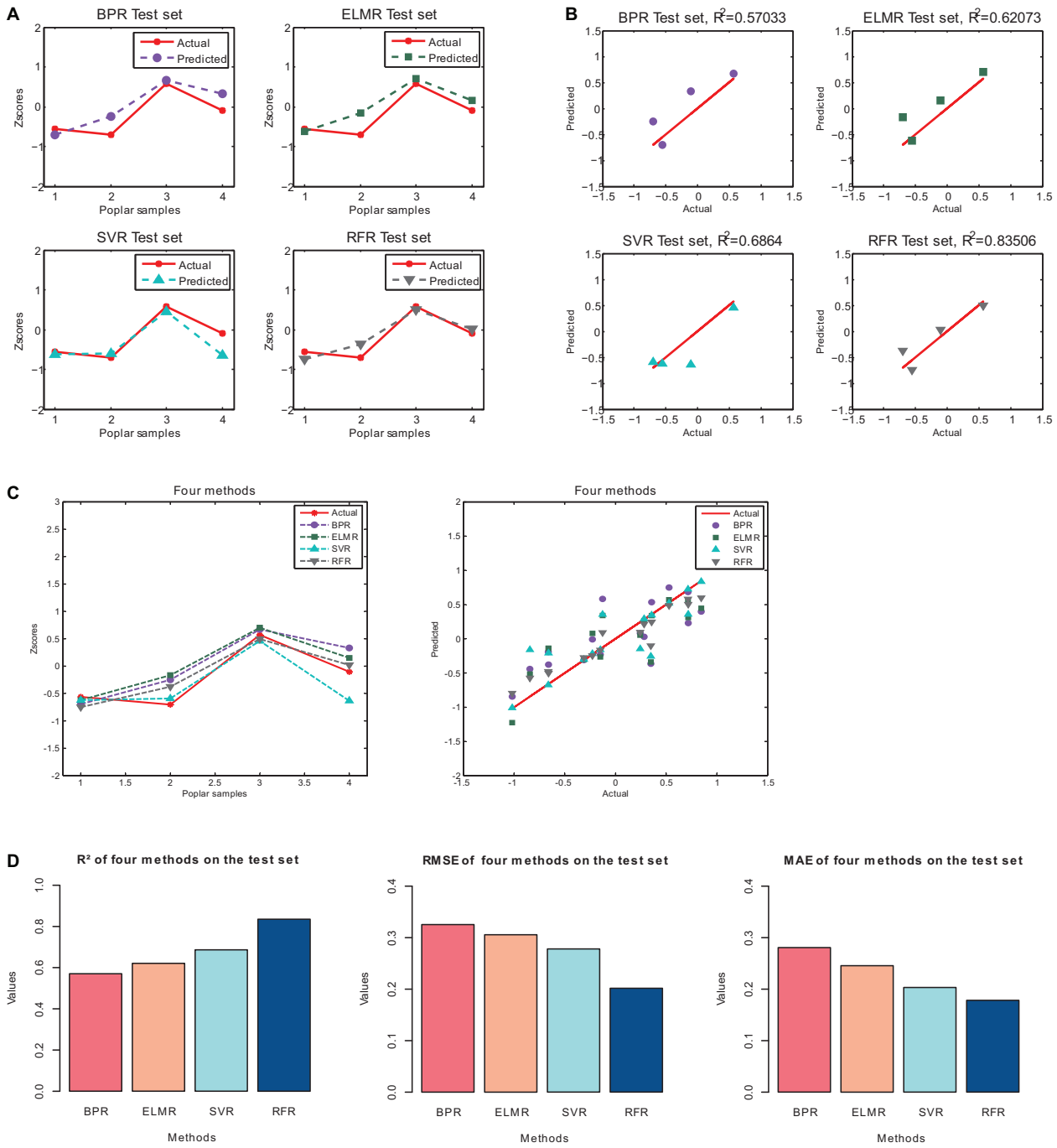

FIGURE 7 | The regression results of the four machine learning methods on the test set. **(A)** Results of Predicted. **(B)** Predicted and actual value. **(C)** Comparison of results of four methods. **(D)** The R^2, RMSE and MAE of the four machine learning methods on the test set.

so, while machine learning has many advantages, it also has limitations. For example, many machine learning models lack interpretability and are prone to overfitting. For this reason, these problems still need to be considered in practical applications.

The risk of resisting flood disasters can be mainly divided into two aspects. One is to directly predict flood disasters in the risk areas, and take preventive measures before the disaster occurs, such as transferring personnel and valuable finances. Generally speaking, the key variables that need to be considered in flood forecasting include 25 factors such as water level, river flood, soil moisture, and rainfall (Maier et al., 2010). Among these key variables affecting flood forecasting, rainfall and the spatial examination of the hydrologic cycle have the most significant effects (Nourani and Komasi, 2013). Although many studies

TABLE 7 | The R^2, RMSE and MAE of the test set.

Methods	BPR	ELMR	SVR	RFR
R^2	0.5703	0.6207	0.6864	0.8351
RMSE	0.3254	0.3057	0.2780	0.2016
MAE	0.2806	0.2456	0.2032	0.1782

have predicted the risk of flooded areas (Sampson et al., 2015; Tehrany et al., 2015; Wang et al., 2015; Darabi et al., 2019), this method still cannot essentially eliminate the impact of flood disasters. At the same time, it is relatively difficult to predict flood disasters. Thus, people have to consider another method to resist flood disasters. Another way to resist the impact of flood disasters is mainly through building dams and afforestation. The key to afforestation is to understand the waterlogging resistance mechanism of plants. The research on the waterlogging resistance mechanism of plants mainly focuses on exploring the ways for plants to resist flood stress (Wang et al., 2013, 2021; Najeeb et al., 2015; Duy et al., 2016). These studies have analyzed the waterlogging resistance mechanism from the molecular level of proteins and metal ions. However, there are few studies on waterlogging resistance prediction, and a complete system is still lacking. Xie and Shen (2021) used the SVR method in machine learning to predict the waterlogging resistance of poplar. However, there are still some limitations in their studies, such as chlorophyll fluorescence features that have not been considered. Compared with the previous research, we considered more accurate feature parameters and more kinds of machine learning methods. Additionally, we improved the prediction system of poplar resistance to waterlogging and added two quantitative definitions of waterlogging resistance evaluation indexes, which has made considerable improvements.

This study used machine learning methods to predict the flood resistance of poplar. First, three indicators of flood resistance were defined and evaluated. Then, the data was processed, and feature selection and modeling evaluation were implemented. The whole process is intuitive and specific, which has perfected the research system of waterlogging tolerance prediction to a considerable extent, and at the same time, it has also promoted the research on the mechanism of waterlogging tolerance. This study helps researchers to screen out poplar varieties with strong waterlogging tolerance during the poplar sapling period. It can further cultivate high-quality poplar saplings to achieve the purpose of precise flood resistance. The results of the experiment show that the machine learning algorithm shows high accuracy in predicting the flood resistance of poplar, especially the random forest regression (RFR) and support vector regression (SVR) methods. The final result has certain practical value. In practical applications, these two algorithms can be used first. However, it must be mentioned that although 160 poplar samples were used throughout the experiment, only 20 poplar varieties were actually used for regression analysis. In addition, in the regression analysis, 80 poplar samples from the experimental group were used and averaged according to varieties. Since the waterlogging tolerance of different individuals may be quite different, the final result may deviate from the actual situation. But within the allowable range of error, our research mainly provides a way of predicting waterlogging tolerance and improving the system for predicting waterlogging tolerance. Future research can consider more poplar varieties to improve the universality and stability of the method. In addition, the quantitative relationship of poplar varieties' impact on flood disasters can be considered. In a word, this research has great theoretical value and practical significance, and the proposed method can meet the actual engineering needs in a considerable range.

CONCLUSION

To predict the flood resistance of poplar, the author first analyzed the differences between the three evaluation indexes of flood resistance. Then, the final evaluation index of waterlogging tolerance was determined, and outliers were eliminated. For the selection of feature parameters, the first screening was carried out according to the significance test and correlation analysis, and then the three methods of hierarchical clustering, Lasso, and stepwise regression were adopted to screen the features for the second time. The selected features are interpretable and promote the understanding of poplar's waterlogging resistance mechanism. Finally, four machine learning methods were used to predict and evaluate the flood resistance of poplar. The results show that the random forest regression and support vector regression methods are more precise. Nevertheless, it must be pointed out that there are only four groups of experiments and controls for each variety. Due to sample differences and randomness, the final result may deviate from the actual situation. Future research can consider more poplar species and sample sizes to improve the versatility and stability of the method.

This research has perfected the prediction system of plant resistance to waterlogging, and has important value for accurate flood resistance and scientific seedling selection. Meanwhile, it has also made a great contribution to a better understanding of the mechanism of waterlogging tolerance. The analysis process of this paper is clear and repeatable. When considering the features related to the flood resistance of poplar, the photosynthesis features, chlorophyll fluorescence features, and environmental features are comprehensively considered. After data processing, feature selection, and other operations, the machine learning models were used to predict the flood resistance of poplar. Finally, the regression results show that the random forest regression (RFR) and support vector regression (SVR) methods have high accuracy. On the test set, the coefficients of determination (R^2) of the two methods are 0.8351 and 0.6864, respectively, the root mean square errors (RMSE) are 0.2016 and 0.2780, and the mean absolute errors (MAE) are 0.1782 and 0.2031. Based on the above conclusions, our research shows that combining photosynthesis, chlorophyll fluorescence, and environmental variables before flooding experiments, modeling and prediction of machine learning methods against waterlogging can achieve high accuracy, which is suitable for actual engineering problems.

DATA AVAILABILITY STATEMENT

The raw data supporting the conclusions of this article will be made available by the authors, without undue reservation.

AUTHOR CONTRIBUTIONS

XX, XZ, JS, and KD participated in the conception and design of this research and revised the manuscript. XZ and KD carried out experiments and organized the database. XX and JS performed the statistical analysis and proposed the methodology. XX implemented visualization and wrote the manuscript. All authors contributed to the article and approved the submitted version.

FUNDING

This research was supported by the National Natural Science Foundation of China (Grant No. 31570665), Fundamental Research Funds for the Central Universities (Grant No. 2662020YLPY017), and the High-end Foreign Experts Recruitment Plan of China (Grant No. G20200017074).

ACKNOWLEDGMENTS

We would like to thank the support of College of Horticulture and Forestry Sciences of Huazhong Agricultural University and other researchers who participated in this experiment.

REFERENCES

Aertsen, W., Kint, V., van Orshoven, J., Ozkan, K., and Muys, B. (2010). Comparison and ranking of different modelling techniques for prediction of site index in Mediterranean mountain forests. *Ecol. Model.* 221, 1119–1130. doi: 10.1016/j.ecolmodel.2010.01.007

Aggarwal, C. C., and Yu, P. S. (2005). An effective and efficient algorithm for high-dimensional outlier detection. *VLDB J.* 14, 211–221. doi: 10.1007/s00778-004-0125-5

Alfieri, L., Bisselink, B., Dottori, F., Naumann, G., de Roo, A., Salamon, P., et al. (2017). Global projections of river flood risk in a warmer world. *Earths Future* 5, 171–182. doi: 10.1002/2016ef000485

Angulo, A. P., and Shin, K. (2019). Mrmr plus and Cfs plus feature selection algorithms for high-dimensional data. *Appl. Intell.* 49, 1954–1967. doi: 10.1007/s10489-018-1381-1

Ao, Y., Zhou, X., Ji, F., Wang, Y., Yang, L., Wang, Q., et al. (2020). Flood disaster preparedness: experience and attitude of rural residents in Sichuan, China. *Nat. Hazards* 104, 2591–2618. doi: 10.1007/s11069-020-04286-0

Arbona, V., Hossain, Z., Lopez-Climent, M. F., Perez-Clemente, R. M., and Gomez-Cadenas, A. (2008). Antioxidant enzymatic activity is linked to waterlogging stress tolerance in citrus. *Physiol. Plant.* 132, 452–466. doi: 10.1111/j.1399-3054.2007.01029.x

Arora, S., and Anand, P. (2019). Binary butterfly optimization approaches for feature selection. *Expert Syst. Appl.* 116, 147–160. doi: 10.1016/j.eswa.2018.08.051

Berhongaray, G., Janssens, I. A., King, J. S., and Ceulemans, R. (2013). Fine root biomass and turnover of two fast-growing poplar genotypes in a short-rotation coppice culture. *Plant Soil* 373, 269–283. doi: 10.1007/s11104-013-1778-x

Bloeschl, G., Hall, J., Viglione, A., Perdigão, R. A. P., Parajka, J., Merz, B., et al. (2019). Changing climate both increases and decreases European river floods. *Nature* 573, 108–111. doi: 10.1038/s41586-019-1495-6

Breiman, L. (2001). Random forests. *Mach. Learn.* 45, 5–32. doi: 10.1023/a:1010933404324

Chen, W., Xie, X., Peng, J., Shahabi, H., Hong, H., Tien, B. D., et al. (2018). GIS-based landslide susceptibility evaluation using a novel hybrid integration approach of bivariate statistical based random forest method. *Catena* 164, 135–149. doi: 10.1016/j.catena.2018.01.012

Choubin, B., Moradi, E., Golshan, M., Adamowski, J., Sajedi-Hosseini, F., and Mosavi, A. (2019). An ensemble prediction of flood susceptibility using multivariate discriminant analysis, classification and regression trees, and support vector machines. *Sci. Total Environ.* 651, 2087–2096. doi: 10.1016/j.scitotenv.2018.10.064

Coleman, M. D., Dickson, R. E., and Isebrands, J. G. (2000). Contrasting fine-root production, survival and soil CO_2 efflux in pine and poplar plantations. *Plant Soil* 225, 129–139. doi: 10.1023/a:1026564228951

Cortes, C., and Vapnik, V. (1995). Support-vector networks. *Mach. Learn.* 20, 273–297. doi: 10.1007/bf00994018

Cui, Z., and Gong, G. (2018). The effect of machine learning regression algorithms and sample size on individualized behavioral prediction with functional connectivity features. *Neuroimage* 178, 622–637. doi: 10.1016/j.neuroimage.2018.06.001

Darabi, H., Choubin, B., Rahmati, O., Haghighi, A. T., Pradhan, B., and Klove, B. (2019). Urban flood risk mapping using the GARP and QUEST models: a comparative study of machine learning techniques. *J. Hydrol.* 569, 142–154. doi: 10.1016/j.jhydrol.2018.12.002

Demir, B., and Bruzzone, L. (2014). A multiple criteria active learning method for support vector regression. *Pattern Recognit.* 47, 2558–2567. doi: 10.1016/j.patcog.2014.02.001

Ding, S., Zhao, H., Zhang, Y., Xu, X., and Nie, R. (2015). Extreme learning machine: algorithm, theory and applications. *Artif. Intell. Rev.* 44, 103–115. doi: 10.1007/s10462-013-9405-z

Domingues, R., Filippone, M., Michiardi, P., and Zouaoui, J. (2018). A comparative evaluation of outlier detection algorithms: experiments and analyses. *Pattern Recognit.* 74, 406–421. doi: 10.1016/j.patcog.2017.09.037

Dou, J., Yunus, A. P., Bui, D. T., Merghadi, A., Sahana, M., Zhu, Z., et al. (2019). Assessment of advanced random forest and decision tree algorithms for modeling rainfall-induced landslide susceptibility in the Izu-Oshima Volcanic Island, Japan. *Sci. Total Environ.* 662, 332–346. doi: 10.1016/j.scitotenv.2019.01.221

Du, H., Zhu, J., Su, H., Huang, M., Wang, H., Ding, S., et al. (2017). Bulked segregant RNA-seq reveals differential expression and SNPs of candidate genes associated with waterlogging tolerance in maize. *Front. Plant Sci.* 8:1022. doi: 10.3389/fpls.2017.01022

Du, K., Xu, L., Wu, H., Tu, B., and Zheng, B. (2012). Ecophysiological and morphological adaption to soil flooding of two poplar clones differing in flood-tolerance. *Flora* 207, 96–106. doi: 10.1016/j.flora.2011.11.002

Du, P., Samat, A., Waske, B., Liu, S., and Li, Z. (2015). Random forest and rotation forest for fully polarized SAR image classification using polarimetric and spatial features. *ISPRS J. Photogramm. Remote Sens.* 105, 38–53. doi: 10.1016/j.isprsjprs.2015.03.002

Duy, N., Rieu, I., Mariani, C., and van Dam, N. M. (2016). How plants handle multiple stresses: hormonal interactions underlying responses to abiotic stress and insect herbivory. *Plant Mol. Biol.* 91, 727–740. doi: 10.1007/s11103-016-0481-8

Forster, E. J., Healey, J. R., Dymond, C., and Styles, D. (2021). Commercial afforestation can deliver effective climate change mitigation under multiple decarbonisation pathways. *Nat. Commun.* 12:3831. doi: 10.1038/s41467-021-24084-x

Gerjets, R., Richter, F., Jansen, M., and Carminati, A. (2021). Hydraulic redistribution by hybrid poplars (*Populus nigra* x *Populus maximowiczii*) in a greenhouse soil column experiment. *Plant Soil* 463, 145–154. doi: 10.1007/s11104-021-04894-0

Granato, D., Santos, J. S., Escher, G. B., Ferreira, B. L., and Maggio, R. M. (2018). Use of principal component analysis (PCA) and hierarchical cluster analysis (HCA) for multivariate association between bioactive compounds and

functional properties in foods: a critical perspective. *Trends Food Sci. Technol.* 72, 83–90. doi: 10.1016/j.tifs.2017.12.006

Guidolin, M., and Pedio, M. (2021). Forecasting commodity futures returns with stepwise regressions: do commodity-specific factors help? *Ann. Oper. Res.* 299, 1317–1356. doi: 10.1007/s10479-020-03515-w

Hallegatte, S., Green, C., Nicholls, R. J., and Corfee-Morlot, J. (2013). Future flood losses in major coastal cities. *Nat. Clim. Change* 3, 802–806. doi: 10.1038/nclimate1979

Han, L., Yang, G., Dai, H., Xu, B., Yang, H., Feng, H., et al. (2019). Modeling maize above-ground biomass based on machine learning approaches using UAV remote-sensing data. *Plant Methods* 15:10. doi: 10.1186/s13007-019-0394-z

Hirabayashi, Y., Mahendran, R., Koirala, S., Konoshima, L., Yamazaki, D., Watanabe, S., et al. (2013). Global flood risk under climate change. *Nat. Clim. Change* 3, 816–821. doi: 10.1038/nclimate1911

Hong, S., Piao, S., Chen, A., Liu, Y., Liu, L., Peng, S., et al. (2018). Afforestation neutralizes soil pH. *Nat. Commun.* 9:520. doi: 10.1038/s41467-018-02970-1

Hong, S., Yin, G., Piao, S., Dybzinski, R., Cong, N., Li, X., et al. (2020). Divergent responses of soil organic carbon to afforestation. *Nat. Sustain.* 3, 694–700. doi: 10.1038/s41893-020-0557-y

Hu, P., Zhang, Q., Shi, P., Chen, B., and Fang, J. (2018). Flood-induced mortality across the globe: spatiotemporal pattern and influencing factors. *Sci. Total Environ.* 643, 171–182. doi: 10.1016/j.scitotenv.2018.06.197

Huang, G.-B., Wang, D. H., and Lan, Y. (2011). Extreme learning machines: a survey. *Int. J. Mach. Learn. Cybern.* 2, 107–122. doi: 10.1007/s13042-011-0019-y

Idowu, S., Saguna, S., Ahlund, C., and Schelen, O. (2016). Applied machine learning: forecasting heat load in district heating system. *Energy Build.* 133, 478–488. doi: 10.1016/j.enbuild.2016.09.068

Johnson, M. D., Hsieh, W. W., Cannon, A. J., Davidson, A., and Bedard, F. (2016). Crop yield forecasting on the Canadian prairies by remotely sensed vegetation indices and machine learning methods. *Agric. For. Meteorol.* 218, 74–84. doi: 10.1016/j.agrformet.2015.11.003

Khosravi, A., Koury, R. N. N., Machado, L., and Pabon, J. J. G. (2018). Prediction of wind speed and wind direction using artificial neural network, support vector regression and adaptive neuro-fuzzy inference system. *Sustain. Energy Technol. Assess.* 25, 146–160. doi: 10.1016/j.seta.2018.01.001

Khosravi, K., Shahabi, H., ThaiPham, B., Adamowski, J., Shirzadi, A., Pradhan, B., et al. (2019). A comparative assessment of flood susceptibility modeling using Multi-Criteria Decision-Making analysis and machine learning methods. *J. Hydrol.* 573, 311–323. doi: 10.1016/j.jhydrol.2019.03.073

Kreuzwieser, J., Hauberg, J., Howell, K. A., Carroll, A., Rennenberg, H., Millar, A. H., et al. (2009). Differential response of gray poplar leaves and roots underpins stress adaptation during hypoxia. *Plant Physiol.* 149, 461–473. doi: 10.1104/pp.108.125989

Lee, E.-J., Kim, K. Y., Zhang, J., Yamaoka, Y., Gao, P., Kim, H., et al. (2021). *Arabidopsis* seedling establishment under waterlogging requires ABCG5-mediated formation of a dense cuticle layer. *New Phytol.* 229, 156–172. doi: 10.1111/nph.16816

Li, J., Cheng, K., Wang, S., Morstatter, F., Trevino, R. P., Tang, J., et al. (2018). Feature selection: a data perspective. *ACM Comput. Surv.* 50:39. doi: 10.1145/3136625

Liu, X., Yang, T., Wang, Q., Huang, F., and Li, L. (2018). Dynamics of soil carbon and nitrogen stocks after afforestation in arid and semi-arid regions: a meta-analysis. *Sci. Total Environ.* 618, 1658–1664. doi: 10.1016/j.scitotenv.2017.10.009

Liu, Z. T., Wu, M., Cao, W. H., Mao, J., Xu, J. P., and Tan, G. Z. (2018). Speech emotion recognition based on feature selection and extreme learning machine decision tree. *Neurocomputing* 273, 271–280. doi: 10.1016/j.neucom.2017.07.050

Loreti, E., van Veen, H., and Perata, P. (2016). Plant responses to flooding stress. *Curr. Opin. Plant Biol.* 33, 64–71. doi: 10.1016/j.pbi.2016.06.005

Lukic, N., Kukavica, B., Davidovic-Plavsic, B., Hasanagic, D., and Walter, J. (2020). Plant stress memory is linked to high levels of anti-oxidative enzymes over several weeks. *Environ. Exp. Bot.* 178:104166. doi: 10.1016/j.envexpbot.2020.104166

Maier, H. R., Jain, A., Dandy, G. C., and Sudheer, K. P. (2010). Methods used for the development of neural networks for the prediction of water resource variables in river systems: current status and future directions. *Environ. Model. Softw.* 25, 891–909. doi: 10.1016/j.envsoft.2010.02.003

Major, I. T., and Constabel, C. P. (2007). Shoot-root defense signaling and activation of root defense by leaf damage in poplar. *Can. J. Bot.* 85, 1171–1181. doi: 10.1139/b07-090

Mekanik, F., Imteaz, M. A., Gato-Trinidad, S., and Elmahdi, A. (2013). Multiple regression and artificial neural network for long-term rainfall forecasting using large scale climate modes. *J. Hydrol.* 503, 11–21. doi: 10.1016/j.jhydrol.2013.08.035

Miche, Y., Sorjamaa, A., Bas, P., Simula, O., Jutten, C., and Lendasse, A. (2010). OP-ELM: optimally pruned extreme learning machine. *IEEE Trans. Neural Netw.* 21, 158–162. doi: 10.1109/tnn.2009.2036259

Mishra, S., and Padhy, S. (2019). An efficient portfolio construction model using stock price predicted by support vector regression. *N. Am. J. Econ. Finance* 50:101027. doi: 10.1016/j.najef.2019.101027

Moazenzadeh, R., Mohammadi, B., Shahaboddin, S., and Chau, K.-W. (2018). Coupling a firefly algorithm with support vector regression to predict evaporation in northern Iran. *Eng. Appl. Comput. Fluid Mech.* 12, 584–597. doi: 10.1080/19942060.2018.1482476

Moghadassi, A. R., Nikkholgh, M. R., Parvizian, F., and Hosseini, S. M. (2010). Estimation of thermophysical properties of dimethyl ether as a commercial refrigerant based on artificial neural networks. *Expert Syst. Appl.* 37, 7755–7761. doi: 10.1016/j.eswa.2010.04.065

Murtagh, F., and Contreras, P. (2012). Algorithms for hierarchical clustering: an overview. *Wiley Interdiscip. Rev. Data Min. Knowl. Discov.* 2, 86–97. doi: 10.1002/widm.53

Najeeb, U., Atwell, B. J., Bange, M. P., and Tan, D. K. Y. (2015). Aminoethoxyvinylglycine (AVG) ameliorates waterlogging-induced damage in cotton by inhibiting ethylene synthesis and sustaining photosynthetic capacity. *Plant Growth Regul.* 76, 83–98. doi: 10.1007/s10725-015-0037-y

Nourani, V., and Komasi, M. (2013). A geomorphology-based ANFIS model for multi-station modeling of rainfall-runoff process. *J. Hydrol.* 490, 41–55. doi: 10.1016/j.jhydrol.2013.03.024

Ou, C., Ray, R., Li, C., and Yong, H. (2016). Multi-index and two-level evaluation of shale gas reserve quality. *J. Nat. Gas Sci. Eng.* 35, 1139–1145. doi: 10.1016/j.jngse.2016.09.056

Paprotny, D., Sebastian, A., Morales-Napoles, O., and Jonkman, S. N. (2018). Trends in flood losses in Europe over the past 150 years. *Nat. Commun.* 9:1985. doi: 10.1038/s41467-018-04253-1

Peng, Y., Zhou, Z., Zhang, Z., Yu, X., Zhang, X., and Du, K. (2018). Molecular and physiological responses in roots of two full-sib poplars uncover mechanisms that contribute to differences in partial submergence tolerance. *Sci. Rep.* 8:12829. doi: 10.1038/s41598-018-30821-y

Probst, P., Wright, M., and Boulesteix, A. L. (2018). Hyperparameters and tuning strategies for random forest. *Wiley Interdiscip. Rev. Data Min. Knowl. Discov.* 9:e1301. doi: 10.1002/widm.1301

Rezaeianzadeh, M., Tabari, H., Yazdi, A. A., Isik, S., and Kalin, L. (2014). Flood flow forecasting using ANN, ANFIS and regression models. *Neural Comput. Appl.* 25, 25–37. doi: 10.1007/s00521-013-1443-6

Sampson, C. C., Smith, A. M., Bates, P. B., Neal, J. C., Alfieri, L., and Freer, J. E. (2015). A high-resolution global flood hazard model. *Water Resour. Res.* 51, 7358–7381. doi: 10.1002/2015wr016954

Sayed, G. I., Hassanien, A. E., and Azar, A. T. (2019). Feature selection via a novel chaotic crow search algorithm. *Neural Comput. Appl.* 31, 171–188. doi: 10.1007/s00521-017-2988-6

Shafizadeh-Moghadam, H., Valavi, R., Shahabi, H., Chapi, K., and Shirzadi, A. (2018). Novel forecasting approaches using combination of machine learning and statistical models for flood susceptibility mapping. *J. Environ. Manage.* 217, 1–11. doi: 10.1016/j.jenvman.2018.03.089

Tehrany, M. S., Pradhan, B., Mansor, S., and Ahmad, N. (2015). Flood susceptibility assessment using GIS-based support vector machine model with different kernel types. *Catena* 125, 91–101. doi: 10.1016/j.catena.2014.10.017

Tian, L., Li, J., Bi, W., Zuo, S., Li, L., Li, W., et al. (2019). Effects of waterlogging stress at different growth stages on the photosynthetic characteristics and grain yield of spring maize (*Zea mays* L.) under field conditions. *Agric. Water Manage.* 218, 250–258. doi: 10.1016/j.agwat.2019.03.054

Tibshirani, R. (1996). Regression shrinkage and selection via the lasso. *J. R. Stat. Soc. Ser. B Methodol.* 58, 267–288. doi: 10.1111/j.25176161.1996.tb02080.x

Voesenek, L. A. C. J., and Bailey-Serres, J. (2013). Flooding tolerance: O_2 sensing and survival strategies. *Curr. Opin. Plant Biol.* 16, 647–653. doi: 10.1016/j.pbi.2013.06.008

Wang, M., Zheng, Q., Shen, Q., and Guo, S. (2013). The critical role of potassium in plant stress response. *Int. J. Mol. Sci.* 14, 7370–7390. doi: 10.3390/ijms14047370

Wang, X., He, Y., Zhang, C., Tian, Y.-A., Lei, X., Li, D., et al. (2021). Physiological and transcriptional responses of *Phalaris arundinacea* under waterlogging conditions. *J. Plant Physiol.* 261:153428. doi: 10.1016/j.jplph.2021.153428

Wang, Z., Lai, C., Chen, X., Yang, B., Zhao, S., and Bai, X. (2015). Flood hazard risk assessment model based on random forest. *J. Hydrol.* 527, 1130–1141. doi: 10.1016/j.jhydrol.2015.06.008

Wang, Z., and Srinivasan, R. S. (2017). A review of artificial intelligence based building energy use prediction: contrasting the capabilities of single and ensemble prediction models. *Renew. Sustain. Energy Rev.* 75, 796–808. doi: 10.1016/j.rser.2016.10.079

Willner, S. N., Levermann, A., Zhao, F., and Frieler, K. (2018). Adaptation required to preserve future high-end river flood risk at present levels. *Sci. Adv.* 4:eaao1914. doi: 10.1126/sciadv.aao1914

Wu, J., Xiong, H., and Chen, J. (2009). Towards understanding hierarchical clustering: a data distribution perspective. *Neurocomputing* 72, 2319–2330. doi: 10.1016/j.neucom.2008.12.011

Xie, X., and Shen, J. (2021). Waterlogging resistance evaluation index and photosynthesis characteristics selection: using machine learning methods to judge poplar's waterlogging resistance. *Mathematics* 9:1542. doi: 10.3390/math9131542

Xiong, Q., Cao, C., Shen, T., Zhong, L., He, H., and Chen, X. (2019). Comprehensive metabolomic and proteomic analysis in biochemical metabolic pathways of rice spikes under drought and submergence stress. *Biochim. Biophys. Acta Proteins Proteomics* 1867, 237–247. doi: 10.1016/j.bbapap.2019.01.001

Xu, R., and Wunsch, D. (2005). Survey of clustering algorithms. *IEEE Trans. Neural Netw.* 16, 645–678. doi: 10.1109/tnn.2005.845141

Yang, L., and Shami, A. (2020). On hyperparameter optimization of machine learning algorithms: theory and practice. *Neurocomputing* 415, 295–316. doi: 10.1016/j.neucom.2020.07.061

Yang, P. Y., Hui, C. J., Tien, D. J., Snowden, A. W., Derfus, G. E., and Opel, C. F. (2019). Accurate definition of control strategies using cross validated stepwise regression and Monte Carlo simulation. *J. Biotechnol.* 306:100006. doi: 10.1016/j.btecx.2019.100006

Yang, S., Feng, Q., Liang, T., Liu, B., Zhang, W., and Xie, H. (2018). Modeling grassland above-ground biomass based on artificial neural network and remote sensing in the Three-River Headwaters Region. *Remote Sens. Environ.* 204, 448–455. doi: 10.1016/j.rse.2017.10.011

Yao, L., and Ge, Z. (2018). Deep learning of semisupervised process data with hierarchical extreme learning machine and soft sensor application. *IEEE Trans. Ind. Electron.* 65, 1490–1498. doi: 10.1109/tie.2017.2733448

Yaseen, Z. M., Deo, R. C., Hilal, A., Abd, A. M., Bueno, L. C., Salcedo-Sanz, S., et al. (2018). Predicting compressive strength of lightweight foamed concrete using extreme learning machine model. *Adv. Eng. Softw.* 115, 112–125. doi: 10.1016/j.advengsoft.2017.09.004

Ye, H., Song, L., Chen, H., Valliyodan, B., Cheng, P., Ali, L., et al. (2018). A major natural genetic variation associated with root system architecture and plasticity improves waterlogging tolerance and yield in soybean. *Plant Cell Environ.* 41, 2169–2182. doi: 10.1111/pce.13190

Yin, X., Hiraga, S., Hajika, M., Nishimura, M., and Komatsu, S. (2017). Transcriptomic analysis reveals the flooding tolerant mechanism in flooding tolerant line and abscisic acid treated soybean. *Plant Mol. Biol.* 93, 479–496. doi: 10.1007/s11103-016-0576-2

Zeng, N., Yang, Z., Zhang, Z., Hu, L., and Chen, L. (2019). Comparative transcriptome combined with proteome analyses revealed key factors involved in alfalfa (*Medicago sativa*) response to waterlogging stress. *Int. J. Mol. Sci.* 20:1359. doi: 10.3390/ijms20061359

Zhang, D., Lin, J., Peng, Q., Wang, D., Yang, T., Soroosh, S., et al. (2018). Modeling and simulating of reservoir operation using the artificial neural network, support vector regression, deep learning algorithm. *J. Hydrol.* 565, 720–736. doi: 10.1016/j.jhydrol.2018.08.050

Zhao, X., Zhang, Y., Xie, S., Qin, Q., Wu, S., and Luo, B. (2020). Outlier detection based on residual histogram preference for geometric multi-model fitting. *Sensors* 20:3037. doi: 10.3390/s20113037

Zheng, X., Zhou, J., Tan, D.-X., Wang, N., Wang, L., Shan, D., et al. (2017). Melatonin improves waterlogging tolerance of *Malus baccata* (Linn.) Borkh. seedlings by maintaining aerobic respiration, photosynthesis and ROS migration. *Front. Plant Sci.* 8:483. doi: 10.3389/fpls.2017.00483

Zhou, C., Bai, T., Wang, Y., Wu, T., Zhang, X., Xu, X., et al. (2017). Morpholoical and enzymatic responses to waterlogging in three *Prunus* species. *Sci. Hortic.* 221, 62–67. doi: 10.1016/j.scienta.2017.03.054

Zhou, W., Chen, F., Meng, Y., Chandrasekaran, U., Luo, X., Yang, W., et al. (2020). Plant waterlogging/flooding stress responses: from seed germination to maturation. *Plant Physiol. Biochem.* 148, 228–236. doi: 10.1016/j.plaphy.2020.01.020

Zhu, M., Li, F. H., and Shi, Z. S. (2016). Morphological and photosynthetic response of waxy corn inbred line to waterlogging. *Photosynthetica* 54, 636–640. doi: 10.1007/s11099-016-0203-0

Zhuo, Y., Tehrani, A. M., and Brgoch, J. (2018). Predicting the band gaps of inorganic solids by machine learning. *J. Phys. Chem. Lett.* 9, 1668–1673. doi: 10.1021/acs.jpclett.8b00124

Zou, H., and Hastie, T. (2005). Regularization and variable selection via the elastic net. *J. R. Stat. Soc. Ser. B Stat. Methodol.* 67, 301–320. doi: 10.1111/j.1467-9868.2005.00503.x

Conflict of Interest: The authors declare that the research was conducted in the absence of any commercial or financial relationships that could be construed as a potential conflict of interest.

Publisher's Note: All claims expressed in this article are solely those of the authors and do not necessarily represent those of their affiliated organizations, or those of the publisher, the editors and the reviewers. Any product that may be evaluated in this article, or claim that may be made by its manufacturer, is not guaranteed or endorsed by the publisher.

APPENDIX A

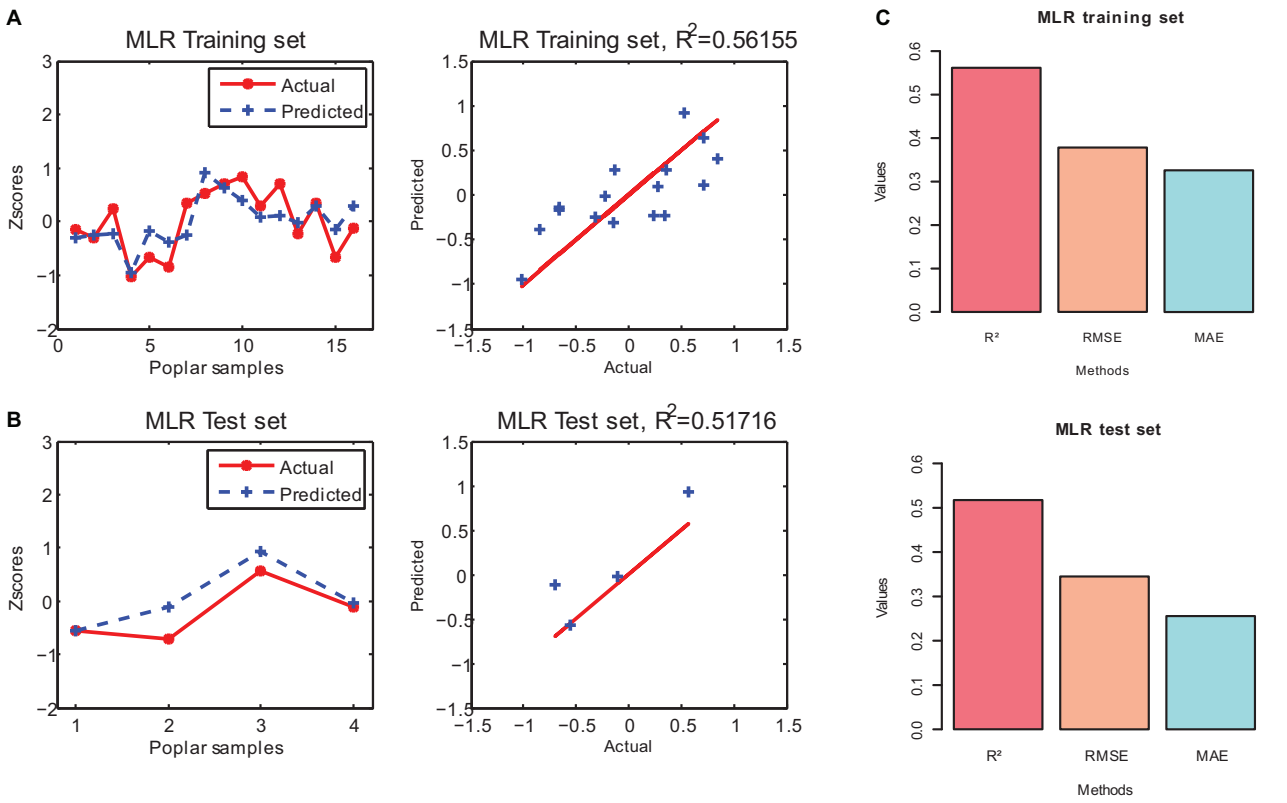

FIGURE A1 | Results of multiple linear regression.

TABLE A1 | The specific meanings and correlation coefficients of 26 features.

Features	Specific meaning	Unit
AHs/Cs	Ball-Berry parameter	Dimensionless
Cond	Conductance to H_2O	mol H_2O m^{-2} s^{-1}
CndCO_2	Total conductance to CO_2	mol CO_2 m^{-2} s^{-1}
CO_2S	CO_2 concentration on Sample cell	μmol CO_2 mol^{-1}
CO_2S/CO_2R	CO_2 concentration on Sample cell/CO_2 concentration on Reference cell	Dimensionless
C_2sfc	CO_2 concentration on Leaf Surface	μmol CO_2 mol^{-1}
Ci_Pa	Intercellular CO_2 partial pressure	Pa
Ci/Ca	Intercellular CO_2/Ambient CO_2	Dimensionless
CndTotal	Total conductance to water vapor	mol H2O m^{-2} s^{-1}
CTleaf	Computed leaf temperature	°C
Fo	Minimal fluorescence (dark)	bit
Fm	Maximal fluorescence (dark)	bit
Fv	Variable fluorescence	bit
H_2OS	H_2O concentration on Sample cell	mmol H_2O mol^{-1}
H_2OS/H_2OR	H_2O concentration on Sample cell/H_2O concentration on Reference cell	Dimensionless
H_2O_i	Intercellular H_2O concentration	mmol H_2O mol^{-1}
H_2Odiff	Difference between Intercellular H_2O and Sample cell H_2O	mmol H_2O mol^{-1}
Photo	Photosynthetic rate	μmol CO_2 m^{-2} s^{-1}
PARabs	Absorbed Photosynthetically active radiation	μmol m^{-2} s^{-1}
PhiCO_2	Quantum yield corresponding to CO_2 assimilation rate	Dimensionless
qN_Fo	Non-photochemical quenching (Calculated by Fo)	Dimensionless
RH_S	Relative humidity in the sample cell	%
RH_S/RH_R	Relative humidity on Sample cell/Relative humidity on Reference cell	Dimensionless
SVTleaf	Saturated vapor pressure calculated by leaf temperature	Pa
Trans	Transpiration rate	mol H_2O m^{-2} s^{-1}
VpdL	Vapor pressure deficit based on Leaf temperature	kPa

frontiers in Plant Science

ORIGINAL RESEARCH
published: 21 February 2022
doi: 10.3389/fpls.2022.839572

Crop Pest Recognition in Real Agricultural Environment Using Convolutional Neural Networks by a Parallel Attention Mechanism

Shengyi Zhao[1], Jizhan Liu[1], Zongchun Bai[2], Chunhua Hu[3] and Yujie Jin[1]*

[1] Key Laboratory of Modern Agricultural Equipment and Technology, Jiangsu University, Zhenjiang, China, [2] Research Institute of Agricultural Facilities and Equipment, Jiangsu Academy of Agricultural Sciences, Nanjing, China, [3] College of Information Science and Technology, Nanjing Forestry University, Nanjing, China

Crop pests are a major agricultural problem worldwide because the severity and extent of their occurrence threaten crop yield. However, traditional pest image segmentation methods are limited, ineffective and time-consuming, which causes difficulty in their promotion and application. Deep learning methods have become the main methods to address the technical challenges related to pest recognition. We propose an improved deep convolution neural network to better recognize crop pests in a real agricultural environment. The proposed network includes parallel attention mechanism module and residual blocks, and it has significant advantages in terms of accuracy and real-time performance compared with other models. Extensive comparative experiment results show that the proposed model achieves up to 98.17% accuracy for crop pest images. Moreover, the proposed method also achieves a better performance on the other public dataset. This study has the potential to be applied in real-world applications and further motivate research on pest recognition.

Keywords: crop, pest recognition, deep learning, convolution neural network, attention mechanism

OPEN ACCESS

Edited by:
Changyuan Zhai,
Beijing Academy of Agricultural and Forestry Sciences, China

Reviewed by:
Saeed Hamood Alsamhi,
Ibb University, Yemen
Byungkon Kang,
SUNY Korea, South Korea
Daniel Felipe Silva Santos,
São Paulo State University, Brazil

****Correspondence:***
Jizhan Liu
1000002048@ujs.edu.cn

Specialty section:
This article was submitted to Sustainable and Intelligent Phytoprotection, a section of the journal Frontiers in Plant Science

Received: *20 December 2021*
Accepted: *21 January 2022*
Published: *21 February 2022*

Citation:
Zhao S, Liu J, Bai Z, Hu C and Jin Y (2022) Crop Pest Recognition in Real Agricultural Environment Using Convolutional Neural Networks by a Parallel Attention Mechanism. Front. Plant Sci. 13:839572. doi: 10.3389/fpls.2022.839572

INTRODUCTION

Agriculture is an important basic industry worldwide, and pests can cause huge losses to crop production in every country (Santangelo, 2018). According to research, nearly half of global crop production will be impacted to varying degrees due to pests every year, which seriously affects the regional economy and people's daily lives (King, 2017). Pest detection has become an important task for the development of agricultural precision because pests have a wide distribution, cause great damage, and reproduce quickly (Wang et al., 2020). Traditional pest detection methods mainly include manual inspection and light trapping, but these methods need manual intervention and experience problems related to insufficient automation and intelligence, such as a large workload, low efficiency, and poor real-time performance (Lim et al., 2018). Due to the diversity of pests, manual identification relies on a large amount of expert knowledge, and it is difficult to obtain accurate and timely information on the number and species of pests in orchards, so it is difficult to widely implement (Li Y. et al., 2020). The automatic recognition of pests can provide a better growth environment for crops and increase the level of agricultural production.

With the rapid development of computer vision and pattern recognition technology, machine learning and deep learning have become the main research directions of agricultural pest detection (Albanese et al., 2021; Liu and Wang, 2021). For example, Fina et al. (2013) proposed a pest identification method using k-means clustering segmentation, but it takes a long time to label features manually in the case of a large dataset. Zhong et al. (2018) used a Prewitt operator and Canny edge detection algorithms to extract the morphological features of pests. Then, a support vector machine (SVM) was used to automatically recognize whiteflies and thrips, and the experimental results showed that the recognition rate was nearly 90%. Liu T. et al. (2016) proposed a method for the detection of wheat aphids based on genetic algorithms, which can accurately identify and count in the complex environment of the field. Yaakob and Jain (2012) used six invariant matrices to extract the shape features of pests, then combined the ARTMAP neural network algorithm and achieved an 85% recognition accuracy in a specific background. Barbedo (2014) developed a soybean whitefly monitoring system based on digital image processing, which can realize the automatic identification and counting of whiteflies and greatly improves work efficiency compared with manual inspection. Although the traditional machine learning recognition algorithm has achieved better results when the number of crop pest species is small, when there are many kinds of pests and the input parameters are limited, the machine learning method has difficulty effectively extracting key feature information, resulting in poor performance of the model robustness (Roy and Bhaduri, 2021).

Deep learning is an autonomous machine learning method that uses multilevel neural networks, and computers can automatically extract key features from a large number of images (Brahimi et al., 2017). Saleh et al. (2021) has demonstrated convolutional neural network (CNN) is a high performance deep learning network, and the CNN has the best performance compared to multiple models (DT, RF, SVM, NB, LR, KNN, RNN, and LSTM). CNN abandons complex preprocessing and feature extraction operations, and uses an end-to-end architecture that effectively combines global and local features and greatly simplify the recognition process. Thus, CNNs have been widely used in crop information recognition for real agricultural environments, and the automatic recognition of pests combined with CNNs is conducive to improving the accuracy of detection and reducing labor costs (Cheng et al., 2017).

Many studies have been carried out on the use of deep learning technology for crop key informations detection to provide accurate information for subsequent spray management, effectively improving the survival rate and yield of vegetables, fruits and field crops. A model of classification of tomato leaf diseases and pests with 89% accuracy was designed (Shijie et al., 2017), but this method can be applied in simple background pest classification and is impossible to integrate into practical applications. Chen et al. (2019) improved the residual network structure, added a high-resolution convolutional layer and the corresponding number of channels, and the accuracy of pest identification reached 91.5%. Wang et al. (2020) fused pest context information into a CNN, which improved the accuracy of pest detection and recognition in complex environments. Liu et al. (2019) proposed an effective multiscale data enhancement method for pest images. This method combines different scale image enhancements into the recognition model, which solves the problem that the traditional single image scale algorithm cannot be applied to the detection and recognition of small target pests. A method using CNN architecture for fruit fly recognition was proposed and achieved an accuracy of 95.68% (Leonardo et al., 2018). Generative Adversarial Networks (GAN) were applied to extend the dataset, and the extended dataset was fed into a pre-trained CNN model, which achieved an accuracy of 92% for plant disease classification (Gandhi et al., 2018). Dawei et al. (2019) designed a diagnostic system based on transfer learning for pest detection, and this approach to train and test 10 types of pests and achieves an average accuracy of 93.84%.Chen et al. (2021) proposed to classify tea pests by fine-tuning the VGG-16 network, and the results showed that the classification has accuracy up to 97.75%.

In recent years, due to the characteristic of extracting discriminative features of the area of interest, the attention mechanism has begun to be widely used in machine translation, generative adversarial and so on (Dong et al., 2019; Xiang et al., 2020). Researchers used the attention mechanism to quickly scan a global image to obtain the region of interest. However, it is still in the exploratory stage in the field of crop pest recognition. Liu et al. (2019) proposed a pest identification method based on CNN technology. This method combined the channel attention mechanism into the CNN. Through experiments on 16 types of field pests, the average accuracy reached 75.46%, and the accuracy was significantly improved. Guo et al. (2020) designed a self-attention mechanism and incorporated it into the CNN structure, which achieved the optimal F1-scores of 93.21% for 11 types of crop diseases and pests. Zhang and Liu (2021) proposed a method based on DenseNet and an attention mechanism, and the model could identify 7 types of navel orange diseases and pests on the test set with 96.90% accuracy. The results in this study are compared with on other studies as summarized in **Table 1**.

By analyzing current work, deep learning methods have been proven to significantly improve pest recognition performance, providing a reference for the recognition of crop pests. However, these studies mostly focus on the improvement and optimization of the diseases and pests recognition model. On the application of deep learning models, Alsamhi et al. (2021) combination of neural networks and IoT devices plays a vital role in improving feedback control efficiency with automatic operation and reductions of fertilizer and pesticides consumption. Agricultural UAVs are a modern agricultural technology with remarkable efficiency in quickly identifying and locating areas of outbreaks of pests and diseases through aerial imaging. And combining UAVs with high-performance IoT sensors enables efficient tasks such as remote crop growth monitoring, soil moisture monitoring, and water quality monitoring (Almalki et al., 2021). Meanwhile, UGVs have also been widely used for crop planting

TABLE 1 | Summary of the comparison of the existing work.

Paper	Object	Model	Types	Accuracy
Shijie et al. (2017)	Diseases and pests	VGG-16 + Transfer learning	9	89.00%
Chen et al. (2019)	Pests	ResNet + Block-cg	38	91.50%
Wang et al. (2020)	Pests	ResNet-50	3	72.30%
Liu et al. (2019)	Pests	CNN + Attention	16	75.46%
Leonardo et al. (2018)	Pests	SVM + VGG-16	10	95.68%
Dawei et al. (2019)	Pests	AlexNet + Transfer learning	10	93.84%
Chen et al. (2021)	Pests	VGGNet-16	14	97.75%
Guo et al. (2020)	Diseases and pests	CNN + Self-attention	11	92.78%
Zhang and Liu (2021)	Diseases and pests	DenseNet + Attention	7	96.90%
Our model	Pests	ResNet-50 + Parallel-attention	10	98.17%

monitoring, and by deploying a crop information detection model on the controller, it has been achieved soil moisture, pH, fertility monitoring and climate conditions monitoring, crop plant diseases and insect pests monitoring, growth and yield monitoring, etc. (Jin et al., 2021).

In the recognition task, pest pixels only occupy a small part of the whole image, and the attention mechanism can improve the learning of important feature channels of pests. The proposed model added a parallel attention module with a CNN structure to automatically extract pest feature information from a real agricultural environment. Feature extraction is focused on the pest feature channel, and invalid feature channel information is eliminated. Thus, the proposed model in this paper can automatically accurately recognize ten types of crop pests.

The main contributions of this paper are summarized as follows:

(1) To meet the recognition requirements of crop pests, this paper collects 10 types of pest images in a real agricultural environment. Thus, data enhancement improves the robustness and accuracy of the model performance in the detection task.
(2) This paper proposes an improved CNN model for the recognition of crop pests. Based on the original residual structure, spatial attention is combined with channel attention to obtain a parallel attention mechanism module. The parallel attention module is deeply integrated into the ResNet-50 network model.
(3) The attention module can establish a multidimensional dependency relationship of the extracted crop pest feature map, is lightweight and can be easily added into the network. Using this method, we achieved highly accurate recognition of crop pests in complex agricultural environments.

This paper is divided into five sections. The model improvement methods are shown in section "The Proposed Approach." Section "Experiment" shows the dataset collection and experiment setup. The performance of the deep learning method is discussed in section "Experimental Results and Discussion," and conclusions and future work are described in section "Conclusion."

THE PROPOSED APPROACH

Spatial/Channelwise Attention Mechanism

Spatial Attention Mechanism

Researchers have proposed a variety of attention mechanisms and applied them to the training tasks of CNN models. At the cost of smaller calculations and parameters, the network performance can be greatly improved (Fukui et al., 2019). The attention mechanism mainly includes the channel attention mechanism and spatial attention mechanism. The spatial attention mainly extracts important regions in the feature and judges the importance of the corresponding feature by the dependence between different positions in the feature. The corresponding weight parameters are assigned to improve the feature expression of the key area. Therefore, spatial attention enables the network to better evaluate the effect of each feature position during the classification feature extraction process and further enhances the modeling ability of the network.

As shown in **Figure 1**, average pooling and maximum pooling operations are performed on the input feature map *F*, and information is gathered separately into two different feature maps and used convolutional layers are applied to generate spatial attention maps *Ms*. Then, feature fusion is realized through a 7×7 convolution operation, and the sigmoid activation function is used to generate a weight map and superimpose it on the original input feature map. Finally, the features of the target pixel area are enhanced.

Channel Attention Mechanism

Channel attention mainly performs correlation modeling on the feature maps of different channels, adaptively obtains the importance of each feature channel through back-propagation parameter learning, and assigns different weight coefficients to each channel.

SENet is one of the classic channel attention modules, as shown in **Figure 2**. Hu et al. (2018) mentioned it in a CVPR ImageNet Workshop speech. The weights of different channels are trained through the cost function, and the weight coefficients of each feature channel are automatically obtained. Then, according to the size of the weight coefficient of each feature channel, the effective feature channel is enhanced, and the invalid feature channel is suppressed.

Parallel Attention Mechanism Design

Based on pest recognition, we know that features from the spatial attention module are highlighted in pest regions from the perspective of spatial position, while features from the channelwise attention module are highlighted from the perspective of channels, which carry more important information

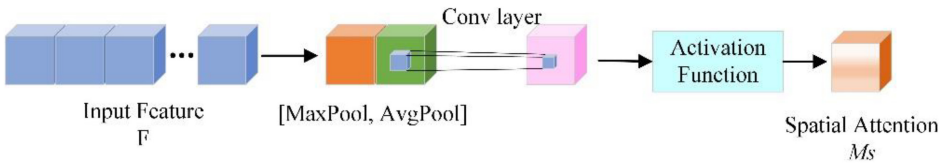

FIGURE 1 | The structure of the spatial attention mechanism.

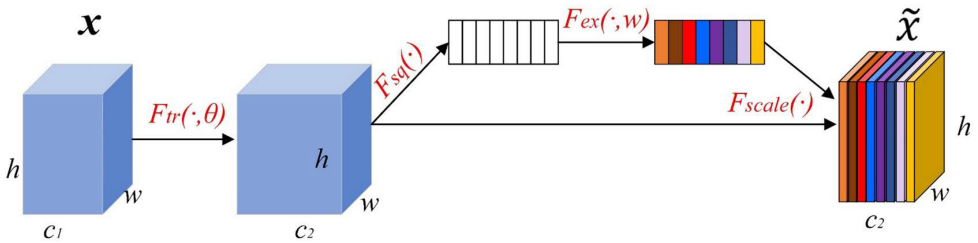

FIGURE 2 | The structure of the channel attention mechanism.

at the channel level. It is necessary to combine multi-attention features together to obtain enhanced attention features. Therefore, this paper proposed a parallel attention mechanism, namely, PCSA, that effectively combines the spatial attention module and the channel attention module in series as that used for pest recognition. In **Figure 3**, the PCSA consists of three parts: channel attention, spatial attention and feature map fusion. It can be directly applied to existing network architectures.

(1) The channel attention mainly redistributes the channel weights in the feature map through one-dimensional convolution, increases the weight of pest-related channels and reduces the weight of the remaining channels. First, the global average pooling calculation is performed on the feature map with input size $C \times H \times W$ through the squeeze operation (F_{sq}) to obtain a $1 \times 1 \times C$ feature vector and it is input into the two fully connected layers. The *ReLU* activation function is used between the two fully connected layers, generated feature maps are first downscaled by FC-1 and then upscaled by FC-2, and the feature channel dimensions of the input and output are the same. The squeeze process can be expressed as follows:

$$F_{sq}(u_c) = \frac{1}{H \times W} \sum_{i=1}^{H} \sum_{j=1}^{W} u_c(i, j)$$

Where $u_c(i,j)$ is the element in row i and column j of the input data. Then, the input feature map F generates a $1 \times 1 \times C$ global feature map. In the excitation operation (F_{ex}), the sigmoid activation function is used to calculate the weight of each feature channel, which is the core of the entire channel attention module. These weights are allocated to the input feature maps. The excitation process can be expressed as follows:

$$F_{ex}(z, W) = \sigma\left(g(z, W)\right) = \sigma\left(W_2 \sigma\left(W_1 z\right)\right)$$

Where σ is the ReLU function, z is the result of the compression process. The parameter W_1 reduces the dimension of channels to $1/r$ of the original in the FC-1, restore the dimension of channels

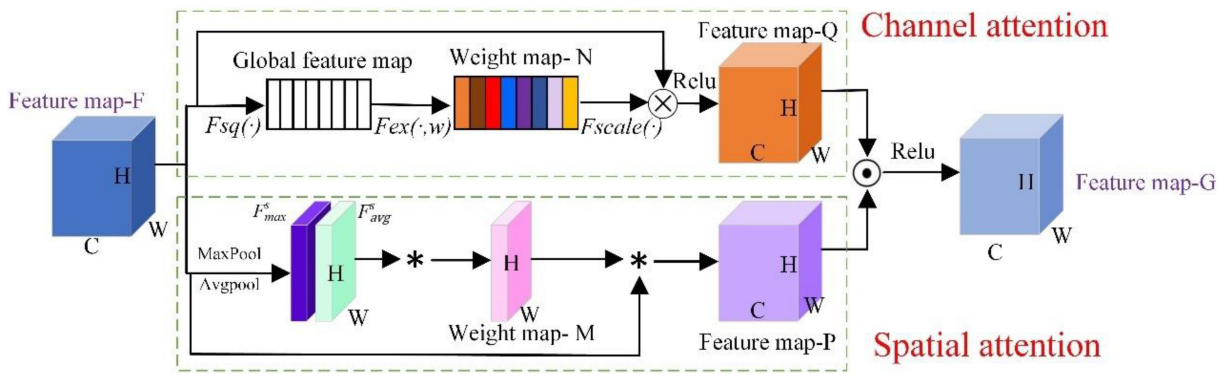

FIGURE 3 | The structure of the parallel attention mechanism.

to the original dimension of channels with parameter W_2 in the FC-2, and W_1 and W_2 are inverse relationships. $W_1 \in R^{\frac{C}{r} * C}$ and $W_2 \in R^{C * \frac{C}{r}}$ are the downgrading and upgrading parameters of the FC-1 and FC-2, r is the scaling parameter to balance model performance and computational complexity. Finally, the output feature channel weight vector is multiplied by the original input feature map through the scale operation (F_{scale}) to complete the original feature calibration in the channel dimension. Therefore, the extracted features have stronger directivity and improved classification performance. The scale process can be expressed as follows:

$$F_{scale}(u_c, s_c) = u_c \odot s_c$$

Where $F_{scale}(u_c, s_c)$ refers to the channelwise multiplication between the scalar s_c and the feature map $u_c \in R^{H \times W}$.

(2) Spatial attention performs average pooling and maximum pooling operations on the feature map F in the channel dimension and generates two single-channel feature maps F^s_{avg} and F^s_{max}. Then, the F^s_{avg} and F^s_{max} feature maps are combined to generate a weight map M, and the feature map F is weighted by the weight map M to generate a feature map P. Finally, in the feature map P, the areas related to the pests are given higher weights, while the other areas have lower weights. The calculation process of the spatial attention module can be expressed as follows:

$$M_s = \left(\left[Avgpool(F) \otimes maxpool(F)\right]\right) = \sigma\left(\left[F^s_{avg} \otimes F^s_{max}\right]\right)$$

Where σ is the ReLU function, s is the 2D feature maps and is the dot product of position data corresponding to F^s_{avg} and F^s_{max} feature maps.

(3) The feature map Q is dot-producted with the feature map P and the feature map G is obtained using the ReLu activation function. The feature map G combines the weight distribution of the channel dimension and the weight distribution of the spatial dimension, thereby obtaining complementary key features, which can highlight the pest feature area and suppress various interferences, so that the model can identify pests more accurately.

Crop Pest Recognition Model of ResNet-50 Fused to PSCA

Feature extraction is the key part of deep learning models, and the convolutional layer of the CNN has powerful feature extraction capabilities. Recently, AlexNet, VGGNet and GoogLeNet have been widely used in face recognition, disease diagnosis, text classification and other tasks and have achieved good results (Ballester and Araujo, 2016). However, these CNNs increase the feature extraction ability by adding to the number of network layers, which will increase the number of model parameters and the computational cost (Tang et al., 2020b). More seriously, it will cause the problems of network redundancy, gradient explosion and disappearance.

The residual network proposed by He et al. (2016) won the championship in the 2015 ImageNet large-scale visual recognition competition. The residual block in the model can avoid the problem of network degradation caused by the deepening of the number of network layers. Compared with AlexNet, VGGNet, and GoogLeNet, ResNet has less computation and higher performance. Compared with ResNet-101 and ResNet-18, ResNet-50 has the advantages of higher accuracy, fewer parameters and faster speed (Li X. et al., 2020). Thus, this study chose ResNet-50 as the feature extraction network.

In **Figure 4**, identity mapping uses the jump connection method to directly add feature X that the network originally wants to learn from the shortcut branch and feature $F_{(X)}$ learned from the weighted layer through the *ReLU* activation function. The bottleneck structure in the ResNet network can effectively reduce the network parameters and computational complexity. The bottleneck structure is composed of two 1×1 convolutional layers and one 3×3 convolutional layer. The input feature vector is reduced from 256 dimensions to 64 dimensions through a 1×1 convolution, a 3×3 convolutional layer is used to learn features, and the feature vector is restored to 256 dimensions through a 1×1 convolutional layer. Finally, the identity map and output are added through the *ReLU* activation function. In this paper, a PCSA is added to the original model structure of ResNet-50 to obtain the ResNet-50-PCSA model. The network architectures of the improved ResNet-50 are depicted in **Figure 5**.

The model mainly includes four stage processes, and each stage is composed of a residual module. The proposed model embeds the PCSA module after the residual module and constitutes 4 bottleneck-PCSA modules, the numbers of which are 3, 6, 6, and 3. The size of the convolution kernels of bottleneck-PCSA is the same. The main difference between models is the number of convolution kernels and the output dimensions of the fully connected layer in the PCSA module. The crop pest images are input into the ResNet-50-PCSA network structure, first through the convolutional layer, BN layer, activation layer and max pool. Then, the pest feature map was obtained through 4 bottleneck-PCSA modules. Finally, the obtained feature map is calculated by AVG pooling, and the number of output feature layers is changed from multidimensional to one-dimensional through the flattened layer and output through the fully connected layer. When deepening the number of network layers, if the internal features of the network have reached the optimal level in a certain layer, the subsequent superimposed network layers will not change the features.

The above is the complete structure and operation process of the ResNet-50-PCSA model. The PCSA subnetwork structure is embedded in ResNet-50. The combination of the feature channel recalibration strategy and residual network can effectively improve network performance and thus does not need to greatly increase the computational cost. Through feature refinement, the learning ability of complex pest features is enhanced.

EXPERIMENT

Dataset Acquisition

The development of deep learning in recent years has proven that the detection and classification tasks of target objects can

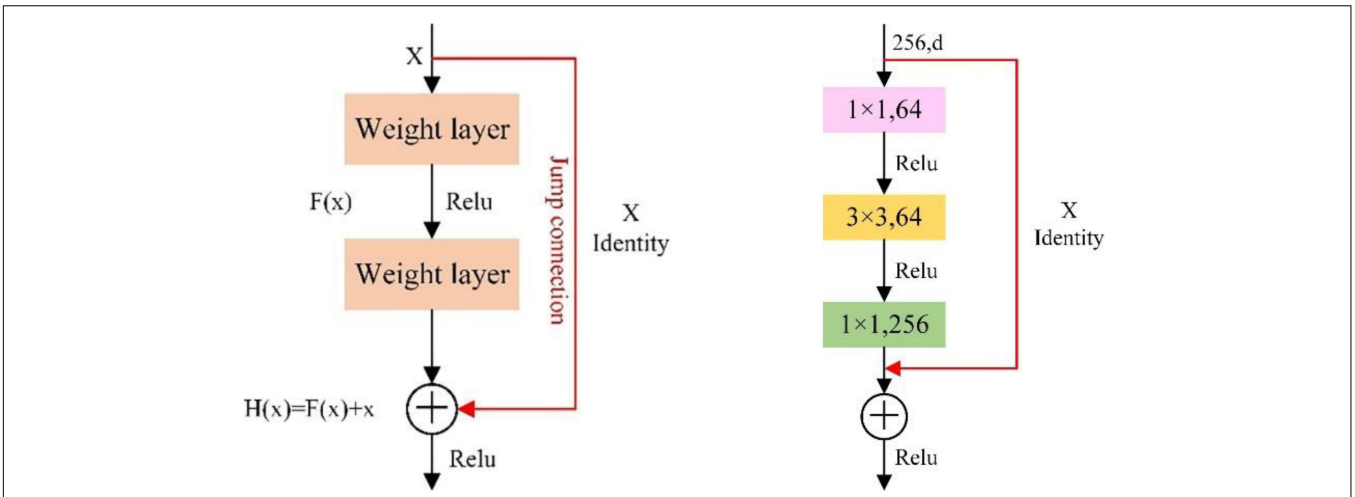

FIGURE 4 | The residual block **(left)** and the bottleneck structure **(right)**.

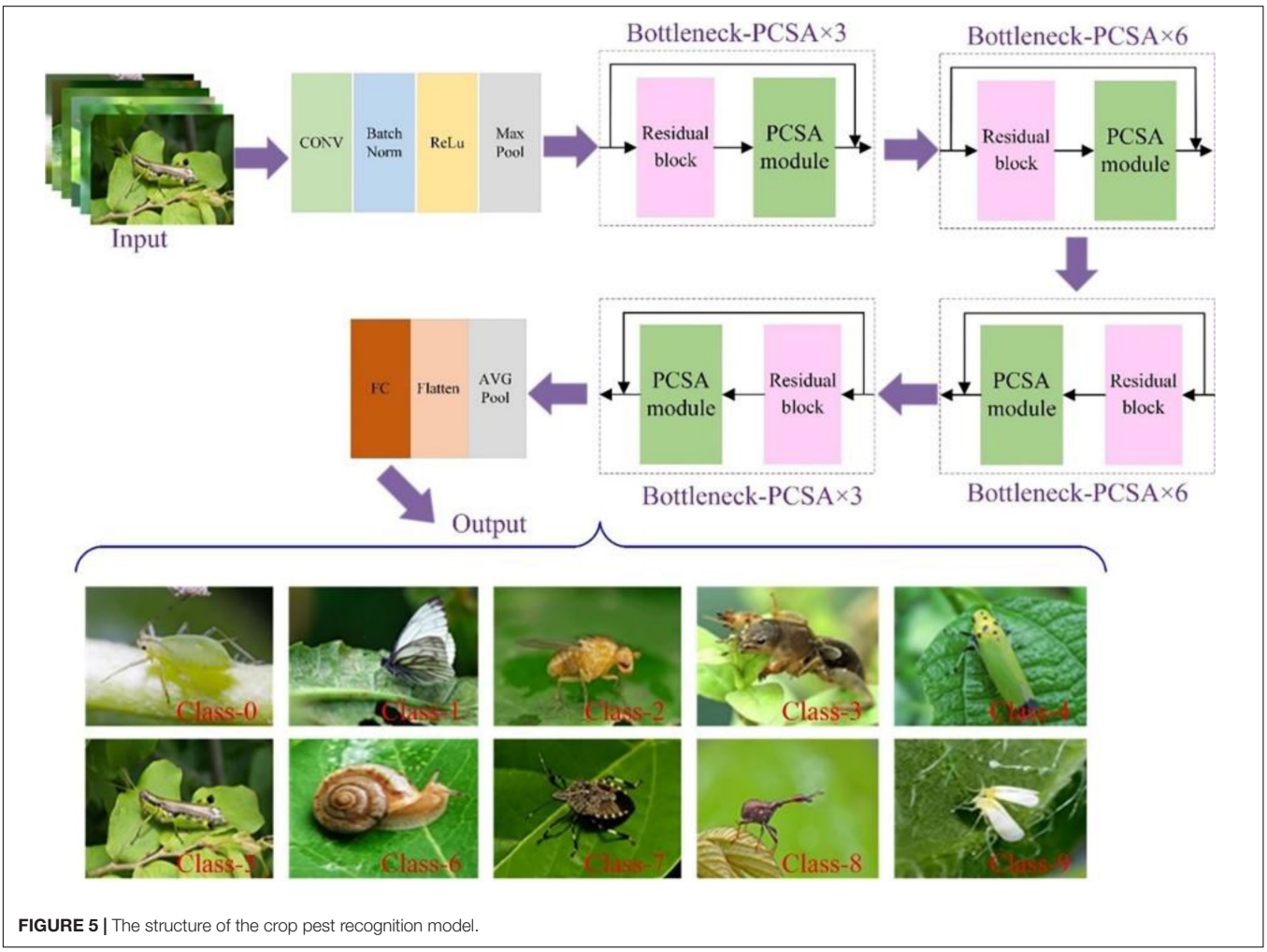

FIGURE 5 | The structure of the crop pest recognition model.

be effectively achieved under high-quality and large-size datasets (Liu W. et al., 2016). For crop pests, their active time and distribution law are related to various environmental factors, such as climate and season, and it is difficult to obtain large images. Therefore, it is not feasible to obtain a large number of pest images through the process of collecting and shooting. This

paper makes use of abundant internet resources to compensate for this deficiency and enriches the content of image data by open-source dataset and web crawler methods.

In this paper, we selected 10 common classes of crop pests, namely, Aphid, Cabbage butterfly, Drosophila, Gryllotalpa, Leafhopper, Locust, Snail, Stinkbug, Weevil, and Whitefly, as shown in **Figure 6**. Because these pests are prone to exist all over the world, they reproduce very quickly and spread widely (Dawei et al., 2019). They mainly feed on the leaves, stems and fruits of crops. If they lay eggs on crops, they are difficult to handle and will cause huge losses in crop yields. Therefore, effective detection and timely control of these 10 types of pests have great significance.

Most of the images in the pest dataset in this paper are collected from the internet, and a few are from the open-source dataset. The web crawler keywords for each type of pest were divided into Chinese and English. Multithreaded collection of the images of each type of pest is completed using three major internet search engines: Google, Bing and Baidu. The open source dataset mainly comes from Kaggle[1] and Forestry[2]. Although the key information is defined in the collection process, there are still many non-pest images and redundant data. Several agricultural technology experts judged and classified the collected images and removed incorrect pest types and poor-quality images. The size of all images was unified by means of image normalization (224×224), and the format was JPG. Overall, there were more than 400 images of each type of pest, and the number of snails and locusts exceeded 800 images.

Data Augmentation

Data augmentation is an important data processing technology in deep learning. It can effectively increase the amount and diversity of training data and improve the generalization ability and robustness of the model (Shorten and Khoshgoftaar, 2019). Data enhancement is divided into online enhancement and offline enhancement; online enhancement is suitable for large datasets, and after the model obtains batch data, it can be enhanced by rotation, translation and folding (Tang et al., 2020a). Offline enhancement directly processes images and is suitable for small datasets. Therefore, this paper used offline augmentation techniques and enhanced images in combination with OpenCV under the PyTorch framework.

a) Spin: Randomly rotating the picture by 0°, 90°, 180°, and 270° will not change the relative position of the pest pixels, simulating the randomness of the shooting angle under natural conditions.
b) Zoom: The images are reduced according to a certain ratio, which helps to identify pests on multiple scales. For the scaled image, the resolution of the image is expanded to 224×224 pixels by filling in fixed color pixels.
c) Gaussian noise is added to the image to simulate the interference information in the natural environment.
d) Color jitter: Changed the image brightness and contrast to simulate the image difference generated by the change of light intensity in the environment of crop growing. The color jitter can be expressed as follows:

$$g(i,j) = b^* f\ (i,j) + a;\ a \in [a_1, a_2]$$

where a is the image contrast, b is the image brightness, $g(i,j)$ is the output image, $f(i,j)$ is the input image, a_1 is the lowest brightness factor in the field and a_2 is the highest brightness factor in the field.

Samples of the data enhancement is shown in **Figure 7**. By using these image offline augmentation techniques, the number of datasets is expanded four times. The total number of original images was 5,245; after data augmentation, the number of images increased to 26,225. The training set and validation set are divided into 8:2 ratios, and detailed information on the dataset are shown in **Table 2**. For the model testing, we collected 150 real images of each pest and formed a testset. In the end, the testset contained 1,500 images.

Experiment Setup

In this study, the weight parameters of the pretrained ResNet-50 model on ImageNet are used for transfer learning to accelerate the convergence speed of the model. The collected dataset contains 10 kinds of pests, so the output layer must be changed from 1,000 (ImageNet pretrained ResNet-50) to 10. The operating platform for this experiment is a Dell T7920 graphics workstation, the operating environment is Windows 10, the CPU is Intel Xeon Gold 6248R, and the GPU is NVIDIA Quadro RTX 5000. The training environment is created by Anaconda3, and the environment configuration is Python 3.6 and PyTorch 1.8.0, torchvision 0.7.0 artificial neural network library. The model parameters were selected as follows: the initial learning rate set to 0.001, a weight decay of 0.00001 and momentum factor is 0.1. Set 100 epochs, after 2 epochs, the model performance does not improve and the learning rate will decrease after that. At the same time, the CUDA 10.2 deep neural network acceleration library is used. The experiment uses a stochastic gradient descent with momentum (SGDM), updates the parameters and optimizes the training process. The parameter update can be expressed as follows:

$$\theta_{i+1} = \theta_i - \alpha \Delta L_R(\theta_i) + m(\theta_i - \theta_{i-1})$$

where i is the number of iterations, θ is the network parameters, $\Delta L_R(\theta_i)$ is the loss function gradient, m is the momentum and α is the learning rate. Meanwhile, before the training and validation of each epoch, the data was randomly shuffled. After each training, the validation set is tested, and the model is saved. Finally, the model with the highest accuracy is selected.

Model Evaluation Index

When evaluating the performance of a model, Precision (P), Recall (R), F_1 Score (F_1) and Detection speed (T_a) are usually selected as evaluation indices.

$$P = \frac{T_P}{T_P + F_P}$$

[1] https://www.kaggle.com/
[2] https://www.forestryimages.org/index.cfm

FIGURE 6 | Sample images for 10 common pest classes.

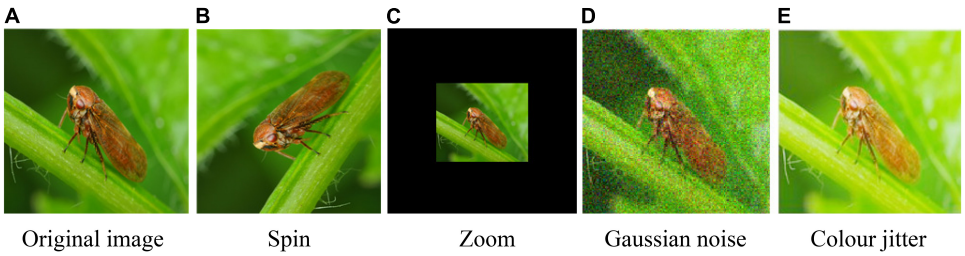

FIGURE 7 | Samples for data augmentation. **(A)** Original image, **(B)** spin, **(C)** zoom, **(D)** Gaussian noise, and **(E)** color jitter.

TABLE 2 | Crop pest dataset detail information.

Pest	Class	Origin images	Augmentation images	Trainset	Validation set
Aphid	0	415	2,075	1,660	415
Cabbage butterfly	1	430	2,150	1,720	430
Drosophila	2	440	2,200	1,760	440
Gryllotalpa	3	485	2,425	1,940	485
Leafhopper	4	455	2,275	1,820	455
Locust	5	820	4,100	3,280	820
Snail	6	850	4,250	3,400	850
Stinkbug	7	420	2,100	1,680	420
Weevil	8	480	2,400	1,920	480
Whitefly	9	450	2,250	1,800	450
Total		5,245	26,225	20,980	5,245

$$R = \frac{T_P}{T_P + F_N}$$

$$F_1 = 2 \times \frac{P \times R}{P + R}$$

Where T_P (true positive) is the number of positive samples predicted as positive samples, F_P (false-positive) is the number of negative samples considered to be positive samples, and F_N (false negative) is the number of positive samples considered to be negative samples.

$$T_a = \frac{T}{N}$$

Where T is the total detection time for the validation set, and N is the total number for the validation set.

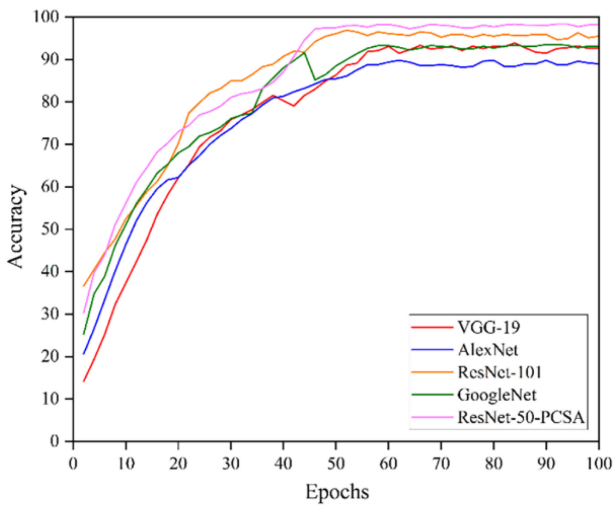

FIGURE 8 | The training accuracy curves.

EXPERIMENTAL RESULTS AND DISCUSSION

Comparison of the Performance of Various Models

To evaluate the performance, the proposed network is compared with several famous CNN networks, such as VGG-19, AlexNet, ResNet-101 and GoogLeNet. These models were configured to use the same optimizer (SGDM), classifier (softmax) and learning rate (0.0001).

The comparison of various CNN model training curves is shown in **Figure 8**. The training iteration epochs are plotted on the x-axis, and the accuracy is plotted on the y-axis. The ResNet-50-PCSA model proposed in this paper has the highest accuracy, and except for the AlexNet model, the accuracy of the other models exceeds 90% because AlexNet is not deep enough compared to other models, and the amount of feature information extracted by the network is less. Meanwhile, the ResNet-50-PCSA model converges fastest, and the model begins to converge after approximately 45 epochs.

TABLE 3 | The evaluation results.

Model	Input	*P*	*R*	F_1	T_a (ms)	Accuracy (%)	Size (Mb)
VGG-19	224	0.9137	0.9130	0.9133	41.81	92.62	482
AlexNet	224	0.8905	0.8891	0.8898	33.37	88.96	227
GoogLeNet	224	0.9331	0.9324	0.9327	33.64	93.35	45
ResNet-101	224	0.9537	0.9548	0.9542	39.05	94.48	167
ResNet-50-PCSA	224	0.9798	0.9816	0.9807	32.29	98.17	91

TABLE 4 | The results of ResNet-50-PCSA compared with ResNet-50.

Model	Input	*P*	*R*	F_1	T_a (ms)	Accuracy (%)	Size (Mb)
ResNet-50	224	0.9386	0.9391	0.9388	31.36	92.41	78
ResNet-50-PCSA	224	0.9798	0.9816	0.9807	32.29	98.17	91

TABLE 5 | The results of PCSA compared with SENet and CBAM.

Model	Input	*P*	*R*	F_1	T_a (ms)	Accuracy (%)	Size (Mb)
ResNet-50-SENet	224	0.9495	0.9496	0.9495	30.62	94.96	72
ResNet-50-CBAM	224	0.9601	0.9603	0.9602	31.98	96.05	86
ResNet-50-PCSA	224	0.9798	0.9816	0.9807	32.29	98.17	91

TABLE 6 | Accuracy for crop pest recognition with 10 classes.

Classes	0	1	2	3	4	5	6	7	8	9
Accuracy (%)	97.08	98.37	97.15	99.34	97.53	98.52	99.15	98.43	98.01	97.10
Average accuracy (%)	**98.17**									

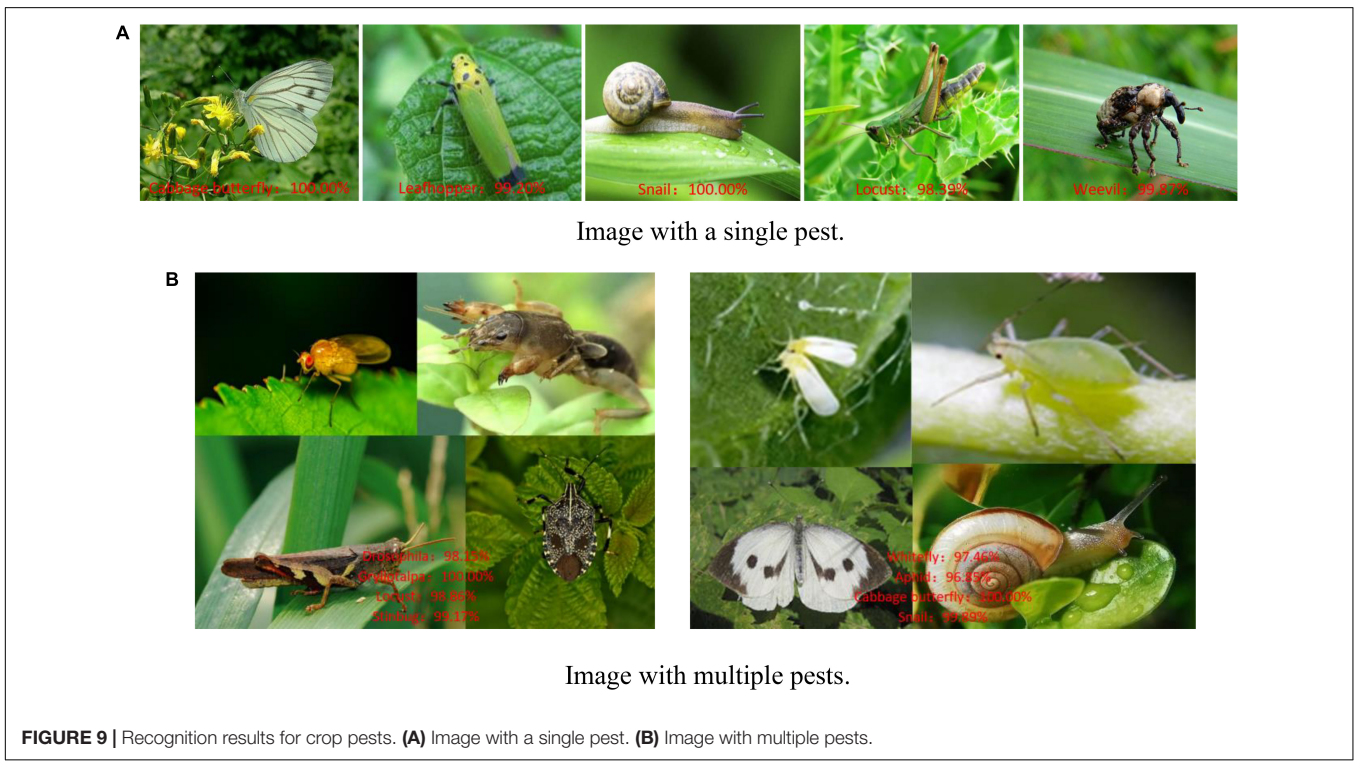

FIGURE 9 | Recognition results for crop pests. **(A)** Image with a single pest. **(B)** Image with multiple pests.

The VGG-19, AlexNet, ResNet-101, and GoogLeNet models have larger fluctuations after convergence, and the ResNet-50-PCSA model converges with the smallest fluctuation range, reflecting good stability.

The detailed evaluation results of different models on crop pests are obtained in **Table 3**. Under the same experimental conditions, the ResNet-50-PCSA model proposed in this paper has the highest precision, recall and F_1 score. The proposed model also has the highest average accuracy, with an accuracy reaching 98.17%. Compared with the VGG-19, AlexNet, GoogLeNet and ResNet-101 models, the average accuracy is 5.55, 9.21, 4.82, and 3.69% higher, respectively, and the proposed model is significantly ahead of the other CNN networks. The ResNet-50-PCSA model has the fastest recognition speed, and the average recognition time for a single pest image is only 32.29 ms. Compared with

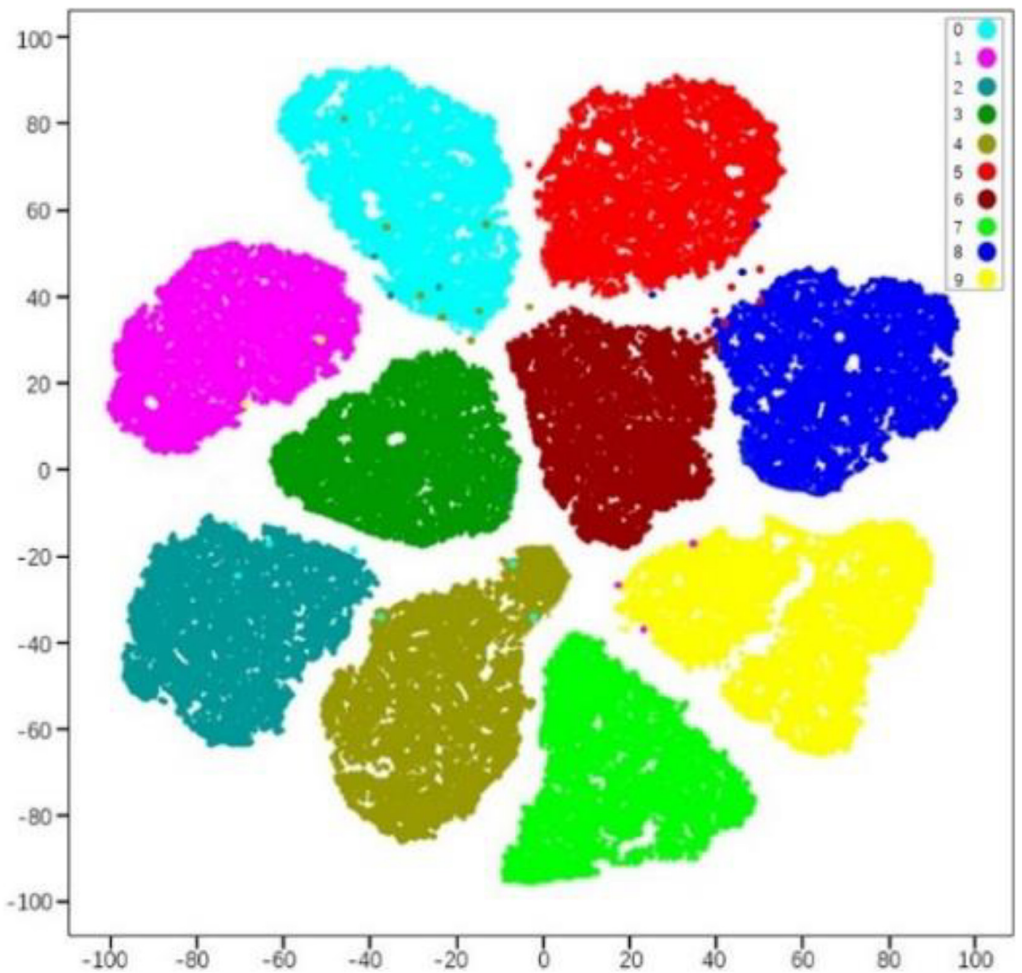

FIGURE 10 | Clustering results of the training set.

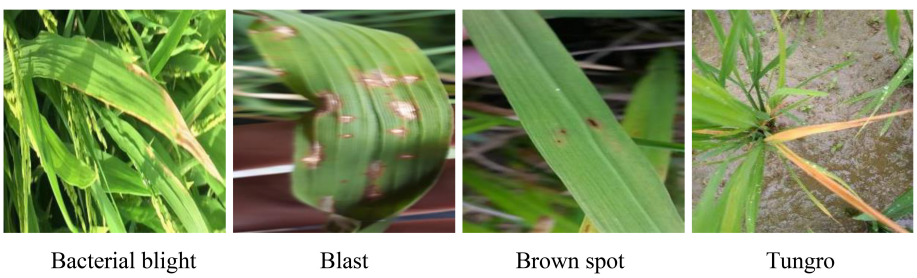

FIGURE 11 | Sample images of the rice leaf dataset.

the second-ranked AlexNet model, the time is reduced by 1.08 ms, which meets the needs of real-time recognition of crop pests. Considering that the model will be deployed to the inspection robot system, VGG-19, AlexNet and ResNet-101 have a large model size, which cannot guarantee real-time detection task requirements. Moreover, the size of the ResNet-50-PCSA model is 91 Mb, which is 46 Mb larger than GoogLeNet. However, ResNet-50-PCSA also meets the requirements of lightweight deployment, and the accuracy is higher than that of GoogLeNet. Synthesizing the above analysis, the proposed model achieves the best performance in terms of accuracy and speed.

Effectiveness of PCSA Module

To prove the effect of adding a parallel attention mechanism on the performance of the original model, keeping the experimental conditions and parameters consistent, a comparison experiment of the performance of the ResNet-50-PCSA and ResNet-50 models was carried out. The results of the comparative experiment of the proposed model and the ResNet-50 model without a parallel attention mechanism on crop pests are shown in **Table 4**.

It can be seen from **Table 4** that the results of the model are improved after adding the parallel attention mechanism. The accuracy of the model is increased by 5.76%, and the precision, recall and F1 score are all higher than those of the original ResNet-50 model. The proposed model can retain more image details due to important feature reuse. However, the ResNet-50-PCSA model average detection time of a single pest image is increased by 0.93 ms, and the model size is increased by 13 Mb. This explains why adding the parallel attention mechanism can slightly increase the computational complexity and complexity of the model.

To further verify the effectiveness of the parallel attention mechanism proposed in this paper, we selected two widely used attention mechanisms as comparative experiments: SENet (Hu et al., 2018) and CBAM (Woo et al., 2018). The CBAM is composed of a serial structure of channel attention and spatial attention; it first learns the key features through the channel attention module and then uses the spatial attention module to learn the location of the key features.

The comparison results of the PCSA module with SENet and CBAM are shown in **Table 5**. In the recognition accuracy of the model, the ResNet-50-PCSA is 3.21 and 2.12% higher than ResNet-50-SENet and ResNet-50-CBAM, respectively. In terms of the average inspection time and model size, the ResNet-50-PCSA is slightly insufficient. ResNet-50-SENet has the fastest recognition speed and smallest model size. The average detection time is only 1.67 ms faster than ResNet-50-PCSA, but the recognition accuracy is significantly lower than ResNet-50-PCSA. The recognition speed of ResNet-50-PCSA still meets actual application requirements. At the same time, the model size of ResNet-50-PCSA is 19 and 5 Mb larger than ResNet-50-SENet and ResNet-50-CBAM, respectively, but it also confirms the requirements of lightweight deployment in machine control panels. Synthesizing the above analysis, the results show that the proposed parallel attention mechanism is effective.

Crop Pest Classification Results

Table 6 shows the ResNet-50-PCSA model accuracy of each pest on the validation set. The indices of 10 classes of pests are represented as follows: 0. Aphid, 1. Cabbage butterfly, 2. Drosophila, 3. Gryllotalpa, 4. Leafhopper, 5. Locust, 6. Snail, 7. Stinkbug, 8. Weevil, 9. Whitefly.

The result suggests that the model correctly recognizes 10 classes of pests with an average accuracy of 98.17%. The model recognition accuracy for aphid, Drosophila, leafhopper, and whitefly is low, but the accuracy also exceeds 97%. The reason is that the color features of aphids and leafhoppers are similar to those of crop leaves, and Drosophila and whiteflies are smaller in size and occupy only a few pixels in the whole image. Furthermore, the model exceeded 99% accuracy on 2 classes of pests (Gryllotalpa, and snail), while the other 4 classes of pests had accuracies between 98.01 and 98.52%.

Figure 9 shows the correct recognition results for randomly selected images using the ResNet-50-PCSA model. The model has a better recognition result of the 5 pest images in **Figure 9A**, and the accuracies of cabbage butterflies and snails are 100.00%. The accuracy of locust is the lowest, but it is also as high as 98.39%, which meets the accuracy requirements in real pest recognition tasks. In **Figure 9B**, we stitch images of different pests into one image and input it into the model. The model also obtained a better

TABLE 7 | The evaluation result of the rice leaf dataset.

Model	Input	P	R	F_1	T_a (ms)	Accuracy (%)
GoogLeNet	256	0.9365	0.9361	0.9363	33.07	93.68
Xception	256	0.9355	0.9353	0.9354	31.51	93.53
ResNet-50	256	0.9480	0.9478	0.9479	30.54	94.81
ResNet-50-PCSA	256	0.9933	0.9935	0.9934	31.39	99.35

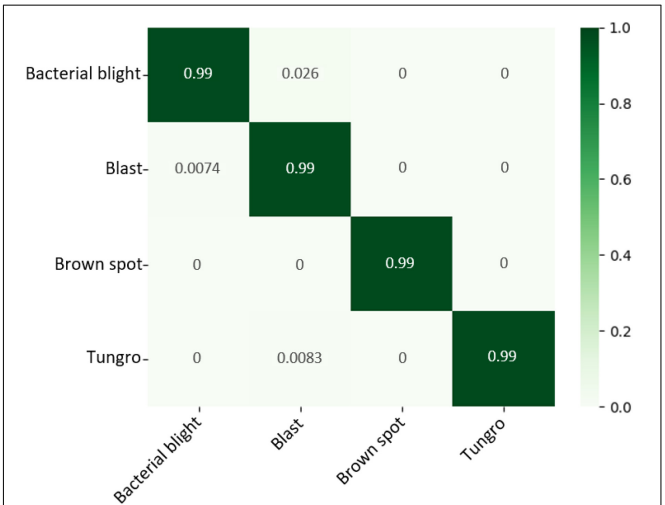

FIGURE 12 | Confusion matrices for rice leaf diseases.

performance and could accurately recognize each pest in the stitched image.

To better show the classification performance of the model on 10 classes of pests, we choose t-SNE clustering for feature spatial distribution representation. The experiment extracts the features of each image from the fully connected layer of the ResNet-50-PCSA model, uses the t-SNE algorithm to visualize the high-dimensional features in a two-dimensional space of 10-class pests, and performs hierarchical clustering analysis on the features. The 2048-dimensional feature clustering results are shown in **Figure 10**. Each color represents the category of different pests, for a total of 10 categories. On the whole, the features reflected by different pests show a better clustering effect, which is the key to accurately distinguishing different pests. The distribution position of the feature clusters of the same variety deviates, mainly because in the real agricultural environment, the color and shape features of some pests are similar.

Based on the above results, it can be seen that the ResNet-50-PCSA model can complete the task of crop pest recognition well and has a high robustness and accuracy. This model can be a useful detection tool in the field of crop diseases.

ResNet-50-PCSA Adaptability on Other Datasets

To further validate the practical application performance of our model, we experiment with the proposed method on other public datasets of rice leaf diseases, and the disease images have real agricultural backgrounds. The dataset contains 5,932 rice leaf disease images, which include bacterial blight, blast, brown spot and tungro. All the patches were treated as data samples and resized to 224×224 pixels, and **Figure 11** shows the four varieties of rice leaf diseases.

Under the same training environments, GoogLeNet, ResNet-50 and Xception were selected for comparative experiments on rice leaf diseases. As shown in **Table 7**, the proposed model in this paper has an average detection accuracy of 99.35% for the 4 classes of rice leaf diseases. Compared with the GoogLeNet, Xception and ResNet-50 models, the accuracy is 5.67, 5.82, and 4.54% higher, respectively. The ResNet-50-PCSA model has the fastest average detection time for a rice leaf image, and the average detection time for a single rice disease image is only 0.85 ms slower than ResNet-50.

The detection result is represented by the confusion matrix in **Figure 12**, and the detection accuracy of 4 classes of rice leaf diseases exceeded 99%. Compared with crop pest recognition, the accuracy of rice leaf disease diagnosis has increased by 1.18%. The main reason is that there are only 4-classes of rice leaf diseases, which is 6-classes less than that of pest recognition. It is proven that the proposed method has a wide range of applicability and has better performance relative to deep-based methods on public datasets. Moreover, it is certified that our method is effective for datasets captured in real agricultural environments.

CONCLUSION

In this work, a pest recognition model based on deep learning was proposed using a manually collected dataset to classify 10 types of crop pests. A total of 5,245 images were downloaded from different websites and manually validated. In the data preparation phase, data augmentation was used to expand the dataset. We successfully designed a parallel attention mechanism and deeply integrated the original ResNet-50 model and recognize the great performance of the proposed network through various experiments. The added attention module can suppress complex backgrounds and extract multiscale pest features more accurately without increasing the number of model parameters. Under the condition of ensuring high accuracy, rapid recognition is realized on images with multiple pests and complex backgrounds. It is verified that our method is of great significance and provides accessible help for the recognition of crop pests.

In this feature, we will use the proposed method to implement a crop pest image recognition system and transplant it into agricultural inspection robots. At the same time, we will also expand a dataset of crop pests in a real agricultural environment to improve the model performance of the robot. It can help farmers accurately distinguish pests, carry out pesticide works according to the types of pests, and successfully realize agricultural modernization and intelligence.

DATA AVAILABILITY STATEMENT

The original contributions presented in the study are included in the article/supplementary material, further inquiries can be directed to the corresponding author/s.

AUTHOR CONTRIBUTIONS

SZ and JL designed the study, performed the experiments, data analysis, and wrote the manuscript. SZ advised on the design of the model and analyzed to find the best method for improve detection accuracy of crop pest. YJ, ZB, and CH collected the data from the website and contributed the information for the data annotation. All authors contributed to the article and approved the submitted version.

FUNDING

This study was supported by the Graduate Research and Innovation Projects of Jiangsu Province (No. KYCX20_3034), the Changzhou Key Research and Development Program (No. CE20202021), the Jiangsu Provincal Key Research and Development Program (No. BE2020383), the Jiangsu Agriculture

1 Science Technology Innovation Fund [No. CX (21)2022], and the Priority Academic Program Development of Jiangsu Higher Education Institutions (No. PAPD-2018-87).

ACKNOWLEDGMENTS

Appreciations are given to the editor and reviewers of the Journal.

REFERENCES

Albanese, A., Nardello, M., and Brunelli, D. (2021). Automated pest detection with DNN on the edge for precision agriculture. *IEEE J. Emerg. Selected Top. Circuits Systems* 11, 458–467.

Almalki, F. A., Soufiene, B. O., Alsamhi, S. H., and Sakli, H. (2021). A low-cost platform for environmental smart farming monitoring system based on IoT and UAVs. *Sustainability* 13:5908.

Alsamhi, S. H., Almalki, F. A., Al-Dois, H., Ben Othman, S., Hassan, J., Hawbani, A., et al. (2021). Machine learning for smart environments in B5G networks: connectivity and QoS. *Comp. Intell. Neurosci.* 2021:6805151. doi: 10.1155/2021/6805151

Ballester, P., and Araujo, R. M. (2016). "On the performance of googlenet and AlexNet applied to sketches," in *Proceedings of the 13th AAAI Conference on Artificial Intelligence*, Phoenix, AZ.

Barbedo, J. G. A. (2014). Using digital image processing for counting whiteflies on soybean leaves. *J. Asia-Pacific Entomol.* 17, 685–694.

Brahimi, M., Boukhalfa, K., and Moussaoui, A. (2017). Deep learning for tomato diseases: classification and symptoms visualization. *Appl. Art. Intell.* 31, 299–315.

Chen, J., Chen, L., and Wang, S. (2019). Pest image recognition of garden based on improved residual network. *Trans. Chin. Soc. Agric. Machi* 50, 187–195.

Chen, J., Liu, Q., and Gao, L. (2021). Deep convolutional neural networks for tea tree pest recognition and diagnosis. *Symmetry* 13:2140. doi: 10.3390/sym13112140

Cheng, X., Zhang, Y., Chen, Y., Wu, Y., and Yue, Y. (2017). Pest identification via deep residual learning in complex background. *Comp. Electron. Agriculture* 141, 351–356. doi: 10.1016/j.compag.2017.08.005

Dawei, W., Limiao, D., Jiangong, N., Jiyue, G., Hongfei, Z., and Zhongzhi, H. (2019). Recognition pest by image-based transfer learning. *J. Sci. Food Agriculture* 99, 4524–4531. doi: 10.1002/jsfa.9689

Dong, L., Zhou, D., and Liu, H. (2019). "A weakly supervised text detection based on attention mechanism," in *Proceedings of the International Conference on Image and Graphics*, (Berlin: Springer), 406–417. doi: 10.1007/978-3-030-34120-6_33

Fina, F., Birch, P., Young, R., Obu, J., Faithpraise, B., and Chatwin, C. (2013). Automatic plant pest detection and recognition using k-means clustering algorithm and correspondence filters. *Int. J. Adv. Biotechnol. Res.* 4, 189–199.

Fukui, H., Hirakawa, T., Yamashita, T., and Fujiyoshi, H. (2019). "Attention branch network: learning of attention mechanism for visual explanation," in *Proceedings of the IEEE/CVF Conference on Computer Vision and Pattern Recognition*, (Piscataway, NJ).

Gandhi, R., Nimbalkar, S., Yelamanchili, N., and Ponkshe, S. (2018). "Plant disease detection using CNNs and GANs as an augmentative approach," in *Proceedings of the 2018 IEEE International Conference on Innovative Research and Development (ICIRD)*, (Piscataway, NJ: IEEE).

Guo, X., Zhou, H., Su, J., Hao, X., Tang, Z., Diao, L., et al. (2020). Chinese agricultural diseases and pests named entity recognition with multi-scale local context features and self-attention mechanism. *Comp. Electron. Agriculture* 179:105830.

He, K., Zhang, X., Ren, S., and Sun, J. (2016). "Deep residual learning for image recognition," in *Proceedings of the IEEE Conference on Computer Vision and Pattern Recognition*, (Piscataway, NJ), 770–778.

Hu, J., Shen, L., and Sun, G. (2018). "Squeeze-and-excitation networks," in *Proceedings of the IEEE Conference on Computer Vision and Pattern Recognition*, (Piscataway, NJ), 7132–7141.

Jin, Y., Liu, J., Xu, Z., Yuan, S., Li, P., and Wang, J. (2021). Development status and trend of agricultural robot technology. *Int. J. Agricultural Biol. Eng.* 14, 1–19. doi: 10.1042/ETLS20200275

King, A. (2017). Technology: the future of agriculture. *Nature* 544, S21–S23.

Leonardo, M. M., Carvalho, T. J., Rezende, E., Zucchi, R., and Faria, F. A. (2018). "Deep feature-based classifiers for fruit fly identification (diptera: Tephritidae)," in *Proceedings of the 2018 31st SIBGRAPI Conference on Graphics, Patterns and Images (SIBGRAPI)*, (Piscataway, NJ: IEEE), 41–47.

Li, X., Li, S., and Liu, B. (2020). Apple leaf disease detection method based on improved Faster R_CNN. *Comp. Eng.* 47, 298–304.

Li, Y., Wang, H., Dang, L. M., Sadeghi-Niaraki, A., and Moon, H. (2020). Crop pest recognition in natural scenes using convolutional neural networks. *Comp. Electron. Agriculture* 169:105174. doi: 10.1016/j.compag.2019.105174

Lim, S., Kim, S., Park, S., and Kim, D. (2018). "Development of application for forest insect classification using cnn," in *Proceedings of the 2018 15th International Conference on Control, Automation, Robotics and Vision (ICARCV)*, (Piscataway, NJ: IEEE), 1128–1131.

Liu, J., and Wang, X. (2021). Plant diseases and pests detection based on deep learning: a review. *Plant Methods* 17:22. doi: 10.1186/s13007-021-00722-9

Liu, L., Wang, R., Xie, C., Yang, P., Wang, F., Sudirman, S., et al. (2019). PestNet: an end-to-end deep learning approach for large-scale multi-class pest detection and classification. *IEEE Access* 7, 45301–45312. doi: 10.1109/access.2019.2909522

Liu, T., Chen, W., Wu, W., Sun, C., Guo, W., and Zhu, X. (2016). Detection of aphids in wheat fields using a computer vision technique. *Biosystems Eng.* 141, 82–93. doi: 10.1016/j.biosystemseng.2015.11.005

Liu, W., Anguelov, D., Erhan, D., Szegedy, C., Reed, S., Fu, C.-Y., et al. (2016). "Ssd: Single shot multibox detector," in *Proceedings of the European Conference on Computer Vision*, (Berlin: Springer), 21–37.

Roy, A. M., and Bhaduri, J. (2021). A deep learning enabled multi-class plant disease detection model based on computer vision. *AI* 2, 413–428. doi: 10.3390/ai2030026

Saleh, H., Alharbi, A., and Alsamhi, S. H. (2021). OPCNN-FAKE: optimized convolutional neural network for fake news detection. *IEEE Access* 9, 129471–129489. doi: 10.1109/access.2021.3112806

Santangelo, G. D. (2018). The impact of FDI in land in agriculture in developing countries on host country food security. *J. World Bus.* 53, 75–84. doi: 10.1016/j.jwb.2017.07.006

Shijie, J., Peiyi, J., and Siping, H. (2017). "Automatic detection of tomato diseases and pests based on leaf images," in *Proceedings of the 2017 Chinese Automation Congress (CAC)*, (Piscataway, NJ: IEEE), 2537–2510.

Shorten, C., and Khoshgoftaar, T. M. (2019). A survey on image data augmentation for deep learning. *J. Big Data* 6, 1–48.

Tang, Z., Yang, J., Li, Z., and Qi, F. (2020b). Grape disease image classification based on lightweight convolution neural networks and channelwise attention. *Comp. Electron. Agriculture* 178:105735. doi: 10.1016/j.compag.2020.105735

Tang, Z., Gao, Y., Karlinsky, L., Sattigeri, P., Feris, R., and Metaxas, D. (2020a). "OnlineAugment: online data augmentation with less domain knowledge," in *Proceedings of the Computer Vision–ECCV 2020: 16th European Conference*, (Glasgow: Springer), 313–329. doi: 10.1007/978-3-030-58571-6_19

Wang, F., Wang, R., Xie, C., Yang, P., and Liu, L. (2020). Fusing multi-scale context-aware information representation for automatic in-field pest detection and recognition. *Comp. Electron. Agriculture* 169:105222. doi: 10.1016/j.compag.2020.105222

Woo, S., Park, J., Lee, J.-Y., and Kweon, I. S. (2018). "CBAM: convolutional block attention module," in *Proceedings of the European Conference on Computer Vision (ECCV)*, eds V. Ferrari, M. Hebert, C. Sminchisescu, and Y. Weiss (Cham: Springer), 3–19. doi: 10.1007/978-3-030-01234-2_1

Xiang, X., Yu, Z., Lv, N., Kong, X., and El Saddik, A. (2020). Attention-Based generative adversarial network for semi-supervised image classification. *Neural Processing Lett.* 51, 1527–1540. doi: 10.1007/s11063-019-10158-x

Yaakob, S. N., and Jain, L. (2012). An insect classification analysis based on shape features using quality threshold ARTMAP and moment invariant. *Appl. Intell.* 37, 12–30. doi: 10.1007/s10489-011-0310-3

Zhang, Y. E., and Liu, Y. P. (2021). Identification of navel orange diseases and pests based on the fusion of densenet and self-attention mechanism. *Comp. Intell. Neurosci.* 2021, 1–12. doi: 10.1155/2021/5436729

Zhong, Y., Gao, J., Lei, Q., and Zhou, Y. (2018). A vision-based counting and recognition system for flying insects in intelligent agriculture. *Sensors* 18:1489. doi: 10.3390/s18051489

Conflict of Interest: The authors declare that the research was conducted in the absence of any commercial or financial relationships that could be construed as a potential conflict of interest.

Publisher's Note: All claims expressed in this article are solely those of the authors and do not necessarily represent those of their affiliated organizations, or those of the publisher, the editors and the reviewers. Any product that may be evaluated in this article, or claim that may be made by its manufacturer, is not guaranteed or endorsed by the publisher.

frontiers in Plant Science

ORIGINAL RESEARCH
published: 10 March 2022
doi: 10.3389/fpls.2022.815218

Autonomous Navigation System of Greenhouse Mobile Robot Based on 3D Lidar and 2D Lidar SLAM

Saike Jiang[1,2], *Shilin Wang*[2,3], *Zhongyi Yi*[2,3], *Meina Zhang*[2] *and Xiaolan Lv*[1,2]*

[1] School of Agricultural Engineering, Jiangsu University, Zhenjiang, China, [2] Institute of Agricultural Facilities and Equipment, Jiangsu Academy of Agricultural Science, Nanjing, China, [3] Key Laboratory for Protected Agricultural Engineering in the Middle and Lower Reaches of Yangtze River, Ministry of Agricultural and Rural Affairs, Nanjing, China

The application of mobile robots is an important link in the development of intelligent greenhouses. In view of the complex environment of a greenhouse, achieving precise positioning and navigation by robots has become the primary problem to be solved. Simultaneous localization and mapping (SLAM) technology is a hot spot in solving the positioning and navigation in an unknown indoor environment in recent years. Among them, the SLAM based on a two-dimensional (2D) Lidar can only collect the environmental information at the level of Lidar, while the SLAM based on a 3D Lidar demands a high computation cost; hence, it has higher requirements for the industrial computers. In this study, the robot navigation control system initially filtered the information of a 3D greenhouse environment collected by a 3D Lidar and fused the information into 2D information, and then, based on the robot odometers and inertial measurement unit information, the system has achieved a timely positioning and construction of the greenhouse environment by a robot using a 2D Lidar SLAM algorithm in Cartographer. This method not only ensures the accuracy of a greenhouse environmental map but also reduces the performance requirements on the industrial computer. In terms of path planning, the Dijkstra algorithm was used to plan the global navigation path of the robot while the Dynamic Window Approach (DWA) algorithm was used to plan the local navigation path of the robot. Through the positioning test, the average position deviation of the robot from the target positioning point is less than 8 cm with a standard deviation (SD) of less than 3 cm; the average course deviation is less than 3° with an SD of less than 1° at the moving speed of 0.4 m/s. The robot moves at the speed of 0.2, 0.4, and 0.6 m/s, respectively; the average lateral deviation between the actual movement path and the target movement path is less than 10 cm, and the SD is less than 6 cm; the average course deviation is $<3°$, and the SD is $<1.5°$. Both the positioning accuracy and the navigation accuracy of the robot can meet the requirements of mobile navigation and positioning in the greenhouse environment.

Keywords: greenhouse, mobile robot, navigation, Lidar, SLAM

OPEN ACCESS

Edited by:
Changyuan Zhai,
Beijing Academy of Agricultural and Forestry Sciences, China

Reviewed by:
Azlan Zahid,
Texas A&M University, United States
Baohua Zhang,
Nanjing Agricultural University, China

***Correspondence:**
Xiaolan Lv
lxlanny@126.com

Specialty section:
This article was submitted to Sustainable and Intelligent Phytoprotection, a section of the journal Frontiers in Plant Science

Received: *15 November 2021*
Accepted: *27 January 2022*
Published: *10 March 2022*

Citation:
Jiang S, Wang S, Yi Z, Zhang M and Lv X (2022) Autonomous Navigation System of Greenhouse Mobile Robot Based on 3D Lidar and 2D Lidar SLAM. Front. Plant Sci. 13:815218. doi: 10.3389/fpls.2022.815218

INTRODUCTION

With the development of mechanization and automation, agriculture has undergone an accelerated upgrading toward information and intelligent agriculture in the world. Also, with the development of high technology and with the incremental labor cost, the application of robots in agriculture has become more and more extensive. Compared with the complex field environment, the greenhouse environment is relatively simple; however, in greenhouses where plants are densely distributed under high temperature and high humidity, and, sometimes, even toxic gases are emitted, there are some potential safety hazards in manual operation (Henten et al., 2013). Therefore, robots enjoy a large application market in picking, plant protection, inspection, and other aspects of greenhouses (Uyeh et al., 2019).

In terms of the autonomous navigation of robots, the navigation solutions based on Global Navigation Satellite System (GNSS) have been fully applied in the field operations environment (Pérez Ruiz and Upadhyaya, 2012). However, as there are many obstructions in greenhouses to cause the loss of satellite signals, the greenhouse environment is not suitable for mobile robots. Path planning and movement, which are safe, fast, and effective, have become the primary difficulties in the application of greenhouse mobile robots.

The guide rail navigation is a common navigation solution for greenhouse mobile robots. It realizes the mobile navigation in greenhouses by laying rails on the ground (Chiu et al., 2013; Hayashi et al., 2014; Lee et al., 2015). Considering the high cost of the rail laying and the occupation of the ground in greenhouses, some robots that use greenhouse pipes as motion guide rails have been developed, and these robots can move along the pipes or on the ground (Zhao et al., 2016; Arad et al., 2020). To further improve the safety and practicability of the robots on guide rails, Balaso et al. (2013) installed a distance sensor, a photoelectric sensor, and an ultrasonic sensor to assist the navigation of the designed multi-functional greenhouse robot. Although the guide rail navigation is simple in operation, the fixed rails greatly limit the movement path and the range of the robot. Magnetic navigation and ribbon navigation through the magnetic stripes and ribbons replace the rails in the guide rail navigation. Magnetic navigation realizes path tracking by detecting the electromagnetic signals installed on the ground (Pan et al., 2019), and the color band navigation uses visual sensors to detect the edge of the color band to achieve navigation (Min et al., 2014). Compared with the guide rail navigation, the installation cost of magnetic stripes and color bands is relatively low and does not occupy the greenhouse space; moreover, their laying and installation are simpler and more flexible. Nevertheless, they could not get rid of the movement restrictions by fixed routes.

Machine vision navigation uses monocular vision or stereo vision sensors to collect environmental information then extract the navigation paths or crop lines based on the Hough Transform (Hough, 1962), the least-Square Methods (Cui et al., 2015; Mao et al., 2019), and the binocular stereo vision algorithms (Zou et al., 2012). Wang et al. (2012) analyzed the distribution characteristics of each component of the road image between the tomato ridges in the Hue, Saturation and Intensity (HSI) color space and then proposed a greenhouse tomato path detection method between the ridges based on the least square method. The experimental results showed that the proposed method could accurately extract the edge information of the target sensitive area; there was a 91.67% accuracy rate of extracting the navigation path between the tomato ridges with different coverage. In view of the problems of poor recognition of visual navigation technology and vulnerability to illumination, Gao and Ming (2014) selected the H component in the HIS color space for subsequent image processing and introduced the K-means algorithm to cluster and to segment the image for the unique color characteristic information of greenhouse. Chen et al. (2021) proposed a Hough transform algorithm for the prediction point by using a new graying factor to segment cucumber plants and soil, and this proposed algorithm is used for prediction points to fit the navigation paths. This algorithm is 35.20 ms faster than the traditional Hough Transform. The robot uses the machine vision sensor, which is carried by itself to autonomously navigate, thus saving the cost of setting up the environment in the early stage. However, the navigation path of the robot needs to be fitted after extracting the greenhouse vegetation or the roadside information each time, so the path of the robot is subject to environmental constraints, which further limits the space for robot movements.

The positioning and navigation method, based on multi-source data fusion, is the current hotspot in the research of the navigation of greenhouse mobile robots. In this navigation environment, the robot can move freely within a greenhouse. In general, the navigation by fusing multi-source data can be divided into two types: one is to achieve precise positioning and navigation by arranging sensors in the environment with the assistance of an inertial measurement unit (IMU), an odometer, and other modules that are carried by the robot itself; the other is to achieve the positioning and navigation directly by the sensor that is carried by the robot itself. Widodo et al. (2012) applied the acoustic positioning system in the greenhouse for the first time. To reduce the time consumed in manual deployment and calibration, Widodo et al. (2013) subsequently designed a self-calibrating acoustic positioning system. Huang et al. (2020a) proposed a spread spectrum sound-based local positioning system for greenhouse robots, and Tsay et al. (2020) added a temperature compensation on this basis. In addition to a sound-based positioning system, Preter et al. (2018) designed a strawberry harvesting robot, which uses an ultra-wideband indoor positioning system, wheel encoders, and a gyroscope to achieve positioning and navigation in the greenhouse. The development of indoor navigation technologies, such as radio frequency identification (Choi et al., 2011; Ming, 2018), Bluetooth low energy (Spachos et al., 2021), and positioning by signal strength (Huang et al., 2020b), provide more options for greenhouse mobile robot navigation. However, for all the above navigation solutions, it is necessary to arrange base stations, tags, and other external sensors in advance in the greenhouse. Although the installation procedures are much simpler than the guide rail navigation, the magnetic navigation, and the color band navigation, the technology of positioning and navigation through the sensors, as carried by the robot itself, eliminates these extra

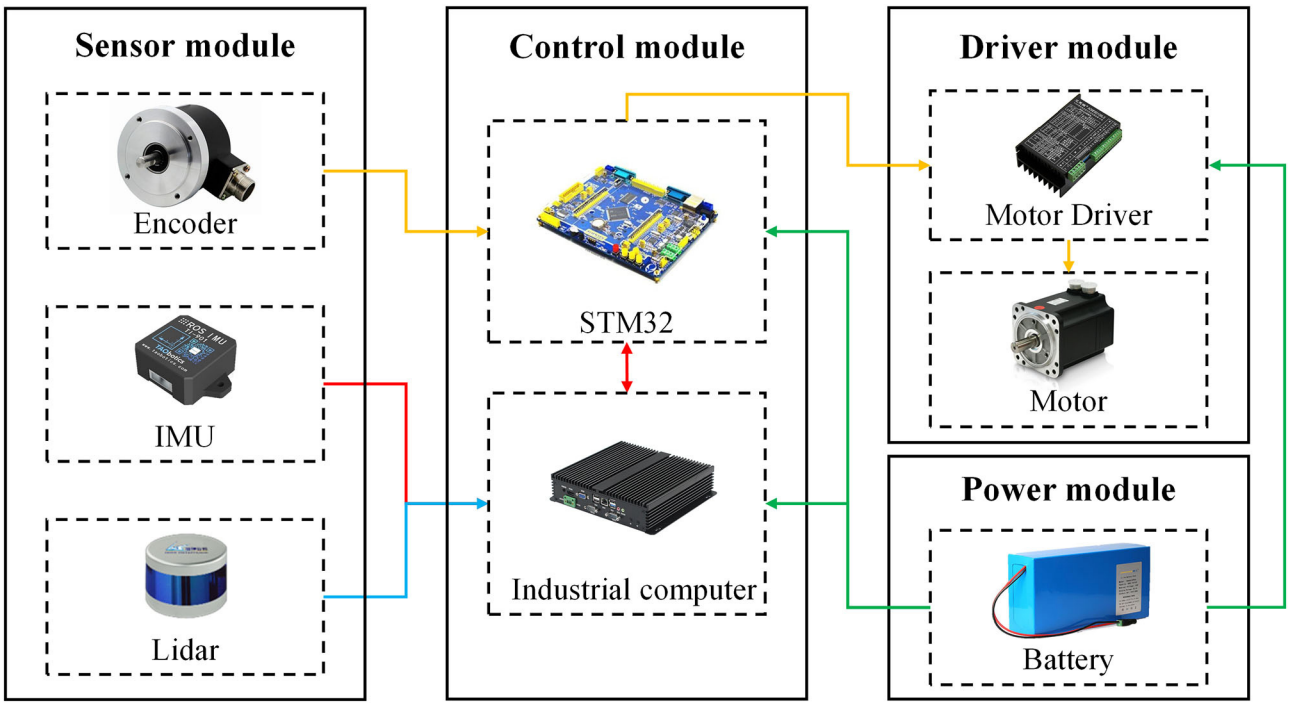

FIGURE 1 | Hardware structure diagram of the robot navigation system.

steps. In an unknown environment, the robot uses the sensors it carries to achieve navigation. The first and most important thing is that the robot knows its location. The SLAM technology can help the robot build an environment map and estimate its posture well. According to the types of sensors, the SLAM technology can be divided into visual SLAM technology and Lidar SLAM technology. In comparison, since the visual sensor is susceptible to the influence of light intensity, the visual SLAM technology has poor mapping performance in the poor light environment; while the Lidar SLAM technology is not affected by light, with higher accuracy, less calculation, and more mature technology (Chan et al., 2009). The SLAM technology, based on two-dimensional (2D) Lidar, has achieved good results in the research of greenhouse mobile robot navigation (Juan et al., 2016; Obregón et al., 2019; Hou et al., 2020; Tiwari et al., 2020). However, the environment detected by 2D Lidar is only on the same horizontal plane as the installation position of the Lidar on the robot. More stringent requirements are needed for the installation of Lidar and the greenhouse environment. At the same time, the Lidar cannot detect the environmental information above and below itself. Therefore, it leaves a huge potential safety hazard in robot navigation. The SLAM technology, based on three-dimensional (3D) Lidar, can detect all the environmental information of the greenhouse, which enhances the safety of the robot when it moves, but it also increases the computational burden of the robot and puts forward higher requirements on the computational performance of the robot.

Based on the Robot Operating System (ROS), this study proposed a new positioning and navigation solution for greenhouse mobile robots by combining the SLAMs of both 3D Lidar and 2D Lidar. First, the 3D point cloud data, collected by multi-line Lidar, were filtered and were fused into 2D data. The 2D information after the fusion contained the location information of key points, within the motion range of the robot, to the maximum extent. Then, the 2D Lidar SLAM algorithm, based on the encoder information and IMU information, was used to build the environment map, and the optimal navigation path was further planned to achieve the positioning and navigation of the greenhouse mobile robot, which not only ensured the safety of the robot mapping navigation but also reduced the energy consumption in data calculation by the robot.

MATERIALS AND METHODS

Hardware System Design

The designed hardware system of the greenhouse mobile robot is mainly composed of the sensor module, the control module, the driver module, and the power module. The hardware system structure is shown in **Figure 1**.

Sensor Module

The sensor module of the robot was mainly composed of an encoder, an IMU, and a Lidar. The encoder is composed of a 1,024-line photoelectric incremental code disc, which collected the real-time speed information of the robot and sent feedback to the bottom controller of the robot. The inertial measurement unit has the 9-axis IMU (HFI-A9, HandsFree, Shenzhen, China), which includes a 3-axis gyroscope, a 3-axis accelerometer, and

a 3-axis magnetometer. The internal integrated posture solver, with the assistance of the dynamic Kalman filter algorithm, can accurately output the real-time posture of the robot in a dynamic environment, thus providing accurate calculation data for the determination of the position of the robot in the greenhouse, such as Euler angles, quaternions, and the most commonly used roll/pitch/yaw direction data. The Lidar contains 16 pairs of Lidar transmitting and receiving modules (C16, Leishen Intelligent, Shenzhen, China). By adopting the time of fight measurement method, with a vertical resolution of 1.33°, the internal motor can be driven at a speed of 5 Hz (or 10 or 20 Hz) for 360° scanning. The 100M Ethernet UDP/IP communication protocol is used for data output and configuration.

Control Module

The STM32F103 embedded system board was adopted in the bottom controller of the robot. The core of the system board is a 32-bit high-performance ARM Cortex-M3 processor with a maximum operating frequency of 72 MHz. It has built-in high-speed memory, abundant enhanced I/O ports, and peripherals connected to two advanced peripheral buses (APBs). The power supply voltage is 2– to 3.6 V, and a series of power-saving modes can ensure the needs of the low-powered applications. The bottom controller is connected to the motor driver, the encoder, and the upper computer. According to the real-time speed information provided by the encoder, the STM32 can use the classic proportional-integral-derivative (PID) algorithm to control the motor rotation through the motor driver, to realize the precise movement of the robot. In addition, to enhance the safety of the robot during the movement, the bottom controller will limit the output of the driver and pull up the robot slowly when the temperature of the motor driver is higher than the protection temperature.

The top control of the robot was equipped with an industrial computer as the upper computer (EPC-P3086, Dongtintech, Shenzhen, China), and the Ubuntu18.04 operating System and ROS were installed respectively. The bottom control and the top control of the robot were connected through the control area network (CAN) bus protocol. The communication baud rate is 500K and the message format is MOTOROLA. Through the CAN bus interface, the PC can realize the control of the linear velocity and angular velocity of the mobile robot. Meanwhile, the PC will also receive real-time feedback of the motion state information of the robot.

Driver Module

A total of four 200-W DC brushless servo motors (SDGA-02C11AB24, Tode, Jiaxing, China) were installed at the front and rear of the robot, and a gearbox of 1:30 was equipped to provide sufficient power for the robot (60TDF-147050-L2-H, Tode, Jiaxing, China). The no-load maximum speed is 1.5 m/s. The driving form of the robot was four-wheel independent driving, using a four-wheel differential steering, which could realize a spot turn. In addition to the above functions, the power module of the robot also adopted the composite design of inflatable rubber wheels and independent suspension, which equipped the robot with strong ground clearance and ground adaptability. The robot climbing angle is up to 30°, and the minimum clearance from the ground is 135 mm, which can meet the flexible movement of the robot on different types of ground in the greenhouse.

Power Module

The power module of the robot adopted a 24-V ternary lithium battery (LS-DL24-30, Lishen Energy, Shenzhen, China). The battery voltage is about 29.2 V when it is fully charged with the capacity of 30 Ah. It has a built-in voltage regulator module and a power display module. Under normal circumstances, it can supply power continuously for 3–5 h. When the battery voltage is less than 22.5 V, the robot chassis will automatically alarm with a buzzer, and it will take about 3 h to fully recharge.

Software System Design

The overall software system of the greenhouse mobile robot was designed based on Ubuntu 18.04, as shown in **Figure 2**. It included an application layer, a control layer, and a driver layer. The most important part was the control layer, which was developed based on ROS. It was responsible for the collection, fusion, and processing of information from robot sensors and then for completing the map construction, path planning, and autonomous positioning and navigation according to control instructions. The ROS has a distributed architecture that allows each functional module in the framework to be individually designed, compiled, and loosely coupled together at run time.

Implementation Principles of Navigation Function

The framework of robot navigation function realization in the greenhouse is shown in **Figure 3**. First, the 3D point cloud data collected by 3D Lidar were filtered and fused into 2D Lidar, and then, the 2D Lidar SLAM algorithm was used to construct the greenhouse environment map based on the data. The positioning of the robot in an unknown environment was mainly realized by the Adaptive Monte Carlo Localization (AMCL) algorithm. Robot target point path planning was the focus of navigation function realization. It was divided into two parts: global path planning and local path planning, which were based on the global cost map and the local cost map, respectively. Finally, the robot integrated the above information in the ROS visualization (RVIZ) tool provided by ROS and used the multi-target navigation settings to realize the robot's mobile navigation in the greenhouse.

Multi-Line Lidar Point Cloud Filtering and Fusion

The data transmission between different nodes in ROS is mainly achieved through the communications of Topic, Service, and Parameter Server. The ROS specifies different standard data message types for different sensors, among which the Lidar data is divided into two types: LaserScan.msg (2D Lidar) and PointCloud2.msg (3D Lidar). In this article, both the acceptance and the transmission of Lidar data involved in the robot used the Topic communication based on TCP. Compared with single-line Lidar, multi-line Lidar contains 3D coordinates and intensity of each point cloud data for each frame. By setting the point cloud conversion node, on the one hand, Lidar's topic can be

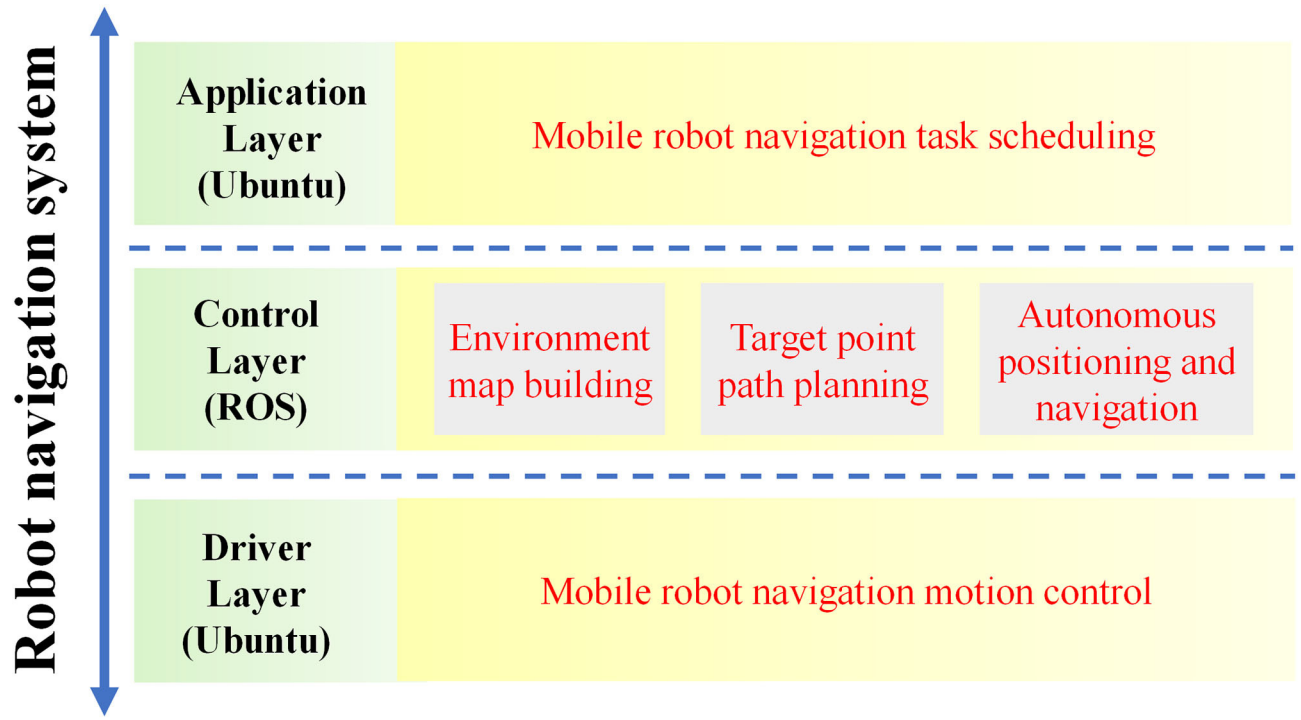

FIGURE 2 | Software structure diagram of the robot.

subscribed through the Topic communication and can constantly accept the 3D point cloud data. The 3D point cloud data beyond the height range of the robot's movement height is filtered, while the 3D point cloud data within the height range is fused layer by layer, and the points with the shortest distance within the same height range are selected as the last output data. On the other hand, the point cloud conversion node releases the Laser topic to the 2D Lidar SLAM node and outputs the filtered and fused Lidar data, thus, greatly retaining the key point environment information within the range of the robot movement in the map.

The specific process of the multi-line Lidar point cloud filtering and fusion algorithm used by the robot is shown in **Figure 4**. Each frame of Lidar point cloud data is composed of its corresponding three-dimensional coordinates. The position information of the point cloud is clear after knowing its coordinate information. Firstly, the 16 pairs of point cloud data, whose height and range fall beyond the threshold range, were sequentially filtered by setting the height threshold and the range threshold, and the point cloud data within the threshold are retained. Then, the point cloud data of the same height were compared at certain size angles. Finally, the data with the smallest range were saved as the final collected data. Through this algorithm, the robot could quickly and effectively compress the greenhouse 3D environment into 2D, which provided accurate and stable environmental information for subsequent mapping and navigation.

The higher the frequency and the greater the resolution of Lidar, the more environmental information can be obtained at the same time, but the huge amount of data also increases the burden of data processing for the robot. Considering the amount of Lidar data and the data processing capability of the computer, the Lidar frequency was set to 10 Hz, its horizontal resolution was 0.18°, and the number of points per second was 320,000. To reduce the loss in the process of Lidar data transmission, the angle increment of Lasersacn output by the point cloud conversion node took the same value as the horizontal resolution of Lidar; the scanning angle range was from and −3.14 to 3.14, and the scan topic publishing frequency and Lidar point cloud topic publishing frequency were the same to set to 5 Hz. The height of the robot was 0.3 m, and the Lidar was installed at 0.25 m above the robot. Since the converted Lidar data were a LaserScan on the same plane as the Lidar, the height threshold was set from −0.47 to 0.1 m. The measurement range of the Lidar was from 0.15 to 150 m. Considering the actual size of the greenhouse, the range threshold was finally from 0.15 to 50 m.

Environment Map Construction

The environment map construction is an important part of the robot navigation and the control system. The quality of map construction directly affects the accuracy of the robot in the navigation and positioning process. The current popular 2D Lidar SLAM algorithms include Hector SLAM, G mapping, Karto SLAM, etc. By comparing the algorithms in the simulation environment, actual environment, and CPU consumption (Santos et al., 2013; Hess et al., 2016), this study finally chose to refer to the Cartographer SLAM algorithm developed by

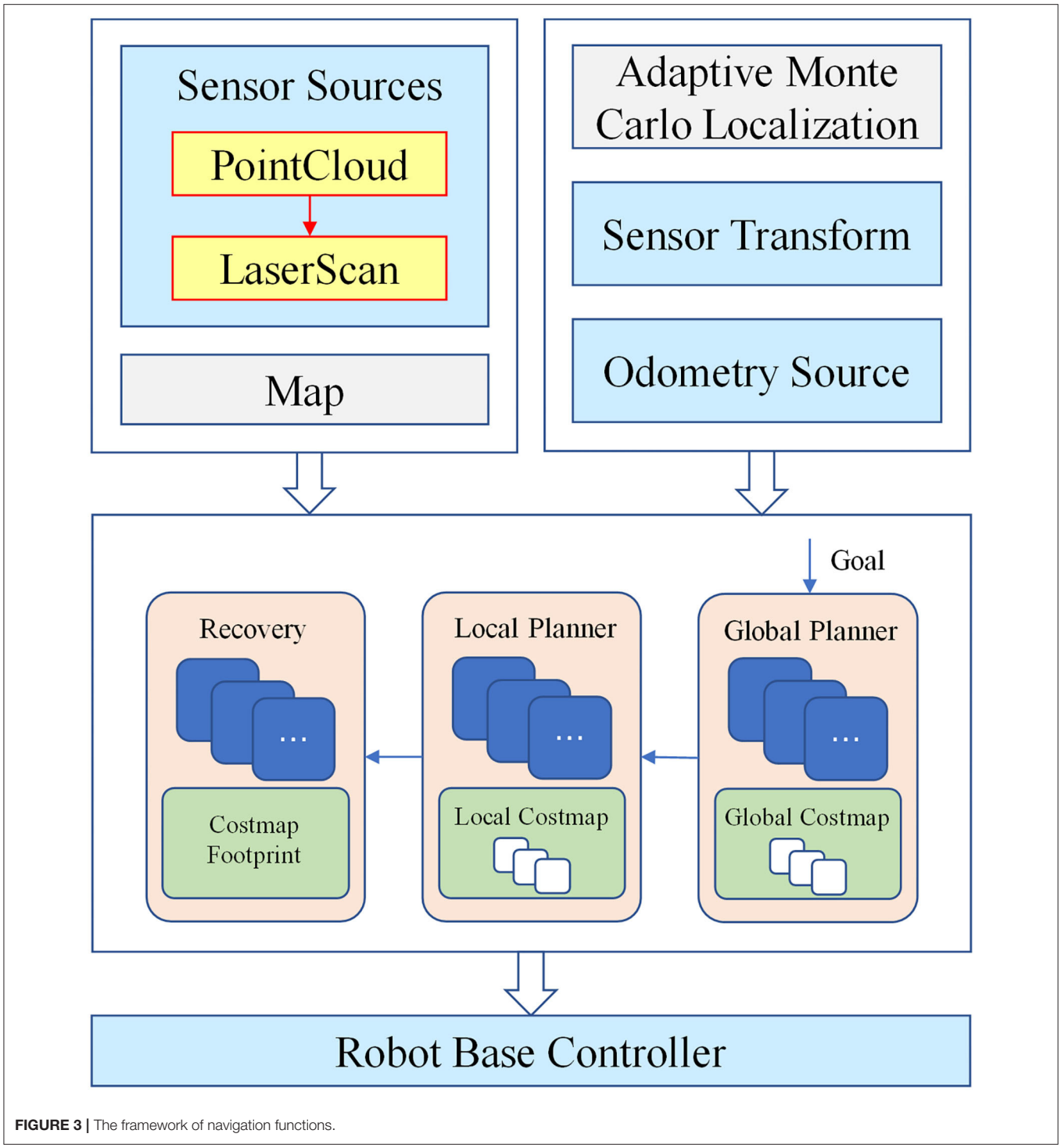

FIGURE 3 | The framework of navigation functions.

Google. The algorithm adopts the idea of constructing a global map based on sub-maps; each frame of the laser scan data obtained is inserted into the submap at the best-estimated position using a scan match, and the generated submap performs a local loop closure and a global loop by a branch-and-bound approach and several precomputed grids. Cartographer is more advantageous in terms of mapping effects, data processing, and sensor requirements. After the algorithm processing, the robot can finally generate a 2D grid map with a precision of 5 cm.

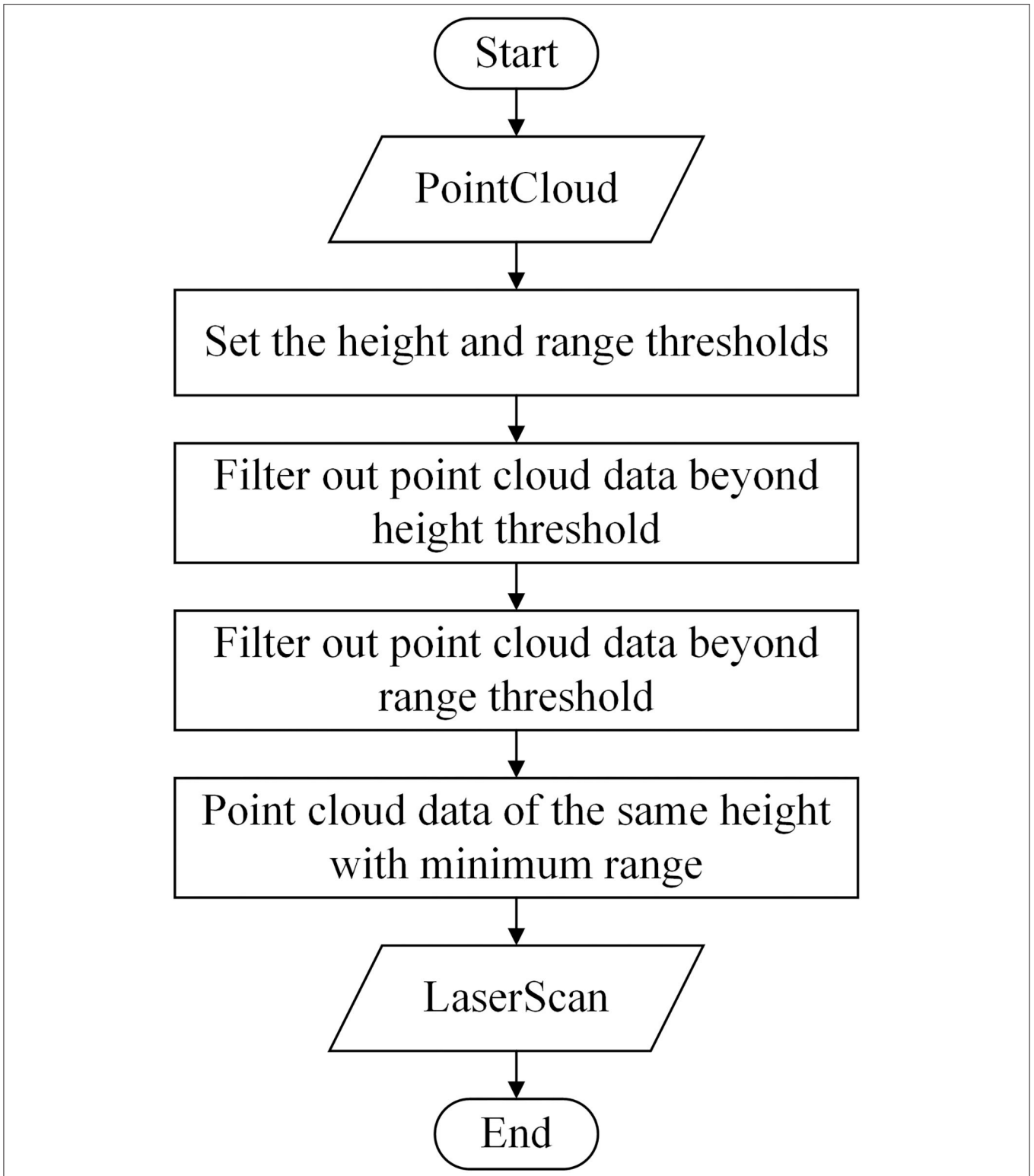

FIGURE 4 | Flowchart of point cloud filtering and fusion.

The Cartographer algorithm is mainly composed of two parts: Local SLAM and Global SLAM. In the part of Local SLAM, odometry and IMU data are used to calculate the estimation value of posture of the robot ξ, $\xi = (\xi_x, \xi_y, \xi_\vartheta)$, and this value is used as the initial value to scan and to match the Lidar data, and the scanned data is recorded as $H = \{h_k\}_{k=1,\cdots,k}, h_k \in R^2$. After

the motion filtering, each frame of Lidar data is superimposed to form a submap. The position of $\{h_k\}$ in submap is expressed as T_ξ, and its transformation formula is as follows:

$$T_\xi p = \underbrace{\begin{pmatrix} cos_{\xi_\theta} & -sin_{\xi_\theta} \\ sin_{\xi_\theta} & cos_{\xi_\theta} \end{pmatrix}}_{R_\xi} p + \underbrace{\begin{pmatrix} \xi_x \\ \xi_y \end{pmatrix}}_{t_\xi} \quad (1)$$

where p represents the coordinates of the robot before the transform, R_ξ represents the rotation matrix, and the t_ξ represents the translation matrix.

The part of Global SLAM is responsible for the loopback detection and back-end optimization, so that small submaps form a whole Global map. The optimization problem of loopback is a nonlinear least squares problem, which can be described as

$$\arg\min_{E^m,E^s} \frac{1}{2} \sum_{ij} \rho(E^2(\xi_i^m, \xi_j^s; \Sigma_{ij}, \xi_{ij})) \quad (2)$$

where $E^m = \{\xi_i^m\}_{i=1,\cdots,m}$ is the submap posture, $E^s = \{\xi_j^s\}_{j=1,\cdots,n}$ is the scan posture, ρ is the loss function, E is the residual function, and these postures are all in the world coordinate system.

To obtain a more accurate map, the robot used the IMU coordinate system as the ROS coordinate system tracked by the SLAM algorithm and the odometer to publish the pose coordinates. The robot controlled the node through a keyboard to walk in the greenhouse at a speed of 0.4 m/s to build a map. After the map was completed, the global environment map was

Algorithm 1 Dijkstra Algorithm

```
Input: map, the starting point S, the goal point G
Output: the shortest path SP
Init openlist[], closedlist[]
While (openlist[] is not empty)
    Centre = the point with the shortest distance in openlist[]
    put Centre from openlist[] to closedlist[]
    If (Centre is not G) Then
        extract path, break
    Else iterate over eight adjacent points
        If (point is in closedlist[] or encounter an obstacle) Then
            skip this point
        Else cumulative the path
            If (point is in openlist[]) Then
                If (the cumulative distance < the original recorded distance) Then
                    replace the data
                Else add the point to openlist[]
                End If
            End If
        End If
        arrange the points in openlist[] from small to large
    End If
End While
```

FIGURE 5 | The pseudo-code of the Dijkstra algorithm.

saved in pgm format through the map server node. In the picture, the probability of the existence of obstacles was represented by different grayscale values and for subsequent navigation.

Path Planning

The path planning of the robot in the greenhouse is completed based on the built map; however, the original map is static and the obstacle information on the map cannot be updated in real time. Therefore, a costmap is introduced in the robot's path planning. Costmap is mainly composed of Static Map Layer, Obstacle Map Layer, and Inflation Layer. The Static Map Layer usually includes the loaded original map data. The Obstacle Map Layer includes the real-time obstacle information detected by sensors. The Inflation Layer expands the obstacle according to the expansion radius parameter to make the robot move more safely.

The path planning of the robot in the greenhouse was divided into two parts: global path planning and local path planning. The robot first used the global path planner to plan a rough path in combination with the global costmap, then the local path planner divided the planned path into many small paths on this basis, and finally, the local path planner performed the local path planning by referring to the local costmap. In this way, not only the obstacles saved in the map could be avoided in the global path planning, but also the new obstacles and dynamic obstacles could be avoided in the local path planning. The robot navigation target points setting was realized through the Publish Point function in the RVIZ visualization interface. When the mouse was clicked on the RVIZ map interface using the Publish Point function, the Topic communication would be used to publish the location information of the point in the map to the outside world. By setting the node to subscribe to the topic and store the set target points in sequence, the target point information was further published to the navigation node in sequence, and the path planning and multi-target point navigation were completed one by one.

The global path planning of the robot adopts the Dijkstra algorithm, and the algorithm is shown in **Figure 5**. First, the starting point and the goal point of the robot navigation is set; then, two arrays to store the points of the path to be determined and the points of the determined path are set up,

Algorithm 2 DWAAlgorithm

Input: robotPose, robotGoal, robotModel
Output: the best v and ω
While (not arrived the goal)
    For v in arrange($v_\omega[]$,v_{reso}) **Do**
        For ω in arrange($v_\omega[]$,ω_{reso}) **Do**
            Traj = Calculate_Traj(x, [v, ω])
            goal_score = Goal_Cost(goal,traj)
            vel_score = Velocity_Cost(traj)
            obs_score = Obstacle_Cost(traj,Obstacle)
            score = goal_score + vel_score + obs_score
            If (min_score >= score) **Then**
                min_score = score
                u = array([v, ω])
                best_traj = traj
            End If
        End For
        return u,best_traj
    End For
End While

FIGURE 6 | The pseudo-code of the DWA algorithm.

respectively; and next, the distance between the center point and the adjacent 8 points is calculated using the starting point as the center point. Later, we stored the point with the smallest distance, considered the point with the smallest distance as the center point, and calculated the distance between the starting point and the adjacent points from the center point again. For the points that have been calculated, we selected the solution with the smallest distance. In this way, the adjacent points are continuously calculated until the target point is encountered, and the shortest path planning route is output. In general, the algorithm calculates and compares the weights of nodes in the graph from the global perspective to obtain the global shortest path.

The Dynamic Window Approach (DWA) algorithm is adopted for the robot's local path planning, and the algorithm is shown in **Figure 6**. The main process includes four parts: initialization, sampling speed samples, sample scoring, and release plan. First, we load the instance of the subclass in BaseLocalPlanner through the class loading module and call its initialization function to obtain the initial state information of the robot and further obtain the trajectory motion model of the robot. Based on the trajectory motion model, the robot can calculate its motion trajectory according to its motion speed. In order to obtain a sample of the robot motion speed, it is necessary to collect the linear speed and the angular speed of each dimension of the robot through sensors within a certain time interval and store them in the corresponding container in the form of a structure. After obtaining the robot speed sample, the corresponding motion trajectory is deduced according to the robot sampling speed simulation, and each trajectory is evaluated through the trajectory evaluation function, as shown in formula (3).

$$G(v,\omega) = \max(\varphi head(v,\omega) + \beta dist(v,\omega) + \delta velo(v,\omega)) \quad (3)$$

where $head(v, \omega)$ and $velo(v, \omega)$ are given by the formula

$$head(v,\omega) = 1 - |\theta| / \pi \quad (4)$$

$$velo(v,\omega) = v/\pi \quad (5)$$

FIGURE 7 | Test environment and robot.

where *head* (v, ω) represents the proximity between the velocity trajectory and the target point, and θ represents the included angle between the motion direction and the destination point. The *dist*(v, ω) represents the distance from the motion estimation to the nearest obstacle at this sampling speed. If there is no obstacle, the value is a constant. *The velo*(v, ω) represents the

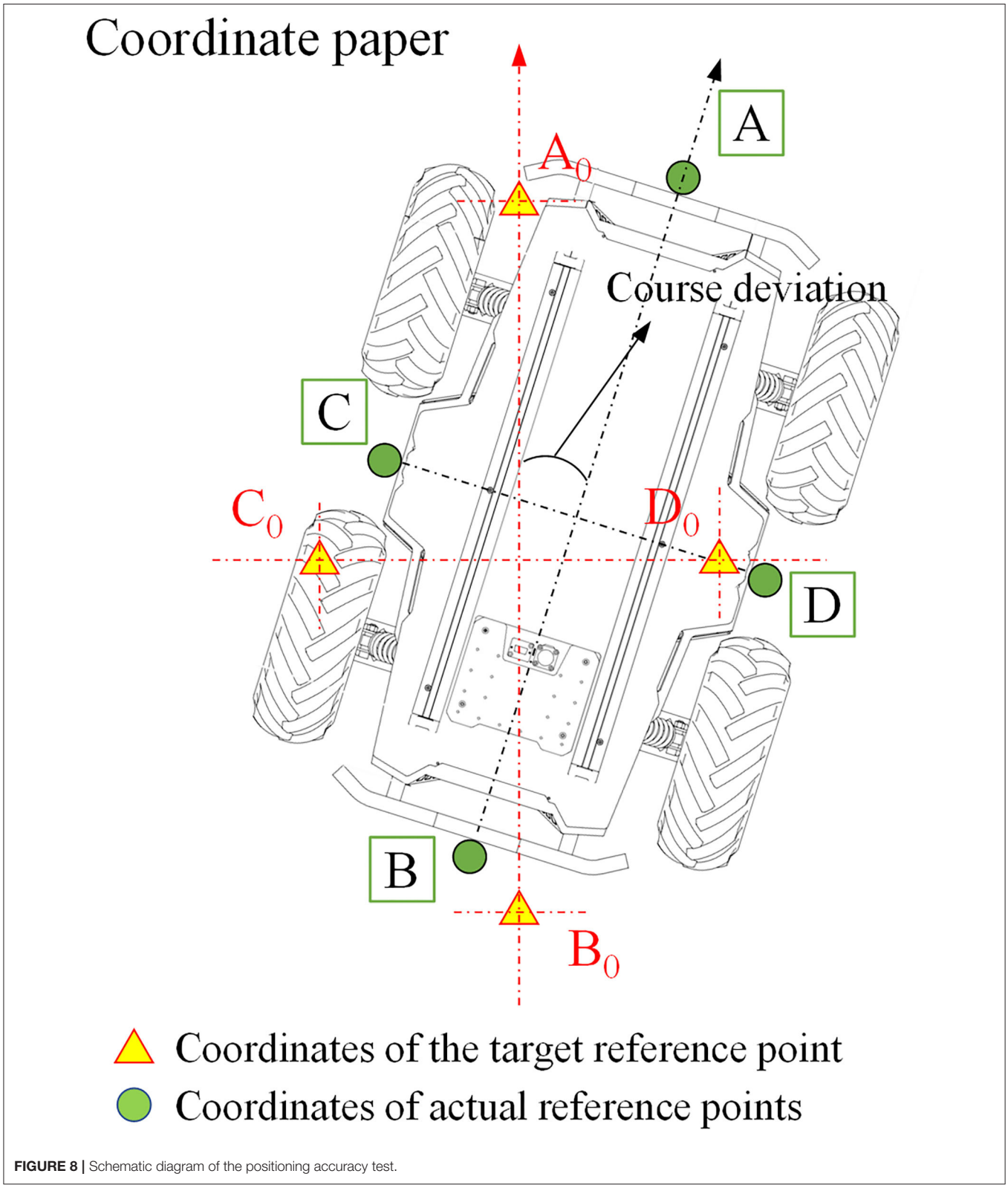

FIGURE 8 | Schematic diagram of the positioning accuracy test.

forward efficiency of the robot under this speed group. The three constant term factors, φ, β, and δ, represent the proportion of the three sub-items in the evaluation function, respectively. Adjusting the three constant factors will affect the actions of the robot in local obstacle avoidance. Finally, all speed groups are evaluated by the above formula, and the speed with the highest score is selected as the current speed command for the movement of the robot.

EXPERIMENTAL RESULTS AND DISCUSSION

The test site is in the Institute of Agricultural Facilities and Equipment, Jiangsu Academy of Agricultural Sciences, Jiangsu province, China, as shown in **Figure 7**. The experimental greenhouse is a glass greenhouse, in which tomatoes are grown in the cultivation tanks, and the row spacing between the cultivation tanks is 1 m.

Robot Positioning Accuracy Test

The robot positioning accuracy test is an effective way to verify the precision and the reliability of the robot navigation system. To accurately measure the position and the posture of the robot at the target points, four target points in the robot greenhouse navigation path were randomly selected, and the positioning coordinate tags were pasted on these four target points. The schematic diagram of the robot positioning accuracy test is shown in **Figure 8**. The four points, such as the front, rear, left, and right, of the robot were randomly selected as the relative reference positions, and a cross laser (Qy-620, Huimei, Dongguan, China) on each of the four points was installed. After the robot reaches the target point and stops, the coordinate position of the laser shot by the laser was recorded accurately on

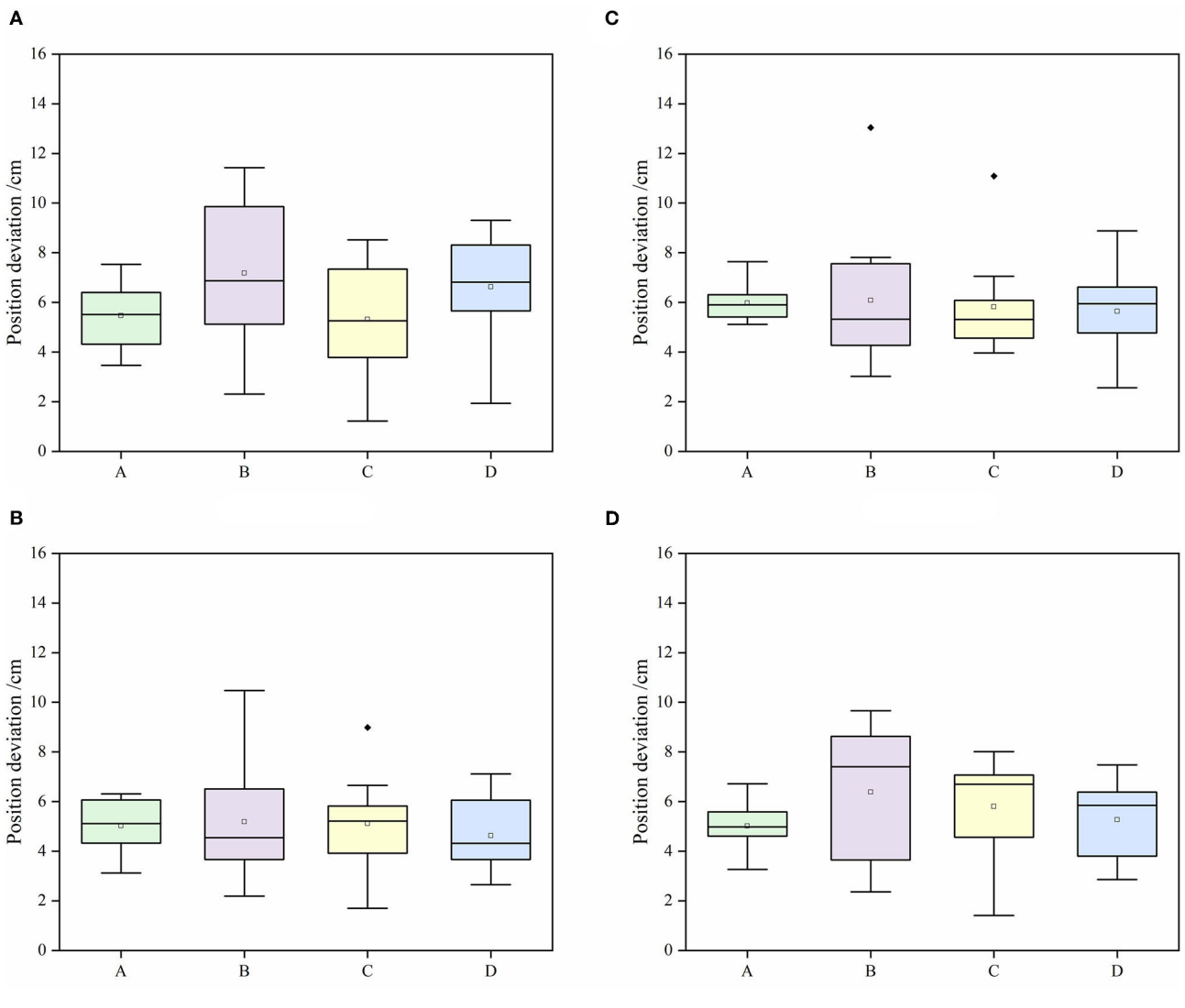

FIGURE 9 | Positioning deviation of the robot at each target point. **(A)** Target 1, **(B)** target 2, **(C)** target 3, **(D)** target 4.

the coordinate tags. The robot completed 10 complete navigation and positioning tests in sequence at a speed of 0.4 m/s. After each test, the robot needed to be repositioned to its initial position to avoid the accumulation of errors during the test and to ensure the independence of the test.

Quantitative analysis is made on the navigation accuracy of the robot. The position deviation and absolute heading deviation of the four relative reference positions on the robot at the four target points are shown in **Figures 9**, **10**.

It can be seen from **Figures 9**, **10** that at a speed of 0.4 m/s, the average absolute position deviation of the robot is less than 8 cm, and the SD is less than 3 cm. The average heading deviation of the robot is less than 3°, and the SD is less than 1°. The precision can meet the requirements of the robot positioning in a greenhouse environment. Although the average positioning accuracy of the robot at the four points is not very different, it is still found that target point 2 and point 3 have abnormal points in the test after comparison. By analyzing the position of the target points, the target point 1 and point 4 are close to the two ends of the cultivation tanks, the target point 2 and point 3 are close to the middle of the cultivation tanks, and the structured feature information of target point 1 and point 4 are more than the target point 2 and point 3, such as greenhouse walls and air conditioners, and the environmental information around target point 2 and point 3 are mostly from cultivation tanks and plant leaf walls, with high similarity. So, we think that adding some different objects with structural features in different positions in the greenhouse can improve the positioning accuracy of the robot. The localization system of the robot was implemented based on AMCL, which used particle filters to track the robot's pose against a known map. In general, the more particles there are, the more accurate the positioning is, but the higher the CPU consumption is as well. To achieve a more accurate positioning of the robot under the existing computing power of the robot, we set the maximum number of particles allowed by the positioning algorithm to 4,000 and the minimum number of particles to 1,000. Through continuous testing, the robot had a good performance under this parameter.

Robot Navigation Accuracy Test

The robot navigation accuracy test is the most direct and effective method to test the robot navigation system. The two most important parameters are the lateral deviation and the heading deviation between the robot and the planned path during the movement process. To obtain the lateral deviation and the heading deviation of the robot, initially, obstacles on the road

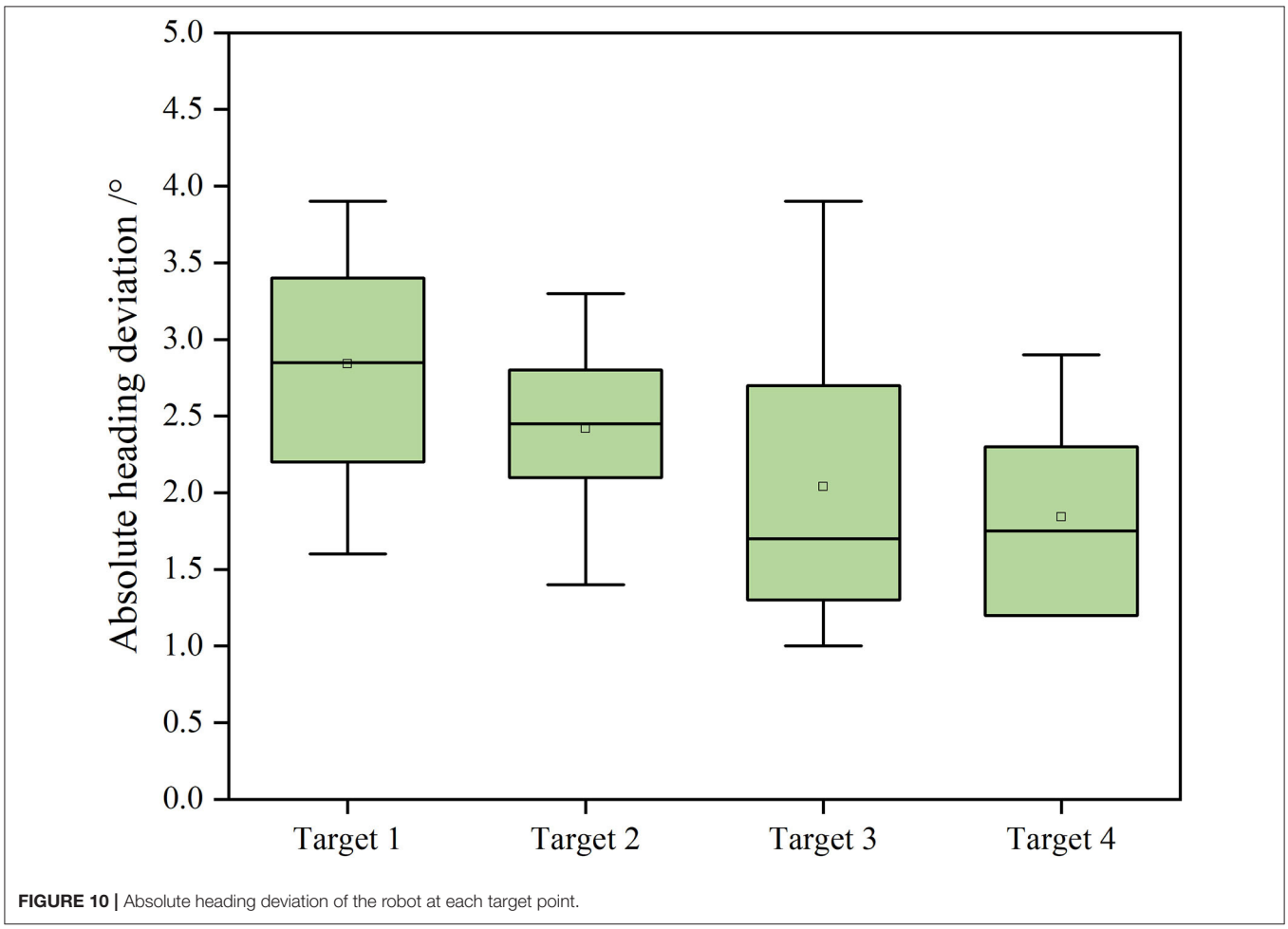

FIGURE 10 | Absolute heading deviation of the robot at each target point.

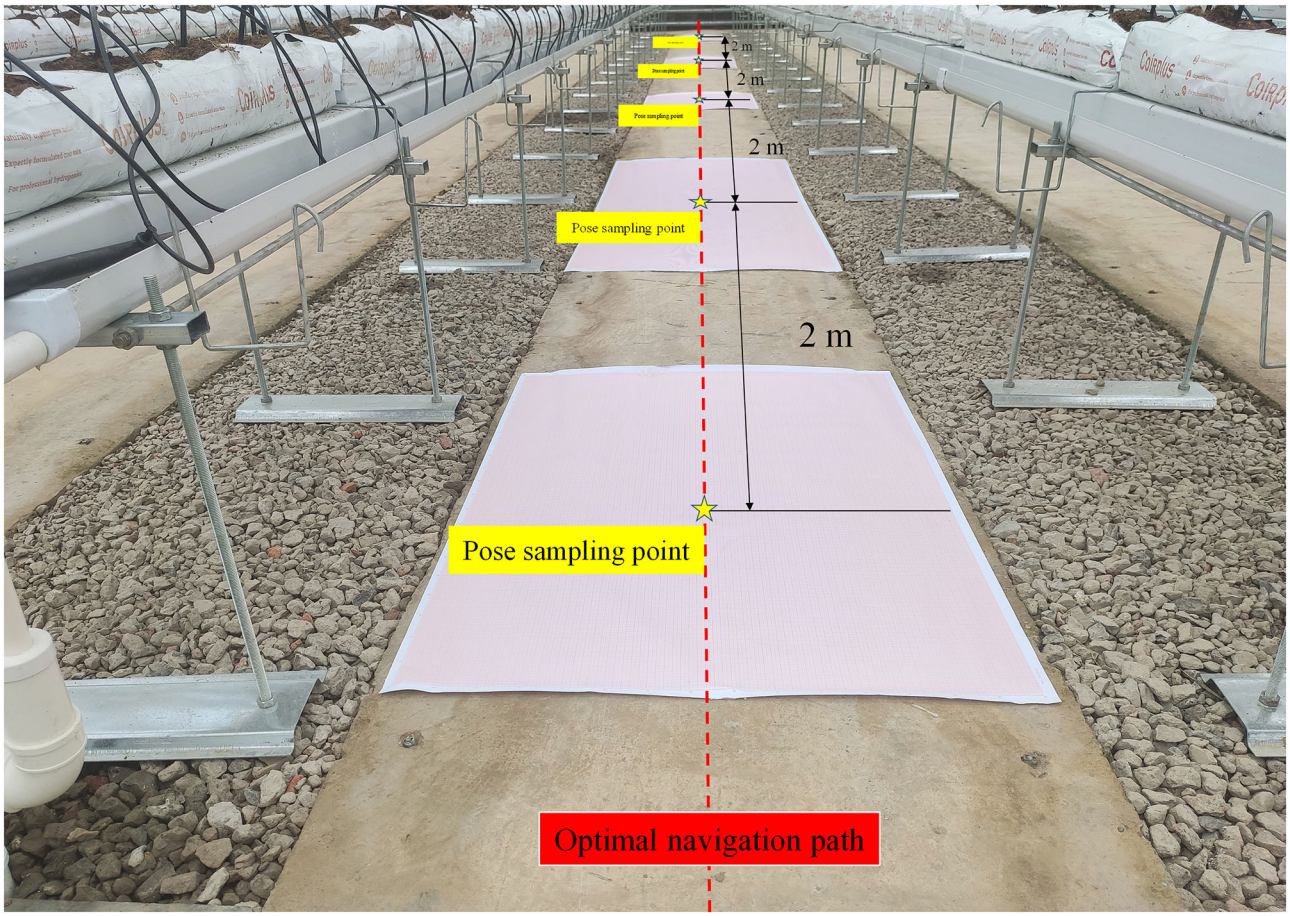

FIGURE 11 | The navigation accuracy test scenario.

between the greenhouse rows were moved away, and then, the robot navigation target points are set. According to the principle of global path and local path planning algorithms, the optimal navigation path of the robot is the straight line between two target points. Hence, as shown in **Figure 11**, a posture sampling point was set every 2 m on the planned paths. To accurately collect the position information of the robot, two cross lasers (Qy-620, Huimei, Dongguan, China) were installed in the front and the rear of the longitudinal center line of the robot. When the robot reached each posture sampling point, it stayed there for 5 s in that position for each sampling point, and the positions of the laser on the coordinate tags were recorded accurately. The robot completed the navigation task at the speed of 0.2, 0.4, and 0.6 m/s, respectively. The experiment was repeated three times at each speed.

As shown in **Figure 12**, the cartesian coordinate system is established on the coordinate paper with the sampling point (x_0, y_0) as the origin, and the target heading of the robot is set to the positive direction of the Y-axis, while the right direction perpendicular to the target heading is the positive direction of the X axis; thus, the coordinate of the sampling point is $(0, 0)$. Suppose the front laser coordinate is (x_1, y_1), the rear laser coordinate is (x_2, y_2), the robot center coordinate is (x, y), then the robot center coordinate is $(\frac{x_1+x_2}{2}, \frac{y_1+y_2}{2})$, the lateral deviation is $|x|$, and the heading deviation is $\arccos(\frac{y_1-y_2}{x_1-x_2})$.

The robot global path planning step size was set to 0.05 m as the grid length in the grid map, and the global path planning frequency was 1 Hz. After numerous tests, when the robot reached the target point, the distance error from the target point in the x-y plane was set to 0.15 m, and the yaw angle error was set to.1 radians, the robot has the best navigation. When these two errors are set smaller, the robot will always hover near the target point. The simulation time of the robot's local path planning was set to 3 s. If the simulation time is too large, it will easily cause the robot to deviate from the global path, especially when the turning radius is large at startup. On the contrary, when the simulation time is too small, it is easy to cause frequent path planning and consume resources, and even oscillation occurs. The step size of the robot's local path planning was set to 0.025 m. After many tests, the three influencing factors in the speed evaluation function were finally set as: $\varphi = 64$, $\beta = 24$, *and* $\delta = 0.5$, respectively.

It can be seen from **Table 1**, with the increase in the moving speed of the robot, both the mean value and SD of the lateral

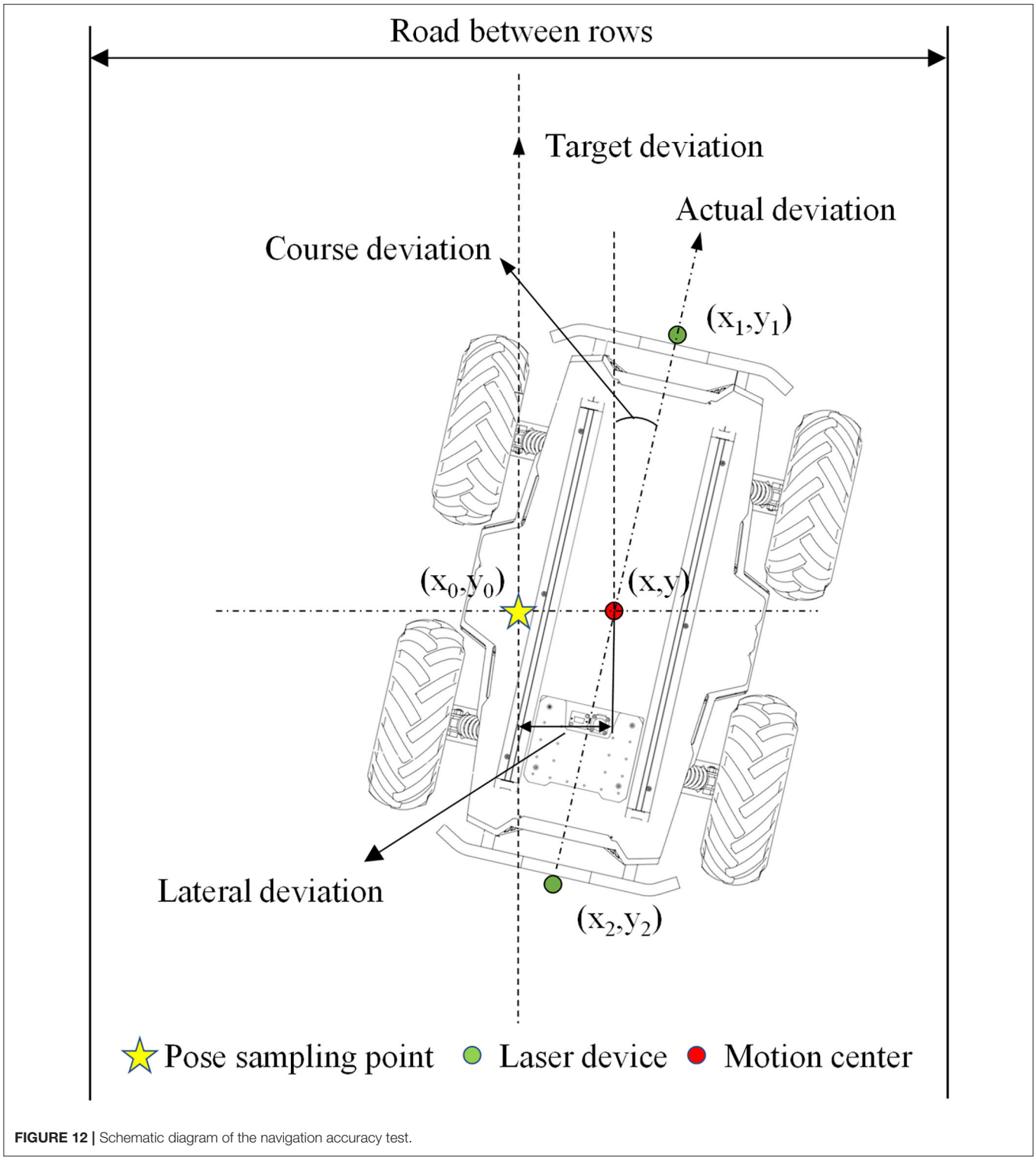

FIGURE 12 | Schematic diagram of the navigation accuracy test.

deviation of the robot and the mean value and SD of the heading deviation of the robot gradually increase, and the change rate of each deviation when the speed is greater than 0.4 m/s is greater than the transformation rate when the speed is less than 0.4 m/s. At a speed of 0.6 m, the average lateral deviation of the robot is 4.4 cm higher than the average at 0.4 m/s, and the maximum lateral deviation even reaches 16.8 cm. We guess this is related to the part that we set and the parameters related to local path planning. We have not yet found the specific reason for the increase of the deviation, which will be one of the problems that

TABLE 1 | Robot navigation deviation.

Speed/(m/s)	Lateral deviation/cm				Course deviation/ (°)			
	Minimum	Maximum	Average	Standard deviation	Minimum	Maximum	Average	Standard deviation
0.2	0.8	7.1	2.8	1.7	0	3.5	1.5	1.2
0.4	0.6	9.5	4.8	3.0	0.3	3.8	1.7	1.1
0.6	0.8	16.8	9.2	5.8	0.7	4.9	2.8	1.1

we need to focus on in the next stages. In general, the average lateral deviation of the robot is less than 9.2 cm, and the SD is less than 5.8 cm. The mean course deviation shall not exceed 2.8°, and the SD shall not exceed 1.2°. As is shown, the precision can meet the requirements of navigation precision of robot in a greenhouse environment.

At present, the greenhouse is moving from informatization to intelligence. To meet the good application of intelligent equipment in greenhouses, most of the greenhouse floors have undergone a ground leveling treatment. Therefore, the robot positioning and navigation test experiment designed was selected to be carried out in a greenhouse with flat ground. After the positioning accuracy test and the navigation accuracy test, the mobile robot navigation control system designed had a good performance, which had an inseparable relationship with the greenhouse standard planting mode and flat ground. Since the Lidar was fixed on the robot, the Lidar was always level with the ground. At the same time, we used the 3D Lidar information to convert the 2D information and integrate the IMU information, so the slope of the greenhouse floor had no effect on the robot's navigation. To expand the application of the robot in different types of greenhouses, the next step is to test the robot on an uneven ground. When the robot was mapping in the greenhouse, we found that there were often some water pipes and other equipment on the ground, but these obstacles did not affect the movement of the robot. To ignore the influence of these obstacles on the mapping, we chose to filter the point cloud. During the fusion process, filtering was selected for the point cloud below 8 cm from the ground. In addition, for the odometry information required for robot mapping, we took the average value of the four encoders of the robot as the odometer data of the robot, which could effectively reduce the data error caused by the slippage of individual wheels of the robot.

The path planning of the robot was realized based on the costmap after the inflation of the obstacle. To ensure that the robot did not collide with the obstacle, the inflation radius should be larger than the radius of the robot's circumcircle. The robot we designed was 0.8 m long and 0.6 m wide. When the expansion radius of the costmap is larger than the robot's circumscribed circle, the robot will not be able to realize the inter-row path planning. To solve this problem, we set the inflation radius of the costmap to 0.4 m, so that we could ensure that when the robot navigated between rows in the greenhouse, the path planning trajectory was within 0.1 m to the left and right of the center of the row. Even if the robot moved along the inflated obstacles between rows, it would not collide with the cultivation tank. However, this setting method was very dangerous when the robot turns between rows. At the same time, due to the limitation of the row spacing in the greenhouse, the yaw angle of the robot in the row cannot be greater than 53°. To ensure the safety of the robot when turning, we inserted a safety target point at the turning point of the robot's navigation route, divided the robot's navigation plan into multiple parts, and performed a global path planning and a local path planning for each segment to ensure that the robot would not interact when cultivation tanks collide. When the robot got into a local dilemma between the rows, we chose to let the robot terminate the navigation. Although this processing strategy avoided robot collision, it was not intelligent enough. In the future, we will further develop a more intelligent and effective local path processing strategy.

CONCLUSION

The proposed autonomous navigation system for the greenhouse mobile robot was designed based on 3D Lidar and 2D Lidar SLAM. The hardware part was mainly composed of 3D Lidar, an IMU, an odometer, and an encoder. The software core control layer was developed based on ROS, and information interaction was realized through a distributed node communication. In order to enhance the safety of the robot during the movement and to reduce the computational power consumption of the computer, 3D environmental information collected by multi-line Lidar was filtered and fused into 2D laser information, and then, localization and map construction were completed using the Cartographer algorithm. After the greenhouse navigation test, the average deviation does not exceed 10 cm, and the average heading deviation does not exceed 3°, which meets the movement requirements of the greenhouse mobile robot. In the process of the robot positioning and navigation, we found that appropriately adding some objects with structured features in the greenhouse environment could effectively improve the positioning accuracy of the robot, and the navigation speed of the robot was closely related to the navigation accuracy. For different navigation speeds, the robot navigation parameters should be reset. At present, this research only solves the simple positioning and navigation of robots in the greenhouse. In the future, we can apply this system to different types of greenhouse mobile robots, and combine the different operating conditions of the robots to develop appropriate navigation strategies based on the existing navigation path planning algorithms. In addition, we can also use 5G, the Cloud Computing Platform, and other modules to further realize the remote control and monitoring of robots.

DATA AVAILABILITY STATEMENT

The original contributions presented in the study are included in the article/**Supplementary Material**, further inquiries can be directed to the corresponding author/s.

AUTHOR CONTRIBUTIONS

SJ performed most of the experiments with the assistance of SW and ZY. SJ, XL, and MZ designed the study, analyzed the data, and wrote the manuscript. All authors contributed to the study conception and design, read, and approved the final manuscript.

FUNDING

This work was supported by the Jiangsu Agricultural Science and Technology Innovation Fund [No. CX(20)1005] and the Jiangsu Modern Agricultural Equipment and Technology Demonstration Promotion Fund (No. NJ2020-23).

ACKNOWLEDGMENTS

We would like to thank Wei Wang, Zhuangwei Xu, and Jian Pan (Institute of Agricultural Facilities and Equipment, Jiangsu Academy of Agricultural Science) for their help during the robot positioning accuracy test and the navigation accuracy test.

SUPPLEMENTARY MATERIAL

The Supplementary Material for this article can be found online at: https://www.frontiersin.org/articles/10.3389/fpls.2022.815218/full#supplementary-material

REFERENCES

Arad, B., Balendonck, J., Barth, R., Ben-Shahar, O., Edan, O., and Hellström, T., et al. (2020). Development of a sweet pepper harvesting robot. *J. Field Robot.* 37, 1027–1039. doi: 10.1002/rob.21937

Balaso, S. D., Arima, S., Ueka, Y., Kono, M., and Takahashi, N. (2013). Development of a multi-operation system for intelligent greenhouses. *IFAC Proceed. Volum.* 46, 287–292. doi: 10.3182/20130327-3-JP-3017.00066

Chan, E., Baciu, G., and Mak, S. C. (2009). Using Wi-Fi signal strength to localize in wireless sensor networks. 2009 wri international conference on communications and mobile computing. *IEEE* 1, 538–42. doi: 10.1109/CMC.2009.233

Chen, J., Qiang, H., Wu, J., Xu, G., Wang, Z. (2021). Navigation path extraction for greenhouse cucumber-picking robots using the prediction-point Hough transform. *Comput. Electron. Agr.* 180, 105911. doi: 10.1016/j.compag.2020.105911

Chiu, Y. C., Chen, S., and Lin, J. F. (2013). Study of an autonomous fruit picking robot system in greenhouses. *Eng. Agric. Environ. Food.* 6, 92–98. doi: 10.1016/S1881-8366(13)80017-1

Choi, B. S., Lee, J. W., Lee, J. J., and Park, K. T. (2011). A hierarchical algorithm for indoor mobile robot localization using RFID sensor fusion. *IEEE Trans. Ind. Electron.* 58, 2226–2235. doi: 10.1109/TIE.2011.2109330

Cui, Y., Qiao, Z., Zou, X., and Wang, B. (2015). Study on the method of visual navigation baseline identification and extraction of agricultural machinery. 2015 6th IEEE International Conference on Software Engineering and Service Science (ICSESS). *IEEE* 2015, 766–769. doi: 10.1109/ICSESS.2015.7339169

Gao, G., and Ming, L. (2014). Study on navigating path recognition for the greenhouse mobile robot based on K-means algorithm. proceedings of the 11th IEEE international conference on networking sensing and control. *IEEE* 2014, 451–456. doi: 10.1109/ICNSC.2014.6819668

Hayashi, S., Yamamoto, S., Saito, S., Ochiai, Y., Kamata, J., and Kurita, M., et al. (2014). Field operation of a movable strawberry-harvesting robot using a travel platform. *Jpn. Agric. Res. Q.* 48, 307–316. doi: 10.6090/jarq.48.307

Henten, E., Bac, C. W., Hemming, J., and Edan, Y. (2013). Robotics in protected cultivation. *IFAC Proceed. Volum.* 46, 170–177. doi: 10.3182/20130828-2-SF-3019.00070

Hess, W., Kohler, D., Rapp, H., and Andor, D. (2016). Real-time loop closure in 2D LIDAR SLAM. 2016 IEEE international conference on robotics and automation (ICRA). *IEEE*. 16:1271–1278. doi: 10.1109/ICRA.2016.7487258

Hou, J., Pu, W., Li, T., and Ding, X. (2020). Development of dual-lidar navigation system for greenhouse transportation robot. *Trans. Chin. Soc. Agric. Eng.* 36, 80–88. doi: 10.11975/j.issn.1002-6819.2020.14.010

Hough, P. (1962). *Method and means for recognizing complex patterns. U.S. Patent No 3,069,654*. Washington, DC:U.S. Patent and Trademark Office.

Huang, Z., Jacky, T. L., Zhao, X., Fukuda, H., Shiigi, T., and Nakanishi, H., et al. (2020a). Position and orientation measurement system using spread spectrum sound for greenhouse robots. *Biosyst. Eng.* 198, 50–62. doi: 10.1016/j.biosystemseng.2020.07.006

Huang, Z., Tsay, L. W. J., Shiigi, T., Zhao, X., Nakanishi, H., and Suzuki, T., et al. (2020b). A noise tolerant spread spectrum sound-based local positioning system for operating a quadcopter in a greenhouse. *Sensors*. 20, 1981. doi: 10.3390/s20071981

Juan, R., Pablo, G. A., Mario, G., Jorge, D. L., Jaime, D. C., and Antonio, B. (2016). Heterogeneous multi-robot system for mapping environmental variables of greenhouses. *Sensors*. 16, 1018. doi: 10.3390/s16071018

Lee, I., Lee, K., Lee, J., and You, K. (2015). Autonomous greenhouse sprayer navigation using automatic tracking algorithm. *Appl. Eng. Agric.* 31, 17–21. doi: 10.13031/aea.3110448

Mao, J., Cao, Z., Wang, H., Zhang, B., and Niu, W. (2019). Agricultural robot navigation path recognition based on k-means algorithm for large-scale image segmentation. 2019 14th IEEE conference on industrial electronics and applications (ICIEA). *IEEE* 2019, 1233–1237. doi: 10.1109/ICIEA.2019.8834296

Min, H. K., Ryuh, B. S., Kim, K. C., Suprem, A., and Mahalik, N. P. (2014). Autonomous greenhouse mobile robot driving strategies from system integration perspective: review and application. *IEEE/ASME Trans. Mechatron.* 20, 01–12. doi: 10.1109/TMECH.2014.2350433

Ming, L. (2018). RFID positioning algorithm based on electronic tracking system (ETPS). *Int. J. RF Technol.* 9, 25–36. doi: 10.3233/RFT-180136

Obregón, D., Arnau, R., Campo-Cossio, M., Arroyo-Parras, J. G., Pattinson, M., and Tiwari, S., et al. (2019). "Precise positioning and heading for autonomous scouting robots in a harsh environment," in *International Work-Conference on the Interplay Between Natural and Artificial Computation*. Springer, Cham, pp. 82–96. doi: 10.1007/978-3-030-19651-6_9

Pan, J., Wei, L., Zhang, K., Sunyang, W. U., and Ren, W. (2019). Design of navigation control system for large-size greenhouse ground mobile irrigator. *J. Irrig. Drain. Eng.* 37, 179–184. doi: 10.3969/j.issn.1674-8530.17.0254

Pérez Ruiz, M., and Upadhyaya, S. (2012). GNSS in Precision Agricultural Operations. *España: Intech*. 12, 448. doi: 10.5772/50448

Preter, A. D., Anthonis, J., and Baerdemaeker, J. D. (2018). Development of a robot for harvesting strawberries. *IFAC-PapersOnLine.* 51, 14–19. doi: 10.1016/j.ifacol.2018.08.054

Santos, J. M., Portugal, D., and Rocha, R. P. (2013). "An evaluation of 2D SLAM techniques available in robot operating system," in 2013 *IEEE International Symposium on Safety, Security, and Rescue Robotics (SSRR)*. (New York, NY: IEEE), pp. 1–6. doi: 10.1109/SSRR.2013.6719348

Spachos, P., Papapanagiotou, I., and Plataniotis, K. (2021). Microlocation for smart buildings in the era of the internet of things: a survey of

technologies, techniques, and approaches. *IEEE Signal Process. Mag.* 35, 140–152. doi: 10.1109/MSP.2018.2846804

Tiwari, S., Zheng, Y., Pattinson, M., Campo-Cossio, M., and Reyes, J. (2020). Approach for autonomous robot navigation in greenhouse environment for integrated pest management. 2020 ieee/ion position, location and navigation symposium (PLANS). *IEEE* 2020, 1286–1294. doi: 10.1109/PLANS46316.2020.9109895

Tsay, L., Shiigi, T., Huang, Z., Zhao, X., and Kondo, N. (2020). Temperature-compensated spread spectrum sound-based local positioning system for greenhouse operations. *IoT*. 1, 147–160. doi: 10.3390/iot10 20010

Uyeh, D. D., Ramlan, F. W., Mallipeddi, R., Park, T., Woo, S., and Kim, J., et al. (2019). Evolutionary greenhouse layout optimization for rapid and safe robot navigation. *IEEE Access* 7, 88472–88480. doi: 10.1109/ACCESS.2019.2926566

Wang, X., Han, X., Mao, H., and Liu, F. (2012). Navigation line detection of tomato ridges in greenhouse based on least square method. *Trans. Chin. Soc. Agric. Mach*. 43, 161–166. doi: 10.6041/j.issn.1000-1298.2012.06.029

Widodo, S., Shiigi, T., Than, N. M., Kurosaki, H., Kikuchi, H., and Yanagida, K., et al. (2013). Design of self-calibration method for sound-based positioning system in greenhouse. *IFAC Proceedings Volumes*. 46, 332–335. doi: 10.3182/20130327-3-JP-3017.00075

Widodo, S., Shiigi, T., Than, N. M., Ogawa, Y., and Kondo, N. (2012). Sound-based ranging system in greenhouse environment with multipath effect compensation using artificial neural network. *Springer, Berlin, Heidelberg*. 2012, 156–163. doi: 10.1007/978-3-642-34478-7_20

Zhao, Y., Liang, G., Liu, C., and Huang, Y. (2016). Dual-arm robot design and testing for harvesting tomato in greenhouse. *IFAC-PapersOnLine*. 49, 161–165. doi: 10.1016/j.ifacol.2016.10.030

Zou, X., Zou, H., and Lu, J. (2012). Virtual manipulator-based binocular stereo vision positioning system and errors modelling. *Mach. Vis. Appl*. 23, 43–63. doi: 10.1007/s00138-010-0291-y

Conflict of Interest: The authors declare that the research was conducted in the absence of any commercial or financial relationships that could be construed as a potential conflict of interest.

Publisher's Note: All claims expressed in this article are solely those of the authors and do not necessarily represent those of their affiliated organizations, or those of the publisher, the editors and the reviewers. Any product that may be evaluated in this article, or claim that may be made by its manufacturer, is not guaranteed or endorsed by the publisher.

frontiers | Frontiers in Plant Science

METHODS
published: 25 May 2022
doi: 10.3389/fpls.2022.876357

Deep Learning-Based Segmentation of Peach Diseases Using Convolutional Neural Network

Na Yao[1,2,3], Fuchuan Ni[1,2], Minghao Wu[1,2], Haiyan Wang[1,2], Guoliang Li[1,2] and Wing-Kin Sung[1,4]*

[1] College of Informatics, Huazhong Agricultural University, Wuhan, China, [2] Hubei Engineering Technology Research Center of Agricultural Big Data, Wuhan, China, [3] College of Information Engineering, Tarim University, Alaer, China, [4] Department of Computer Science, National University of Singapore, Singapore, Singapore

OPEN ACCESS

Edited by:
Changyuan Zhai,
Beijing Academy of Agricultural and Forestry Sciences, China

Reviewed by:
Sijia Yu,
Rutgers, The State University of New Jersey – Busch Campus, United States
Marcin Wozniak,
Silesian University of Technology, Poland
Shunjun Wei,
University of Electronic Science and Technology of China, China

***Correspondence:**
Fuchuan Ni
fcni_cn@mail.hzau.edu.cn

Specialty section:
This article was submitted to Sustainable and Intelligent Phytoprotection, a section of the journal Frontiers in Plant Science

Received: 15 February 2022
Accepted: 04 April 2022
Published: 25 May 2022

Citation:
Yao N, Ni F, Wu M, Wang H, Li G and Sung W-K (2022) Deep Learning-Based Segmentation of Peach Diseases Using Convolutional Neural Network. Front. Plant Sci. 13:876357. doi: 10.3389/fpls.2022.876357

Peach diseases seriously affect peach yield and people's health. The precise identification of peach diseases and the segmentation of the diseased areas can provide the basis for disease control and treatment. However, the complex background and imbalanced samples bring certain challenges to the segmentation and recognition of lesion area, and the hard samples and imbalance samples can lead to a decline in classification of foreground class and background class. In this paper we applied deep network models (Mask R-CNN and Mask Scoring R-CNN) for segmentation and recognition of peach diseases. Mask R-CNN and Mask Scoring R-CNN are classic instance segmentation models. Using instance segmentation model can obtain the disease names, disease location and disease segmentation, and the foreground area is the basic feature for next segmentation. Focal Loss can solve the problems caused by difficult samples and imbalance samples, and was used for this dataset to improve segmentation accuracy. Experimental results show that Mask Scoring R-CNN with Focal Loss function can improve recognition rate and segmentation accuracy comparing to Mask Scoring R-CNN with CE loss or comparing to Mask R-CNN. When ResNet50 is used as the backbone network based on Mask R-CNN, the segmentation accuracy of segm_mAP_50 increased from 0.236 to 0.254. When ResNetx101 is used as the backbone network, the segmentation accuracy of segm_mAP_50 increased from 0.452 to 0.463. In summary, this paper used Focal Loss on Mask R-CNN and Mask Scoring R-CNN to generate better mAP of segmentation and output more detailed information about peach diseases.

Keywords: segmentation, location, peach diseases, focal loss, Mask R-CNN

INTRODUCTION

Peach is an important and popular fruit, and its production is severely affected by peach diseases. The common peach diseases are brown rot, anthracnose, scab, bacterial shot hole, gummosis,

powdery mildew, and leaf curl. The diseases reduce the yield of peach and cause harm to human health. Thus, it is important to find rapid and accurate methods to identify peach diseases and further locate and segment the areas of the lesion in earlier stages.

Currently, a few studies have been conducted on plant disease classification and on locating and segmenting areas of the lesion. There are three approaches. The first approach uses traditional image processing methods or deep learning methods to segment disease or pest areas initially. This preliminary segmentation is the intermediate step for feature extraction, which is the basic step for classification or location in the next step. Yang et al. (2018) used the Prewitt operator and the Canny operator for edge segmentation of single-headed pests based on the high contrast between the pest target and the background in the binary image, and then classified two types of pests by SVM, with the average recognition accuracy rate of 93.5%. Jin and Qian (2020) used fine-tune FCN to separate the diseased areas of green vegetables from the farmland images and then recognized the area by identifying the markers placed at a fixed distance on the ground, which can realize the location of the diseased area. The second approach focuses on classifying and identifying the diseases and further locating the lesion areas. Lu et al. (2017) used VGG-FCN-VD16 and VGG-FCN-S to classify the diseases and locate lesion areas, achieving the mean recognition accuracies of 97.95 and 95.12%, respectively. The third approach uses deep learning methods directly to segment the lesion site. Lin et al. (2019) used U-Net Ronneberger et al. (2015) network to segment cucumber leaves with powdery mildew and improved the segmentation effect by improving the loss function, thus achieving an average pixel accuracy of 96.08%, intersection over union of 72.11%, and dice accuracy of 83.45% on 20 test samples. Dai (2020) proposed a multi-scale fusion U-Net network to segment rice diseases. The first approach of segmentation is usually used for extracting preliminary features, such as the approximate location of the target. The second approach can provide disease classification and location based on the object detection task. The third approach can segment the lesion areas based on the semantic segmentation task. This study used deep learning methods to achieve classification, localization, and segmentation of peach diseases by instance segmentation task.

In deep learning methods, segmentation is initially carried out using FCN Long et al. (2015) network, and then other improved networks, such as DeconvNet Noh et al. (2016) and SegNet, are applied Badrinarayanan et al. (2017) Other networks for segmentation, such as DeepLab Chen et al. (2014) and PSPNet Zhao et al. (2017), are also available. The above-mentioned methods are based on semantic segmentation tasks. The FAST R-CNN (Girshick, 2015) approach can classify, identify, and locate targets, while Mask R-CNN (He et al., 2017) can not only classify and locate targets, but can also perform instance segmentation based on this information. At present, Mask R-CNN has been used for blade segmentation (Zhong et al., 2020), robot item recognition (Shi et al., 2019), pig inventory (Hu et al., 2020), and other applications. Some of the improved methods based on Mask R-CNN are Cascade R-CNN (Cai and Vasconcelos, 2019) and Deformable Convolutional Networks (Dai et al., 2017; Zhu et al., 2019). HRNet (Sun et al., 2019a,b) was also proposed for segmentation tasks. Mask Scoring R-CNN (Huang et al., 2019) adds a branch network on the basis of Mask R-CNN to train and regress mask scores.

This study focuses on identifying and locating major peach diseases and segmenting lesion areas using deep learning methods. The peach disease image dataset was collected from peach orchards by Prof. Luo's team, College of Plant Science and Technology, HZAU, which included seven categories of peach disease images. The seven categories are as follows: (1) brown rot fungi infecting fruits and leaves, (2) anthracnose fungi infecting fruits and leaves, (3) scab fungus infecting fruits, branches, and leaves, (4) shot hole bacterium infecting fruits, branches, and leaves, (5) gummosis fungi infecting branches, (6) powdery mildew fungus infecting fruits and leaves, and (7) leaf curl fungus infecting leaves. These diseases cause damage to different parts of the peach plant. For example, the brown rot disease mainly infects the fruits, causing the fruit to rot, and also affects the leaves leading to the dryness of leaves. Gummosis mainly affects the branches, leading to tree weakness, decreased fruit quality, and ultimately causing the death of branches and trees. As the seven diseases were extensively studied in the laboratory, laboratory personnel were familiar with the characteristics of the diseases. For example, a certain disease mainly infects fruits, while some infect leaves and branches in particular. Therefore, the disease images were mainly obtained from the infected fruits. Each disease is further divided into early, middle, and end stages based on the severity of the disease. Finally, the total number of disease categories totals 21. The project comprises a team of experts on fruit disease prevention and control posts in the National Peach Industry Technology System, which can further ensure the accuracy of its classification. For similar diseases and diseases that are easy to be confused, accurate conclusions can be drawn through tissue isolation of pathogenic bacteria or direct monospore isolation, pathogen morphology observation, and molecular biological identification. The samples were collected by two methods. The first approach included collecting pictures of existing resources in the laboratory or obtaining some pictures from other experts through cooperation in the Peach System, and the second method included taking a large number of pictures indoors or in orchards.

For identifying disease, locating and segmenting lesion areas, two deep neural networks (Mask R-CNN and Mask Scoring R-CNN) are used to classify 21 diseases of peach trees and segment the lesions to obtain more detailed information about the lesions. To overcome the problem due to imbalance of samples and hard samples, by improving the loss function with focal loss (Lin et al., 2017) of Mask R-CNN and Mask Scoring R-CNN, the segmentation effect can be improved.

The remaining manuscript is organized as follows. Section 2 introduces "Materials and Methods." Section 3 presents the "Results and related Discussion." Finally, Section 4 presents our "Conclusion."

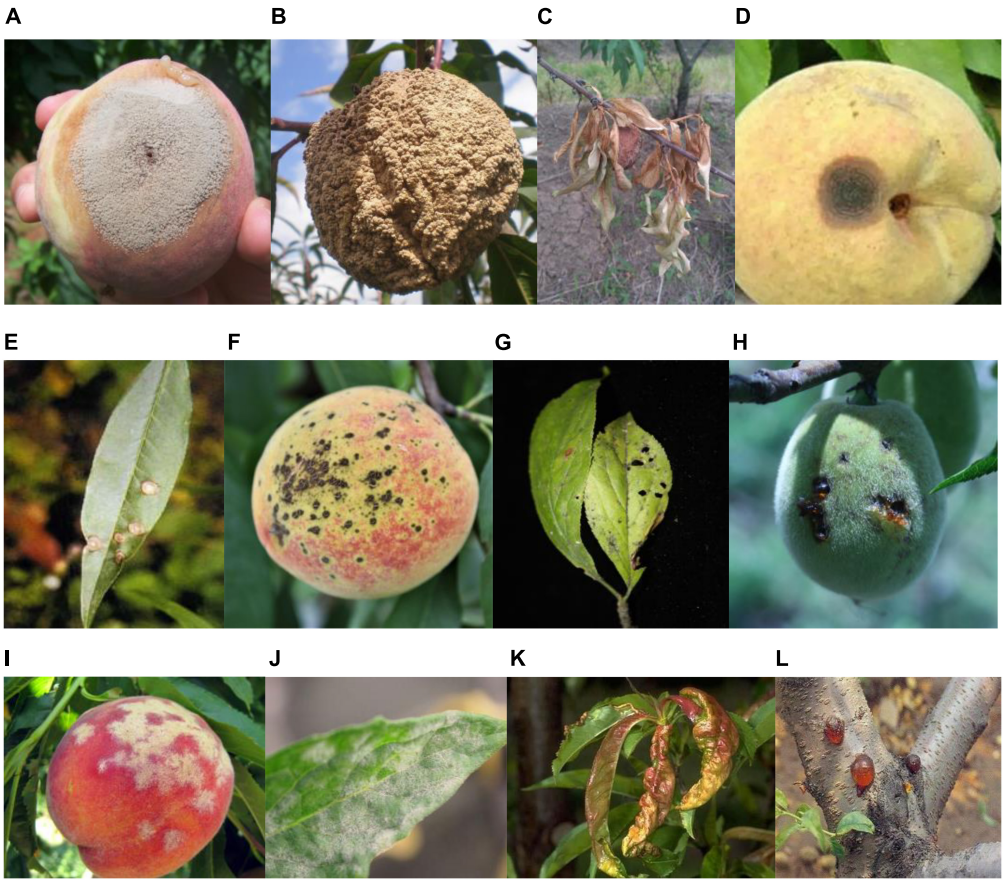

FIGURE 1 | Major plant diseases of peach. **(A)** Brown rot of fruit, **(B)** brown rot of fruit, **(C)** brown rot of leaf, **(D)** anthracnose of fruit, **(E)** anthracnose of leaf, **(F)** scab of fruit, **(G)** scab of leaf, **(H)** bacterial shot hole of fruit, **(I)** powdery mildew of fruit, **(J)** powdery mildew of leaf, **(K)** leaf curl of a leaf, and **(L)** gummosis of a branch (Yao et al., 2021).

TABLE 1 | Classification of peach disease image dataset.

Class	Part	Sample	Class	Part	Sample
Brown rot	Fruits	88	Bacterial shot hole	Fruits	193
	Leaves	6		Leaves	229
Anthracnose	Fruits	129		Branches	5
	Leaves	28	Gummosis	Branches	91
Scab	Fruits	614	Powdery mildew	Fruits	32
	Leaves	35		Leaves	18
	Branches	5	Leaf curl	Leaves	87

MATERIALS AND METHODS

Peach Disease Image Dataset and Image Annotation

The original images of peach diseases (see **Figure 1**, Yao et al., 2021 for detail) were collected to form the Peach Disease Image Dataset (PDID). The numbers of images acquired for brown rot disease, anthracnose disease, scab disease, bacterial shot hole disease, gummosis disease, powdery mildew disease, and leaf curl disease were 94, 157, 654, 427, 91, 50, and 87, respectively (see **Table 1** for detail). As can be seen, the distribution of the number of images in PDID is imbalanced.

Figure 1 Seven categories of disease images.

In order to distinguish the severity of each disease in more detail, we divided each disease into three levels: early disease, middle disease, and end disease. After division, the number of classes changed from 7 to 21, which are as follows: early brown rot, middle brown rot, end brown rot, early anthracnose, middle anthracnose, end anthracnose, early scab, middle scab, end scab, early gummosis, middle gummosis, end gummosis, early leaf curl, middle leaf curl, end leaf curl, early bacterial shot hole, middle bacterial shot hole, and end bacterial shot hole. However, the number of images per class is still small. To increase the number of images, we performed data augmentation (flipping, rotation, adding noise, and changing saturation) on the images. Finally, the number of samples included in the study was 5,627. These samples were divided into 4,051 training samples, 1,013 validation samples, and 563 testing samples.

Labelme software was used to mark the lesion area in the images of different peach diseases. **Figure 2** shows the marking process of early gummosis and end brown rot. After a picture is marked, it is saved as a json file, and the key points and disease

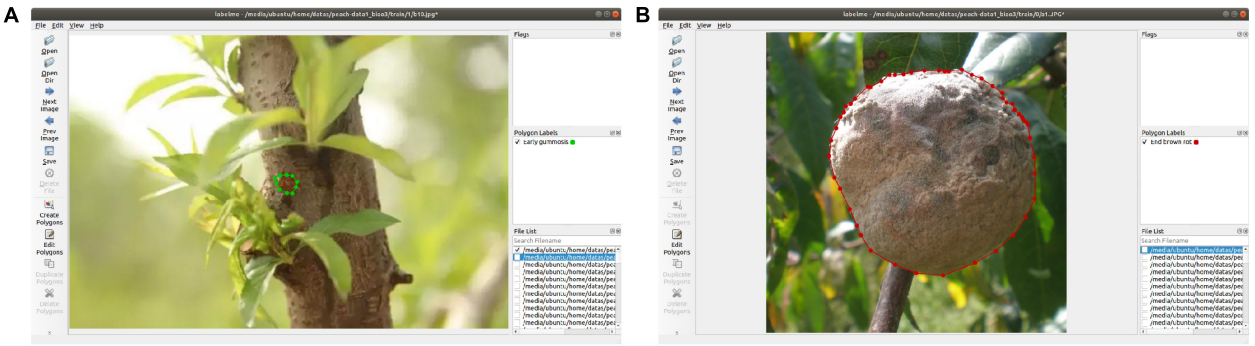

FIGURE 2 | Marking process: **(A)** early gummosis and **(B)** end brown rot.

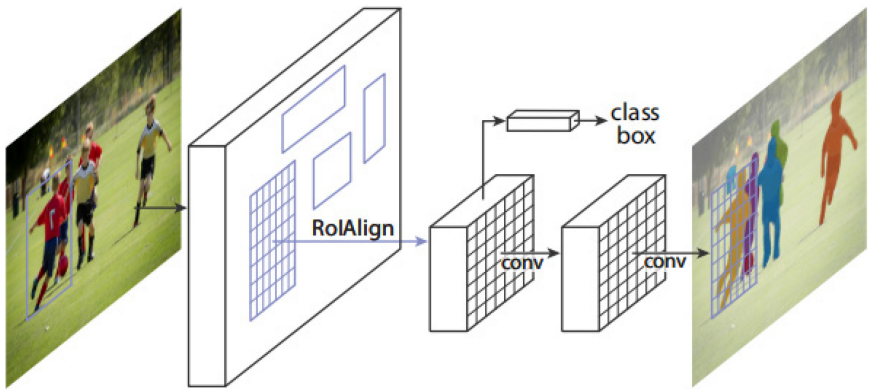

FIGURE 3 | The Mask R-CNN framework for instance segmentation (He et al., 2017).

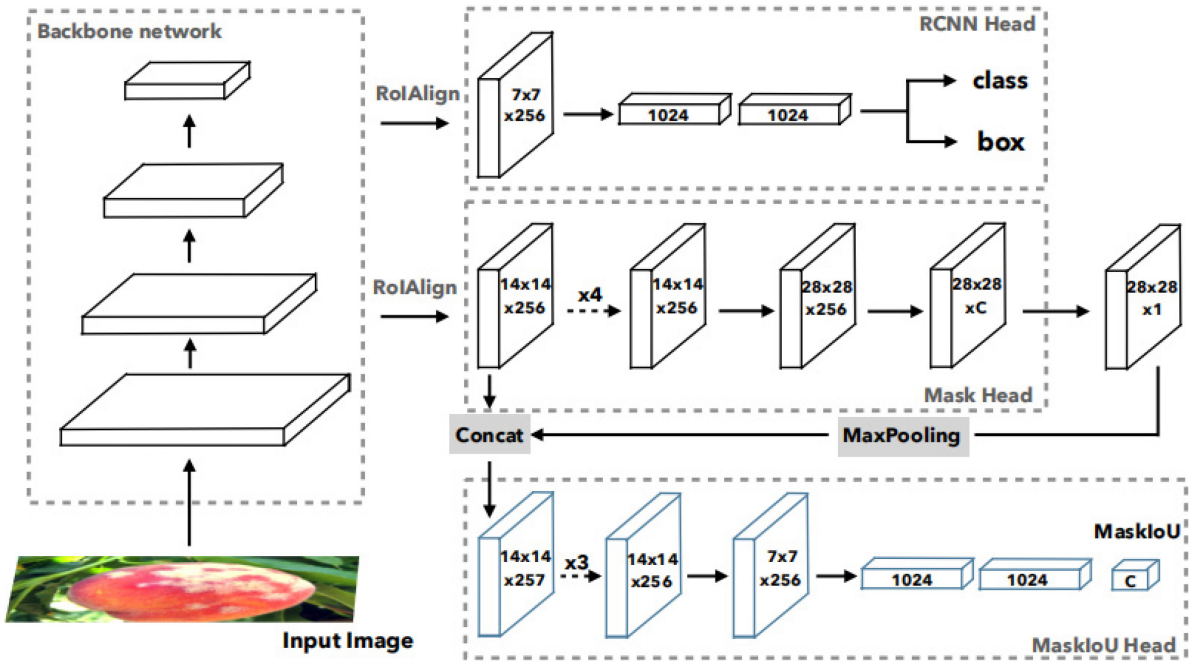

FIGURE 4 | Network architecture of Mask Scoring R-CNN (Huang et al., 2019).

TABLE 2 | Training parameter and test results based on Mask R-CNN with different loss functions.

Network	Bbox_mAP_50	Segm_mAP_50	Loss	Backbone	Epoch	γ	α
Mask R-CNN	0.396	0.236	CE	R50	12		
Mask R-CNN	0.416	0.224	FL	R50	12	5	0.95
Mask R-CNN	0.428	0.197	FL	R50	12	2	0.25
Mask R-CNN	0.463	0.219	FL	R50	12	2	0.55
Mask R-CNN	0.515	0.236	FL	R50	12	2	0.75
Mask R-CNN	0.540	0.246	FL	R50	12	2	0.85
Mask R-CNN	0.534	0.254	FL	R50	12	2	0.95
Mask R-CNN	0.518	0.219	FL	R50	12	1	0.95
Mask R-CNN	0.465	0.222	FL	R50	12	3	0.95
Mask R-CNN	0.443	0.215	FL	R50	12	4	0.95

TABLE 3 | Training parameter and test results based on Mask Scoring R-CNN with different loss functions.

Network	Bbox_mAP_50	Segm_mAP_50	Loss	Backbone	Epoch	γ	α
Mask Scoring R-CNN	0.367	0.246	CE	R50	12		
Mask Scoring R-CNN	0.367	0.224	FL	R50	12	5	0.95
Mask Scoring R-CNN	0.425	0.243	FL	R50	12	5	0.75
Mask Scoring R-CNN	0.451	0.251	FL	R50	12	5	0.55
Mask Scoring R-CNN	0.425	0.240	FL	R50	12	5	0.25
Mask Scoring R-CNN	0.472	0.274	FL	R50	12	4	0.45
Mask Scoring R-CNN	0.408	0.238	FL	R50	12	3	0.35
Mask Scoring R-CNN	0.346	0.196	FL	R50	12	1	0.05
Mask Scoring R-CNN	0.450	0.259	FL	R50	12	2	0.25

names are included in the json file. Mask R-CNN and Mask Scoring R-CNN use the same dataset format, and convert the saved json file to COCO dataset format.

Mask R-CNN

Mask R-CNN and Mask Scoring R-CNN are representatives of typical instance segmentation tasks, and Mask Scoring R-CNN is the improved version of Mask R-CNN. In order to obtain more effective information about the peach disease, two instance segmentation networks (Mask R-CNN and Mask Scoring R-CNN) with focal loss are used to segment peach diseases. As Mask Scoring R-CNN is based on Mask R-CNN, this paper used focal loss in Mask R-CNN and Mask Scoring R-CNN separately.

The Mask R-CNN framework for instance segmentation task is shown in **Figure 3** (He et al., 2017). Mask R-CNN adopts a two-stage procedure. The first stage is RPN. In the second stage, in parallel to predicting the class and box offset, Mask R-CNN also outputs a binary mask for each RoI. Mask R-CNN follows the spirit of Fast R-CNN that applies bounding box classification and regression in parallel. Formally, during training, Mask R-CNN defines a multi-task loss on each sampled RoI as $L = L_{cls} + L_{box} + L_{mask}$. The classification loss $L_{cls}$and bounding box loss $L_{box}$are the same as those defined by a previous study (Girshick, 2015). The mask branch has a Km^2-dimensional output for each RoI, which encodes K binary masks of resolution$m \times m$, one for each of the K classes. It applies a per-pixel sigmoid and defines L_{mask}as the average binary cross-entropy loss. For an RoI associated with ground-truth class k, L_{mask} is only defined on the k-th mask. The definition of L_{mask} allows the network to generate masks for every class without competition among the classes. The dedicated classification branch is relied upon to predict the class label used to select the output mask, which decouples mask and class prediction.

TABLE 4 | Training parameter and test results based on Mask R-CNN with different loss functions.

Network	Bbox_ mAP_50	Segm_ mAP_50	Loss	Backbone	Epoch	γ	α
Mask R-CNN	0.396	0.236	CE	R50	12		
Mask R-CNN	0.534	0.254	FL	R50	12	2	0.95

Mask Scoring R-CNN

In Mask R-CNN framework, the score of instance segmentation hypothesis is determined by the largest element in its classification scores, which can be obtained in R-CNN. But classification score and ground truth mask are not well correlated in Mask R-CNN. So, Mask Scoring R-CNN was proposed. **Figure 4** (Huang et al., 2019) shows the network architecture of Mask Scoring R-CNN, which is a Mask R-CNN with an additional MaskIoU head module that learns the MaskIoU aligned mask score. The input image is fed into a backbone network to generate RoIs *via* RPN and RoI features *via* RoIAlign. The R-CNN head and Mask head are standard components of Mask R-CNN. For predicting MaskIoU, the predicted mask and RoI feature are used as input. The MaskIoU head has four convolution layers (all have kernel = 3 and the final one uses

stride = 2 for downsampling) and three fully connected layers (the final one outputs C classes MaskIoU.). During inference, the predicted MaskIoU is multiplied by the classification score to get the new calibrated mask score as the final mask confidence. Mask Scoring R-CNN definesS_{mask} as the score of the predicted mask. The ideal $S_{mask}$is equal to the pixel-level IoU between the predicted mask and its matched ground truth mask, which also should have only a positive value for the ground truth category and zero for other classes, since a mask belongs to one class only. This requires the mask score to work well on two tasks: classifying the mask to the right category and regressing the proposed MaskIoU for the foreground object category. So, $S_{mask} = S_{cls} \bullet S_{iou}$is denoted for all object categories. S_{cls}focuses on classifying the proposal to the corresponding class, and S_{iou}focuses on regressing the MaskIoU. A classification score can be obtained in the classification task in the R-CNN stage. The MaskIoU head aims to regress the IoU between the predicted mask and its ground truth mask. The predicted MaskIoU scores are multiplied with classification score to get the new calibrated mask score as the final mask confidence. The concatenation of features from the RoIAlign layer and the predicted mask is the input of MaskIoU head. When concatenating, it uses a max pooling layer with kernel size of 2 and stride of 2 to enable the predicted mask to have the same spatial size as the RoI feature. MaskIoU head consists of four convolution layers and three fully connected layers. For the four convolution layers, it follows Mask head and sets the kernel size and filter number to 3 and 256, respectively, for all the convolution layers. For the three fully connected (FC) layers, it follows the R-CNN head and set the outputs of the first two FC layers to 1,024 and the output of the final FC to the number of classes.

Image Pre-processing

The samples in the dataset are RGB images. Generally, images were processed as follows: First, Z-Score normalization was performed. Precisely, mean value $m_x$and standard deviationss_x were calculated. Then, for each pixel value$x$as input, input x is changed to$x^{'} = x - m_x/s_x$, so that the normalized data was a standard normal distribution with zero mean and unit variance. After that, several augmentations, including random flipping, resize, and Pad (size = 32), were used for training and validating the dataset. The augmentation was helpful for enhancing the generalization ability of the model and preventing overfitting.

Improved Method

As the number of samples in the peach disease image dataset is relatively small and the samples in this dataset were imbalanced, standard machine learning techniques have low accuracy. To improve the segmentation accuracy, focal Loss was used for this dataset.

The focal loss is defined as follows:

$$FL(p_t) = -\alpha_t(1 - p_t)^{\gamma}\log(p_t) \quad (1)$$

where $p_t = \begin{cases} p & \text{if } y = 1 \\ 1 - p & \text{otherwise} \end{cases}$ and $\alpha_t = \begin{cases} \alpha & \text{if } y = 1 \\ 1 - \alpha & \text{otherwise} \end{cases}$, for binary classification, y∈{ ± 1} specifies the ground truth class, and p∈[0, 1] is the model's estimated probability for the class with

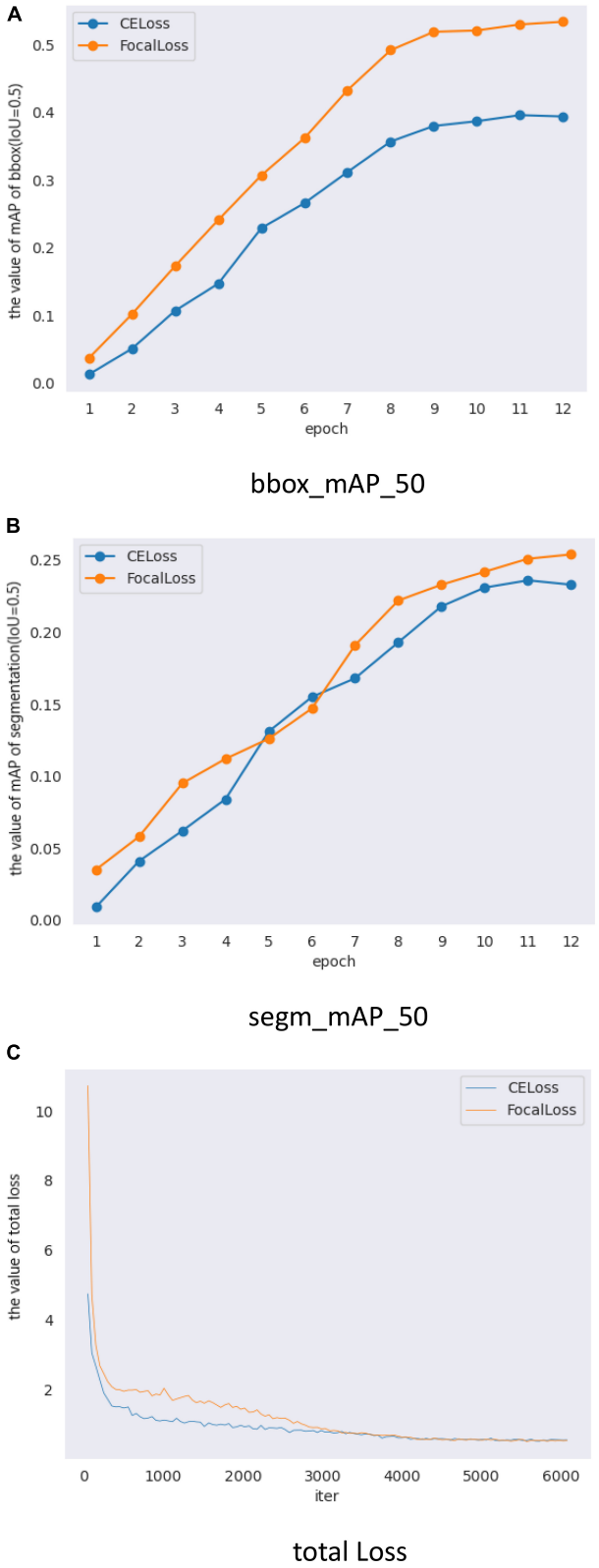

FIGURE 5 | Mask R-CNN with different loss validation parameters and loss functions. **(A)** Comparison of mAP_50 of bbox (IoU = 0.5) on different loss, **(B)** Comparison of mAP_50 of segmentation (IoU = 0.5) on different loss, and **(C)** Comparison of total loss.

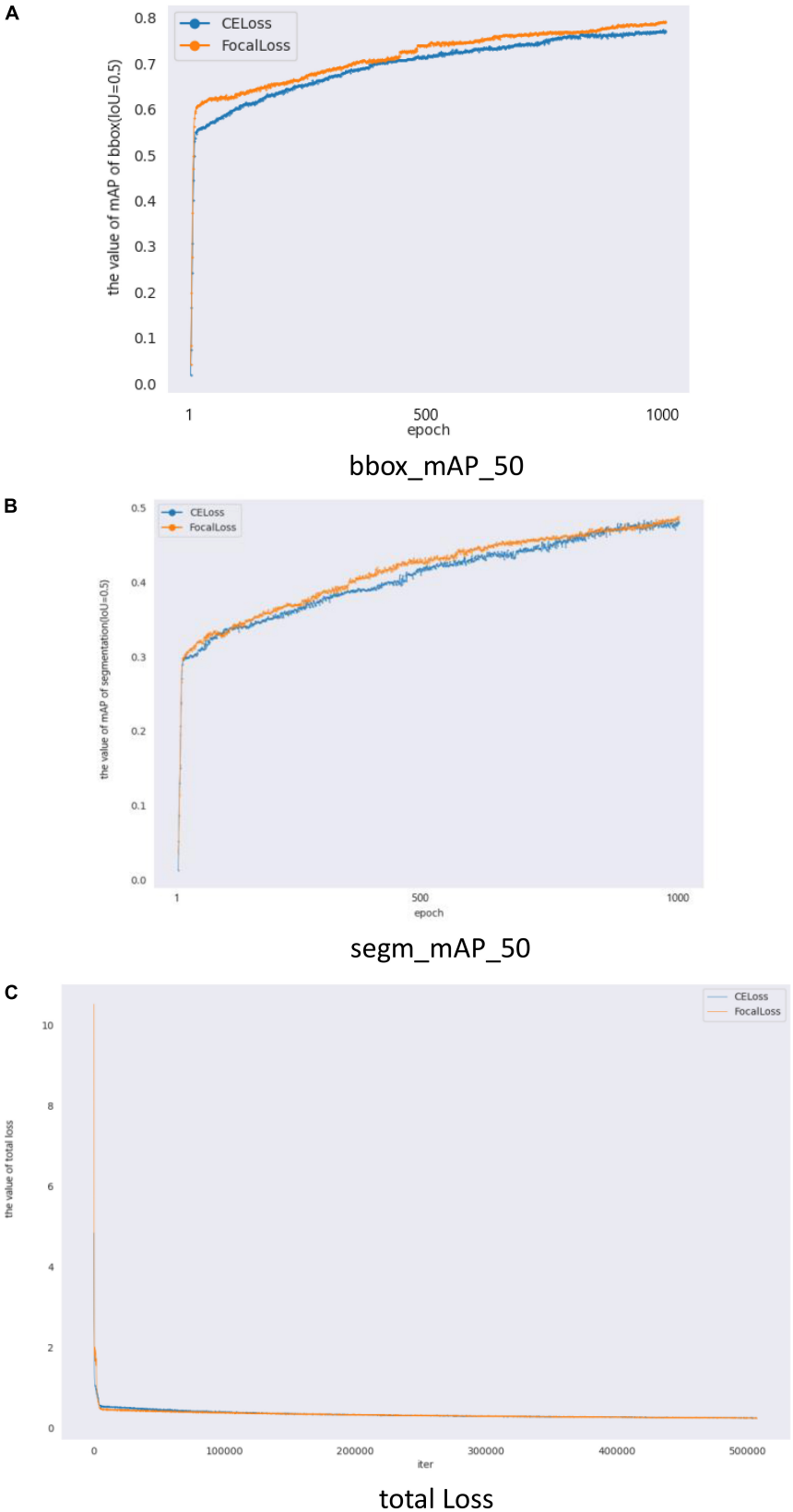

FIGURE 6 | Mask R-CNN with different loss validation parameters and loss functions. **(A)** Comparison of mAP_50 of bbox (IoU = 0.5) on different loss, **(B)** Comparison of mAP_50 of segmentation (IoU = 0.5) on different loss, and **(C)** Comparison of total loss.

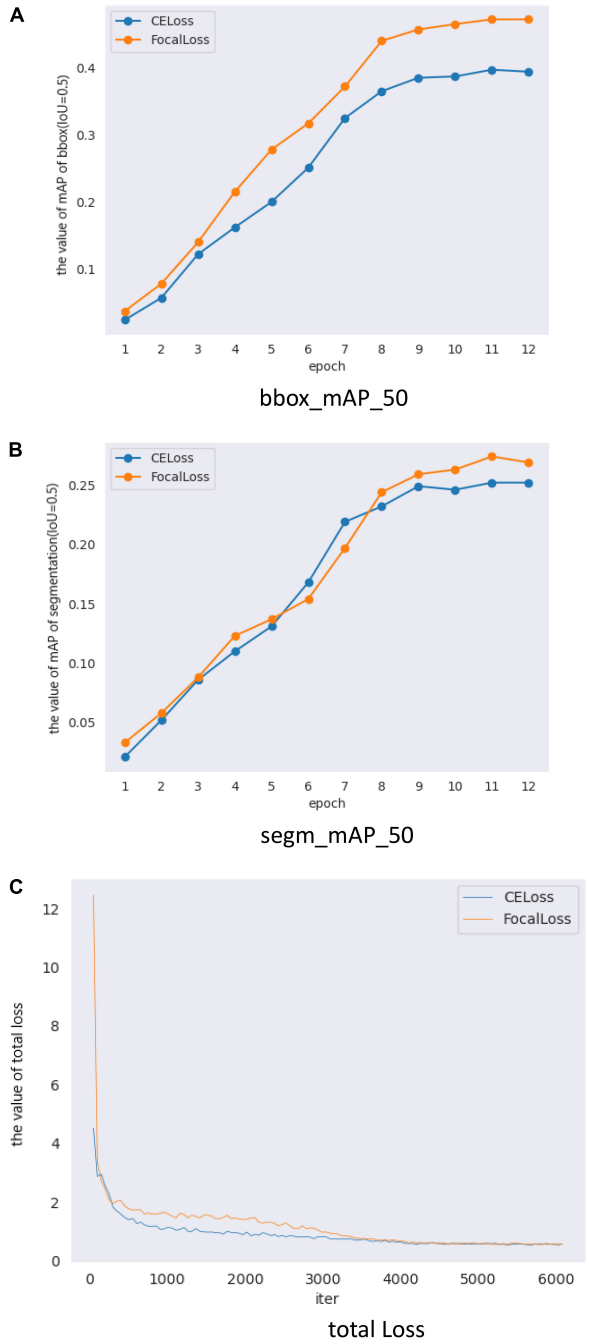

FIGURE 7 | Mask Scoring R-CNN with different loss validation parameters and loss functions. **(A)** Comparison of mAP_50 of bbox (IoU = 0.5) on different loss, **(B)** Comparison of mAP_50 of segmentation (IoU = 0.5) on different loss, and **(C)** Comparison of total loss.

label $y = 1$. Weighting factor $\alpha \in [0, 1]$ for class 1 and 1-α for class-1. While αbalances the importance of positive/negative examples, it does not differentiate between easy/hard examples. This focal loss function gives smaller weights to easy examples. This helps the training method to focus on hard negatives. A modulating factor $(1 - p_t)^{\gamma}$ is added to the cross-entropy loss, with tunable focusing parameter $\gamma \geq 0$.

When an example is misclassified and $p_t$is small, the modulating factor is near 1, and the loss is unaffected. When p_t is near 1, the factor $(1 - p_t)^{\gamma}$ is close to 0, and the loss for well-classified examples is downweighted. The focusing parameter γsmoothly adjusts the rate at which easy examples are downweighted. When $\gamma = 0$, FL is equivalent to CE, and as γ is increased, the effect of the modulating factor is likewise increased. Intuitively, the modulating factor reduces the loss contribution from easy examples and extends the range in which an example receives low loss.

TABLE 5 | Training parameter and test results based on Mask R-CNN with different loss functions.

Network	Bbox_ mAP_50	Segm_ mAP_50	Loss	Backbone	Epoch	γ	α
Mask R-CNN	0.749	0.452	CE	Rx101	1000		
Mask R-CNN	0.771	0.463	FL	Rx101	1000	2	0.95

TABLE 6 | Training parameter and test results based on Mask Scoring R-CNN with different loss functions.

Network	Bbox_ mAP_50	Segm_ mAP_50	Loss	Backbone	Epoch	γ	α
Mask Scoring R-CNN	0.387	0.252	CE	R50	12		
Mask Scoring R-CNN	0.472	0.274	FL	R50	12	4	0.45

TABLE 7 | Training parameter and test results based on Mask Scoring R-CNN with different loss functions.

Network	Bbox_ mAP_50	Segm_ mAP_50	Loss	Backbone	Epoch	γ	α
Mask Scoring R-CNN	0.479	0.311	CE	Rx101	12		
Mask Scoring R-CNN	0.544	0.336	FL	Rx101	12	4	0.45

TABLE 8 | Results of the method proposed in this study compared to other methods.

Network	Bbox_ mAP_50	Segm_ mAP_50	Loss	Backbone	Epoch	γ	α
Mask R-CNN	0.534	0.254	FL	R50	12	2	0.95
Mask Scoring R-CNN	0.472	0.274	FL	R50	12	4	0.45
Cascade R-CNN	0.450	0.243	CE	R50	12		
Cascade-DCN	0.447	0.250	CE	R50	12		
Mask-DCN	0.397	0.222	CE	R50	12		
Mask-DCNV2	0.232	0.127	CE	R50	12		
HRNet	0.303	0.183	CE	HRNet	12		

Implementation

The experiment of classification was performed on a CentOS workstation equipped with two Intel(R) Xeon(R) E5-2683 v4

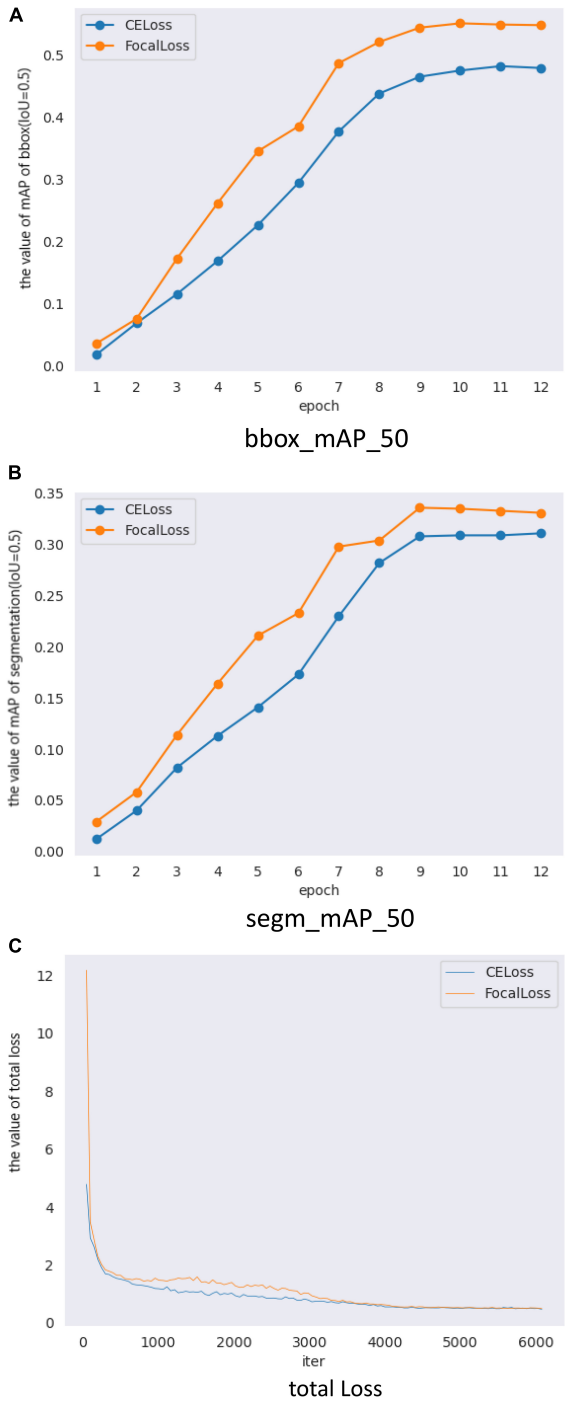

FIGURE 8 | Mask Scoring R-CNN with different loss validation parameters and loss functions. **(A)** Comparison of mAP_50 of bbox (IoU = 0.5) on different loss, **(B)** Comparison of mAP_50 of segmentation (IoU = 0.5) on different loss, and **(C)** Comparison of total loss.

CPU (55G RAM) and accelerated by two Tesla P100-PCIE GPU (16 GB memory). The model implementation in this paper was powered by the deep learning framework of Pytorch.

RESULTS AND DISCUSSION

In this study, mAP (mean average precision) is used as an evaluation indicator, which is usually used in instance segmentation tasks. The experiments based on MMDetection and bbox_mAP_50 represent mAP of BBox when IoU is 0.5. Also, segm_mAP_50 represents mAP of segmentation when IoU is 0.5, while R50 represents ResNet50.

Using focal loss, the empirical values given in the current study (Dai et al., 2017) are $\gamma = 2$ and$\alpha = 0.25$, but different data distributions require different parameters, so different gamma (γ) and alpha (α) values were tested, and the results are presented in **Table 2**. When $\gamma = 2$ and $\alpha = 0.95$, the result is improved using Mask R-CNN. But when Mask Scoring R-CNN was used, $\gamma = 4$ and $\alpha = 0.45$ provides better results, as given in **Table 3**. FL represents the focal loss in **Tables 2**, **3**, and the learning rate is 0.00025 in all the experiments.

In all the experiments of this study, the following parameters are similar: neck using FPN, loss_BBox of Rpn-head using L1 Loss, loss-cls of BBox-head using CE, and loss-BBox of BBox-head using L1 loss in roi_head and loss-mask of mask-head using CE. The focal loss was used in RPN. When focal loss and CE loss were used in RPN, the obtained BBox_mAP_50 and segm_mAP_50 metrics are presented in **Table 4**. The test results shows BBox_mAP_50 increased from 0.396 to 0.534 and segm_mAP_50 increased from 0.236 to 0.254 (**Table 4**). Mask R-CNN with a different loss function used the same training parameters (epoch, learning rate, and batch size). **Figure 5A** shows the validation mAP of BBox (IoU = 0.5) from 1 to 12 epochs when training the dataset with different loss functions, displaying that the validation mAP of BBox is higher with focal loss than with CE loss. **Figure 5B** shows the validation mAP of segmentation (IoU = 0.5) from 1 to 12 epochs when training the dataset with different loss functions, displaying that the validation mAP of segmentation is higher with focal loss than with CE loss. However, the increment in the map of segmentation is lower than BBox. **Figure 5C** shows the total loss value of the *y*-axis changes with the changed iter value of the *x*-axis when training the dataset with different loss functions. The results presented in **Figure 5** and **Table 4** show that the application of Mask R-CNN with focal loss achieves better performance compared with CE loss.

In general, deeper networks and larger epochs can provide better results. When epoch (1,000) and backbone (ResNetx101) are changed, the results obtained are displayed in **Figure 6** and **Table 5**. **Figure 6A** shows the validation mAP of BBox (IoU = 0.5) from 1 to 1,000 epochs when training the dataset with different loss functions, displaying validation mAP of BBox is higher with focal loss than with CE loss. **Figure 6B** shows validation mAP of segmentation (IoU = 0.5) from 1 to 1,000 epochs when training the dataset with different loss functions, displaying validation mAP of segmentation is higher with focal loss than with CE loss. **Figure 6C** shows the total loss value of the *y*-axis changes with the changed iter value of the *x*-axis when training the dataset with different loss functions. The results presented in **Figure 6**

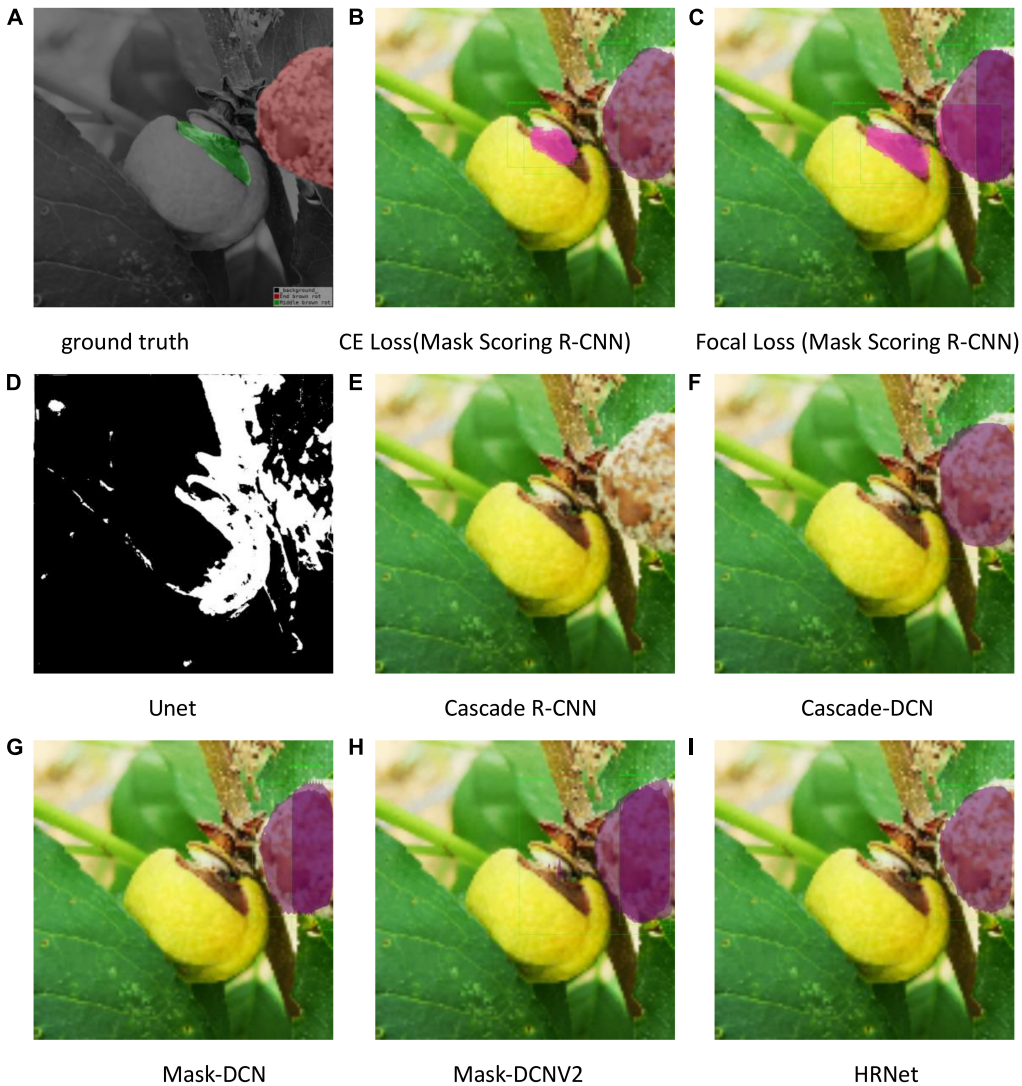

FIGURE 9 | Test results of different methods. **(A)** Ground truth, **(B)** CE Loss on Mask Scoring R-CNN, **(C)** Focal Loss on Mask Scoring R-CNN, **(D)** Unet, **(E)** Cascade R-CNN, **(F)** Cascade-DCN, **(G)** Mask-DCN, **(H)** Mask-DCNV2, and **(I)** HRNet.

and **Table 5** also show that the application of Mask R-CNN with focal loss achieves better performance compared to CE loss. Rx101 represents ResNetx101 in **Table 5**. The test results in **Table 5** show that BBox_mAP_50 increased from 0.749 to 0.771 and segm_mAP_50 increased from 0.452 to 0.463. It can be seen that with the increase of epochs and the deepening of network depth, a better effect is achieved. Despite changing epoch and backbone, the results presented in **Figure 6** and **Table 5** show that Mask R-CNN with focal loss achieves better performance compared to CE loss.

Figure 7 and **Table 6** show the results of Mask Scoring R-CNN. When focal loss and CE loss are used in RPN, the obtained BBox_mAP_50 and segm_mAP_50 metrics are presented in **Table 6**. The test results show BBox_mAP_50 increased from 0.387 to 0.472 and segm_mAP_50 increased from 0.252 to 0.274 (**Table 6**). **Figure 7A** shows the validation mAP of BBox (IoU = 0.5) from 1 to 12 epochs when training the dataset with different loss functions, displaying that the validation mAP of BBox is higher with focal loss than with CE loss. **Figure 7B** shows validation mAP of segmentation (IoU = 0.5) from 1 to 12 epochs when training the dataset with different loss functions, displaying that validation mAP of segmentation is higher with focal loss than with CE loss. **Figure 7C** shows the total loss value of the *y*-axis changes with the changed iter value of the *x*-axis when training the dataset with different loss functions. The results presented in **Figure 7** and **Table 6** show that the application of Mask Scoring R-CNN with focal loss achieves better performance compared to CE loss. Comparing the data presented in **Tables 4**, **6**, it can be found that the mAP of segmentation based on Mask Scoring R-CNN is higher than that based

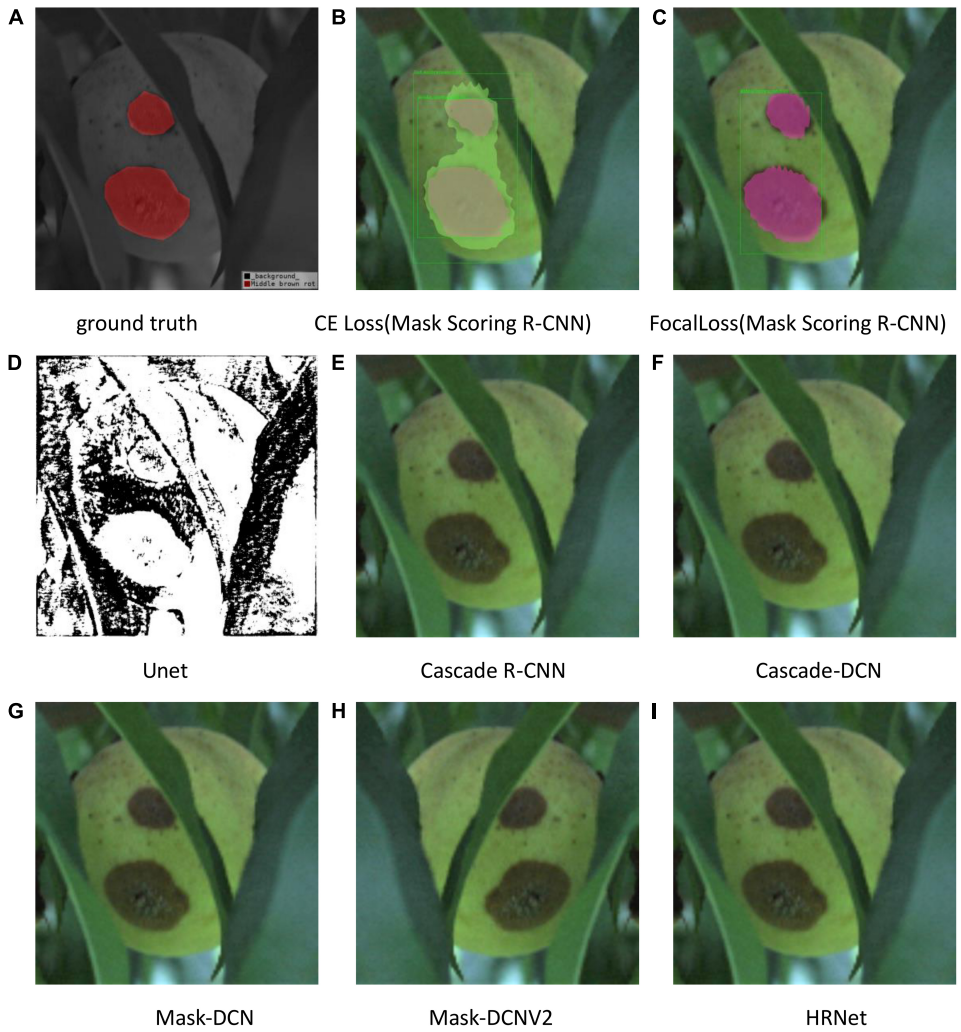

FIGURE 10 | Test results of different methods. **(A)** Ground truth, **(B)** CE Loss on Mask Scoring R-CNN, **(C)** Focal Loss on Mask Scoring R-CNN, **(D)** Unet, **(E)** Cascade R-CNN, **(F)** Cascade-DCN, **(G)** Mask-DCN, **(H)** Mask-DCNV2, and **(I)** HRNet.

on Mask R-CNN and also that the focal loss produces effective results.

When we only changed the backbone from ResNet50 to ResNetx101, the results of training and testing are shown in **Figure 8** and **Table 7**. The test results in **Table 7** show that BBox_mAP_50 increased from 0.479 to 0.544 and segm_mAP_50 increased from 0.311 to 0.336. It can be seen that an increase in network depth can improve object detection and segmentation effect. Although the backbone was changed, the results presented in **Figure 8** and **Table 7** show that Mask Scoring R-CNN with focal loss achieves better performance compared to CE loss.

Table 8 shows the results of Mask R-CNN/Mask Scoring R-CNN with focal loss compared to other methods. Cascade-DCN represents Cascade R-CNN with deformable convolutional networks. Mask-DCN represents Mask R-CNN with deformable convolutional networks. Mask-DCNV2 represents Mask R-CNN with deformable convolutional networks V2. Other hyperparameters of these six methods are similar. The last HRNet used the same learning rate and epoch, but the backbone was different. Using focal loss with Mask R-CNN and Mask Scoring R-CNN provides better segmentation results compared to other methods.

The test results are shown in **Figures 9**–**11**. All peach diseases were tested. Mask Scoring R-CNN with focal loss consistently produced better segmentation results: (1) Mask Scoring R-CNN with CE loss provides a segmentation that cannot cover some ground truth regions. Mask Scoring R-CNN with focal loss provides more correct segmentation results for the diseases brown rot, gummosis, leaf curl, and anthracnose. The test results for the brown rot disease are shown in **Figures 9**, **11**. (2) Mask Scoring R-CNN with CE loss produces a segmentation that covers regions not in the ground truth. Mask Scoring R-CNN with focal loss gives fewer false segmentations for the diseases like bacterial shot hole and brown rot. The test result for the disease brown rot is shown in **Figure 10**. (3) Mask Scoring R-CNN with CE loss presents no detection and segmentation, while

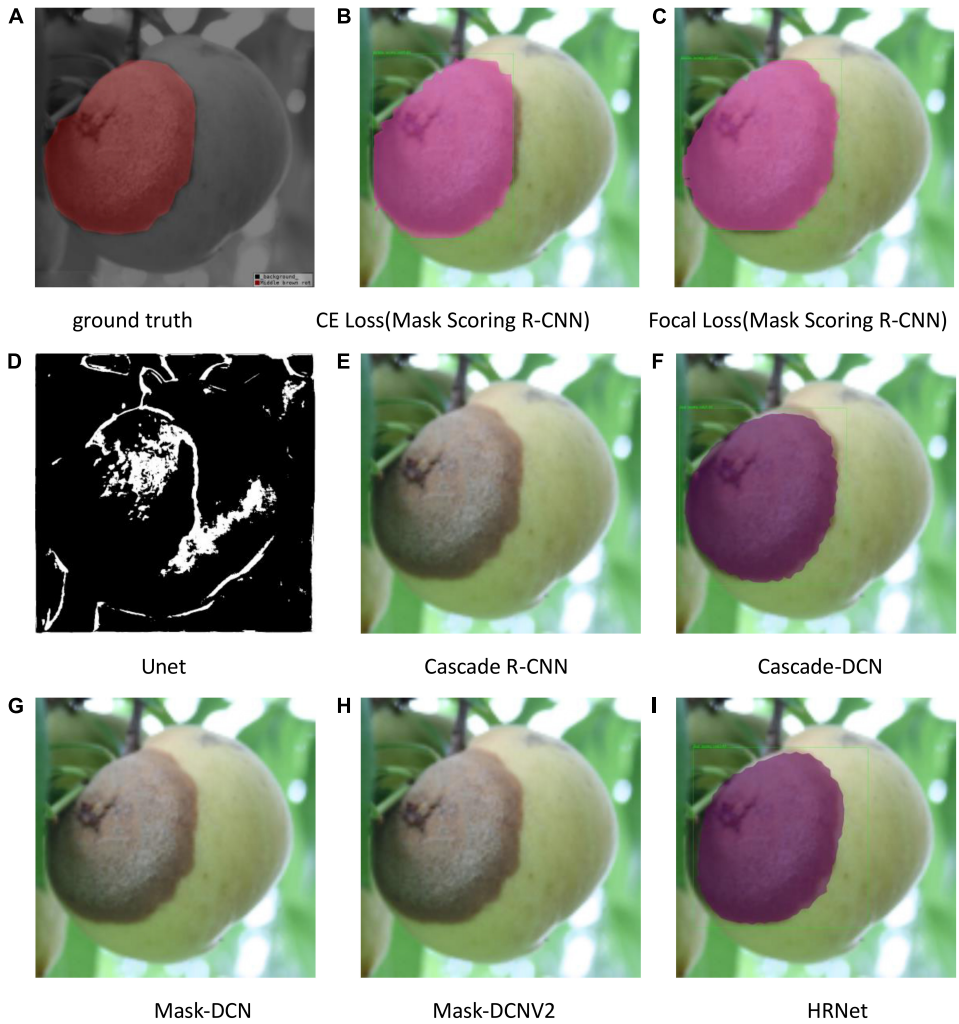

FIGURE 11 | Test results of different methods. **(A)** Ground truth, **(B)** CE Loss on Mask Scoring R-CNN, **(C)** Focal Loss on Mask Scoring R-CNN, **(D)** Unet, **(E)** Cascade R-CNN, **(F)** Cascade-DCN, **(G)** Mask-DCN, **(H)** Mask-DCNV2, and **(I)** HRNet.

TABLE 9 | Training parameters and test results on original dataset.

Network	Bbox_ mAP_50	Segm_ mAP_50	Loss	Backbone	Epoch	γ	α
Mask R-CNN	0.280	0.260	CE	R50	12		
Mask R-CNN	0.294	0.267	FL	R50	12	5	0.95
Mask Scoring R-CNN	0.293	0.264	CE	R50	12		
Mask Scoring R-CNN	0.301	0.279	FL	R50	12	5	0.75
Mask Scoring R-CNN	0.333	0.313	CE	Rx101	24		
Mask Scoring R-CNN	0.371	0.333	FL	Rx101	24	5	0.75

Mask Scoring R-CNN with focal loss provides detection and segmentation. The data presented in **Figures 9D–11D** are tested by the U-Net model, which illustrates that the results are poor. Since the three test images have complex backgrounds, the lesion areas were not segmented well from the background. However, when the lesion areas and background are relatively simple, the segmentation is better.

The results obtained by conducting the same experiments on the original dataset are summarized in **Table 9**. The original dataset (PDID) includes seven peach diseases, with 1,560 images. The ratio of training samples, validation samples, and test samples is 7:2:1. **Table 9** shows that focal loss can improve the mAP of BBox and segmentation on both Mask R-CNN and Mask Scoring R-CNN tasks. But, the parameters of γandαneed to get the optimal value through experiments. The parameters will be different when the dataset is different.

CONCLUSION

In this study, the output of this method provides information regarding the names of peach disease, disease severity levels,

and masked lesion areas. Hence, detailed information about the diseases, not limited to disease names, can be obtained. Usually, disease names can be obtained by classification tasks. Data pertaining to disease names, disease severity level, and masked lesion areas are usually achieved by instance segmentation tasks. This study used the focal loss to improve the effect of instance segmentation. Due to the difficulty in obtaining the pictures of peach disease, the peach disease dataset often has unbalanced or hard samples. We used focal loss in the first stage, and segmentation results were found to be improved. Focal loss was used in Mask R-CNN and Mask Scoring R-CNN for classification, location, and segmentation of peach diseases, while getting better segmentation results. When using Mask R-CNN with ResNet50 as a backbone network, the focal loss parameters gamma (γ) was 2.0 and alpha (α) was 0.95. When Mask Scoring R-CNN was used with ResNet50 and ResNetx101 as the backbone network, the focal loss parameters gamma was 4.0 and alpha was 0.45. We also observed that the deeper the backbone network, the better the effect of focal loss. When dataset is changed, the parameters of $\gamma$and$\alpha$are different. Additionally, the U-Net model was used to segment the lesion areas of peach disease images, but the results showed that this model has a poor accuracy in complex background images. So, the method adopted in this study can improve the segmentation results and can also provide the disease names and severity (early, middle, and end), by displaying the lesion areas by mask. Thus, this technique can provide more detailed information for effective disease treatment and analysis.

DATA AVAILABILITY STATEMENT

The raw data supporting the conclusions of this article will be made available by the authors, without undue reservation.

AUTHOR CONTRIBUTIONS

FN devised the study in collaboration with W-KS, GL, and HW. MW carried out experimental work partly. All authors read and approved the manuscript.

FUNDING

This work was supported by the Key Special Project National Key R&D Program of China (grant number: 2018YFC1604000), partly by the earmarked fund for Modern Agro-Industry Technology. Research System (no. CARS-30), Natural Science Foundation of Hubei Province (grant number: 2019CFC855), partly by Supported by "the Fundamental Research Funds for the Central Universities", Huazhong Agricultural University (grant number: 2662017PY119).

ACKNOWLEDGMENTS

We thank all the colleagues from Prof. Luo chaoxi's team, College of Plant Science and Technology, HZAU for helping collecting and labeling the peaches' images.

REFERENCES

Badrinarayanan, V., Kendall, A., and Cipolla, R. (2017). "SegNet: a deep convolutional encoder-decoder architecture for image segmentation," in *IEEE Transactions on Pattern Analysis & Machine Intelligence*, Piscataway, NJ: IEEE. doi: 10.1109/TPAMI.2016.2644615

Cai, Z., and Vasconcelos, N. (2019). Cascade R-CNN: high quality object detection and instance segmentation. *IEEE Trans. Pattern Anal. Mach. Intell.* 43, 1483–1498. doi: 10.1109/TPAMI.2019.2956516

Chen, L. C., Papandreou, G., Kokkinos, I., Murphy, K., and Yuille, A. L. (2014). Semantic image segmentation with deep convolutional nets and fully connected CRFs. *arXiv* [Preprint]. doi: 10.48550/arXiv.1412.7062

Dai, J., Qi, H., Xiong, Y., Li, Y., Zhang, G., Hu, H., et al. (2017). "Deformable convolutional networks," in *Proceeding of the IEEE International Conference on Computer Vision*, Venice.

Dai, Z. (2020). *Rice Disease Detection Technology Based on Semantic Segmentation*. Chengdu: Xihua University.

Girshick, R. (2015). "Fast r-cnn," in *Proceedings of the 2015 IEEE International Conference on Computer Vision*, Santiago, 1440–1448.

He, K., Gkioxari, G., Dollár, P., and Girshick, R. (2017). "Mask r-cnn," in *Proceedings of the 2017 IEEE International Conference on Computer Vision*, Venice, 2961–2969.

Hu, Y., Cang, Y., and Qiao, Y. (2020). Design of intelligent pig counting system based on improved instance segmentation algorithm. *Trans. Chin. Soc. Agric. Eng.* 36, 177–183.

Huang, Z., Huang, L., Gong, Y., Huang, C., and Wang, X. (2019). "Mask scoring R-CNN," in *2019 IEEE/CVF Conference on Computer Vision and Pattern Recognition (CVPR)*, Long Beach, CA: IEEE.

Jin, L., and Qian, L. (2020). Image semantic segmentation and localization of brassica chinensis disease area based on deep learning. *J. Anhui Agric. Sci.* 48, 235–238.

Lin, K., Gong, L., Huang, Y., Liu, C., and Pan, J. (2019). Deep learning-based segmentation and quantification of cucumber powdery mildew using convolutional neural network. *Front. Plant Sci.* 10:155. doi: 10.3389/fpls.2019.00155

Lin, T. Y., Goyal, P., Girshick, R., He, K., and Dollár, P. (2017). "Focal loss for dense object detection," in *IEEE Transactions on Pattern Analysis & Machine Intelligence, 2999-3007*, Piscataway, NJ: IEEE.

Long, J., Shelhamer, E., and Darrell, T. (2015). Fully convolutional networks for semantic segmentation. *IEEE Trans. Patt. Anal. Mach. Intell.* 39, 640–651.

Lu, J., Hu, J., Zhao, G., Mei, F., and Zhang, C. (2017). An in-field automatic wheat disease diagnosis system. *Comput. Electron. Agric.* 142, 369–379. doi: 10.1016/j.compag.2017.09.012

Noh, H., Hong, S., and Han, B. (2016). "Learning deconvolution network for semantic segmentation," in *2015 IEEE International Conference on Computer Vision (ICCV)*, Santiago: IEEE.

Ronneberger, O., Fischer, P., and Brox, T. (2015). *U-Net: Convolutional Networks for Biomedical Image Segmentation*. Cham: Springer.

Shi, J., Zhou, Y., and Zhang, Q. (2019). Service robot item recognition system based on improved Mask RCNN and Kinect. *Chin. J. Sci. Instrum.* 40, 216–228.

Sun, K., Xiao, B., Liu, D., and Wang, J. (2019a). "Deep high-resolution representation learning for human pose estimation," in *Proceedings of the IEEE/CVF Conference on Computer Vision and Pattern Recognition*, Long Beach, CA, 5693–5703.

Sun, K., Zhao, Y., Jiang, B., Cheng, T., Xiao, B., Liu, D., et al. (2019b). High-resolution representations for labeling pixels and regions. *arXiv*. [preprint], Avaliable at: https://arxiv.org/abs/1904.04514 (accessed April 19, 2022).

Yang, X., Liu, M., Xu, J., and Zhao, L. (2018). Image segmentation and recognition algorithm of greenhouse whitefly and thrip adults for automatic monitoring device. *Trans. Chin. Soc. Agric. Eng.* 34, 164–170.

Yao, N., Ni, F., Wang, Z., Luo, J., Sung, W. K., and Luo, C., et al. (2021). L2MXception: an improved Xception network for classification of peach diseases. *Plant Methods* 17:36. doi: 10.1186/s13007-021-00736-3

Zhao, H., Shi, J., Qi, X., Wang, X., and Jia, J. (2017). "Pyramid scene parsing network," in *Proceedings of the 2017 IEEE Conference on Computer Vision and Pattern Recognition*, Honolulu, HI, 2881–2890.

Zhong, W., Liu, X., Yang, K., and Li, F. (2020). Research on multi-target leaf segmentation and recognition algorithm under complex background based on Mask-R CNN. *Acta Agric. Z.* 32, 2059–2066.

Zhu, X., Hu, H., Lin, S., and Dai, J. (2019). "Deformable ConvNets V2: more deformable, better results," in *IEEE/CVF Conference on Computer Vision and Pattern Recognition (CVPR)*, Long Beach, CA: IEEE.

Conflict of Interest: The authors declare that the research was conducted in the absence of any commercial or financial relationships that could be construed as a potential conflict of interest.

frontiers | Frontiers in Plant Science

ORIGINAL RESEARCH
published: 28 June 2022
doi: 10.3389/fpls.2022.915543

Detection of Small-Sized Insects in Sticky Trapping Images Using Spectral Residual Model and Machine Learning

*Wenyong Li[1], Zhankui Yang[1,2], Jiawei Lv[1,3], Tengfei Zheng[1,4], Ming Li[1] and Chuanheng Sun[1]**

[1] National Engineering Research Center for Information Technology in Agriculture, Beijing, China, [2] College of Computer Science and Technology, Beijing University of Technology, Beijing, China, [3] College of Information Science and Technology, Zhongkai University of Agriculture and Engineering, Guangzhou, China, [4] College of Information, Shanghai Ocean University, Shanghai, China

One fundamental component of Integrated pest management (IPM) is field monitoring and growers use information gathered from scouting to make an appropriate control tactics. Whitefly (*Bemisia tabaci*) and thrips (*Frankliniella occidentalis*) are two most prominent pests in greenhouses of northern China. Traditionally, growers estimate the population of these pests by counting insects caught on sticky traps, which is not only a challenging task but also an extremely time-consuming one. To alleviate this situation, this study proposed an automated detection approach to meet the need for continuous monitoring of pests in greenhouse conditions. Candidate targets were firstly located using a spectral residual model and then different color features were extracted. Ultimately, Whitefly and thrips were identified using a support vector machine classifier with an accuracy of 93.9 and 89.9%, a true positive rate of 93.1 and 80.1%, and a false positive rate of 9.9 and 12.3%, respectively. Identification performance was further tested *via* comparison between manual and automatic counting with a coefficient of determination, R^2, of 0.9785 and 0.9582. The results show that the proposed method can provide a comparable performance with previous handcrafted feature-based methods, furthermore, it does not require the support of high-performance hardware compare with deep learning-based method. This study demonstrates the potential of developing a vision-based identification system to facilitate rapid gathering of information pertaining to numbers of small-sized pests in greenhouse agriculture and make a reliable estimation of overall population density.

Keywords: pest detection, sticky trap, small objects detection, image processing, machine learning

OPEN ACCESS

Edited by:
Lei Shu,
Nanjing Agricultural University, China

Reviewed by:
Muhammad Musa Khan,
South China Agricultural University, China
Tonghai Liu,
Tianjin Agricultural University, China

***Correspondence:**
Chuanheng Sun
sunch@nercita.org.cn

Specialty section:
This article was submitted to Sustainable and Intelligent Phytoprotection, a section of the journal Frontiers in Plant Science

Received: *08 April 2022*
Accepted: *24 May 2022*
Published: *28 June 2022*

Citation:
Li W, Yang Z, Lv J, Zheng T, Li M and Sun C (2022) Detection of Small-Sized Insects in Sticky Trapping Images Using Spectral Residual Model and Machine Learning. Front. Plant Sci. 13:915543. doi: 10.3389/fpls.2022.915543

INTRODUCTION

Integrated pest management (IPM) has been widely applied to the agricultural practices in the field to minimize yield loss and reduce the use of chemical insecticides (Boissard et al., 2008; Espinoza et al., 2016; Rustia et al., 2020). This approach utilizes underlying presence of natural enemies, or likelihood of presence in the field (Wen and Guyer, 2012; Yang et al., 2021). Therefore, the accurate detection of pest species is essential for maximizing the successful IPM.

In greenhouses, one of the most common approaches used for pest detection is using sticky traps to capture insects and subsequently count the presence (and number) of target pest species on these traps. Based on the density and severity of pests in the greenhouse, growers apply appropriate control tactics (Ebrahimi et al., 2017). However, traditional manual identification and counting of insects on a trap is a time-consuming and labor-intensive task. Given these underlying challenges associated with the identification and counting of insect pests in the greenhouse, an automatic pest detection approach is vital to the modern agricultural production.

With advancements in imaging technology and computer software, image-based approaches have been developed in recent years for the detection of small-sized pests in greenhouse agriculture, including traditional machine learning and deep learning methods. In the term of traditional machine learning, Solis-Sánchez et al. utilized shape features (e.g., eccentricity and area) and adaptive threshold discriminant method to detect whiteflies (Solis-Sánchez et al., 2010). To improve feature robustness, they extracted invariant features to discriminate and identify different insect species and an improved precision was achieved compared to previous work (Solis-Sánchez et al., 2011). Besides, Xia et al. (2012) introduced a multifractal analysis approach for detecting whiteflies on a sticky trap *in situ* using a mobile robot to collect insects. Furthermore, to improve pest counting efficiency, Xia et al. (2015) proposed an automatic pest identification method suitable for long term monitoring *in situ* with less computational cost by applying YCbCr color space for segmentation and Mahalanobis distance for identification of pest species (Xia et al., 2015). Espinoza et al. proposed an image processing system that involved object segmentation, as well as morphological and color property estimations, to detect whitefly and thrips (Espinoza et al., 2016). However, these color-based object segmentation methods were not robust to various conditions in the field, such as variable illumination and sticky glue degeneration. Rather than directly counting the pests captured on the traps, Sun et al. presented a counting algorithm to treat trapped pests as "noise" in a two-dimensional (2D) image with two-dimensional Fourier transform (2DFT) serving as a specific noise collector (Sun et al., 2017), but it could not separate pests from real environmental noises and thus did not resolve the species identification problem. In contrast to conventional machine learning methods, deep learning methods automatically ascertain the comprehensive features from the training dataset, avoiding complex image processing procedures during object segmentation and labor-intensive feature engineering to meet various outdoor conditions. Rustia et al. developed a cascaded approach that detects and filters out non-insect objects from the detected objects using a convolutional neural network (CNN) detector in the first stage and then further classifies the obtained insect objects into different species using a multi-class CNN classifier (Rustia et al., 2020). Li et al. (2021) proposed a deep learning model on the basis of the Faster R-CNN architecture to optimize the detection accuracy of tiny pests in sticky trap images from agricultural greenhouses.

Although the above-mentioned studies have achieved good performance and solved some special problems, there is still space for improvement in this area of research. For instance, these methods based on traditional machine learning are not flexible due to the object segmentation bases on threshold strategies. In deep learning area, the typical classification models using the CNN structure rely on large datasets to train the models, but actually, it is hard to obtain a large labeled dataset in many cases (Li and Yang, 2020). Furthermore, greenhouse pests such as whitefly (*Bemisia tabaci*) and western flower thrips (*Frankliniella occidentalis*) are small in size, which will cause information loss during the multi-layer convolution in deep learning architecture. Although many object detectors based on deep learning perform well on medium and large objects, they perform poorly on the task of detecting small objects (Tong et al., 2020). This is because small objects lack appearance information needed to distinguish them from background or similar categories. However, comparing to image background, these tiny pests could be regarded as many "novelty" objects in the sticky trapping images. Since the spectral residual model is independent of features, categories, or other forms of prior knowledge of the objects, it has been widely in small object detection (Zhou and Zhang, 2007; Cui et al., 2012; Deng and Duan, 2013). Therefore, we investigate whether it can be also applied to detect very small pests under natural greenhouse conditions.

In this study, we propose a spectral residual model-based method in combination with a support vector machine (SVM) classifier to identify the most important pests in greenhouse of northern China, namely whitefly (*Bemisia tabaci*) and thrips (*Frankliniella occidentalis*). This work provides a major step toward population estimation in greenhouses and providing accurate, rapid and reliable results to aid in decision making processes for pesticide application and pest management approaches.

MATERIALS AND METHODS

Data Collection

Red-green-blue (RGB) color images were captured automatically by a pest monitoring device (**Figure 1**) in a greenhouse located in Fangshan district, Beijing, China (39°38′19.29″N, 116°01′29.98″E). The device consisted of a solar panel, sticky trap, image acquisition module and storage battery. The device was deployed in the center of the greenhouse, and the height of the sticky trap (25 × 30 cm, Pheorbio®) was above the crop at 1.5 m from ground level. The sticky trap is a typical attractant trap used widely for collection of pests of interest whereby insects became adhered to the sticky surface. The experiment was carried out on green pepper plants cultivated under greenhouse conditions.

Two species, adult-stage whitefly (*B. tabaci*) and thrips (*F. occidentalis*) were selected as the detection target in this study. Solid-color traps were used to avoid "noise" in the digital images caused by grids, as previously reported elsewhere (Xia et al., 2015; Espinoza et al., 2016). Images of the sticky trap (25 × 20 cm) were collected and transmitted to a remote server at 2,560 × 1,920 pixels every 2 h daily (8:00 a.m. to 18:00 p.m.). Generally, the sticky paper is replaced every 6 days to maintain

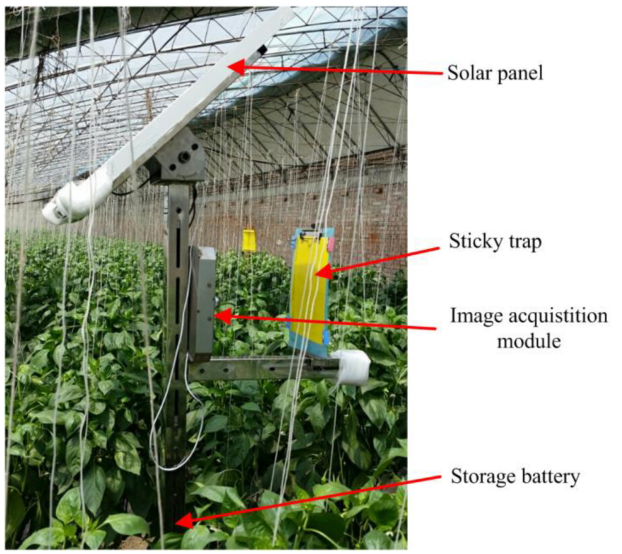

FIGURE 1 | Image acquisition equipment and sticky trap for detection of insect pests in greenhouse conditions (Li et al., 2021).

good trapping effectiveness. Therefore, in this study, eighteen original images were selected to extract training samples from six consecutive days, that is, three original images were selected each day in the period (one image in the morning, midday, and afternoon, respectively). Likewise, eighteen original images were selected to create test samples from another six consecutive days. Thereafter, sample images of three classes, two target species and background, were extracted with a square box of 32 × 32 pixels manually from the original images. Ultimately, 500 sample images for each class, totally 1,500 sample images, were randomly selected from the first eighteen original images to construct the training dataset. And all target species (whitefly and thrips) on the second eighteen original images were used as test dataset.

Detection Method

The proposed detection method consisted of three stages: candidate object location, feature extraction and multi-class recognition. The candidate object location is a pipeline to detect the location of objects (section "Candidate Object Location"), feature extraction devotes to extract feature of the detected objects (section "Feature Extraction") and these obtained objects were then further classified into whitefly, thrips and background in the stage of multi-class recognition (section "Multi-Class Recognition Model"). These procedures are outlined in the following subsections.

Candidate Object Location

Before performing feature extraction and pattern recognition, the locations of candidate targets within the image are determined. The locationpipeline in the sticky trapping images involved several subroutines, as shown in **Figure 2**. First, a color-based segmentation approach is design to extract the sticky paper region from the original image. Then, the sticky trapping image is divided into sub-block images and objects in each sub-block image are locally detected using a saliency region detection model. Subsequently, a threshold is determined and used to obtain the location of the objects.

Extraction of Sticky Paper Region

The sticky paper region, denoted as the region of interest (RoI) in this study, is extracted from the original image. First, the original image (**Figure 3A**) is transformed into YCbCr color space from the RGB color space and the RoI could be distinguished from background based on the Cb component of YCbCr color space (**Figure 3B**). Subsequently, the Cb component is processed into a binary image (**Figure 3C**) using the Ostu method (Otsu, 1979) and a morphological fill operation. Finally, the RoI image (**Figure 3D**) is obtained by performing a logical conjunction between the original image (**Figure 3A**) and the binary image (**Figure 3C**).

Image Blocking

The small-sized insect pests in this study can be distinguished more accurately at a small scale as opposed to a global (i.e., whole RoI) image. Thus, the RoI image is divided into multiple sub-blocks using a sliding window and each block size was 64 × 64 pixels, as shown in **Figure 4**.

Saliency Region Detection

In the sub-block image, small-size insects in local window were regarded as "novelty" objects or saliency regions. These insects can be identified and localized using the saliency region detection method. In this study, a spectral residual model (Zhou and Zhang, 2007) is used to locate the small-size insects in each sub-block image. To construct the saliency map, the spectral residual is extracted by analyzing the log-spectrum of the input sub-block image. Given a sub-block image $I(x)$, the saliency map image $S(x)$ can be obtained using the following equations:

$$A(f) = |F[I(x)]| \tag{1}$$

$$P(f) = \varphi(F[I(x)]) \tag{2}$$

$$L(f) = \log(A(f)) \tag{3}$$

$$R(f) = L(f) - h_n(f)^* L(f) \tag{4}$$

$$S(x) = g(x)^* F^{-1}[\exp(R(f) + iP(f))]^2 \tag{5}$$

where F and F^{-1} denote the Fourier Transform (FT) and Inverse Fourier Transform (IFT), respectively. $A(f)$ and $P(f)$ denote the amplitude and phase spectrum of the image, respectively. $L(f)$ and $R(f)$ denote the log spectrum and spectral residual. $h_n(f)$ and $g(x)$ denote local average and Gaussian filter, respectively.

The pipeline of saliency region detection is illustrated in **Figure 5**. First, the log-spectrum using two-dimensional fast Fourier transform (2DFFT) and a logarithm to the input sub-block image (**Figure 5A**) are calculated. As shown in **Figure 5B**, most of the log-spectrum distribute in the low frequency portion

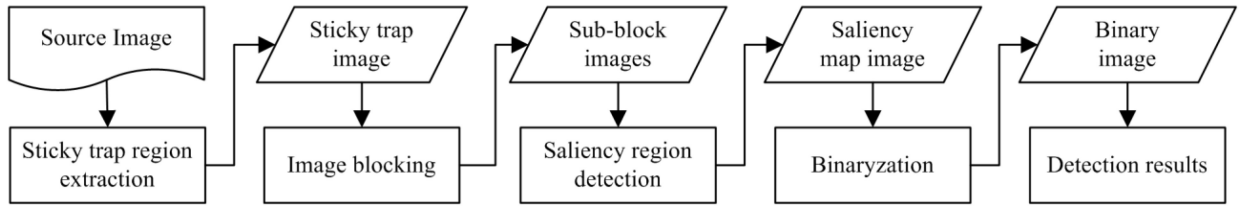

FIGURE 2 | Flow chart of the candidate object location pipeline from source image to detection results.

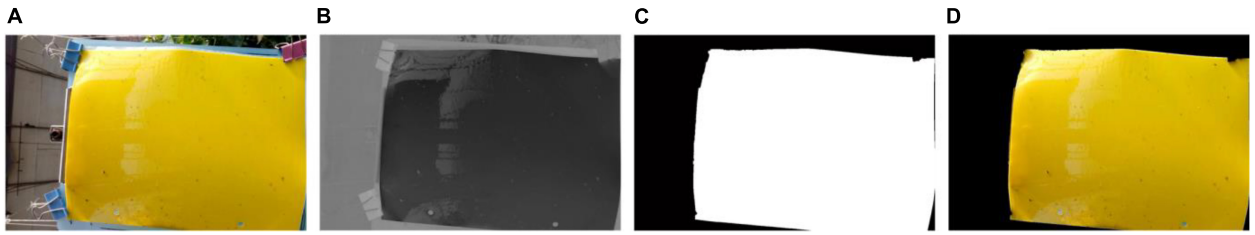

FIGURE 3 | Illustration of the sticky trap region extraction using image processing technology: **(A)** original image, **(B)** Cb component in YCbCr color space, **(C)** binary image, and **(D)** extraction result of the specific region of interest.

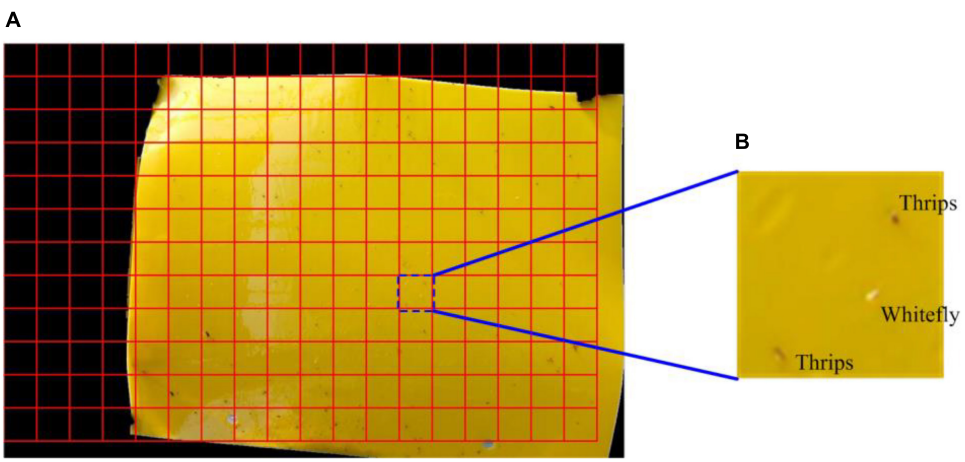

FIGURE 4 | Image blocking diagram. **(A)** This sticky trapping image is divided into a specific region of interest with a specific scale and **(B)** an illustration of an enlarged sub-block image.

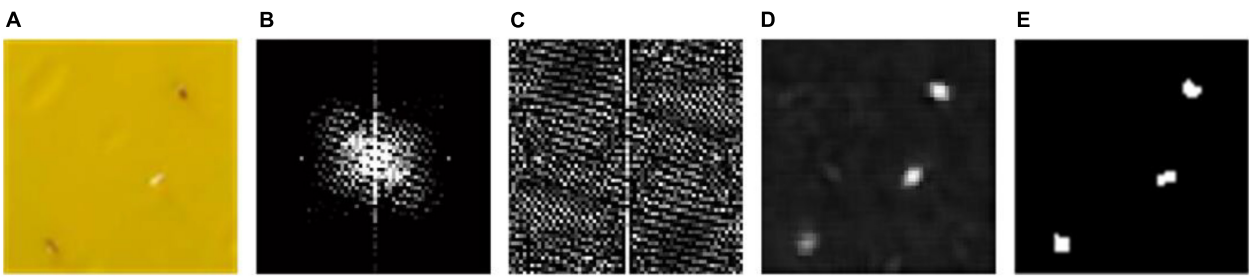

FIGURE 5 | Illustration of saliency region detection for insect pests collected on sticky traps and identified with image acquisition software: **(A)** a sub-block image from the sticky trap, **(B)** log-spectrum distribution of the sub-block, **(C)** the spectral residual image, **(D)** a saliency map of the insect pests and **(E)** binary image of the saliency map.

(white regions of the center), which represents the input image includes slowly changing background and a few salient objects. The spectral residual is obtained by the log-spectrum minus the average spectrum which can be approximated using a local average filter (e.g., step size = 3). However, it can be found from **Figure 5C** that the spectral residual contains high frequency information, which is sharply different from the log-spectrum. After using a two-dimensional inverse Fourier transform (2DIFFT), the saliency map in spatial domain is constructed and the novelty objects (candidate insects in this study) of the image can be seen more clearly in the saliency map (**Figure 5D**).

Image Binarization

The saliency map is an explicit representation of candidate insects in the image. Furthermore, there may be multiple objects within a saliency region. In this section, a threshold segmentation method combined with watershed theory (Meyer, 1994; Dorj et al., 2017) is designed to detect insects within this saliency region. First, the saliency map image is transformed into a binary image using an adaptive threshold value and then watershed algorithm (Tarabalka et al., 2010; Zhang et al., 2014) is selected to segment multiple objects. Since the intensity of the histogram of the saliency map only had a peak and the peak is close to the darkest side, as shown in **Figure 6**, the threshold value is adaptively determined by using a triangle theory. The steps are as followed:

S1: Constructing a line from the peak to the first darkest point on the intensity histogram.

S2: Calculating the distance from each point of histogram to the line.

S3: The location Ta which has the largest distance d is the threshold value.

A binary image could be obtained by using the proposed threshold method. Furthermore, the size of target pests is approximately from 5 pixels to 25 pixels in a sub-block image. Therefore, non-target objects whose sizes are less than 5 pixels or more than 25 pixels are removed from the binary image. Ultimately, the remaining isolated individuals represent the location results (**Figure 5E**).

Feature Extraction

To identify insect species on the RoI image, all isolated insects are segmented and their features are extracted from sub-block images. As shown in **Figure 7**, the sample pest i on a sub-block image (**Figure 7A**) could be segmented into an isolated pest (**Figure 7C**) by performing a logical conjunction operation between the sub-block image and the detected region (**Figure 7B**). As shown in **Figure 7C**, the shape of segmented object is different from its original appearance because of inaccurate segmentation for some pixels of the insects, especially in the boundary of insect region. Therefore, the insect contours are not smooth and the insects can't be accurately identified based solely on shape feature. However, for the two species (whitefly and thrips), different color variation occurs as shown in **Figure 4B**. Therefore, the color feature is a critical factor to identify the insect species. To determine the optimal color feature, four color models widely used in computer vision-based applications (Kurtulmus et al., 2011; Hu et al., 2012; Reyes et al., 2017; Tan et al., 2018) are evaluated: RGB (red, green and blue), HSV (hue, saturation and value), YCbCr (luminance, blue-difference and red-difference) and L*a*b* (lightness, green-red, and blue-yellow).

The features of each segmented sample are represented by average values of R, G, and B components in RGB space, H, S, and V component in HSV space, Y, Cb, and Cr components in YCbCr space, L*, a*, and b* in L*a*b* color space, respectively. The transformations are shown in Eqs (6)–(9).

$$\overline{R} = \frac{\sum_{i=1}^{n_j} R_{\mathrm{i}}}{n_j},\ \overline{G} = \frac{\sum_{i=1}^{n_j} G_{\mathrm{i}}}{n_j},\ \overline{B} = \frac{\sum_{i=1}^{n_j} B_{\mathrm{i}}}{n_j} \tag{6}$$

$$\overline{H} = \frac{\sum_{i=1}^{n_j} H_{\mathrm{i}}}{n_j},\ \overline{S} = \frac{\sum_{i=1}^{n_j} S_{\mathrm{i}}}{n_j},\ \overline{V} = \frac{\sum_{i=1}^{n_j} V_{\mathrm{i}}}{n_j} \tag{7}$$

$$\overline{Y} = \frac{\sum_{i=1}^{n_j} Y_{\mathrm{i}}}{n_j},\ \overline{Cb} = \frac{\sum_{i=1}^{n_j} Cb_{\mathrm{i}}}{n_j},\ \overline{Cr} = \frac{\sum_{i=1}^{n_j} Cr_{\mathrm{i}}}{n_j} \tag{8}$$

$$\overline{L^*} = \frac{\sum_{i=1}^{n_j} L_{\mathrm{i}}^*}{n_j},\ \overline{a^*} = \frac{\sum_{i=1}^{n_j} a_{\mathrm{i}}^*}{n_j},\ \overline{b^*} = \frac{\sum_{i=1}^{n_j} b_{\mathrm{i}}^*}{n_j} \tag{9}$$

where $\overline{R}$, $\overline{G}$, $\overline{B}$, $\overline{H}$, $\overline{S}$, $\overline{V}$, $\overline{Y}$, $\overline{Cb}$, $\overline{Cr}$ $\overline{L^*}$, $\overline{a^*}$, and $\overline{b^*}$ denote the average value of corresponding color component over all pixels. n_j denotes the number of image pixel of the jth segmented insect sample. The three average components of a sample in each color space constructed a three-dimensional vector f_{i1}, f_{i2}, f_{i3}, as shown in **Figure 7D**, which is used as the input of the classifier (discussed in Section "Multi-Class Recognition Model") for species classification.

Multi-Class Recognition Model

After features extraction, a following step is to develop an efficient model to identify different insect species. In this study, the supervised learning model, support vector machine (SVM) (Chen et al., 2010; Li et al., 2010; Saruta et al., 2013), is used as a classifier to discriminate objects between whitefly, thrips or background. For the SVM model, all samples are viewed as points in p-dimensional space and these points in separate categories are divided through a clear gap that is as wide as possible (Rumpf et al., 2010). New examples are then mapped into the same space and predicted to a certain category based on which side of the gap they fall (Larese et al., 2014). In this study, each sample in the training set is marked as belonging to a whitefly, a thrips or background object and all samples are formed into pairs of features-label examples such $\{\mathrm{x}_i, y_i\}$, where x_i is the three-dimensional feature vector and y_i is a class label. Our ultimate goal is to find the "maximum-margin hyperplane" that can divide the groups of samples. One of many possible hyperplanes can be expressed by the following equation:

$$f(\mathrm{x}_i) = w^T \mathrm{x}_i + b = 0 \tag{10}$$

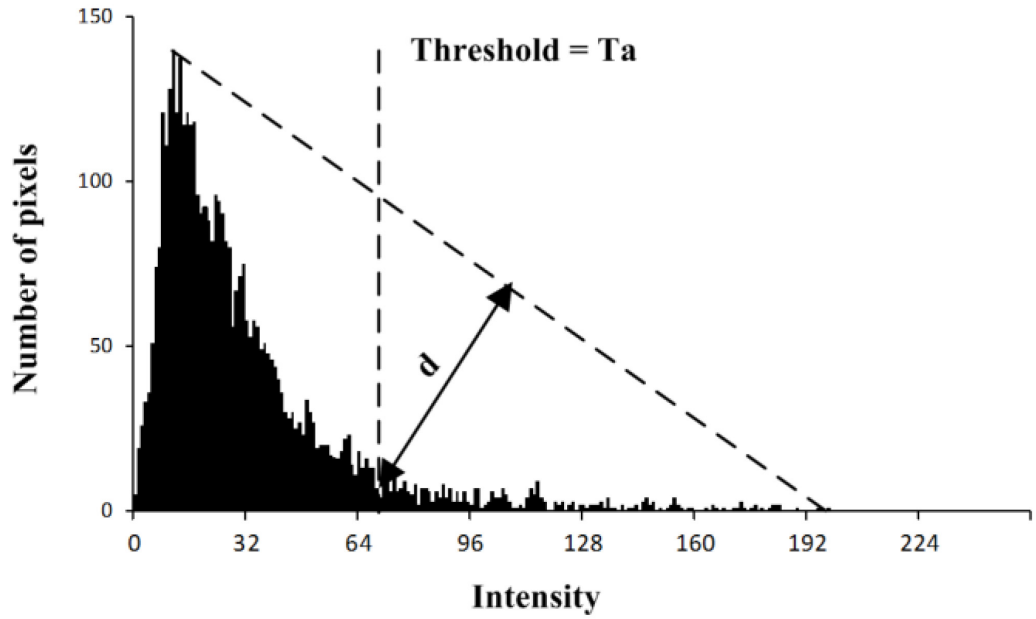

FIGURE 6 | Determination of the threshold value for each saliency map.

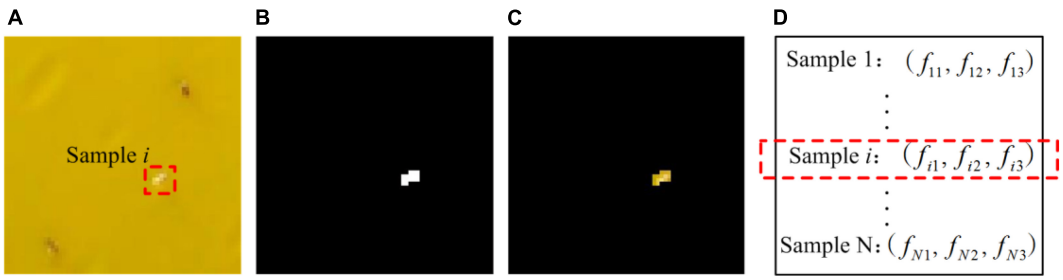

FIGURE 7 | Images documenting feature extraction of individual insects. **(A)** Sub-block image, **(B)** a detected region, **(C)** an isolated insect, **(D)** feature vector in color space.

where $w \in R^d$ and $b \in R$. A support vector classifier selects the hyperplane that maximizes the margin. This optimization problem can be posed as follows:

$$\min_{w,b} \|w\|, y_i(w^T x_i + b) - 1 \geq 0 \tag{11}$$

In this study, the LIBSVM package (Chang and Lin, 2015), which supports support vector classification (C-SVC, mu-SVC) and regression (epsilon SVR, nu-SVR), is used to conduct the identification model development.

Performance Evaluation

The detection results are evaluated using metrics, such as the true positive rate (TPR), false positive rate (FPR) and detection accuracy. These metrics have been widely used in object classification and detection areas (Xia et al., 2012; Nasirahmadi et al., 2017; Shrestha et al., 2018). TPR refers to the effectiveness of a classifier to identify positive samples, whitefly and thrips in this study. A high TPR value means that most of the positive samples are detected successfully. While FPR indicates that how effectively a classifier could identify negative samples. A low FPR value indicates the identification results contain a low percentage of false alarms and a high percentage of true positives. These parameters are calculated as follows:

$$TPR = \frac{TP}{TP + FN} \tag{12}$$

$$FPR = \frac{FP}{TN + FP} \tag{13}$$

$$Accuracy = \frac{TP + TN}{TP + TN + FP + FN} \tag{14}$$

where TP, TN, FP, and FN denote true positive (correctly identified), true negative (correctly rejected), false positive (incorrectly identified) and false negative (incorrectly rejected), respectively.

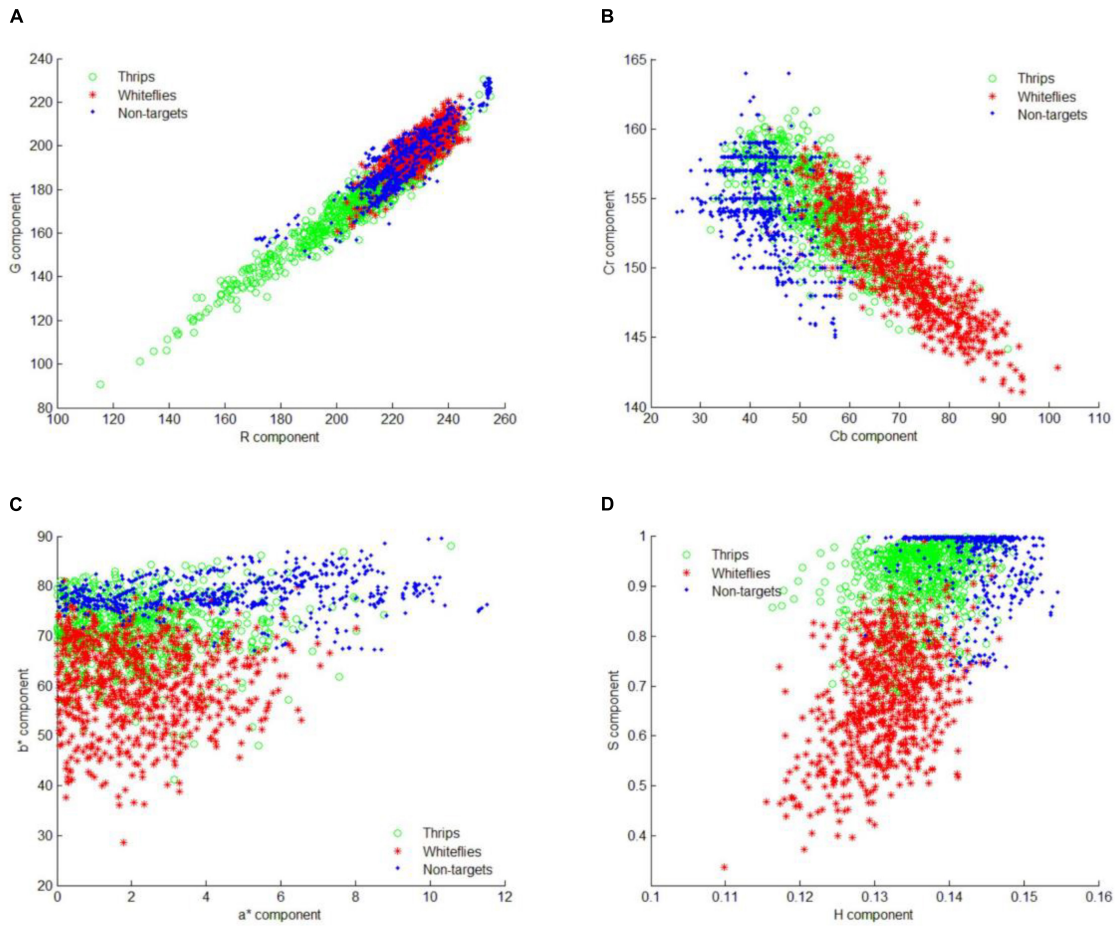

FIGURE 8 | Feature distribution of all the training samples. **(A)** Sample distribution in RGB color space, **(B)** sample distribution in L*a*b* color space, **(C)** sample distribution in YCbCr color space, and **(D)** sample distribution in HSV color space.

RESULTS

Sample Distribution in Different Color Space

After saliency region detector scanning across all images, the locations of most potential objects are detected. To identify those objects into different species, the feature distribution of whitefly, thrips and background are analyzed in four color spaces. The component of R, G, a*, b*, Cb, Cr, H, S in RGB, L*a*b*, YCbCr and HSV color space are illustrated in **Figure 8**. The distributions of different features showed that there is considerable overlap between targets (whitefly and thrips) and background in the RGB color feature space. Therefore, it is difficult to classify whitefly and thrips from the background category (**Figure 8A**). As shown in **Figure 8B**, whitefly can be separated from background category in L*a*b* color space but thrips still can't be separated from background category. Furthermore, the distribution of YCbCr features was similar to L*a*b* color space and thrips can't be separated from category. In addition, there is some confusion between whitefly and thrips (**Figure 8C**). **Figure 8D** documents the distribution of the three categories in HSV color space, which shows that it is relatively easy to classify the three categories. Therefore, the components of H, S and V are used to detect different insect species in current study.

Detection Results

The images captured from the field are complicated due to variable conditions such as unstable illumination, light reflection and various objects. **Figure 9** shows some examples of insect detection of different species in three sub-blocked images with different image quality.

As shown in **Figure 9A**, it is a good-quality image with smooth background. However, most of background in **Figure 9B** is whitened because of the sticky glue degenerated over time, and light reflection causes low-quality image in **Figure 9C**, which brings difficulties to the insect detection. The location results using the saliency region detection method are numbered as shown in **Figures 9D–F**, respectively. Every identified object is located using a bounding box, red for thrips, blue for whitefly and green for background category (non-target) in **Figures 9G–I**, respectively. The results showed that all whiteflies and thrips in **Figure 9A** are detected successfully. However, there were

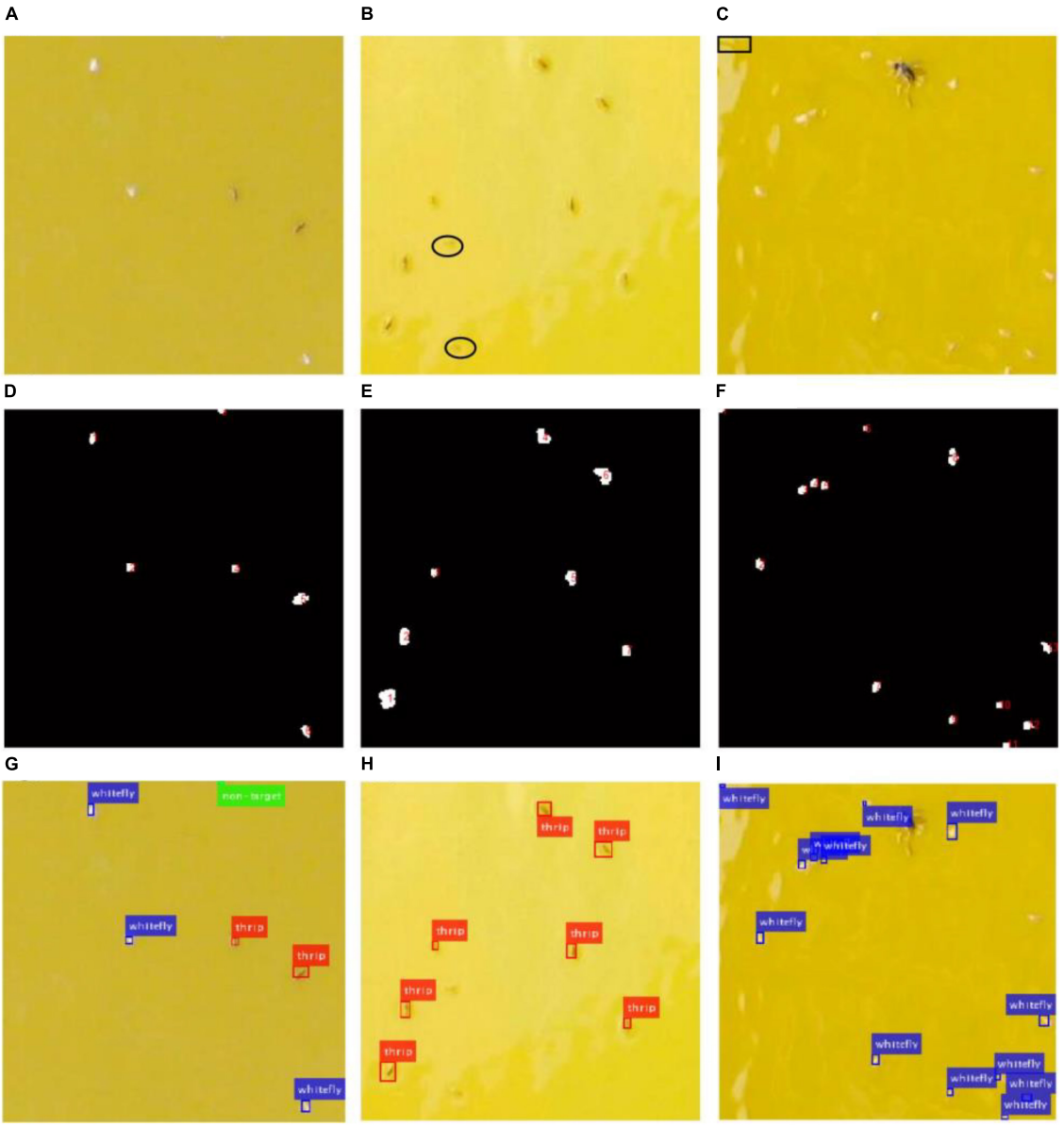

FIGURE 9 | Original images, location results and detection results of three image samples with different quality. **(A,D,G)** Are for sample 1, **(B,E,H)** are for sample 2, **(C,F,I)** are for sample 3.

some missing detections marked with black ellipse in **Figure 9B**. Furthermore, some spots (marked with black rectangle) caused by sticky glue are falsely classified as whiteflies in **Figure 9C**.

The insect detection performance is evaluated using TPR, FPR and accuracy which are described in section "Performance Evaluation." Initially, the two pest species in the testing dataset are separately marked manually and subsequently the evaluation metrics are calculated according to the detection results using Eqs (11)–(13). The overall detection performance on the three categories is shown in **Table 1**. The TPRs for whitefly and background categories were over 90% and the lowest TPR rate of 80.1% is obtained by the thrips category. The reason may be that some insects are attached to the sticky traps for a long time, and they became obscure due to weathering and dryness causing lack of detection. Additionally, the size of thrips is particularly small, ranging from 5 pixels to 20 pixels, such that it merged with the background thereby becoming indistinct. The feature distribution between the background and thrips in section "Sample Distribution in Different Color Space" may further verify the result. However, these recently trapped insects are easier to locate and identify.

The detection method for all categories produced false positives. The lowest FPR of 9.9% is for whitefly but is higher for thrips (12.3%) and background detection (11.6%). These are

TABLE 1 | Detection performance for small-size pests (whitefly and thrips) by the SVM classifier using field sticky trap images (n = 18, mean ± SD).

Objects	Performance metrics		
	TPR	FPR	Accuracy
Whitefly	0.931 ± 0.031	0.099 ± 0.019	0.939 ± 0.015
Thrips	0.801 ± 0.037	0.123 ± 0.039	0.898 ± 0.022
Background	0.930 ± 0.021	0.116 ± 0.037	0.933 ± 0.014

typically caused by degeneration of glue on the sticky trap and these produced "noise" in the form of point, stripe and bulk spot. The latter two noises could be easily filtered by this proposed location method. However, spot noises are easier misclassified into pest targets, especially whiteflies due to their size and color being similar to the targets.

The accuracy metric for whitefly is the highest at 93.9% followed by 93.3% for background category and 89.8% for thrips. The identification accuracy is further evaluated by correlation analysis between the proposed method and manual counting, as shown in **Figure 10**. The coefficient of determination, R^2, reached values of 0.9785 and 0.9572 for whitefly and thrips in the test dataset, respectively. Compared with manual counting, the proposed detection algorithm tended to overestimate the abundance of whitefly and underestimate thrips. Additionally, there are higher FPR for whitefly and increased TPR for thrips in the test dataset.

DISCUSSION

Principle and Feasibility Analysis

This study clearly demonstrates the utility of using a remote imaging approach combining image processing and pattern recognition technology to locate and identify whitefly and thrips on sticky trap in greenhouse conditions. The detection of whitefly and thrips on the sticky trap is primarily composed of two procedures: candidate target location and subsequent identification. Compared with detection in a large image, the small-sized whiteflies and thrips are more accurately recorded on small visual areas. The image blocking procedure is included in the study to split original image into small sub-blocking images to increase area occupancy rate. From the perspective of information theory, an image consists of two parts: the novelty part (saliency regions) and redundant information (Zhou and Zhang, 2007). The background in a sub-blocking image is the statistical redundant component and whitefly and thrips in the image could be regarded as the novelty component. There are different spectral responses for the novelty and redundant parts of the frequency domain. After removing the frequency response of the redundant part from the whole spectrum, the novelty part can be obtained. The most important advantage is that the saliency region detection model is independent of species, features, or other forms of prior knowledge of the objects.

The second step after object location is multi-class identification. The segmented objects in the first step not only contain whitefly and thrips, but also include the non-target category. However, the identification of whiteflies and thrips from non-targets is challenging and feature extraction is a key step in the classification process. Similar studies on the insect detection extracted shape features such as size, body eccentricity and solidity to classify species (Solis-Sánchez et al., 2011; Wang et al., 2012; Espinoza et al., 2016). However, due to the small size characteristics of whiteflies and thrips, the contours of the pests are not smooth after they are extracted from background and could not be accurately identified based on shape features. Despite the challenges, color feature analysis revealed different feature distribution in HSV color space and three color components (H, S, and V) are used as feature input of SVM classifier to identify whiteflies and thrips in this study.

Robustness Analysis

The image-based pest identification method has previously demonstrated high performance on collected images in the laboratory conditions (Cho et al., 2007; Boissard et al., 2008). However, field condition are very different from the laboratory environment since the sticky trap images captured in greenhouse can be influenced by various factors including sticky glue degeneration, light reflection and unstable variable illumination conditions (Xia et al., 2012). For example, Cho et al. (Cho et al., 2007) utilized the RGB and YUV color model to separate three different species. In addition, insect segmentation by YCbCr color model has revealed better results than other methods among different color models (Xia et al., 2015), but these segmentation

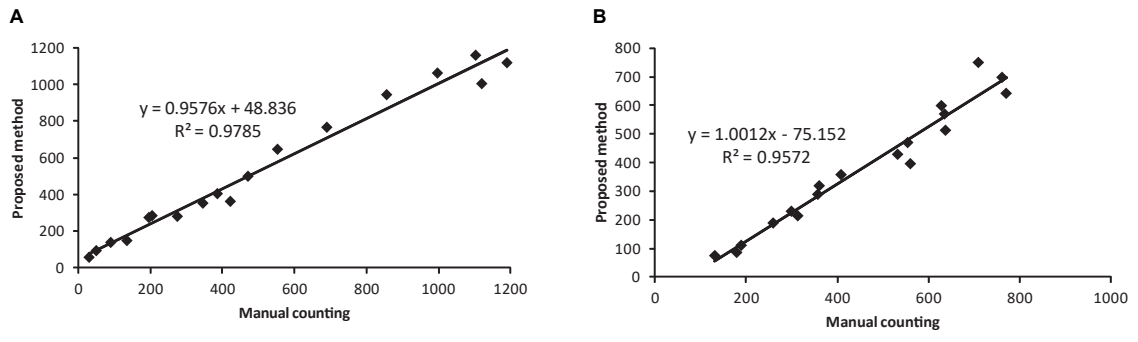

FIGURE 10 | Comparison of results between the proposed detection method and manual counting for **(A)** whitefly and **(B)** thrips using the testing dataset.

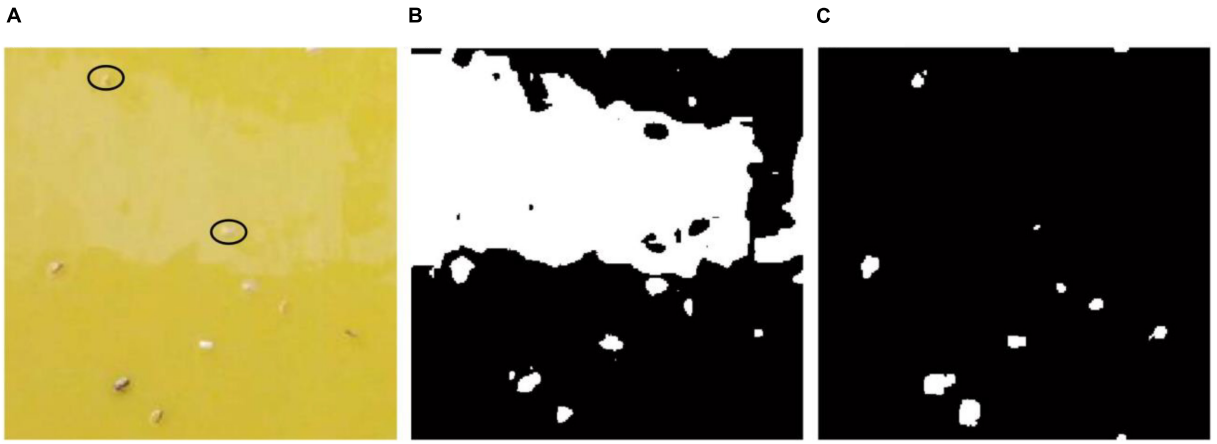

FIGURE 11 | Pest segmentation results of a sub-blocking image with noise by different methods. **(A)** Original image, **(B)** segmentation result of YCbCr color model, **(C)** segmentation result of the proposed method.

TABLE 2 | Comparison between the proposed and previous methods for detection of whitefly and thrips using sticky trap images.

Method	Imaging scene	Segmentation	Features	Classification method	Pest species	Average accuracy (%)
Qiao et al. (2008)	Field-based	Thresholding	Color and size	Comparative method	Whitefly	76.9
Xia et al. (2015)	Lab-based	Thresholding	Color and size	Mahalanobis distance	Whitefly, aphids, thrips	91.0
Espinoza et al. (2016)	Lab-based	Thresholding	Morphology and color	ANN	Whitefly and thrips	94.0
Li et al. (2021)	Field-based	No	Deep learning automatically	Softmax	Whitefly and thrips	94.4
The proposed method	Field-based	Spectral residual model	Color	SVM	Whitefly and thrips	91.9

methods based on the color model have some shortcomings when applied into field images. As shown in **Figure 11A**, there is some noise in upper part of the image caused by degeneration of sticky glue and light reflection. The segmentation result (**Figure 11B**) using the YCbCr color model shows these objects (marked with black ellipse in **Figure 11A**) are entirely missed. However, these objects in the noise region still can be segmented by the proposed method (**Figure 11C**). Although the multifractal analysis method was designed against noise when used under field conditions and showed high performance regarding accuracy, only one species of pest, whiteflies, had been detected and the image collected device and procedure was relatively complex (Xia et al., 2012). Rather than directly counting the pests captured on the traps, Sun et al. (2017) treated trapped pests as noise with 2DFT serving as a noise collector. This method obtained a high correlation with human counting when there was no other noise, but the Fourier transform in a case when there are noise and pests at low population density is similar to another case when pests at high population density and no noise. In addition, it could not address the problem associated with multi-class identification.

In current study, the pests are regarded as novelty objects and located by the saliency region detection method which is independent of color features and other forms of prior knowledge of the objects. Therefore, good robustness of pest segmentation in field images could be obtained by the proposed method.

Conversely, since some pests are attached to the trap for a long time, there is limited resolution in the imaging and the pest region in the saliency map is unclear, which will cause missing detection after binary image processing. Contrasting with the Otsu algorithm (Otsu, 1979), the threshold selected by the triangle method (section "Candidate Object Location") can improve the detection rate since it utilized the single-peaked feature of a histogram, but there are still some pests with low novelty that are not reliably detected. In actual application, the optimal option is replacement of the sticky trap on schedule to avoid loss of resolution and missing data due to sticky trap degeneration.

Comparisons With Previous Methods

Regarding to insect pest detection using sticky traps, several image-based methods had been reported, including handcrafted feature-based and deep learning-based methods. However, it is difficult to compare the performances of these previous studies with the proposed one quantitatively because of the use of different dataset which is not publicly available. Therefore, a qualitative analysis had been made in this study. Comparisons of the proposed approach with some methods for detecting greenhouse pests, such as whitefly and thrips, using sticky trap images are summarized in **Table 2**. Two previous method proposed by Xia et al. (2015) and Espinoza et al. (2016) used

images scanned in the laboratory as research materials, but the comparison showed that the prediction results of the proposed method outperformed the method of Xia et al. (2015). While the detection results reported by Espinoza et al. (2016) presented the higher accuracy, the study used thresholding method to segment targets, which causes the results were likely influenced by the segmentation threshold. Qiao et al. (2008) reported a fact that a small threshold loses relevant information, while a large threshold produces more noise, so its accuracy is much lower than that of the proposed method. It must be acknowledged that the performance of the proposed model is lower than that of deep-learning-based method reported by Li et al. (2021), however, the method based on deep learning technology has high complexity and depends on high-performance hardware, such as GPUs[1].

Pest Identification and Management

During our experiments in a greenhouse planted with pepper, whitely and thrips are the two main pests. Although only whitefly and thrips are identified in this study, the proposed method can have additional applications into the detection of multiple pests in greenhouse agriculture. The methodology for the detection of more than three species is similar to that proposed in section "Detection Method" except that more categories will be required to extract information to allow for the construction of a new baseline dataset.

In ecological studies, IPM usually relies on pest population density assessment in a given area and is often estimated based on trap counts (Petrovskii et al., 2012; Pinto-Zevallos and Vänninen, 2013). Therefore, precision identification and counting of pests in a sticky trap image is of critical importance for the estimation of population density. However, the relationship between trap counts of whitefly and thrips and the actual population density in the greenhouse is not clear. Such validation studies would form a critical future basis for pest management using image processing of pest populations in greenhouses (or open field situations).

CONCLUSION

This study proposed a novel approach for the detection of adult-stage whiteflies and thrips on sticky traps in greenhouses. The approach consisted of three modules: object location, feature extraction and multi-class recognition. The sticky trap image was divided into sub-block images and novelty objects within each sub-block image were located using a saliency region detection model. Furthermore, average values of three components in HSV color space were extracted to train a SVM classifier. Ultimately, HSV color features were calculated and used as input of the trained SVM model to identify whether a detected object was a whitefly or a thrips.

The study shows that adult thrips can be identified with a TPR of 80.1%, FPR of 12.3% and accuracy of 89.8%. Better performance is attained for the identification of whitefly, with a value of 93.1% for TPR, 9.9% for FPR, and 93.9% for accuracy. The proposed method in this study provides the possibility of counting different species of pests in greenhouse conditions by an automated pipeline, alleviating the time-consuming and inaccurate approach associated with grower-based identification of minute insect pests. The findings of the study contribute valuable information pertaining to population density estimation of small insect pests in greenhouse conditions and have broad utility to other systems allowing for decision making processes regarding integrated pest management approaches.

[1] https://www.nvidia.cn/

DATA AVAILABILITY STATEMENT

The raw data supporting the conclusions of this article can be obtained after consulting the corresponding author, without undue reservation.

AUTHOR CONTRIBUTIONS

WL and TZ conceived and explored literature. ZY and JL analyzed data. WL wrote the manuscript. ML and CS reviewed and edited the manuscript. All authors read and approved the manuscript.

FUNDING

This research was supported by the National Natural Science Foundation of China (Grant nos. 31871525 and 61601034), the Promotion and Innovation of Beijing Academy of Agriculture and Forestry Sciences and Young Beijing Scholars Program. All of the mentioned support and assistance are gratefully acknowledged.

REFERENCES

Boissard, P., Martin, V., and Moisan, S. (2008). A cognitive vision approach to early pest detection in greenhouse crops. *Comput. Electron. Agric.* 62, 81–93.

Chang, C.-C., and Lin, C.-J. (2015). *LIBSVM—A Library for Support Vector Machines*. Available online at: http://www.csie.ntu.edu.tw/∼cjlin/libsvm/ (accessed October 23, 2021).

Chen, K., Sun, X., Qin, C., and Tang, X. (2010). Color grading of beef fat by using computer vision and support vector machine. *Comput. Electron. Agric.* 70, 27–32. doi: 10.1016/j.meatsci.2018.03.005

Cho, J., Choi, J., Qiao, M., and Ji, C.-w (2007). Automatic identification of whiteflies, aphids and thrips in greenhouse based on image analysis. *Int. J. Math. Comput. Simu.* 1, 46–57.

Cui, X., Liu, Q., Zhang, S., Yang, F., and Metaxas, D. N. (2012). Temporal spectral residual for fast salient motion detection. *Neurocomputing* 86, 24–32. doi: 10.1016/j.neucom.2011.12.033

Deng, Y., and Duan, H. (2013). Hybrid C2 features and spectral residual approach to object recognition. *Optik - Int. J. Light Electron Optics* 124, 3590–3595. doi: 10.1016/j.ijleo.2012.11.063

Dorj, U.-O., Lee, M., and Yun, S.-s (2017). An yield estimation in citrus orchards via fruit detection and counting using image processing. *Comput. Electron. Agric.* 140, 103–112. doi: 10.1016/j.compag.2017.05.019

Ebrahimi, M. A., Khoshtaghaza, M. H., Minaei, S., and Jamshidi, B. (2017). Vision-based pest detection based on SVM classification method. *Comput. Electron. Agric.* 137, 52–58. doi: 10.1016/j.compag.2017.03.016

Espinoza, K., Valera, D. L., Torres, J. A., López, A., and Molina-Aiz, F. D. (2016). Combination of image processing and artificial neural networks as a novel approach for the identification of *Bemisia tabaci* and *Frankliniella occidentalis* on sticky traps in greenhouse agriculture. *Comput. Electron. Agric.* 127, 495–505. doi: 10.1016/j.compag.2016.07.008

Hu, J., Li, D., Duan, Q., Han, Y., Chen, G., and Si, X. (2012). Fish species classification by color, texture and multi-class support vector machine using computer vision. *Comput. Electron. Agric.* 88, 133–140. doi: 10.1016/j.compag.2012.07.008

Kurtulmus, F., Lee, W. S., and Vardar, A. (2011). Green citrus detection using 'eigenfruit', color and circular gabor texture features under natural outdoor conditions. *Comput. Electron. Agric.* 78, 140–149.

Larese, M. G., Namías, R., Craviotto, R. M., Arango, M. R., Gallo, C., and Granitto, P. M. (2014). Automatic classification of legumes using leaf vein image features. *Pattern Recognit.* 47, 158–168. doi: 10.1016/j.patcog.2013.06.012

Li, D., Yang, W., and Wang, S. (2010). Classification of foreign fibers in cotton lint using machine vision and multi-class support vector machine. *Comput. Electron. Agric.* 74, 274–279. doi: 10.1016/j.compag.2010.09.002

Li, W., Wang, D., Li, M., Gao, Y., Wu, J., and Yang, X. (2021). Field detection of tiny pests from sticky trap images using deep learning in agricultural greenhouse. *Comput. Electron. Agric.* 183:106048. doi: 10.1016/j.compag.2021.106048

Li, Y., and Yang, J. (2020). Few-shot cotton pest recognition and terminal realization. *Comput. Electron. Agric.* 169:105240. doi: 10.1016/j.compag.2020.105240

Meyer, F. (1994). Topographic distance and watershed lines. *Signal Process.* 38, 113–125.

Nasirahmadi, A., Edwards, S. A., and Sturm, B. (2017). Implementation of machine vision for detecting behaviour of cattle and pigs. *Livest. Sci.* 202, 25–38. doi: 10.1016/j.livsci.2017.05.014

Otsu, N. (1979). A threshold selection method from gray-level histograms. *IEEE Trans. Syst. Man Cybern.* 9, 62–66.

Petrovskii, S., Bearup, D., Ahmed, D. A., and Blackshaw, R. (2012). Estimating insect population density from trap counts. *Ecol. Complex.* 10, 69–82. doi: 10.1016/j.ecocom.2011.10.002

Pinto-Zevallos, D. M., and Vänninen, I. (2013). Yellow sticky traps for decision-making in whitefly management: what has been achieved? *Crop Protect.* 47, 74–84. doi: 10.1016/j.cropro.2013.01.009

Qiao, M., Lim, J., Ji, C. W., Chung, B.-K., Kim, H.-Y., Uhm, K.-B., et al. (2008). Density estimation of *Bemisia tabaci* (Hemiptera: Aleyrodidae) in a greenhouse using sticky traps in conjunction with an image processing system. *J. Asia Pacific Entomol.* 11, 25–29. doi: 10.1016/j.aspen.2008.03.002

Reyes, J. F., Correa, C., and Zúñiga, J. (2017). Reliability of different color spaces to estimate nitrogen SPAD values in maize. *Comput. Electron. Agric.* 143, 14–22. doi: 10.1016/j.compag.2017.09.032

Rumpf, T., Mahlein, A. K., Steiner, U., Oerke, E. C., Dehne, H. W., and Plümer, L. (2010). Early detection and classification of plant diseases with support vector machines based on hyperspectral reflectance. *Comput. Electron. Agric.* 74, 91–99. doi: 10.1016/j.compag.2010.06.009

Rustia, D. J. A., Chao, J. J., Chiu, L. Y., Wu, Y. F., Chung, J. Y., Hsu, J. C., et al. (2020). Automatic greenhouse insect pest detection and recognition based on a cascaded deep learning classification method. *J. Appl. Entomol.* 145, 1–17. doi: 10.1111/jen.12834

Saruta, K., Hirai, Y., Tanaka, K., and Inoue, E. (2013). Predictive models for yield and protein content of brown rice using support vector machine. *Comput. Electron. Agric.* 99, 93–100.

Shrestha, S., Topbjerg, H. B., Ytting, N. K., Skovgard, H., and Boelt, B. (2018). Detection of live larvae in cocoons of *Bathyplectes curculionis* (Hymenoptera: Ichneumonidae) using visible/near-infrared multispectral imaging. *Pest Manag. Sci.* 74, 2168–2175. doi: 10.1002/ps.4915

Solis-Sánchez, L. O., Castañeda-Miranda, R., García-Escalante, J. J., Torres-Pacheco, I., Guevara-González, R. G., Castañeda-Miranda, C. L., et al. (2011). Scale invariant feature approach for insect monitoring. *Comput. Electron. Agric.* 75, 92–99. doi: 10.1016/j.compag.2010.10.001

Solis-Sánchez, L. O., García-Escalante, J. J., Castañeda-Miranda, R., Torres-Pacheco, I., and Guevara-González, R. (2010). Machine vision algorithm for whiteflies (*Bemisia tabaci* Genn.) scouting under greenhouse environment. *J. Appl. Entomol.* 133, 546–552.

Sun, Y., Cheng, H., Cheng, Q., Zhou, H., Li, M., Fan, Y., et al. (2017). A smart-vision algorithm for counting whiteflies and thrips on sticky traps using two-dimensional Fourier transform spectrum. *Biosys. Eng.* 153, 82–88. doi: 10.1016/j.biosystemseng.2016.11.001

Tan, K., Lee, W. S., Gan, H., and Wang, S. (2018). Recognising blueberry fruit of different maturity using histogram oriented gradients and colour features in outdoor scenes. *Biosys. Eng.* 176, 59–72. doi: 10.1016/j.biosystemseng.2018.08.011

Tarabalka, Y., Chanussot, J., and Benediktsson, J. A. (2010). Segmentation and classification of hyperspectral images using watershed transformation. *Pattern Recognit.* 43, 2367–2379.

Tong, K., Wu, Y., and Zhou, F. (2020). Recent advances in small object detection based on deep learning: a review. *Image Vis. Comput.* 97:103910. doi: 10.1016/j.imavis.2020.103910

Wang, J., Lin, C., Ji, L., and Liang, A. (2012). A new automatic identification system of insect images at the order level. *Knowl. Based Syst.* 33, 102–110. doi: 10.1016/j.knosys.2012.03.014

Wen, C., and Guyer, D. (2012). Image-based orchard insect automated identification and classification method. *Comput. Electron. Agric.* 89, 110–115. doi: 10.1016/j.compag.2012.08.008

Xia, C., Chon, T.-S., Ren, Z., and Lee, J.-M. (2015). Automatic identification and counting of small size pests in greenhouse conditions with low computational cost. *Ecol. Inform.* 29, 139–146. doi: 10.1016/j.ecoinf.2014.09.006

Xia, C., Lee, J.-M., and Li, Y. (2012). In situ detection of small-size insect pests sampled on traps using multifractal analysis. *Opt. Eng.* 51, 027001–027001.

Yang, Z., Li, W., Li, M., and Yang, X. (2021). Automatic greenhouse pest recognition based on multiple color space features. *Int. J. Agric. Biol. Eng.* 14, 188–195. doi: 10.25165/j.ijabe.20211402.5098

Zhang, X., Jia, F., Luo, S., Liu, G., and Hu, Q. (2014). A marker-based watershed method for X-ray image segmentation. *Comput. Method Programs Biomed.* 113, 894–903. doi: 10.1016/j.cmpb.2013.12.025

Zhou, X., and Zhang, L. (2007). "Saliency detection: a spectral residual approach," in *Proceedings of the 2007 IEEE Conference on Computer Vision and Pattern Recognition*, (Piscataway, NJ: IEEE). 1–8.

Conflict of Interest: The authors declare that the research was conducted in the absence of any commercial or financial relationships that could be construed as a potential conflict of interest.

frontiers | Frontiers in Plant Science

TYPE Original Research
PUBLISHED 15 July 2022
DOI 10.3389/fpls.2022.924749

OPEN ACCESS

EDITED BY
Changyuan Zhai,
Beijing Academy of Agricultural and Forestry Sciences, China

REVIEWED BY
Ilias Travlos,
Agricultural University of Athens, Greece
Fenghui Yuan,
University of Minnesota Twin Cities, United States

*CORRESPONDENCE
Jizhan Liu
1000002048@ujs.edu.cn

SPECIALTY SECTION
This article was submitted to Sustainable and Intelligent Phytoprotection, a section of the journal Frontiers in Plant Science

RECEIVED 20 April 2022
ACCEPTED 29 June 2022
PUBLISHED 15 July 2022

CITATION
Wu S, Liu J, Zhen J, Lei X and Chen Y (2022) Resistance characteristics of broad-leaf crop canopy in air-assisted spray field and their effects on droplet deposition. *Front. Plant Sci.* 13:924749. doi: 10.3389/fpls.2022.924749

Resistance characteristics of broad-leaf crop canopy in air-assisted spray field and their effects on droplet deposition

Shuo Wu, Jizhan Liu*, Junquan Zhen, Xiaojie Lei and Yao Chen

Key Laboratory of Modern Agricultural Equipment and Technology, Ministry of Education, Jiangsu University, Zhenjiang, China

Air-assisted spray technology is widely applied in high-efficiency pesticide applications. The resistance characteristics of the crop canopy reflect its energy dissipation effect on the assisted airflow, connecting the structure of the crop canopy, assisted airflow velocity, and droplet deposition effect. Using a common broad-leaf crop canopy as the research object, the resistance characteristics of the crop canopy in the air-assisted field were investigated in this study by performing theoretical analysis and wind tunnel tests. Further, the feasibility of using the resistance characteristics of the crop canopy was assessed to evaluate its droplet deposition effect. The results showed that under the conditions of different number of leaf layers and initial leaf azimuth angles, the canopy pressure drop experiences a non-linear increasing trend with increasing assisted airflow velocity and that its regression function conforms to the Darcy–Forchheimer function. Moreover, when the initial azimuth angles of single- and multi-layer leaves were 90°–270°, the change rate of the canopy pressure drop with airflow velocity was 7–9m/s, and there was a critical wind speed. However, with an increasing number of leaf layers in the crop canopy and changes in the initial leaf azimuth angle, the corresponding changes between the maximum canopy pressure drop and resistance coefficient were non-linear. Thus, it is proposed that the resistance characteristics of multi-layer leaves cannot be quantified as the results of the linear superposition of the resistance characteristics of several single-layer leaves—that is, it should be regarded as a whole research object. Combined with the analysis of the influence of the crop canopy resistance on droplet deposition, it is considered that when the crop canopy has multiple leaf layers in the airflow direction, the existing air-assisted spray technology cannot guarantee droplet deposition and canopy penetration simultaneously.

KEYWORDS

air-assisted spray, crop canopy, resistance characteristics, droplet deposition, pesticide spraying

Introduction

Crop protection is an important agronomic practice that helps ensure crop yield and quality, with pesticide usage being one of the more effective and widely employed crop-protection methods (Davydov et al., 2018). However, droplet drift, poor canopy penetration, and poor target deposition in pesticide spraying can lead to problems such as pesticide and water wastage, environmental pollution, and food safety concerns (Carvalho, 2006).

Air-assisted spray technology can reduce droplet drift and improve canopy penetration and droplet deposition uniformity by transporting pesticide droplets to the target surface and driving canopy leaves by means of airflow. This method is simple, reliable, and easy to control, making it one of the most widely used spray techniques (Hong et al., 2018). Its integration with pesticide adjuvants, electrostatic spraying, targeted spraying, variable-rate spraying, and other technologies has also become a development trend in crop protection research (Krogh et al., 2003; Stajnko et al., 2012; Patel, 2016; Abbas et al., 2020).

However, Foqué et al. compared the droplet deposition results of vertical sprays with and without air assistance and found that, in some cases, vertical spray deposition was significantly better without air assistance than with it (Foqué et al., 2012). Similarly, our team has been engaged in the research and development of strawberry pesticide spraying technology and equipment for some time. We found that a continuous increase in airflow velocity does not always improve droplet deposition (Wang et al., 2020), because, although the ability of the airflow to change the physical characteristics of the pesticide—such as the droplet size and motion—effectively to improve the canopy penetration and deposition, the motion of crop leaves affected by the assisted airflow force has an equally important effect on droplet deposition. Not all of the crop leaf motion affected by the assisted airflow force in air-assisted spray technology is positive (Derksen et al., 2008).

Therefore, the authors conducted related research on the motion characteristics of strawberry leaves in an air-assisted spray field and their effects on droplet deposition (Wu et al., 2021). Efficient droplet deposition of the crop canopy required that when a leaf moved due to the assisted airflow, contact was ensured between the front and back of the leaves and the droplets, and a reasonable state of motion was achieved to ensure effective deposition. Moreover, the initial position and attitude of crop leaves relative to the assisted airflow affected their state of motion. When the initial azimuth angle of the strawberry leaves was 90°–270°, the airflow more than the critical wind speed drove the leaves to produce a high-frequency, high-amplitude state of vibration that produced a good deposition effect for droplets of small diameters.

Although the initial position and attitude of crop leaves relative to the assisted airflow and speed of the assisted airflow affect droplet deposition, it can be difficult to obtain the initial position and attitude of all leaves in the crop canopy in real time. Moreover, the group effect of crop leaves makes the movement of the group significantly different from that of a single leaf. Consequently, it can be difficult to evaluate the droplet deposition effect of the crop canopy directly through the initial position and attitude of the leaf group relative to the assisted airflow and assisted airflow velocity.

Based on droplet deposition methods—such as the use of water-sensitive paper—to evaluate the crop canopy droplet deposition effect under different air-assisted spray conditions, an efficient deposition mechanism can be achieved by combining high-speed photography with droplet tracing technology, a widely used research method in the field of crop protection (Sánchez-Hermosilla and Medina, 2004; Wang et al., 2008). However, this traditional method can be hampered by expensive equipment, cumbersome processes, and repetition. How to realize the rapid and low-cost evaluation of the effect of droplet deposition on the crop canopy remains a difficult technical problem.

The resistance characteristics of the crop canopy reflect its effects on the airflow energy dissipation at the macro level, which are closely related to the characteristics of the crop canopy—that is, the number of leaves, their initial positions, and the attitude of the leaves relative to the assisted airflow—and assisted airflow velocity (Lhomme, 1991; Fang et al., 2020). In air-assisted spray operations, the airflow and droplets interact with each other, so the resistance characteristics of the crop canopy are closely related to the droplet deposition effect (Liu et al., 2021a). Clearly, the resistance characteristics of the crop canopy can easily form the basis for establishing the relationship among the crop canopy structure, assisted air velocity, and droplet deposition effect. In addition, it is easy to perform rapid measurement at low cost.

Consequently, a broad-leaved crop canopy was considered the research object in this study. Based on the relevant theories and wind tunnel tests, the resistance characteristics of single and multi-layer leaves in the assisted airflow field were studied. The effects of the number of leaf layers, initial position and attitude of the leaves relative to the assisted airflow, and effect of the assisted airflow velocity on the resistance characteristics were analyzed. The feasibility of evaluating the deposition effect of crop canopy droplets based on the resistance characteristics of the crop canopy was assessed. This research provides a theoretical basis for and insight that will facilitate rapid, low-cost research and development of crop protection technology and equipment.

Theory

Motion of broad-leaf crop leaves in air-assisted spray field

As leaves are the basic elements of the crop canopy, their motion in the air-assisted spray field constitutes the mathematical basis of relevant theoretical and experimental studies. In a previous study, we proposed a visual descriptive method for leaf motion in an air-assisted spray field, as detailed below (Wu et al., 2021).

As shown in Figure 1, the base coordinate system, $e_X e_Y e_Z$, is used to represent zero rigid bodies such as the plant roots or ground. The $\vec{e}_X$ -axis in the base coordinate system, $e_X e_Y e_Z$, is parallel and opposite to the horizontal component of the airflow, $\vec{V}$. Concurrently, the dynamic relative reference system, OXYZ, for leaf motion can be established in the base coordinate system, $e_X e_Y e_Z$.

The dynamic relative reference system, OXYZ, has the following features: Point O is the mass center of the leaf; the OX-axis is parallel to the horizontal component of the airflow, $\vec{V}$, and has the opposite direction; the OY-axis is vertically orientated; the elliptic ABCD simplifies the representation of the leaf; and line segments CD and AB represent the long and wide axes of the leaf, respectively. Line segment CE represents the slender stem, and point C represents the thin and short petiole connecting the stem and the leaf. The angle between the normal vector, $\vec{n}$, on the front surface of the leaf, ABCD, and the OZ-axis is the inclination angle, θ, of the leaf. The angle between the normal vector, $\vec{n}$, on the front surface of the leaf, ABCD, on the OXY horizontal plane and the OX-axis is the azimuth angle, φ, of the leaf, counterclockwise being the positive direction. The characteristic normal vector, $\vec{n}$, of the position and posture of the leaf relative to the dynamic relative reference system, OXYZ, is (sinθcosφ, −sinθsinφ, cosθ), and the position vector, $\vec{r}$, of the dynamic relative reference system, OXYZ, relative to the base coordinate system, $e_X e_Y e_Z$, is (x_o, y_o, z_o). Therefore, the position and posture of the leaf relative to the base coordinate system, $e_X e_Y e_Z$, can be expressed by (x_o, y_o, z_o, sinθcosφ, sinθsinφ, cosθ), characterized by the vector $\vec{n}_{\text{basic}}$.

The motion of the leaf in the base coordinate system in the air-assisted spray field can be expressed as follows:

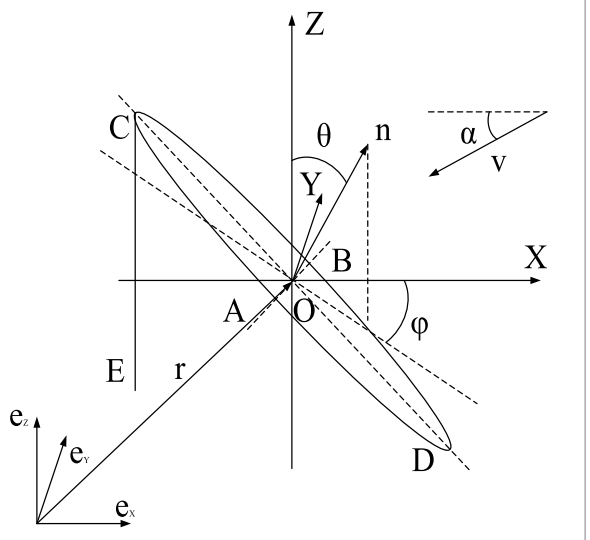

FIGURE 1
Visual description of leaf movement of broad-leaved crops in air-assisted spray field.

$$\vec{n}_{\text{basic,first}} \times A_{\text{trans}} = \vec{n}_{\text{basic,final}} \quad (1)$$

where $\vec{n}_{\text{basic,first}}$ is a vector of the initial position and posture of the leaf relative to the base coordinate system, $e_X e_Y e_Z$, at the beginning; $\vec{n}_{\text{basic,first}}$ is a vector of the initial position and posture of the leaf relative to the base coordinate system, $e_X e_Y e_Z$; and A_{trans} is the position and posture change matrix of the leaf as influenced by the airflow relative to the base coordinate system, $e_X e_Y e_Z$.

Mechanism of capturing droplets in crop leaves

The process of droplet capture in crop leaves can be complicated, with the droplets, airflow, and leaves interacting during contact. However, the contact between leaves and droplets is the premise of effective deposition. To simplify the analysis, only the influence of the airflow on leaf movement was considered in this study, ignoring the influence of the airflow on the droplets and that of the droplets and leaves on the airflow during the contact process between the leaves and droplets.

In a previous study, as shown in Figure 2—combined with the relevant research conclusions of Dorr et al.—the contact process between droplets and plant leaves was thought to occur in three stages: that is, the pre-contact, spreading, and rebound, sputtering, or deposition stages (Dorr et al., 2016; Wu et al., 2021). Droplets are accelerated by the nozzle injection pressure and sprayer airflow in the pre-contact stage, having initial kinetic, potential, and surface energies, with the total energy being E_1. After a droplet collides with a leaf surface, the initial kinetic energy and potential energy of the droplet are converted into surface energy because of the enlargement of the droplet surface area, with the energy dissipation during the collision being $E_{\text{diss,0–1}}$. When the diffusion radius reaches its maximum, the droplet begins to shrink under the action of surface tension, during which the energy dissipation is $E_{\text{diss,1–2}}$.

When the droplet reaches its maximum contraction stage, the total energy, E_2, can be expressed as follows:

$$E_2 = E_1 - E_{\text{diss,0–1}} - E_{\text{diss,1–2}} \quad (2)$$

When E_2 is not sufficiently large to overcome the constraints of the droplet potential energy, adhesion to the leaf, surface tension, and other factors, the droplet does not separate from the leaf, but rather is effectively deposited on its surface. The motion of the leaf influences the initial total energy, E_1, of the droplet as well as the state change of the droplet energy dissipation during its contact with the leaf, thus influencing the effective deposition of droplets on the leaf surface. Efficient droplet capture by the crop canopy requires movement of the leaves, induced by the sprayer airflow, ensuring that both the front and back surfaces of the leaves make contact with the droplets—that is, reasonable motion of the leaves ensures the effective deposition of spray droplets.

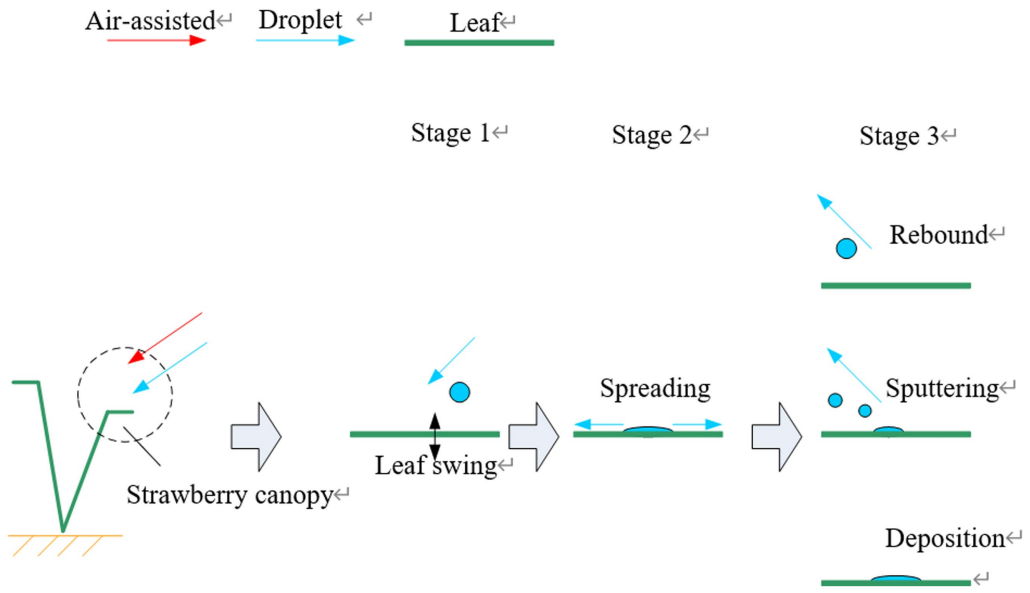

FIGURE 2
Schematic of droplet capture by leaves.

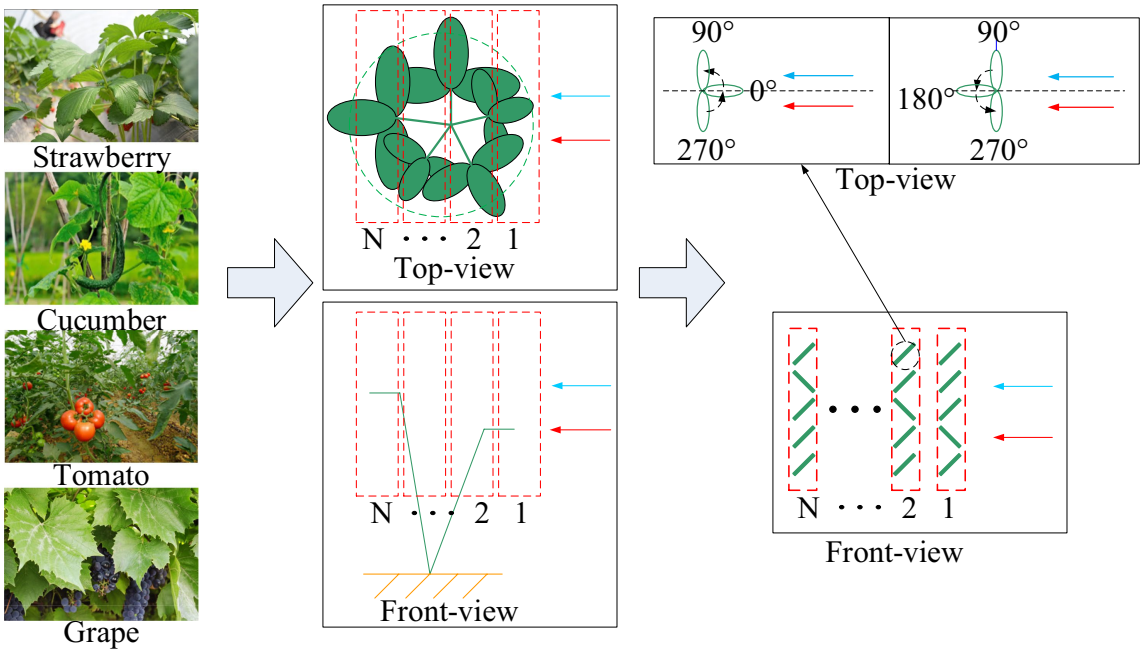

FIGURE 3
Schematic diagram of quantitative analysis of the droplet capture process in the crop canopy.

As shown in Figure 3, in order to obtain sunlight throughout the day fully, the crop leaves generally grow around. According to the definition of the azimuth angle of the leaf in Section "Motion of broadleaf crop leaves in air-assisted spray field," the initial azimuth angles of the leaves in the crop canopy relative to the assisted airflow are generally 0°–360°. In this study, the crop canopy was stratified along the direction of the assisted airflow and droplets. The assisted airflow and droplets will attenuate after passing through each leaf layer. In an actual crop canopy, the leaves will overlap, and simultaneously, multiple leaves in a local area range will jointly affect the droplet capture process of the next leaf layer. To analyze the droplet capture

process of crop canopy quantitatively, it was assumed for simplicity that the leaves in each layer of the crop canopy would not overlap and each leaf in each layer would only affect the motion and droplet capture process of the corresponding leaves after the direction of their respective airflow and droplets. In a previous study, combining a droplet capture test of crop leaf motion in the air-assisted spray field and the above theoretical analysis, we found that when the initial azimuth angle of the leaf relative to the assisted airflow was 90°–270°, with the appropriate inclination of the applicator fan being the high-frequency and high-amplitude vibration state of the leaf driven by the assisted airflow greater than the critical wind speed, there were good positive and negative uniform deposition effects on droplets of small diameters (Wu et al., 2021). Therefore, on the premise that the initial azimuth angle of the leaf is known, the droplet capture effect can be analyzed. The attenuation analysis of assisted airflow is based on the airflow resistance characteristics of canopy. In this study, the leaf sample layout scheme of the canopy airflow resistance characteristics test and the correlation analysis between the canopy airflow resistance characteristics and droplet capture were based on the above assumptions.

Description method and theory of crop canopy resistance characteristics

After the assisted airflow passes through the crop canopy, some of its energy is dissipated by it. The resistance characteristics of the crop canopy macroscopically reflect the energy dissipation effect of the crop canopy on assisted airflow, which is closely related to the number of leaves, the initial position and attitude of leaves relative to the assisted airflow, and the velocity of the assisted airflow.

In this study, the Darcy–Forchheimer function in Equation (3) can be used to characterize the resistance characteristics of the crop canopy (Molina-Aiz et al., 2006; Nield and Bejan, 2006; Dullien, 2012):

$$\frac{\partial p}{\partial L} = -\left(D \cdot \mu \cdot v + 0.5 \cdot C \cdot p \cdot v^2\right) \tag{3}$$

To facilitate the wind tunnel test, Equation (3) can be integrated to obtain Equation (4):

$$\Delta p = D \cdot \mu \cdot L \cdot v + 0.5 \cdot C \cdot \rho \cdot L \cdot v^2 + A \tag{4}$$

where p is the pressure loss of the assisted airflow after passing through the crop canopy (Pa), L is the length of the crop canopy along the direction of the assisted airflow (m), D is the viscosity coefficient ($\mathrm{m}^{-2} \cdot \mathrm{s}^{-2}$), μ is the aerodynamic viscosity at the experimental temperature and has a value of $1.79 \times 10^{-5} \mathrm{Pa} \cdot \mathrm{s}$, ρ is the air density at the experimental temperature and has a value of $1.189 \mathrm{kg} \cdot \mathrm{m}^{-3}$, v is the assisted airflow velocity ($\mathrm{m} \cdot \mathrm{s}^{-1}$), C is the resistance coefficient, and Δp is the dynamic pressure loss of the assisted airflow through the crop canopy, collectively referred to as the canopy pressure drop.

In this study, the canopy pressure drop and resistance coefficient were used to assess the resistance characteristics of the crop canopy comprehensively.

Materials and methods

Leaf sample selection and basic properties

As shown in Figure 4, simulated broad-leaf crop leaves composed of resin were selected for the experiment, to overcome a series of problems including the individual differences among real crop leaves and the potential effects of repeated tests on their physical properties (Liu et al., 2021a). The sample sizes and physical parameters are listed in Table 1.

Establishment of crop canopy resistance characteristic measurement system

As shown in Figure 5, we designed and built a linear wind tunnel measurement system to measure the resistance characteristics of the crop canopy, including the tunnel body, power module, and measurement module (Molina-Aiz et al., 2006).

The tunnel body includes the air inlet, power section, stability section, rectification section, contraction section, test section, expansion section, and air outlet; the power module includes a three-phase DC motor (Shengxiang Machinery Factory, Wuxi, China), frequency converter (Jintian Technology Co., Ltd., Guangdong, China), leaf, and fairing; the measurement module includes a leaf sample-fixing device,

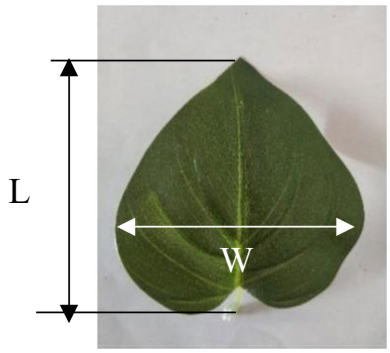

FIGURE 4
Sample leaf of simulated broad-leaved group.

TABLE 1 Sample size and physical parameters.

Parameter	Value
Leaf length L (mm)	73.46
Leaf width W (mm)	62.24
Leaf area (mm^2)	3,078
Density ($kg{\cdot}m^{-3}$)	900
Petiole length (mm)	15.74
Petiole modulus of elasticity (MPa)	22.5
Elastic modulus of leaf (MPa)	2.36
Ra (μm)	0.16

hot-wire anemometer (KIMO, Bordeaux, France), and digital micromanometer (DP1000, Hangzhou, China). The sampling frequency of the hot-wire anemometer was 10 Hz, and the accuracy was 0.01 m/s. The range of the digital micromanometer was 0–200 Pa, with an accuracy of 0.1 Pa. The technical parameters of the tunnel body and power module are summarized in Table 2.

Airflow resistance characteristic test of multi-position attitude of single leaf

As depicted in Figures 6, a leaf sample fixing and rotating device was constructed, including a thin metal rod, a clamp, and suction cups. The thin metal rod was fixed in the wind tunnel test section by utilizing suction cups, a clamp was fastened to the rod to affix the leaf sample, and the rod could rotate around the suction cups.

The single-factor control variable method was adopted in this study, as illustrated in Figure 7. The initial azimuth, φ, of the leaf sample relative to the assisted airflow was controlled by the rotation of the leaf sample fixing device, and the airflow velocity in the test section was controlled by a frequency converter with a varied range of 0–12 m/s. This airflow velocity range is commonly used in the air-assisted spray. The airflow velocity at the front of the leaf sample was measured using an airflow velocity sensor in front of the sample. The pressures at the front and rear air outlets of the leaf sample were measured using a pressure sensor and micromanometer. The distance between the airflow velocity sensor and the sample was 280 mm. The distance between the pressure sensor and the sample was 280 mm. This information will not be repeated below.

The specific test arrangements are listed in Table 3. To reduce the number of tests, we set eight eigenvalues for the initial azimuth angle of the leaf sample relative to the assisted airflow. Each group of tests was repeated three times, and the average value was calculated.

Airflow resistance characteristic test of multi-position attitude of multi-layer leaf

We divided the crop canopy into multiple leaf sample layers in the direction of the assisted airflow, as shown in Figure 8. According to the simplification and assumption mentioned in Section "Mechanism of capturing droplets in crop leaves," the leaves in the different layers of the crop canopy will not overlap, and each leaf in each layer will only affect the motion and droplet capture process of the corresponding leaves after the direction of their respective airflow and droplets. The influence of each leaf layer on the rear leaf layer can be regarded as the linear superposition of the effects of multiple leaves on the corresponding leaves at the rear. Therefore, we set one leaf sample in each leaf layer. In fact, the number of leaves in each layer of a crop canopy is very large. If the control variable method is used to study the influence of the azimuth difference of the leaves in each layer on the overall resistance characteristics of the crop canopy, the task will become impossible. Therefore, based on the simplified assumption that the resistance characteristics of multiple leaves in each sample layer have linear relationships with those of the individual leaves, we set one leaf sample in each leaf sample layer. The initial azimuth angle, φ, of the leaf sample relative to the assisted airflow was controlled by rotating the leaf sample fixing device, and the airflow velocity in the test section was controlled to 0–12 m/s by a frequency converter. The airflow velocity at the front of the leaf sample was measured using an airflow velocity sensor in front of the sample. The pressures at the front and rear air outlets of the leaf sample were measured using a pressure sensor and micromanometer. To reduce the number of tests, we used two or three leaf sample layers, and the number of leaf samples in each leaf layer was set to two with significantly different initial azimuth angles of 0° and 180°, the specific arrangements of which are listed in Table 4.

Each group of experiments was repeated three times, and the average value was calculated. For convenience, each group of multi-layer leaf tests is described in the form $N(\varphi_1, \varphi_2, \varphi_3)$, where N is the number of leaf sample layers, φ_1, φ_2, and φ_3 are the initial azimuths of the leaf samples in the first, second, and third layers, respectively.

Results and discussion

Airflow resistance characteristics of a single leaf at different initial azimuth angles

In the motion analysis of crop leaves in an airflow field, when the state of motion of the leaves changes suddenly, the airflow velocity corresponding to the change of motion is called the critical wind speed (Shao and Chen, 2011; Tadrist et al., 2015). In this study, the change in canopy pressure drop of leaf samples was an important basis for evaluating whether the state of motion changed.

Through comparison, as shown in Figure 9, we found that under different initial azimuth conditions, the canopy pressure drop of a single leaf exhibited a non-linear increase with a

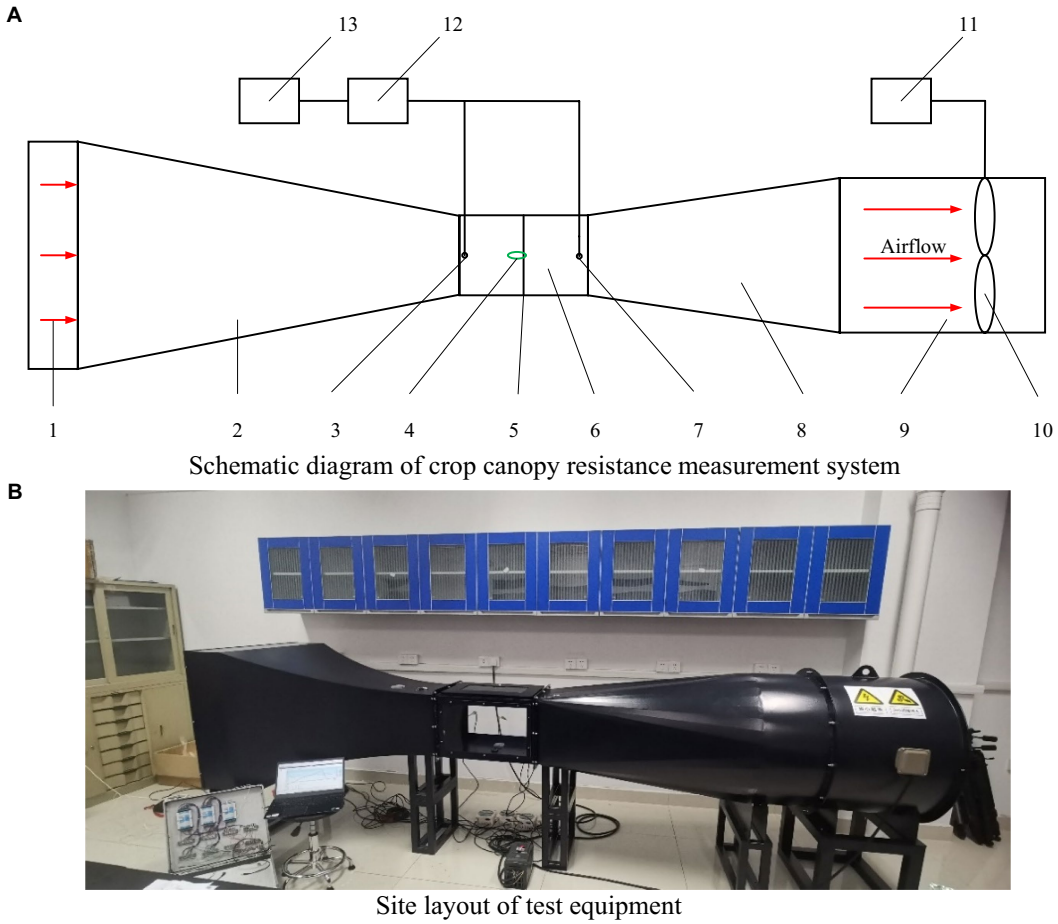

FIGURE 5
Measurement system of crop canopy resistance characteristics. **(A)** Schematic diagram of crop canopy resistance measurement system. **(B)** Site layout of test equipment. 1. Rectifier air inlet; 2. Contraction section; 3. Airflow velocity sensor and pressure sensor; 4. Leaf sample; 5. Leaf sample-fixing device; 6. Test section; 7. Pressure sensor; 8. Diffusion section; 9. Power section; 10. Axial flow motor; 11. Frequency converter; 12. Data collector; 13. Computer.

continuous increase in the assisted airflow velocity. When the initial azimuth angle was 90°, 135°, 180°, 225°, and 270°, the critical wind speed was 7–9 m/s. When the assisted air velocity was less than the critical wind speed, an increase in the assisted air velocity did not significantly improve the leaf canopy pressure drop. However, when the air velocity was greater than the critical wind speed, the leaf canopy pressure drop increased rapidly with increasing assisted air velocity. Moreover, when the initial azimuth was 0°, 45°, and 315°, there was no critical wind speed, marking a sudden change in the canopy pressure drop with increasing assisted airflow velocity. As shown in Figure 10, this finding was obtained because when the initial azimuth of the leaf was 0°, 45°, and 315°, the assisted airflow and front face of the leaf formed an effective airflow load surface, with the airflow load driving the leaf inclination with increasing airflow velocity and the windward area also gradually increasing, resulting in a gradually increasing canopy pressure drop. When the initial azimuth of the leaf was 90°, 135°, 180°, 225°, and 270° and the air velocity was less than the critical wind speed, and the increase in assisted air velocity did not significantly improve the windward area of the leaf. However, when the assisted air velocity was greater than the critical wind speed, the leaf presented an unstable high-frequency and high-amplitude vibration state, greatly dissipating the assisted air energy, resulting in a rapid increase in the canopy pressure drop.

Simultaneously, we performed quadratic polynomial regression fitting on the test data. The obtained curve corresponding to Equation (5) conforms to the configuration of Equation (4), where the determination coefficient R^2 is 0.83–0.98:

$$\Delta p = K_1 v + K_2 v^2 + A \quad (5)$$

TABLE 2 The technical parameters of the tunnel body and power module.

Parameter	Value
Overall size (length × width × height)	4,000 × 900 × 1,350 mm
Motor power (w)	650
Fan impeller diameter (mm)	800
Test section size (length × width × height)	400 × 400 × 600 mm
Wind speed in test section ($m \cdot s^{-1}$)	0.5–20.0
Relative standard deviation of velocity uniformity in test section	≤2.0%
Relative deviation of velocity stability in test section	≤2%
Airflow deflection angle	≤2°

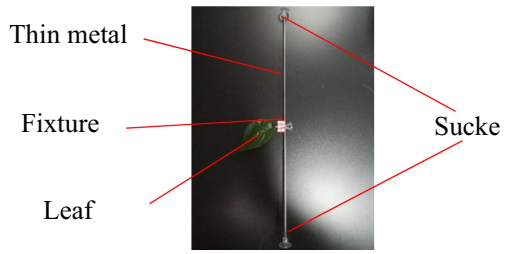

FIGURE 6
Leaf sample fixation and rotation device.

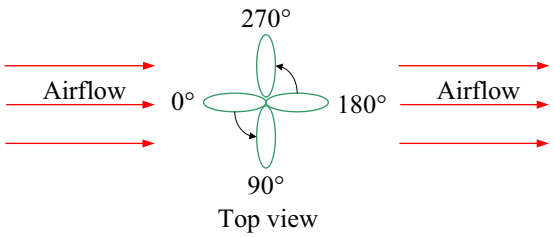

FIGURE 7
Azimuth adjustment diagram of leaf sample.

Referring to Equation (4), we calculated the maximum canopy pressure drop and resistance coefficient C of the leaf under different initial azimuth conditions using the coefficients K_1 and K_2 of the regression fitting curve of Equation (5), as shown in Figures 11, 12 (Sanz, 2003; Song and Fu, 2020). When the initial azimuth of the leaf was 180°, the maximum canopy pressure drop and airflow resistance coefficient were greater than those at other initial azimuth angles, with values of 7.37 ± 0.77 Pa and 0.35 ± 0.02, respectively. When the leaf azimuth was 90°, 225°, and 270°, the maximum canopy pressure drop and airflow resistance coefficient were less than those at other azimuth positions, with values of 3.75 ± 0.56 Pa and 0.19 ± 0.01, 3.10 ± 0.53 Pa and 0.12 ± 0.01, and 3.09 ± 0.65 Pa and 0.11 ± 0.02, respectively. When the initial azimuth of the leaf was at other positions, the difference between the maximum canopy pressure drop and airflow resistance coefficient was not obvious.

The reason for this finding is that the maximum canopy pressure drop and resistance coefficient of the leaf reflected the dissipation capacity of the leaf to the airflow energy. This energy dissipation capacity includes two parts—that is, when the assisted airflow passes through the leaf canopy, part of the energy is

TABLE 3 Test scheme of airflow resistance characteristics of single leaf at multiple positions.

Test Number	Initial azimuth angle φ (°)
1	0
2	45
3	90
4	135
5	180
6	225
7	270
8	315

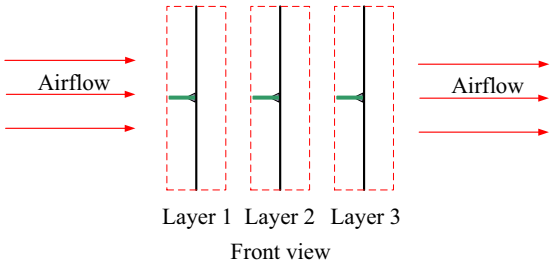

FIGURE 8
Schematic diagram of leaf sample layer division.

TABLE 4 Test scheme of airflow resistance characteristics for multi-position attitude of multi-layer leaves.

Test number	Number of leaf sample layers N	Initial azimuth of each leaf layer (φ_1, φ_2, φ_3)
1	2	(0°, 0°)
2	2	(0°, 180°)
3	2	(180°, 180°)
4	2	(180°, 0°)
5	3	(0°, 0°, 0°)
6	3	(0°, 0°, 180°)
7	3	(0°, 180°, 0°)
8	3	(0°, 180°, 180°)
9	3	(180°, 180°, 0°)
10	3	(180°, 180°, 180°)
11	3	(180°, 0°, 0°)
12	3	(180°, 0°, 180°)

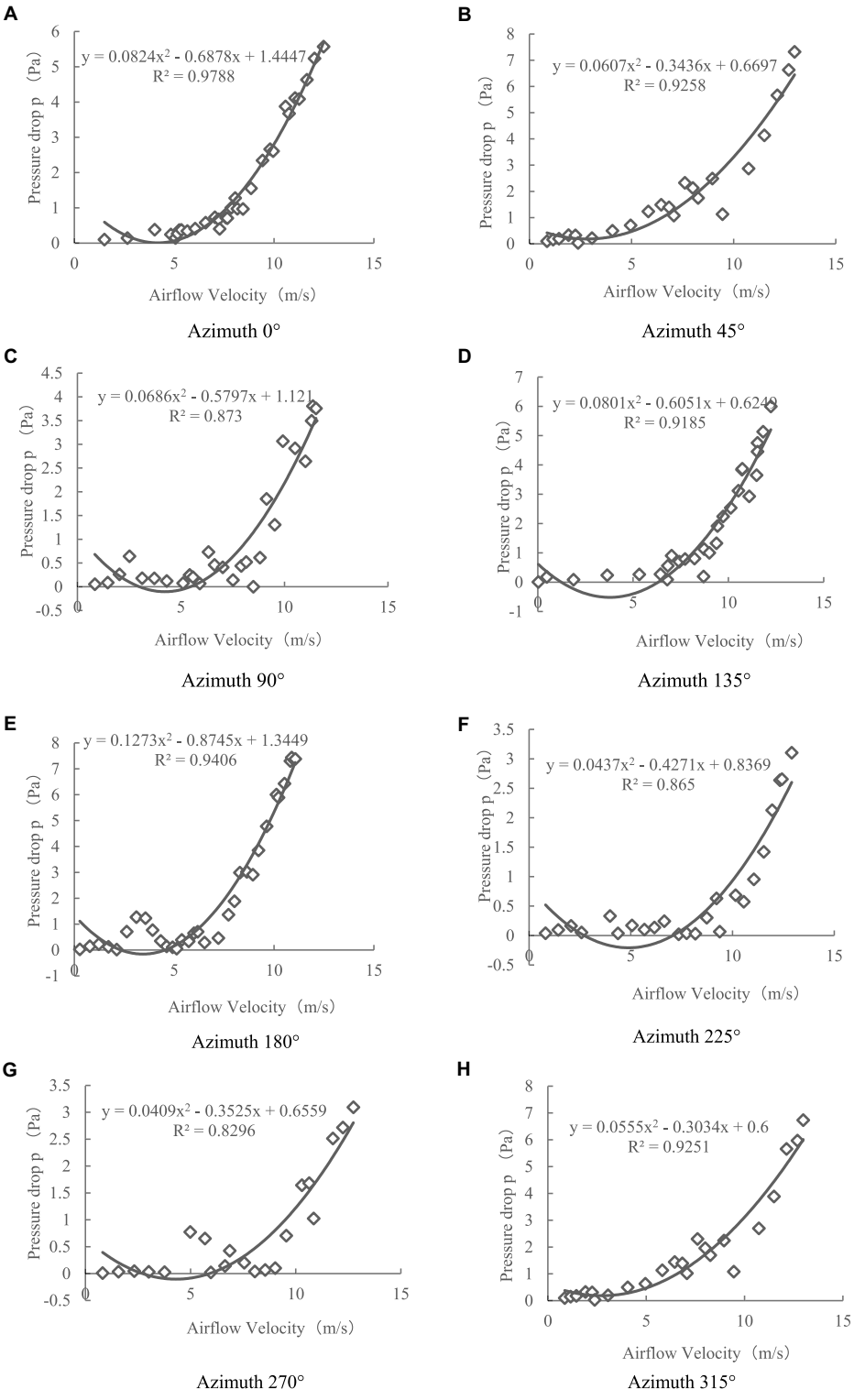

FIGURE 9
Variation of canopy pressure drop with airflow velocity under different azimuth conditions. **(A)** Azimuth 0°. **(B)** Azimuth 45°. **(C)** Azimuth 90°. **(D)** Azimuth 135°. **(E)** Azimuth 180°. **(F)** Azimuth 225°. **(G)** Azimuth 270°. **(H)** Azimuth 315°.

dissipated due to friction, leaf upwind blocking, and other factors and the other part is transformed into the kinetic energy of the leaf. However, when the leaf azimuth changes constantly, the weight of energy dissipation of factors such as friction, leaf upwind resistance, and leaf kinetic energy conversion is an ever-changing process.

Airflow resistance characteristics of multi-leaf and multi-position attitude

Through the comparison in Figure 13, we found that with an increasing number of leaf layers, the canopy pressure drop still increases in a linear nonlinear proportion with continual increases in the assisted airflow velocity, with a critical wind speed in the 7–9 m/s range. When the air velocity is less than the critical wind speed, an increase in the assisted air velocity does not significantly improve the canopy pressure drop. However, when the air velocity is greater than the critical wind speed, the pressure drop increases rapidly.

We performed quadratic polynomial regression fitting on the experimental data to obtain the curve of Equation (5) and used the coefficients K_1 and K_2 of the fitting curve of Equation (5) to calculate the maximum canopy pressure drop and resistance coefficient of the leaves under different leaf layers and initial azimuth angles. The comparisons in Figures 14, 15 indicate that when the number of leaf layers is two, the maximum canopy pressure drop and resistance coefficient of the leaf are not more than those of a single leaf and that they have numerical ranges of 2.53–6.10 ± 0.55 Pa and 0.08–0.29 ± 0.55, respectively. When the number of leaf layers is three, the maximum canopy pressure drop and resistance coefficient of the leaf are clearly more than those of the single-layer leaf, and their numerical ranges are 3.83–12.09 ± 0.77 Pa and 0.04–0.38 ± 0.02, respectively. Moreover, the ratio of the number of leaf layers with an initial azimuth of 180° to the number of leaf layers with an initial azimuth of 0° directly affects the maximum pressure drop and resistance coefficient of the crop canopy. When the number of leaf layers with an initial azimuth of 180° is large, the maximum pressure drop of the crop canopy is relatively small. As the number of leaf layers in the crop canopy and the differences in the initial azimuths of the leaves in the layer increase, the corresponding change between the maximum canopy pressure drop and the resistance coefficient is non-linear and difficult to quantify, as the result of the linear superposition of the resistance characteristics of multiple single-layer leaves. Thus, it is recommended that when there are multiple leaf layers in a canopy, it should be regarded as a single research object.

Relationships between resistance characteristics of crop canopy and droplet deposition effect

In the process of air-assisted spraying, there should be a positive correlation between the energy dissipation effect of the canopy on the assisted airflow and its ability to capture droplets (Cox et al., 2000; Endalew et al., 2010a). Based on this premise, we analyzed the relationship between the resistance characteristics of the crop canopy and the fog droplet deposition effect.

When the crop canopy had only a single leaf in the direction of the assisted airflow, the canopy pressure drop increased non-linearly with increasing assisted airflow velocity, meaning that the droplet-catching ability of the leaf also increased. When the initial azimuth angle of the leaf was 0°–90° or 270°–360°, an increase in the windward load area increased the canopy pressure drop, but the droplet deposition on the back of the leaf could not be guaranteed. When the initial azimuth angle of the leaf was 90°–270°, if the wind speed of the assisted airflow was greater than the critical wind speed, the unsteady high-frequency and high-amplitude vibration state of the leaf increased the canopy pressure drop, with the leaf exhibiting a good droplet deposition effect on both sides, which is consistent with the conclusions of previous studies. Consequently, for single-layer leaves, we could evaluate the corresponding initial azimuth and droplet deposition effect by considering when the canopy pressure drop value changed with the airflow velocity and whether there was a critical wind speed, combining the maximum canopy pressure drop value and resistance coefficient.

When the crop canopy had multiple leaves in the direction of the assisted airflow, the leaves in the first layer inevitably captured most of the droplets when the velocity of the assisted

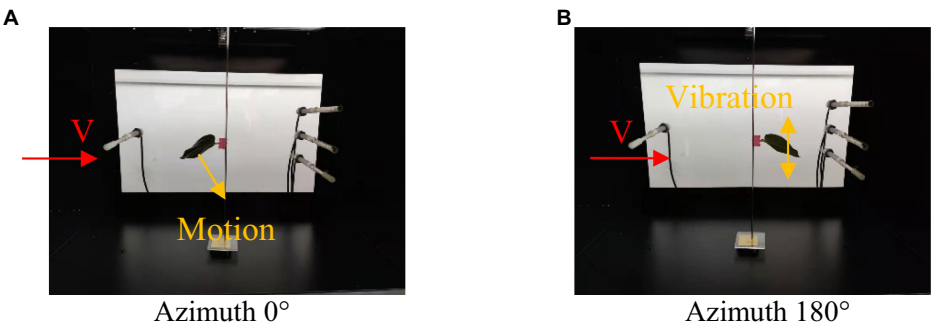

FIGURE 10
Motion of leaves at different airflow velocities, *V*, and azimuth angles, φ. **(A)** Azimuth 0°. **(B)** Azimuth 180°.

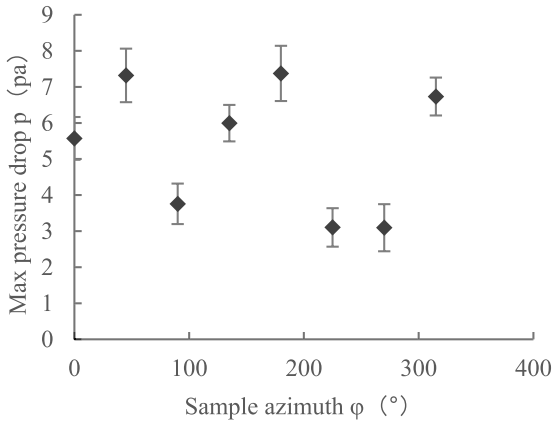

FIGURE 11
Variation of maximum canopy pressure drop with initial azimuth.

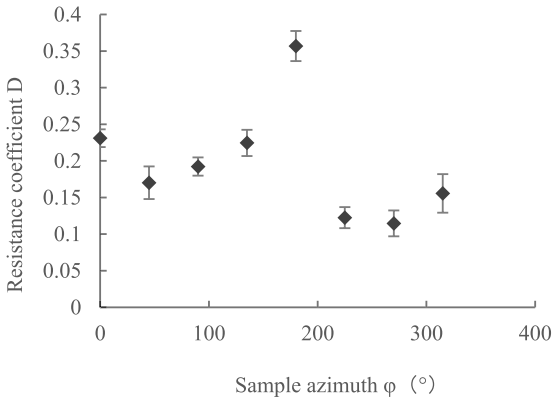

FIGURE 12
Variation of drag coefficient with initial azimuth.

airflow was greater than the critical wind speed, resulting in poor canopy penetration. When the assisted airflow velocity was kept below the critical wind speed and the initial azimuth angle of each layer of leaves was 90°–270°, although canopy penetration could be guaranteed, the droplet deposition effect of the corresponding leaf layer was worse. Moreover, as the number of leaf layers in the crop canopy increased and the initial azimuth angles of the leaves within the canopy changed, the corresponding changes in the maximum pressure drop and resistance coefficient were non-linear and difficult to quantify. It was difficult to judge the number of leaf layers and the specific canopy structure based on the resistance characteristics of the crop canopy with the characteristics of multiple leaves. Consequently, it was considered that existing air-assisted spray technology could not guarantee the droplet deposition effect and canopy penetration at the front layer when the canopy had multiple leaves in the assisted airflow direction.

Application potential of resistance characteristics in the evaluation of air-assisted spraying effect

Combining CFD technology with field testing is a common method of studying the distribution and attenuation law of the coupled field of airflow and droplets in the inner space of a crop canopy (Endalew et al., 2010b,c). The distribution and attenuation law of the coupling field between the assisted airflow and droplets in the inner space of a complex crop canopy is always a research problem. The existing CFD technology can only simplify the crop canopy into a porous medium model for calculation and analysis. The distribution and attenuation law of the coupled field of the assisted airflow and droplets in the internal space of the crop canopy completely ignores the characteristics of the crop leaves and canopy under airflow stress, and accuracy cannot be guaranteed. Based on the field test of the distribution and attenuation law of the coupling field between the assisted airflow and droplets in the inner space of the crop canopy, the canopy was layered along the assisted airflow direction, and the relationships between the distribution and attenuation and the canopy leaf area index, porosity, resistance coefficient, and other structural characteristic parameters were established (Sun et al., 2015; Sun and Liu, 2019). However, the influence of the motion characteristics of the crop canopy under assisted airflow force on the changes in the canopy leaf area index, porosity, resistance coefficient, and other structural characteristic parameters was still ignored. Liu et al. considered the potential influence of the airflow stress movement characteristics of a crop canopy on droplet deposition (Liu et al., 2021b). However, only under certain working conditions, the canopy deformation characteristics of cotton crop are small, so it is difficult to apply his approach to other crops, and it is impossible to establish a universal and efficient theoretical model. Section "Introduction" mentioned that the evaluation of the droplet deposition effect of the crop canopy under different air-assisted spraying conditions based on water-sensitive paper and other droplet deposition measurement methods has the problems of expensive equipment, a complicated process, and repetition. In this study, the effects of airflow-forced movement characteristics of crop canopy on air-assisted spraying were considered, and the effects of number of the leaf layer, initial position, and attitude of leaves relative to the assisted airflow as well as assisted airflow speed on the resistance characteristics of the crop canopy were analyzed. Finally, the application potential of crop canopy resistance characteristics in air-assisted spraying effect evaluation was verified.

Conclusion

In general, our experimental data showed that the number of leaf layers and the initial azimuth of leaves in the crop canopy significantly affected the resistance characteristics of the canopy and that these resistance characteristics were also being closely

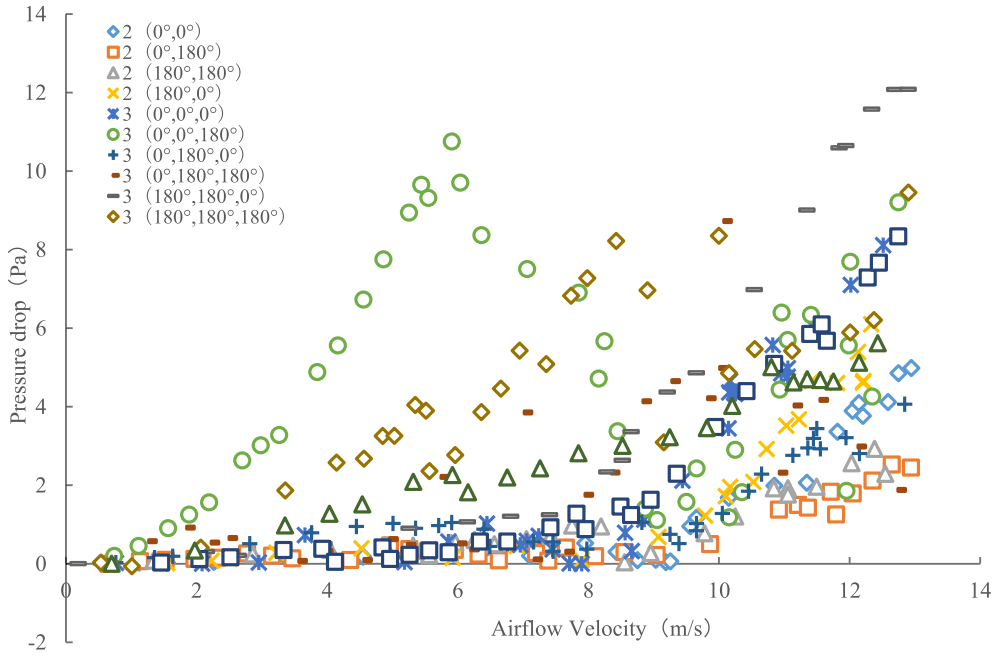

FIGURE 13
Variation of canopy pressure drop with air velocity with different numbers of leaf sample layers.

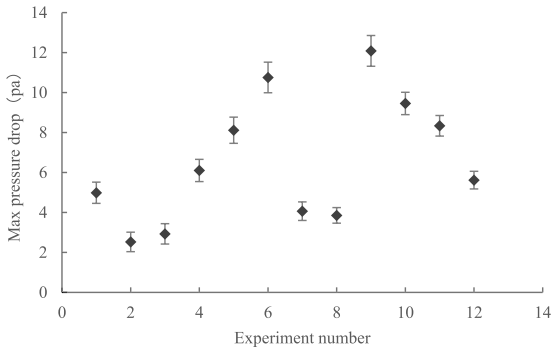

FIGURE 14
Variation of maximum canopy pressure drop with the number of leaf layers and initial azimuth.

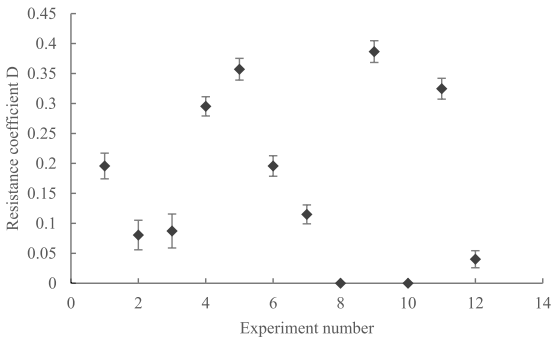

FIGURE 15
Variation of resistance coefficient with the number of leaf layers and initial azimuth.

related to the effects of droplet deposition. Using a broad-leaved crop canopy as an example, the following conclusions can be drawn.

Under the conditions of different leaf layers and initial leaf azimuth angles in different leaf layers, the canopy pressure drop increases non-linearly with increasing assisted airflow velocity. The curve equation obtained by regression fitting conformed to the Darcy–Forchheimer equation. When the initial azimuth of the single-layer leaf was 90°–270°, there was a critical wind speed in the 7–9 m/s range, and when the assisted air velocity was less than this critical wind speed, an increase in the assisted air velocity did not significantly improve the canopy pressure drop. However, when the air velocity was greater than the critical wind speed, the canopy pressure drop of the leaf increased rapidly with increasing assisted air velocity.

For a single leaf, when the initial azimuth angle of the leaf was 180°, the maximum canopy pressure drop and airflow resistance coefficient were greater than those of the other initial azimuth positions, at 7.37 Pa and 0.35, respectively. When the leaf azimuth angle was 90°, 225°, and 270°, the maximum canopy pressure drop and airflow resistance coefficient were smaller than those of other azimuth positions, with values of 3.75 and 0.19, 3.10 and 0.12, and 3.09 and 0.11, respectively. When the initial azimuth was in other positions, the differences

between the maximum canopy pressure drops and airflow resistance coefficients were not obvious.

When the number of leaf layers was two, the maximum canopy pressure drop and resistance coefficient were not more than those of a single leaf, with values of 2.53–6.10 Pa and 0.08–0.29, respectively. When there were three leaf layers, the maximum canopy pressure drop and resistance coefficient were clearly larger than those of a single leaf, with values of 3.83–12.09 Pa and 0.04–0.38, respectively. Moreover, the ratio of the number of leaf layers with an initial azimuth angle of 180° to the number of leaf layers with an initial azimuth angle of 0° directly affected the maximum pressure drop and resistance coefficient of the crop canopy. The maximum pressure drop of the crop canopy was relatively small when the initial azimuth angle was 180°.

We analyzed the relationships between the resistance characteristics of the crop canopy and droplet deposition effect. For single-layer leaves, we evaluated the corresponding initial azimuth and droplet deposition effect based on whether the canopy pressure drop changed with air velocity and whether there was a critical wind speed and combined the maximum canopy pressure drop and resistance coefficient. When the crop canopy had multiple leaves in the assisted airflow direction, the existing air-assisted spray technology could not guarantee the droplet deposition effect and canopy penetration simultaneously.

Our experiment had several limitations. Although we focused on the resistance characteristics of single and multi-layer leaves in an assisted airflow field, the number of leaf layers in the crop canopy and initial azimuth angle of the leaves in the layer significantly affect their resistance characteristics. However, in the real world, the leaves are different and the leaf population structure of the crop canopy is much more complex than that set in this study. When the assisted airflow passes through the crop canopy, its change law becomes more complex, and the movement law of the leaf population is significantly different from that examined in this study. Moreover, due to connections between stems, many leaves move in concert, which needs to be investigated further. This study indicates that when the number of layers of the crop canopy exceeds 1 in the direction of assisted airflow, air-assisted spraying technology cannot guarantee that every layer of leaves in the crop canopy has a good droplet deposition effect in theory. Solving this problem is of great significance for the research and development of crop protection technologies and equipment.

Data availability statement

The original contributions presented in the study are included in the article/supplementary material, further inquiries can be directed to the corresponding author.

Author contributions

SW, JL, and JZ designed the study, performed the experiments and data analysis, and wrote the manuscript. JZ and YC advised on the design of the experiments. All authors contributed to the article and approved the submitted version.

Funding

The work was supported by the Jiangsu Provincial Key Research and Development Program (BE2020383) and the Changzhou Science and Technology Bureau (CE20202014).

Acknowledgments

Appreciations are given to the editor and reviewers of the Journal.

Conflict of interest

The authors declare that the research was conducted in the absence of any commercial or financial relationships that could be construed as a potential conflict of interest.

Publisher's note

References

Abbas, I., Liu, J., Faheem, M., Noor, R. S., Shaikh, S. A., Solangi, K. A., et al. (2020). Different real-time sensor technologies for the application of variable-rate spraying in agriculture. *Sens. Actuators A* 316:112265. doi: 10.1016/j.sna.2020.112265

Carvalho, F. P. (2006). Agriculture, pesticides, food security and food safety. *Environ. Sci. Pol.* 9, 685–692. doi: 10.1016/j.envsci.2006.08.002

Cox, S., Salt, D., Lee, B., and Ford, M. (2000). A model for the capture of aerially sprayed pesticide by barley. *J. Wind Eng. Ind. Aerodyn.* 87, 217–230. doi: 10.1016/S0167-6105(00)00038-6

Davydov, R., Sokolov, M., Hogland, W., Glinushkin, A., and Markaryan, A. (2018). The application of pesticides and mineral fertilizers in agriculture. *MATEC Web Conf.* 245:11003. doi: 10.1051/matecconf/201824511003

Derksen, R., Zhu, H., Ozkan, H., Hammond, R., Dorrance, A., and Spongberg, A. (2008). Determining the influence of spray quality, nozzle type, spray volume, and air-assisted application strategies on deposition of pesticides in soybean canopy. *Trans. ASABE* 51, 1529–1537. doi: 10.13031/2013.25301

Dorr, G. J., Forster, W. A., Mayo, L. C., McCue, S. W., Kempthorne, D. M., Hanan, J., et al. (2016). Spray retention on whole plants: modelling, simulations and experiments. *Crop Prot.* 88, 118–130. doi: 10.1016/j.cropro.2016.06.003

Dullien, F. A. (2012). *Porous Media: Fluid Transport and Pore Structure*. San Diego, California: Academic Press.

Endalew, A. M., Debaer, C., Rutten, N., Vercammen, J., Delele, M. A., Ramon, H., et al. (2010a). Modelling pesticide flow and deposition from air-assisted orchard

spraying in orchards: a new integrated CFD approach. *Agric. For. Meteorol.* 150, 1383–1392. doi: 10.1016/j.agrformet.2010.07.001

Endalew, A. M., Debaer, C., Rutten, N., Vercammen, J., Delele, M. A., Ramon, H., et al. (2010b). A new integrated CFD modelling approach towards air-assisted orchard spraying—Part II: validation for different sprayer types. *Comput. Electron. Agric.* 71, 137–147. doi: 10.1016/j.compag.2009.11.007

Endalew, A. M., Debaer, C., Rutten, N., Vercammen, J., Delele, M. A., Ramon, H., et al. (2010c). A new integrated CFD modelling approach towards air-assisted orchard spraying. Part I. Model development and effect of wind speed and direction on sprayer airflow. *Comput. Electron. Agric.* 71, 128–136.

Fang, H., Li, K., Wu, G., Cheng, R., Zhang, Y., and Yang, Q. (2020). A CFD analysis on improving lettuce canopy airflow distribution in a plant factory considering the crop resistance and LEDs heat dissipation. *Biosyst. Eng.* 200, 1–12. doi: 10.1016/j.biosystemseng.2020.08.017

Foqué, D., Pieters, J. G., and Nuyttens, D. (2012). Spray deposition and distribution in a bay laurel crop as affected by nozzle type, air assistance and spray direction when using vertical spray booms. *Crop Prot.* 41, 77–87. doi: 10.1016/j.cropro.2012.05.020

Hong, S.-W., Zhao, L., and Zhu, H. (2018). CFD simulation of pesticide spray from air-assisted sprayers in an apple orchard: tree deposition and off-target losses. *Atmos. Environ.* 175, 109–119. doi: 10.1016/j.atmosenv.2017.12.001

Krogh, K., Halling-Sørensen, B., Mogensen, B., and Vejrup, K. (2003). Environmental properties and effects of nonionic surfactant adjuvants in pesticides: a review. *Chemosphere* 50, 871–901. doi: 10.1016/S0045-6535(02)00648-3

Lhomme, J.-P. (1991). The concept of canopy resistance: historical survey and comparison of different approaches. *Agric. For. Meteorol.* 54, 227–240. doi: 10.1016/0168-1923(91)90007-D

Liu, X., Song, L., Cui, H., Liu, Y., Liu, X., and Wu, M. (2021a). Influence of air droplets stress and canopy porosity change on deposition performance in air-assisted spray. *Trans. Chin. Soc. Agric. Mach.* 52, 117–126. doi: 10.6041/j.issn.1000-1298.2021.08.01

Liu, X., Song, L., Cui, H., Liu, Y., Liu, X., and Wu, Q. (2021b). Decoupling study on the effects of airflow droplet stress and canopy pore change on sedimentation performance. *Trans. Chin. Soc. Agric. Mach.* 1376. doi: 10.1063/1.3651957

Molina-Aiz, F., Valera, D., Alvarez, A., and Madueno, A. (2006). A wind tunnel study of airflow through horticultural crops: determination of the drag coefficient. *Biosyst. Eng.* 93, 447–457. doi: 10.1016/j.biosystemseng.2006.01.016

Nield, D. A., and Bejan, A. (2006). *Convection in Porous Media*. New York, NY: Springer.

Patel, M. K. (2016). Technological improvements in electrostatic spraying and its impact to agriculture during the last decade and future research perspectives–a review. *Eng. Agric. Environ. Food* 9, 92–100. doi: 10.1016/j.eaef.2015.09.006

Sánchez-Hermosilla, J., and Medina, R. (2004). Adaptive threshold for droplet spot analysis using water-sensitive paper. *Appl. Eng. Agric.* 20, 547–551. doi: 10.13031/2013.17454

Sanz, C. (2003). A note on k-ε modelling of vegetation canopy air-flows. *Bound. Layer Meteorol.* 108, 191–197. doi: 10.1023/A:1023066012766

Shao, C., and Chen, Y. (2011). Deformation and vibration of a *Platanus acerifolia* tree leaf in wind. *AIP Conf. Proc.* 495–497.

Song, M., and Fu, H. (2020). Relationship between structural parameters and resistance characteristics of three-dimensional canopy. *J. Donghua Univ.* 46:7.

Stajnko, D., Berk, P., Lešnik, M., Jejčič, V., Lakota, M., Štrancar, A., et al. (2012). Programmable ultrasonic sensing system for targeted spraying in orchards. *Sensors* 12, 15500–15519. doi: 10.3390/s121115500

Sun, C., and Liu, C. (2019). Construction and application of a model for air spray droplet canopy penetration. *Trans. Chin. Soc. Agric. Eng.* 35, 25–32. doi: 10.11975/j.issn.1002-6819.2019.15.004.

Sun, C., Qiu, W., Ding, W., and Gu, J. (2015). Optimization and experiment of key operating parameters of pear air spray. *Trans. Chin. Soc. Agric. Eng.* 31, 30–38. doi: 10.11975/j.issn.1002-6819.2015.24.005

Tadrist, L., Julio, K., Saudreau, M., and Langre, E. (2015). Leaf flutter by torsional galloping: experiments and model. *J. Fluids Struct.* 56, 1–10. doi: 10.1016/j.jfluidstructs.2015.04.001

Wang, F., Feng, J., and Zhao, Y. (2008). The head-on colliding process of binary liquid droplets at low velocity: high-speed photography experiments and modeling. *J. Colloid Interface Sci.* 326, 196–200. doi: 10.1016/j.jcis.2008.07.002

Wang, J., Liu, J., Zhao, S., Zhai, J., and Wu, S. (2020). Design and experiment of pendular small sprayer for elevated strawberry. *J. Agric. Mechaniz. Res.* 42:7.

Wu, S., Liu, J., Wang, J., Hao, D., and Wang, R. (2021). The motion of strawberry leaves in an air-assisted spray field and its influence on droplet deposition. *Trans. ASABE* 64, 83–93. doi: 10.13031/trans.14143

frontiers | Frontiers in Plant Science

TYPE Original Research
PUBLISHED 22 July 2022
DOI 10.3389/fpls.2022.920902

OPEN ACCESS

EDITED BY
Xiongkui He,
China Agricultural University,
China

REVIEWED BY
Ilias Travlos,
Agricultural University of Athens, Greece
Yanbo Huang,
United States Department of Agriculture (USDA), United States

*CORRESPONDENCE
Ercheng Zhao
eczhao@126.com
Chunhong Jia
chjia55@163.com

SPECIALTY SECTION
This article was submitted to Sustainable and Intelligent Phytoprotection, a section of the journal Frontiers in Plant Science

RECEIVED 15 April 2022
ACCEPTED 13 June 2022
PUBLISHED 22 July 2022

CITATION
Zhang J, Xie Y, Zhang C, Zhang P, Jia C and Zhao E (2022) Early evaluation of adjuvant effects on topramezone efficacy under different temperature conditions using chlorophyll fluorescence tests. *Front. Plant Sci.* 13:920902. doi: 10.3389/fpls.2022.920902

Early evaluation of adjuvant effects on topramezone efficacy under different temperature conditions using chlorophyll fluorescence tests

Jinwei Zhang[1], Yaqiong Xie[2], Chunhua Zhang[3], Peng Zhang[3], Chunhong Jia[1]* and Ercheng Zhao[1]*

[1]Institute of Plant Protection, Beijing Academy of Agriculture and Forestry Sciences, Beijing, China, [2]MAP Field Crop Division, Sinochem Agriculture Holdings, Beijing, China, [3]Beijing Grand Agro Chem Co., Ltd., Beijing, China

Proper selection of adjuvant applications is an important strategy to enhance herbicide efficacy and reduce active ingredient input especially under adverse environmental conditions. In this study, a two-factor split-plot-design experiment was conducted to evaluate the effects of two adjuvants on the efficacy of topramezone on the grassy weed species giant foxtail (*Setaria faberi* Herrm.) and the broadleaved weed species velvetleaf (*Abutilon theophrasti* Medik.) under three different temperature conditions. The two tested adjuvants were methylated seed oil (MSO) and organosilicone. Three temperature levels, 35/30°C, 25/20°C, and 15/10°C (day/night), were used in the laboratory and greenhouse experiment. Plant chlorophyll fluorescence measurements shortly after herbicide application and classic whole-plant bioassay methods were used to evaluate the herbicide efficacy among the different treatments. Results indicated that the maximum quantum efficiency (Fv/Fm) of the top leaf of the weeds treated with topramezone mixed with MSO was significantly lower than that of the weeds treated with topramezone mixed with organosilicone and without an adjuvant at 2–3days after treatment under all three temperature levels. The herbicide response of the plants treated with topramezone mixed with organosilicone and topramezone alone was not significantly different. These results corresponded well with the results of the classic whole-plant test. MSO has been shown to be good at enhancing the efficacy of topramezone on these weed species under all three temperature conditions. The measurement of chlorophyll fluorescence is a promising technique for evaluating the effects of adjuvants on the efficacy of herbicides shortly after herbicide treatment.

KEYWORDS

topramezone, adjuvant, methylated seed oil, chlorophyll fluorescence test, early efficacy evaluation

Introduction

To enhance their efficacy, many postemergence herbicides have to be applied together with adjuvants (Hart et al., 1992; Bunting et al., 2004; Bautista et al., 2020). An adjuvant is any substance in an herbicide formulation or added to a spray tank to improve herbicidal activity or application characteristics (Foy, 1989). There are various types of adjuvants with varying degrees of effectiveness at improving herbicide efficacy. Selecting the proper adjuvant for herbicides is difficult but very important because the efficacy of herbicides on weeds is usually dependent on the herbicide type, weed species, the selected adjuvant, environmental conditions and so on (Penner, 2000). This can reduce the herbicide active ingredient input and environmental risk. Methylated seed oil (MSO) is a fatty acid from seed oil esterified with methanol. Reports have shown that MSO enhances the efficacy of several herbicides on certain weed species, as MSO contributes to increasing the penetration of herbicides into plants (Thompson et al., 1996; Young and Hart, 1998; Sharma and Singh, 2000; Pester et al., 2001; Bukun et al., 2010; Zhang et al., 2013a). Organosilicone surfactants were introduced to work as adjuvants for pesticides in the 1980s, and since then, their chemical structure and synergistic mechanism have been extensively researched (Stevens, 1993; Knoche, 1994). Because of the numerous advantages of these two adjuvants, MSO and organosilicone are typically the most commonly used adjuvants for pesticide application in China. Topramezone, a hydroxyphenylpyruvate dioxygenase inhibitor, was commercially introduced in 2006 (Grossmann and Ehrhardt, 2007) and registered in China in 2010. When applied as a postemergence herbicide, it controls a wide spectrum of annual grass and broadleaved weeds (Zhang et al., 2013a) and is safe for maize (Soltani et al., 2007; Gitsopoulos et al., 2010). In China, MSO is the only recommended adjuvant for this herbicide, as is the case in other countries. Thus, trying to find a new adjuvant for topramezone application will provide additional options for weed control in maize.

Environmental factors, such as temperature, relative humidity, soil moisture, rain, and wind, contribute to the amount and rate of herbicide uptake and the final efficacy (Zabkiewicz, 2000). In particular, the environmental temperature is variable at different latitudes or under certain small-scale regional conditions even in the same crop growing season. Temperature can influence the absorption, translocation, and metabolism of herbicide active ingredients in plants. Similarly, the effect of an adjuvant on herbicide efficacy varies under different environmental temperature conditions. One of the main functions of a right and good adjuvant is to overcome or minimize adverse factors. There has been long history on the effect of environmental conditions on the efficacy of herbicides (Hammerton, 1967; Peregoy et al., 1990; Hinz and Owen, 1994; Levene and Owen, 1995). However, as an increasingly extensive-used herbicide in maize field in China, from the Northeast to the Southwest region, there has been very few research on the impact and interaction effects of adjuvant type and environmental temperature conditions on the efficacy of this herbicide.

It is valuable and useful to evaluate the effect of an adjuvant on the efficacy of herbicides under different environmental conditions, especially under adverse conditions. A fast and nondestructive herbicide efficacy evaluation approach shortly after herbicide treatment could be an efficient method for agronomists to screen the right adjuvant for a certain herbicide. With the rapid development of plant phenotypic analysis, methods such as RGB imaging, multispectral imaging, hyperspectral imaging, thermal imaging, chlorophyll fluorescence, 3D sensing, and others have been introduced to test the response of plants under environmental (biotic and abiotic) stress efficiently (Lee et al., 2010; Belin et al., 2013; Huang et al., 2015; Lowe et al., 2017). Utilizing the improvement of these technologies, scientists in weed science also want to evaluate the efficacy of herbicides on weeds and their safety on crops (Streibig et al., 2014; Travlos et al., 2021). Chlorophyll fluorescence test has been used as a sensitive indicator of the physiological status of plants. It can monitor spatial and temporal variations by providing images of photosynthesis activity (Schreiber, 2004; Abbaspoor and Streibig, 2007; Belin et al., 2013). By utilizing this technology, Woodyard et al. (2009) evaluate the joint activity of mesotrione and atrazine in a tank-mix application on sensitive and resistant broadleaved weeds, Kaiser et al. (2013) and Wang et al. (2016, 2018) measured the herbicide resistance of *Alopecurus myosuroides* in the greenhouse and field conditions, and Li et al. (2018) identified herbicide stress in soybean shortly after treatment.

Understanding the effect of the two common used adjuvants in China in different environmental conditions, especially detecting it in a much efficient way, is beneficial to enhance herbicide efficacy and reduce active ingredient input. The objectives of this research were (a) to detect the effects of two adjuvant types (MSO and organosilicone) on the efficacy of topramezone under different environmental temperature conditions and (b) to determine whether the plant chlorophyll fluorescence test can be used as a nondestructive method to evaluate the effect of adjuvants on the efficacy of herbicides shortly after herbicide treatment.

Materials and methods

Chemicals and plant materials

In this study, the applied solution was prepared using a commercial herbicide and adjuvant products, including Baowei™ (336 g a.i. L^{-1} topramezone, SC, BASF Co., Ltd.), GY-HMax™ (methylated soybean oil, an MSO adjuvant, Central Research Institute of China Chemical Science and Technology), and BREAK-THRU® (S240, an organosilicone adjuvant, Omya. Agro. AG, Switzerland). The spray herbicide solutions were prepared according to the data in Table 1.

10.3389/fpls.2022.920902

TABLE 1 Herbicide solution preparation for the experiment.

Treatment	Herbicide dose (g a.i. ha^{-1})	Adjuvant dose (%)
Topramezone alone	6.3	0
Topramezone with MSO*	6.3	0.300 (v/v)
Topramezone with organosilicone	6.3	0.025 (v/v)
Control	0	0

*MSO means methylated seed oil.

The dicotyledonous weed velvetleaf (*Abutilon theophrasti* Medic.) and monocotyledonous weed giant foxtail (*Setaria faberi* Herrm.) were selected as sample plants in this study, because they were two of the most common infested weed species in maize field in China. The weed seeds (provided by Herbiseed Co., UK) were pregerminated in plastic pots (11 × 11 × 6 cm) filled with vermiculite (2–3 cm) in a greenhouse (25/20 ± 1°C day/night, 122 μmol m^{-2} s^{-1} supplemental light for 12 h, and 55 ± 10% RH). After germination, the velvetleaf seedlings were transplanted into 11 × 11 × 12 cm plastic pots (3 plants per pot), and the giant foxtail seedlings were transplanted into 7 × 7 × 8 cm compostable pots (4 plants per pot). All the pots were filled with a mixture of vermiculite: peat: clay (1:1:1 by volume). The plants were irrigated daily with tap water. The homogeneous plants were selected as plant samples for the experiment when they had developed 3–4 true leaves.

Experimental design and tests

The sample plants were moved into a growth chamber 2 days before herbicide application and were watered according to their demand. After 2 days of cultivation in the chamber, herbicides were applied using a track sprayer (Aro, Langenthal, Switzerland) with a spray volume of 200 l ha^{-1} (nozzle: 8002 EVS, Teejet® Spraying Systems Co., Wheaton, IL, United States) at 3.2 kPa. The sample plants were cultivated in the growth chamber for 2 more days and then moved back to the greenhouse. The plants were watered daily with tap water. The aboveground biomass of the plants was harvested 3 weeks after herbicide application and dried at 80°C for 48 h before weight measurement. The experiment was established as a two-factor split-plot design, with environmental temperature treatment in the main plots and adjuvant treatments in the subplots. Three replicates were used for each treatment, and the whole experiment was repeated once.

The temperature of the artificial growth chamber (KBF720, Binder GmbH, Tuttlingen, Germany) was set to produce a high temperature (35/30°C, day/night), moderate temperature (25/20°C, day/night) and low temperature (15/10°C, day/night). The photoperiod was adjusted to 12/12 h (day/night), and the relative humidity was adjusted to 75% for both the day and night time.

To evaluate herbicide efficacy, the PSII maximum quantum efficiency (Fv/Fm) of the fourth leaf (the top leaf of the plant), defined as Fv/Fm, was measured and recorded using a chlorophyll fluorometer (Imaging-PAM, M-Series MAXI Version, Heinz Walz GmbH, Effeltrich, Germany) at 2, 3, 4 and 5 days after treatment (DAT). The F_v/F_m was calculated according to equation (1):

$$F_v / F_m = (F_m - Fo) / F_m \quad (1)$$

where Fm is the maximal fluorescence yield and F0 is the dark fluorescence yield. For the determination of F_0, the plants were dark adapted for 30 min prior to the measurement. All measurements were conducted in a dark room under green illumination to avoid other photosynthetically active radiation except that emitted by the Imaging-PAM light source. After dark adaptation, the plants were illuminated with a light-saturated pulse of 2,634 μm m^{-2} s^{-1} photosynthetic photon flux density (PPFD) and a wavelength of 450 nm for F_v/F_M determination. Usually, all PSII reaction centers are open after dark adaptation, and nonphotochemical energy dissipation is minimal. During the saturation pulse, the fluorescence yield is maximal. The Imaging-PAM fluorometer also measures other parameters related to chlorophyll fluorescence, including effective quantum yield. The maximum quantum efficiency of PSII, however, was selected for this study because it remains unchanged until the next F0 and Fm determination.

While measuring the F_v/F_m value, chlorophyll fluorescence images were taken using a charge coupled device(CCD)camera mounted above the plant pots. The spatial resolution of the camera was 640 by 480 pixels, and the field of view was 10 by 13 cm. Only the plants were measured; the background was removed from the images. Fluorescence intensities are displayed as false colors. Light-emitting diodes (LEDs) were placed around the lens of the camera. Blue (450 nm) LED light provides pulse-modulated excitation light and simultaneously serves as actinic illumination and saturation pulses. The red long-pass filter in front of the CCD chip confined the detection window to wavelengths longer than 620 nm. In total, nine individual velvetleaf and twelve giant foxtail plants were measured for each treatment.

Statistical analysis

To estimate the significance of the herbicide effect, the variable relative index (RI) of F_v/F_m and plant dry weight (DW) were calculated according to the following equations:

$$RI_{F_v/F_m} = \frac{(F_v / F_m)_{treatment}}{(F_v / F_m)_{control}} \quad (2)$$

$$RI_{DW} = \frac{(DW)_{treatment}}{(DW)_{control}} \quad (3)$$

The data were subjected to univariate analysis *via* the GLM process using SPSS 22.0 (version 22.0) software. The assumptions of variance analysis were tested by ensuring that the residuals were random and homogenous, with a normal distribution, using residual plots and the Shapiro–Wilk normality test. The data from two repeated experiments were combined for analysis because there were no interaction effects between the two experiments. When there was a significant interaction between the treatments of temperature and adjuvant (P<0.05), the means were separated by Fisher's protected LSD test at the 5% level of probability.

Results

Effects of adjuvants as revealed by plant chlorophyll fluorescence measurements

The relative maximum quantum efficiency (F_v/F_m) index (RI_{F_v/F_m}) of the giant foxtail treated with topramezone plus MSO under the high and moderate temperature conditions was significantly lower ($p < 0.05$) than that of the topramezone alone treatment group from 2 DAT to 5 DAT. Under low temperature conditions, similar differences between the two groups appeared after 4 DAT. In the case of topramezone applied mixed with organosilicone, there was no significant difference in the RI_{F_v/F_m} value compared with that of the treatment of herbicide applied alone in any of the three temperature conditions. Additionally, the RI_{F_v/F_m} value of the giant foxtail ranked as moderate < high < low for each adjuvant treatment from 3 DAT to 5 DAT (Table 2).

The chlorophyll fluorescence images taken at 5 DAT showed that the weed treated with herbicide mixed with MSO was injured more severely than the weeds treated with herbicide alone and mixed with organosilicone under all 3 temperature conditions (the false color of the normal plant leaves was blue, while the false color of the leaves changing from green to yellow and even to black demonstrated that the plants were injured more severely). In addition, the plants treated under high and moderate temperature conditions were injured more severely than those treated under low temperature conditions for each herbicide treatment (Figure 1).

Similar to the case of giant foxtail, the RI_{F_v/F_m} value of velvetleaf treated with topramezone together with a tank-mix of MSO under the high and moderate temperature conditions was significantly lower ($p < 0.05$) than that of the topramezone alone treatment group from 2 DAT to 5 DAT, while there were no differences under the low temperature conditions. With respect to the treatment of topramezone together with a tank-mix of organosilicone, there was no significant difference compared with the treatment of topramezone alone under any of the three temperature conditions. With respect to all three herbicide treatments, the RI_{F_v/F_m} value of the treated velvetleaf under moderate and high temperature conditions was significantly lower ($p < 0.05$) than that under low temperature conditions (horizontal comparison). The chlorophyll fluorescence images taken at 5 DAT also showed that velvetleaf plants treated with herbicide together with a tank-mix of MSO were more injured than those treated with herbicide alone and together with organosilicone under moderate and high temperature conditions, while the difference was not apparent under low temperature conditions (Figure 2).

The abovementioned results indicated that the MSO adjuvant significantly enhanced the efficacy of topramezone under all temperature conditions for giant foxtail and under high and moderate temperature conditions for velvetleaf, while the effect of organosilicone on enhancing the efficacy was not significant for either weed species. Additionally, the efficacy of topramezone was better under relatively high temperatures than under relatively low temperature conditions for giant foxtail and velvetleaf after it was tank-mixed with MSO (Table 3).

Effects of adjuvants according to whole-plant biomass measurements

The relative dry weight index (RI_{DW}) of both weed species treated with topramezone together with MSO was significantly lower ($p < 0.05$) than that treated with topramezone applied alone and together with organosilicone under all three temperature conditions, while the difference between the last two treatments was not significant under any of the three temperature conditions at 3 weeks after treatment (WAT). Additionally, the RI_{DW} value under the different temperature conditions ranked as high < moderate < low for both weed species for each adjuvant treatment (Table 4).

The images taken at 3 WAT also apparently showed that both weed species treated with topramezone together with MSO were injured more than those treated with the other adjuvant and applied alone under all temperature conditions (Figures 3, 4). The results demonstrated that the MSO adjuvant significantly but not the organosilicone adjuvant enhanced the efficacy of topramezone under all temperature conditions for both weed species and that the efficacy of topramezone was better under relatively high temperature conditions than under relatively low temperature conditions.

Discussion

Effects of two adjuvants on enhancing the efficacy of topramezone under different environmental temperatures

In our study, both the leaf chlorophyll fluorescence measurements and whole-plant bioassay results demonstrated that the MSO adjuvant significantly enhanced the efficacy of

10.3389/fpls.2022.920902

TABLE 2 Effects of two adjuvants on the maximum quantum efficiency (F_v/F_m) of giant foxtail (*Setaria faberi* Herrm.) at 2–5days after treatment (DAT).

Days After Treatment (DAT)	Adjuvant	RI_{F_V/F_m}		
		High temperature	Moderate temperature	Low temperature
2	Alone	0.97 ± 0.07aA	0.98 ± 0.04aA	0.99 ± 0.02aA
	Org	0.89 ± 0.13abA	0.95 ± 0.06abA	1.00 ± 0.02aA
	MSO	0.89 ± 0.20bB	0.86 ± 0.08bB	0.99 ± 0.02aA
3	Alone	0.79 ± 0.25aB	0.57 ± 0.19abC	0.96 ± 0.03aA
	Org	0.78 ± 0.20aB	0.60 ± 0.19aC	0.98 ± 0.04aA
	MSO	0.73 ± 0.19aB	0.55 ± 0.16bC	0.96 ± 0.05aA
4	Alone	0.56 ± 0.26aB	0.32 ± 0.09aC	0.68 ± 0.17aA
	Org	0.42 ± 0.21abB	0.36 ± 0.12aC	0.75 ± 0.20aA
	MSO	0.37 ± 0.22bA	0.26 ± 0.07bC	0.54 ± 0.09bA
5	Alone	0.45 ± 0.23aB	0.28 ± 0.08aC	0.49 ± 0.16aA
	Org	0.36 ± 0.17aB	0.23 ± 0.09aC	0.57 ± 0.27aA
	MSO	0.27 ± 0.08bB	0.13 ± 0.04bC	0.39 ± 0.15bA

The topramezone dose was 6.3 g a.i. ha^{-1}; control means treated with tap water; Alone means that topramezone was applied alone; Org means that topramezone was applied with a tank-mix of organosilicone; MSO means topramezone was applied with a tank-mix of MSO. The means in the same column followed by a common letter are not significantly different at p = 0.05 (vertical comparison). The means in the same row followed by a capital common letter are not significantly different at p = 0.05 (horizontal comparison).

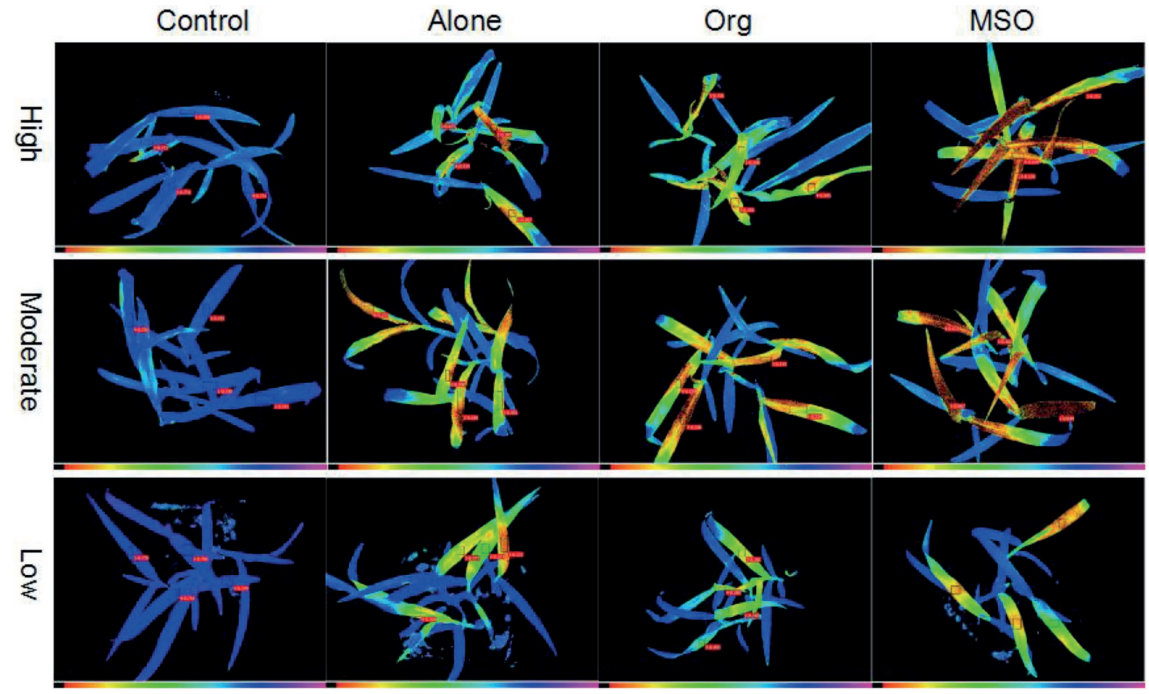

FIGURE 1
Chlorophyll fluorescence images of giant foxtail at 5 days after treatment. The topramezone dose was 6.3 g a.i. ha^{-1}; control means treated with tap water; Alone means topramezone was applied alone; Org means topramezone was applied with a tank-mix of organosilicone; MSO means topramezone was applied with a tank-mix of MSO.

topramezone under all temperature conditions for both weed species, especially for those under relatively high temperatures. Zollinger (2010) summarized that the MSO adjuvant had the unique advantage of enhancing herbicide efficacy when applied at reduced rates under adverse environmental conditions (e.g., hot weather, low relative humidity, and high temperature). In our case, when the plants were cultivated in the 35/30°C (day/night) conditions (the high temperature conditions), the dose of herbicide we applied (6.3 g a.i. ha^{-1}) was only 1/4 of the recommended dose (the recommended

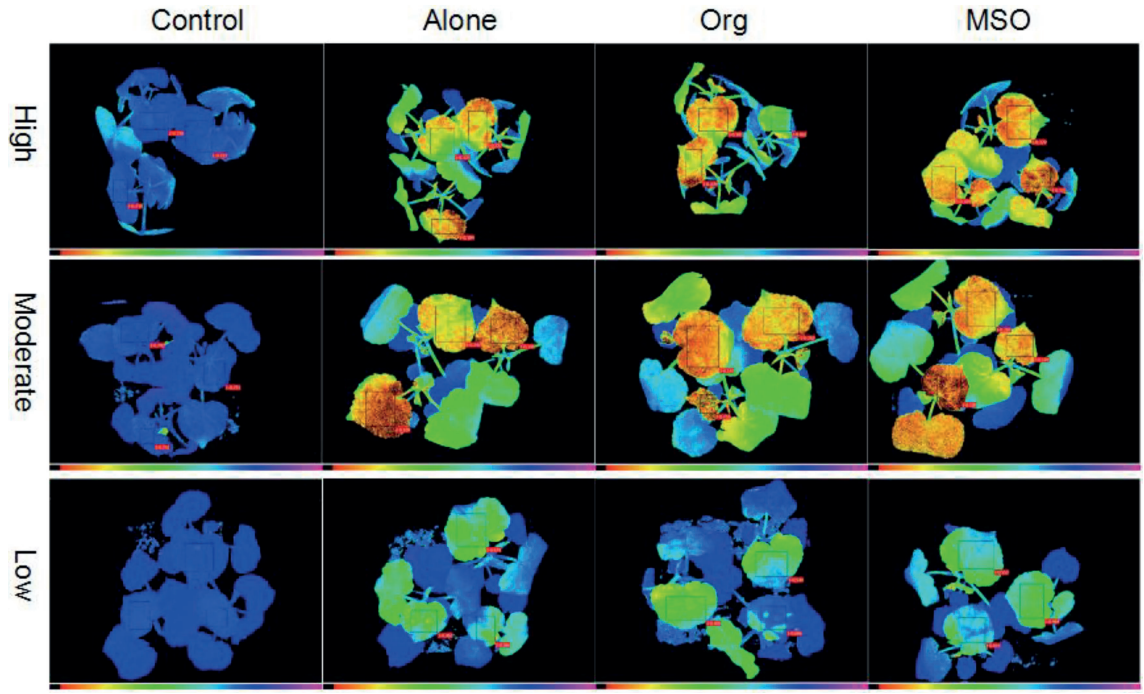

FIGURE 2
Chlorophyll fluorescence images of velvetleaf at 3 days after treatment. The topramezone dose was 6.3 g a.i. ha^{-1}; control means treated with tap water; Alone means topramezone was applied alone; Org means topramezone was applied together with a tank-mix of organosilicone; MSO means topramezone was applied together with a tank-mix of MSO.

TABLE 3 Effects of two adjuvants on the maximum quantum efficiency (F_v/F_m) of velvetleaf (*Abutilon theophrasti* Medik.) at 2–5days after treatment (DAT).

Days After Treatment (DAT)	Adjuvant	RI_{F_V}/F_m		
		High temperature	Moderate temperature	Low temperature
2	Alone	0.92 ± 0.07aB	0.92 ± 0.07aB	0.99 ± 0.03aA
	Org	0.88 ± 0.10abA	0.88 ± 0.08abA	1.00 ± 0.03aA
	MSO	0.86 ± 0.09bB	0.84 ± 0.08bB	0.99 ± 0.03aA
3	Alone	0.72 ± 0.15aB	0.69 ± 0.14aB	0.87 ± 0.20aA
	Org	0.72 ± 0.16aB	0.63 ± 0.17abB	0.90 ± 0.15aA
	MSO	0.59 ± 0.09bB	0.54 ± 0.12bB	0.86 ± 0.23aA
4	Alone	0.58 ± 0.19aB	0.52 ± 0.20aB	0.79 ± 0.17aA
	Org	0.45 ± 0.13abB	0.47 ± 0.24abB	0.83 ± 0.15aA
	MSO	0.39 ± 0.10bB	0.38 ± 0.16bB	0.78 ± 0.19aA
5	Alone	0.46 ± 0.11aB	0.48 ± 0.18aB	0.70 ± 0.12aA
	Org	0.34 ± 0.12abB	0.39 ± 0.31abB	0.67 ± 0.19aA
	MSO	0.25 ± 0.09bB	0.32 ± 0.21bB	0.69 ± 0.08aA

The topramezone dose was 6.3 g a.i. ha^{-1}; control means treated with tap water; Alone means that topramezone was applied alone; Org means that topramezone was applied together with a tank mix of organosilicone; MSO means topramezone was applied together with a tank mix of MSO. The means in the same column followed by a common letter are not significantly different at P = 0.05 (vertical comparison). The means in the same row followed by a capital common letter are not significantly different at p = 0.05 (horizontal comparison).

dose of topramezone registered in China is 22.5–27.0 g a.i. ha^{-1}). Therefore, our result is mostly consistent with the results in the report of Zollinger. Our previous research (Zhang et al., 2013b) showed that MSO enhanced the efficacy of topramezone on giant foxtail and velvetleaf by decreasing the solution surface tension and leaf-droplet contact angle and by increasing both the spread area and wetting time on weed leaf surfaces. This resulted in a decreased crystal amount of the active ingredient and an increased foliar uptake and final translocation of the active ingredient in the plants.

TABLE 4 Effects of two adjuvants on the dry weight of giant foxtail (*Setaria faberi* Herrm.) and velvetleaf (*Abutilon theophrasti* Medik.) at 3weeks after application.

Weed	Adjuvant	RI_{DW}		
		High temperature	Moderate temperature	Low temperature
Giant foxtail	Alone	0.36 ± 0.08aB	0.38 ± 0.09aAB	0.51 ± 0.19aA
	Organosilicone	0.29 ± 0.14abB	0.41 ± 0.20aAB	0.46 ± 0.18abA
	MSO	0.21 ± 0.08bB	0.32 ± 0.06bAB	0.40 ± 0.08bA
Velvetleaf	Alone	0.41 ± 0.22aB	0.46 ± 0.30aB	0.66 ± 0.37aA
	Organosilicone	0.38 ± 0.23aB	0.38 ± 0.30aB	0.59 ± 0.38abA
	MSO	0.23 ± 0.04bB	0.25 ± 0.07bB	0.48 ± 0.20bA

The topramezone dose was 6.3 g a.i. ha^{-1}; control means treated with tap water; Alone means that topramezone was applied alone; Org means that topramezone was applied together with a tank mix of organosilicone; MSO means topramezone was applied together with a tank mix of MSO. The means in the same column followed by a common letter are not significantly different at P = 0.05 (vertical comparison). The means in the same row followed by a capital common letter are not significantly different at p = 0.05 (horizontal comparison).

FIGURE 3
Images of giant foxtail taken at 3 weeks after herbicide application. The topramezone dose was 6.3 g a.i. ha^{-1}; control means treated with tap water; Alone means topramezone was applied alone; Org means topramezone was applied together with organosilicone; MSO means topramezone was applied together with MSO.

Additionally, studies have shown that the absorption and translocation of herbicide active ingredients in plants decreased under high temperature stress, which ultimately decreased herbicide efficacy (Hawxby et al., 1972; Devine et al., 1983; Coetzer et al., 2001). Thus, the application of MSO adjuvants could contribute to the enhancement of herbicide efficacy, especially under adverse environmental conditions.

Adjuvant organosilicone had no effect on the efficacy of topramezone under any of the three temperature conditions. Organosilicone adjuvants usually enhance the efficacy of certain herbicides by reducing the surface tension of the spray solution, promoting infiltration of the active ingredient into stomata, and increasing droplet spreading over the leaf surface (Field et al., 1992). Though a large number of studies have demonstrated good effects of organosilicone on enhancing the efficacy of herbicides with many different modes of action, there are still some reports indicating antagonistic action between L-77 (a type of organosilicone adjuvant) and glyphosate (Sharma and Singh, 2000). This is similar to the findings in our study; hence, the reason (perhaps from the perspective of deposition, retention, uptake, translocation and so on) needs to be further studied in future.

Chlorophyll fluorescence measurement as a method to evaluate the effect of adjuvants on herbicide

Measuring changes in the chlorophyll fluorescence induction curve (Kautsky curve) has been used in plant photosynthesis research (Christensen et al., 2003; Korres et al., 2003). This method is effective at providing a snapshot of the physiological status of a plant exposed to various stress factors and contains important information about the photosynthetic apparatus. Because of its nondestructive, highly sensitive, rapid speed and easy-to-operate characteristics, this method has been used to measure the effects of herbicides that inhibit photosystem II and those with other modes of action (Habash et al., 1985; Percival et al., 1992; Klem et al., 2002). With the development of this technology and new instruments, Wang et al. (2018) demonstrated that chlorophyll fluorescence can be used to identify the effects of ALS (acetolactate synthase) and ACCase (acetyl CoA carboxylase) inhibitor herbicides on the PSII of weed species and crops under different growing conditions. Similar to other 4-hydroxyphenylpyruvate dioxygenase (4-HPPD) inhibitors, topramezone blocks the formation of homogentisate by

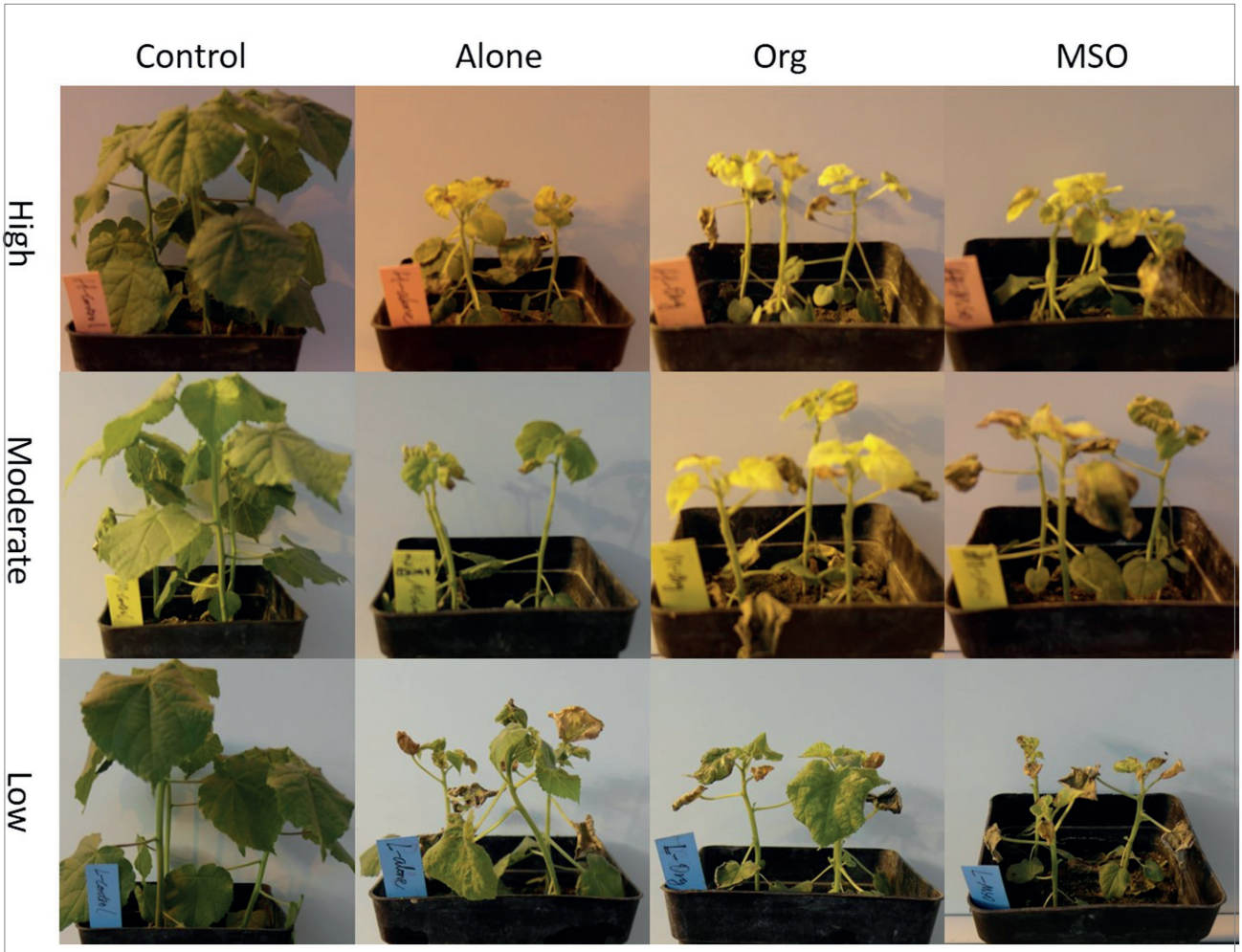

FIGURE 4
Images of velvetleaf taken at 3 weeks after application. The topramezone dose was 6.3 g a.i. ha^{-1}; control means treated with tap water; Alone means topramezone was applied alone; Org means topramezone was applied together with organosilicone; MSO means topramezone was applied together with MSO.

inhibiting 4-HPPD (Grossmann and Ehrhardt, 2007). As homogentisic acid is a precursor of the most common plastoquinone (PQ-9), the electron transport efficiency between PSI and PSII decreases after the inhibition of HPPD (Xu et al., 2019), and the photosynthesis of herbicide-treated plants becomes interrupted. Thus, less energy can be used by the plants *via* photosynthesis and is therefore reemitted as chlorophyll fluorescence in a shorter wavelength compared with that which occurs in unstressed status. Therefore, chlorophyll fluorescence imaging technology should theoretically be capable of evaluating the efficacy of such mode of herbicides.

In our case, we employed chlorophyll fluorescence imaging technology to evaluate the effects of adjuvants on herbicide efficacy under different environmental temperature conditions. The classic whole-plant bioassay and plant chlorophyll fluorescence measurement results at 2-5 DAT under high and moderate environmental temperatures corresponded well with each other for both the grassy weed giant foxtail and the broadleaved weed velvetleaf. This is quite similar to the result of Vranjes et al. (2019) when they did their research on the response of *chenopodium album* and *abutilon theophrasti* to the treatment of mesotrione. The RI_{F_v/F_m} value of the treatment involving the herbicide applied together with MSO in a tank mixture was significantly decreased compared with that of the treatment involving the herbicide applied alone. In the case of low temperature, the chlorophyll fluorescence measurement at 2-5 DAT was not consistent for velvetleaf, and the RI_{F_v/F_m} value did not significantly vary among the different adjuvant treatments. Hence, chlorophyll fluorescence measurements are capable of evaluating the effects of adjuvants on the efficacy of herbicides under relatively high environmental temperature conditions for some grassy weed species, but attention should be paid under relatively low temperature conditions and for some broadleaved weed species. As stated above, this technology has already been applied for herbicide efficacy evaluation in the field accompanying the improvement of technology and new instruments (Wang

et al., 2016, 2018; Li et al., 2018). Hence this method will accelerate the progress of screening the right adjuvant for herbicides and improve the digital component of classic herbicide bioassays practically.

Conclusion

Selecting an appropriate spray adjuvant for herbicides under different environmental conditions is an important strategy to enhance the efficacy of herbicides, reduce the application dose, and enhance environmental safety. Both the weed leaf chlorophyll fluorescence test and the whole-plant bioassay results demonstrated that the MSO adjuvant significantly enhanced the efficacy of topramezone under all temperature conditions for both weeds, the grassy weed species giant foxtail (*Setaria faberi* Herrm.) and the broadleaved weed species velvetleaf (*Abutilon theophrasti* Medik.), especially under relatively high temperature conditions. However, the organosilicone adjuvant had no effect on the efficacy of the herbicide on either weed species under any of the temperature conditions. The underlying reason (perhaps from the aspect of deposition, retention, uptake, translocation and so on) needs to be further studied. There was a relatively good correlation between chlorophyll fluorescence measurements and whole-plant bioassay results for both weed species under high and moderate temperature conditions. Hence, chlorophyll fluorescence measurements should be capable of evaluating the effects of adjuvants on herbicide efficacy under certain environmental conditions. However, attention should still be paid under relatively low temperature conditions for broadleaved weed species.

Data availability statement

The raw data supporting the conclusions of this article will be made available by the authors, without undue reservation.

Author contributions

JZ contributed to conceptualization, methodology, data curation, and manuscript writing. YX contributed to investigation, validation and resources. CZ helped in investigation and resources. PZ contributed to investigation and resources. CJ contributed to supervision and funding acquisition. EZ helped in supervision, validation and resources. All authors contributed to the article and approved the submitted version.

Funding

This research was supported by the China National Key Research and Development Project (No. 2017YFD0201808).

Conflict of interest

JZ was employed by Institute of Plant Protection, Beijing Academy of Agriculture and Forestry Sciences. YX employed by MAP Field Crop Division, Sinochem Agriculture Holdings. CZ and PZ were employed by Beijing Grand Agro Chem Co., Ltd.

The remaining authors declare that the research was conducted in the absence of any commercial or financial relationships that could be construed as a potential conflict of interest.

Publisher's note

All claims expressed in this article are solely those of the authors and do not necessarily represent those of their affiliated organizations, or those of the publisher, the editors and the reviewers. Any product that may be evaluated in this article, or claim that may be made by its manufacturer, is not guaranteed or endorsed by the publisher.

References

Abbaspoor, M., and Streibig, J. C. (2007). Monitoring the efficacy and metabolism of phenylcarbamates in sugar beet and black nightshade by chlorophyll fluorescence. *Pest Manag. Sci.* 63, 576–585. doi: 10.1002/ps.1382

Bautista, C. P., Guadalupe, J., Travlos, I., Tataridas, A., and Prado, R. D. (2020). Effect of adjuvant on glyphosate effectiveness, retention, absorption and translocation in *lolium rigidum* and *conyza canadensis*. *Plan. Theory* 9, 297. doi: 10.3390/plants9030297

Belin, É., Rousseau, D., Boureau, T., and Caffier, V. (2013). Thermography versus chlorophyll fluorescence imaging for detection and quantification of apple scab. *Comput. Electron. Agric.* 90, 159–163. doi: 10.1016/j.compag.2012.09.014

Bukun, B., Lindenmayer, R. B., Nissen, S. J., Westra, P., Shaner, D. L., and Brunk, G. (2010). Absorption and translocation of aminocyclopyrachlor and aminocyclopyrachlor-methyl ester in Canada thistle (*Cirsium arvense*). *Weed Sci.* 58, 96–102. doi: 10.1614/WS-09-086.1

Bunting, J. A., Sprague, C. L., and Riechers, D. E. (2004). Absorption and activity of foramsulfuron in giant foxtail (*Setaria faberi*) and woolly cupgrass (*Eriochloa villosa*) with various adjuvants. *Weed Sci.* 52, 513–517. doi: 10.1614/WS-03-135R

Christensen, M. G., Teicher, H. B., and Streibig, J. C. (2003). Linking fluorescence induction curve and biomass in herbicide screening. *Pest Manag. Sci.* 59, 1303–1310. doi: 10.1002/ps.763

Coetzer, E., Al-Khatib, K., and Loughin, T. M. (2001). Glufosinate efficacy, absorption, and translocation in amaranth as affected by relative humidity and temperature. *Weed Sci.* 49, 8–13. doi: 10.1614/0043-1745(2001)049[0008:GEAATI]2.0.CO;2

Devine, M. D., Bandeen, J. D., and McKERSIE, B. D. (1983). Temperature effects on glyphosate absorption, translocation, and distribution in quackgrass (*Agropyron repens*). *Weed Sci.* 31, 461–464. doi: 10.1017/S0043174500069393

Field, R. J., Dobson, N. N., and Tisdall, L. J. (1992). "Species-specific sensitivity to organosilicone surfactant-enhancement of glyphosate uptake," in *Adjuvants for Agrochemicals*. ed. C. L. Foy (Florida, USA: CRC Press Boca Raton), 423–431. doi: 10.1201/9781351069502-40

Foy, C. L. (1989). "Adjuvants: terminology, classification, and mode of action," in *Adjuvants and agrochemicals*. eds. P. N. P. Chow, C. A. Grant and A. M. Hinshalwood (United States: CRC Press)

Gitsopoulos, T. K., Melidis, V., and Evgenidis, G. (2010). Response of maize (*Zea mays* L.) to post-emergence applications of topramezone. *Crop Prot.* 29, 1091–1093. doi: 10.1016/j.cropro.2010.06.020

Grossmann, K., and Ehrhardt, T. (2007). On the mechanism of action and selectivity of the corn herbicide topramezone: a new inhibitor of 4-hydroxyphenylpyruvate dioxygenase. *Pest Manag. Sci.* 63, 429–439. doi: 10.1002/ps.1341

Habash, D. M., Percival, P., and Baker, N. R. (1985). Rapid chlorophyll fluorescence technique for the study of penetration of photosynthetically active herbicides into leaf tissue. *Weed Res.* 25, 389–395. doi: 10.1111/j.1365-3180.1985.tb00660.x

Hammerton, J. L. (1967). Environmental factors and susceptibility to herbicides. *Weeds* 15, 330–336. doi: 10.2307/4041001

Hart, S. E., Kells, J. J., and Penner, D. (1992). Influence of adjuvants on the efficacy, absorption, and spray retention of primisulfuron. *Weed Technol.* 6, 592–598. doi: 10.1017/S0890037X00035855

Hawxby, K., Basler, E., and Santelmann, P. W. (1972). Temperature effects on absorption and translocation of trifluralin and methazole in peanuts. *Weed Sci.* 20, 285–289. doi: 10.1017/S0043174500035669

Hinz, J. R., and Owen, M. D. (1994). Effect of drought stress on velvetleaf (*Abutilon theophrasti*) and bentazon efficacy. *Weed Sci.* 42, 76–81. doi: 10.1017/S0043174500084198

Huang, S., Qi, L., Ma, X., Xue, K., Wang, W., and Zhu, X. (2015). Hyperspectral image analysis based on BoSW model for rice panicle blast grading. *Comput. Electron. Agric.* 118, 167–178. doi: 10.1016/j.compag.2015.08.031

Kaiser, Y. I., Menegat, A., and Gerhards, R. (2013). Chlorophyll fluorescence imaging: a new method for rapid detection of herbicide resistance in *Alopecurus myosuroides*. *Weed Res.* 53, 399–406. doi: 10.1111/wre.12043

Klem, K., Špundová, M., Hrabalova, H., Nauš, J., Váňová, M., Masojidek, J., et al. (2002). Comparison of chlorophyll fluorescence and whole-plant bioassays of isoproturon. *Weed Res.* 42, 335–341. doi: 10.1046/j.1365-3180.2002.00293.x

Knoche, M. (1994). Organosilicone surfactant performance in agricultural spray application: a review. *Weed Res.* 34, 221–239. doi: 10.1111/j.1365-3180.1994.tb01990.x

Korres, N. E., Froud-Williams, R. J., and Moss, S. R. (2003). Chlorophyll fluorescence technique as a rapid diagnostic test of the effects of the photosynthetic inhibitor chlorotoluron on two winter wheat cultivars. *Ann. Appl. Biol.* 143, 53–56. doi: 10.1111/j.1744-7348.2003.tb00268.x

Lee, W. S., Alchanatis, V., Yang, C., Hirafuji, M., Moshou, D., and Li, C. (2010). Sensing technologies for precision specialty crop production. *Comput. Electron. Agric.* 74, 2–33. doi: 10.1016/j.compag.2010.08.005

Levene, B. C., and Owen, M. D. (1995). Effect of moisture stress and leaf age on bentazon absorption in common cocklebur (*Xanthium strumarium*) and velvetleaf (*Abutilon theophrasti*). *Weed Sci.* 43, 7–12. doi: 10.1017/S0043174500080747

Li, H., Wang, P., Weber, J. F., and Gerhards, R. (2018). Early identification of herbicide stress in soybean (*Glycine max* (L.) Merr.) using chlorophyll fluorescence imaging technology. *Sensors* 18:21.

Lowe, A., Harrison, N., and French, A. P. (2017). Hyperspectral image analysis techniques for the detection and classification of the early onset of plant disease and stress. *Plant Methods* 13:80. doi: 10.1186/s13007-017-0233-z

Penner, D. (2000). Activator adjuvants 1. *Weed Technol.* 14, 785–791. doi: 10.1614/0890-037X(2000)014[0785:AA]2.0.CO;2

Percival, M. P., Blowers, M. H., Green, J. W., and Baker, N. R. (1992). "Chlorophyll fluorescence-a noninvasive technique for rapid investigation of the effects of adjuvants on herbicide and plant growth regulator uptake by leaves," in *Adjuvants for Agrichemicals*. ed. C. F. Foy (United States, Boca Raton: CRC Press), 187–193.

Peregoy, R. S., Kitchen, L. M., Jordan, P. W., and Griffin, J. L. (1990). Moisture stress effects on the absorption, translocation, and metabolism of haloxyfop in johnsongrass (*Sorghum halepense*) and large crabgrass (*Digitaria sanguinalis*). *Weed Sci.* 38, 331–337. doi: 10.1017/S0043174500056630

Pester, T. A., Nissen, S. J., and Westra, P. (2001). Absorption, translocation, and metabolism of imazamox in jointed goatgrass and feralrye. *Weed Sci.* 49, 607–612. doi: 10.1614/0043-1745(2001)049[0607:ATAMOI]2.0.CO;2

Schreiber, U. (2004). "Pulse-amplitude-modulation (PAM) fluorometry and saturation pulse method: an overview," in *Chlorophyll Fluorescence: A Signature of Photosynthesis*. eds. G. Papageorgiou and F. Govindjee (Dordrecht, the Netherlands: Kluwer Academic Publishers), 279–319.

Sharma, S. D., and Singh, M. (2000). Optimizing foliar activity of glyphosate on *Bidens frondosa* and *Panicum maximum* with different adjuvant types. *Weed Res.* 40, 523–533. doi: 10.1046/j.1365-3180.2000.00209.x

Soltani, N., Sikkema, P. H., Zandstra, J., O'Sullivan, J., and Robinson, D. E. (2007). Response of eight sweet corn (*Zea mays* L.) hybrids to topramezone. *Hortic. Sci.* 42, 110–112. doi: 10.21273/HORTSCI.42.1.110

Stevens, P. J. (1993). Organosilicone surfactants as adjuvants for agrochemicals. *Pestic. Sci.* 38, 103–122. doi: 10.1002/ps.2780380206

Streibig, J. C., Rasmussen, J., Andújar, D., Andreasen, C., Berge, T. W., Chachalis, D., et al. (2014). Sensor-based assessment of herbicide effects. *Weed Res.* 54, 223–233. doi: 10.1111/wre.12079

Thompson, W. M., Nissen, S. J., and Masters, R. A. (1996). Adjuvant effects on imazethapyr, 2,4-D and picloram absorption by leafy spurge (*Euphorbia esula*). *Weed Sci.* 44, 469–475. doi: 10.1017/S0043174500094200

Travlos, I., Tsekoura, A., Antonopoulos, N., Kanatas, P., and Gazoulis, I. (2021). Novel sensor-based method (quick test) for the in-season rapid evaluation of herbicide efficacy under real field conditions in durum wheat. *Weed Sci.* 69, 147–160. doi: 10.1017/wsc.2021.8

Vranjes, F., Vrbnicanin, S., Nedeljkovic, D., Savic, A., and Bozic, D. (2019). The response of *Chenopodium album* L. and *Abutilon theophrasti* Medik. To reduced doses of mesotrione. *J. Environ. Sci. Health B* 54, 1–7.

Wang, P., Li, H., Jia, W., Chen, Y., and Gerhards, R. (2018). A fluorescence sensor capable of real-time herbicide effect monitoring in greenhouses and the field. *Sensors* 18, 3771. doi: 10.3390/s18113771

Wang, P., Peteinatos, G., Li, H., and Gerhards, R. (2016). Rapid in-season detection of herbicide resistant *Alopecurus myosuroides* using a mobile fluorescence imaging sensor. *Crop Prot.* 89, 170–177. doi: 10.1016/j.cropro.2016.07.022

Woodyard, A. J., Hugie, J. A., and Riechers, D. E. (2009). Interactions of mesotrione and atrazine in two weed species with different mechanisms for atrazine resistance. *Weed Sci.* 57, 369–378. doi: 10.1614/WS-08-175.1

Xu, K., Racine, F., He, Z., and Juneau, P. (2019). Impacts of hydroxyphenylpyruvate dioxygenase (HPPD) inhibitor (mesotrione) on photosynthetic processes in *Chlamydomonas reinhardtii*. *Environ. Pollut.* 244, 295–303. doi: 10.1016/j.envpol.2018.09.121

Young, B. G., and Hart, S. E. (1998). Optimizing foliar activity of isoxaflutole on giant foxtail (*Seteria faberi*) with various adjuvants. *Weed Sci.* 46, 397–402. doi: 10.1017/S0043174500090792

Zabkiewicz, J. A. (2000). Adjuvants and herbicidal efficacy-present status and future prospects. *Weed Res.* 40, 139–149. doi: 10.1046/j.1365-3180.2000.00172.x

Zhang, J., Jäck, O., Menegat, A., Zhang, Z., Gerhards, R., and Ni, H. (2013a). The mechanism of methylated seed oil on enhancing biological efficacy of topramezone on weeds. *PLoS One* 8:e74280. doi: 10.1371/journal.pone.0074280

Zhang, J., Zheng, L., Jäck, O., Yan, D., Zhang, Z., Gerhards, R., et al. (2013b). Efficacy of four post-emergence herbicides applied at reduced doses on weeds in summer maize (*Zea mays* L.) fields in North China plain. *Crop Prot.* 52, 26–32. doi: 10.1016/j.cropro.2013.05.001

Zollinger, R., (2010). Optimizing herbicide performance through adjuvants: resolving misconception and confusion. *Proceeding of the 2010 Wisconsin Crop Mnagement Conference*. 49, 39–45.

frontiers | Frontiers in Plant Science

TYPE Original Research
PUBLISHED 28 July 2022
DOI 10.3389/fpls.2022.953753

OPEN ACCESS

EDITED BY
Bugao Xu,
University of North Texas, United States

REVIEWED BY
Arthur Novikov,
Voronezh State University of Forestry and Technologies named after G.F. Morozov, Russia
Soumi Mitra,
Baylor College of Medicine, United States

*CORRESPONDENCE
Xiongkui He
xiongkui@cau.edu.cn
Yajia Liu
liuyajia@cau.edu.cn

SPECIALTY SECTION
This article was submitted to Sustainable and Intelligent Phytoprotection, a section of the journal Frontiers in Plant Science

RECEIVED 26 May 2022
ACCEPTED 05 July 2022
PUBLISHED 28 July 2022

CITATION
Qi P, Wang Z, Wang C, Xu L, Jia X, Zhang Y, Wang S, Han L, Li T, Chen B, Li C, Mei C, Pan Y, Zhang W, Müller J, Liu Y and He X (2022) Development of multifunctional unmanned aerial vehicles versus ground seeding and outplanting: What is more effective for improving the growth and quality of rice culture? *Front. Plant Sci.* 13:953753. doi: 10.3389/fpls.2022.953753

Development of multifunctional unmanned aerial vehicles versus ground seeding and outplanting: What is more effective for improving the growth and quality of rice culture?

Peng Qi[1,2,3], Zhichong Wang[4], Changling Wang[1,2,3], Lin Xu[1,2], Xiaoming Jia[1,2], Yang Zhang[4], Shubo Wang[1,2,3], Leng Han[1,2,3], Tian Li[1,2,3], Bo Chen[5], Chunyu Li[5], Changjun Mei[6], Yayun Pan[7], Wei Zhang[8], Joachim Müller[4], Yajia Liu[1,2,3]* and Xiongkui He[1,2,3]*

[1]College of Science, China Agricultural University, Beijing, China, [2]Centre for Chemicals Application Technology, China Agricultural University, Beijing, China, [3]College of Agricultural Unmanned System, China Agricultural University, Beijing, China, [4]Tropics and Subtropics Group, Institute of Agricultural Engineering, University of Hohenheim, Stuttgart, Germany, [5]Yuren UAV (Zhuhai) Co., Ltd., Zhuhai, China, [6]Agricultural and Rural Bureau of Huaiyuan, Huaiyuan, China, [7]Anhui Difa Agricultural Technology Co., Ltd., Huaiyuan, China, [8]Anhui Zhongke Intelligent Sense Technology Co., Ltd., Wuhu, China

The agronomic processes are complex in rice production. The mechanization efficiency is low in seeding, fertilization, and pesticide application, which is labor-intensive and time-consuming. Currently, many kinds of research focus on the single operation of UAVs on rice, but there is a paucity of comprehensive applications for the whole process of seeding, fertilization, and pesticide application. Based on the previous research synthetically, a multifunctional unmanned aerial vehicle (mUAV) was designed for rice planting management based on the intelligent operation platform, which realized three functions of seeding, fertilizer spreading, and pesticide application on the same flight platform. Computational fluid dynamics (CFD) simulations were used for machine design. Field trials were used to measure operating parameters. Finally, a comparative experimental analysis of the whole process was conducted by comparing the cultivation patterns of mUAV seeding (T1) with mechanical rice direct seeder (T2), and mechanical rice transplanter (T3). The comprehensive benefit of different rice management processes was evaluated. The results showed that the downwash wind field of the mUAV fluctuated widely from 0 to 1.5 m, with the spreading height of 2.5 m, and the pesticide application height of 3 m, which meet the operational requirements. There was no significant difference in yield between T1, T2,

and T3 test areas, while the differences in operational efficiency and input labor costs were large. In the sowing stage, T1 had obvious advantages since the working efficiency was 2.2 times higher than T2, and the labor cost was reduced by 68.5%. The advantages were more obvious compared to T3, the working efficiency was 4 times higher than in T3, and the labor cost was reduced by 82.5%. During the pesticide application, T1 still had an advantage, but it was not a significant increase in advantage relative to the seeding stage, in which operating efficiency increased by 1.3 times and labor costs were reduced by 25%. However, the fertilization of T1 was not advantageous due to load and other limitations. Compared to T2 and T3, operational efficiency was reduced by 80% and labor costs increased by 14.3%. It is hoped that this research will provide new equipment for rice cultivation patterns in different environments, while improving rice mechanization, reducing labor inputs, and lowering costs.

KEYWORDS

multifunctional UAV, seeding, fertilizing, plant protection, mechanization, CFD simulation, rice

Introduction

Rice is one of the most important crops throughout the world. As a staple food for more than half of the world's population, rice is cultivated in more than 100 countries, and 90% is produced in Asia (Bhandari, 2019; Fukagawa and Ziska, 2019). The rice cultivation area in China is about 30 million hm^2, accounting for 30% of the crop cultivation area in China and 20% of the rice cultivation area around the world. The total rice production is nearly 20 million tons in China, accounting for 40 of total grain production in China and 35% of the total rice production all over the world (Zhu et al., 2007; He et al., 2008). With 60% of the Chinese population relying on rice as a staple food, rice has the largest area of cultivation, and the highest yield, which occupies an extremely important position in food security. (Feng et al., 2020).

However, there are many segments and complex agronomic technical measures in rice cultivation, which lead to the low-efficiency mechanization of the whole production process. There are great differences in the mechanization levels of rice seedling, transplanting, fertilization and pesticides management, machine harvest, postharvest transportation, and grain drying (Chen et al., 2017b). The rice cultivation process is divided into four main parts: tillage, seeding, management, and harvest. The tillage and harvest are mechanized, but the seeding and management still cannot meet the requirements of modern agriculture (Li et al., 2012; Song et al., 2018b). Especially in the hilly areas, the arable land is small and scattered, where the terrain is rugged. There are also problems with the use of mechanical operations on the plains. For example, the soil is compacted resulting in uneven seed emergence, and there is an inconvenience in the use of small farm machinery (Lan et al., 2017). They are time-consuming, inconvenient, and labor-intensive, which seriously affect the progress of mechanization (Bao and Li, 2004; Zhang and Zhou, 2019).

With the development of modern manufacturing, many forms of agricultural equipment are used in rice production. Unmanned aerial vehicle (UAVs), with the advantages of fewer site requirements, low energy consumption, high safety, and no space restrictions, has been widely used in rice agricultural production (Wang et al., 2019). The continuous improvement of agronomic technology, intelligent supporting technology, and equipment for the whole process of rice production have been introduced, which promoted many scholars to use UAV applications for rice management (Zhang and Gong, 2014; Zhou et al., 2017, 2019). Firstly, for the effect of plant protection UAV operating parameters on droplets and control effectiveness, some previous explorations have been conducted. Wang et al. (2017) studied the effect of spray parameters of small, unmanned helicopters on the deposition of droplets. The experimental results showed that the droplet distribution decreased from the upper to the lower layer of the rice canopy and decreased with the increase of flight speed. Chen et al. (2016) studied the effect of HY-B-10L unmanned helicopter spray parameters on the droplet deposition distribution in the hybrid rice canopy. The results showed that the vertical wind field above the plant canopy weakened with increasing height, and the amount of droplet deposition gradually decreased; the lower the operating speed, the more droplets were deposited below the aircraft. Xue et al. (2013) applied N-3 UAV to

investigate the effect of different flight heights on the control of rice *Planthopper* and *Cnaphalocrocis medinalis*. The results showed that low flight altitude was effective in controlling rice *Planthopper* and *C. medinalis*, and the application volume was directly proportional to the control effect at the same flight altitude. Secondly, for agricultural UAV seeding, our researchers have conducted a lot of research. In 2014, Li et al. (2016) conducted UAV spreading experiments. The results showed that a 0.09 hm^2 rice field only required 305 s to complete rice seed spreading. Cheng and Li (2020) studied the effects of direct seeding on rice growth characteristics and yield. The results showed that UAV direct seeding had significant advantages over hole-direct seeding and manual sowing in seedling quality indexes. The yield of UAV direct seeding was 454.9 kg/667 m^2, which was higher than that of manual sowing at 417.9 kg/667 m^2, but lower than that of hole direct seeding at 509.3 kg/667 m^2. Thirdly, UAVs had also been studied for agricultural fertilization. Ren et al. (2021) designed a rice fertilizer spreading system. The test results showed that fertilizer spreading uniformity was significantly influenced by flow rate, UAV flight speed, centrifugal disc speed, and drop-in position angle, all of which interacted with each other. The best fertilizer spreading performance was achieved when the drop-in position angle was forty, the centrifugal disc speed was 1,100 r/min, the fertilizer flow rate was 3,460 particles/s, and the flight speed was 5 m/s. The coefficient of variation was 8.86% currently. The fertilizer application efficiency of the UAV was about 12.5 times that of manual fertilizer application.

In 2012, there were less than 10 Chinese agricultural UAV manufacturers and only a few hundred agricultural UAVs. With the promulgation of the Centra Document No. 1 in 2014, the number of UAV enterprises have increased by nearly hundreds, and the sales amount has reached 60 thousand units by 2020. Correspondingly, agricultural UAV ownership has reached 110 thousand units (Yubin and Guobin, 2018; Yongwang et al., 2020). The rapid development of the UAV industry and the rise in labor costs have accelerated the use of UAVs in the rice cultivation process. Especially in areas where large ground machinery cannot operate rice cultivation, the application of UAVs has broad prospects.

Currently, UAVs are widely used in different aspects of agriculture, but mostly single function. UAVs have developed rapidly in agricultural fields, such as disease and insect pest control, pollination, and agricultural information acquisition by remote sensing, but the development of UAV air sowing is relatively backward (Wan et al., 2021). Considering the characteristics of different application of UAVs in seeding, fertilization, and pesticide application in rice cultivation, the idea to design an multifunctional unmanned aerial vehicle (mUAV) is proposed (**Figure 1**), which can combine all these functions. The focus of this article mainly included the following aspects: (1) The mUAV were structured as a modularity of different functions. A sophisticated flight platform was designed and improved, which was based on modular design theory connected to different functional devices, and these different modules corresponded to different functions. This structure

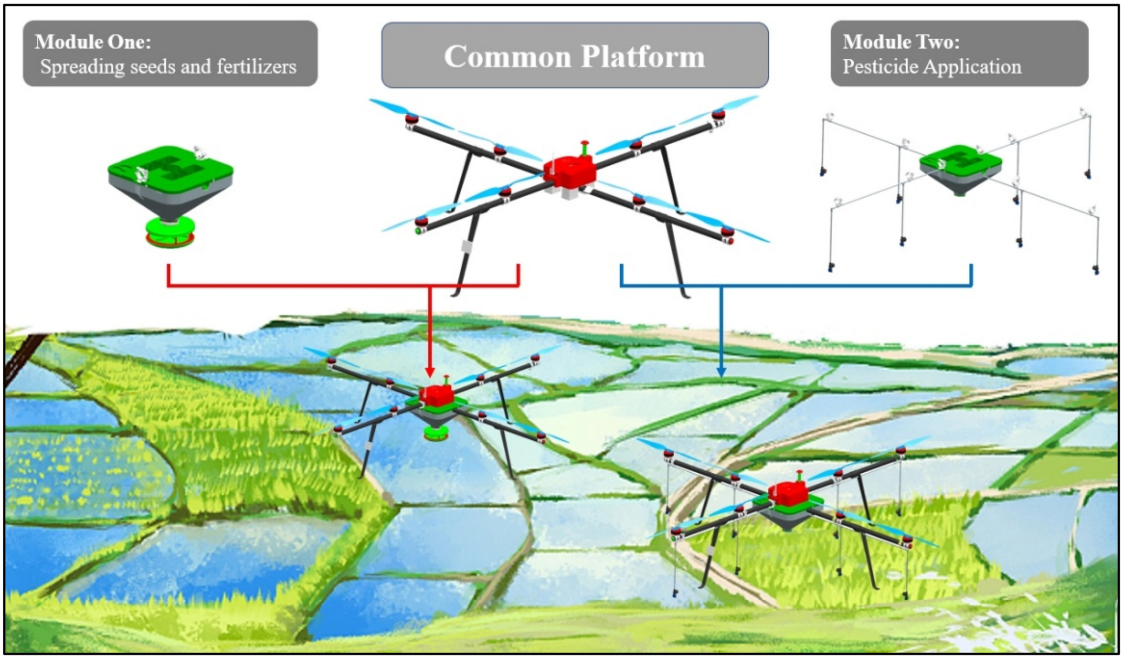

FIGURE 1
mUAV total design solution.

could increase the utilization rate of machinery and reduce the idle rate of agricultural machinery. It could also reduce the acquisition cost of agricultural machinery and protect farmers' income. (2) The appropriate range of operational parameters was selected for the different functional modular devices. Two approaches were used to evaluate the operational patterns separately. Numerical simulation analysis was prioritized, which focused on the downwash airflow motion regulation. Afterwards, field tests were combined for verification, which clarified the particle distribution at the target under the action of downwash airflow. It was hoped that the content of these studies would provide some guidance for practical use by farmers. (3) Comparative field trials were conducted in the mUAV, mechanical seeding, and mechanical transplanting the latter two, of which were the mainstream mechanized operations in society. Each of the three types of equipment was applied to the whole process of rice cultivation to summarize and analyze the impact of labor cost, as well as rice yield in the whole process of rice cultivation. It was hoped that the comparison test would provide a reference basis for farmers to recognize and understand the advantages and weaknesses of the mUAV when they chose the mUAV for their operations.

Materials and methods

Multi-rotor unmanned aerial vehicle platform and multifunctional component design

In this research, based on the current UAV models, an eight-rotor UAV with 20 kg loading capacity was designed based on "Yuren" automatic flight control system. Multifunctional component system was designed based on this UAV platform. Its core working components were mainly divided into three parts: flight control platform, spreading system, and spraying system. The spreading system and the spraying system were connected with the rotary arm through the quick release buckle to realize the agricultural various agricultural operation requirements of sowing, spreading fertilizer, and spraying. A three-dimensional model of the whole structure was constructed using Unigraphics NX (Siemens PLM Software), as shown in Figure 2. The basic parameters were listed in Table 1.

TABLE 1 Basic parameters of the multifunctional UAV.

Parameters	Values
Dimensions/mm^3	3,740 × 3,740 × 800
Fight velocity/ms^{-1}	0–7
Fight altitude/m	0.5–5
Number of nozzles	8
Number of rotors	8
Spaying width/m	8–10
Spreading fertilizer width/m	9–12
Seeding width/m	5–7
Maximum load/kg	20
Battery capacity/mA·h	5,500

Operational parameters optimization

Multifunctional unmanned aerial vehicle wind field computational fluid dynamics simulation by using ANSYS

The wind field below the UAV rotor was mainly composed of the UAV rotor wind field and the external environment wind

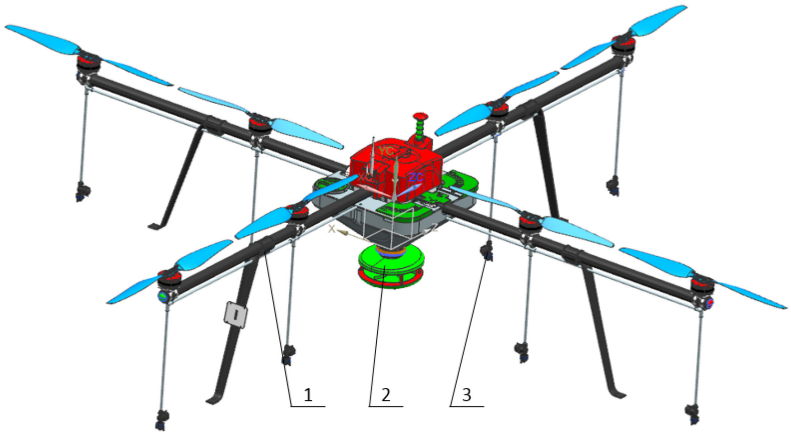

FIGURE 2
3D overall design of mUAV. 1 represents the public flight control platform, 2 represents the device for spreading seed or fertilizer, and 3 represents the entire system used for pesticide application.

field, which was the main factor affecting the particle trajectory. During the stable flight of the UAV, a strong rotor wind field would be generated, which had a certain coercive effect on the particle movement. Therefore, the computational fluid dynamics (CFD) method was used to explore the influence of the mUAV rotor wind field on the particle movement. Through the research on the distribution characteristics and development regularity of the mUAV rotor wind field, the influence of the mUAV rotor wind field on the particle movement can be more accurately explored and understood.

An accurate 3D model of mUAV played a key factor in CFD simulation, but the complex structure led to difficulties in modeling and boundary conditions. As shown in Figure 2, the mUAV is a full-size structure, which was not necessary because the shape of the mUAV was a complex-curved surface. Therefore, simplifying the structure was very necessary for CFD simulation. The simplified result was shown in Figure 3.

In the 3D coordinates, the forward motion in X direction was the front of the MUVA flight, the forward motion in Y direction was the right offset, and the forward motion in Z direction was the descent direction.

The mUAV was located at the center of the coordinate system ($X = 0$, $Y = 0$, $Z = 0$) and the distances between the mUAV and the ground were 1–6 m. The entire computational domain was a cylinder with a radius of 8 m, as shown in Figure 4A. The rotation direction of the mUAV blades was shown in Figure 4B.

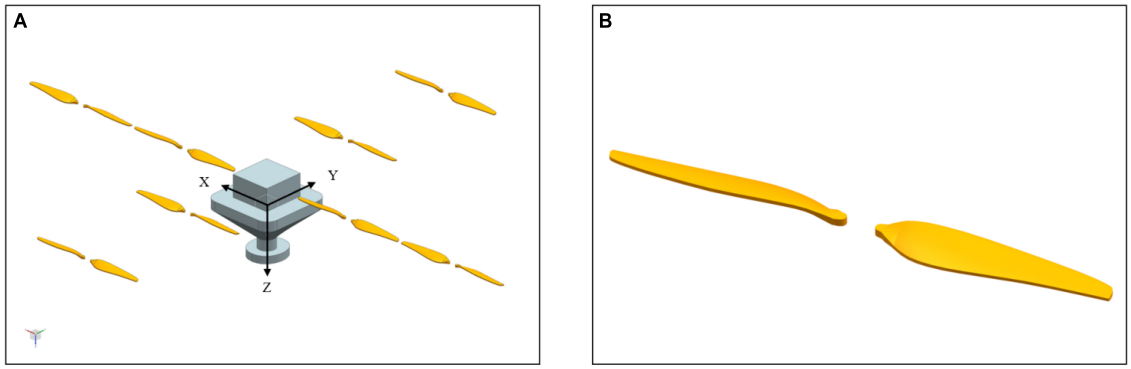

FIGURE 3
The simplified structure for numerical simulation processes. **(A)** Represents the simplified rotor and other structures, while **(B)** represents the specific structure of each propeller after simplification.

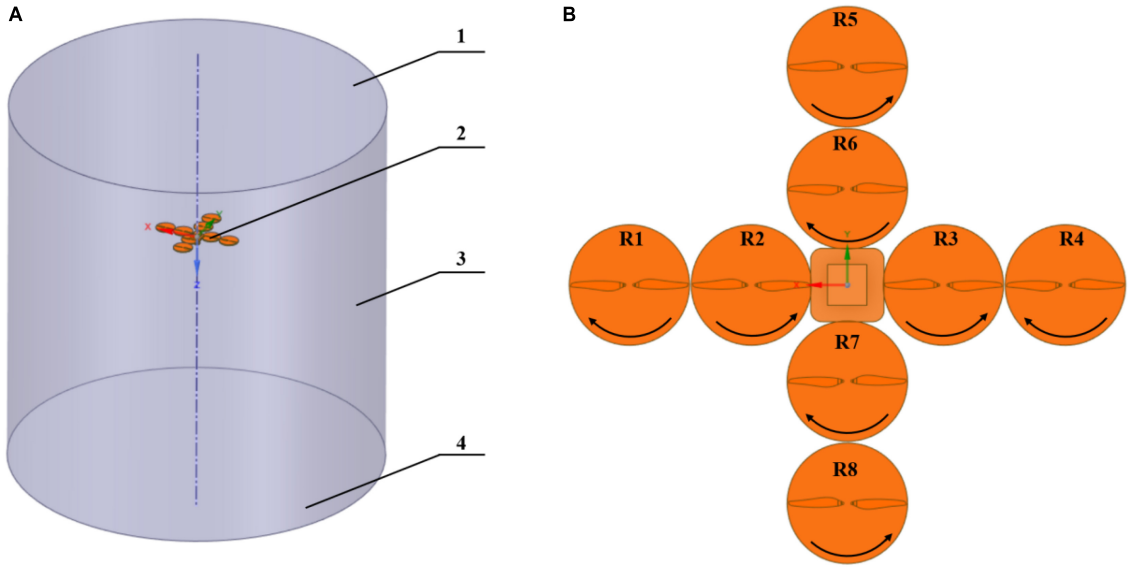

FIGURE 4
Computational domain settings in numerical simulation. **(A)** Stands for the name of the boundary condition, where 1 represents the top surface of the computational domain, 2 represents the location of the mUAV, 3 represents the space wall, and 4 represents the ground. **(B)** Stands the top view of the rotor in the computational domain, where R1–R8 represents each rotor, respectively, and the corresponding black portion of arrows represent the direction of rotation of that rotor in the computational domain.

The eight rotors of the mUAV were the rotational domain and the cylindrical air was the stationary domain. The interface meshes were established for accurate calculation between rotors domain and air domain.

The SpaceClaim software (Release 2021 R1, Ansys, Inc., PA, United States) was used to develop the CFD models of simplified mUAV model, Mesh in Workbench was used for meshing and as the solver. The unstructured tetrahedral mesh was applied, and the size of the grids was defined. The mesh size of the rotational domain was defined as 10 mm, the mesh of the stationary domain was defined as 400 mm, and the mesh quality was improved by defining the dimensions of faces and lines separately. Also, it had turn on features, such as Capture Curvature and Proximity to improve mesh quality. Transient SST k-ε model was employed (Wang et al., 2001; Omar et al., 2016), the computation lasted 1,000 steps with a time step of 0.005 s. The workstation was used to calculate the results of the rotational speed of the rotating domain at 2,500 r/min.

Experimental parameters

Seeds and fertilizers were evenly distributed in the soil, which was beneficial to seed emergence and balanced fertilizer nutrition. Therefore, refer to the test regulations of the technical specifications in EN13739-1 (2011) Agricultural machinery – Solid fertilizer broadcasters and full width distributors – Environmental protection and NY/T1003 (2006) Technical specifications of quality evaluation for fertilizing machinery, the distribution of particles in the field was an important test parameter. To reduce the particle bouncing and other factors affecting the collection efficiency, particle size uniformity detector (AAMS-SALVARANI BVBA, Germany) was used as a dedicated tester to collect particles. During the test, Pocketwind IV Anemometer (Lechler GmbH·Agricultural Nozzles and Accessories, Germany) was used as a device for recording wind speed and temperature of the environment. If the wind speed exceeded 4 m/s and the temperature exceeded 30°C, it would be regarded as invalid data. In the experiment, about 667 m^2 of open space was selected as the UAV operation area, and the center of the area was used as the collection location of the detector. When the UAV was operating, the detector area would be fully covered to ensure accurate data. The speed of the UAV was set between 2 and 2.5 m/s and keep the flight height at 1.5, 2, and 2.5 m, respectively. After the UAV landed safely, the particles in each detector were recorded.

For the sowing test (Figure 5A), to simulate the real working environment, the fields, which were soaked in water, were selected. The detectors were fixed in the test field with an interval of 2 m and perpendicular to the UAV course. The detector was divided into 6 × 6 partitions, with an outer size of 500 mm × 500 mm, which can easily count the number of seeds in each small partitions. There was some variation in the location of fertilizer test site (Figure 5B), which was selected on a dryland. In addition to using a collector, Φ200 mm × 500 mm size circular collectors were used to collect fertilizer particles in a 3 × 6 array at 1,500 mm × 1,200 mm intervals.

The plant protection application experiment was conducted at the jointing-booting stage of paddy. The fixed rods were inserted into the paddy field, which were arranged in a 3 × 9 matrix with a cortege spacing of 3,000 mm × 1,000 mm (Figure 6A). One end of the double-head clamp was fixed on the fixed rod, and the other end clamped the droplet collector (Polyethylene Card, PVC), as shown in Figure 6B. The two droplet collectors were located at the top and middle ends of the same fixed rod. It was placed horizontally, which accounted for 100 and 50% of the length of the rice, respectively. The Allura red solution with a concentration of 10 g/L was prepared as a droplet deposition tracer, which was put into the UAV tank before flight. The UAV was operated with the parameters shown in Table 2. The Wind Master model (Gill Instruments Ltd., United Kingdom) was used on site to

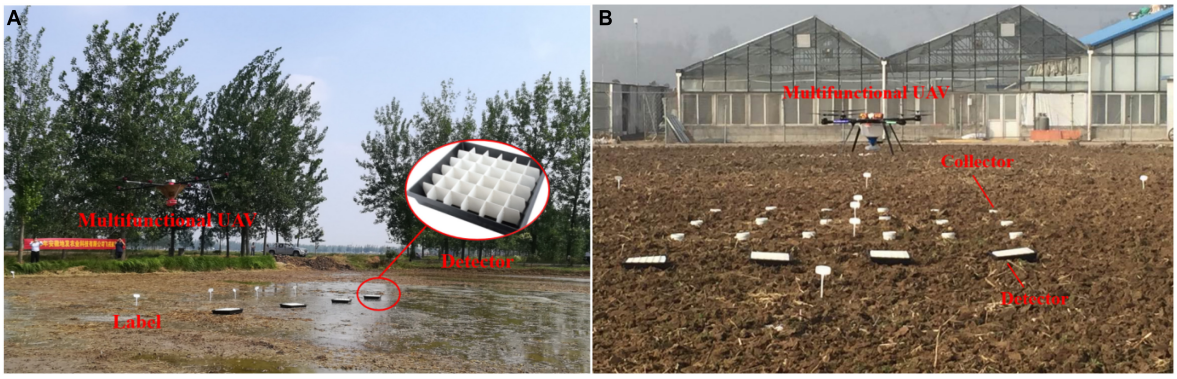

FIGURE 5
Test site for rice seeding and fertilization. **(A)** Represents the rice seeding test site, where detector is to collect the rice seeds that fall on the ground; Label is to identify the location. **(B)** Represents the fertilizer spreading test site, where detector is used to collect ground fertilizer particles, and collector is used as another way to collect ground fertilizer particles.

FIGURE 6
Rice pesticide application test site. **(A)** Represents the field sampling site of rice field, where the sampling points are arranged on the fixed rod. **(B)** Represents a partial schematic of each fixed rod, where the double-head clamp connects the fixed rod to the droplet collector.

TABLE 2 Spray test and environmental parameters.

Test number	Flight height (m)	Flight speed ($m \cdot s^{-1}$)	Wind speed ($m \cdot s^{-1}$)	Temperature (°C)
1	1.0	6.0	2.7	34.6
2	2.0	6.0	2.5	32.5
3	3.0	6.0	2.2	31.2
4	3.0	4.0	2.6	30.4
5	3.0	5.0	2.7	32.7
6	4.0	6.0	1.7	30.5

monitor the environmental parameters. After the UV landed, the sampling bottle collected 50 ml of liquid in the tank. After the droplet collectors were naturally dried, each droplet collector was individually packaged in a plastic sealing bag and stored in darkness.

Refer to ISO22866 (2005) and ISO24253-1 (2015) standards. Deionized water (50 ml) was added to the plastic sealing bag of polyethylene film, then the plastic sealing bag was placed in a shaker at 500 r/min for 10 min. The eluate was measured with a 722 spectrophotometer. The droplet deposition refers to the mass of the droplet per unit area, which was calculated using the following Eq. 1 (Qin et al., 2014; Wang et al., 2020):

$$\beta_{dep} = \frac{(\rho_{smpl} - \rho_{blk}) \times F_{eal} \times V_{dii}}{\rho_{spray} \times A_{col}} \quad (1)$$

β_{dep}: Droplet deposition $[\frac{\mu g}{cm^2}]$; ρ_{smpl}: Sample Collection Values; ρ_{blk}: Blank Control Values; F_{eal}: Calibration Factor (per fluorimeter scale unit) $[\frac{\mu g}{L}]$; V_{dii}: Volume of dilution liquid used to solute tracer from collector [L]; ρ_{spray}: Tracer concentration in spray liquid $[\frac{\mu g}{L}]$; A_{col} : the area of the collector for catching the spray deposition$[cm^2]$.

The uniformity of the particles or spray deposition on the sampling places are reported as the coefficient of variation (CV) of the measured deposition values, and a lower CV value indicates a better uniformity of deposition distribution. Equation 2 describes the calculation of the CV (%) using the ISO standard 24253-1.

$$CV = \frac{\sqrt{\sum_{i=1}^{n} \frac{\left(X_i - \bar{X}\right)^2}{(n-1)}}}{\bar{X}} \times 100\% \quad (2)$$

X_i : Samples from each collection point; $\bar{X}$: Corresponding to the average value of the collected samples; n: Number of samples collected.

All statistical analyses were performed using IBM SPSS Statistics for Windows (IBM Corp., Armonk, NY, United States). Two-way analysis of variance (ANOVA) was adopted to explore the effects of broadcast and spray on distribution uniformity on the field. In all trials, the mean values of distribution uniformity at different parameters, together with those of percentage, were compared using one-way ANOVA via the Duncan test ($\alpha = 0.05$).

Application experiment of rice cycle cultivation management

To better understand the performance of mUAV operated in an outdoor environment, comprehensive comparison experiments were conducted at different growth stages of rice using different agricultural machinery.

There were three main modes of local rice cultivation: The first one was rice direct seeder cultivation, which was an important way to fully mechanize rice cultivation. The second one was mechanized rice transplanter, which is also an important mode and guarantees and supports mechanization planting. The third was artificial transplanting, which is a traditional rice transfer method that had been gradually replaced by mechanical transplanting. Therefore, the comprehensive comparative experiment was set up with three cultivation patterns: the first experimental field was the multifunctional UAV directly sowing, fertilizing, and applying pesticide. The second experimental field was sown with a rice direct seeder, and fertilizer and pesticide were applied using other ground machinery. The third experimental field was sown with a rice transplanter, while other ground machinery was used to apply fertilizer and pesticides. The area of each experiment area was 2.2 hm^2, which were marked as T1, T2, and T3 respectively.

Full mechanization referred to the mechanization of efficient production technologies in rice production, such as tillage, planting, plant protection, fertilization, harvesting, drying, and straw treatment. According to the agricultural characteristics and experimental requirements of rice cultivation, there were five main segments: tillage, seeding, planting, fertilization, and harvesting. This experiment was conducted to compare the feasibility of UAV application in the whole process of rice and a comprehensive comparison with two mechanical planting methods. The test site was in Zhuangqiao Village, Wanfu Town, Huaiyuan County, Bengbu City, Anhui Province in 2020, and the trial included evaluation of labor costs, rice yield and profit, cost analysis of transplanting, etc. To match the actual production conditions, the agricultural materials and equipment used during the experiments process were provided by local cooperatives.

Agronomic process of different cultivation modes of rice

Ploughing stage

All experimental fields were cultivated with a 1804D model tractor (YTO GROUP CORPORATION, China) and a 1GS-3300 model rotary tiller (YTO GROUP CORPORATION, China) with a width of 3,000 mm for the purpose of breaking the soil stubble. At the same time, 40 kg/667 m^2 base fertilizer was applied, and the soil and fertilizer were mixed using rotary tillage. In the field, a ditch with a depth and width of 300 mm × 300 mm was dug at an interval of 4,000 mm for water retention and to prevent waterlogging. The herbicide was sprayed by a 3WPZ-1500B self-propelled boom sprayer (Qingzhou Aike Machinery Technology Co., Ltd., Qingzhou, China). The difference was that T1 and T3 irrigations were kept for 7 days, and the water was drained, while T2 did not require further treatment. As shown in **Figure 7**.

Sowing stage

In the T1 experimental area, the seeds were soaked 24 h in advance and germinated to a length of 1.5–2 mm (Tao et al., 2011), and the seeds were sown into soil at 5 kg/667 m^2 using a UAV broadcast. In the T2 experimental area, the seeds were only soaked about 12 h until just about to germinate, and the seeds sown into soil at 6 kg/667 m^2 using a rice direct seeder (Huaiyuan County Sanliu Agricultural Machinery Co., Ltd., Huaiyuan, China). In the T3 experimental area, the seeds were cultivated 20 days in advance, which was the seedling raising period, and then the seedlings were collected and transported, then 4–7 seedlings per hole were inserted into the experimental field with a row spacing of 140 mm × 300 mm using a NSD8 model mechanical rice transplanter (Kubota Agricultural Machinery (Suzhou) Co., Ltd., Suzhou, China). According to the agronomic characteristics, T1 and T2 were selected as suitable for direct seeding with the same seed variety, and T3 was selected as another variety suitable for transplanting.

Top dressing stage

Topdressing was mainly in the tillering and booting period, and the amount of fertilization was 15 kg/667 m^2 each time, for a total of two times. The main difference between the three experimental areas were the use of different equipment. In the T1 area, the feeding port suitable for the caliber was installed to the UAV broadcast, and then the top-dressing operation was carried out. In the T2 and T3 experimental areas, to reduce the

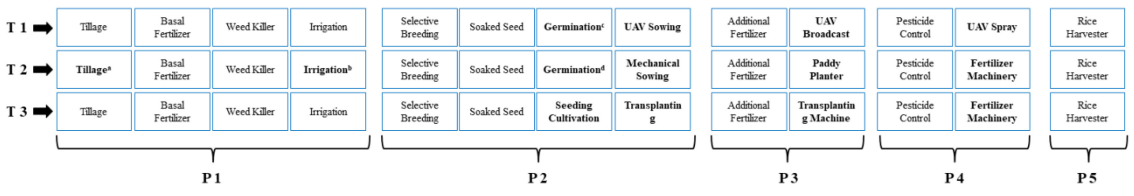

FIGURE 7
Agricultural process of rice cultivation in different experimental areas. [a] Compared to T1 and T3, the workload in the T2 region is reduced by about half, [b] compared to T1 and T3, the T2 area is only about 60% irrigated, keeping the soil from drying out, but not having standing water, [c] the seeds germinated to 2 mm, which took about 20 h, [d] the seeds were just ready to germinate, but did not grow, taking about 8 h. T1 represents mUAV experiment area, T2 represents mechanical rice direct seeder area, T3 represents mechanical rice transplanter area. P1 represents soil preparation stage, P2 represents seeding stage, P3 represents fertilization stage, P4 represents pesticide application, and P5 represents harvester stage.

cost of agricultural equipment, the sports chassis of the 3WPZ-1500B self-propelled machine, and the separately purchased fertilizer spreader were used to work together.

Pesticide application stage

In the actual management of diseases and pests, pest prevention is the main method of pest and disease control. Therefore, according to the needs of agricultural control and the occurrence of pests and diseases, pesticides were generally sprayed before the occurrence of pests and diseases. The pesticides were mainly insecticides and fungicides, which were sprayed 3–4 times during the rice cultivation process. The main differences between the three experimental fields were the agricultural equipment and the amount of pesticide applied. In the T1 experimental area, the application system was installed on the UAV platform, and the pesticides were mixed and diluted with an application rate of 1.5−2 L/667 m^2. The 3WPZ-1500B self-propelled boom sprayer was used in the T2 and T3 experimental areas to spray with the application rate of 15−20 L/667 m^2.

Harvest stage

The rice yield was evaluated, reference to the National Grain High Yield Creation Yield Measurement, Acceptance Method, and the DB32/T 1093-2015 Standard. Five units were selected in the diagonal direction of each experimental area, each unit of 20 × 667 m^2 was used as a production measurement unit. Five sampling points were randomly selected in each production measurement unit. For the experimental field with obvious row spacing and plant spacing, representative rice panicles within a certain range were selected from each sampling point, and the number of panicles per 667 m^2 was calculated. Representative mature rice ears with ten holes per unit were selected to measure the plant height and root length of rice. After natural air-drying, the number of grains per ear, seed setting rate, and thousand-grain weight were determined, and the theoretical yield per 667 m^2 was calculated. For the experimental field where the row spacing and plant spacing cannot be clearly distinguished, a square frame of 1,000 mm × 1,000 mm was made with hard iron wire, and the number of ears and yield per 667 m^2 were calculated. Finally, the 4LZ-200 rice combine harvester (Luoyang Zhongshou Machinery Equipment Co., Ltd., Luoyang, China) was used to harvest rice.

Results

Characteristics of downwash airflow at different heights

As shown in **Figure 8**, the velocity of the downwash flow field was varied along the *Z*-axis in the range of 1–6 m from the ground for the UAV.

Higher wind speeds were generated at the wingtips of the rotor blades, and two distinct areas of acceleration appeared below each rotor blade. An upward (*Z*-axis negative direction) airflow appeared in the center of the mUAV broadcast. The vertically downward scrubbing airflow created a negative pressure that caused the surrounding air to converge on the downward scrubbing airflow. The vertically downward airflow touched the ground, causing the airflow to flow sideways, and this airflow met the airflow that was brought to the center, forming a vortex.

At the same time, various combinations of altitudes can be seen. As the flight height of the mUAV increased, the velocity change tended to level off at the position near the ground, the airflow gradually increased along the radius direction, and the vortex gradually moved away from the center.

In all the interfaces shown in **Figure 8**, a straight line was set at 0.5 m intervals along the *Z*-axis direction. This straight line indicated that the velocity changed at different distances in the *Y*-axis (**Figure 9**).

Four small peaks and one trough were observed at 0.5 m (**Figure 9A**) and 1 m (**Figure 9B**) below the UAV at all test heights. The wind speed at this point was unstable and there was an effect of wind speed in the opposite direction (*Z*-axis negative direction). Since the mUAV was so low to the ground, the strong airflow hit the ground and bounced off the ground, which referred as the ground effect.

An upward (*Z*-axis negative direction) velocity was observed in the range of 0.5–1.5 below the mUAV at flight heights of 1 and 2 m. Until the flight altitude of 3 m (**Figure 9C**), the velocity direction was still downward (positive *Z*-axis direction) despite the sharp change in the center of the mUAV. Moreover, above 1.5 m from the bottom of the mUAV, the velocity change tended to smooth out.

In addition, the flow field below the mUAV became more stable with the increasing flight altitude, and the same trend was observed at flight altitudes of 4–6 m (**Figures 9D–F**).

According to the above simulation results, it was suggested that the mUAV should operate at a height of 2 m or more.

Variation of spread distribution with height

When the mUAV was used for seeding tests, the flight altitude had an (positive or negative) effect on the uniformity of spreading, which was 24.36, 22.83, and 13.05% in the horizontal direction for the three altitudes tested. As shown in **Figure 10A**, the fluctuations were relatively large at the position of test point (1,4) and less in the middle (2,3).

When the mUAV performed fertilizer spreading was tested, there was the same trend at different heights, and the weight of particles collected by the detector that showed more in the middle and less on both sides. The variability was greater on

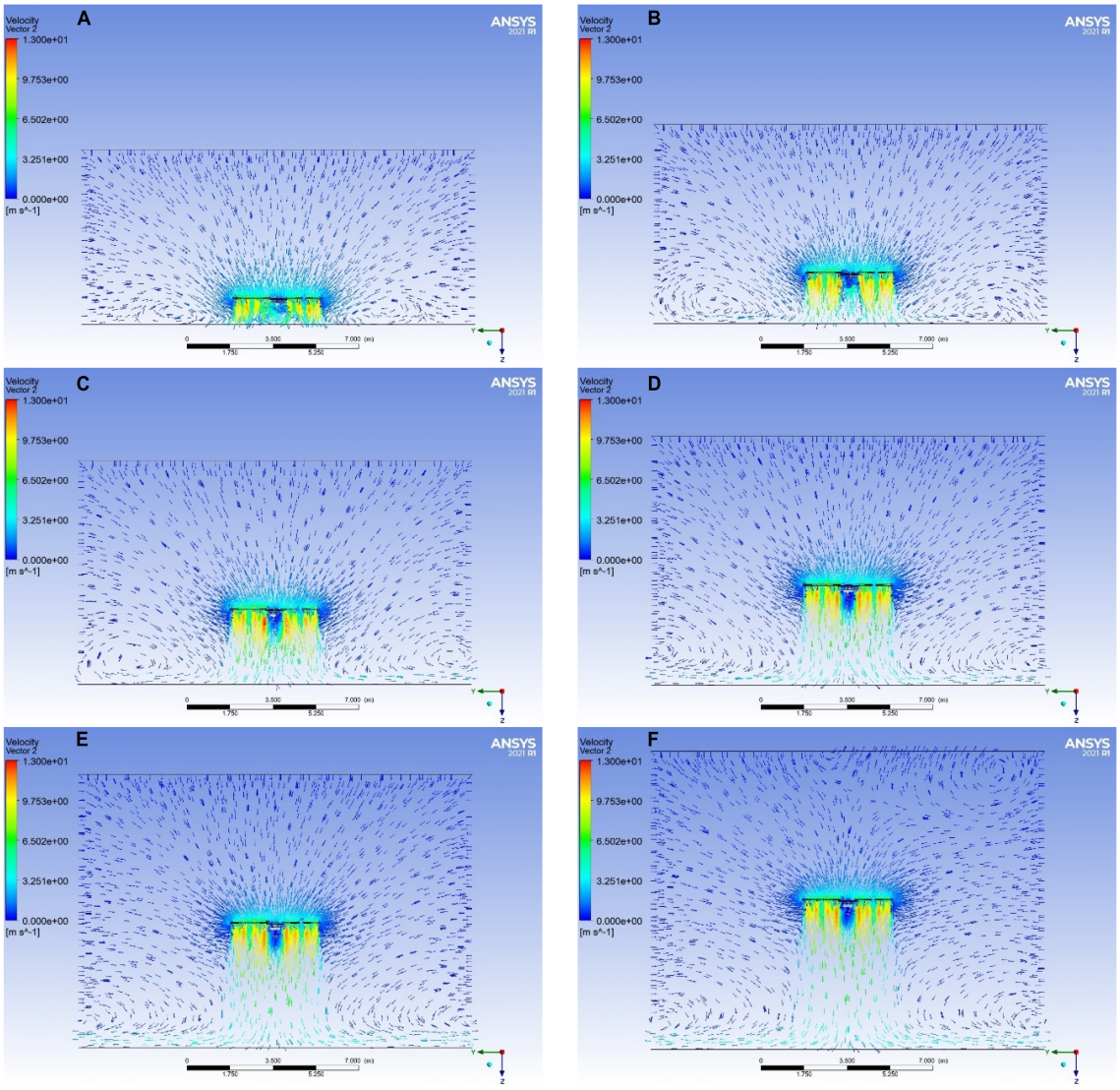

FIGURE 8
Flow field velocity vector illustration of the mUAV flying at different altitudes. **(A–F)** Indicate that the mUAV is flying at 1, 2, 3, 4, 5, and 6 m above the ground, respectively.

the right side than on the left side, as shown in Figure 10B. In the circular detector (Figure 10C), the left collector had a large particle dispersion and good uniformity of dispersal to the off-right of the mUAV route. The CV in the horizontal direction fluctuated from 11.98 to 23.68% over the range of test heights.

According to the simulation results (Figure 9), the mUAV tended to have a smoother downwash airflow with an increasing height, which was more conducive to the uniform distribution of particles. However, the actual motion of the particles in the air varied greatly under the influence of the ambient wind field forces. The higher the flight height, the longer the fall time in the air and the more uncontrolled the trajectory of the particles, which led to greater uncertainty in the particle fall point. As shown above, 2.5 m would not be the most suitable height, but it could meet the requirements of agronomic spreading and minimize the influence of ambient wind field forces.

Variation of spray distribution with height and velocity

As shown in Figure 11A, the deposition of droplets in the upper and middle of rice was affected by the flight height of the mUAV. The low flight (H = 1 m) can significantly increase the deposition of the upper and middle, and the deposition in the upper and middle layers was 0.0849 and 0.0446 μL cm^{-2}. From H = 2 m to H = 3 m, there was no significant difference in the deposition between the upper

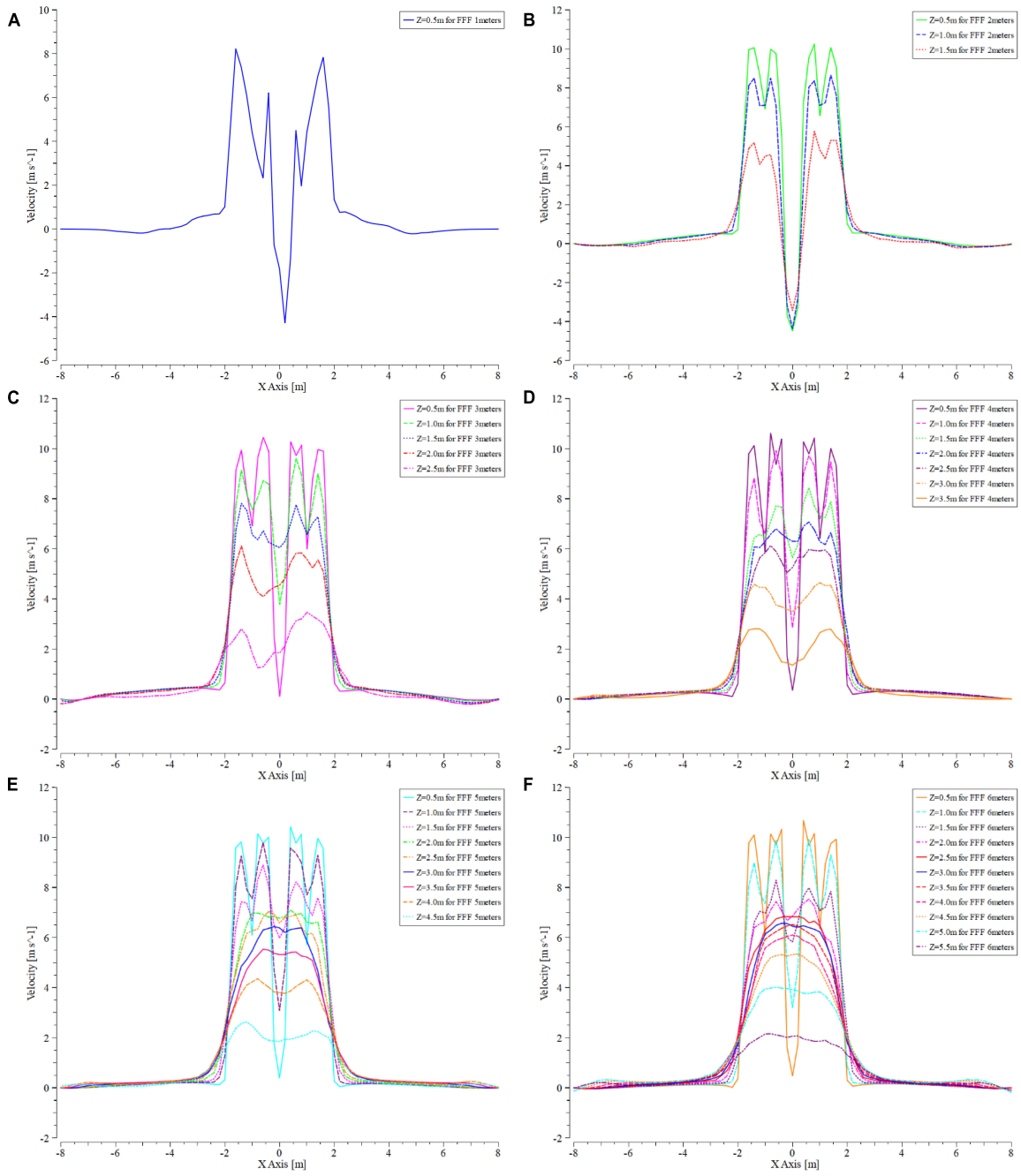

FIGURE 9
Variation curve of velocity at different altitudes during simulation. **(A–F)** Indicate that the mUAV is flying at 1, 2, 3, 4, 5, and 6 m above the ground, respectively. The "Z" in each figure indicates the distance from below the mUAV, "for FFF meters" indicates the altitude at which the mUAV is flying. The curves in each graph indicate the wind speed of the mUAV at distance "Z," where positive values indicate a vertical downward wash and negative values indicate a vertical upward wash.

and middle of rice, but the deposition at H = 3 m was higher than that at H = 2 m and H = 4 m. In the range of UAV flight speed of 4–6 m s^{-1} (Figure 11B), low flight speed could significantly increase the deposition of droplets in the upper layer, but it had no significant effect on the deposition of the middle.

When the mUAV was flying at an altitude of 1–6 m above the ground, Figure 12 showed the wind speed profiles for different flight heights of 0.5 m above the ground. The intensity of the downwash airflow was highest and unstable when the mUAV was flying at 1-m height, which resulted in a high air mass flow rate and an increase in the number of particles per unit

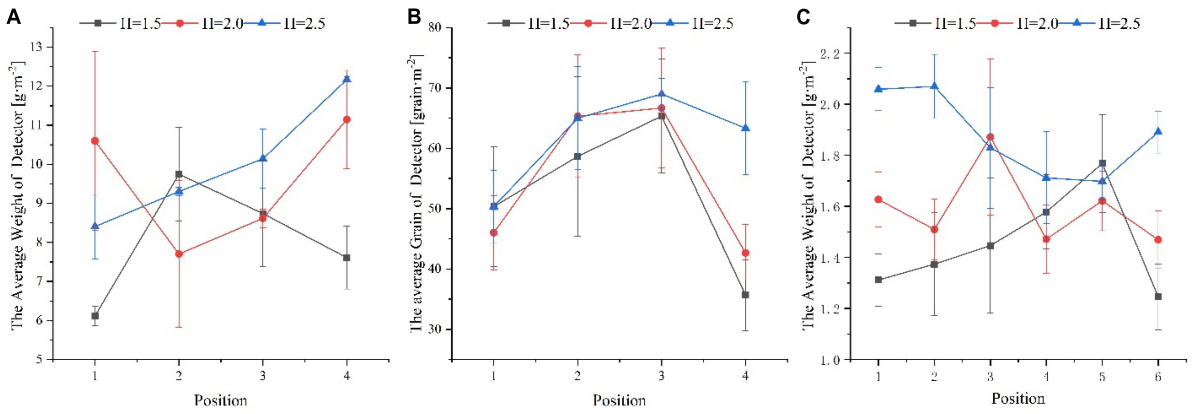

FIGURE 10
The uniformity of spreading in the horizontal direction at different heights. **(A)** Represents uniformity of horizontal distribution of sown seeds. **(B)** Represents uniformity of horizontal distribution of fertilizer in square collectors. **(C)** Represents uniformity of horizontal distribution of fertilizer in circular collectors. In all figures, the horizontal coordinates indicate the collector number, and the vertical coordinates indicate the distribution, where "h" indicates the flight height of the mUAV from the ground.

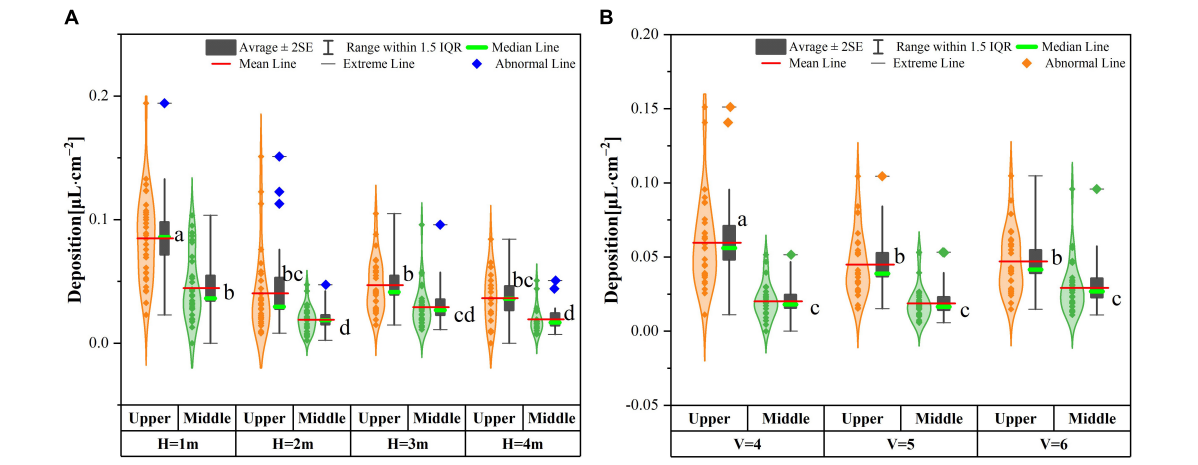

FIGURE 11
Distribution characteristics of droplet deposition in the rice canopy. **(A)** Represents deposition distribution affected by flight heights, **(B)** Represents deposition distribution at affected by flight speeds. Where "H" represents the mUAV flight height, "V" represents the mUAV flight speed, "Upper" represents the upper rice layer, and "Middle" represents the middle rice layer. a, b, c, and d indicate a significant difference at $P < 0.05$.

time of droplet movement, which eventually manifested itself as an increase in deposition. One possibility inferred from this was that the downwash airflow velocity of the mUAV above the canopy should be less than 5 m/s to evenly distribute the deposition above and below the canopy.

Under the same speed conditions, the droplet deposition in the upper and middle layers tended to decrease with the increase of flight height, which may be affected because of droplet drift caused by the increase of height. Under the condition of the same flight height, the deposition of the upper and middle also decreased with the increase of the speed. This was caused by the low flight speed, which led to the increase of the spraying flow droplet deposition. According to the CV values of the droplet's deposition and distribution in the rice canopy, the 3-m flying height with a speed of 5 ms^{-1} were selected/recommended during the spraying operation.

Yield of different cultivation patterns

After analysis of the yield components, it was found that the panicles distribution density, spikelet per panicle, as well as thousand grain weight, were all significantly affected by the methods of cultivation (Table 3). Meanwhile, the performance of T1 with T2 in the number of panicles per square was similar, while T3 had the lowest value ($P < 0.05$) among these methods.

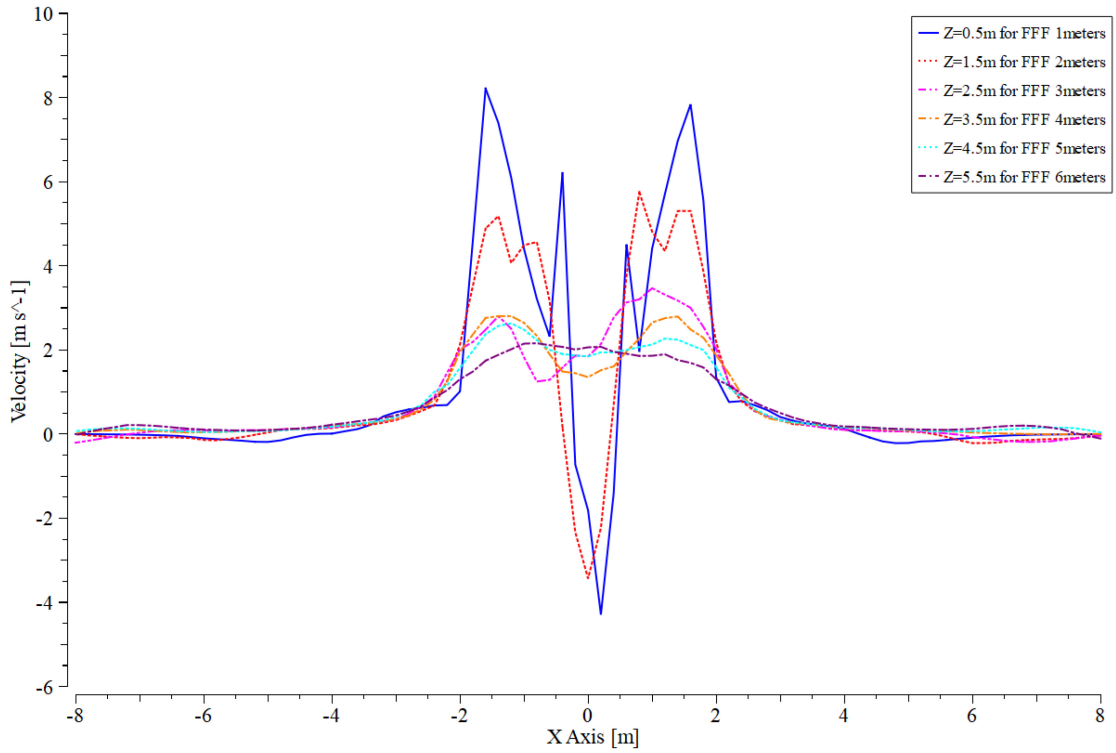

FIGURE 12
Velocity variation curve at 0.5 m from the ground at different flight heights. Where "*Z* = 0.5 m for 1 m," "*Z* = 1.5 m for 2 m," "*Z* = 2.5 m for 3 m," "*Z* = 3.5 m for 4 m," "*Z* = 4.5 m for 5 m," "*Z* = 5.5 m for 6 m," the size of the downwash airflow at 0.5 m from the ground when the UAV is flying at 1, 2, 3, 4, 5, and 6 m, respectively.

T1 and T2 were 19.7 and 9.5% higher than T3, respectively. The cultivation methods did not have an obvious difference of the number of spikelets per panicle. T2 increased the value ($P < 0.05$) by 24.6% compared with T3. The thousand grain weight were similar between T1 and T2, approximately 14.6% less in T1 compared with T3 area. However, there were no significant differences in seed-setting rate and predicted yield among the three experimental areas.

Comparison of benefits of different cultivation methods

The experimental site in this study was professionally managed by a cooperative production, and the statistics were based on workers employed and agricultural equipment purchased by the company.

As shown in the Table 4, the T1 area (mUAV broadcast) had significant advantages in the seeding session. Its operational efficiency was 2.2 times and 4 times higher than T2 and T3, respectively. The effect of pesticide spraying in T1 area was also higher than T2 and T3 area by 33%. However, the fertilizer application efficiency in T1 was five times lower than T2 and T3.

According to the management company salary standard, the driver should be paid RMB 200 per day, and the support staff should be paid RMB 150 per day. All agronomic segments required one driver and several support staff. The number of employees used for planting was the regular operation configuration. The seeding segment in T1 area had one less support staff than T2 and T3 areas, and the fertilizer stage had two less support staff than T2 and T3 areas.

As shown in Figure 7 in the process of P1 to P5, rice harvesting cost (P5) was the same and the difference in labor cost was mainly in P1 to P4. The labor cost was calculated based on the number of employees, the number of operations, and the work efficiency (Table 5).

In soil preparation stage, it was mainly because T2 did not require 100% irrigation, but only about 60% of the irrigation. As a result, T2 area has a 32.6% reduction in labor costs compared to T1 and T3 areas. T2 and T3 had high loads of ground equipment, which consequently led to 16.5% higher labor cost for fertilizer application in T1 than T2 and T3. Pesticide spraying by mUAV (T1) had the advantage of reducing labor costs by 25% in T1 area compared to the other two areas. The UAV had an advantage over the rice direct seeder, but the advantage was not significant with higher only 8.7%. Compared to transplanting, the mUAV significantly reduced labor costs by 34.1%.

TABLE 3 Effect of different cultivation methods on grain yield and its components of rice.

Test area	No. of panicle per square (No/m^2)	No. of spikelet per panicle	Seed-setting rate (%)	Thousand grain weight (g)	Yield (kg/667 m^2)
T1	374.83a	121.93ab	94.52a	22.57b	577.41a
T2	342.83ab	140.37a	94.80a	23.50b	600.99a
T3	313.17b	112.67b	95.57a	26.42a	554.43a

a, b indicates a significant difference at $P < 0.05$.

TABLE 4 Efficiency and number of employees of sowing, fertilizing, and application operations in different experimental areas.

Test area	Agronomic sessions	Work efficiency (667 m^2/day)	Labor cost (RMB/day)	Number of employees/day	Number of operations*
T1	Sowing	200	350	2	1
	Fertilization	160	350	2	2
	Spraying	400	350	2	3
T2	Sowing	90	500	3	1
	Fertilization	800	1,500	4	2
	Spraying	300	350	2	3
T3	Sowing	50	500	3	1
	Fertilization	800	1,500	4	2
	Spraying	300	350	2	3

* Number of operations throughout the growth cycle of rice.

TABLE 5 Labor cost of soil preparation, sowing, fertilizing, and spraying in different experimental areas*.

Test area	Soil preparation cost**/ RMB	Sowing cost/RMB	Fertilization cost/ RMB	Spraying cost/ RMB	Total cost/ RMB
T1	766.67	175.00	437.50	262.50	1641.67
T2	516.67	555.56	375.00	350.00	1797.22
T3	766.67	1000.00	375.00	350.00	2491.67

*Based on 66.7 thousand m^2. **Including all labor costs for irrigation during the rice cultivation process.

Discussion

With the increasing application of UAVs in precision agriculture, the CFD was applied to the improve the downwash airflow of agricultural UAVs, from which the particle motion in the airflow was analyzed. For example, Yang et al. (2017, 2018a) simulated the velocity distribution of the downwash airflow field and the spatial distribution of droplets during the hovering condition of multi-rotor aircraft based on the Fluent k-ε turbulence model, which was verified by combining with indoor hovering experiments. From the wind field simulation results, it reflected the overall wind field spatial distribution pattern, and the simulated value of the average wind speed at the marker point was within 9% error with the experimental measurement results.

In this study, we simulated the wind field of the designed mUAV to provide a theoretical basis for the parameter setting of the field test. The different flow velocity of the downwash airflow from the center outward caused the effect of the flow field spreading outward from top to bottom. This resulted in an increase in spray width, and the spray width was proportional to the flight height (Yang et al., 2018b). The airflow along the outer rotor caused two peaks in a certain range. The effect became relatively poor (Zhang et al., 2016) when the multi-rotor UAV was operated at an altitude below 1 m. In addition, when the wind speed was smaller horizontally and larger (Chen et al., 2017a) vertically downward, the rotor's downwash airflow had better deposition uniformity. Particles in the air were mainly affected by wind field forces and gravity, etc. When out of the downwash airflow region, they were mainly affected by the environmental wind speed, which was non-constant, and this affected the final position of the particles. These factors led to uneven distribution of rice seeds, fertilizer particles, and pesticide droplets. There was a risk of drift loss of pesticide droplets (Zhang et al., 2015; Wen et al., 2018). Therefore, based on the premise of satisfactory distribution uniformity and mUAV flight safety, the following operational parameters were selected in this work for experiments with a width of

4 m and a flight height 2−6 m at regular flight speed and lower flight height.

The simulation parameters were given as a guide, the specific operating parameters needed to be derived from actual tests. Song et al. (2018a) designed an air-powered UAV rice spreading device that used airflow to blow seeds out in different directions. The results showed that the UAV's operating height in the range of 1−2.8 m had no significant effect on the spreading width and spreading uniformity. Considering the factors of spreading width and uniformity CV, as well as the field operating environment, the flight height of 2 m was considered to be the appropriate operation height of this UAV platform. Liu et al. (2020) studied the effect of quadrotor UAV spreading parameters on the seed distribution of *Astragalus membranaceus*. The results showed that the flight height was the most important factor affecting the uniformity of seed distribution. Meanwhile, the height of 1.5 m was recommended as the optimal operation height. Wang et al. (2016a,b) analyzed the distribution characteristics of droplets in different parts of space by comparing different UAVs, different flight modes, flight speeds, flight heights, and crosswinds using a spatial mass balance test. The results showed that the wind speed was fast and strong when the UAV flew at 2 m height. As the height increased, the airflow in the vertical direction weakened significantly. Although the increased flight altitude reduced the dispersion of droplet deposition rate and improved the uniformity of droplet distribution, there was a significant upward trend in the percentage of downwind drift. The above results showed that it was a double-edged sword that the method of adjustment of distribution uniformity by flight height. The airflow motion gradually decreased with increase of height, and there was a gradual diffusion change from vertical downward motion to horizontal motion (Shi, 2015). Simply increasing the flight height had an effect on the uniformity of distribution. However, as the flight height increased, the particles were weakened by the force of the downwash airflow, and it was susceptible to interference from ambient wind speed. Therefore, the operating parameters chosen in this study were flight height of about 2.5 m for broadcast application, and height of 3 m for pesticide application.

The application of UAVs in the whole process of rice cultivation or in individual segments can be seen to satisfy the requirements of modern paddy cultivation. Li et al. (2016) used a small multi-rotor UAV for rice broadcasting, the results showed that CV was far smaller than that of artificial broadcasting. The average yield of field broadcasted by UAV was 7,705.5 kg/hm^2, implying that rice air broadcasting by UAV was feasible. Zhu et al. (2021) conducted a comparative trial of five cultivation methods: mechanical transplanting, unmanned machine seeding, mechanical precision hole sowing, mechanical seedling throwing, and manual seeding. The results showed that the number of seedlings in descending order was manual seeding, UAV seeding, mechanical precision hole sowing, mechanical transplanting, and mechanical seedling throwing. The total effective number of spikes was higher in the treatments of unmanned seeding and mechanical transplanting. The theoretical yield of each treatment was in the order of mechanical precision hole sowing, mechanical seedling throwing, UAV seeding, mechanical transplanting, and manual seeding. The analysis of the labor cost in the seedling planting process showed that the mechanical precision hole sowing or UAV seeding method was worthy of promotion. Zheng et al. (2021) conducted a comparison test on four different seeding methods: mechanical powder seeding, precision hole direct seeding, UAV seeding, and manual seeding. The results showed that the highest number of seedlings and the highest effective spikes were achieved in the UAV seeding treatment, with the effective spikes reaching 3,811,500 spikes/hm^2. The actual yield of UAV seeding was 6,549 kg/hm^2, which was 1.2% lower than that of mechanical precision hole seeding. Moreover, the lowest labor cost was 40.5 Yuan/hm^2 for the UAV broadcast. The results of our work showed similar trends, with the number of seedlings per square in descending order of mUAV direct seeder, mechanical rice direct seeder, and mechanical rice transplanter. The theoretical yields were in the downhill order of mechanical direct seeder, mUAV direct seeder, and mechanical transplanter.

With the strict emission limits for environmental protection regulations and limits for exhaust pollutions from diesel engines of non-road mobile machinery (GB20891, 2014), the UAV used electrical energy as power, compared to traditional agricultural machinery burning diesel to obtain power, which reduced pollutant emissions. The results of Xu et al. (2012) showed that the average fuel consumption for the whole process of rice production in the southern double-season rice area was 95.08 L/hm^2, of which 36.65 and 37.88 L/hm^2 was for tillage and harvesting, respectively, 12.15 L/hm^2 for transplanting, and 8.4 L/hm^2 for mechanized plant protection. Data from the National Bureau of Statistics of China (NBS, 2021) showed that it was 4,734 hectares in the sown area of early-season rice in 2021. It was only 42.26% of mechanical rice cultivation rate of China in 2015. In this study, it provided a viable solution for rice cultivation in the application of mUAV in seeding, fertilizing, and applying pesticides, which contributed tremendously to the reduction of labor commitment and mechanization enhancement.

In addition, the cost of farm machinery was different in the three segments of seeding, fertilization, and spraying. The total input cost of farm machinery used in the mUAV seeding, mechanical seeding, and mechanical transplanting was about 110 thousand RMB, 215 thousand RMB, and 235 thousand RMB. However, the tractor used in the mechanical direct seeder and transplanter test area can also be used in the tillage stage. Therefore, it reduced the cost of farm machinery inputs in mUAV pilot area with certain extent, and it was increased rate of farm machinery utilization, but it would also increase the rate of depreciation.

At present, China's agricultural UAVs are mostly used in plant protection, UAV broadcast applications are still in the preliminary research and trial application stage. There are still many problems with UAV applications.

In the fertilization process, the mUAV had no advantage over ground fertilization machinery. Although the number of workers was reduced, the operating efficiency and labor costs were lower than those of ground machinery. This was mainly due to the weight limitation of mUAV, as traditional ground machinery can be loaded up to 800–1,000 kg. UAVs had great advantages over manual fertilization. The results of the study by Ren et al. (2021) showed that the efficiency of UAV fertilization was about 12.5 times higher than manual fertilization, and the cost of UAV fertilization was reduced to 18.45 RMB/hm^2. Liu et al. (2019) designed a spreading device for granular herbicides, and the results showed that the control effect was not significantly different from manual application, and the operational productivity reached 80–120 667 m^2/h, which was 15–25 times higher. Diao et al. (2020) compared it to mechanical precision hole seeding and UAV direct seeding trials. The results showed that the yield of both was comparable. Although the UAV was slightly lower than the mechanical precision hole seeding, the operational cost was reduced by about 50% and the operational efficiency was increased by more than 5 times. There are limitations in the UAV fertilizer application process, the same problems existed with ground machinery in the middle and late stages of rice growth and in complex hilly areas (Xie et al., 2013), such as poor adaptability, high operational intensity, and severe crushing of rice (Chen et al., 2012; Qi et al., 2016; Shi et al., 2018; Song et al., 2018b). Therefore, there is still a great market demand for mUAV fertilizer application.

In the soil preparation process, there were two main ways of mechanized rice direct seeding, water direct seeding, and dry direct seeding. Water direct seeding was primarily applied in the south, rice seeds was germinated working in a leveled soil without waterlogging. Dry direct seeding was mostly applied in the north, which can be directly in the sowing of seeds without germination, but it has higher requirements for the plot (Luo et al., 2019). At this stage, the mUAV pilot area had advantages over the water broadcast pilot area, with lower labor costs. However, mUAV had no advantage compared to dry broadcast.

After the rice emerged in the experiment, it was observed that the seedlings emerged unevenly at both ends of the field, which might be due to uneven sowing caused by the change in speed when the mUAV was changing rows and turning. As the same time, the shape of the centrifugal spreading was circular, which easily led to overseeding between adjacent widths and result in poor uniformity (Qin and Liu, 2006). Zhou et al. (2018) studied the effect of UAV spreading methods on the characteristics of rice plants in terms of lodging resistance. The results showed significant differences in the main physical characteristics of the stalks between the different spreading methods, which showed that the stalks were thin at the 2nd and 3rd internodes. Also, the plants were taller, with less folding resistance and a higher lodging index. Apart from that, conventional spreaders buried the seeds into the soil, but the seeds from the UAVs were exposed on the surface of the field which were vulnerable to the sun or being fed by birds, which affected the seeds' rooting and germination. On the other hand, rice seeds must be germinated before spreading. If the turntable was rotated too fast, it hit the wall which caused damage to the seed buds. Maximum range was also limited, the continuous flight capacity of the battery was generally 10–20 min, which led to the efficiency of the UAV work that could not be fully developed. The field operation required to carry several batteries, which were high-cost. It is also a problem that the UAV industry currently confronts.

However, as of 2016 (Luo et al., 2019), China's comprehensive rice mechanization level was 79.2%, with tillage, sowing, and harvesting levels of 99.3, 44.5, and 87.1%, respectively. This is only the achievement of moving from the primary stage to the intermediate stage, indicating that we still need to continue our efforts to completely solve the problem of mechanization of rice cultivation in China. China should learn from the advanced equipment and technology of developed countries to develop a proper route for itself, agricultural mechanization development of China cannot directly copy the way of other country, and agricultural mechanization of China can only be realized step by step (Yang et al., 2003).

Conclusion and outlook

Conclusions: In this study, a mUAV with three functions of seeding, spreading fertilizer, and applying pesticide was developed. CFD numerical simulation was used to initially obtain downwash airflow characteristics, and feasible operating parameters were obtained through practical operation test methods in the field. Through the whole rice cultivation comparison test with mechanical direct seeder and mechanical transplanter, the mUAV was summarized and analyzed in terms of operational efficiency, labor input, and yield in the management process.

The main conclusions were drawn as follows. (1) The modular design of the mUAV, its products could be used in the three segments of rice seeding, pesticide application and fertilization, and its ability could meet the requirements of rice production. Compared with other mechanical cultivation methods, this mUAV operation method could reduce the input of machinery types. (2) The range of operations allowed for the mUAV was verified in numerical simulations and from the perspective of real measurements. There was a strong initial value of airflow directly below the rotor, and a height of more than 1.5 m is recommended. It was recommended to fly at a height of 2.5 m for seeding and 3 m for pesticide application. (3) A comprehensive comparison was conducted

in the whole rice cultivation and the results showed that the efficiency of sowing seeds by mUAV was 2.2 times and 4 times higher than that of mechanical direct seeding and transplanting, respectively. The labor cost was reduced by 68.5 and 82.5%, respectively. The efficiency of mUAV application was 1.3 times higher than mechanical direct seeding and rice transplanting. The cost of labor was reduced by 25%. However, the mUAV fertilization was not as efficient as mechanical direct seeder and transplanter, with 80% lower operational efficiency and 14.3% higher labor costs.

Outlook: Although the development of UAV research and applications in China started slowly and initially relied heavily on state funding, several research institutions and universities have conducted research on agricultural UAV. Especially in recent years, China has been paying more and more attention to the development and research of agricultural UAV. By the end of 2015, more than 3,000 agricultural UAV had been put into agricultural production in China, the number of flight controllers had exceeded 2,500, and there were more than 400 manufacturing companies in related industries. As of 2020, China's agricultural UAV holdings were about 100,000 units, with an additional demand of 50,000 units in 2020 alone, which showed that agricultural UAV were in a phase of rapid development. With the massive transfer of agricultural population, rural labor capacity was insufficient, which made the utilization of agricultural resources inefficient, and it even seriously affected the production efficiency of agriculture. In some areas, there were also problems such as desertion, which was not conducive to the rational optimization of the rural industrial structure. Especially in remote hilly mountainous areas, ordinary ground machinery could not work in the fields, and there was a great lack of machinery in the rice production process. The mUAV could be controlled remotely and could also automatically route its operations. This not only solved the difficult problem that some ground machinery hardly worked in the paddy field, but also did not cause damage to the rice. The emergence of the mUAV has become an important breakthrough in solving this problem.

Data availability statement

The original contributions presented in this study are included in the article/supplementary material, further inquiries can be directed to the corresponding authors.

Author contributions

PQ performed most of the experiments with the assistance of CW, LX, and XJ. PQ designed the study, analyzed the data, and wrote the manuscript with ZW, YZ, SW, and JM. PQ designed and improved the UAV with the help of BC and CL. YP helped PQ to manage the rice field. PQ, XH, and YL were involved in all the contents throughout. All authors contributed to the study conception and design, read, and approved the final manuscript.

Funding

This work was carried out due to financial support from the World Bank "Climate Smart Staple Crop Production Project" (CWB Pro No. 144531/GEF Pro No. 5221), the National Key Research and Development Program of China (2020YFD1000202), the National Modern Agricultural Industrial Technology System of China (No. CARS-28-20), and Deutsche Forschungsgemeinschaft (DFG, German Re- search Foundation)-328017493/GRK 2366 (Sino-German International Research Training Group AMAIZE-P).

Acknowledgments

We acknowledged the contributions of specific colleagues, institutions, or agencies that aided the efforts of the authors.

Conflict of interest

BC and CL were employed by Yuren UAV (Zhuhai) Co., Ltd. YP was employed by Anhui Difa Agricultural Technology Co., Ltd. WZ was employed by Anhui Zhongke Intelligent Sense Technology Co., Ltd.

The remaining authors declare that the research was conducted in the absence of any commercial or financial relationships that could be construed as a potential conflict of interest.

Publisher's note

References

Bao, C., and Li, B. (2004). Research development of rice transplanter in Japan. *Trans. Chin. Soc. Agric. Mach.* 35, 162–166. doi: 10.3969/j.issn.1000-1298.2004.01.042

Bhandari, H. (2019). *Global Rice Production, Consumption and Trade: Trends and Future Directions. Koreascience.or.Kr, 2019*. Available online at: http://www.koreascience.or.kr/article/CFKO201932468198493.page (accessed May 15, 2022).

Chen, S., Lan, Y., Li, J., Zhou, Z., Jin, J., and Liu, A. (2016). Effect of spray parameters of small unmanned helicopter on distribution regularity of droplet deposition in hybrid rice canopy. *Trans. Chin. Soc. Agric. Eng.* 32, 40–46. doi: 10.11975/j.issn.1002-6819.2016.17.006

Chen, S., Lan, Y., Li, J., Zhou, Z., Liu, A., and Xu, X. (2017b). Comparison of the pesticide effects of aerial and artificial spray applications for rice. *J. South China Agric. Univ.* 38, 103–109. doi: 10.7671/j.issn.1001-411X.2017.04.017

Chen, S., Lan, Y., Bradley, K. F., Li, J., Liu, A., and Mao, Y. (2017a). Effect of wind field below rotor on distribution of aerial spraying droplet deposition by using multi-rotor UAV. *Trans. Chin. Soc. Agric. Mach.* 48, 105–113. doi: 10.6041/j.issn.1000-1298.2017.08.011

Chen, S., Zhang, S., Sun, X., and Li, Y. (2012). Design and experiment of self-propelled high-ground- clearance spreader for paddy variable-rate fertilization. *Trans. Chin. Soc. Agric. Eng.* 28, 16–21. doi: 10.3969/j.issn.1002-6819.2012.11.003

Cheng, P., and Li, Q. (2020). Effects of different seeding methods on rice yield. *Agric. Mach. Technol. Ext.* 56–57, 59. doi: 10.3969/j.issn.1671-3036.2020.02.022

Diao, Y., Zhu, C., Ren, D., Yu, J., Luo, X., Ouyang, Y., et al. (2020). Key points and prospect of rice direct seeding technology by unmanned aerial vehicle. *China Rice* 26, 22–25. doi: 10.3969/j.issn.1006-8082.2020.05.005

EN13739-1 (2011). Agricultural Machinery-Solid Fertilizer Broadcasters and Full Width Distributors- Environmental Protection-Part 1. Brussels: Europäischen Komitee für Normung (CEN).

Feng, Y., Wang, Q., Zhao, H., Song, Q., Sun, Y., and Zeng, X. (2020). Research status and prospect of the direct seeding technology of rice in China. *China Rice* 26, 23–27. doi: 10.3969/j.issn.1006-8082.2020.01.006

Fukagawa, N. K., and Ziska, L. H. (2019). Rice: importance for global nutrition. *J. Nutr. Sci. Vitaminol. (Tokyo)* 65, S2–S3. doi: 10.3177/jnsv.65.S2

GB20891 (2014). *Limits and Meaurement Methods for Exhaust Pollutants From Diesel Engines of Non-Road Mobile Machinery*. Beijing: Ministry of Ecology and Environment of the People's Republic of China.

He, R., Luo, H., and Li, Y. (2008). Comparison and analysis of different rice planting methods in China2008,24(1):167-171.(in Chinese with English abstract). *Trans. Chin. Soc. Agric. Eng.* 24, 167–171. doi: 10.3321/j.issn:1002-6819.2008.01.032

ISO22866 (2005). *Equipment for Crop Protection-Methods for Field Measurement of Spray Drift*. Geneva: ISO.

ISO24253-1 (2015). *Crop Protection Equipment-Spray Deposition Test for Field Crop*. Geneva: ISO.

Lan, Y. B., Chen, S. D., and Fritz, B. K. (2017). Current status and future trends of precision agricultural aviation technologies. *Int. J. Agric. Biol. Eng.* 10, 1–17. doi: 10.3965/j.ijabe.20171003.3088

Li, C., Tang, Y., Wu, C., and Huang, G. (2012). Effect of sowing patterns on growth, development and yield formation of wheat in rice stubble land. *Trans. Chin. Soc. Agric. Eng.* 28, 36–43. doi: 10.3969/j.issn.1002-6819.2012.18.006

Li, J. Y., Lan, Y. B., Zhou, Z. Y., Zeng, S., Huang, C., Yao, W. X., et al. (2016). Design and test of operation parameters for rice air broadcasting by unmanned aerial vehicle. *Int. J. Agric. Biol. Eng.* 9, 24–32. doi: 10.3965/j.ijabe.20160905.2248

Liu, Q., Lan, Y., Shan, C., Mao, Y., Zhao, D., and Lu, W. (2020). the effects of sowing parameters of four-rotor UAV on seed distribution of *Astragalus membranaceus*. *J. Agric. Mech. Res.* 42, 127–132. doi: 10.3969/j.issn.1003-188X.2020.11.023

Liu, Y., Wang, M., Xu, X., Zhang, P., and De, X. (2019). Field efficacy trials on the control of weeds in rice by UAVead. *Pestic. Sci. Adm.* 40, 45–51. doi: 10.3969/j.issn.1002-5480.2019.09.011

Luo, X., Wang, Z., Zeng, S., Zang, Y., Yang, W., and Zhang, M. (2019). Recent advances in mechanized direct seeding technology for rice. *J. South China Agric. Univ.* 40, 1–13. doi: 10.7671/j.issn.1001-411X.201905069

NBS (2021). Available online at: http://www.stats.gov.cn/xxgk/jd/sjjd2020/202108/t20210825_1820903.html (accessed May 15, 2022).

NY/T1003 (2006). *Technical Specifications of Quality Evaluation for Fertilizing Machinery*. Beijing: Ministry of Agriculture and Rural Affairs of the People's Republic of China.

Omar, Z., Qiang, K. Y., Mohd, S., and Rosly, N. (2016). CFD simulation of aerial crop spraying. *IOP Conf. Ser. Mater. Sci. Eng.* 160:012028. doi: 10.1088/1757-899X/160/1/012028

Qi, X., Zhou, Z., Yang, C., Luo, X., Gu, X., Zang, Y., et al. (2016). Design and experiment of key parts of pneumatic variable-rate fertilizer applicator for rice production. *Qi xingyuanZhou ZhiyanYang ChengLuo XiwenGu XiuyanZang YuLiu Wulan* 32, 20–26. doi: 10.11975/j.issn.1002-6819.2016.06.003

Qin, C., and Liu, J. (2006). Study and design on spreading mechanism of centrifugal fertilizer spinner. *J. Agric. Mech. Res.* 10, 100–102. doi: 10.3969/j.issn.1003-188X.2006.10.035

Qin, W., Xue, X., and Zhou, L. (2014). Effects of spraying parameters of unmanned aerial vehicle on droplets deposition distribution of maize canopies. *Trans. Chin. Soc. Agric. Eng.* 30, 50–56. doi: 10.3969/j.issn.1002-6819.2014.05.007

Ren, W., Wu, Z., Li, M., Lei, X., Zhu, S., and Chen, Y. (2021). Design and experiment of UAV fertilization spreader system for rice. *Trans. Chin. Soc. Agric. Mach.* 52, 88–98. doi: 10.6041/j.issn.1000-1298.2021.03.009

Shi, Q. (2015). Numerical simulation for downwash flow field of small-size unmanned helicopter hedgehopping. *J. Drain. Irrig. Mach. Eng.* 33, 521–525. doi: 10.3969/j.issn.1674-8530.15.0073

Shi, Y., Chen, M., Wang, X., Morice, O. O., Li, C., and Ding, W. (2018). Design and experiment of variable-rate fertilizer spreader with centrifugal distribution cover for rice paddy surface fertilization. *Trans. Chin. Soc. Agric. Mach.* 49, 86–113. doi: 10.6041/j.issn.1000-1298.2018.03.010

Song, C., Zhou, Z., Luo, X., Jiang, R., Lan, Y., and Zhang, H. (2018b). Review of agricultural materials broadcasting application on unmanned helicopter. *J. Agric. Mech. Res.* 40, 1–9. doi: 10.3969/j.issn.1003-188X.2018.09.001

Song, C., Zhou, Z., Jiang, R., Luo, X., He, X., and Ming, R. (2018a). Design and parameter optimization of pneumatic rice sowing device for unmanned aerial vehicle. *Trans. Chin. Soc. Agric. Eng.* 34, 80–88. doi: 10.11975/j.issn.1002-6819.2018.06.010

Tao, G., Yi, S., Li, Z., and Shi, D. (2011). Temperature field analysis of water immersion temperature rice seed soaking germination equipment. *Trans. Chin. Soc. Agric. Mach.* 42, 90–94. doi: 10.3969/j.issn.1000-1298.2011.10.017

Wan, J., Qi, L., Zhang, H., Lu, Z., and Zhou, J. (2021). Research status and development trend of UAV broadcast sowing technology in China. In American Society of Agricultural and Biological Engineers Annual International Meeting. *ASABE* 2021, 31–42. doi: 10.13031/aim.202100017

Wang, C., He, X., Wang, X., Jane, B., Andreas, H., Wang, Z., et al. (2016a). Testing method of spatial pesticide spraying deposition quality balance for unmanned aerial vehicle. *Trans. Chin. Soc. Agric. Eng.* 32, 54–61. doi: 10.11975/j.issn.1002-6819.2016.11.008

Wang, C., He, X., Wang, X., Wang, Z., Wang, S., Li, L., et al. (2016b). Distribution characteristics of pesticide application droplets deposition of unmanned aerial vehicle based on testing method of deposition quality balance. *Trans. Chin. Soc. Agric. Eng.* 32, 89–97. doi: 10.11975/j.issn.1002-6819.2016.24.012

Wang, C., He, X., and Zeng, A. (2020). Measuring method and experiment on spray drift of chemicals applied by UAV sprayer based on an artificial orchard test bench. *Trans. Chin. Soc. Agric. Eng.* 36, 56–66. doi: 10.11975/j.issn.1002-6819.2020.13.007

Wang, C., Song, J., He, X., Wang, Z., and Wang, S. (2017). Effect of flight parameters on distribution characteristics of pesticide spraying droplets deposition of plant-protection unmanned aerial vehicle. *Trans. Chin. Soc. Agric. Eng.* 33, 109–116. doi: 10.11975/j.issn.1002-6819.2017.23.014

Wang, L., Zhou, J., Xu, Y., Li, Z., and Zhang, B. (2019). Application status and prospect of agricultural UAV. *Agrochemicals* 58:634.

Wang, Q., Melaaen, M. C., and De Silva, S. R. (2001). Investigation and simulation of a cross-flow air classifier. *Powder Technol.* 120, 273–280. doi: 10.1016/S0032-5910(01)00282-0

Wen, S., Han, J., Lan, Y., Yin, X., and Lu, Y. (2018). Influence of wing tip vortex on drift of single rotor plant protection unmanned aerial vehicle. *Trans. Chin. Soc. Agric. Mach.* 49:160. doi: 10.6041/j.issn.1000-1298.2018.08.015

Xie, Y., Xu, J., and Liang, Y. (2013). Design of high-speed broad width pneumatic conveying concentration feeding precision seeding and fertilizing machine. *Agric. Sci. Equip.* 2013, 19–21. doi: 10.16313/j.cnki.nykjyzb.2013.05.025

Xu, L., Yang, M., and Huang, Y. (2012). Analysis on influencing factors of fuel consumption for mechanical paddy riceproduction in double-cropping areas in southern China. *Trans. Chin. Soc. Agric. Eng.* 28, 33–39. doi: 10.3969/j.issn.1002-6819.2012.23.005

Xue, X., Qin, W., Sun, Z., Zhang, S., Zhou, L., and Wu, P. (2013). Effects of N-3 UAV spraying methods on the efficiency of insecticidesagainst planthoppers and *Cnaphalocrocis medinalis*. *J. Plant Prot.* 40, 83–88. doi: 10.13802/j.cnki.zwbhxb.2013.03.013

Yang, F. B., Xue, X. Y., Zhang, L., and Sun, Z. (2017). Numerical simulation and experimental verification on downwash air flow of six-rotor agricultural unmanned aerial vehicle in hover. *Int. J. Agric. Biol. Eng.* 10, 41–53. doi: 10.25165/j.ijabe.20171004.3077

Yang, M., Yang, L., Li, Q., and Chen, J. (2003). Agricultural mechanization system of rice production of Japan and proposal for China. *Transctions Chin. Soc. Agric. Eng.* 19, 77–82. doi: 10.3321/j.issn:1002-6819.2003.05.016

Yang, Z., Ge, L., Qi, L., Cheng, Y., and Wu, Y. (2018b). Influence of UAV rotor down-wash airflow on spray width. *Trans. Chin. Soc. Agric. Mach.* 49, 116–122. doi: 10.6041/j.issn.1000-1298.2018.01.014

Yang, F., Xue, X., Cai, C., and Zhou, Q. (2018a). Effect of down wash airflow in hover on droplet motion law for multi-rotor unmanned plant protection machine. *Trans. Chin. Soc. Agric. Eng.* 34, 64–73. doi: 10.11975/j.issn.1002-6819.2018.02.009

Yongwang, G., Xiaojing, Y., Yubin, L., and Huizhu, Y. (2020). *Application Guide of Agricultural Aviation Plant Protection Technology*. Beijing: Agriculture Press.

Yubin, L., and Guobin, W. (2018). General situation and prospect of UAV industry in China. *Agric. Eng. Technol.* 38, 17–27. doi: 10.16815/j.cnki.11-5436/s.2018.09.004

Zhang, H., and Gong, J. (2014). Research status and development discussion on high-yielding agronomy of mechanized planting rice in China. *Sci. Agric. Sin.* 47, 1273–1289. doi: 10.3864/j.issn.0578-1752.2014.07.004

Zhang, J., and Zhou, H. (2019). Substitution elasticity of labor and machinery in the production of rice under the background of mechanization: based on the survey data of rice farmers in Jiangsu Province. *J. South. Agric.* 50, 432–438. doi: 10.3969/j.issn.2095-1191.2019.02.31

Zhang, P., Lv, Q., Yi, S., Liu, Y., He, S., Xie, R., et al. (2016). Evaluation of spraying effect using small unmanned aerial vehicle (UAV) in citrus orchard. *J. Fruit Sci.* 33, 34–42. doi: 10.13925/j.cnki.gsxb.20150182

Zhang, S., Xue, X., Qin, W., Sun, Z., Ding, S., and Zhou, L. (2015). Simulation and experimental verification of aerial spraying drift on N-3 unmanned spraying helicopter. *Trans. Chin. Soc. Agric. Eng.* 31, 87–93. doi: 10.3969/j.issn.1002-6819.2015.03.012

Zheng, X., Lu, M., Pang, Z., He, Z., and Xie, G. (2021). Comparison of different direct seeding methods of early Indica rice. *XianDai NongYe KeJi* 5:13. doi: 10.3969/j.issn.1007-5739.2021.11.002

Zhou, L., Li, M., Wu, Z., Chen, Y., Ma, R., and Ren, W. (2018). Study on lodging resistance of uav seeding rice in hilly areas. *J. Henan Agric. Univ.* 52, 599–603.

Zhou, T., Zhang, Y., Yang, Y., and Zhang, J. (2019). Monitoring rice fertilization by remote sensing technology-application of unmanned aerial vehicle in improving rice taste quality. *Sci. Technol. Cereal. Oils Foods* 27, 27–30. doi: 10.16210/j.cnki.1007-7561.2019.06.005

Zhou, Z., Ming, R., Zang, Y., He, X., Luo, X., and Lan, Y. (2017). Development status and countermeasures of agricultural aviation in China. *Trans. Chin. Soc. Agric. Eng.* 33, 1–13. doi: 10.11975/j.issn.1002-6819.2017.20.001

Zhu, B., Li, H., Dong, M., Duan, H., Li, Z., and Cheng, J. (2021). Effects of different planting methods on yield and economic benefit of high quality medium indica rice variety Huanghuazhan. *Hubei Agric. Sci.* 60, 20–22. doi: 10.14088/j.cnki.issn0439-8114.2021.24.004

Zhu, F., Chen, H., and Xu, Y. (2007). Countermeasure and perspective of mechanization of rice planting in China. *North Rice* 5, 13–18. doi: 10.3969/j.issn.1673-6737.2007.05.005

frontiers | Frontiers in Plant Science

TYPE Original Research
PUBLISHED 01 August 2022
DOI 10.3389/fpls.2022.960686

OPEN ACCESS

EDITED BY
Lei Shu,
Nanjing Agricultural University, China

REVIEWED BY
Xiangjun Zou,
South China Agricultural University, China
Wen-Cheng Lai,
National Yunlin University of Science and Technology, Taiwan
Quan Qiu,
Beijing Institute of Petrochemical Technology, China
Pei Wang,
Southwest University, China
Siniša Mitrić,
University of Banja Luka, Bosnia and Herzegovina

*CORRESPONDENCE
Yajia Liu
liuyajia@cau.edu.cn
Xiongkui He
xiongkui@cau.edu.cn

SPECIALTY SECTION
This article was submitted to Sustainable and Intelligent Phytoprotection, a section of the journal Frontiers in Plant Science

RECEIVED 03 June 2022
ACCEPTED 30 June 2022
PUBLISHED 01 August 2022

CITATION
Wang S, Song J, Qi P, Yuan C, Wu H, Zhang L, Liu W, Liu Y and He X (2022) Design and development of orchard autonomous navigation spray system. *Front. Plant Sci.* 13:960686. doi: 10.3389/fpls.2022.960686

Design and development of orchard autonomous navigation spray system

Shubo Wang, Jianli Song, Peng Qi, Changjian Yuan, Hecheng Wu, Lanting Zhang, Weihong Liu, Yajia Liu* and Xiongkui He*

Centre for Chemicals Application Technology, College of Science, College of Agricultural Unmanned System, China Agricultural University, Beijing, China

Driven by the demand for efficient plant protection in orchards, the autonomous navigation system for orchards is hereby designed and developed in this study. According to the three modules of unmanned system "perception-decision-control," the environment perception and map construction strategy based on 3D lidar is constructed for the complex environment in orchards. At the same time, millimeter-wave radar is further selected for multi-source information fusion for the perception of obstacles. The extraction of orchard navigation lines is achieved by formulating a four-step extraction strategy according to the obtained lidar data. Finally, aiming at the control problem of plant protection machine, the ADRC control strategy is adopted to enhance the noise immunity of the system. Different working conditions are designed in the experimental section for testing the obstacle avoidance performance and navigation accuracy of the autonomous navigation sprayer. The experimental results show that the unmanned vehicle can identify the obstacle quickly and make an emergency stop and find a rather narrow feasible area when a moving person or a different thin column is used as an obstacle. Many experiments have shown a safe distance for obstacle avoidance about 0.5 m, which meets the obstacle avoidance requirements. In the navigation accuracy experiment, the average navigation error in both experiments is within 15 cm, satisfying the requirements for orchard spray operation. A set of spray test experiments are designed in the final experimental part to further verify the feasibility of the system developed by the institute, and the coverage rate of the leaves of the canopy is about 50%.

KEYWORDS

orchard plant protection, crawler sprayer, autonomous navigation, laser lidar, obstacle avoidance

Introduction

Among orchard management operations, plant protection management is provided with the highest labor intensity (Liu et al., 2020). Exploring an automatic sprayer with a high degree of automation and a high pesticide utilization is a hot spot for agricultural machinists. There are mainly two thorny problems in the development of automated orchard sprayers: one is to achieve efficient penetration of pesticides in a low dense canopy and reduce the loss of chemical solution (Meng et al., 2022; Wang C. et al., 2022), while the other is to let the machine traverse the orchard autonomously without manual control in the orchard with a closed canopy and blocked vision (Bergerman et al., 2015; Ye et al., 2018; Zhang et al., 2020). Considerable research has been conducted on the above two issues.

The leaves can rotate under the blowing of the centrifugal fan, and those of the fruit tree can be fully sprayed because of the air assistance of the air-driven sprayer (Boatwright et al., 2020; Boatwright and Schnabel, 2020). In general, the effect is better than that of hydraulic atomization, making the way of wind assistance more frequently adopted in the orchard. In the field of air-driven orchard sprayers, the development process proposed by the developed countries in Europe is relatively richer, where the development has always been committed to solving environmental problems such as low utilization of spray pesticides and pesticide pollution of soil and atmosphere (Fox et al., 2008; Boatwright and Schnabel, 2020). The porous air bag orchard spray, the multi-airway orchard spray and the small orchard air-driven sprayer have been developed consecutively (Fox et al., 2008). At this stage, the planting mode of orchards has been standardized and transformed accordingly, which has promoted the development and application of air-assisted sprayers in small and medium-sized orchards, making it a main force of orchard spray plant protection management machinery under the dwarf dense planting mode (Owen-Smith et al., 2019; An et al., 2020).

Another thorny problem of orchard spray is to realize automatic driving. In the complex and closed environment of the orchard, many sensors and positioning devices may be subject to a low accuracy or even failure (Fei and Vougioukas, 2022). Exploring a reliable autonomous driving scheme in orchard has been extensively studied. After decades of exploration, a complete unmanned system scheme with "perception-decision-making-control" progression has been formed (Bergerman et al., 2015; Jones et al., 2019). At the level of "perception," sensors are mainly used to obtain orchard environmental data, including fruit tree information, road information, etc., which will be then applied to make the next-stage decision; at the level of "decision making," the obtained environmental information is further processed, and then the travel track is extracted for judging whether there are obstacles; and at the level of "control," the controller is designed to drive the system to follow the trajectory. The result of this research shows that in the entire autonomous driving process, it is the most difficult task to effectively perceive the orchard environment, perform real-time positioning, and effectively avoid obstacles. Visual sensors or radar sensors are generally used as the perception part, the representative literature, and the advantages and disadvantages are listed in **Table 1**.

In general, GNSS-based orchard navigation and positioning is based on satellite map or known structured orchard map, which fails to realize obstacle avoidance and navigation in unknown environment. Millimeter wave radar can only sense obstacles, but it cannot build a global map. Therefore, the above two methods are generally combined with other sensors to guide the unmanned system through the fusion strategy. Therefore, the development of autonomous obstacle avoidance and navigation orchard vehicles based on binocular vision, lidar, or multi-sensor fusion has been extensively studied. A previous study (Chen et al., 2021) adopted a binocular vision method to build a simultaneous localization and mapping (SLAM), which realized the perception of orchard environment through vision and generated a detailed global map supporting long-term, flexible, and large-scale orchard picking. On the basis of binocular vision, the study discussed in Liu et al. (2022) proposed a trinocular vision system for orchard vehicle based on a wide-angle camera and binocular stereo vision system, which finally realized orchard row detection and obstacle detection simultaneously. Besides, based on the vision technology, the study discussed in Li Y. et al. (2020) proposed a visual perception method based on convolutional neural network, and realized obstacle detection and colligation avoidance in robot harvesters. Ravankar et al. (2021) used lidar sensors to navigate unmanned vehicles in the vineyard, and developed a point cloud processing algorithm to avoid dynamic obstacles in the vineyard while smoothing the robot's trajectories. A previous study (Ji et al., 2021) built a tracker platform based on 3D/2D lidar and GNSS/AHRS to acquire fusion point cloud data, and finally realized obstacle perception and target tracking. The study explained in Kragh and Underwood (2020) adopted the fusion of lidar and visual sensors and proposed a multimodal fusion algorithm from the scene analysis domain for obstacle detection in agriculture with moving ground vehicles. One of the previous studies (Emmi et al., 2021) proposed the field autonomous navigation system based on 2D lidar and RGB cameras, and realized the robot positioning in a hybrid topological map through data fusion. Previous research (Rovira-Más et al., 2020) proposed an autonomous navigation strategy based on the integration of three sensing devices, namely, 3D vision, lidar, and ultrasonics. It is pointed out that this augmented perception overcomes the problem of GNSS frame loss and achieves high navigation accuracy in grapes.

Based on the above research, an automatic spray working in orchard is developed in this study using laser radar and millimeter wave radar sensing technology. At the same time, the air spray method is used for pesticides spraying. The crawler

TABLE 1 Classification of driverless perception and decision system working in orchard.

	Advantage	Shortcoming
GNSS (Guevara et al., 2020; Mao et al., 2022)	It can work in the orchard all day and is completely unaffected by the weather	In the orchard, the loss of signal caused by canopy occlusion, multipath effect, radio frequency interference, etc., results in great errors to GNSS navigation and even led to invalid navigation
Binocular vision (Stefas et al., 2016; Lin et al., 2021; Ma et al., 2021; Vrochidou et al., 2022)	Low cost and abundant information (depth map and RGB map)	The accuracy is poor, and is seriously reduced in dim light and at night, failing to meet the needs of overnight operation in orchards
Lidar (Bergerman et al., 2015; Blok et al., 2019; Jones et al., 2019; Guevara et al., 2020; Zhang et al., 2020)	The cost is high, and is greatly affected by bad weather such as rain and snow	The cost is high, and is greatly affected by bad weather such as rain and snow
Millimeter wave radar (Li X. et al., 2020; Wang et al., 2021)	It has a strong penetrability and is not affected by light, and can meet all kinds of weather in the orchard	The atmospheric attenuation is large and the detection distance is short, so it cannot be perceived in a large range

chassis and laser radar navigation scheme are adopted according to the standard hedgerow orchard planting mode (as shown in Figure 1). Finally, the full autonomous spray operation is realized in the orchard environment. The main contributions of this work are summarized as follows: (1) An orchard navigation strategy based on laser radar is proposed, and at the same time, combined with ultrasonic radar, the accurate perception of obstacles and high-precision planning of navigation route are realized. (2) An air spray device is developed to realize the twice atomization of liquid medicine and improve the penetration rate of droplets.

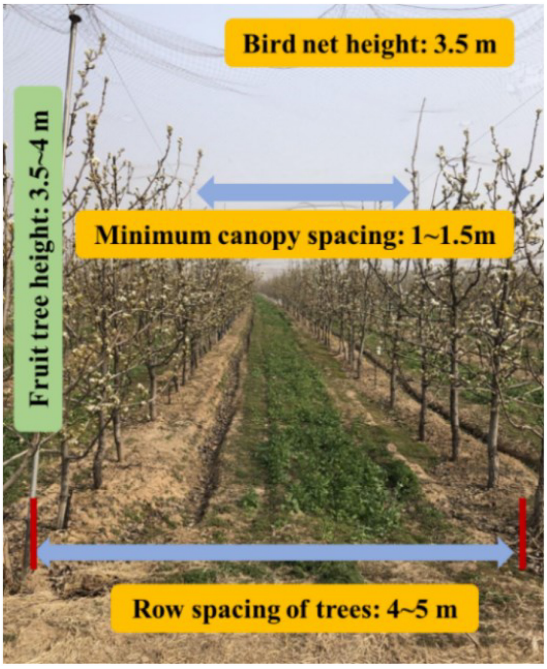

FIGURE 1
Overview of orchard environment.

The rest of this article is organized as follows: section "Design of hardware system" introduces the hardware part of the system, including the chassis, sensor module, spray system, and other core modules; section "Design of software system" proposes the environment perception and navigation based on lidar, as well as the control strategy; section "Experiments and discussions" discusses the experiments of obstacle avoidance and navigation accuracy under unfair conditions, also the preliminary spray experiment; and section "Conclusion" summarizes the full study.

Design of hardware system

As shown in Figure 2, the electric air-driven crawler sprayer is composed of power unit, traveling system, transmission device, control device, pneumatic system, spray device, etc. The main components of the electric air-driven crawler sprayer

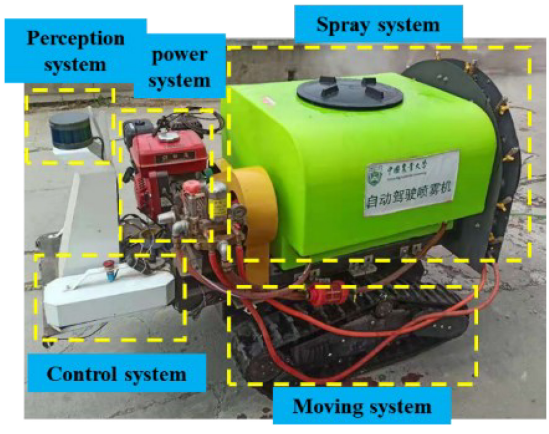

FIGURE 2
Hardware module of orchard autonomous navigation spray system.

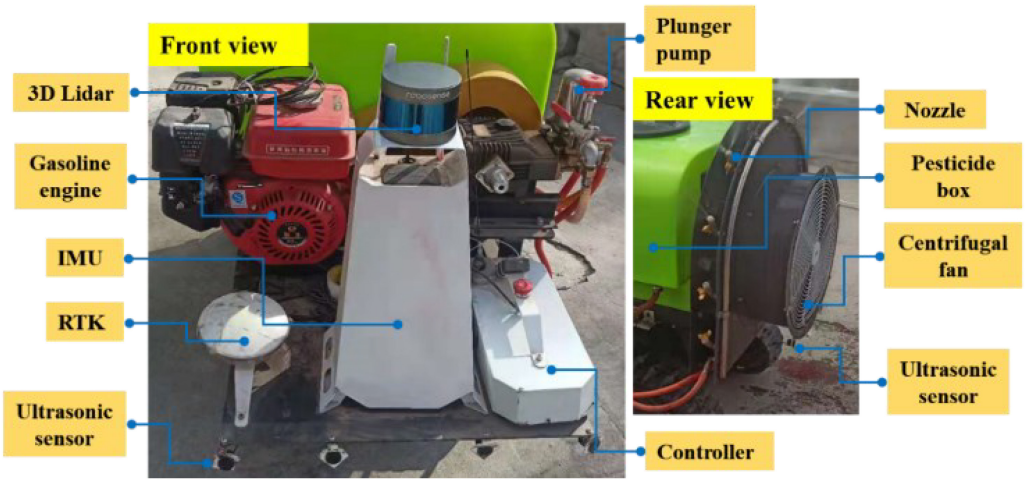

FIGURE 3
The main hardware distribution of the orchard autonomous navigation spray system.

shown in Figure 3 are remote control track chassis, frame, 200-L medicine tank, 48-V Servo electrode, centrifugal fan, water ring, 170-F gasoline engine and centrifugal pulley. The chassis and spray device are powered by different units, respectively. The track chassis is electric, and the 170-F gasoline engine is used as the power unit for the spray device to transmit the power to the centrifugal fan at the rear to ensure sufficient power. Actions such as forward, turning, and moving backward of the machine are realized by the electric part driving the left and right gear motors. The pump pressure of the Model 25A plunger pump can be adjusted by the pressure valve preset, which adopts centrifugal belt installation installed on the output shaft of 170-F gasoline engine, and applies belt transmission between the fan pulley and the plunger pump pulley to form a three-axis linkage. When the output speed of the gasoline engine exceeds 600 rpm/min, the pulley of the walking device begins to work. The fan rotation and the power of the plunger pump are provided by the transmission of the gasoline engine, and the installation height of the plunger pump can be adjusted according to the demand during the actual working process to fully provide tension to the power transmission belt.

Chassis drive

Considering that the platform is mainly used for spray operation in hedgerow orchards, the mechanical part of the navigation robot hardware platform is correspondingly improved. Therefore, the chassis needs to be equipped with a medicine box and spray system weighing about 250 kg. Given that the liquid medicine will shake with the movement of the platform during the operation and the situation of the muddy road, as shown in the Figure 4, the medicine box is embedded into the chassis for obtaining a low-center of gravity-tracked chassis structure. The chassis design parameters are shown in Table 2.

Sensors and information processing modules

The sensor module, processor framework, and communication transmission process are shown in Figure 5, where it can be observed that the core of the sensor module is the lidar sensor and the sprayer is equipped with RS-LiDAR-16, i.e., RoboSense[1] 16-wire laser radar. The RS-LiDAR-16 emits and receives high-frequency laser beams through 16 groups of built-in laser components, and carries out real-time 3D imaging through 360° rotation. The measurement distance can reach 150 m, the accuracy is within ±2 cm, and 300,000 points clouds can be formed per second on

1 https://www.robosense.cn/en

FIGURE 4
Structure diagram of crawler chassis diagram.

TABLE 2 Chassis hardware structure parameters.

Index	Load (kg)	Width (m)	Length (m)
Parameter	250	1.2	1.2
Index	**Ground clearance (mm)**	**Turning radius (m)**	**Top speed km/h**
Parameter	150	<7	≥4

average. The vertical angle measurement is 15–15° for ensuring the real-time perception of the environment in the orchard. Also, N100 IMU of Wheeltec Company[2] is applied to the inertial measurement unit (IMU) with a three-axis accelerometer, a three-axis gyroscope, and a three-axis magnetometer, among which, the accelerometer resolution is less than 0.5 mg, and the range is ±16 g; the gyroscope resolution is less than 0.02°/s; and the range is ±2,000°/s; the magnetometer resolution is 1.5 mg, and the range is ±4,900. The N100 IMU can meet the effective output of inertia parameters such as attitude angle and velocity in orchard environments. The model used by the ultrasonic obstacle avoidance sensor is DYP-A19-V1.0 (Best Sensor)[3], whose measuring range is 28–450 cm, with an accuracy of ±(1 + 0.3% of the current ranging). The CPU of the control host is i7 4700M, equipped with 8-G memory and 128-G storage for realizing the solution of sensor data, information storage, and output.

2 http://wheeltec.net/product/html/?144.html

3 http://www.dypsensor.com/en/proData.aspx?cid=142&pid=122

FIGURE 5
Sensor and information processing module information transmission process.

Spray system module

Orchard electric air-driven crawler sprayer can satisfy the requirements for modern orchard plant protection spray operation, and the spray unit is powered by a diaphragm pump. The sprayer follows two atomization processes. First, the liquid medicine is extracted from the medicine box and atomized once through the spray system, when the diaphragm pump is the power source. Then, the liquid medicine passes through the infusion tube and is transported to each nozzle at the ring baffle, and the high-pressure air flow is generated by the centrifugal fan to produce a second atomization of the droplets.

As shown in Figure 6, the spray device of the orchard electric air-driven crawler sprayer is mainly composed of a centrifugal fan, an arc-shaped aqueduct on both sides of the tail and nozzles. Ten spray nozzles are arranged in a circle along both sides at the end of the machine, and five nozzles are evenly arranged on each pipe ring. Each nozzle is equipped with a switch that can be adjusted independently, and the nozzle angle can be adjusted as well; from bottom to top on the left are nozzles No. 1, 2, 3, 4, and 5, respectively, and the nozzles are symmetrically distributed both on the right and the left. The detailed parameters are shown in Table 3. The application of a segmented water ring can ensure

FIGURE 6
Sprinkler distribution map.

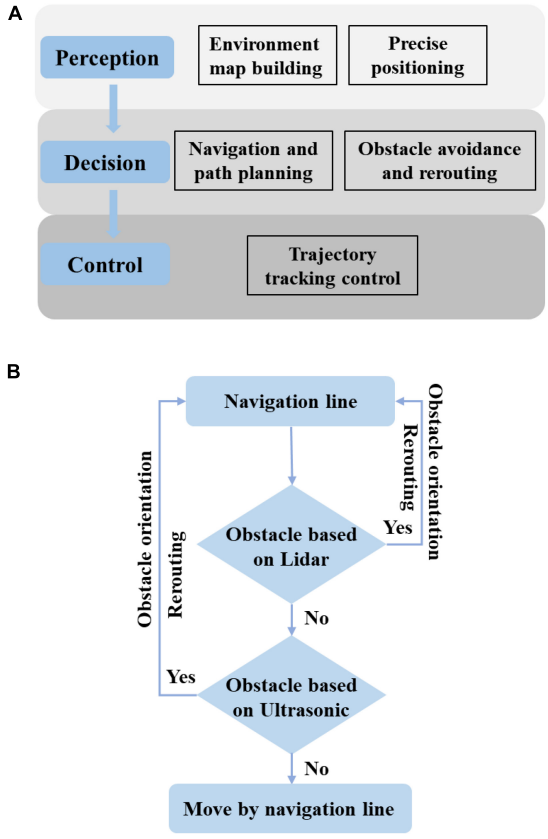

FIGURE 7
Software block diagram of unmanned spray truck based on "perception decision control". **(A)** Relationship between three layers. **(B)** Obstacle avoidance fusion output based on decision-level fusion.

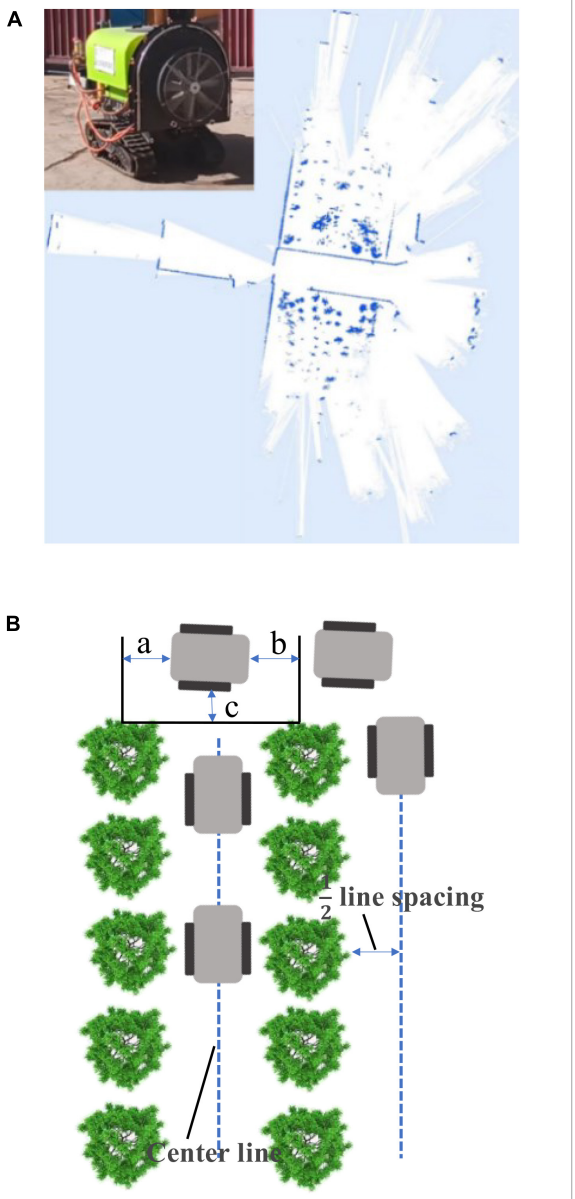

FIGURE 8
Construction of local map based on RS-LiDAR-16. **(A)** Local map acquisition. **(B)** Schematic diagram of navigation line.

that the pressure of each sprinkler is basically the same, and the direction and angle of the nozzle can be adjusted according to the actual growth of the fruit trees in the pear orchard during the spray operation.

Design of software system

The navigation system is provided with the function of switching between manual control and autonomous driving, so that the user can remotely control the chassis to the orchard before operation and switch to the autonomous navigation mode after the navigation task is planned during operation, thereby realizing full autonomous operation. After operation, the user can remotely control the chassis out of the orchard, and handle emergencies by remote control at the same time. As shown in Figure 7A, the overall system is divided into three parts, i.e., perception, decision, and control. First, the local map is constructed based on lidar; then, the operation path is planned in accordance with the constructed map and finally, the planned path is transmitted to the trajectory controller for the unmanned vehicle traveling according to the preset trajectory. At the same time, it can realize automatic obstacle avoidance, including obstacle detection, type recognition, and selective bypassing of static and dynamic obstacles, which are also involved in the perception layer and decision-making layer. As shown in Figure 7B, two sensors based on ultrasonic radar and laser radar are used for obstacle perception. Given that the longitudinal sensing range of laser radar is only 30, it is difficult to perceive ground obstacles. The ultrasonic radar located under the vehicle is used for obstacle fusion sensing. The two sensing

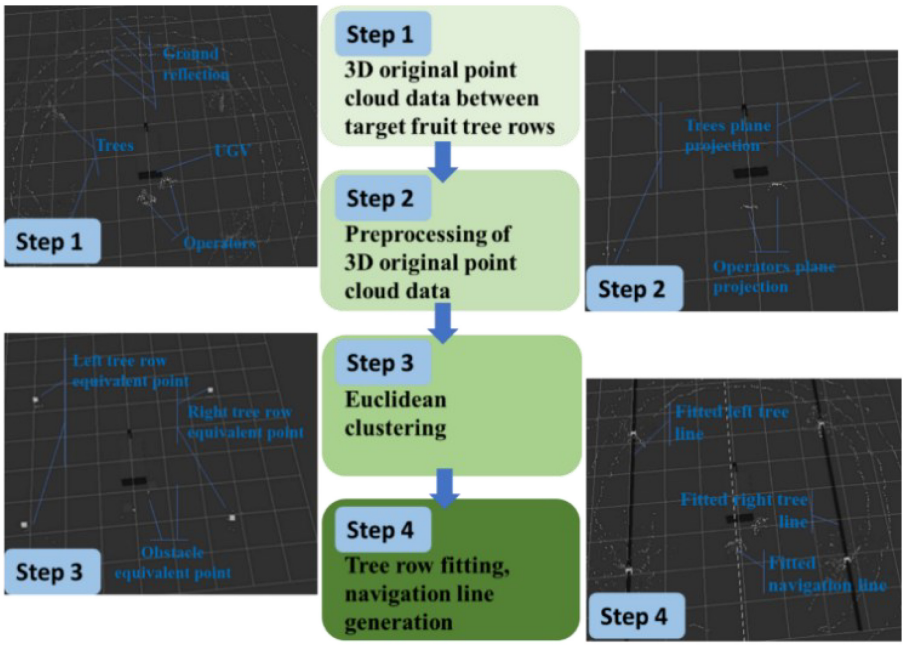

FIGURE 9
Navigation line extraction rules among fruit trees.

strategies are fused based on the decision-making layer, and the weighted decision-making method is adopted. Each laser radar and ultrasonic radar have 50% weight. When the proportion of perceived obstacles is greater than or equal to 50%, the path needs to be replanned, that is, when any sensor senses an obstacle, the path needs replanning. The overall software is secondary developed based on Autopilot Kit.[4]

Environment perception and navigation based on laser radar

As shown in Figure 8A, the automatic tracking navigation can be realized by constructing a local map through laser radar. The navigation system detects the fruit trees and takes the two lines of center lines as the traveling track to carry out the traveling operation when the spray truck travels in the orchard, and can automatically complete the turning and move to the next row of operation when reaching the ground, as shown in Figure 8B. The navigation rules are as follows: The centerline is taken as the travel track when traveling in two rows; the trajectory is determined by a distance of one-half row when there are fruit trees on only one side; when the spray truck reaches the end-member of field, $a = b = 1/2$ line spacing (determined at the center), and C is not less than the safe distance. The next center position is determined as the spray truck moves on to the next row and turns to move on to the next row of work.

As shown in Figure 9, the navigation line extraction rules of the spray truck between fruit trees are divided into four steps: Step 1: Data collecting of the 3D original point cloud data between the rows of the target orchard; Step 2: Data preprocessing (clipped and dimensionality reduction) of the 3D original point cloud data; Step 3: European clustering; and Step 4: Tree row fitting and the navigation line generation. Because the extreme weather, such as rain, fog, and high temperature, is not suitable for spray operation, this study does not consider extreme weather navigation line extraction.

The original point cloud data of the 3D space obtained between the rows of the target orchard are collected, as shown in Figure 9 (Step 1), where the block is a mobile robot model; other white point clouds are the relative positions of the objects in the 3D scene; the coordinate origin, such as the point clouds on the left and right sides of the mobile robot are fruit trees; those in front are ground reflections; and those in the back are the mobile robot operators. Point clouds have a 360° horizontal full coverage and a vertical coverage from the ground to above the fruit trees. The RS-LiDAR-16 laser radar adopted in this study is a 16-wire laser radar with a horizontal field of view of 360°, a vertical field of view of 30° (±15°), and a maximum detection distance of 200 m.

In Step 2, the preprocessing of the 3D original point cloud data is mainly completed *via* clipping and dimensionality

4 https://www.agilex.ai/solution/5?lang=zh-cn

reduction. The 3D clipping mainly involves data clipping based on the *x*-, *y*-, and *z*- axes, and the specific clipping process is as follows: The clipping threshold of *xyz* is set according to the plant spacing, row spacing, and the average net trunk length of fruit trees; that of *x*-axis is at least three times of single row spacing; that of *y*-axis is at least 1.5 times of single row spacing; and that of *z*-axis does not exceed the average net trunk length. The clipping purpose is to select a certain visual range, reduce the amount of data, and improve the processing speed.

The dimensionality reduction of the cropped data mainly aims to project the cropped 3D data into a given 3D space plane ($x = 0$, $y = 0$, $z = 1$), thereby realizing the dimensionality data reduction from 3D to 2D, and simplifying the geometric problem, as shown in **Figure 9** (Step 2). The left and right points in the figure are the projection of the trunk in the plane ($x = 0$, $y = 0$, $z = 0$), while the middle point denotes the projection of the operator in the plane ($x = 0$, $y = 0$, $z = 1$).

Euclidean clustering method is used in Step 3 for clustering the effective points after search. The midpoint of each category of the data is calculated to replace the corresponding category, and equivalent points of two left tree row, the obstacle, and the right tree row are all marked as shown in **Figure 9** (Step 3).

Finally, the left tree row straight line and the right tree row straight line are made to fit using the least square method in Step 4. The left tree row equation and the right tree row equation are obtained as shown in **Figure 9** (Step 4), and the fitted left and right tree row lines are marked, respectively. Finally, the center line of the left and right tree rows is adopted for calculating the navigation line, and the fitted navigation line is also marked in the map.

Control strategy

The hereby designed tracked vehicle controls the speed and direction of the driving wheels on both sides for an accurate tracking of the desired trajectory as shown in **Figure 10**, where Oxy is the geodetic coordinate system; Cx_cy_c is the tracked vehicle coordinate system;C is the coincidence point between the geometric center and the centroid of the tracked vehicle; and $2L$ is the center distance of the tracked vehicle.

The status quantity of tracked vehicle is $q=(x,y,\theta)^{\mathrm{T}}$, where (x,y) represents the position of tracked vehicle, and the kinematic model of tracked vehicle is calculated as:

$$\begin{bmatrix} \dot{x} \\ \dot{y} \\ \dot{\theta} \end{bmatrix} = \begin{bmatrix} \cos\theta & 0 \\ \sin\theta & 0 \\ 0 & 1 \end{bmatrix} \begin{bmatrix} v \\ \omega \end{bmatrix} \tag{1}$$

where v is the vehicle speed; ω is the angular velocity of vehicle centroid; v_R is the right track speed; and v_L is the left track speed.

It can be seen that $u=[v,\omega]^{\mathrm{T}}$ is the control quantity of crawler, when the track vehicle control problem turns into tracking the track vehicle reference trajectory by finding a suitable control

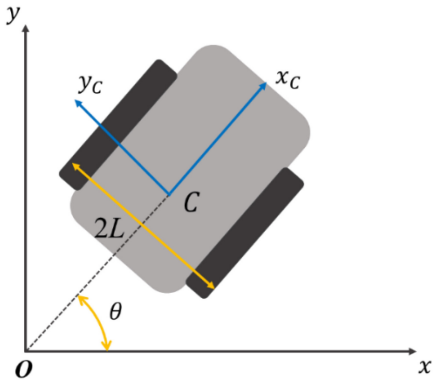

FIGURE 10
Definition of crawler coordinate system.

quantity under the condition of given initial state information and speed information. Deriving the kinematic model further, it can be obtained as follows:

$$\begin{bmatrix} v \\ \omega \end{bmatrix} = \frac{1}{2} \begin{bmatrix} 1 & 1 \\ -\frac{1}{L} & \frac{1}{L} \end{bmatrix} \begin{bmatrix} v_L \\ v_R \end{bmatrix} \tag{2}$$

The control of speed and steering angle is particularly important during the operation of tracked plant protection vehicle. Assuming the nozzle sprays liquid medicine at a constant flow rate, the unmanned vehicle is required to travel at a constant speed. Whether the unmanned vehicle needs human participation in the control at the boundary turn of the plot is determined by whether the steering angle can be accurately controlled. In addition, during the operation of the plant protection unmanned vehicle, the total mass of the vehicle will be reduced with the spraying of liquid medicine, and the shaking of liquid medicine in the medicine box, air resistance, non-linear friction, and the unmodeled part of the system will cause multi-source and unknown interference to the agricultural unmanned vehicle. For solving these problems, the active disturbance rejection control (ADRC) control strategy is adopted for the controller of the plant protection unmanned vehicle. The control system is designed based on the discussions in Wang S. et al. (2022), as shown in **Figure 11**, with the following two ADRC controllers involved: One receives the desired speed and outputs the speed control quantity while the other receives the desired angular speed and outputs the angular speed control quantity. At the same time, the tracked vehicle transmits the actual speed and angular speed to the controller.

Experiments and discussions

In this section, we discuss on several groups of obstacle avoidance experiments, such as navigation accuracy experiments and fog drop coverage tests that are designed;

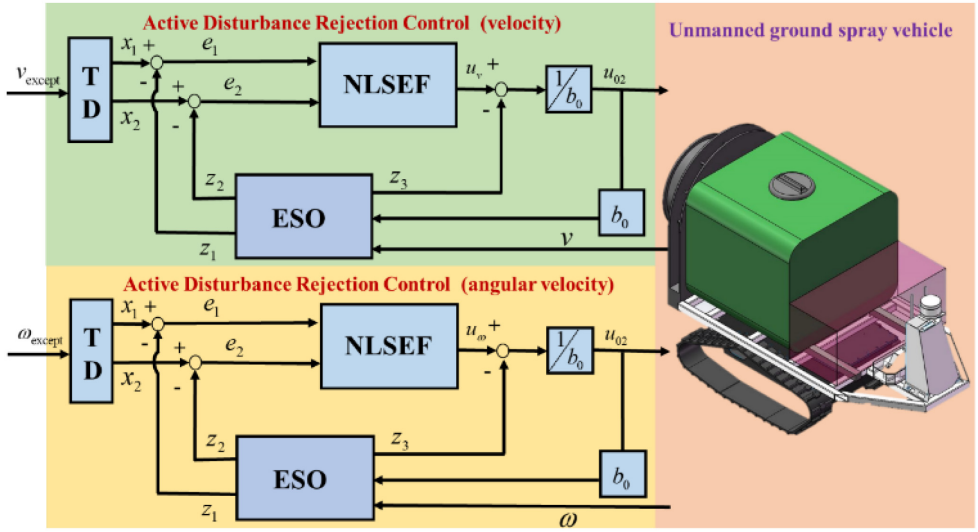

FIGURE 11
System control block diagram based on ADRC (ESO, extended state observer; TD, tracking differentiator; NLSEF, non-linear state error feedback).

also discussed are the obstacle avoidance experiments that include static obstacle experiments and dynamic obstacle experiments. The specific experimental process is shown in Figure 12.

Obstacle avoidance performance test

Static obstacle test

Fixed human obstacles

In this experiment, the size of the selected work area was about 10 m × 15 m. First, the closed-loop track was formed by manually manipulating the UGV as shown in Figure 13, where the orange arrow indicates the direction of travel. During manual operation, the lidar combined with the IMU data would map the working area, and then switch to the automatic mode, when the UGV would return to the starting point of the manual operation, and follow the manual operation track automatically for trajectory tracking control. At this time, two fixed persons were set as obstacles in the track as shown in the figure. The upper part of the figure depicts the key five-frame pictures of the UGV avoiding obstacle 1, where it can be observed that the UGV could identify and avoid obstacles well: the UGV in the test started braking at a distance of about 0.5 m from the obstacle, bypassed the person from the right, and quickly returned to the set track to continue driving. The lower part of the figure describes the key five-frame pictures of the UGV avoiding obstacle 2. Similar to facing obstacle 1, the UGV started braking at a distance of about 0.5 m from the person, turned left to avoid the person, and finally returned to the preset track. In the fixed-person obstacle experiment, the height of the person was about 1.8 m and the width was about 0.5 m. The UGV could avoid obstacles well and return to the preset track as expected.

Fixed pole obstacles

To further test the UGV's capability of recognizing the size of obstacles, resin tubes and wooden strips were selected for obstacle avoidance experiments. The height of the resin tube was about 1.5 m and the diameter was about 0.05 m; the height of the wood strip was about 1.5 m and the diameter was about 0.04 m. The same terrain (10 m × 15 m) was selected for two groups of experiments whose preset trajectories were different. The placement position of obstacles varied as well.

As shown in Figure 14, the upper part of the figure displays the key five-frame pictures of the UGV avoiding obstacle 1 when the wooden strip was used as an obstacle. It can be seen from the image of Frame 1 in the figure that the unmanned vehicle recognized the obstacle and braked sharply when it was about 0.5 m away from the wooden strip. Frames 1, 2, 3, and 4 show that the UGV started to bypass the obstacle at this time, while Frame 5 presents that the UGV had completed the detour process and was returning to the preset track. The lower part of the figure shows the five key frames of the UGV bypassing obstacle 2 of the resin tube. Similar to the wooden strip experiment, the UGV stopped about 0.5 m away from the obstacle, continued to bypass the obstacle, and returned to the preset track as expected.

The second set of experiment was also carried out, and the preset track was redesigned in the experiment, as shown in Figure 15. The upper and lower parts of the figure still show the five key frames of the UGV avoiding obstacles

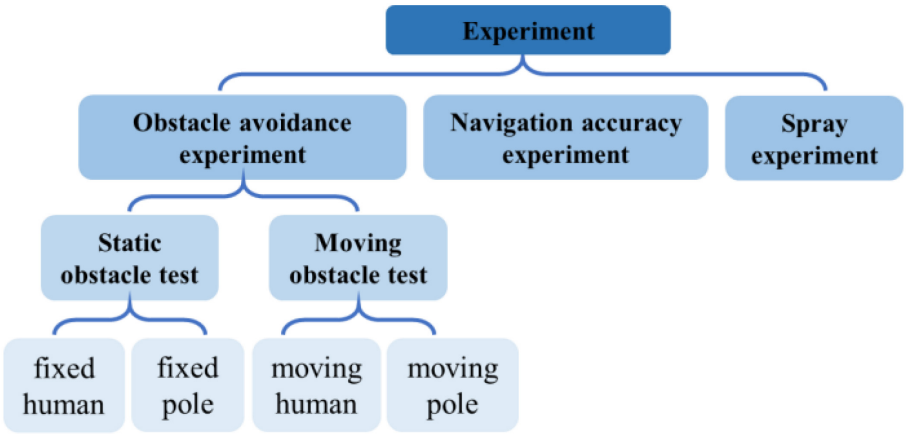

FIGURE 12
Experimental flow chart.

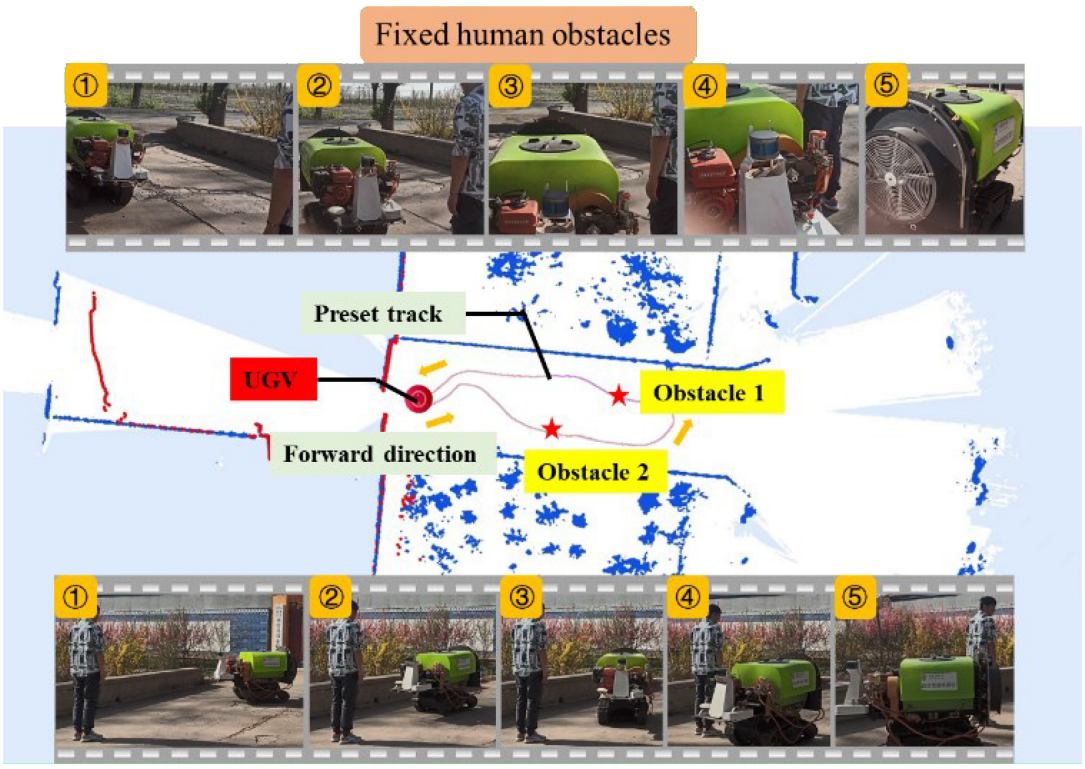

FIGURE 13
Experiment of fixed human obstacle.

when the wood strips and resin pipes were used as obstacles, respectively. Similar to the previous set of experimental results, the unmanned vehicle stopped quickly at a distance of 0.5 m from the obstacle, avoided the obstacle by detouring, and finally returned to the preset track. Replacing the curve preset track with the straight-line preset track can better display the process of UGV bypassing obstacles and returning to the preset track. Besides, the UGV deviated from the preset track by about 0.3–0.5 m while bypassing the obstacles.

Moving obstacle test

Moving human obstacles

To further test the obstacle avoidance performance of the UGV, dynamic obstacles were set in this section. As shown

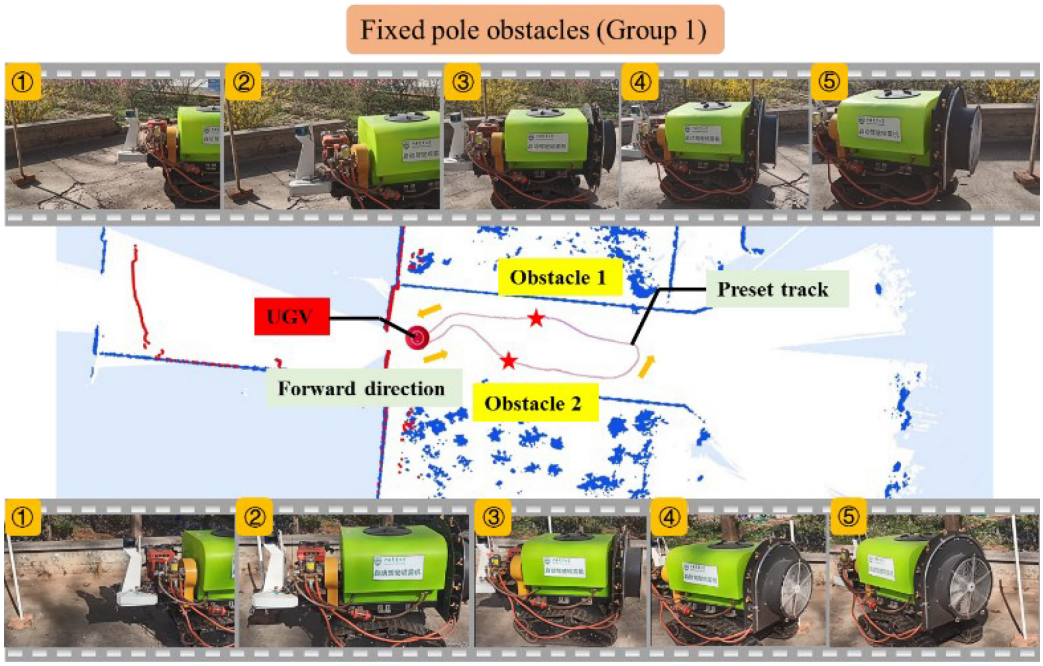

FIGURE 14
Experiment of fixed pole obstacle (Group 1).

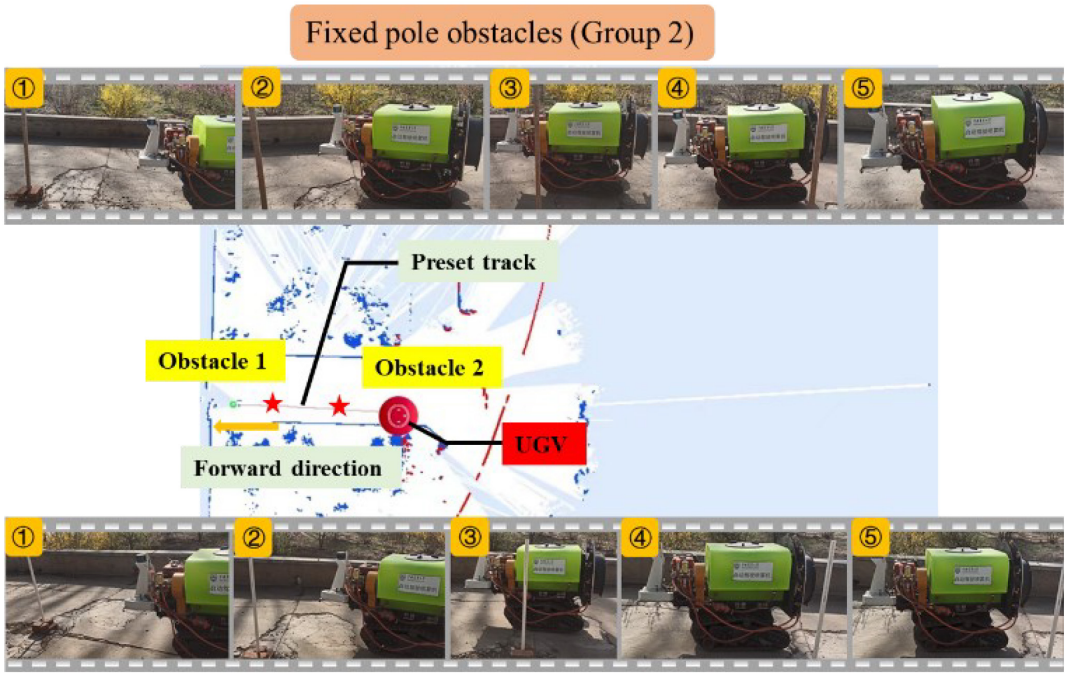

FIGURE 15
Experiment of fixed pole obstacle (Group 2).

in Figure 16, the travel track of the UGV, and two groups of moving person obstacles were all set in advance during the travel process. The UGV followed the red arrow to travel to the other side when passing the moving person obstacle 1, and followed the red arrow to start and stop on the track when passing the moving person obstacle 2. The upper part of Figure 16 depicts

the six key frames of the UGV avoiding obstacle 1 with a moving person as the obstacle. It can be seen from the image of Frame 1 that the UGV was traveling according to the preset track at this time, and in Frame 2, the person had started to set off, and the tracks of human and UGV would coincide. In Frames 3 and 4, the UGV completely coincided with the person's movement track, when the UGV started to stop suddenly and tried to detour. The person continued to move. It can be seen in Frame 5 that the UGV had an obvious detour, and the heading angle was deflected, but the moving person had left the preset track at this time. In Frame 6, the person had completely left the preset track, the UGV returned to the preset track and continued to move forward.

The lower part of Figure 16 depicts the seven key frames of the UGV avoiding obstacle 2 with a moving person acting as the obstacle. It can be seen from Frame 1 that the UGV was traveling according to the preset track at this time, and in Frame 2, the person had started to set off, and the tracks of human and the UGV would coincide. In Frame 3, the person had stopped on the UGV preset track, and the UGV started to stop suddenly. Frames 4, 5, and 6 show that the UGV bypassed the stopped person and started to approach the preset track. Frame 7 shows that the UGV had completed the obstacle avoidance of the moving person, completely returned to the preset track, and continued to travel. The experiments of two different modes of moving people as obstacles show that the UGV also had good detection and obstacle avoidance performance for unknown moving obstacles. Especially for the sudden obstacles, it could quickly brake and make evasive actions, and return to the preset track.

Moving pole obstacles

To further test the obstacle avoidance ability of UGV for small-sized and moving obstacles, the experiment of hand-held moving resin rods as obstacles was carried out. As shown in Figure 17, two groups of moving resin rods were set as obstacles during the UGV's traveling process, the hand-held moving rod was placed in front of the UGV for 5 s and then withdrawn when the UGV passed the moving resin rod 1, and when the UGV passed the moving resin rod 2, the hand-held moving rod had been placed in front of the UGV for 30 s.

The upper part of Figure 17 describes the key six-frame picture of the UGV bypassing obstacle 1 with the moving rod acting as the obstacle. It can be seen from Frame 1 in Figure 16 that the UGV traveled according to the preset trajectory. In Frames 1 and 2, the resin rod was picked up and placed in front of the UGV, when the UGV started to brake and make an emergency stop to avoid obstacles. The emergency stop was maintained until Frames 4 and 5. In Frame 6, the moving resin rods were evacuated and the UGV started to move on.

The lower part of Figure 17 shows the 10 key frames of the UGV bypassing obstacle 2 with the moving rod acting as the obstacle. It can be seen from Frames 1, 2, and 3 that the UGV traveled according to the preset trajectory, when the resin rod was picked up and placed in front of the UGV, and the UGV started to brake and make an emergency stop to avoid obstacles. Compared with the previous groups of experiments, the moving rod was placed in front of the UGV for a longer time, about 30 s. It can be seen from Frame 5 that the UGV started to deflect the heading angle to the left, trying to avoid obstacles, but if it moved forward to the left, human would appear as obstacles. In Frames 5 and 6, the UGV turned around the yaw angle and deflected to the right, and began to prepare for detour, and then in Frames 7 and 8, the UGV bypassed the obstacle from the side. In Frame 9, the obstacle was successfully avoided and the preset track was approached. In Frame 10, it completely returned to the preset trajectory and continued to move forward to complete the obstacle avoidance process.

In the moving rod experiment, the diameter of the moving rod was only 0.05 m. When the moving rod suddenly appeared in front of the UGV, the UGV detected it, and when the obstacle stayed for a long time, the UGV made a detour. The above groups of experiments verify the real-time detection performance of the designed UGV for small-sized and moving obstacles.

Navigation accuracy experiment

To verify the navigation accuracy of the UGV automatic navigation system, the evaluation was performed by designing and measuring the difference between the manual navigation route and the automatic navigation route. As shown in Figure 18, the paint would flow out from the paint bag and form a paint line on the ground for recording the travel track in real time by hanging the paint bag at the tail of UGV under the real environment. The manual control was the white paint line; the automatic navigation was the yellow paint line; the length of the selected track line was about 8 m; and a point was selected every one meter as the measurement point (x_1,x_2,x_3,$x_4$$x_5$,$x_6$,$x_7$,$x_8$); and the automatic navigation performance was evaluated by measuring the distance between the yellow paint line and the white paint line. As shown in the formula provided in Eq. (3), the average value was taken as the navigation accuracy of the planned route.

$$\text{Navigation accuracy} = \left| \frac{x_1 + x_2 + x_3 + x_4 + x_5 + x_6 + x_7 + x_8}{8} \right| \tag{3}$$

Navigation accuracy experiment (Group 1)

The size of the operation area was about 10 m × 15 m in the first set of navigation accuracy experiment. First, the UGV was manually controlled to form the trajectory shown in Figure 19, when the paint bag hanging at the tail of the UGV was filled with white paint, forming a white paint trajectory line on the ground. Then, the UGV was switched to the automatic mode and returned to the starting point of manual control, and automatically followed the manually operated track for the

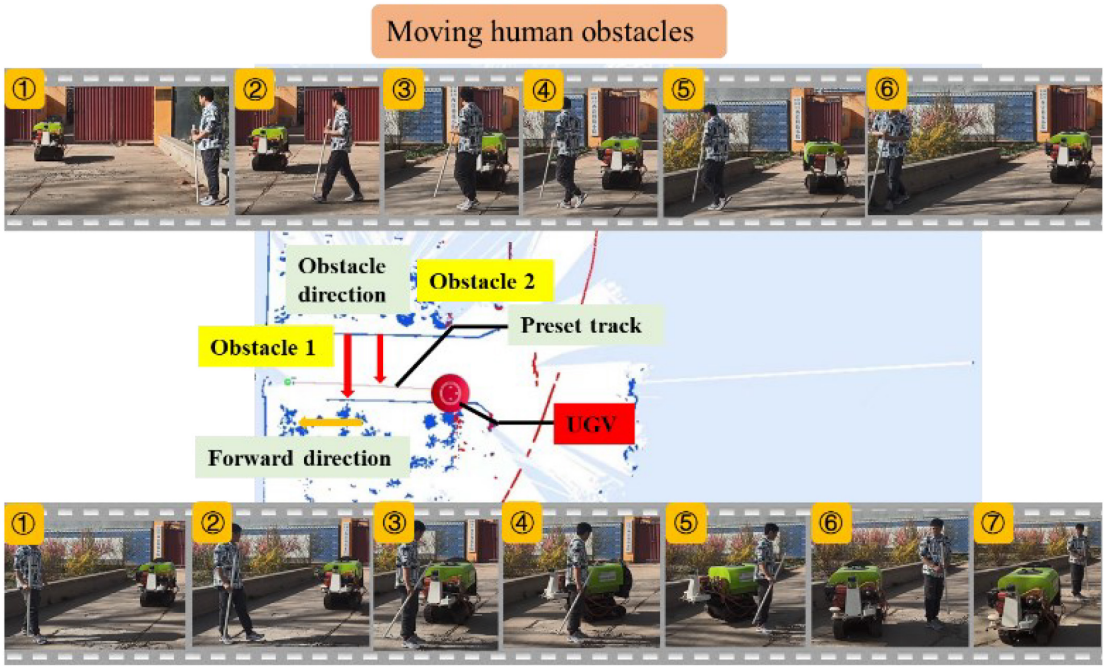

FIGURE 16
Experiment of moving person obstacle.

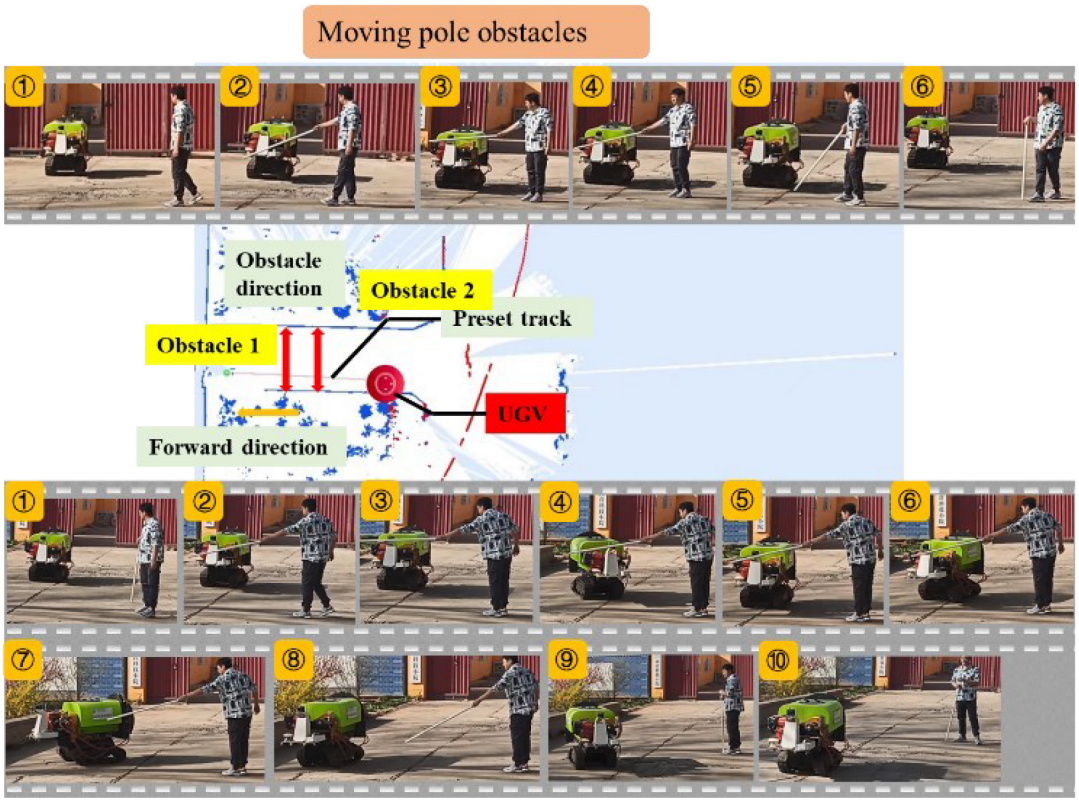

FIGURE 17
Experiment of moving pole obstacle.

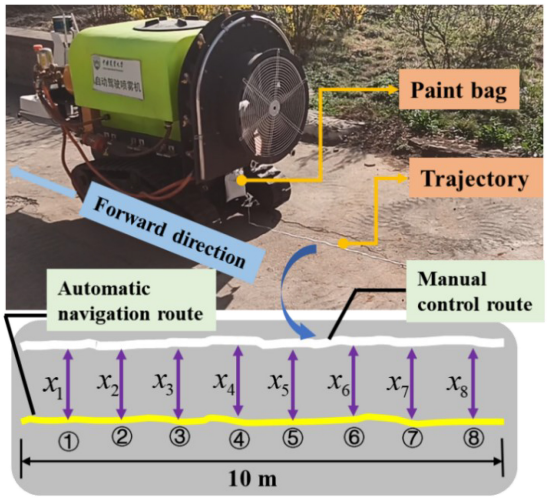

FIGURE 18
Navigation accuracy test scheme.

track tracking control. At this time, the paint bag hanging at the tail of the UGV was yellow paint, forming a yellow paint track line on the ground. The eight selected points were shown in Figure 19, and the measurement results were shown in Table 4. It can be concluded from Table 4 that the error of each point was within 15 cm in the eight selected points, and the average navigation accuracy was 13.625 cm, meeting the navigation accuracy requirements of the UGV working in the orchard.

Navigation accuracy experiment (Group 2)

The size of the operation area was about 10 m × 10 m in the second group of navigation accuracy experiment. The UGV was still manually controlled to form a white paint track line on the ground at first, and was then switched to the automatic mode for the tracking control, forming a yellow paint track line on the ground. Similarly, eight points were selected as the sampling points, as shown in Figure 20. The measurement results of each point were shown in Table 5, where it can be observed that the error of each point was still within 15 cm, and the average accuracy was 10.3125 cm, which, compared with the first group of accuracy experiments, was much improved. Given that the test site of the second group was flatter than the first group, there was less shaking of the UGV.

In the above two groups of accuracy experiments, the error of all sampling points was within 15 cm, and the navigation accuracy was about 10 cm in the relatively flat area, meeting the navigation requirements of the orchard spray system.

Spray experiment

The standard orchard demonstration area in Xiying Village was selected for the spray test. The specific parameters of the

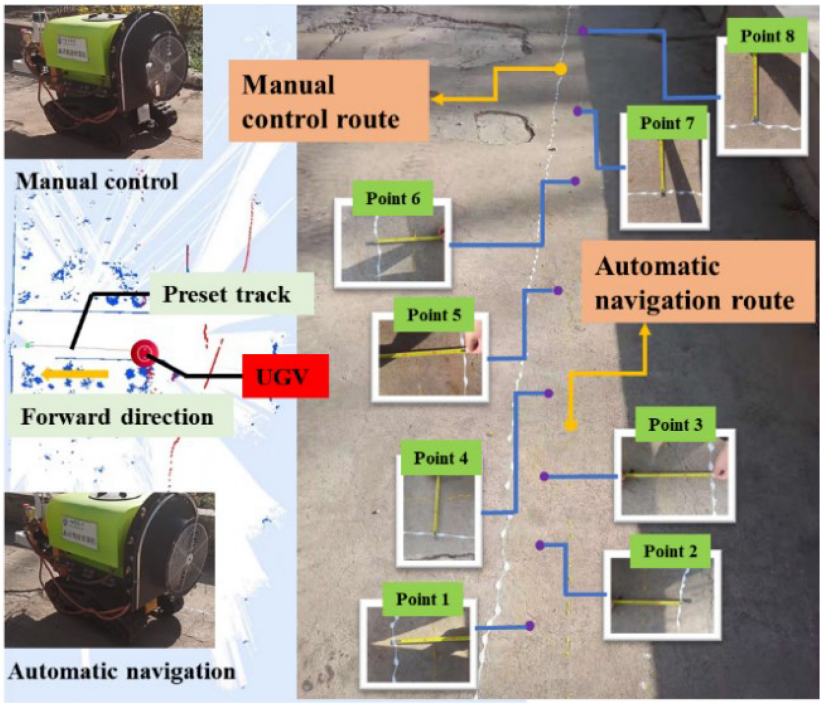

FIGURE 19
Navigation accuracy experiment (Group 1).

TABLE 3 List of nozzle parameters from No. 1 to 5.

Nozzle serial number	1	2	3	4	5
Spray pitch (cm)	8	8	8	8	8
Sprinkler angle (°)	0	18	36	54	72
Sprinkler height (cm)	30	46	60	75	88
Wind velocity (m/s)	20	20	20	20	20
Spray volume (L/min)	1.7	1.7	1.7	1.7	1.7

1, 2, 3, 4, and 5 represent the nozzle numbers of the nozzles of the orchard electric air-driven crawler sprayer.

TABLE 4 Navigation accuracy test value of each sampling point (Group 1).

Collection point	Point 1	Point 2	Point 3	Point 4	Point 5
Measured value	12 cm	14 cm	14 cm	15 cm	14 cm
Collection point	**Point 6**	**Point 7**	**Point 8**		**Average**
Measured value	13 cm	14 cm	13 cm		13.625 cm

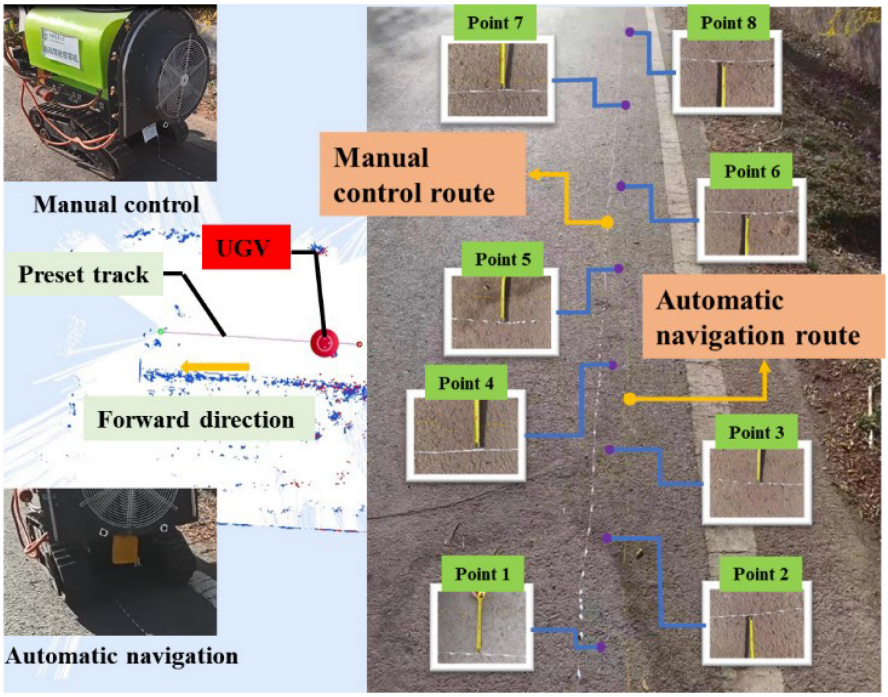

FIGURE 20
Navigation accuracy experiment (Group 2).

planting mode were as follows: The orchard area was more than 300 acres; the spacing of each row of fruit trees was about 3 m; the spacing between the trees was 1.5 m; the growth height of the fruit trees was 3 m; and the height of the trunk was about 0.5 m. The canopy of fruit trees was of small crown and sparse layer type, with a crown diameter length of 1.5 m, which could be divided into three layers in the vertical direction. The whole tree retained one main branch, while the side branches were less reserved and the branches were simple. The angle with the central trunk was between 60° and 80°, and the pruning method resembled the spindle shape.

Three trees set the five positions of east, south, west, north and middle in the canopy were selected. The first layer was 1 m away from the ground, and every 50 cm from the bottom to the top of the canopy was used as a layer, and then, the second layer and the third layer in the same way. Besides, the water-sensitive paper was fixed on the leaves of the east, south, west, north, and middle with an alligator clip, and three trees

TABLE 5 Navigation accuracy test value of each sampling point (Group 2).

Collection point	Point 1	Point 2	Point 3	Point 4	Point 5
Measured value	14 cm	12 cm	11 cm	10 cm	10.5 cm
Collection point	**Point 6**	**Point 7**	**Point 8**		**Average**
Measured value	10 cm	3 cm	12 cm		10.3125 cm

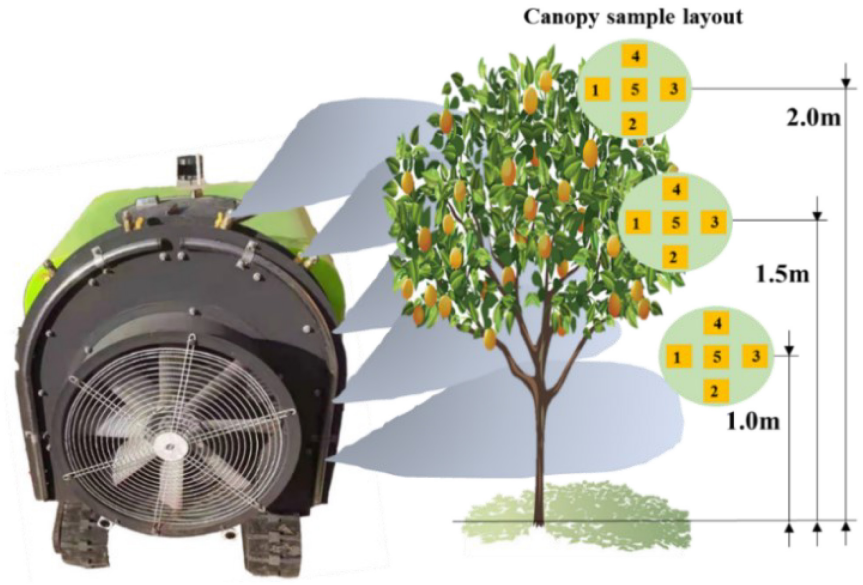

FIGURE 21
Spray diagram and collection point layout.

TABLE 6 Coverage of each sampling area under different layers.

Sampling point	1	2	3	4	5
Upper layer/100%	75.2	69.5	46.5	59.4	60.3
Middle layer/100%	50.7	33.9	43.3	58.5	45.2
Lower level/100%	79.2	43.5	27.5	56.5	51.4

were continuously arranged from west to east along the traveling direction of machines and tools. The arrangement of canopy droplet samples was shown in Figure 21. The scanner was used for obtaining the spray landing area of droplets on each piece of water-sensitive paper, and finally obtaining the coverage per unit area as shown in Table 6.

The coverage rate of the leaves of the canopy was almost no more than 80%, most of them gathering at 50%, when the spray effect was consistent with the growth conditions of the pear trees.

Conclusion

At this stage, automation technology has been widely transferred to orchard equipment, which has promoted the intelligent development of agricultural equipment. Aiming at the problem of automatic spray in complex and closed orchard environment, a 3D laser lidar orchard map construction strategy is adopted in this study, and at the same time, the air spray is selected to realize two atomization of the liquid medicine and improve the penetration rate of the droplets. The 3D laser lidar can facilitate all-weather orchard operations compared to the characteristics of visual navigation greatly affected by light, which is necessarily important for the large-scale occurrence of diseases and pests, also the urgent need for fast operation time. Millimeter wave radar is selected for obtaining multi-source information of obstacle avoidance, which improves the accuracy of obstacle avoidance. However, the autonomous navigation spray system developed in this study fails to take much account of the spray system, such as variable spray and profiling spray technology. To this end, the precision spray technology

will be further explored to achieve independent and accurate pesticide spraying in the orchard environment on the basis of automatic navigation.

Data availability statement

The original contributions presented in the study are included in the article/**Supplementary material**, further inquiries can be directed to the corresponding authors.

Author contributions

SW, JS, PQ, CY, HW, LZ, and WL: conceptualization, methodology, software, validation, formal analysis, investigation, resources, data curation, writing the original draft, reviewing and editing, and visualization. YL and XH: supervision, funding acquisition, and project administration. All authors contributed to the article and approved the submitted version.

Funding

This work was funded by the National Key Research and Development Program of China (Grant No. 2020YFD1000202), the National Modern Agricultural Industrial Technology System of China (Grant No. CARS-28-20), Sanya Institute of China Agricultural University Guiding Fund Project (Grant No. SYND-2021-06), and Deutsche Forschungsgemeinschaft (DFG, German Research Foundation)-328017493/GRK 2366.

Conflict of interest

The authors declare that the research was conducted in the absence of any commercial or financial relationships that could be construed as a potential conflict of interest.

Publisher's note

All claims expressed in this article are solely those of the authors and do not necessarily represent those of their affiliated organizations, or those of the publisher, the editors and the reviewers. Any product that may be evaluated in this article, or claim that may be made by its manufacturer, is not guaranteed or endorsed by the publisher.

Supplementary material

The Supplementary Material for this article can be found online at: https://www.frontiersin.org/articles/10.3389/fpls.2022.960686/full#supplementary-material

References

An, Q., Li, D., Wu, Y., and Pan, C. (2020). Deposition and distribution of myclobutanil and tebuconazole in a semidwarf apple orchard by hand-held gun and air-assisted sprayer application. *Pest Manag. Sci.* 76, 4123–4130. doi: 10.1002/ps.5968

Bergerman, M., Maeta, S. M., Zhang, J., Freitas, G. M., Hamner, B., Singh, S., et al. (2015). Robot farmers: Autonomous orchard vehicles help tree fruit production. *IEEE Robot. Autom. Mag.* 22, 54–63. doi: 10.1109/MRA.2014.2369292

Blok, P. M., van Boheemen, K., van Evert, F. K., IJsselmuiden, J., and Kim, G.-H. (2019). Robot navigation in orchards with localization based on Particle filter and Kalman filter. *Comput. Electron. Agricult.* 157, 261–269. doi: 10.1016/j.compag.2018.12.046

Boatwright, H., and Schnabel, G. (2020). "Evaluation of laser-guided air-blast sprayer on pest and disease control in peach orchards," in *Proceedings of the Meeting of the southern division of the American Phytopathological Society (APS)*, Vol. 110, Charleston, SC, 2.

Boatwright, H., Zhu, H., Clark, A., and Schnabel, G. (2020). Evaluation of the intelligent sprayer system in peach production. *Plant Dis.* 104, 3207–3212. doi: 10.1094/PDIS-04-20-0696-RE

Chen, M., Tang, Y., Zou, X., Huang, Z., Zhou, H., Chen, S., et al. (2021). 3D global mapping of large-scale unstructured orchard integrating eye-in-hand stereo vision and SLAM. *Comput. Electron. Agricult.* 187:106237. doi: 10.1016/j.compag.2021.106237

Emmi, L., Le Flécher, E., Cadenat, V., and Devy, M. (2021). A hybrid representation of the environment to improve autonomous navigation of mobile robots in agriculture. *Precis. Agricult.* 22, 524–549. doi: 10.1007/s11119-020-09773-9

Fei, Z., and Vougioukas, S. (2022). Row-sensing templates: A generic 3D sensor-based approach to robot localization with respect to orchard row centerlines. *J. Field Robot.* doi: 10.1002/rob.22072

Fox, R. D., Derksen, R. C., Zhu, H., Brazee, R. D., and Svensson, S. A. (2008). A history of air-blast sprayer development and future prospects. *Trans. ASABE* 51, 405–410. doi: 10.13031/2013.24375

Guevara, J., Cheein, F. A. A., Gené-Mola, J., Rosell-Polo, J. R., and Gregorio, E. (2020). Analyzing and overcoming the effects of GNSS error on LiDAR based orchard parameters estimation. *Comput. Electron. Agricult.* 170:105255. doi: 10.1016/j.compag.2020.105255

Ji, Y., Li, S., Peng, C., Xu, H., Cao, R., Zhang, M., et al. (2021). Obstacle detection and recognition in farmland based on fusion point cloud data. *Comput. Electron. Agricul.* 189:106409. doi: 10.1016/j.compag.2021.106409

Jones, M. H., Bell, J., Dredge, D., Seabright, M., Scarfe, A., Duke, M., et al. (2019). Design and testing of a heavy-duty platform for autonomous navigation in kiwifruit orchards. *Biosyst. Eng.* 187, 129–146. doi: 10.1016/j.biosystemseng.2019.08.019

Kragh, M., and Underwood, J. (2020). Multimodal obstacle detection in unstructured environments with conditional random fields. *J. Field Robot.* 37, 53–72. doi: 10.1002/rob.21866

Li, X., Tao, X., Zhu, B., and Deng, W. (2020). Research on a simulation method of the millimeter wave radar virtual test environment for intelligent driving. *Sensors* 20:1929. doi: 10.3390/s20071929

Li, Y., Iida, M., Suyama, T., Suguri, M., and Masuda, R. (2020). Implementation of deep-learning algorithm for obstacle detection and collision avoidance for robotic harvester. *Comput. Electron. Agricult.* 174:105499. doi: 10.1016/j.compag.2020.105499

Lin, G., Zhu, L., Li, J., Zou, X., and Tang, Y. (2021). Collision-free path planning for a guava-harvesting robot based on recurrent deep reinforcement learning. *Comput. Electron. Agricult.* 188:106350. doi: 10.1016/j.compag.2021.106350

Liu, S., Wang, X., Li, S., Chen, X., and Zhang, X. (2022). Obstacle avoidance for orchard vehicle trinocular vision system based on coupling of geometric constraint and virtual force field method. *Expert Syst. Applic.* 190:116216. doi: 10.1016/j.eswa.2021.116216

Liu, Y., Li, L., Liu, Y., He, X., Song, J., Zeng, A., et al. (2020). Assessment of spray deposition and losses in an apple orchard with an unmanned agricultural aircraft system in China. *Trans. ASABE* 63, 619–627. doi: 10.13031/trans.13233

Ma, Y., Zhang, W., Qureshi, W. S., Gao, C., Zhang, C., Li, W., et al. (2021). Autonomous navigation for a wolfberry picking robot using visual cues and fuzzy control. *Inf. Process. Agricult.* 8, 15–26. doi: 10.1016/j.inpa.2020.04.005

Mao, W., Liu, H., Hao, W., Yang, F., and Liu, Z. (2022). Development of a combined orchard harvesting robot navigation system. *Remote Sens.* 14:675. doi: 10.3390/rs14030675

Meng, Y., Zhong, W., Liu, Y., Wang, M., and Lan, Y. (2022). Droplet distribution of an autonomous UAV-based sprayer in citrus tree canopy. *J. Phys. Conf. Ser.* 2203:012022. doi: 10.1088/1742-6596/2203/1/012022

Owen-Smith, P., Perry, R., Wise, J., Raja Jamil, R. Z., Gut, L., Sundin, G., et al. (2019). Spray coverage and pest management efficacy of a solid set canopy delivery system in high density apples. *Pest Manag. Sci.* 75, 3050–3059. doi: 10.1002/ps.5421

Ravankar, A., Ravankar, A. A., Rawankar, A., and Hoshino, Y. (2021). Autonomous and safe navigation of mobile robots in vineyard with smooth collision avoidance. *Agriculture* 11:954. doi: 10.3390/agriculture11100954

Rovira-Más, F., Saiz-Rubio, V., and Cuenca-Cuenca, A. (2020). Augmented perception for agricultural robots navigation. *IEEE Sens. J.* 21, 11712–11727. doi: 10.1109/JSEN.2020.3016081

Stefas, N., Bayram, H., and Isler, V. (2016). Vision-based UAV navigation in orchards. *IFAC Papersonline* 49, 10–15. doi: 10.1016/j.ifacol.2016.10.003

Vrochidou, E., Oustadakis, D., Kefalas, A., and Papakostas, G. A. (2022). Computer vision in self-steering tractors. *Machines* 10:129. doi: 10.3390/machines10020129

Wang, C., Liu, Y., Zhang, Z., Han, L., Li, Y., Zhang, H., et al. (2022). Spray performance evaluation of a six-rotor unmanned aerial vehicle sprayer for pesticide application using an orchard operation mode in apple orchards. *Pest Manag. Sci.* 78, 2449–2466. doi: 10.1002/ps.6875

Wang, S., Chen, J., and He, X. (2022). An adaptive composite disturbance rejection for attitude control of the agricultural quadrotor UAV. *ISA Trans.* Online ahead of print, doi: 10.1016/j.isatra.2022.01.012

Wang, Z., Yu, G., Zhou, B., Wang, P., and Wu, X. (2021). A train positioning method based-on vision and millimeter-wave radar data fusion. *IEEE Trans. Intell. Transport. Syst.* 23, 4603–4613. doi: 10.1109/TITS.2020.3046497

Ye, Y., He, L., Wang, Z., Jones, D., Holinger, G. A., Taylor, M. E., et al. (2018). Orchard manoeuvring strategy for a robotic bin-handling machine. *Biosyst. Eng.* 169, 85–103. doi: 10.1016/j.biosystemseng.2017.12.005

Zhang, S., Guo, C., Gao, Z., Sugirbay, A., Chen, J., Chen, Y., et al. (2020). Research on 2d laser automatic navigation control for standardized orchard. *Appl. Sci.* 10:2763. doi: 10.3390/app10082763

frontiers | Frontiers in Plant Science

TYPE Review
PUBLISHED 08 August 2022
DOI 10.3389/fpls.2022.870956

OPEN ACCESS

EDITED BY
Lei Shu,
Nanjing Agricultural University, China

REVIEWED BY
Xing Wei,
Purdue University, United States
Soumi Mitra,
Baylor College of Medicine, United States
Tania Prinsloo,
University of Pretoria, South Africa

*CORRESPONDENCE
Jean Paul Douzals
jean-paul.douzals@inrae.fr
Yubin Lan
ylan@scau.edu.cn

SPECIALTY SECTION
This article was submitted to Sustainable and Intelligent Phytoprotection, a section of the journal Frontiers in Plant Science

RECEIVED 07 February 2022
ACCEPTED 11 July 2022
PUBLISHED 08 August 2022

CITATION
Chen P, Douzals JP, Lan Y, Cotteux E, Delpuech X, Pouxviel G and Zhan Y (2022) Characteristics of unmanned aerial spraying systems and related spray drift: A review. *Front. Plant Sci.* 13:870956. doi: 10.3389/fpls.2022.870956

Characteristics of unmanned aerial spraying systems and related spray drift: A review

Pengchao Chen[1], Jean Paul Douzals[2]*, Yubin Lan[1]*, Eric Cotteux[2], Xavier Delpuech[3], Guilhem Pouxviel[2] and Yilong Zhan[1]

[1]National Center for International Collaboration Research on Precision Agricultural Aviation Pesticides Spraying Technology, College of Electronic Engineering and Artificial Intelligence, South China Agricultural University, Guangzhou, China, [2]UMR ITAP, National Research Institute for Agriculture, Food and Environment, Université de Montpellier, Montpellier, France, [3]Institut Français de la Vigne et du vin (IFV), Montpellier, France

Although drift is not a new issue, it deserves further attention for Unmanned Aerial Spraying Systems (UASS). The use of UASS as a spraying tool for Plant Protection Products is currently explored and applied worldwide. They boast different benefits such as reduced applicator exposure, high operating efficiency and are unconcerned by field-related constraints (ground slope, ground resistance). This review summarizes UASS characteristics, spray drift and the factors affecting UASS drift, and further research that still needs to be developed. The distinctive features of UASS comprise the existence of one or more rotors, relatively higher spraying altitude, faster-flying speed, and limited payload. This study highlights that due to most of these features, the drift of UASS may be inevitable. However, this drift could be effectively reduced by optimizing the structural layout of the rotor and spraying system, adjusting the operating parameters, and establishing a drift buffer zone. Further efforts are still necessary to better assess the drift characteristics of UASS, establish drift models from typical models, crops, and climate environments, and discuss standard methods for measuring UASS drift.

KEYWORDS

unmanned aerial spraying systems, spray drift, downwash airflow, drift measurement, relative movement

Introduction

Unmanned Aerial Spraying Systems (UASS) consist drones that carry a spraying device. They are operated by a control system and comprise sensors to spray plant protection products. UASS have been developed rapidly during recent years as a spray tool for the application of plant protection products (He et al., 2018; Wang L. et al., 2022). According to existing reports, the use of UASS to carry out chemical spraying covers most parts of the world. In East Asia, where field conditions are limiting and

where the original plant protection equipment is still in use, there is an urgent demand for UASS on the market (Lan and Chen, 2018). The number of UASS has exploded in this region. In 2014 China owned less than 1,000 plant protection drones, with an annual operating area lesser than 0.28 million ha. By the end of 2020, the number of drones in China reached 106,000, with a total yearly working area of 64 million ha (Zhang et al., 2021). In Europe, due to restrictions in application of plant protection products with aerial technology (128/CE/2009), UASS have not yet been used at a large scale yet (Reger et al., 2018). However, in mountainous grape-growing areas, producers and researchers have shown strong interest for UASS (Sarri et al., 2019; Bloise et al., 2020). The UASS can spray in the hilly and steep slope areas without being restricted by field obstacles (Delpuech et al., 2022). This has positive practical significance for separating the applicator from the tanks and replacing the backpack sprayer (Wang et al., 2020). In addition, although agricultural aviation is active on the American continent, with mainly manned fixed-wing aircraft, which are widely used in the United States, Canada, and Brazil, experimental research on UASS is also being carried out (Teske et al., 2018; Richardson et al., 2019; Li et al., 2021a,b).

UASS boast advantages in pesticide spraying. On the one hand, compared to any other ground spraying technique, the drone isolates the tank from the applicator, thus favoring operator safety (Qin et al., 2016; Morales-Rodríguez et al., 2022). As with other aerial techniques, physical damage to crops can be avoided. It can easily spray above high standing crops (bananas, corn, and rubber) and operate over complex terrain (steep slopes, terraces) where backpack sprayers are confronted to critical operator issues regarding tediousness and safety (Lan and Chen, 2018; Cavalaris et al., 2022). Moreover, exploitation costs are reduced by shortening the time of spray application and by lowering the amount of plant protection products applied (Morales-Rodríguez et al., 2022). Carbon-based fuel can also be replaced by electricity derived from renewable energies. It thus lowers the carbon impact and save costs since carbon-based fuel can be replaced by energy that, technically, could be easy to generate in a farmyard (Hussain and Nishat, 2022). Currently, UASS has been widely used over flat fields or terraces with low-lying crops, including grain crops such as wheat, corn, rice, and cash crops such as cotton, citrus, and grapes (Pan et al., 2016; Sarri et al., 2019; Wang L. et al., 2019; Chen et al., 2020a; Meng et al., 2020; Chen H. et al., 2021). Spraying with UASS has proven to be feasible in the prevention and control of crop diseases and pests by spraying insecticides or fungicides (Meng et al., 2018; Yan et al., 2022). In the case of trees grown on steep slopes, the quality of the application is partially limited by the flight altitude of the sensor and terrain following technology with the help of lidar for example (Meng et al., 2022b; Wang C. et al., 2022). Moreover, a denser crop canopy also presents limitations in terms of droplet penetration (Chen et al., 2020b; Yu et al., 2022). For these latter reasons, the application with UASS on 3D crops in mountainous and hilly areas is still being investigated.

Although the market is open to UASS, the risk of environmental drift caused by drone spray is also noteworthy (Wang et al., 2020a, 2021). The risk of spray drift could be closely related to operational efficiency and operating parameters. On one hand, the operating efficiency of a single UASS has increased from 2 to 3 hectares per hour to the current 15–20 hectares per hour within the past 5 years (Chen H. et al., 2021). The result of single-machine efficiency implies that more chemicals can be sprayed in a short time (Wang Z. et al., 2022), however more pesticide droplets may also be scattered in the air (Liu et al., 2021). The overall environmental risks due to efficiency improvements need to be assessed. On another hand, drift can be minimized when low flying altitude is applied (1–3 m). Due to the varying growth heights of crops, the actual flying altitude is rather generally comprised between 3 and 10 m (Wang et al., 2019b, 2021). The flight speed generally ranges between 1 and 6 m/s (Chen H. et al., 2021). Flying altitude and speed may cause the droplets to move in the air for a longer time. Nevertheless, they are also susceptible to the natural lateral wind and environmental climate, forcing which result in drift (Chen H. et al., 2021).

Studies on drone drift include theoretical (CFD simulations) and experimental studies. Current research on theoretical analysis focuses on the changes in the wind field of the UASS rotor and the movement of droplets affected by the wind field using calculations and simulations (Zhu et al., 2019; Tang et al., 2020, 2021; Zhang et al., 2022). Experimental research is mainly carried out in wind tunnels or in the field combined, with present-day climate environment and crop types. Current experimental studies on drift include the characteristics of UASS drift, drift distance, and the influence of operating parameters or spraying systems on the drift (Wang et al., 2020, 2020a, 2021). However, current research on UASS drift is still scarce. Data on the spray drift of drones and their impact on the environment are scarce, and the factors affecting drift are still being studied. Existing technical standards do not address the drift of UASS, including how to test drift in the field and wind tunnels (Wang et al., 2020). In addition to the European ban on aerial sprayers, no relevant country or region implements a specific legislation on drone drift (Reger et al., 2018).

Although drift is not a new concern, it requires further attention toward new equipment that is being widely used. This literature review focuses on the emerging issue of drift caused by UASS. Articles from scientific journals were searched and analyzed from 2014 by setting keywords, such as UAV/UASS plus spraying or drift, etc., including a part of Chinese literature indexed by the engineering index. Section "Characteristics of unmanned aerial spraying systems and spray drift" describes UASS platforms, the spraying systems and the characteristics of spray drift generated by drones. Drift evaluation protocols test methods developed for drones, and

the possible environmental risks are also included. Section "Factors influencing unmanned aerial spraying systems drift" rather focuses on more fundamental processes where spraying is combined with the displacement of the UASS. This chapter reviews the factors that affect the drift of the UASS including atomization, downwash airflow, and the relative movement. The atomization factor caused by the structural design of the spraying system includes the selection of nozzles, the layout of nozzles and rotors, and the properties of the liquid (Chen P. et al., 2021). For the downwash airflow, the number and size of rotors and payload were investigated. The relative movement refers to changes in the UASS flight process that may either come from itself or from the surrounding environment, including the UASS flight parameters and natural lateral wind (Wang et al., 2020). The issue of evaporation during spraying is not considered in this article. Finally, since current research on the drift of UASS sprayers is still limited, the lack of research studies and the future research that needs to be developed are discussed in Section "Discussion and further recommendations."

Characteristics of unmanned aerial spraying systems and spray drift

Characteristics of unmanned aerial spraying systems

Unmanned aerial spraying systems platform

Fuel-powered agricultural helicopters first appeared in Japan in the 1980s (Chen H. et al., 2021). With the recent technical developments, electrical single-rotor or multi-rotor models have gradually replaced fuel-powered helicopters (He et al., 2017; Chen H. et al., 2021). **Table 1** summarizes the technical parameters of a few typical UASS. The structure of electrical rotary-wing plant protection UASS mainly comprises the rotor, tank, spraying system, control system, environmental sensor, energy system, etc. The rotor provides lift for the UASS and at the same time generates a unique downwash wind field (Zhan et al., 2022). Drone rotors available on the market are built with single rotors, two rotors, four rotors, six rotors, and eight rotors. The tank is the major element of UASS, and its volume is related to the maximum payload weight. According to **Table 1**, the tank volume in new models has been increasing in recent years. The initial payload range is 8–15 L, and some current models can reach up to 20–40 L. The control system and environmental sensing sensors are the fastest elements of the drone update iteration, evolving from the initial manual control mode, semi-automatic (ex. Trajectory from Point A to Point B mode) control mode to fully autonomous mode. Positioning sensors have evolved from the Global Navigation Satellite System (GNSS) with meter-level errors to Real Time Kinematic (RTK) with centimeter-level errors. In addition, air pressure sensors, ultrasonic sensors, radar, binocular vision, and other sensors used for altitude determination, distance measurement, and obstacle avoidance are constantly updated (Wang L. et al., 2019; Chen H. et al., 2021).

Spraying system

The nozzle represents an essential part of the UASS spraying system. As illustrated in **Figures 1**, **2**, commonly used nozzles for UASS include hydraulic and centrifugal nozzles (He et al., 2018). Hydraulic nozzles are derived from ground spray equipment and are currently the most common type of nozzle for UASS. The chemical solution is atomized through the nozzle cavity under a given pressure and forms a liquid film. The liquid film is continuously stretched and formed into a filamentary shape under the pressure difference. When the liquid film collides with relatively static air, it splits into fine droplets (ASAE ANSI/ASABE, 2020; He et al., 2018). The hydraulic nozzle atomization can be modified by adjusting the pressure, changing the surface tension of the solution or equipping the nozzle with air inclusion or Venturi nozzles (Al Heidary et al., 2014).

The centrifugal spraying system adopted by UASS mainly consists of a rotary disc centrifugal nozzle. The rotary disc-type centrifugal nozzle comprises multiple radial grooves on the inner wall of the rotary disc (Qingqing et al., 2017). The groove ends are generally equilateral pins. The existence of radial grooves can reduce the slippage of the solution and allow the solution and rotary disc to share similar circumferential speeds (He et al., 2018). The solution in the nozzle enters the high-speed rotating turntable through the draft tube, and the droplets fly out in a spiral tangential direction along the edge of the turntable under the action of centrifugal force, forming droplets of uniform size (Gao, 2013; Qingqing et al., 2017). With a centrifugal nozzle, the spray mix relies on gravity to enter the turntable and is ejected from the radial direction under centrifugal force on radial pins (Qingqing et al., 2017). The required spray pressure is therefore, slight, resulting in a narrow droplet spectrum but also a weak droplet penetration. However, as the droplets flowing out of the nozzle do not interfere with one another, the distribution of droplet deposition is more uniform and controllable (Hayashi and Takeda, 1986). The spectrum of the atomized droplets can be adjusted by controlling the rotational speed of the spray disc in order to meet different droplet size requirements. Under the different voltages, the rotation speed of the nozzle can vary from 0 to 17,000 revolutions per minute (RPM) (Wang et al., 2020). The spray disc is not easy to clog and is particularly suitable for spraying wettable powders and suspension agents with low solubility (Qingqing et al., 2017; Wang et al., 2020). It is adapted to a high concentration of UASS chemical liquid. However, centrifugal nozzles produce fine droplets, and as their direction of movement is horizontal, the risk of drift is high (Wang et al., 2020).

TABLE 1 The technical parameters of some typical UASS.

Model (Manufacturer, release time)	Dimensions (Frame arms unfolded, mm)	Rotors (Number*diameter *pitch, mm)	Payload (Kg)	Fully loaded weight (Kg)	Geolocation technology
T30 (DJI, 2021)	2,858 × 2,685 × 790	6*38*508	30	66.5	RTK,Horizontal ± 10 cm, vertical ± 10 cm
T16 (DJI, 2019)	2,520 × 2,212 × 720	6*33 × 177.8	16	40.7	
MG-1P (DJI, 2018)	1,460 × 1,460 × 578	4*21*177.8	10	22.5	GNSS/RTK
V40 (XAG, 2021)	2,795 × 828 × 731	2*47*457.2	16	44	RTK,Horizontal ± 10 cm, vertical ± 10 cm
P40 (XAG,2021)	2,110 × 2,127 × 555	4*40*352.1	20	45	
P20 (XAG, 2019)	1,830 × 1,822 × 452	4*33*292.1	10	28	

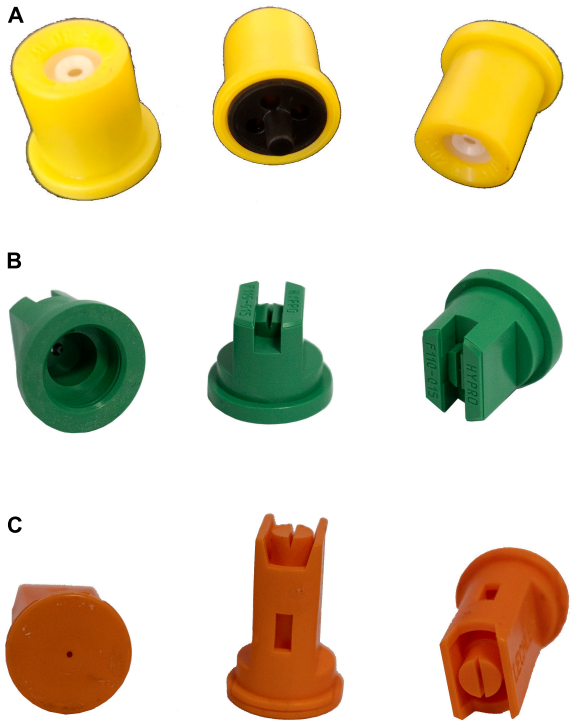

FIGURE 1
Examples of Hydraulic nozzles. **(A)** Hollow cone nozzle (TR80-02c, Lechler), **(B)** flat fan nozzle (HYPRO, 110-015), **(C)** air induction nozzle (IDK 120-01, Lechler).

In the early stages of UASS development, the flow rate could be modified by changing the nozzle type or adjusting the flight speed (Chen et al., 2020a). However, changing the nozzle implies a change in the size of the droplets. The influence of the flight speed on the droplet distribution and drift can thus be ignored. At present, the flow rate can be essentially modified by increasing the number of water pumps and nozzles and by adjusting the pump flowrate. The number of pumps and nozzles carried by drones has also been increasing as operational efficiency is being developed (Chen H. et al., 2021).

According to **Table 2**, the difference between both spraying systems is the range of values of the nozzle Volume Median Diameter (VMD). For the hydraulic spraying system, the droplet size is affected by the nozzle type, operating pressure, and the nature of the solution. For centrifugal nozzles, the significant factor is the speed of the spray plate. The droplet size is strongly related to drift (Al Heidary et al., 2014). Choosing a nozzle with a larger VMD can reduce the risk of drifting in the spraying system, such as air induction nozzles that are widely used in boom sprayers. However, choosing anti-drift nozzles on UASS may not always be suitable for crop protection. Due to load limitation, the improvement of the spraying quality of UASS implies a reduction in the atomized particle size in order to ensure a higher droplet density and coverage. However, by

FIGURE 2
Centrifugal nozzle (2018, XAG Co., Ltd).

reducing the size of the droplets, the risk of drift is increased. For UASS, improving the spray quality and reducing the risk of drift have contradictory effects.

Characteristics of unmanned aerial spraying systems spray drift

Downwash and outside airflow

The most significant feature of rotary-wing UASS is to carry one or more rotors (Li J. et al., 2018). However, rotor movement can also cause vortex or turbulence (Fengbo et al., 2017; Wang et al., 2020). When the wing generates a positive lift due to the pressure difference between the upper and lower wing surfaces, the high-pressure airflow below follows the wingtips, then rolls upwards and flows toward the lower pressure upper side of the wing, forming a spiral-shaped vortex (Wen et al., 2018). Wingtip vortices are not unique to drones, and they can also occur in helicopters and fixed-wing aircraft (Mickle, 1996). However, the high-speed rotor of the drone will cause the movement of the droplets under the rotor to be more complex. With a stronger rotor downwash, the vortex in flight is stronger (Zhan et al., 2022). Under the entrapment of the vortex, a greater number of droplets spread to both sides of the route, further worsening the downwind drift (Wang et al., 2020a). This vortex generated by the joint action of the rotor downwash airflow and the outside air is a major factor affecting the drift of UASS spray (Tang et al., 2021). Two types of outside airflow exist: the relative air movement caused by the drone's forward speed and the natural wind. Wen et al. (2018) showed that a spiral wake occurs behind the aircraft when the flight speed exceeds 3 m/s. The higher the speed, the longer the spiral vortex prevails in the air. Moreover, when the drone hovers, instead of drifting, the droplets fall directly to the ground with the downwash of the main rotor (Wen et al., 2018). Results concerning hovering situations are derived from software simulations, therefore, the same observations might not be made in the case of field trials. On one hand, even when no environmental wind blows, fine droplets sprayed by UASS with centrifugal nozzles can drift beyond 4 m downwind due to the effect of the rotor wind and the Brownian motion (Wang et al., 2020). On the other hand, since the UASS operate above the canopy droplets in the air can easily drift outside the crop with a crosswind (Li L. et al., 2018). Consequently, UASS drift cannot be totally avoided under the combined effects of the rotor wind field, natural wind, and sprayer movement.

Unmanned aerial spraying systems drift measurement method

Drone drifting still lacks a standard testing method, and existing research mainly refers to the ISO22866 standard (Iso, 2005). The drift phenomenon can be evaluated through sedimentation and/or airborne drift according to the spatial position of collectors (Grella et al., 2017). Sedimentation drift involves the collection of ground deposition at different distances downwind that is typically used to assess water course exposure (Wang J. et al., 2018). Airborne drift consists of the collection of droplets during their transport in the atmosphere typically at several meters from the field edge and at different heights reaching several meters above the ground (Wang et al., 2021). This airborne drift can be used to evaluate the transport of droplets and further consequences in terms of resident exposure (Al Heidary et al., 2014).

In the existing literature, UASS drift tests are mainly carried out in the field (Wang et al., 2019a, 2020, 2021). **Table 3** summarizes the test methods from certain field tests found in the literature. The drift collection is made in the downwind direction and perpendicular to the UASS flight direction (Wang et al., 2020). For the different spatial positions of the collectors, spray drift is detected by extracting a dye tracer from the polyethylene wire, active sampler or rotary impactors for catching airborne drift. Petri dishes, Mylar cards or filter papers are used as collectors to sample sedimentation drift (Wang et al., 2019a, 2021; Ahmad et al., 2022). According to the statistics in **Table 3** provided by the literature, the sampling points of sediment drift are usually arranged in non-target areas ranging from 1 to 50 m, while airborne drift includes one or more sampling points within 50 m.

The He research team proposed a 3D mass balance test method consisting of a 5 m × 5 m × 2 m tunnel frame with Ø2 mm drift collection lines on four sides (left–right–ground–top) to collect the droplets sprayed inside the tunnel by a UASS () (Wang et al., 2016). Quantitative information can thus be obtained along the four directions, although information is lacking at different distances on the ground. Wang et al. (2021) used a near-ground drift test platform with Petri dishes to collect sedimented droplets at different distances downwind from the UASS route. Wang et al. (2019a) and Wang et al. (2020) arranged the collection poles at a height of 1 m within a 2–50 m range in the downwind direction and fixed Mylar plates (5 × 8 cm) to each collection pole. The

TABLE 2 Characteristics and comparison of different UASS spraying systems.

Spraying system	Nozzles	VMD (μm)	Droplet size adjustment method
Hydraulic spraying system	Flat fan	110–200	Adjust pressure, solution properties, nozzle type
	Hollow cone	90–150	
	Air induction	220–400	
Centrifugal spraying system	Centrifugal	90–300	Change the speed of the spray plate

TABLE 3 Field test methods for UASS spray drift evaluation in the literature.

UASS sprayer	Fluorescence tracer	Testing method (Sampling location)	Material	References
Z-3	Rhodamine-B	Sediment (2–100 m) and Airborne (2, 50 m)	polyester card (ϕ = 90 mm) and polyester fiber (ϕ = 1 mm)	Xinyu et al., 2014
Yamaha R-MAX II	/	Sediment (7.5–48 m) and Airborne	Deposition sheet (40 * 25 cm) and SKC AirCheck HV30 sample pump	Brown and Giles, 2018
3WQF120-12	Brillant sulfoflavin dye (BSF)	Sediment (1–20 m) and Airborne (5,10,20 m)	Petri dishes and rotary impactors	Wang X. et al., 2018
3WQF80-10	BSF	Airborne drift	A cuboid aluminum sampling frame (5 m × 5 m × 2 m)	Wang X. et al., 2018
X-4	Tartrazine solution	Sediment and Airborne (5,10 m)	filter paper and water sensitive paper	Li J. et al., 2018
3QF120-12	Rhodamine-B	Sediment (1–50 m) and Airborne (10,25,50 m)	mylar card (10 × 8 cm), monofilament line (Ø = 0.45 mm)	Wang X. et al., 2018
MG-1S	Allure red	Sediment drift (0.5–12.5 m)	Mylar cards	Chen et al., 2020a,b; Chen S. et al., 2020
P20 (XAG)	Rhodamine-B	Sediment (2–50 m) and Airborne (2,12 m)	mylar plate (5 × 8 cm^2) and monofilament line (φ = 0.6 mm)	Wang et al., 2020
3WQF120-12, 3WM6E-10, 3WM8A-20	Pyranine	Sediment (2 m) and Airborne (2–20 m)	Petri dishes, rectangle collection frames with polyethylene tubes (5.5 × 2.0 m), rotary samplers	Wang et al., 2021

airborne drift near the ground was estimated after recovering the Mylar plates. Assessing sedimentation drift is the most common method in spray drift research, and it reflects the real value of ground drift at different distances from the downwind direction. However, data on the vertical spatial distribution of drift is still lacking. In order to efficiently understand the spatial distribution of droplets on the downwind side of a UASS flight path, both sediment and airborne drift need to be considered.

Since field tests can be easily affected by weather conditions, wind tunnels are a solution to provide stable and controllable wind conditions, allowing for repeatable operations (Iso International Standard, 2009). Wang et al. (2020b) placed the single rotor and nozzle of the drone in a wind tunnel. The rotor refers to one single spray unit of a quadrotor UASS "3WQFTX-10" (Anyang Quanfeng Aviation Plant Protection Technology Co., Ltd., China), with a size of 76.2 cm. Ling et al. (2018) placed a UASS carrying a spraying system inside a 2 m × 2 m wind tunnel for spray testing. The UASS model used here was a miniature version. Although these studies attempted to test the UASS in a wind tunnel, the use of a single rotor or the reduction in the size of the UASS may differ from reality. A research team from South China Agricultural University and Nanjing Research Institute for Agricultural Mechanization, China, built a set of UASS test platforms (as illustrated in **Figure 3**). The test platform can hold up to 4, 6, and 8 rotors (adjusted as needed). The rotor speed can be adjusted within the range of 600–2,500 RPM. The spraying system is located under the rotor, and can be installed with a hydraulic spraying system or a centrifugal spraying system, where the position of the nozzle relative to the rotor can be adjusted freely. In addition, the test platform can adjust the pitch angle from –30° to 30°. Liu et al. (2021) combined the UASS platform with the wind tunnel and placed the platform at the extremity of the wind tunnel in order to build an indoor drift test device. Although the sampling area is not located inside the wind tunnel, this

FIGURE 3
The UASS spraying test bench in South China Agricultural University.

method is a good attempt to reduce disturbances from natural environmental conditions.

Potential environmental risks

The UASS uses low application volume rates for spraying because of the limited payload (Zhan et al., 2022). Compared with ground sprayers, the amount of spray per unit area of drones is less even though the rate of active substance can be equivalent (Qin et al., 2016; Wang G. et al., 2019). The drift rate (as normalized by the application volume, ISO 22866) is therefore not significantly reduced. The conclusions of the study by Wang G. et al. (2019) are that pesticide droplets from multi-rotor drones drift further away than with a traditional backpack sprayer. In addition, the amount of drift in the air is greater (Wang G. et al., 2019). Indeed, according to a study by Li L. et al. (2018) the multiple rows of vertical crop canopies can effectively prevent droplets from moving during ground equipment spraying, thus resulting in a lower extent of drift outside the crop than with UASS. The Wang field experiment study also demonstrated that the UASS drift of almost all treatments at 50 m was lower than the detection limits, and that the drift distance of the UASS model was much shorter than that of an aerial manned aircraft sprayer (Wang et al., 2020). However, the above conclusions are particular cases that depend on the spraying system, crop type and operation scenario.

Xu et al. (2020) performed preliminary research on applicator exposure in a rice paddy by multi-rotor UASS. They clearly highlighted that the risk of exposure using UASS applicators was almost zero due to the separation between the applicator and application machine. In contrast, backpack sprayer application resulted in entire body exposure of the applicator to the pesticide. Yan et al. (2021) compared the amount of insecticide droplet drift with the mortality of bees for multi-rotor plant protection UASS and for electric backpack sprayers. After pesticide application by the multi-rotor drone and electric backpack sprayer, the droplet deposition at a distance of 5 m downwind was 0.107 9 $\mu g\ cm^{-2}$ and 0.002 2 $\mu g\ cm^{-2}$ respectively. The number of bee deaths caused by the plant protection drone application drift was 62.9 fold that of the electric backpack sprayer (Yan et al., 2021). Current UASS drift research focuses on sediment and airborne drift, while the impact on non-target organisms is still limited. Further tests are still necessary to evaluate the environmental risks of drone drift.

Factors influencing unmanned aerial spraying systems drift

Atomization and sprays

Nozzles

The nozzle is at the core of the spraying system as it plays a key role in spray atomization. Spray atomization refers to the process of spraying a liquid into a gas medium at high speed through a nozzle, dispersing and fragmenting it, and finally forming fine particle droplets (He et al., 2018). Both the size of the droplets generated by atomization and the proportion of fine droplets have an impact on the drift (Al Heidary et al., 2014). In the spraying process of ground spray equipment, air induction fan nozzles are used in specific anti-drift scenarios. **Table 4** summarizes drift test results from UASS equipped with different nozzles in the field. Regardless of the different UASS models and test areas, IDK 120-015 presents a better anti-drift effect than TR 80-0067. Hollow cone nozzles produce finer droplets and are often used for pest control in orchards; IDK nozzles produce larger droplet sizes than flat fan nozzles. The average VMD (DV50) values of IDK 120-015 and TR 80-0067 in this test were 114.9 and 312.6 μm, respectively, and the proportions of droplets with a particle size smaller than 75 μm were 16.1 and 1.8%, respectively. The air induction nozzle can produce coarser droplets, thus reducing the risk of droplet drifting (Wang et al., 2020a).

A correct selection of nozzles has significant effects in reducing drift (Herbst et al., 2020; Wang et al., 2020). According to **Table 4** the result of 90% of total sedimentary drift locations correlates strongly with droplet size (Dv50). The influence of the nozzle on drift depends on the droplet size (Dv50) produced by atomization. The larger the droplet size, the better anti-drift performance (Wang et al., 2020). Larger droplets, which hardly moved upwards with the vortex, traveled much shorter distances and floated at lower altitudes. When the size of the droplets increased, their maximum drifting distance gradually decreased and was less affected by crosswind speed and direction (Wang J. et al., 2018, Wang et al., 2020, 2021). This conclusion has been verified in several of the studies presented in **Table 4**. When the crosswind blew from the right-hand side, large droplets (200

TABLE 4 Comparison of the 90% drift distance with different nozzles and UASS in the literature.

Nozzles	UASS	Dv50/μm	Wind speed (m/s)	Distance 90% of total sedimentary drift (m)	References
Centrifugal nozzle (XAG company)	P20 (4-Rotor)	100	1.16 ± 0.06	13.2	Wang et al., 2020
		150	1.30 ± 0.05	12.0	
		200	0.61 ± 0.03	5.7	
Hollow cone nozzle, TR 80-0067	3WQF120-12 (Helicopter)	114.9 ± 0.7	3.31 ± 0.17	9.99	Wang et al., 2021
	3WM6E-10 (6-Rotor)		3.79 ± 0.58	11.53	
	3WM8A-20 (6-Rotor)		3.47 ± 0.37	11.70	
Air-injector nozzle, IDK 120-015	3WQF120-12 (Helicopter)	312.6 ± 1.8	3.11 ± 0.40	9.13	
	3WM6E-10 (6-Rotor)		3.45 ± 0.46	7.90	
	3WM8A-20 (6-Rotor)		3.37 ± 0.56	13.62	
Flat fan nozzle, LU 120-02	3WQF120-12	268.6	2.82 ± 0.76	10.05	Wang J. et al., 2018

and 400 μm) tended to deposit faster and closer to the swath, while fine droplets (50 and 100 μm) were displaced by the crosswind with a strong non-uniform spatial distribution and a tendency to float toward the far left-hand side (Tang et al., 2021). The drift distance of droplets gradually decreases as the droplet size increases. Research by Wang et al. (2020) shows that large droplets are more affected by gravity and mainly deposit on the lower half of the 2 m, while fine droplets remain suspended in the air and are less affected by gravity, thus leading to a higher slope of airborne drift at 12 m.

Layout of nozzles

The location of the nozzle under the rotor affects the movement of the droplets (Chen H. et al., 2021). As illustrated in the **Figure 4**, four standard layouts of rotors and nozzles are possible. (i) The nozzle can be located directly below the rotor, (ii) the nozzle can be located directly below the rotor (extended), (iii) the nozzle can be located inside the rotor, or (iv) the nozzle can be separated from the rotor (spray boom). However, studies on the impact of the spatial layout of rotors and nozzles on spray drift are still scarce. The typical nozzle arrangements are spray boom and vertical suspension under the rotor. The sensitivity to spray drift depends on the position of the nozzle. Indeed, the nozzles at the two extremities of the boom are sensitive to the rotor vortex. The closer the nozzle to the wingtip of the rotor, the greater the amount of droplets drawn by the wingtip vortex (Wang J. et al., 2017). To reduce spray drift, the length of the boom (similar to **Figure 4D**) should not be greater than the diameter of the rotor (Chen H. et al., 2021) as has been advised for larger aerial spraying systems. A reduction in the distance between nozzles can also decrease the droplet drift caused by wingtip vortices (Wen et al., 2018).

Adjuvant and formulation

Adjuvant can significantly reduce the surface tension of the solution (Meng et al., 2021, 2022a). In a field trial study, Silwett DRS-60, ASFA + B, T1602, Break-thru Vibrant, QF-LY and Tmax could reduce spray drift by 65, 62, 59, 46, 42, and 19%, respectively, in comparison with water. The adequate concentration of adjuvants can reduce the percentage of fine droplets and thus significantly decrease the risk of drift in agricultural spraying (Wang X. et al., 2018). Wind tunnel experiments in different meteorological condition also demonstrated that the addition of spray adjuvants to the spray solution can affect the level of spray drift level (Wang et al., 2020a). The effect of adjuvant has also been found to lessen drift by modifying the surface tension of the solution, thus contributing to a reduction of the proportion of fine droplets. It therefore plays a significant role in reducing the drift risk of UASS.

Ultra-low volume spraying by UASS entails exigent demands in pesticide formulations. The drift of herbicides generally produces a higher impact on the environment than for fungicides and insecticides. In the early stage of UASS application, the blind use of herbicides to affect non-target organisms is a common strategy (Shan et al., 2021). While Japan developed drone sprayers earlier, herbicides were processed in the form of granules specifically for drone application according to the properties of drone aircraft spraying (Yuan et al., 2018). Granules can be employed in paddy fields such as rice, thus reducing environmental risks

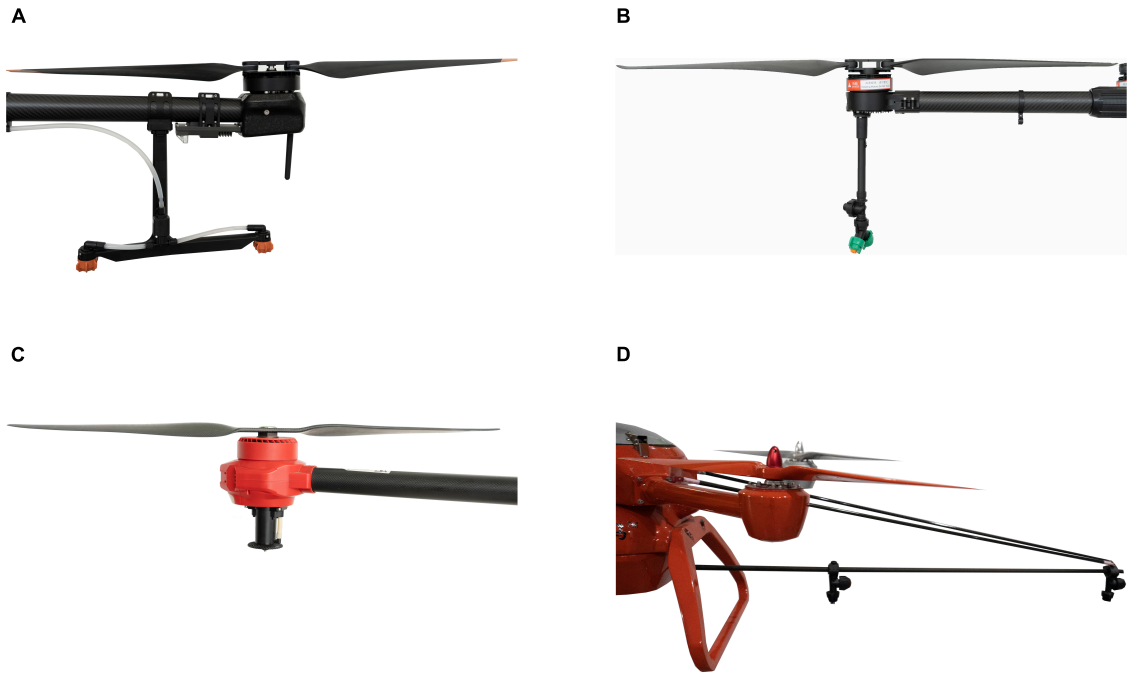

FIGURE 4
The relative position of the rotor and the nozzle. **(A)** Inside under the rotor (T30, from DJI), **(B)** below the rotor (extended, 3WWDZ-16, from Tuogong), **(C)** below the rotor (P30, from XAG), **(D)** boom (kongzhongbaoma, from SCAU).

for non-target areas. Further efforts in the future will still be necessary to develop adequate pesticide formulations for UASS (Yuan et al., 2018).

Downwash airflow

Rotor airflow is a typical feature in UASS (Zhan et al., 2022). The airflow of the rotor directly affects the movement of the droplets in space. It is the main factor that affects the airborne delivery of droplets to the target but also the leading cause of drift (Li J. et al., 2018). The following section summarizes the factors that cause variations in rotor airflow, including rotor and payload.

Rotors

The UASS are divided into single rotor and multi-rotor Systems. **Figure 5** introduces several multirotor UASS and **Table 5** summarizes the effective coverage area and average wind pressure of certain UASS. A single-rotor therefore covers a larger effective area than a multi-rotor. However, the take-off weight of the multi-rotor is not lower than that of the single-rotor. In terms of the downward wind pressure generated by the rotor, the multi-rotor performs better than the single-rotor; however its effect on drift cannot yet be explained.

Even though data on the way the type and number of rotors affect drift is still lacking, the influence of rotors on drift has been acknowledged (Richardson et al., 2019). As mentioned in **Table 4**, Wang studied the drift characteristics of hollow cone and air-injector nozzles mounted on UASS with different numbers of rotors (Wang et al., 2021). Based on 90% of the total drift distance, they demonstrated that the single rotor case always provided lowest drift distances. Following a computer simulation, Tang et al. (2021) observed that the largest droplets (200 and 400 μm) would be deposited near the swath, while the smallest droplets (50 and 100 μm) would remain airborne on the far left-hand side. Since the application height of the helicopter was low, a spanwise vortex appeared near the ground on the left-hand side of the helicopter. As a result, fine droplets were lifted due to the strong downwash flow while larger droplets were deposited before entering the vortex (Tang et al., 2021). These findings could be further exploited in order to significantly reduce the spray drift. In the case where a stronger downwash airflow would be produced, the effect of the vortex would be more prominent, and a greater amount of droplets would drift toward both sides of the route owing to the vortex wake of the UASS sprayer (Wang et al., 2021). Focusing on droplet deposition, the droplets were concentrated on 19.37% of the surface without a downwash flow field. The deposition area was a regular rectangle with a width of 2.6 m, which is the target area. When a downwash flow field was activated, the drift distance of the droplets increased and a greater amount of droplets traveled to non-target areas. The width of the droplet deposition area was 12.8 m, and droplets were observed on 41.06% of the test

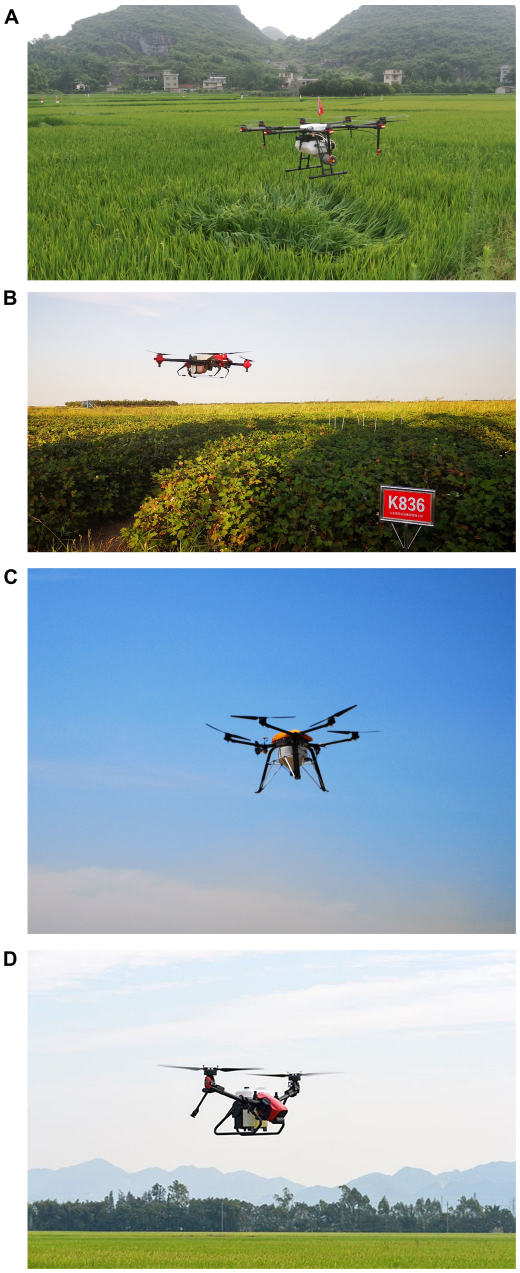

FIGURE 5
The UASS with different numbers of rotors. **(A)** Eight-rotor UASS (MG-1P, from DJI), **(B)** quadrotor UASS (P30, from XAG), **(C)** six-rotor UASS (M45, from GKXN,China), **(D)** two-rotor UASS (V40, from XAG).

area (Shi et al., 2019). Furthermore, it is generally believed that apart from favoring the displacement and deposition of droplets, the external high-speed airflow would also lead to a second atomization, resulting in a larger variation in droplet sizes (Butler Ellis et al., 2002; Ferguson et al., 2015; Wang et al., 2021).

Payload

The tank represents the most significant constituent of airborne equipment as it defines the payload and productivity. Its shape and size affect the UASS weight and control performance of the entire body and can even affect the distribution of the downwash airflow (Li J. et al., 2018). The spray method found on UASS is an air assisted spraying system similar to that of an orchard sprayer. Airspeed and air volume are the main factors in orchard spray technology that affect the distribution of deposits inside and outside the fruit tree canopy (Zhai et al., 2018). The airspeed and air volume of the orchard sprayer are obtained by adjusting the speed of the fan (Balsari et al., 2019). The difference between the UASS and the orchard sprayer is that the wind speed and air volume produced by the orchard sprayer are stable and controllable. The wind field generated by the UASS rotor is affected by external factors and is relatively uncontrollable. Indeed, the lift generated by the UASS rotor(s) is related to the load that is constantly changing because of the continuous discharge of the tank mixture (Zhan et al., 2022). According to a study, the RPM of each rotor blade was found to decrease by 14–20% as the payload decreased from 10 to 0 kg (Ismail et al., 2021). Therefore, in present-day spraying activities, changes in RPM could produce a downwash airflow pattern that constantly varies from the starting point up to the finishing point. This could have an effect on the distribution of the pesticide along the flight pathway (Ismail et al., 2021).

At present, 90% of electric multi-rotor drones have a tank capacity smaller than 15 L (Wang et al., 2020), but the developmental trend is now to increase the load. Some drone companies have even released electric drones with 40 L payloads, such as DJI's T40 and XAG's P40. The load factor (the ratio of load/total weight) has become an essential factor that can change wind strength of the rotor. As the weight of the UASS decreases, the downwash decreases, thus reducing its ability to draw droplets toward the ground and thereby further increasing airborne drift (Teske et al., 2018). The extent to which the payload affects drift still needs to be further investigated with subsequent research.

Relative movement

The drone constantly moves during the spraying process. Due to its displacement or to variations in external factors, the airflow can change (Wang L. et al., 2019; Tang et al., 2020). First of all, the forward movement of the UASS itself involves flight parameters, including flight speed, flight height, and flight direction. Secondly, variations in the external natural environment take place, such as natural wind blowing in the field. This section summarizes and discusses the factors related to relative motion and potential effects on spray drift.

TABLE 5 Comparison of effective wind field area and average wind pressure of some UASS.

Type	Model	Rotor diameter (mm) * number	Cover effective area[a]/m^2	Standard takeoff weight/kg	Average wind pressure[b]/($kg \cdot m^{-2}$)
Oil single rotor	3WQF120-12	2,410 * 1	4.56	42	9.21
Electric single rotor	S40-A	2,400 * 1	4.52	40	8.85
Electric multi-rotor	V40 2021	1,194 * 2	2.24	44	19.64
	P40 2021	1,016 * 4	3.24	45	13.89
	P80 2021	1,194 * 4	4.48	80	17.86
	T16	838.2 * 6	3.3	41	13.67
	T30	965.2 * 6	4.38	66.5	15.18

[a]The cover effective area is equal to the coverage area of the rotor multiplied by the number of rotors.
[b]The average wind pressure is equal to the take-off weight divided by the effective coverage area.

Flying speed

While the rotary wing drone hovers, the wingtip vortex flows outwards to the sides of the fuselage (Wen et al., 2018). However, as the drone moves forward, a spiral wake vortex develops behind the fuselage (Wen et al., 2019). The greater the flight speed and the higher the flight altitude, the farther the diffusion distance of the wake vortex. Wen et al. (2018) studied a single-rotor UASS in a CFD simulation analysis. Results indicated that 38% of droplets drifting in the air were due to the spiral wake vortex when the flight speed was 5 m s-1, the flight altitude was 3 m, and the particle size was less than 100 μm. The 100 μm droplets account for about 80% of the total number of drifting droplets (Wen et al., 2018; Wang et al., 2020). In the case when the drone flew too fast (more than 5 m s-1), the direction of the downwash airstream of the rotor changed from vertical downward to obliquely downward due to the relative moving external wind, which weakened the pressure effect on sprayed droplets. The horizontal velocity component of the downwash airflow contributed to an increase in the external wind speed flowing opposite to the flight direction, and thus aggravating the spray drift toward the rear of the fuselage (Wang et al., 2020). Consequently, the flight speed was found to produce a significant effect on spray drift characteristics for UASS aerial application indeed, a reduction in flight speed could effectively decrease the potential spray drift (Teske et al., 2018; Wang et al., 2020,a; Zhang H. et al., 2020).

Flight altitude

Airflow control has been achieved in orchard spraying by adjusting the distance between the nozzle and the spray target (Balsari et al., 2019). Generally, a reduction in the distance from the target should ensure sufficient air volume and air speed, while simultaneously decreasing the drift during spraying. The flight altitude refers to the height of the drone relative to the crop, which is the shortest distance the droplets need to travel to reach the surface of the target. Changes in altitude ought to affect the strength of the rotor wind field (Wen et al., 2018; Zhang H. et al., 2020). Indeed, the higher the altitude, the weaker the downwash airflow of the rotor at the top of canopy, and more easily sprayed droplets can drift with the crosswind (Wang et al., 2019a). Wang used a QuanFeng120 UASS in a pineapple field under various meteorological conditions. When the operation altitude was less than 2.5 m, the mean speed varied between 1.14 and 2.82 m/s, and the 90% spray drift distance remained within a 10 m range (Wang J. et al., 2018). Considering an operation altitude up to 3.5 m and the natural wind speed ranging between 2.02 and 3.59 m/s, the 90% spray drift distance can reach 33.54–46.50 m (Wang J. et al., 2018). Various experimental studies all come to the same conclusion that the maximum flight altitude should not be above 2.5 m in order to reduce the extent of droplet drifting (Wang J. et al., 2018).

Flight direction

Two concepts of flight direction are investigated here. The first concerns the forward and backward movement of the aircraft during route planning. Wang C. et al. (2018) studied the influence of forward and backward motion on droplet deposition in a tunnel frame of 5 m × 5 m × 2 m with 2 mm diameter drift collection lines on four sides (left—right—ground–top). When the UASS flew forward, the deposition rate ratio of downwind varied between 57.3 and 64.8%, while the bottom part varied between 30.3 and 38.8%. However, the deposition rate ratio of downwind decreased to 24.4–28.7% when flying backward, and the bottom part increased to 51.5–60.4%. As a result, the deposition rate of the bottom part of backward flight can reach 60% in comparison with forward flight. Therefore, the backward direction had a better result and allowed for a reduction in drift, optimizing the deposition rate on the target plant and the utilization of pesticides (Wang C. et al., 2018). However, this result was caused by the asymmetric structure of the single rotor UASS, and may not be applicable to the symmetrical multi-rotor UASS.

The second concept is the movement (perpendicular or parallel) of the flight route relative to the row of crops. When an application operation proceeds in a perpendicular direction to the row orientation, a higher proportion of drift can be observed in comparison with an application operation that runs parallel to the row orientation. This is attributed to the high proportion (> 50%) of gaps in the canopy parallel to the wind direction

(Brown and Giles, 2018). Consequently, a UASS flying backward or parallel to the direction of a row of vines should significantly reduce the risk of drift. However, these research data remain very specific, and such a conclusion may vary according to the different UASS models and crop types.

Crosswind

The main feature of rotary-wing UASS is airflow, and often natural wind interferes directly with the airflow distribution of the rotor during operation (Li J. et al., 2018). Similarly to any other type of spraying system, the influence of crosswind on the drift of UASS remains significant (Wang C. et al., 2018). Studies have demonstrated how, under conditions of average temperature of 31.5°C and average relative humidity of 34.1%, the effect of crosswind can be more significant than the flight height and flight speed of the UASS (Wang X. et al., 2017). Consistently with the effect of flight altitude, crosswinds tend to reduce the strength of the vertical downward rotor wind field, thus causing droplets to deposit along the downwind side, reducing the amount of deposition in the target area and increasing the proportion of drift (Wang X. et al., 2018).

Discussion and further recommendations

Optimization of spraying system and structure layout

At present, the Chinese market alone is concerned by more than 178 types of agricultural drones, and the spraying systems carried by the drones are also very diverse (He, 2018). The spraying systems proposed by manufacturers can differ significantly, and models from a single manufacturer but produced at different periods can also be different. However, these drones dating from different periods are widespread in the market. Due to this fact, a universal operating rule or anti-drift suggestion is difficult to establish. Therefore, the UASS system structure design still needs to be further improved corresponding technical standards need to be set. Drone manufacturers have focused on improving the drone platform during the previous development processes, such as positioning accuracy, autonomous control, and environmental sensing devices. However, the spraying system, as a core component of the drone, has been ignored (Li J. et al., 2018). Spraying studies are scarcely conducted before drone manufacturers release drones, while they are more frequently based on existing drones for testing. In subsequent developments, an upgrade of the drone spraying system could become a primary solution.

The choice of spray head type should take into account the application scene, the spray purpose, and its chemical formulation. It is recommended that target crops and environmental conditions be included, but this rather relies on experimental data. The centrifugal nozzle presents certain advantages in terms of droplet size, controllability and a reduced relative span (Qingqing et al., 2017). However, most of the droplet classification of current centrifugal spraying systems lies within the fine particle range. The reduction in the drift of the centrifugal spraying system using chemicals and adjuvant is also an issue that deserves improvement. In addition, the simple choice of hydraulic anti-drift nozzles to reduce drift may lead to reduced spray coverage. Therefore, it is necessary to equilibrate the relationship between drift and deposition distribution for hydraulic nozzles. The selection of formulations may require a focus on the risks related to herbicides. Drones carrying rice seeds and fertilizer granules have appeared and are employed in China (Song et al., 2018). The spreading of herbicide particles using drone based spreading devices may become a novel direction of research.

Optimization of the layout of nozzles and rotors is significant factor in reducing drift (Wen et al., 2018). The characteristics of the nozzle vary with the requirements of the application scenario (Chen et al., 2020a). A combination between the characteristics of the rotor wind field and of the nozzle spray should be made in order to select the most optimal spatial layout. This would be the most crucial and effective solution to solve the issues in spray drifting. The selection of the appropriate nozzle according to the rotor downwash flow field, although a critical issue for UASS, has not been sufficiently described in the existing literature. On one hand, the number of rotors and downwash flow field intensity is strictly an engineering issue related to the design, stability and payload capacity of UASS (Zhang H. et al., 2020). Since rotors are conveniently employed to support nozzles, the downwash field flow may contribute toward droplet penetration into the foliage (Zhang S. et al., 2020). On the other hand, the choice of the nozzle is depends on agronomical specifications (expected dosage/ha, spray quality, as well as technical possibilities in terms of nozzle flowrate, nozzle technology, etc. Such a pragmatic approach leads to a few practical consequences in terms of spray deposition and spray drift which are well described in the literature. The physical description of the rotor and nozzle combination is possible in a fixed position but may become more complex when considering the travel speed and influence of atmospheric conditions. In this sense, the effective horizontal spray distribution (spray swath) for UASS is not easily predictable and still needs to be experimentally investigated. In addition, the load in the tank, which constantly decreases during the spraying flight, tends to affect the rotor thrust. Attention should therefore be paid to the manner in which the rotor wind field variations can affect the spray quality and drift.

Drift test database and modeling

The development of drone spray technology is relatively new, and the UASS spray drift data base is still limited

(Wang et al., 2020,b). According to the study developed in Part 3, the drift of UASS is simultaneously affected by multiple operating parameters. Current research focuses on the influence of a specific factor or a small number of factors on drift while ignoring the interactions between multiple factors (Chen P. et al., 2021). The choice of operating parameters can be easily affected by the experience level of the operator, and the use of models can reduce the risk of drift caused by human decision-making errors (Chen et al., 2022). The selection of operating parameters for drone sprayers relies on a large number of field trials. The conduction of further assessments on larger-scale application fields would help to optimize operating parameters and fully understand the potential and limitations of UASS spray technology. According to recent observations, future research should incorporate more parameters, including system parameters, operating parameters, and environmental parameters, into the scope of the study so as to build a more accurate spray model. The existing AGDISP (Agricultural Dispersal) and CHARM (Comprehensive Hierarchical Aeromechanics Rotorcraft Model) were not originally designed for UASS sprayers. The previous models could not include all UASS platforms, rotor configurations, and spraying system types. However they could still act as a reference for UASS drift models (Chen H. et al., 2021). Therefore, a large accumulation of simulation or field data can provide the opportunity to establish a suitable model for UASS. Nevertheless, as the weather and crop structure in field experiments remain uncontrollable variables, it is challenging for these variables to be integrated into a decisive strategy (Bartzanas et al., 2013). Numerical modeling techniques such as CFD can effectively quantify the impact of mechanical designs, environmental parameters and weather conditions in a virtual environment. In addition to the drone itself, wind conditions and crop canopy are also important influencing factors. Hong et al. (2021) proposes a review of fluid dynamic approaches of spray drift taking into account influencing factors (including droplet size, wind conditions, and canopy interaction) into account to build accurate spray models, however this review does not concern the specific case fo UASS. In the future, a greater number of CFD studies will be implemented for the range of conditions for evaluating multi-rotor UASS to be expanded, thereby forming a modeling method to optimize UASS performance systematically.

In summary, the drift of UASS is an inevitable phenomenon. However, the establishment of reasonable measures, such as suggesting drift buffers throughout test data or models, is a necessary step toward drift reduction. Test data can help optimize the model in order to guide the process of selecting operating parameters. In addition, the structural design of the UASS sprayer system is still at a stage of continuous improvements, while the accumulation of test data should contribute to further improve the system.

Standardization of measurement methods

Table 3 in section "Unmanned aerial spraying systems drift measurement method" highlights a lack of consistent test protocols in existing research projects. Many UASS spraying systems are available, and the types of sampling collectors and collection locations are also diverse. Therefore, a summary and comparison of existing research data are difficult to make. The ISO22866 standard provides a field drift test method, which can be used to compare the drift characteristics and environmental risks between different types of spray equipment. However, it may not be suitable for the UASS drift test. For example, it is necessary to determine a unified test method according to various typologies of UASS, including a number of spraying systems and spatial layouts. Including the upwind drift data caused by the UASS wingtip vortex into the scope of the evaluation is a necessary step. NY/T 3213 is China's first agricultural UASS industry standard (Zhang S. et al., 2020). The standard determines the modeling rules, quality requirements, inspection methods, and rules of the UASS. However, the standard only defines the measurement of the UASS spray width, and the UASS drift test method is not mentioned. In order to further clarify the drift characteristics of UASS and to establish a drift model or database of UASS, it is necessary to first determine the corresponding field test method.

Major difficulties still arise when testing drone spray in wind tunnels. The principle of drift testing in wind tunnel is that it should have a sufficient size so that the airflow is not disturbed by the inner wall or sprayer (or its installation) (Iso 22856, 2008). Moreover, height and downwind distance of the wind tunnel should be sufficient to contain enough sampling equipment or collectors. According to **Table 3**, the length of the UASS is generally greater than 2 m, the height range lies between 0.5 and 0.7 m, and the size range of the rotor is 0.53–1.19 m. According to the specifications of the wind tunnel for spray testing mentioned in the literature (Ling et al., 2018; Ding et al., 2019; Liao et al., 2019; Wang et al., 2020,b), the width of most wind tunnel cross-sections ranges between 1.2 and 3 m, while the height is 1.1–2 m high. As the length of the rotor itself interferes with the current cross-sectional dimensions of the wind tunnel, the whole machine or the rotor are difficult to place inside the wind tunnel. The test method of UASS drift should take into account the characteristics of the UASS system. For example, the rotor wind field may impact the movement of the droplets as well as the secondary atomization. However, the ISO 22856 standard mentions that the spray generator mounting, control, and supply lines are to be arranged in order to minimize disturbance to the airflow, thus leading to a contradiction. It is therefore crucial to revise the field and indoor drift test methods based on the characteristics of UASS spraying systems.

Conclusion

The rapid development of drone sprayers has provided novel opportunities for chemical spraying techniques, but the drift of the UASS is also a noteworthy feature. The high-speed motion of the rotor causes the droplets to be drawn in by vortices on both sides of the wingtips, while the forward motion of the aircraft causes the vortices to produce long trailing vortices at the rear. Under the combined action of the lateral wind and the wake vortex, the droplets are easily dispersed toward the non-target areas. However, drone drifting is not an uncontrollable phenomenon. UASS drift has been found to be affected by the droplet size, layout of nozzles, number and size of rotors, payload, flying speed, flying altitude, and crosswind. By optimizing the structural layout of the rotor and spraying system, adjusting the operating parameters, and establishing a drift buffer zone, the drift of the droplets can be effectively reduced. For this new spray equipment, it is necessary for researchers to further investigate the drift characteristics of UASS, establish drift models of typical models, crops, and climate environment, and discuss standard methods for measuring UASS drift.

Author contributions

JD, YL, and PC: conceptualization. PC: formal analysis and writing—original draft preparation. PC, JD, EC, XD, and GP: investigation. JD and YL: resources, supervision, and funding acquisition. JD, YL, EC, XD, and GP: writing—review and editing. YZ: visualization. All authors have read and agreed to the published version of the manuscript.

Funding

This research was supported by the 111 Project (D18019), China Scholarship Council (202008440662), and the Pulvedrone project funded by the French Ministry of Agriculture (CASDAR).

Conflict of interest

The authors declare that the research was conducted in the absence of any commercial or financial relationships that could be construed as a potential conflict of interest.

Publisher's note

All claims expressed in this article are solely those of the authors and do not necessarily represent those of their affiliated organizations, or those of the publisher, the editors and the reviewers. Any product that may be evaluated in this article, or claim that may be made by its manufacturer, is not guaranteed or endorsed by the publisher.

Supplementary material

The Supplementary Material for this article can be found online at: https://www.frontiersin.org/articles/10.3389/fpls.2022.870956/full#supplementary-material

References

Ahmad, F., Zhang, S., Qiu, B., Ma, J., Xin, H., Qiu, W., et al. (2022). Comparison of water sensitive paper and glass strip sampling approaches to access spray deposit by UAV sprayers. *Agronomy* 12:1302. doi: 10.3390/agronomy12061302

Al Heidary, M., Douzals, J. P., Sinfort, C., and Vallet, A. (2014). Influence of spray characteristics on potential spray drift of field crop sprayers: a literature review. *Crop Prot.* 63, 120–130. doi: 10.1016/j.cropro.2014.05.006

ASAE ANSI/ASABE (2020). *Spray nozzle classification by droplet spectra. Standard 572.3*. St. Joseph, MI: American Society of Agricultural and Biological Engineers.

Balsari, P., Grella, M., Marucco, P., Matta, F., and Miranda Fuentes, A. (2019). Assessing the influence of air speed and liquid flow rate on the droplet size and homogeneity in pneumatic spraying. *Pest. Manag. Sci.* 75, 366–379. doi: 10.1002/ps.5120

Bartzanas, T., Kacira, M., Zhu, H., Karmakar, S., Tamimi, E., Katsoulas, N., et al. (2013). Computational fluid dynamics applications to improve crop production systems. *Comput. Electron. Agric.* 93, 151–167. doi: 10.1016/j.compag.2012.05.012

Bloise, N., Ruiz, M. C., D'Ambrosio, D., and Guglieri, G. (2020). "Preliminary design of a remotely piloted aircraft system for crop-spraying on vineyards," in *Proceedings of the 2020 IEEE International Workshop on Metrology for Agriculture and Forestry (MetroAgriFor)*. (Trento: IEEE), 1–6. doi: 10.1109/MetroAgriFor50201.2020.9277607

Brown, C. R., and Giles, D. K. (2018). Measurement of pesticide drift from unmanned aerial vehicle application to a vineyard. *Transac. Asabe* 61, 1539–1546. doi: 10.13031/trans.12672

Butler Ellis, M. C., Swan, T., Miller, P., Waddelow, S., Bradley, A., and Tuck, C. R. (2002). PM—power and machinery: design factors affecting spray characteristics and drift performance of air induction nozzles. *Biosyst. Eng.* 82, 289–296. doi: 10.1006/bioe.2002.0069

Cavalaris, C., Karamoutis, C., and Markinos, A. (2022). Efficacy of cotton harvest aids applications with unmanned aerial vehicles (UAV) and ground-based field sprayers–a case study comparison. *Smart Agric. Technol.* 2:100047. doi: 10.1016/j.atech.2022.100047

Chen, H., Lan, Y., Fritz, B. K., Hoffmann, W. C., and Liu, S. (2021). Review of agricultural spraying technologies for plant protection using unmanned aerial vehicle (UAV). *Int. J. Agric. Biol. Eng.* 14, 38–49. doi: 10.25165/j.ijabe.20211401.5714

Chen, P., Lan, Y., Douzals, J., Ouyang, F., Wang, J., and Xu, W. (2020a). Droplet distribution of Unmanned Aerial Vehicle under several spray volumes and canopy heights in the cotton canopy. *Int. J. Precis. Agric. Aviat.* 3, 74–79. doi: 10.33440/j.ijpaa.20200304.136

Chen, P., Lan, Y., Huang, X., Qi, H., Wang, G., Wang, J., et al. (2020b). Droplet deposition and control of planthoppers of different nozzles in two-stage rice with a quadrotor unmanned aerial vehicle. *Agronomy* 10:303. doi: 10.3390/agronomy10020303

Chen, P., Ouyang, F., Wang, G., Qi, H., Xu, W., Yang, W., et al. (2021). Droplet distributions in cotton harvest aid applications vary with the interactions among the unmanned aerial vehicle spraying parameters. *Ind. Crop. Prod.* 163:113324. doi: 10.1016/j.indcrop.2021.113324

Chen, P., Xu, W., Zhan, Y., Wang, G., Yang, W., and Lan, Y. (2022). Determining application volume of unmanned aerial spraying systems for cotton defoliation using remote sensing images. *Comput. Electron. Agric.* 196:106912. doi: 10.1016/j.compag.2022.106912

Chen, S., Lan, Y., Zhou, Z., Deng, X., and Wang, J. (2021). Research advances of the drift reducing technologies in application of agricultural aviation spraying. *Int. J. Agric. Biol. Eng.* 14, 1–10. doi: 10.25165/j.ijabe.20211405.6225

Chen, S., Lan, Y., Zhou, Z., Ouyang, F., Wang, G., Huang, X., et al. (2020a). Effect of droplet size parameters on droplet deposition and drift of aerial spraying by using plant protection UAV. *Agronomy* 10:195. doi: 10.3390/agronomy10020195

Delpuech, X., Gorioux, H., and Pouxviel, G. (2022). *Évaluation de la Qualité de la Pulvérisation par Drone en Vignoble de forte pente: Article Prenant sa Source de l'article "Pulvérisation par Drone en vignoble de forte pente"(Phytoma-La santé des végétaux n° 741, février 2021)*. Paris: vine and wine. doi: 10.20870/IVES-TR.2022.5402

Ding, S., Xue, X., Qin, W., Gu, W., Cai, C., and Cui, L. (2019). Influencing factors research and performance experiment on droplets deposition at low wind speed. *Int. J. Precis. Agric. Aviat.* 2, 46–51. doi: 10.33440/j.ijpaa.20190201.0017

Fengbo, Y., Xinyu, X., Ling, Z., and Zhu, S. (2017). Numerical simulation and experimental verification on downwash air flow of six-rotor agricultural unmanned aerial vehicle in hover. *Int. J. Agric. Biol. Eng.* 10, 41–53. doi: 10.25165/j.ijabe.20171004.3077

Ferguson, J. C., O'Donnell, C. C., Chauhan, B. S., Adkins, S. W., Kruger, G. R., Wang, R., et al. (2015). Determining the uniformity and consistency of droplet size across spray drift reducing nozzles in a wind tunnel. *Crop Prot.* 76, 1–6. doi: 10.1016/j.cropro.2015.06.008

Gao, Y. Y. (2013). *Study on Distribution of Pesticide Droplets in Gramineous Crop Canopy And Control Effect Sprayed By Unmanned Aerial Vehicle*. Harbin: Northeast Agric. Univ.

Grella, M., Marucco, P., Manzone, M., Gallart, M., and Balsari, P. (2017). Effect of sprayer settings on spray drift during pesticide application in poplar plantations (*Populus* spp.). *Sci. Total Environ.* 578, 427–439. doi: 10.1016/j.scitotenv.2016.10.205

Hayashi, H., and Takeda, S. (1986). Spray drying characteristics by a centrifugal pressure nozzle with large orifice diameter. *Dry. Technol.* 4, 331–342. doi: 10.1080/07373938608916333

He, X. (2018). Rapid development of unmanned aerial vehicles (UAV) for plant protection and application technology in China. *Outlooks Pest Manag.* 29, 162–167. doi: 10.1564/v29_aug_04

He, X., Bonds, J., Herbst, A., and Langenakens, J. (2017). Recent development of unmanned aerial vehicle for plant protection in East Asia. *Int. J. Agric. Biol. Eng.* 10, 18–30. doi: 10.3965/j.ijabe.20171003.3248

He, Y., Xiao, S., Fang, H., Dong, T., Tang, Y., Nie, P., et al. (2018). Development situation and spraying decision of spray nozzle for plant protection UAV. *Transac. Chin. Soc. Agric. Eng.* 34, 113–124. doi: 10.11975/j.issn.1002-6819.2018.13.014

Herbst, A., Bonds, J., Wang, Z. C., Zeng, A. J., He, X. K., and Goff, P. (2020). The influence of unmanned agricultural aircraft system design on spray drift. *J. Kulturpfl.* 72, 1–11. doi: 10.5073/JfK.2020.01.01

Hong, S., Park, J., Jeong, H., Lee, S., Choi, L., Zhao, L., et al. (2021). Fluid dynamic approaches for prediction of spray drift from ground pesticide applications: A review. *Agronomy* 11:1182. doi: 10.3390/agronomy/11061182

Hussain, A., and Nishat, A. S. (2022). *The Energy Challenge: Moving from Fossil Fuels to Biofuels, Hydrogen, and Green Energy Sources*. New York, NY: New York City College of Technology.

Ismail, S. A., Yahya, A., Su, A. S. M., Asib, N., and Mustafah, A. M. (2021). Drone payload and flying speed effects on rotor blades' RPM and traveling pattern for agricultural chemical spraying. *Basrah J. Agric. Sci.* 34, 157–170. doi: 10.37077/25200860.2021.34.sp1.16

Iso, I. (2005). *Equipment for Crop Protection-Methods for field Measurements of Spray Drift*. Geneva: International Organization for Standardization, 1–17.

Iso International Standard (2009). *Equipment for Crop Protection—Methods for the Laboratory Measurement of spray Drift—Wind Tunnels*. Geneva: ISO.

Lan, Y., and Chen, S. (2018). Current status and trends of plant protection UAV and its spraying technology in China. *Int. J. Precis. Agric. Aviat.* 1:1. doi: 10.33440/j.ijpaa.20180101.0002

Li, J., Lan, Y., and Shi, Y. (2018). Research progress on airflow characteristics and field pesticide application system of rotary-wing UAV. *Transac. Chin. Soc. Agric. Eng.* 34, 104–118. doi: 10.3969/j.issn.1002-6819.2018.12.013

Li, L., Liu, Y., He, X., Song, J., Zeng, A., Zhichong, W., et al. (2018). *Assessment of Spray Deposition and Losses in the Apple Orchard from Agricultural Unmanned Aerial Vehicle in China*. St. Joseph, MI: American Society of Agricultural and Biological Engineers. doi: 10.13031/aim.201800504

Li, X., Giles, D. K., Andaloro, J. T., Long, R., Lang, E. B., Watson, L. J., et al. (2021a). Comparison of UAV and fixed-wing aerial application for alfalfa insect pest control: evaluating efficacy, residues, and spray quality. *Pest Manag. Sci.* 77, 4980–4992. doi: 10.1002/ps.6540

Li, X., Giles, D. K., Niederholzer, F. J., Andaloro, J. T., Lang, E. B., Watson, L. J., et al. (2021b). Evaluation of an unmanned aerial vehicle as a new method of pesticide application for almond crop protection. *Pest Manage. Sci.* 77, 527–537. doi: 10.1002/ps.6052

Liao, J., Hewitt, A. J., Wang, P., Luo, X., Zang, Y., Zhou, Z., et al. (2019). Development of droplet characteristics prediction models for air induction nozzles based on wind tunnel tests. *Int. J. Agric. Biol. Eng.* 12, 1–6. doi: 10.25165/j.ijabe.20191206.5014

Ling, W., Du, C., Ze, Y., Xindong, N., and Shumao, W. (2018). Research on the prediction model and its influencing factors of droplet deposition area in the wind tunnel environment based on UAV spraying. *IFAC PapersOnLine* 51, 274–279. doi: 10.1016/j.ifacol.2018.08.174

Liu, Q., Chen, S., Wang, G., and Lan, Y. (2021). Drift evaluation of a quadrotor unmanned aerial vehicle (UAV) sprayer: effect of liquid pressure and wind speed on drift potential based on wind tunnel test. *Appl. Sci.* 11:7258. doi: 10.3390/app11167258

Meng, Y., Lan, Y., Mei, G., Guo, Y., Song, J., Wang, Z. G., et al. (2018). Effect of aerial spray adjuvant applying on the efficiency of small unmanned aerial vehicle for wheat aphids control. *Int. J. Agric. Biol. Eng.* 11, 46–53. doi: 10.25165/j.ijabe.20181105.4298

Meng, Y., Su, J., Song, J., Chen, W., and Lan, Y. (2020). Experimental evaluation of UAV spraying for peach trees of different shapes: effects of operational parameters on droplet distribution. *Comput. Electron. Agric.* 170:105282. doi: 10.1016/j.compag.2020.105282

Meng, Y., Wang, M., Wang, Z., Hu, H., and Ma, Y. (2021). Surface tension and spreading coefficient of single-and mix-pesticide solutions with aerial spraying organosilicone adjuvant. *Int. J. Precis. Agric. Aviat.* 4, 6–13. doi: 10.33440/j.ijpaa.20210401.159

Meng, Y., Zhong, W., Liu, C., Su, J., Su, J., Lan, Y., et al. (2022a). UAV spraying on citrus crop: impact of tank-mix adjuvant on the contact angle and droplet distribution. *PeerJ* 10:e13064. doi: 10.7717/peerj.13064

Meng, Y., Zhong, W., Liu, Y., Wang, M., and Lan, Y. (2022b). *Droplet Distribution of an Autonomous UAV-Based Sprayer in Citrus Tree Canopy*. Bristol: IOP Publishing. doi: 10.1088/1742-6596/2203/1/012022

Mickle, R. E. (1996). Influence of aircraft vortices on spray cloud behavior. *J. Am. Mosq. Control Assoc. Mosq. News* 12, 372–379.

Morales-Rodríguez, P. A., Cano Cano, E., Villena, J., and López-Perales, J. A. (2022). A comparison between conventional sprayers and new UAV sprayers: A study case of vineyards and olives in extremadura (Spain). *Agronomy* 12:1307. doi: 10.3390/agronomy12061307

Pan, Z., Lie, D., Qiang, L., Shaolan, H., Shilai, Y., Yande, L., et al. (2016). Effects of citrus tree-shape and spraying height of small unmanned aerial vehicle on droplet distribution. *Int. J. Agric. Biol. Eng.* 9:45. doi: 10.3965/j.ijabe.20160904.2178

Qin, W., Qiu, B., Xue, X., Chen, C., Xu, Z., and Zhou, Q. (2016). Droplet deposition and control effect of insecticides sprayed with an unmanned aerial vehicle against plant hoppers. *Crop Prot.* 85, 79–88. doi: 10.1016/j.cropro.2016.03.018

Qingqing, Z., Xinyu, X., Weicai, Q., Chen, C., and Liangfu, Z. (2017). Optimization and test for structural parameters of UAV spraying rotary cup atomizer. *Int. J. Agric. Biol. Eng.* 10, 78–86. doi: 10.3965/j.ijabe.20171003.3119

Reger, M., Bauerdick, J., and Bernhardt, H. (2018). Drones in agriculture: current and future legal status in Germany, the EU, the USA and Japan. *Landtechnik* 73, 62–79. doi: 10.15150/lt.2018.3183

Richardson, B., Rolando, C. A., Kimberley, M. O., and Strand, T. M. (2019). Spray application efficiency from a multi-rotor unmanned aerial vehicle configured for aerial pesticide application. *Trans. Asabe* 62, 1447–1453. doi: 10.13031/trans.13509

Sarri, D., Martelloni, L., Rimediotti, M., Lisci, R., Lombardo, S., and Vieri, M. (2019). Testing a multi-rotor unmanned aerial vehicle for spray application in high slope terraced vineyard. *J. Agric. Eng.* 50, 38–47. doi: 10.4081/jae.2019.853

Shan, C., Wang, G., Wang, H., Xie, Y., Wang, H., Wang, S., et al. (2021). Effects of droplet size and spray volume parameters on droplet deposition of wheat herbicide application by using UAV. *Int. J. Agric. Biol. Eng.* 14, 74–81. doi: 10.25165/j.ijabe.20211401.6129

Shi, Q., Mao, H., and Guan, X. (2019). Numerical simulation and experimental verification of the deposition concentration of an unmanned aerial vehicle. *Appl. Eng. Agric.* 35, 367–376. doi: 10.13031/aea.13221

Song, C., Zhou, Z., Jiang, R., Luo, X., He, X., and Ming, R. (2018). Design and parameter optimization of pneumatic rice sowing device for unmanned aerial vehicle. *Transac. Chin. Soc. Agric. Eng.* 34, 80–88. doi: 10.11975/j.issn.1002-6819.2018.06.010

Tang, Q., Chen, L., Zhang, R., Deng, W., Xu, M., Xu, G., et al. (2021). Effects of application height and crosswind on the crop spraying performance of unmanned helicopters. *Comput. Electron. Agric.* 181:105961. doi: 10.1016/j.compag.2020.105961

Tang, Q., Zhang, R., Chen, L., Xu, G., Deng, W., Ding, C., et al. (2020). High-accuracy, high-resolution downwash flow field measurements of an unmanned helicopter for precision agriculture. *Comput. Electron. Agric.* 173:105390. doi: 10.1016/j.compag.2020.105390

Teske, M. E., Wachspress, D. A., and Thistle, H. W. (2018). Prediction of aerial spray release from UAVs. *Transac. Asabe* 61, 909–918. doi: 10.13031/trans.12701

Wang, C., He, X., Wang, X., Wang, Z., Pan, H., and He, Z. (2016). Testing method of spatial pesticide spraying deposition quality balance for unmanned aerial vehicle. *Transac. Chin. Soc. Agric. Eng.* 32, 54–61. doi: 10.25165/j.ijabe.20181102.3187

Wang, C., He, X., Wang, X., Wang, Z., Wang, S., Li, L., et al. (2018). Testing method and distribution characteristics of spatial pesticide spraying deposition quality balance for unmanned aerial vehicle. *Int. J. Agric. Biol. Eng.* 11, 18–26.

Wang, C., He, X., Zeng, A., Herbst, A., and Wanlin, G. (2020a). Measuring method and experiment on spray drift of chemicals applied by uav sprayer based on an artificial orchard test bench. *Transac. Chin. Soc. Agric. Eng.* 36, 56–66. doi: 10.11975/j.issn.1002-6819.2020.13.007

Wang, C., Zeng, A., He, X., Song, J., Herbst, A., and Gao, W. (2020b). Spray drift characteristics test of unmanned aerial vehicle spray unit under wind tunnel conditions. *Int. J. Agric. Biol. Eng.* 13, 13–21. doi: 10.25165/j.ijabe.20201303.5716

Wang, C., Herbst, A., Zeng, A., Wongsuk, S., Qiao, B., Qi, P., et al. (2021). Assessment of spray deposition, drift and mass balance from unmanned aerial vehicle sprayer using an artificial vineyard. *Sci. Total Environ.* 777:146181. doi: 10.1016/j.scitotenv.2021.146181

Wang, C., Liu, Y., Zhang, Z., Han, L., Li, Y., Zhang, H., et al. (2022). Spray performance evaluation of a six-rotor unmanned aerial vehicle sprayer for pesticide application using an orchard operation mode in apple orchards. *Pest Manag. Sci.* 78, 2449–2466. doi: 10.1002/ps.6875

Wang, G., Han, Y., Li, X., Andaloro, J., Chen, P., Hoffmann, W. C., et al. (2020). Field evaluation of spray drift and environmental impact using an agricultural unmanned aerial vehicle (UAV) sprayer. *Sci. Total Environ.* 737:139793. doi: 10.1016/j.scitotenv.2020.139793

Wang, G., Lan, Y., Yuan, H., Qi, H., Chen, P., Ouyang, F., et al. (2019). Comparison of spray deposition, control efficacy on wheat aphids and working efficiency in the wheat field of the unmanned aerial vehicle with boom sprayer and two conventional knapsack sprayers. *Appl. Sci.* 9. doi: 10.3390/app9020218

Wang, J., Lan, Y., Wen, S., Hewitt, A. J., Yao, W., and Chen, P. (2019a). Meteorological and flight altitude effects on deposition, penetration, and drift in pineapple aerial spraying. *Asia Pac. J. Chem. Eng.* 15. doi: 10.1002/apj.2382

Wang, J., Lan, Y., Yao, W., Chen, P., Lin, J., and Yan, Y. (2019b). Effects of working height of single-rotor unmanned aerial vehicle on drift and droplets deposition distribution of areca tree. *Nongye Jixie Xuebao* 50, doi: 10.6041/j.issn.1000-1298.2019.07.011

Wang, J., Lan, Y., Zhang, H., Zhang, Y., Wen, S., Yao, W., et al. (2018). Drift and deposition of pesticide applied by UAV on pineapple plants under different meteorological conditions. *Int. J. Agric. Biol. Eng.* 11, 5–12. doi: 10.25165/j.ijabe.20181106.4038

Wang, J., Xu, W., Wen, J., Wang, X., and Luo, B. (2017). Numerical simulation on gas-liquid phase flow of large-scale plant protection unmanned aerial vehicle spraying. *Transac. Chin. Soc. Agric. Mach.* 48.

Wang, L., Huang, X., Li, W., Yan, K., Han, Y., Zhang, Y., et al. (2022). Progress in agricultural unmanned aerial vehicles (UAVs) applied in China and prospects for Poland. *Agriculture* 12:397. doi: 10.3390/agriculture12030397

Wang, L., Lan, Y., Zhang, Y., Zhang, H., Tahir, M. N., Ou, S., et al. (2019). Applications and prospects of agricultural unmanned aerial vehicle obstacle avoidance technology in China. *Sensors* 19:642. doi: 10.3390/s19030642

Wang, X., He, X., Song, J., Wang, Z., Wang, C., Wang, S., et al. (2018). Drift potential of UAV with adjuvants in aerial applications. *Int. J. Agric. Biol. Eng.* 11, 54–58. doi: 10.25165/j.ijabe.20181105.3185

Wang, X., He, X., Wang, C., Wang, Z., Li, L., Wang, S., et al. (2017). Spray drift characteristics of fuel powered single-rotor UAV for plant protection. *Transac. Chin. Soc. Agric. Eng.* 33, 117–123. doi: 10.11975/j.issn.1002-6819.2017.01.016

Wang, Z., Hussain, M., Huang, G., Yin, J., Guo, Y., Mo, Y., et al. (2022). Better droplet deposition and internode shortening effects of plant growth regulator EDAH on maize applied by small unmanned aerial vehicle than electric knapsack sprayer. *Agriculture* 12:404. doi: 10.3390/agriculture12030404

Wen, S., Han, J., Lan, Y. B., Yin, X. C., and Lu, Y. H. (2018). Influence of wing tip vortex on drift of single rotor plant protection unmanned aerial vehicle. *Trans. Chin. Soc. Agric. Mach.* 49:127â. doi: 10.6041/j.issn.1000-1298.2018.08.015

Wen, S., Han, J., Ning, Z., Lan, Y., Yin, X., Zhang, J., et al. (2019). Numerical analysis and validation of spray distributions disturbed by quad-rotor drone wake at different flight speeds. *Comput. Electron. Agric.* 166:105036. doi: 10.1016/j.compag.2019.105036

Xinyu, X., Kang, T., Weicai, Q., Lan, Y., and Zhang, H. (2014). Drift and deposition of ultra-low altitude and low volume application in paddy field. *Int. J. Agric. Biol. Eng.* 7:23. doi: 10.3965/j.ijabe.20140704.003

Xu, S., Jianli, S., Shilin, W., Xiaoming, J., Lin, X., and Yajia, L. (2020). Study on droplet drift and applicator exposure in rice flight prevention by multi-rotor plant protection UAV. *Chin. J. Pest. Sci.* 22, 1085–1093. doi: 10.16801/j.issn.1008-7303.2020.0148

Yan, X., Xin, S., Xiaohui, L., Du Yahui, Daibin, Y., and Huizhu, Y. (2021). The spray drift risk of plant protection unmanned aerial vehicle (UAV spraying neonicotinoid pesticides to honey bees. *J. Plant Prot.* 48, 477–482. doi: 10.13802/j.cnki.zwbhxb.2021.2021836

Yan, X., Yuan, H., Chen, Y., Shi, X., Liu, X., Wang, Z., et al. (2022). Broadcasting of tiny granules by drone to mimic liquid spraying for the control of fall armyworm (*Spodoptera frugiperda*). *Pest Manag. Sci.* 78, 43–51. doi: 10.1002/ps.6604

Yu, K., Liu, Y., Gong, Z., Liang, Y., Du, L., Zhang, Z., et al. (2022). Chemical topping improves the efficiency of spraying harvest aids using unmanned aerial vehicles in high-density cotton. *Field Crops Res.* 283:108546. doi: 10.1016/j.fcr.2022.108546

Yuan, H. Z., Xue, X. Y., Yan, X. J., Qin, W. C., Kong, X., Zhou, Y. Y., et al. (2018). Applications and prospects in the unmanned aerial system for low-altitude and low-volume spray in crop protection. *Plant Protect.* 44, 152–158. doi: 10.16688/j.zwbh.2018307

Zhai, C., Zhao, C., Ning, W., Long, J., Wang, X., Weckler, P., et al. (2018). Research progress on precision control methods of air-assisted spraying in orchards. *Transac. Chin. Soc. Agric. Eng.* 34, 1–15. doi: 10.11975/j.issn.1002-6819.2018.10.001

Zhan, Y., Chen, P., Xu, W., Chen, S., Han, Y., Lan, Y., et al. (2022). Influence of the downwash airflow distribution characteristics of a plant protection UAV on spray deposit distribution. *Biosyst. Eng.* 216, 32–45. doi: 10.1016/j.biosystemseng.2022.01.016

Zhang, H., Qi, L., Wan, J., Musiu, E. M., Zhou, J., Lu, Z., et al. (2022). Numerical simulation of downwash airflow distribution inside tree canopies of an apple orchard from a multirotor unmanned aerial vehicle (UAV) sprayer. *Comput. Electron. Agric.* 195:106817. doi: 10.1016/j.compag.2022.106817

Zhang, H., Qi, L., Wu, Y., Musiu, E. M., Cheng, Z., and Wang, P. (2020). Numerical simulation of airflow field from a six–rotor plant protection drone using lattice Boltzmann method. *Biosyst. Eng.* 197, 336–351. doi: 10.1016/j.biosystemseng.2020.07.018

Zhang, S., Qiu, B., Xue, X., Sun, T., and Peng, B. (2020). Parameters optimization of crop protection UAS based on the first industry standard of China. *Int. J. Agric. Biol. Eng.* 13, 29–35. doi: 10.25165/j.ijabe.20201303.5439

Zhang, Y., Huang, X., Lan, Y., Wang, L., Lu, X., Yan, K., et al. (2021). Development and prospect of UAV-based aerial electrostatic spray technology in China. *Appl. Sci.* 11:4071. doi: 10.3390/app11094071

Zhu, H., Li, H., Zhang, C., Li, J., and Zhang, H. (2019). Performance characterization of the UAV chemical application based on CFD simulation. *Agronomy* 9:308. doi: 10.3390/agronomy9060308

frontiers | Frontiers in Plant Science

TYPE Original Research
PUBLISHED 23 August 2022
DOI 10.3389/fpls.2022.959429

OPEN ACCESS

EDITED BY
Nikolaos Papadopoulos,
University of Thessaly,
Greece

REVIEWED BY
Kittisak Jermsittiparsert,
University of City Island, Cyprus
Lefteris Benos,
Centre for Research and Technology Hellas, Greece
Kevi Mace,
California Department of Food and Agriculture, United States
Robert Orpet,
Washington State University, United States

*CORRESPONDENCE
Xiongkui He
xiongkui@cau.edu.cn
Jianli Song
songjianli@cau.edu.cn

SPECIALTY SECTION
This article was submitted to Sustainable and Intelligent Phytoprotection, a section of the journal Frontiers in Plant Science

RECEIVED 01 June 2022
ACCEPTED 08 August 2022
PUBLISHED 23 August 2022

CITATION
Jiang Y, He X, Song J, Liu Y, Wang C, Li T, Qi P, Yu C and Chen F (2022) Comprehensive assessment of intelligent unmanned vehicle techniques in pesticide application: A case study in pear orchard. *Front. Plant Sci.* 13:959429. doi: 10.3389/fpls.2022.959429

Comprehensive assessment of intelligent unmanned vehicle techniques in pesticide application: A case study in pear orchard

Yulin Jiang[1,2,3], Xiongkui He[1,2]*, Jianli Song[1]*, Yajia Liu[1], Changling Wang[1,2], Tian Li[1], Peng Qi[1], Congwei Yu[1] and Fu Chen[3]

[1]College of Science, China Agricultural University, Beijing, China, [2]College of Agricultural Unmanned System, China Agricultural University, Beijing, China, [3]Key Laboratory of Farming System, Ministry of Agriculture and Rural Affairs, College of Agronomy and Biotechnology, China Agricultural University, Beijing, China

The intelligent pesticide application techniques in orchards have grown rapidly worldwide due to the decrease in agricultural populations and the increase in labor costs. However, whether and how intelligent pesticide application techniques are better than conventional pesticide application remains unclear. Here, we evaluated the performance of the unmanned aircraft vehicle (UAV) and unmanned ground vehicle (UGV) on pesticide application, ecological environment protection, and human's health protection compared to conventional manual methods. We quantified characteristics from the aspects of working effectiveness, efficiency, environmental pollution, water saving and carbon dioxide reduction. The results showed that the UAV application has the advantages of a higher working efficiency and less environmental pollution and natural resource consumption compared to the UGV and conventional manual methods despite of its worse spray performance The UGV application techniques could improve spray performance at the cost of high environmental pollution. The conventional spray gun technique was unfriendly to environmental and resource protection although it showed a better spray performance. Thus, the balance of improving spray performance and controlling environmental pollution is the key to improve the performance of UAV and UGV technology in the future. The study could be useful in the development of intelligent pesticide application techniques and provide scientific support for the transition of intelligent management in orchards.

KEYWORDS

plant protection, UAV, UGV, application performance, ecological assessment, orchard

Introduction

Orchard area and fruit production have rapidly increased to meet the higher demand for fruit consumption over the past decades. The global orchard area and fruit production increased by approximately 22 and 54%, respectively (FAO, 2020). As the country with largest population in the world, China has the largest orchard area and the highest fruit production in the world (Jiang et al., 2021). The fruit industry is not only an advantageous industry in China but also a labor-intensive industry. Plant protection is an important part of orchard management with high labor demands (He et al., 2017). However, rapid urbanization during past decades has led to severe labor shortages in the orchard industry, and the challenges associated with the aging population in the county is becoming increasingly prominent (Zhao et al., 2021). At present, most management of orchard pesticide application relies on manual operation, which is characterized by high labor intensity, low efficiency and low standardization (Zhai et al., 2018; Liu et al., 2021). Moreover, pesticide application has potential damage both in human and environment (Pan et al., 2020; Cai et al., 2021). In general, green and sustainable development is an important objective of global agricultural transformation (Abbas and Sagsan, 2019; Guo et al., 2020). Cleaner production with a reduction in greenhouse gas emissions and resource consumption in agricultural management is urgent and important based on global climate change (Young et al., 2015). How to strengthen ecological environmental protection during the utilization of pesticides in orchard is a key issue in national development plans (Li et al., 2022). In addition, legislation and ethics have to go hand in hand when considering the design of legal solutions due to the value-laden nature of the concerns associated with robotic systems (EU, 2016; Benos et al., 2022).

Generally, the air-assisted spray method (a machine with pump and air-assisted equipment) and the human spray gun method (a machine with pump and several spray guns) are widely used in orchard plant protection (Khot et al., 2012; Lu et al., 2021). The former method has been recognized as a high-efficiency pesticide application technology and is widely used for pest control in orchards (Li et al., 2022). However, it is only suitable in standardized orchards with fixed wide spacing and relatively flat pavement (Wang et al., 2022). Human spray guns can make up for this shortcoming. However, high labor costs limit its application in large-scale orchard management (An et al., 2020). To solve these problems, intelligent pesticide application technology can be an alternative choice in orchard plant protection, which has been growing rapidly worldwide as a new method for the application of plant protection products, especially in East Asian and Southeast Asian countries (He et al., 2017; He, 2018). Unmanned aircraft vehicles (UAVs) and unmanned ground vehicles (UGVs) are two major kinds of intelligent equipment that have been widely adapted for agricultural management (Kefauver et al., 2017; Zhang et al., 2019). Intelligent pesticide application technology fits the current development requirements of modern agriculture: high efficiency, high quality and economically efficient as well as standardization and informatization (Wang et al., 2016; Lan and Chen, 2018). It has a major advantage in low labor demand, which is important for orchard management in the future. Moreover, intelligent equipment can also ignore terrain obstacles and planting patterns, which is important for orchards in hilly areas and disorderly planting orchards, such as orchards in southwestern China (Wang et al., 2022). Some intelligent equipment has the ability to work at night, which can significantly improve working efficiency. Finally, the outstanding progress in vision sensors in conjunction with that of machine learning has allowed the sustainable targeted application (Benos et al., 2021).

A comprehensive evaluation of the stability and effectiveness of intelligent pesticide application techniques during actual operation scenario is important for technological improvement and popularization; however, this exploration is still limited. Many studies have focused on parameter optimization in specific equipment. For example, the influence of operating techniques on the spray effect through ground machine application, including travel speed, nozzle type, and spray pressure, has been explored by many researchers (Nuyttens et al., 2007; Li et al., 2021a, 2022; Grella et al., 2022). Similarly, flight height and velocity, tree shape, UAV type and drift have been widely studied for UAV application (Tang et al., 2018; Meng et al., 2020; Wang et al., 2021). On the other hand, previous studies have also focused on equipment design and remolding to improve application performance (Li et al., 2017; He, 2019). These studies were meaningful for improving the equipment and application effectiveness. However, it is difficult to achieve farmer recognition. Previous study showed that farmers from larger farms focus more on financial benefits from robots and prefer large autonomous tractors. Conversely, small-scale or organic farmers consider environmental benefits of field crop robots relatively more important and favor small robots (Spykman et al., 2021). Few studies have focused on the effects of different pesticide application techniques on the ecological environment. It was essential to carry out a comprehensive comparison between conventional and intelligent technology and evaluate the difference between different pesticide application techniques in terms of both economic and ecological benefits. Some studies have compared UAV application methods to air-assisted spray methods in terms of spraying performance (Sarri et al., 2019; Martinez-Guanter et al., 2020; Li et al., 2021a). However, most studies were concentrated in a small area (less than 0.1 ha), which is quite distinct from the actual operation situation. On the other hand, the ecological characteristics of separate application techniques, such as environmental pollution, resource consumption and greenhouse gas emission, should also be evaluated due to the national green and sustainable development strategy in agricultural management, but it is still limited.

Thus, to understand the comprehensive performance of intelligent pesticide application technology and conventional technology in orchards, a comparison study through field positioning experiments was conducted. This study aimed to clarify the characteristics of different pesticide application techniques from the aspects of working effectiveness, efficiency, environmental pollution, water savings and CO_2 reduction and to

put forward suggestions for the development of orchard plant protection in the future, providing scientific support for the transition of intelligent management in orchards.

Materials and methods

Study area

A pear (*Pyrus bretschneideri*) orchard was selected as the target study area, which was located in Pinggu district, Beijing (Figure 1). The 4-year-old pear orchard covered an area of approximately 13 hectares. The dwarfing and dense planting mode was adapted in the target pear orchard. The distances between rows and trees were 4 and 1.5 m, respectively. The average height of the trees was approximately 3 m. Tests were conducted during October 2021. The daily daytime temperature ranged from 18 to 25°C, while the humidity was 45%. The wind speed was below 1 m/s during the experiment.

Sprayer characteristics

Five orchard pesticide application equipment were adapted in the study, including three mainstream orchard unmanned aircraft vehicles, one unmanned ground vehicle and one conventional manual spray gun (Figure 2). The basic parameters of the different equipment are shown in Table 1. All treatments were modeled on the actual operation parameter environment, which was promoted by the guidance of local orchardists and professional operators.

Experimental design

Three treatments were set in this study: spraying by unmanned aircraft vehicle (UAV), spraying by unmanned ground vehicle (UGV) and spraying by conventional spray gun (CONV). The average level of three major UAVs was adapted in order to represent the common performance about UAV application techniques. To better simulate the actual working environment, a 1 ha test field was set in the T1 and T2 treatments, which contained approximately 40 rows of pear trees. The large working area included at least 1 battery change or water refill. Considering the relatively low working efficiency in conventional manual application, a 0.08 ha test field was set in T3, which contained 5 rows of pear trees. Three types of unmanned aircraft vehicles were adapted for the test, and two repetitions were set for each piece of equipment. Meanwhile, both the T2 and T3 treatments were repeated 3 times. All

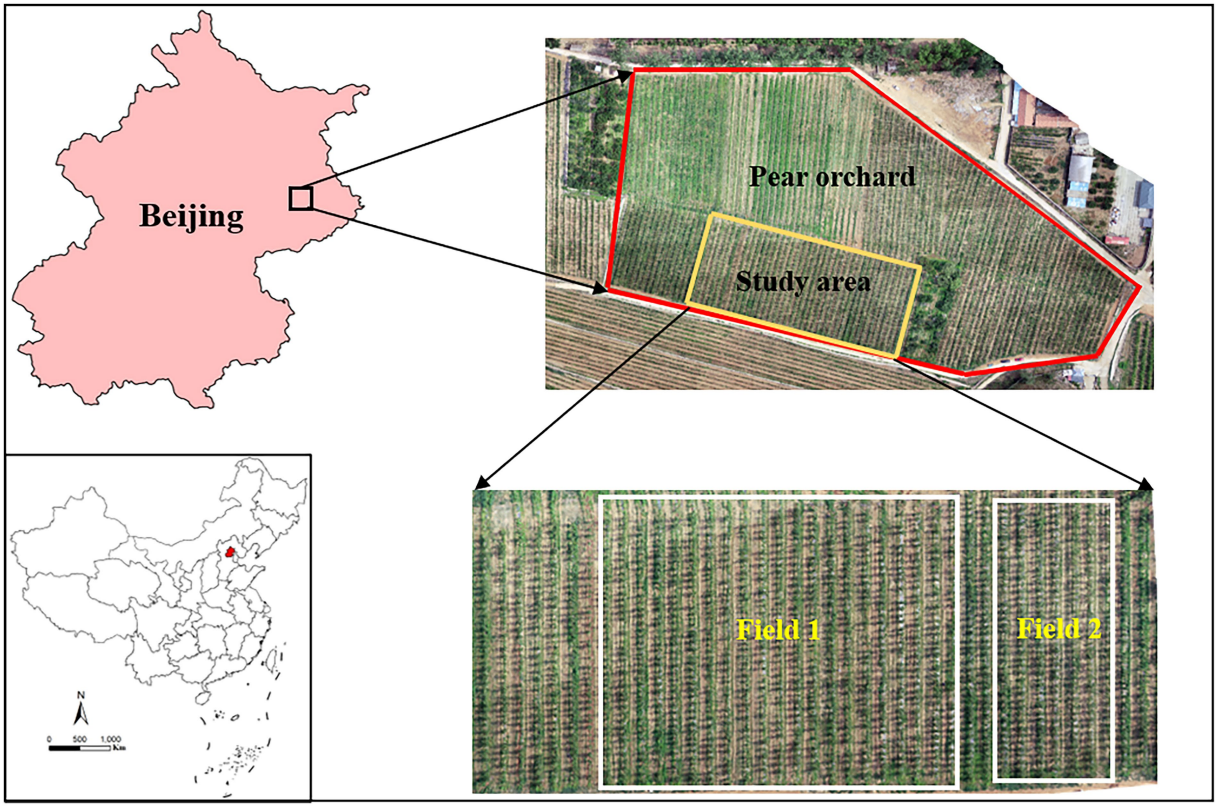

FIGURE 1
Location of the study area and test fields. Field 1 represents the test field of the unmanned aerial vehicle and ground machine spraying method; Field 2 represents the test field of the conventional artificial method.

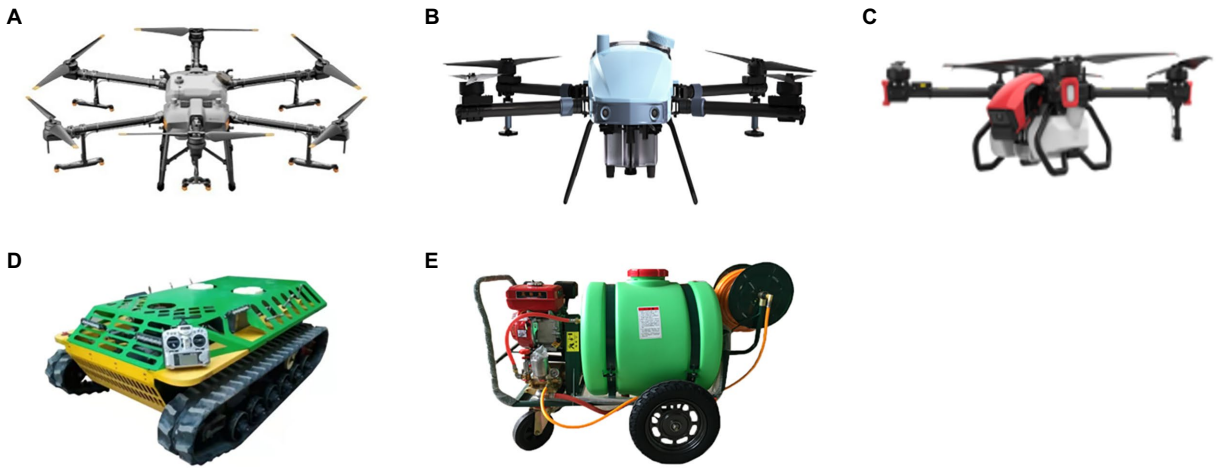

FIGURE 2
Major pesticide application equipment used in the study, including unmanned aircraft vehicles **(A–C)**, unmanned ground vehicles **(D)** and conventional manual spray guns **(E)**.

TABLE 1 Equipment and application parameters of unmanned aircraft vehicles (UAV), unmanned ground vehicle (UGV) and conventional manual spray guns (CONV) used in the trials.

Parameter	UAV-1	UAV-2	UAV-3	UGV	CONV
Tank capacity	30 l	20 l	40 l	200 l	300 l
Working speed	1.1 m/s	1.5 m/s	2.6 m/s	1 m/s	3.5 m/min
Spray width	7 m	3.5 m	3.2 m	6–8 m	10–12 m
Flight height	4.5 m	3.3 m	5.5 m	–	–
Flow rate	2.98 l/min	3.01 l/min	2.82 l/min	8 l/min	22 l/min
Engine power	7.2KW	7.2KW	7.2KW	9.5KW	4.8 KW

The engine power of the UAV represents the battery charge engine power.

intelligent application equipment were operated manually by professional operator and tried to keep uniformity in repetition. Through positioning experiments, the characteristics of different pesticide application techniques in spraying performance, working efficiency, environmental pollution and resource consumption were comprehensively analyzed.

Spray effectiveness test

Five consecutive trees were sampled in the middle row of each test field, and sample trees were no less than 10 m from the beginning and end of the row to ensure that the equipment was working stably when passing through (Figure 3A). The sample tree was divided into three layers, including upper, middle and lower layers, and the height of each layer was 2, 1.5, and 1 m, respectively. The number of sample points set in the upper, middle and lower layers was 4, 5 and 8, respectively (Figure 3B). The well-grown leaf which was fully expanded was chosen as the sample leaf, and 2 white art papers (60 mm × 40 mm) were attached on both the adaxial side and abaxial side of it. Ponceau 4R, a kind of food coloring with no risk of environmental pollution and human damage, was added as a replacement for pesticide in the test. All samples were scanned with a scanner (DS-1610, Epson, Beijing, China) at 400 dpi to obtain images. ImageJ, an image processing program, was used for the analysis to obtain spray coverage (Zhu et al., 2011).

The deposit coverage on both the adaxial side (CAD) and abaxial side (CAB) of the leaf was calculated in different layers during the test. The ratio of deposit coverage on the abaxial side and whole leaf (RBW) was calculated to account for droplet distribution uniformity on leaves (Li et al., 2022). The coefficient of variation, CV (%) was also calculated in the study.

$$RBW = \frac{CAB}{CAB + CAD} \quad (1)$$

$$CV = \frac{SD}{\overline{X}} \times 100\% \quad (2)$$

where SD represents the standard deviation of each treatment and x represents the mean value of each treatment.

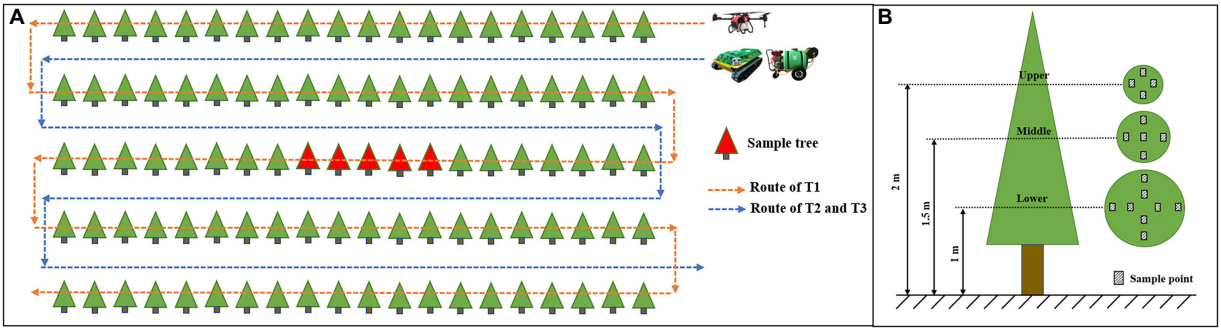

FIGURE 3
Layout of the test **(A)** and sample point **(B)**. The yellow line represents the flight route of the UAV; the blue line represents the route of UGVs and humans; the red triangle represents the sample trees; and the black rectangle represents the sample point.

Environmental pollution test

Pesticide application pollution mainly includes ground residue, machine residue and human body residue (Musiu et al., 2019; Rani et al., 2021). Deposit coverage was used to evaluate the degree of pollution in different positions. For the ground residue test, white art papers were attached to the ground at the center of rows and trees (Figure 4A). For the machine residue test, white art papers were randomly attached around the equipment, including the rotor, arm, tank, and shell (Figure 4C). For the human body residue test, white art papers were randomly pasted on the head, arm, chest and leg (Figure 4B). All samples were also scanned with a scanner (DS-1610, Epson, Beijing, China) at 400 dpi to obtain images, and ImageJ was used for the analysis to obtain average spray coverage.

Working efficiency test

Working efficiency (WE, ha/h) referred to the area of application completed in unit time. This study provides significant guidance for orchard management between different application techniques. The calculation formula was as follows:

$$\mathrm{WE}=\frac{A}{\sum_{i=1}^{n} T_i} \tag{3}$$

where T_i represents the overall application time in process i (h). The process includes dosing, battery change and machine transfer. A represents the application area (ha). In this study, stopwatch was used to record the progress of application. For UAV application, time recording was initiated at the route planning and ended at the complement of the last line of trees. For the ground machine and conventional manual techniques, time was started at dosing and ended at the complement of the last line of trees. Considering the difference in the application area between treatments, the application area per unit time was uniformly converted.

Water consumption test

Orchard workers usually use a fixed amount of pesticide, although the application technique varies. Thus, we calculated the overall water consumption among the different treatments. The calculation formula was as follows:

$$W=\sum_{i=1}^{n} W_b - W_e \tag{4}$$

where W represents the overall water consumption in the test (L). W_b represents the volume of water in the beginning (L); W_e represents the volume in the end (L); and n represents the time of dosing. The average water consumption per unit area was uniformly converted.

Machine CO_2 emission test

Machine CO_2 emissions (E_{CO2}, kg) refer to the CO_2 directly generated by the combustion of gasoline used in agricultural production. The emission was equal to the amount of gasoline multiplied by the CO_2 emission coefficient of gasoline. The calculation formula was as follows:

$$E_{C02}=\frac{\left(G_b-G_e\right)}{A}\times 2.9251 \tag{5}$$

where G_b represents the gasoline in the beginning and G_e represents the gasoline in the end, kg; A represents the application area, ha. The CO_2 emission coefficient of gasoline in China was 2.9251, $kgCO_2$-eq/kg. The determination of the CO_2 emission coefficient was referred from Intergovernmental Panel on Climate Change (IPCC) guidelines for greenhouse gas inventory and provincial guidance for greenhouse gas inventory complications (Paustian et al., 2006; Yan et al., 2022). In the UAV application treatment, the oil consumption of the generator used for battery charging was mainly recorded. Gasoline consumption of the engine was recorded in the UGV treatment while gasoline consumption of the pump was recorded in the conventional spray gun treatment.

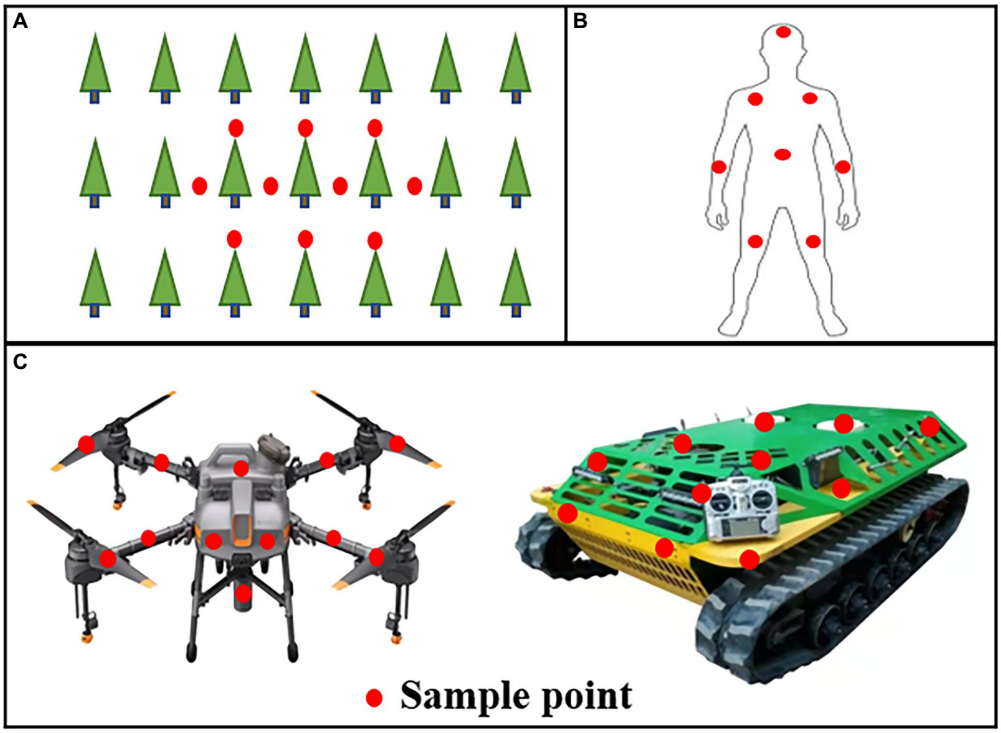

FIGURE 4
Layout of the sample site in the test of ground residue **(A)**, human body residue **(B)** and machine residue **(C)**. The red circle represents the sample point.

Data processing and analysis

Feature normalization was adapted in the study to make different types of data in the same range. StandardScaler was one of the feature normalization methods which had been widely adapted in data processing. After normalization, the mean value of each column of the matrix was 0 and the standard deviation was 1. The calculation formula was as follows:

$$X = \frac{(x - \mu)}{\sigma} \tag{6}$$

where X represents the result after feature normalization; x represents the initial data; μ represents the average value of dataset; σ represents the standard deviation of dataset.

All statistical analysis were conducted by SPSS 26.0 software (IBM Crop., Armonk, NY, United States). Before the statistical tests, assumptions of normality and homoscedasticity of the datasets were tested using the Shapiro–Wilk and Levene tests, respectively. One-way analysis of variance was applied to test the effects of different pesticide application techniques on spray performance, environmental residue, working efficiency and resources consumption. Significant differences between various treatments were identified by the least significant difference test at the $p < 0.05$ level. Data visualization was performed using the R package ggplot 2.

Results and discussion

Assessment of spraying performance

Various deposit coverages occurred in different layers between different spraying techniques (Table 2). The average deposit coverages of UAV, UGV, and CONV in the test were 3.4, 60.3 and 34.9%, respectively. Similar to previous studies, deposit coverage on the adaxial side was higher than that on the abaxial side in all treatments (Grella et al., 2020; Salcedo et al., 2020). According to the UAV's low-volume-spray characteristics, the deposit coverage in UAV was significantly lower than that in the other treatments. The average deposit coverage was approximately 3.4%. The deposit coverage decreased from the upper to lower layer on both the adaxial and abaxial side. The deposit coverage on the abaxial side of the lower layer was approximately 1.1%. In addition, the average CV of UAV (66.2%) was higher than that of the other treatments. This result indicated that UAV application technology is unstable, which could affect the overall pest control in the orchards. Generally, it could achieve pest control effects when the deposit coverage exceeds 1% during UAV application (Wang et al., 2022) due to its high-concentration spraying property. The results indicated that UAV application could adapt to orchard pest control. However, unstable effectiveness would reduce acceptance for farmers because of the uncertainty in the control effect. Previous research also showed mediocre performance in UAV spraying (Li et al., 2021c). In

TABLE 2 Comparison of deposit coverage on the adaxial side (CAD) and abaxial side (CAB) of the leaf between different layers and spraying techniques.

Layer	Treatment	CAD		CAB	
		Mean (%) ± SE	CV (%)	Mean (%) ± SE	CV (%)
Upper	UAV	6.8 ± 1.6c	66.4	1.6 ± 0.2c	46.2
	UGV	51.8 ± 6.4a	41.1	34.3 ± 8.9a	48.3
	CONV	23.1 ± 4.2b	42.3	16.2 ± 6.5b	46.5
Middle	UAV	5.7 ± 0.9c	63.5	1.4 ± 0.9c	65.7
	UGV	79.6 ± 5.6a	27.0	42.2 ± 6.9a	59.2
	CONV	47.4 ± 3.7b	19.6	33.3 ± 8.3ab	45.5
Lower	UAV	3.2 ± 0.2c	28.5	1.1 ± 0.2c	57.5
	UGV	91.1 ± 3.1a	17.5	62.6 ± 4.8a	40.3
	CONV	52.6 ± 7.8b	17.9	36.7 ± 5.4b	42.6

Mean represents average values of 18–27 biological replicates. ± indicates standard error of each dataset. The different letters in the same column indicate significant differences at the $p < 0.05$ by ANOVA test with LSD as *post hoc* test.

contrast to field crops, pest control in orchards is stricter because it will affect the economic benefit significantly.

Unmanned ground vehicle application technology showed the highest deposit coverage on both the adaxial and abaxial sides of leaves among all treatments. In contrast to the UAV, the deposit coverage increased from the upper to the lower layer. This was mainly because the ground machine sprays from the bottom to the top through high-pressure assistance. It had a relatively low average CV (37.1%) in different layers, which is more stable than UAV application. Generally, deposit coverage of approximately 30–70% in ground pesticide application equipment is normal, and some high-application-volume operations even approach 100% (Gil et al., 2021; Wang et al., 2022). Although ground machines have better performance in pesticide application, high environmental pollution and pesticide residues should be given more attention.

Conventional spray gun technology showed similar characteristics to UGV in different layers. The deposit coverage in each layer was lower than that in ground machine technology, and the average CV was 42.2%. The results showed that the conventional method has satisfactory performance in orchard plant protection. However, human application is uncertain. It depends on the experience of the farmers, degree of fatigue and other factors associated with the farmers, which could directly affect the performance of plant protection in practice (Foque et al., 2012). At present, there is no deposit coverage standard for fruit trees, and it is difficult to compare the performance of different application techniques. The perspectives of uniformity and penetration are usually selected as indices of application evaluation (Wang et al., 2022). For further study, a reasonable assessment index system should be built through big data surveys and multipoint experiments.

Assessment of environmental pollution

Deposit coverage on the ground, machine and human body were estimated in the study, which could represent the environmental pollution in different spraying technologies. The average level of environmental pollution during pesticide application was CONV > UGV > UAV (Figure 5). UAV showed a relatively lower environmental residual than the other treatments. Deposit coverage on the ground, machine and human body were 22, 15 and 6%, respectively. Although UAV application technology uses a low-volume spraying method, it can still cause ground residue in actual applications. Drift of droplets could lead to uncertainty in pesticide application (Wang et al., 2021). On the other hand, a suitable flight route is also important to in the application of a sprayer above the canopy of the tree. Machine pollution of UAV application technology mainly came from the interaction of air flow and environmental wind, which allow droplets to drift to the surface of the machine. Human body pollution in UAV application could also come from droplet drift. Drift characteristics increase the uncertainty of environmental pollution in agricultural UAV applications (Liu et al., 2020; Martinez-Guanter et al., 2020). It would be harmful to the surrounding environment when we use UAV technology in agricultural management, such as pesticide and herbicide application.

High ground residual and machine residual values occurred in UGV, which were significantly higher than those in UAV. The deposit coverages of UGV on the ground and machined were 93 and 88%, respectively. High-volume spraying under UGV technology could achieve better performance on leaves at the cost of environmental pollution. It also demonstrated that the pesticide utilization efficiency of UGV application technology could be improved, which was meaningful for green and sustainable development in agricultural management. However, UGV showed a lower residual on the human body, with an of average 2% coverage. The remote operation using in UGV technology could effectively reduce the exposure of humans in the application environment and protect operators from pesticide damage.

Conventional spray gun showed the highest environmental pollution compared to UAV and UGV. The deposit coverage on the ground and machine were close to UGV. Human body residue amount was significantly higher than others, which could lead to

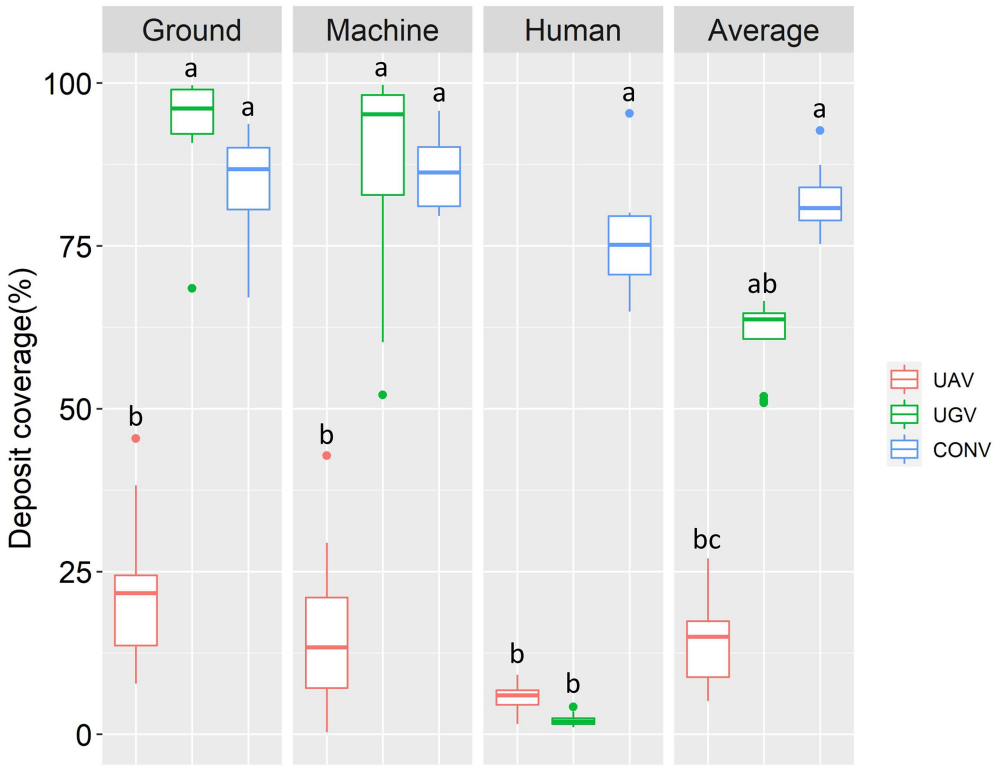

FIGURE 5
The droplet residue on the ground, machine and human body of unmanned aircraft vehicle technique (UAV), unmanned ground vehicle technique (UGV) and conventional manned technique (CONV). Different letters in the same column indicate significant differences at the $p<0.05$ level under ANOVA test with LSD as *post hoc* test. UAV had 18 biological replicates while UGV and CONV had 13 biological replicates.

greater potential threat to the operator. It is easy to understand that operators were fully exposed to the application environment, which could result in a large amount of residue on the body. Operator health has received increasing social attention because of the high operator exposure, which has been accused of negative health issues such as respiratory, dermatological, neurological, reproductive, endocrine, and gastrointestinal diseases (Nuyttens et al., 2009). Conventional pesticide application technology was not sustainable unless personnel safety was addressed.

Generally, the results indicated that intelligent plant protection technology could reduce environmental pollution and human damage compared to conventional methods. However, there is still much room for improvement to reduce the ground and machine residue to further increase the pesticide utilization efficiency. For UAV application technology, drift influence should be evaluated both in theory and in practice. Meanwhile, for UGV application technology, volume control and spray angle improvement may be useful for the reduction in environmental pollution.

Assessment of working efficiency

Working efficiency could directly affect cost estimation and technology promotion. The results showed that the working efficiency of UAV application was approximately 1.82 ha/h, which was the highest among all treatments (Table 3). This result was lower than data recommended from UAV companies or some previous studies. However, these studies did not consider the time of dosing, charging, or changing the battery. The properties are very important in practice. The duration of a single flight of a UAV was usually no more than 20 min, and it needed to be maintained through battery replacement in large-scale operation. Although each battery replacement and charging time could be shortened by engaging experienced workers, multiple uses during application would result in longer time of application. Meanwhile, all UAV operations should be carried out on the ridge, and the round-trip operation also requires time. The results in this study could be closer to the actual application.

The working efficiency of UGV application following UAV was approximately 1.29 ha/h. The results might be higher because the test field was in a standardized orchard, which was easier for UGV working. The flat terrain allowed the ground machine to move at a constant speed, and rational planting allowed the machine to turn around more easily. However, in some disorderly planting orchards, the ground machine often needs to return to the original path and then proceed to the next row. For some hilly orchards, the moving speed could also be difficult to control,

TABLE 3 Comparison of the working efficiency and resource consumption of different spraying technologies.

Treatment	Area (ha)	Time (h)	Efficiency	Water usage	Gasoline usage	CO_2 emission
			ha/h ± SE	L/ha ± SE	L/h ± SE	kg/ha ± SE
UAV	1.00	0.55	1.82 ± 1.1a	105 ± 1.1c	3.00 ± 0.5a	3.60 ± 0.5b
UGV	1.00	0.78	1.28 ± 0.9b	360 ± 6.2b	1.52 ± 0.4b	3.15 ± 1.3b
Conventional	0.08	0.84	0.09 ± 0.01c	3,375 ± 101.9a	1.48 ± 0.2b	39.00 ± 4.2a

All values in table represent average values of 3–9 biological replicates. ± indicates standard error of each dataset. Different letters in the same column indicate significant differences at the $p < 0.05$ level under ANOVA test with LSD as *post hoc* test.

which would affect the working efficiency of the intelligent ground machine.

Conventional technology showed the lowest working efficiency compared to others, which was approximately 0.09 ha/h. The result could be lower than actual application because of the efficiency of a single operator. In most orchard pesticide applications, there are usually at least two people working simultaneously using spray gun technology. One pump could connect to 4 spray guns at the same time. Thus, the actual working efficiency was difficult to calculate considering different orchard scales or management. However, compared with intelligent application technology, working efficiency assessment based on a single-person working environment is still meaningful.

In general, the higher working efficiency that occurred in the UAV and UGV applications showed the advancement of intelligent pesticide application techniques. The working efficiency of the UAV was almost 20 times higher than that of the conventional method. UGV could also improve efficiency, which was approximately 14 times that of conventional technology. Due to the shortage of the agricultural population and the increase in labor costs, intelligent pesticide application technology will be an alternative in the future due to its significantly high efficiency.

Assessment of water-saving potential

The economical utilization of resources is also an important aspect for the comparison of different pesticide application techniques. The results showed that the variation characteristics of water consumption among the different treatments were UAV < UGV < Conventional (Table 3). The average water usage in UAV application was approximately 105 l/ha. The lower water consumption was mainly due to its low-volume and high-concentration spraying characteristics. The water consumption under UGV application was approximately 360 l/ha, which was almost three times higher than that under UAV application. The water consumption of conventional technology was approximately 3,375 l/ha, which was significantly higher than that of the other treatments. The results indicated that intelligent plant protection equipment has a significant advantage in water savings during pesticide application compared to conventional methods, especially in UAV application technology. New spraying technology could save approximately 3,000 l/ha water resources within a single-time application. Generally, orchards usually need at least 8 pesticide applications during the growing season. The adaptation of intelligent application technology could have vast water saving potential in orchard management. Meanwhile, in actual orchard plant protection, farmers usually adapt the same amount of pesticide regardless of the application technique to ensure control effectiveness. Thus, current intelligent application techniques cannot reduce pesticide consumption. However, with the development of variable pesticide application technology, it will be possible to achieve both water and pesticide savings through intelligent techniques in the future (Chen et al., 2021).

Assessment of CO_2 emission reduction potential

UAV application showed higher gasoline consumption compared to UGV and conventional technology. The average gasoline consumption of UAV application was approximately 3 l/h, while gasoline consumption of UGVs and conventional technology was 1.52 and 1.48 l/ha, respectively (Table 3). UAV technology was recognized as cleaner energy equipment because of replacing fuel with electric power (Matlock et al., 2019). However, in practical operation, UAV application needs to maintain its endurance through long-term battery charging, which still requires a high amounts of gasoline consumption of gasoline. The results showed that the gasoline consumption of UAV application in fixed time was twice that in UGV application and the conventional method. The average CO_2 emissions of machines through the combination of working efficiency and gasoline usage were also calculated in the study. The average CO_2 emissions of the UAV, UGV and conventional techniques were 3.60, 3.15 and 39.00 kg/ha, respectively. Although UAV application consumes more gasoline in a fixed time, high working efficiency could eliminate its negative effect on CO_2 emissions to a certain degree. In contrast, conventional application technology has much higher CO_2 emissions due to its low working efficiency. UGV application showed better performance in reducing CO_2 emissions than the other treatments. The results indicated that intelligent pesticide application technology could effectively reduce CO_2 emissions

from the machine itself compared with the conventional method. The application of intelligent techniques in orchards is of great significance to the national carbon neutrality strategy.

Perspectives and implications

The innovation on pesticide application technique is important and urgent for orchard management due to the rapid decrease in agricultural labor and the increase in labor costs. Intelligent pesticide application techniques should be developed to cope with the current dilemma in orchard management (He, 2018). However, different pesticide application techniques have their own characteristics (Figure 6), and there is still no satisfactory application technique to date. UAV application technology could significantly improve the working efficiency, which has been recognized by most researchers (Li et al., 2021b). It also had a significant advantage in pollution control and water resource reduction during pesticide application due to its low-volume spraying. Higher working efficiency also led to lower carbon dioxide emissions from the machine itself. However, spraying uniformity was the greatest challenge for UAV application technology, which could directly affect the effectiveness of pest control in orchard management (Qin et al., 2018). A previous study had also showed that spraying performance of UAV technique was much poorer than conventional methods, especially in spray uniformity and penetration (Wang et al., 2022). Even in field crops application with lower canopy, the spray performance and pest control effectiveness under UAV application were still unsatisfied (Li et al., 2021b). The research emphasis of UAV application technology should focus on improving the application effect and reducing drifting pollution. Nozzle improvement, droplet control, airflow control and operation parameter optimization are of great significance in improving the application effectiveness of UAV technology (Wang et al., 2022). For the orchard manager, UAV spraying technology could only be considered if the spraying uniformity and penetration have been improved and can achieve better performance in pest or disease control.

Fewer studies had evaluated the performance of UGV application technique in orchard management in past years. Interestingly, our study proved that UGV application technology also has advantages in working efficiency improvement, water savings and carbon dioxide emission reduction compared to conventional methods. UGV application technology had a better spraying uniformity with the price of higher pesticide pollution, which differed from UAV spraying technology. For orchard managers, UGV application technology could be a better choice for the replacement of conventional methods considering the stable application performance and low natural resource waste. However, how to control environmental pollution during actual practice is also important to the development of UGV application

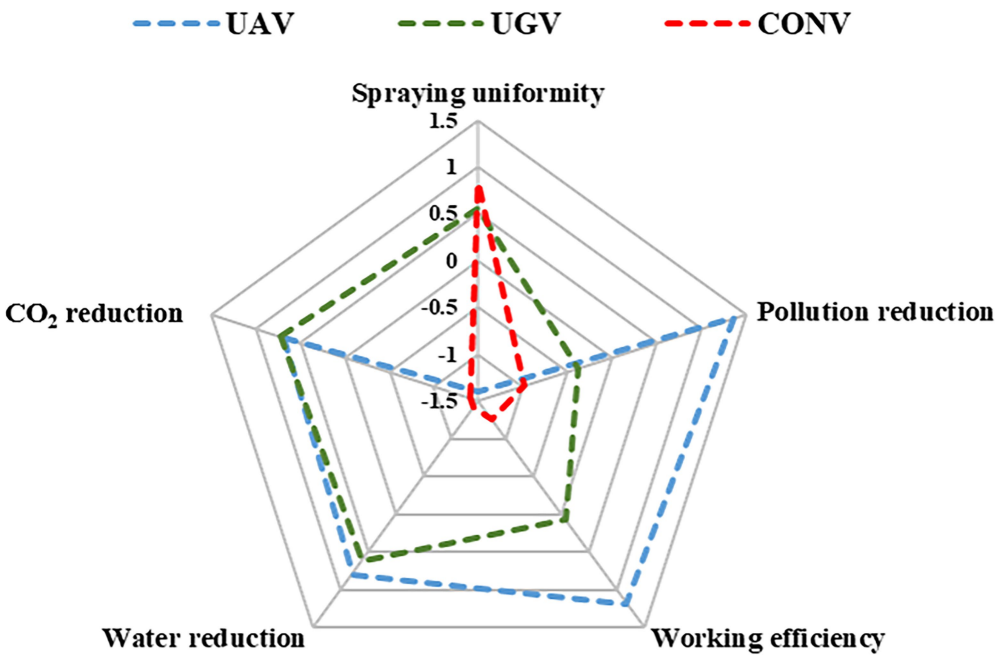

FIGURE 6
Comprehensive comparison of characteristics in different pesticide application techniques. Blue line represents unmanned aircraft vehicle technique (UAV), green represents unmanned ground vehicle technique (UGV) and red line represents conventional manned technique (CONV). Data was normalized and 0 represents the average value of each column. Positive values represent performance above average in each column whereas negative values represent performance below average.

technology in the future. It is possible to reduce environmental pollution and increase pesticide utilization efficiency through the adjustment of flow and spray angle. On the other hand, considering the cost of intelligent equipment and the planting scale of orchards, conventional spray gun technology could also be a valid choice. However, with orchard standardization and scale management, intelligent pesticide application techniques will play an important role in the future of orchard management. Different scales and types of orchards could influence the performance of different pesticide application techniques. To improve the application performance and environmental pollution of intelligent application techniques, we should also pay more effort in better detection sensors together with more accurate machine learning algorithms. Precision application technology which is based on monitoring sensors and recognition algorithms, as well as control of spray parameters will play an important role in intelligent equipment in the future.

This study systematically clarified the characteristics of intelligent unmanned vehicle techniques in pesticide application from the aspects of working effectiveness, efficiency, environmental pollution, water saving and carbon dioxide reduction, which are important for the development of intelligent equipment in orchard. It should be noted that our study was conducted in a standardized orchard. To cover a wider range of working environments, we will further consider the effects of orchard type, planting scale, ecological area, and other factors on the performance of different pesticide application techniques. Moreover, a meta-analysis could also help to achieve more accurate and universal results. Meanwhile, all intelligent equipment in this study were operated manually which may cause various among receptions. As the development of automatic navigation and application in UAV and UGV, the artificial error can be avoided for further research.

Conclusion

This study clarified the characteristics of different pesticide application techniques from the aspects of working effectiveness, efficiency, environmental pollution and resource protection. UAV application techniques have advantages of high working efficiency and low environmental pollution and natural resource consumption. However, it performed worse in spray performance compared to the UGV and conventional manual methods. UGV application techniques could improve spray performance at the cost of high environmental pollution. The conventional spray gun technique also showed good spray performance. However, the tradition method was unfriendly to environmental protection and the green development of agriculture. Intelligent pesticide application techniques could be an alternative to conventional methods. Improving spray performance and controlling environmental pollution are major directions for UAV and UGV technology improvement in the future.

Further research should be undertaken to investigate the comprehensive performance of intelligent application techniques in different kinds of orchards. A meta-analysis can be carried out to make the results more accurate and universal. This study comprehensively evaluated the characteristics of different pesticide application techniques and put forward suggestions for the development of orchard plant protection in the future, providing scientific support for the transition of intelligent management in orchards and the development of smart agriculture in China.

Data availability statement

The raw data supporting the conclusions of this article will be made available by the authors, without undue reservation.

Author contributions

YJ performed most of the experiments with the assistant of TL, PQ, CY, and FC provides guidance of work while XH and JS contributed to the study conception and design. All authors contributed to the article and approved the submitted version.

Funding

This work was supported by the National Natural Science Foundation of China (no. 31761133019), China Agriculture Research System of MOF and MARA (CARS-28), and the 2115 Talent Development Program of China Agricultural University.

Acknowledgments

We thank the managers of orchard for their kindly help and support. We also thank all reviewers and the editor for their suggestions, which substantially improved the manuscript.

Conflict of interest

The authors declare that the research was conducted in the absence of any commercial or financial relationships that could be construed as a potential conflict of interest.

Publisher's note

References

Abbas, J., and Sagsan, M. (2019). Impact of knowledge management practices on green innovation and corporate sustainable development: a structural analysis. *J. Clean. Prod.* 229, 611–620. doi: 10.1016/j.jclepro.2019.05.024

An, Q. S., Li, D., Wu, Y. L., and Pan, C. P. (2020). Deposition and distribution of myclobutanil and tebuconazole in a semidwarf apple orchard by hand-held gun and air-assisted sprayer application. *Pest Manag. Sci.* 76, 4123–4130. doi: 10.1002/ps.5968

Benos, L., Sørensen, C. G., and Bochtis, D. (2022). Field deployment of robotic Systems for Agriculture in light of key safety, labor, ethics and legislation issues. *Curr. Robot Rep.* 3, 49–56. doi: 10.1007/s43154-022-00074-9

Benos, L., Tagarakis, A. C., Dolias, G., Berruto, R., Kateris, D., and Bochtis, D. (2021). Machine learning in agriculture: a comprehensive updated review. *Sensors* 21, 3758. doi: 10.3390/s21113758

Cai, J. Y., Xiong, J. J., Hong, Y., and Hu, R. F. (2021). Pesticide overuse in apple production and its socioeconomic determinants: evidence from Shaanxi and Shandong provinces. *China. J. Cleaner Prod.* 315:128179. doi: 10.1016/j.jclepro.2021.128179

Chen, H. B., Lan, Y. B., Fritz, B. K., Hoffmann, W. C., and Liu, S. B. (2021). Review of agricultural spraying technologies for plant protection using unmanned aerial vehicle (UAV). *Int. J. Agric. Biol. Eng.* 14, 38–49. doi: 10.25165/j.ijabe.20211401.5714

EU (2016). European Parliament. Ethical aspects of cyber-physical systems. Available at: https://www.europarl.europa.eu/thinktank/en/document/EPRS_STU(2016)563501 (Accessed June 28, 2016).

FAO (2020). Food and agriculture Organization of the United Nations. Available at: http://www.fao.org/faostat/zh/#data/QC (Accessed December 22, 2020).

Foque, D., Pieters, J. G., and Nuyttens, D. (2012). Comparing spray gun and spray boom applications in two ivy crops with different crop densities. *HortScience* 47, 51–57. doi: 10.21273/HORTSCI.47.1.51

Gil, E., Salcedo, P., Solser, A., Ortega, P., Llop, J., Campos, J., et al. (2021). Realative efficiencies of experimental and conventional foliar sprayers and assessment of optimal LWA spray volumes in trellised wine grapes. *Pest. Manag. Sci.* 77, 2462–2476. doi: 10.1002/ps.6276

Grella, M., Marucco, P., Zwertvaegher, I., Gioelli, F., Bozzer, C., Biglia, A., et al. (2022). The effect of fan setting, air-conveyor orientation and nozzle configuration on airblast sprayer efficiency: insights relevant to trellised vineyards. *Crop Prot.* 155:105921. doi: 10.1016/j.cropro.2022.105921

Grella, M., Miranda-Fuentes, A., Marucco, P., and Balsari, P. (2020). Field assessment of a newly-designed pneumatic spout to contain spray drift in vineyards: evaluation of canopy distribution and off-target losses. *Pest Manag. Sci.* 76, 4173–4191. doi: 10.1002/ps.5975

Guo, M., Nowakowska-Grunt, J., Gorbanyov, V., and Egorova, M. (2020). Green technology and sustainable development: assessment and green growth frameworks. *Sustainability* 12, 6571. doi: 10.3390/su12166571

He, X. (2018). Rapid development of unmanned aerial vehicles (UAV) for plant protection and application technology in China. *Outlooks Pest Manag.* 29, 162–167. doi: 10.1564/v29_aug_04

He, X. K. (2019). Research and development of crop protection machinery and chemical application technology in China (in Chinese). *Chin. J. Pest. Sci.* 21, 921–930. doi: 10.16801/j.issn.1008-7303.2019.0089

He, X., Bonds, J., Herbst, A., and Langenakens, J. (2017). Recent development of unmanned aerial vehicle for plant protection in East Asia. *Int J Agric Biol Eng.* 10, 18–30.

Jiang, Y. L., Yin, X. G., Wang, X. H., Zhang, L., Lu, Z., Lei, Y. D., et al. (2021). Impacts of global warming on the cropping systems of China under technical improvements from 1961 to 2016. *Agron. J.* 113, 187–199. doi: 10.1002/agj2.20497

Kefauver, S. C., Vicente, R., Vergara-Diaz, O., Fernandez-Gallego, J., Kerfal, S., Lopez, A., et al. (2017). Comparative UAV and field phenotyping to assess yield and nitrogen use efficiency in hybrid and conventional barley. *Front. Plant Sci.* 8, 1733. doi: 10.3389/fpls.2017.01733

Khot, L. R., Ehsani, R., Albrigo, G., Larbi, P. A., Landers, A., Campoy, J., et al. (2012). Air-assisted sprayer adapted for precision horticulture: spray patterns and deposition assessments in small-sized citrus canopies. *Biosyst. Eng.* 113, 76–85. doi: 10.1016/j.biosystemseng.2012.06.008

Lan, Y., and Chen, S. (2018). Current status and trends of plant protection UAV and its spraying technology in China. *Int. J. Precis. Agric. Aviat.* 1, 1–9. doi: 10.33440/j.ijpaa.20180101.0002

Li, X., Giles, D. K., Andaloro, J. T., Long, R., Lang, E. B., Waston, L. J., et al. (2021b). Comparison of UAV and fixed-wing aerial application for alfalfa insect pest control: evaluating efficacy, residues, and spray quality. *Pest Manag. Sci.* 77, 4980–4992. doi: 10.1002/ps.6540

Li, X., Giles, D. K., Niederholzer, F. J., Andaloro, J. T., Lang, E. B., and Watson, L. J. (2021c). Evaluation of an unmanned aerial vehicle as a new method of pesticide application for almond crop protection. *Pest Manag. Sci.* 77, 527–537. doi: 10.1002/ps.6052

Li, L. L., He, X. K., Song, J. L., Wang, X. N., Jia, X. M., and Liu, C. H. (2017). Design and experiment of automatic profiling orchard sprayer based on variable air volume and flow rate. *Trans. Chin. Soc. Agric. Eng.* 33, 70–76. doi: 10.11975/j.issn.1002-6819.2017.01.009

Li, J., Li, Z., Ma, Y., Cui, H., Yang, Z., and Lu, H. (2021a). Effects of leaf response velocity on spray deposition with an air-assisted orchard sprayer. *Int. J. Agric. Biol. Eng.* 14, 123–132. doi: 10.25165/j.ijabe.20211401.5435

Li, T., Qi, P., Wang, Z. C., Xu, S. Q., Huang, Z., Han, L., et al. (2022). Evaluation of the effects of airflow distribution patterns on deposit coverage and spray penetration in multi-unit air-assisted sprayer. *Agronomy* 12, 944. doi: 10.3390/agronomy12040944

Liu, Z., Guo, P., Liu, H., Fan, P., Zeng, P., Liu, X., et al. (2021). Gradient boosting estimation of the leaf area index of apple orchards in UAV remote sensing. *Remote Sens.* 13, 3263. doi: 10.3390/rs13163263

Liu, Y., Li, L., Liu, Y. J., He, X., Song, J., Zeng, A., et al. (2020). Assessment of spray deposition and losses in apple orchards from unmanned agricultural aircraft system in China. *Trans. ASABE* 63, 619–627. doi: 10.13031/trans.13233

Lu, X. Y., Gong, Y., Liu, D. J., Wang, G., Chen, X., Zhang, X., et al. (2021). CFD simulation and experiment on the flow field of air-assisted ultra-low-volume sprayer in facilities. *Int. J. Agric. Biol. Eng.* 14, 26–34. doi: 10.25165/j.ijabe.20211402.6013

Martinez-Guanter, J., Agüera, P., Agüera, J., and Pérez-Ruiz, M. (2020). Spray and economics assessment of a UAV-based ultra-low-volume application in olive and citrus orchards. *Precis. Agric.* 21, 226–243. doi: 10.1007/s11119-019-09665-7

Matlock, J., Sharikov, P., Warwick, S., Richards, J., and Suleman, A. (2019). Evaluation of energy efficient propulsion technologies for unmanned aerial vehicle. *Trans. Can. Soc. Mech. Eng.* 43, 481–489. doi: 10.1139/tcsme-2018-0231

Meng, Y., Su, J., Song, J., Chen, W. H., and Lan, Y. (2020). Experimental evaluation of UAV spraying for peach trees of different shapes: effects of operational parameters on droplet distribution. *Comput. Electron. Agric.* 170:105282. doi: 10.1016/j.compag.2020.105282

Musiu, E. M., Qi, L. J., and Wu, Y. L. (2019). Spray deposition and distribution on the targets and losses to the ground as affected by application volume rate, airflow rate and target position. *Crop Prot.* 116, 170–180. doi: 10.1016/j.cropro.2018.10.019

Nuyttens, D., Baetens, K., De Schampheleire, M., and Sonck, B. (2007). Effect of nozzle type, size and pressure on spray droplet characteristics. *Biosyst. Eng.* 97, 333–345. doi: 10.1016/j.biosystemseng.2007.03.001

Nuyttens, D., Braekman, P., Windey, S., and Sonck, B. (2009). Potential dermal pesticide exposure affected by greenhouse spray application technique. *Pest Manag. Sci.* 65, 781–790. doi: 10.1002/ps.1755

Pan, D., He, M. M., and Kong, F. B. (2020). Risk attitude, risk perception, and farmers' pesticide application behavior in China: A moderation and mediation model. *J. Clean. Prod.* 276:124241. doi: 10.1016/j.jclepro.2020.124241

Paustian, K., Ravindranath, N. H., and Amstel, A. V. (2006). 2006 IPCC Guidelines for National Greenhouse Gas Inventories. International Panel on Climate Change.

Qin, W. C., Xue, X. Y., Zhang, S. M., Gu, W., and Wang, B. K. (2018). Droplet deposition and efficiency of fungicides sprayed with small UAV against wheat powdery mildew. *Int. J. Agric. Biol. Eng.* 11, 27–32. doi: 10.25165/j.ijabe.20181102.3157

Rani, L., Thapa, K., Kanojia, N., Sharma, N., Singh, S., Grewal, A. S., et al. (2021). An extensive review on the consequences of chemical pesticides on human health and environment. *J. Clean. Prod.* 283:124657. doi: 10.1016/j.jclepro.2020.124657

Salcedo, R., Zhu, H., Zhang, Z., Wei, Z., Chen, L., Ozkan, E., et al. (2020). Foliar deposition and coverage on young apple trees with PWM-controlled spray systems. *Comput. Electron. Agric.* 178:105794. doi: 10.1016/j.compag.2020.105794

Sarri, D., Martelloni, L., Rimediotti, M., Lisci, R., Lombardo, S., and Vieri, M. (2019). Testing a multi-rotor unmanned aerial vehicle for spray application in high slope terraced vineyard. *J Agric Eng.* 50, 38–47. doi: 10.4081/jae.2019.853

Spykman, O., Gabriel, A., Ptacek, M., and Gandorfer, M. (2021). Farmers' perspectives on field crop robots-evidence from Bavaria, Germany. *Comput. Electron. Agric.* 186:106176. doi: 10.1016/j.compag.2021.106176

Tang, Y., Hou, C. J., Luo, S. M., Lin, J. T., Yang, Z., and Huang, W. F. (2018). Effects of operation height and tree shape on droplet deposition in citrus trees using an unmanned aerial vehicle. *Comput. Electron. Agric.* 148, 1–7. doi: 10.1016/j.compag.2018.02.026

Wang, C., He, X., Wang, X., Bonds, J., and He, Z. (2016). Testing method of spatial pesticide spraying deposition quality balance for unmanned aerial vehicle. *Trans. Chin. Soc. Agric. Eng.* 32, 54–61. doi: 10.11975/j.issn.1002-6819.2016.11.008

Wang, C. L., Herbst, A., Zeng, A. J., Wongsuk, S., Qiao, B. Y., Qi, P., et al. (2021). Assessment of spray deposition, drift and mass balance from unmanned aerial vehicle sprayer using an artificial vineyard. *Sci. Total Environ.* 777:146181. doi: 10.1016/j.scitotenv.2021.146181

Wang, C. L., Liu, Y., Zhang, Z. H., Han, L., Li, Y. F., Zhang, H., et al. (2022). Spray performance evaluation of a six-rotor unmanned aerial vehicle sprayer for pesticide application using an orchard operation mode in apple orchards. *Pest Manag. Sci.* 78, 2449–2466. doi: 10.1002/ps.6875

Yan, S. J., Deng, A. X., Shang, Z. Y., Tang, Z. W., Chen, C. Q., Zhang, J., et al. (2022). Characteristics of carbon emission and approaches of carbon mitigation and sequestration for carbon neutrality in China's crop production (in Chinese). *Crop J.* 48:12.

Young, J., Kingwell, R., Bathgate, A., and Thomson, A. (2015). Agricultural greenhouse gas emission reporting: the implications for farm management. *J. Sustain. Agric.* 40, 261–276. doi: 10.1080/21683565.2015.1131221

Zhai, C., Zhao, C., Wang, N., Long, J., Wang, X., Weckler, P., et al. (2018). Research progress on precision control methods of air-assisted spraying in orchards. *Trans. Chin. Soc. Agric. Eng.* 34, 1–15. doi: 10.11975/j.issn.1002-6819.2018.10.001

Zhang, J., Virk, S., Porter, W., Kenworthy, K., Sullivan, D., and Schwartz, B. (2019). Applications of unmanned aerial vehicle based imagery in turfgrass field trials. *Front. Plant Sci.* 10:279. doi: 10.3389/fpls.2019.00279

Zhao, Q. Y., Bao, H. X. H., and Zhang, Z. L. (2021). Off-farm employment and agricultural land use efficiency in China. *Land Use Policy* 101:105097. doi: 10.1016/j.landusepol.2020.105097

Zhu, H., Salyani, M., and Fox, R. D. (2011). A portable scanning system for evaluation of spray deposit distribution. *Comput. Electron. Agric.* 76, 38–43. doi: 10.1016/j.compag.2011.01.003

frontiers | Frontiers in Plant Science

ORIGINAL RESEARCH
published: 13 September 2022
doi: 10.3389/fpls.2022.900939

Control Efficacy and Deposition Characteristics of an Unmanned Aerial Spray System Low-Volume Application on Corn Fall Armyworm *Spodoptera frugiperda*

Changfeng Shan[1], *Jiajun Wu*[2], *Cancan Song*[1], *Shengde Chen*[3], *Juan Wang*[4], *Haihong Wang*[2], *Guobin Wang*[1]* and *Yubin Lan*[1,3,5]*

[1] College of Agricultural Engineering and Food Science, Shandong University of Technology, Zibo, China, [2] Corteva Agroscience Technology (Shanghai) Co., Ltd., Shanghai, China, [3] College of Electronic Engineering, College of Artificial Intelligence, South China Agricultural University, Guangzhou, China, [4] Mechanical and Electrical Engineering College, Hainan University, Haikou, China, [5] Department of Biological and Agricultural Engineering, Texas A&M University, College Station, TX, United States

OPEN ACCESS

Edited by:
Xiongkui He,
China Agricultural University, China

Reviewed by:
Jane Bonds,
Consultant, Panama City Beach, United States
Soumi Mitra,
New Mexico State University, United States

***Correspondence:**
Guobin Wang
guobinwang@sdut.edu.cn
Yubin Lan
ylan@sdut.edu.cn

Specialty section:
This article was submitted to Sustainable and Intelligent Phytoprotection, a section of the journal Frontiers in Plant Science

Received: 21 March 2022
Accepted: 17 May 2022
Published: 13 September 2022

Citation:
Shan C, Wu J, Song C, Chen S, Wang J, Wang H, Wang G and Lan Y (2022) Control Efficacy and Deposition Characteristics of an Unmanned Aerial Spray System Low-Volume Application on Corn Fall Armyworm Spodoptera frugiperda. Front. Plant Sci. 13:900939. doi: 10.3389/fpls.2022.900939

As a major global pest, fall armyworm (FAW), *Spodoptera frugiperda,* invaded China in 2019, which has seriously threatened the safety of China's food production and raised widespread concerns. As a new low-volume application technology, an unmanned aerial spray system (UASS) is playing an important role in the control of FAW in China. However, the studies on the effect of the water application volume on the efficacy of FAW using UASS have been limited. In this study, Kromekote® cards were used to sample the deposition. The method of using a sampling pole and sampling leaf for the determination of deposition. Four water application volumes (7.5, 15.0, 22.5, and 30.0 L/ha) were evaluated with regard to the corn FAW control efficacy. A blank control was used as a comparison. The control efficacy was assessed at 1, 3, 7, and 14 days after treatment (DAT). The tested results showed that sampling methods have a significant effect on deposition results. The number of spray deposits and coverage on the sampling pole were 35 and 40% higher than those on the sampling leaves, respectively. The deposition and control efficacy gradually increased as the water application volume increased. The control efficacy at 14 DAT under different water application volumes was in the range of 59.4–85.4%. These data suggest that UASS spraying can be used to achieve a satisfying control of FAW, but the control efficacy of the water application volume of 30.0 and 22.5 L/ha did not differ significantly. Considering work efficiency, a water application volume of 22.5 L/ha is recommended for field operation.

Keywords: unmanned aerial spray system, spray volume, droplet deposition, control efficacy, plant protection

INTRODUCTION

The fall armyworm (FAW), *Spodoptera frugiperda,* is a major global pest. The FAW displays outstanding adaptable and migratory capacity and is an agricultural pest characterized by outbreaks. When the temperature is suitable, FAW can lay eggs once every 2–3 days, about 1,500 eggs are laid at a time, and a life cycle can be completed in 30–45 days (Cui et al., 2019). It can travel a 1,600 km migration distance within 30 h if the weather conditions are suitable (Lu et al., 2021). It originated in North America and invaded Africa in 2016. In 2 years, it spread across 44 countries in Africa and caused great damage to corn cultivation (Goergen et al., 2016). Since 2018, FAW has been expanding northward and southward into Asia, and the degree of occurrence has seriously increased, with it now has spread to 16 countries in Asia. In January 2019, it invaded Yunnan Province, China. Since then, it has seriously threatened the safety of China's food production. After 6 months, it was found in more than 22 provinces, seriously threatening the grain production (Jing et al., 2019). It has attracted wide attention internationally due to its strong adaptability, migration ability (Westbrook et al., 2015), and the characteristics of outbreak damage (Johnson, 1987). FAW larvae attack a large number of cultivated plant species (Casmuz et al., 2010), such as corn, sorghum, cotton, peanut, and soybean. In sub-Saharan Africa, more than $13 billion a year is at risk of crops being destroyed by the FAW (Harrison et al., 2019). In the United States, an outbreak year can cost as much as $500 billion in yield loss (Mitchell, 1979; Montezano et al., 2018). In Brazil, about $600 million was spent in 2009 to control FAW (Ferreira Filho et al., 2010). When 55–100% of corn plants were infected with FAW in the mid-to-late corn stage, the yield decreased by 15–73% (Hruska and Gould, 1997). Currently, FAW control is primarily achieved by spraying insecticides with large volume sprays. A crop protection unmanned aerial spray system (UASS) represents a new pesticide spraying technology adapted to the development of modern agriculture. UASS has many advantages compared with manned aircraft and traditional application machinery, including high efficiency, low drift, no need to take off from an airport, a lower price and labor operation cost, and no damage to the physical structure of crops and soil (Zhang et al., 2015). Meanwhile, it is more suitable for complex and tall crops where no machine can normally move. It can fly quickly to the exact location to accurately process the target area, and be pre-programmed to navigate its way around. Furthermore, the use of a low or ultra-low spray volume can reduce pesticide use by 15.0–20.0%, which can be used as an important technical support for the pesticide reduction program in China (Lan and Chen, 2018; Meng et al., 2019).

In recent years, the use of and research on UASS have rapidly developed across the world (Huang et al., 2013; Berner and Chojnacki, 2017). In the most recent 5 years, research on UASS has been carried out in China, the United States, Brazil, Poland, and other countries (Faiçal et al., 2014, 2017; Pachuta et al., 2018). Researchers have studied the addition of additives (He et al., 2017; Xiao et al., 2019), droplet deposition (Qin et al., 2016; He et al., 2017; Zhang et al., 2017; Wang et al., 2019a), control efficacy (Qin et al., 2016; Zhang et al., 2017; Wang et al., 2019a; Xiao et al., 2019), etc., in UASS. Xiao et al. (2019) studied the effects of aviation spray adjuvants on cotton defoliation and boll opening. The results showed that adding aviation spray adjuvants could increase the defoliation rate by 3.1–34.6% and the bell opening rate by 6.7–29.6%. He et al. (2017) studies showed that increasing the water application volume can significantly increase the deposition density of droplets while adding spray adjuvants can significantly increase the deposition and effective deposition rate of droplets. Wang et al. (2019a) studied the effect of a low water application volume on droplet deposition and control efficacy, and the results indicated that different water application volumes significantly influenced the droplet deposition and control efficacy of wheat pests and diseases. Qin et al. (2016) found that flight parameters not only affect the control efficacy of rice planthoppers (*Nilaparvata lugens*) but also affect the droplet distribution uniformity in a rice canopy. Zhang et al. (2017) used UASS to study the effect of different citrus tree shapes on droplet deposition and control efficacy. The results showed that the droplet distribution performance and control efficacy of hedgerow-shaped plants were the best. Xin et al.'s (2018) research showed that with the increase of the UASS water application volume, the thidiazuron and diuron residues in cotton leaves also increased. Phani et al. (2021) studied the effects of different pesticides on the control effect of FAW using high-volume spraying, and screened out the pesticides with better control effect. Yan et al. (2021) studied the control effect of FAW by using a plant protection UASS to spray solid particles of pesticides. Lu et al. (2021) used a plant protection UASS to study the effect of spraying time on the control effect of FAW and recommend the best spraying time. Different application parameters have a great effect on the control of different pests and diseases by plant protection UASS. Meanwhile, in the prevention and control of pests and diseases, excessive water application volume will not only cause the loss of pesticides but also reduce work efficiency, while too low water application volume often fails to achieve the effect of pest control. However, none of the above studies involved the effect of different water application volumes of plant protection UASS on the control effect of FAW. It is unknown whether the plant protection UASS low water consumption spray can effectively control the FAW. Therefore, a crop protection UASS was used to study the effects of four different water application volumes on the control efficacy of FAW, and determine the optimal water application volume.

In the dose transfer process, the deposition structure plays an important role. This is because it associates the target organism with the pesticide application (Ebert et al., 1999). The deposit structure has a significant effect on the control of pests and diseases. However, different sampling materials and sampling arrangement methods have been used to obtain different deposition results. Therefore, the choice of sampling material and sampling arrangement method is very important for the deposition results. Commonly used sampling materials include Kromekote® cards, water-sensitive paper, Petri dishes, and filter paper (Brain et al., 2017). The most common sampling methods include the arrangement of sampling materials on a slant on the plant leaf (Qin et al., 2016; Wang et al., 2019b) or horizontally on the sampling pole (Kharim et al., 2019; Wang et al., 2019a). However, different sampling methods lead to different deposition results, which makes it difficult to compare

the data in different papers. Therefore, this study compared the droplet deposition using different sampling methods under the same spray conditions.

An experiment was carried out in Yunnan Province, China to study the control efficacy of UASS on FAW. Due to the climate characteristics of this experiment site, the air humidity is relatively high, and the water-sensitive paper is easily affected by moisture, which can easily affect the test results. The use of stainless steel samplers is more troublesome for subsequent acquisition of test data (droplet density and coverage), while Kromekote cards are similar to water-sensitive paper, which is not easily disturbed by external conditions and has a better stability. Therefore, the experiment chose the Kromekote® card as the deposition acquisition material, and DepositScan was used to obtain the droplet density and coverage. The experiment compared the effect of four different water application volumes (7.5–30.0 L/ha) on the control efficacy of FAW in corn.

MATERIALS AND METHODS

Sprayers

The spraying equipment is an eight-rotor electrical-powered UASS (MG-1P, Shenzhen DJI Technology Co., Ltd., Guangzhou, China). The spraying equipment is shown in **Figure 1**. The MG-1P UASS is powered by lithium-ion batteries, which provide a flight time of about 15 min on one charge. It can be operated remotely or automatically and can fly according to a pre-programmed route. The MG-1P platform was equipped with four XR11001 or XR110015 nozzles (TeeJet Technologies, Wheaton, IL). Due to the limited range of the UASS flight speed, the water application volumes in this test were difficult to achieve when only using a change in flight speed. Therefore, the tests used XR11001 and XR110015 nozzles to achieve different water application volumes. The nozzles were mounted under rotors and angled vertically downward and in a parallel direction with reference to the direction of flight. The arrangement of the four nozzles was rectangular, and the length and width were 132 and 56 cm, respectively. The spray pressure, output rate, and flight height of the UASS were set through the remote controller. When using XR11001 or XR110015 nozzles, the spray pressure and output rate were 2.0 bar and 0.32 L/min or 2.5 bar and 0.54 L/min, respectively.

Experimental Design

The experiment was conducted in September 2019 at Corteva Yunnan research center, Kunming City, Yunnan Province (E103°8′52″; N24°46′47″), China (the field is private land, and

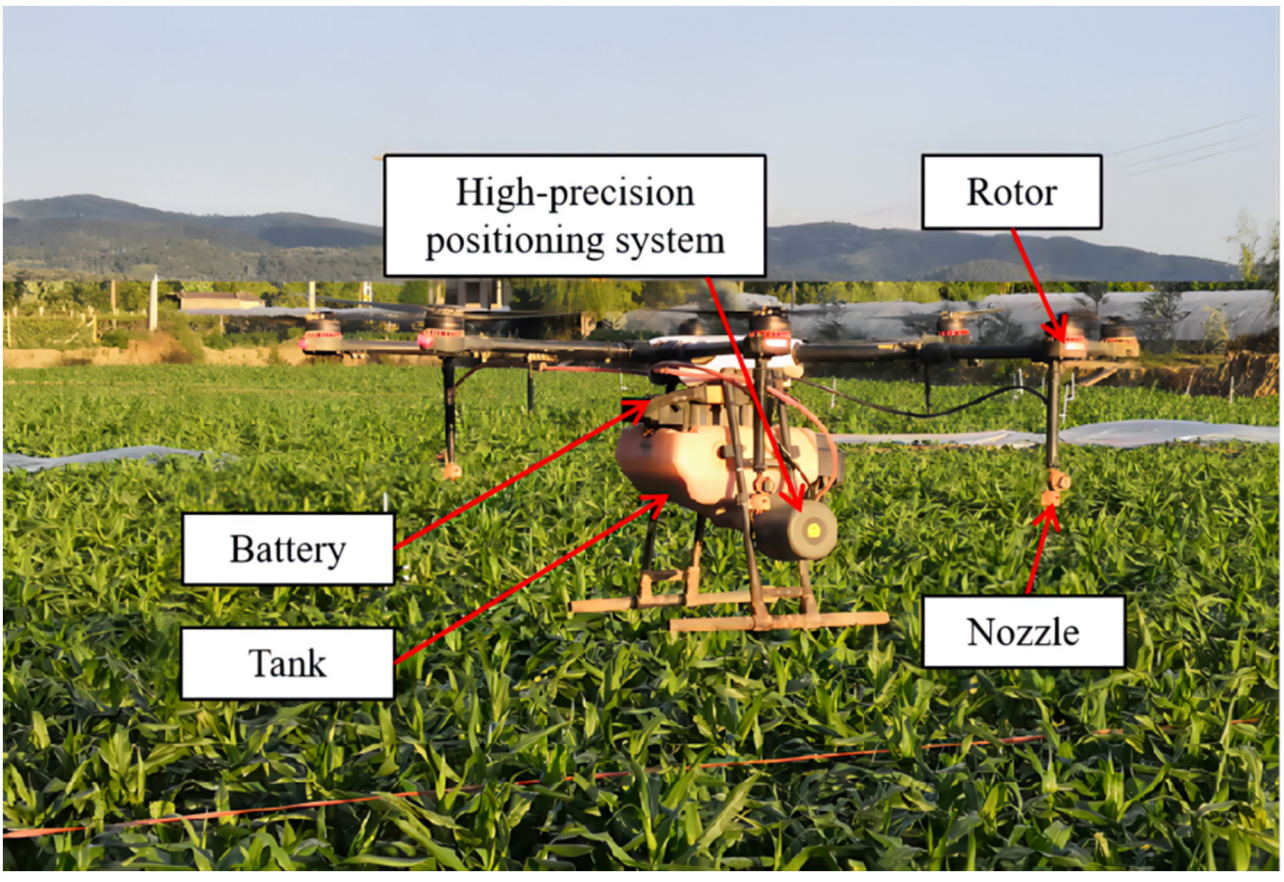

FIGURE 1 | The DJI MG-1P eight-rotor electric unmanned aerial spray system (UASS).

the owner of the land permitted to conduct the study on this site). The corn variety in the experimental site field was Tian Cui 311, and the sowing time was July 20, 2019. The corn plant height, row spacing, and plant spacing during application were about 0.4, 0.4, and 0.3 m, respectively. The corn growth periods were small, with flaring open stages. FAW kills the growing point of corn plants, causing numerous holes in the whorls and upper leaves (Yan et al., 2021). The field observation and survey rate of the harmed corn plants reached above 10%, and most of the corn plants reached the damage level of 3 (Davis scale) (Davis et al., 1992).

The dimension of the experimental field was about 170 m × 118 m, and it was divided into five treatments. Each treatment was replicated three times for a total of 12 plots. Each plot was a 50 m × 22 m area. Then, 10 m buffer zones between plots were set to avoid the drift pollution of droplets. Among them, there were four treatments for the DJI MG-1P UASS and one treatment for the blank control. In the experiment, the effect of water application volumes on the spray deposition and control effect was studied. The DJI MG-1P UASS used four different water application volumes of 7.5, 15.0, 22.5, and 30.0 L/ha.

Sampling Point Arrangement

Two sampling methods were used to analyze the influence of different sampling methods on the deposition results (**Figure 2**). The first sampling method was Kromekote® cards horizontally arranged at a distance of 5 cm from the crop canopy using a sampling pole. This method has the characteristic that the deposition sampling efficiency is not related to the crop canopy. This standard method can be used to compare the results with other research in further work. The second sampling method was Kromekote® cards arranged on the first corn leaf from the top with a stapler at an angle of almost 50 ± 10 degrees. The droplet deposition on the first leaf from the top of the corn had an important role in the control efficacy of FAW. There were two main considerations in using this sampling method. On the one hand, the droplet was mainly deposited on the first leaf from the top of the corn; on the other hand, the FAW mainly lays eggs and hatches on the first leaf from the top of the corn (Yan et al., 2021). For analyzing the droplet deposition, 11 sampling points were uniformly arranged in the experiment plot.

Water Application Volume

In the experiment, the spray height was 2.0 m. Under the spray pressure of 2.0 and 2.5 bar, the droplet size of the XR11001 nozzle and XR110015 nozzle was 90.4–121.2 μm (Jeon and Tian, 2010) and 154.2–183.0 μm (Guo et al., 2020), respectively. Different water application volumes of UASS were achieved by changing the flight speed and nozzles. The corresponding

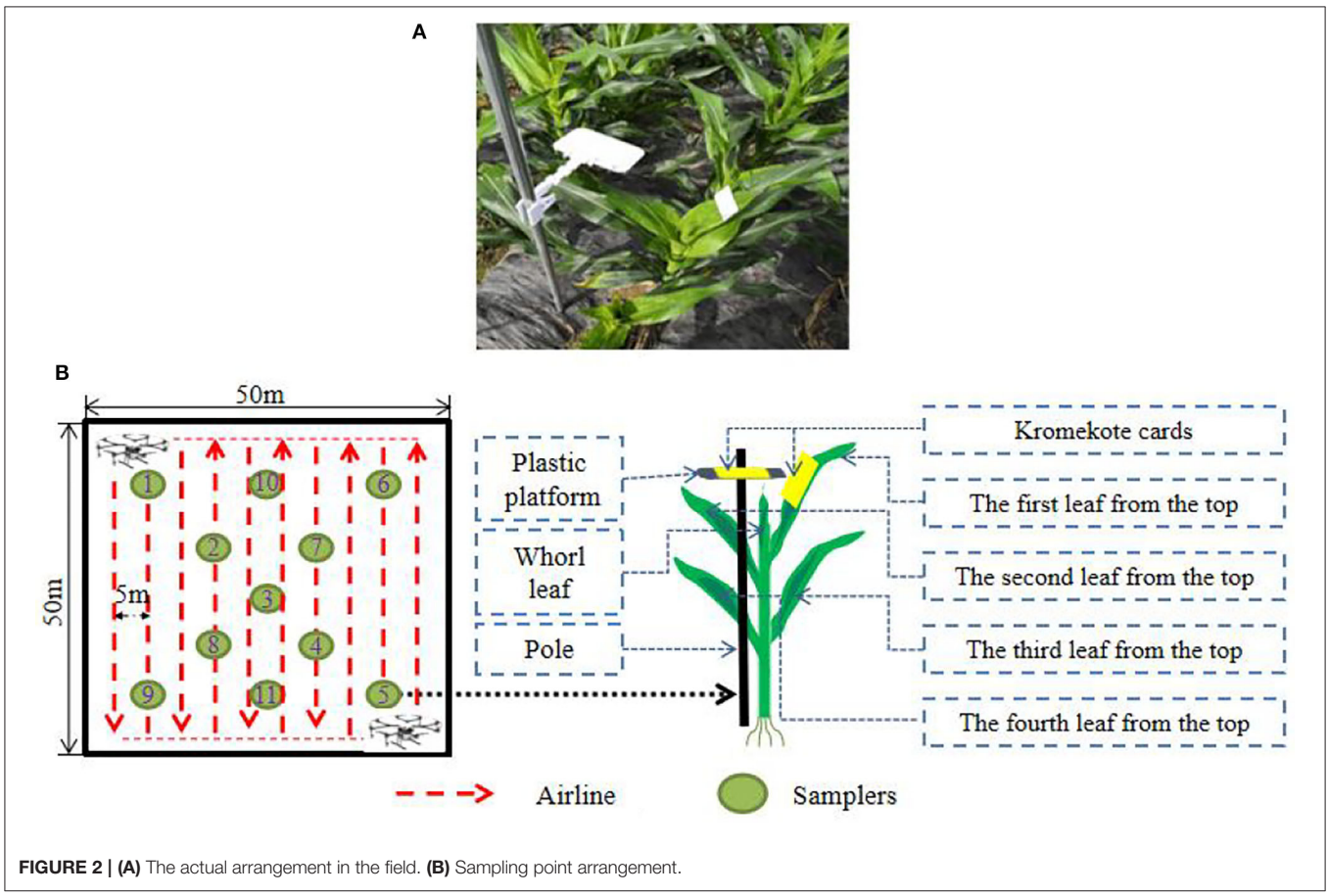

FIGURE 2 | (A) The actual arrangement in the field. **(B)** Sampling point arrangement.

TABLE 1 | The speed of flight under different water application volumes.

Nozzles	Water application volume (L/ha)	Spray pressure(bar)	Droplet size (μm)	Output rate(L/min)	Swath width (m)	Flight speed(m/s)
XR11001	7.5	2.0	90.4–121.2	0.32	5.0	5.7
XR110015	15.0	2.5	154.2–183.0	0.54		4.8
	22.5					3.2
	30.0					2.4

flight speed according to the water application volume was ascertained under the conditions of spray pressure, output rate, and swath width. The flight speed was calculated according to Formula (1) (American Society of Agricultural Engineers, 1995). When the water application volumes were 7.5, 15.0, 22.5, and 30.0 L/ha, the corresponding flight speeds were as shown in **Table 1**.

$$V = \frac{K_3 \times Q}{RS} \quad (1)$$

where, R is the water application volume, L/ha; Q is the output rate, L/min; K_3 is a constant, 600; V is the flight speed, km/h; and S is the swath width, m.

Measurement of Droplet Deposition

Before application, 10.0 g/L of Allura Red (80% purity, purchased from Beijing Oriental Care Trading Ltd., China) was added to the tank using a tracer. The tracer is used to measure the deposition of droplets on Kromekote® cards (Qin et al., 2018). After application, the Kromekote® cards contained in a self-sealing bag were brought to the laboratory for collection and processing. Kromekote® cards were scanned at a resolution of 600 dpi with a scanner (Model GT-1500 Seiko Epson Corporation. Japan). Then, the imagery software DepositScan (USDA, Wooster, OH, USA) was utilized to extract and analyze the droplet density and coverage on the scanned photos (Xiao et al., 2019).

The climatic conditions were recorded using a weather meter (Model NK-5500, Nielsen-Kellerman Co., Boothwyn, PA, 209 USA), which indicated temperatures of 22.9–29.5°C, relative humidity of 45.4–72.2%, and wind velocities of 0.4–2.2 m/s during the deposition test.

Control Efficacy

The insecticide used in this experiment was a 25% Spinetoram water-dispersible granule (Delegate®) produced by Corteva™ agriscience Company, USA. The dosage for each treatment was 30 g a.i/ha.

The efficacy experiment was based on the insecticide field efficacy test guideline (II) standards and the Davis scale. A five-point sampling method per plot was selected. The FAW numbers and the damage index of three plants of corn per point before spraying were investigated and the corns were marked with a red string (Wang et al., 2019a,b). Then, 1, 3, 7, and 14 days after application, the number of FAW and the damage index of corn in the same location and plant were investigated again. The overall control efficacy against corn FAW was calculated without regard to the instars of the corn FAW. The control efficacy was obtained based on the population numbers of live insects in each zone before and after spraying. The control efficacy was calculated according to Equations (2) and (3) (Wang et al., 2019b). The damage index of the corn method referred to the investigation method of Davis et al. (1992). **Figure 3** shows a visual map of the corn FAW damage to leaf feeding. A numerical scale (0–9) was employed, where 0 indicates no visible damage and 9 indicates heavy damage, which is also known as the Davis scale. This method can quickly and easily distinguish small differences in plant damage. It was based on the types and numbers of feeding lesions at 7 and 14 days after infestation. The damage index of each treatment area was calculated according to the damage index Equation (4).

$$\begin{aligned}\text{Mortality (\%)} = {} & (\text{The number of pests before application} \\ & - \text{The number of pests after application})/ \\ & \text{The number of pests before application} \times 100 \quad (2)\end{aligned}$$

$$\begin{aligned}\text{Control effect (\%)} = {} & [\text{Observed mortality (\%)} \\ & - \text{Control mortality (\%)}] \\ & /[100 - \text{Control mortality (\%)}] \times 100 \quad (3)\end{aligned}$$

$$\text{Damage index} = \frac{\sum(\text{Number of damage leaves at each level} \times \text{Corresponding level value})}{\text{Total number of investigation} \times 9} \times 100 \quad (4)$$

Data Analysis

A significant difference was obtained using analysis of variance (ANOVA) by Duncan's test at a significance level of 95% with SPSS v17.0 (SPSS Inc., an IBM Company, Chicago, IL, USA), and Excel software (Microsoft Office 2019, Microsoft Corporation, Redmond, Washington, USA) was used to calculate the coefficient of variation (CV). The CV was used to show the uniformity of droplet deposition and can be presented as (Xiao et al., 2019).

$$CV = \frac{S}{\overline{X}} \times 100\%, \quad (5)$$

$$S = \sqrt{\sum_{i=1}^{n}(X_i - \overline{X})^2/(n-1)} \quad (6)$$

where, S is the standard deviation (SD) of the samples in the same test group, X_i is the droplet density or coverage of each sampling point, $\overline{X}$ is the mean value of the droplet density or coverage in each test group, and n is the number of sampling points in each test group.

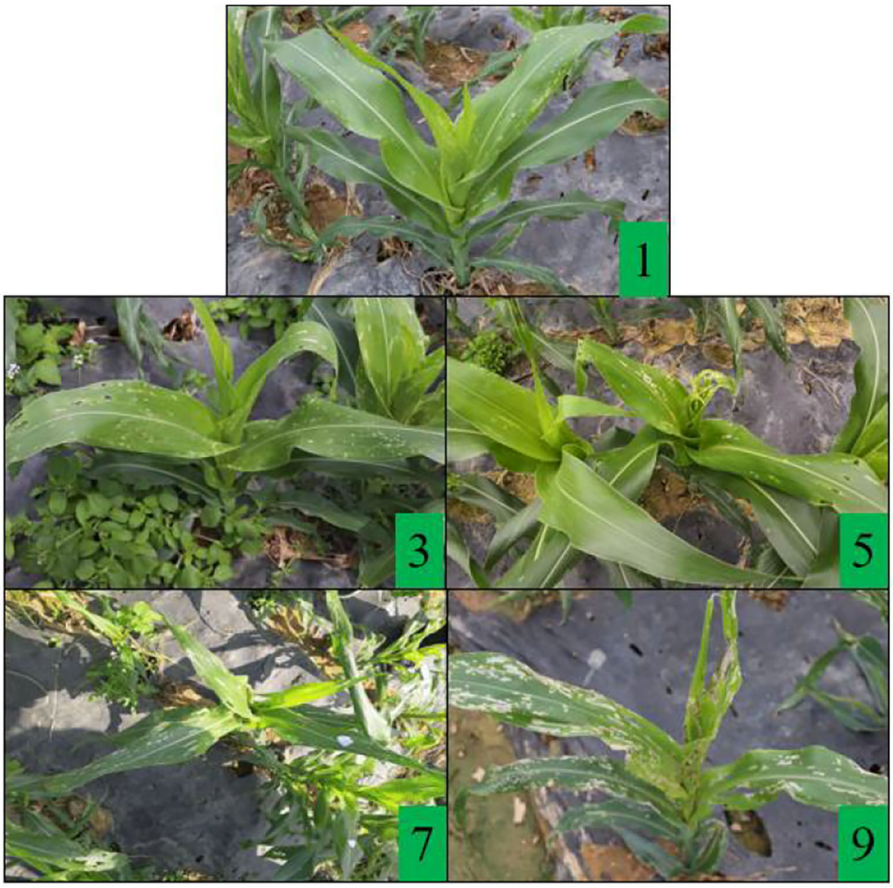

FIGURE 3 | A visual map of some different damage levels of corn fall armyworm. (1) There was only needle-like damage on the leaves, and the damaged area was <5%. (3) There were pin-eye or small annular lesions on the leaves, and the damaged leaf area is between 6 and 15%. (5) Several small and medium irregular holes appeared on the leaves, and the damaged area was between 16 and 25%. (7) There are many large, elongated lesions on the leaves, ranging from 26 to 50% of the damaged area. (9) Corn leaves are destroyed and it is difficult to restore normal growth.

RESULTS

Visual Photos of Droplet Deposition

The droplet deposition has a great effect on the control efficacy. **Figure 4** is a visual photo of the droplet deposition of the MG-1P UASS with different water application volumes and sampling methods. Three qualitative conclusions can be drawn from the visual photos: (1) the water application volume has a significant effect on the droplet density and coverage; (2) the droplet density and coverage obtained by sampling on the pole were higher than those obtained by sampling on the leaf; and (3) a significant difference in the deposition was observed at different sampling points, indicating poor deposition uniformity.

Quantitative Analysis of Deposition Characteristics

Effect of Sampling Methods on Droplet Deposition

The droplet deposition (droplet density and coverage) values obtained by different sampling methods are shown in **Figure 5**. Under the water application volumes of 7.5–30.0 L/ha, the droplet density and coverage achieved by the sampling on the pole method were 24.3 droplet/cm^2 and 8.4%, respectively; by the sampling on the leaf method, they were 18.0 droplet/cm^2 and 6.0%, respectively. The droplet density and coverage obtained by the sampling on the pole method were 35.0 and 40.0% higher than those obtained by the sampling on the leaf method, and the difference was significant ($p < 0.01$). The CV values of deposition obtained by the two sampling methods were all higher than 60.0%, indicating that the uniformity of the deposition was poor.

Effect of Water Application Volumes on Droplet Deposition

The droplet density and coverage under different water applications are shown in **Figure 6**. When the water applications volume of the UASS was in the range of 7.5–30.0 L/ha, the droplet density was 12.5–37.0 droplet/cm^2 and the coverage was 5.9–11.8%. The droplet density and coverage increased as the water application volumes increased. Through linear fitting of the data, a good linear relationship was found between the droplet deposition (droplet density and coverage) and water application

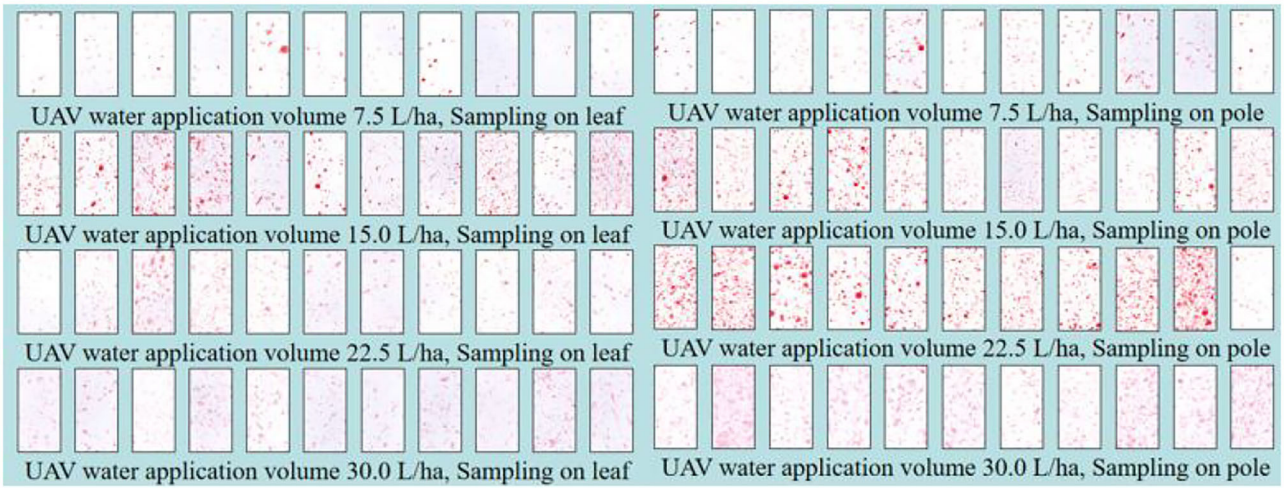

FIGURE 4 | A visual aid showing deposition on the representative Kromekote® cards by UASS application.

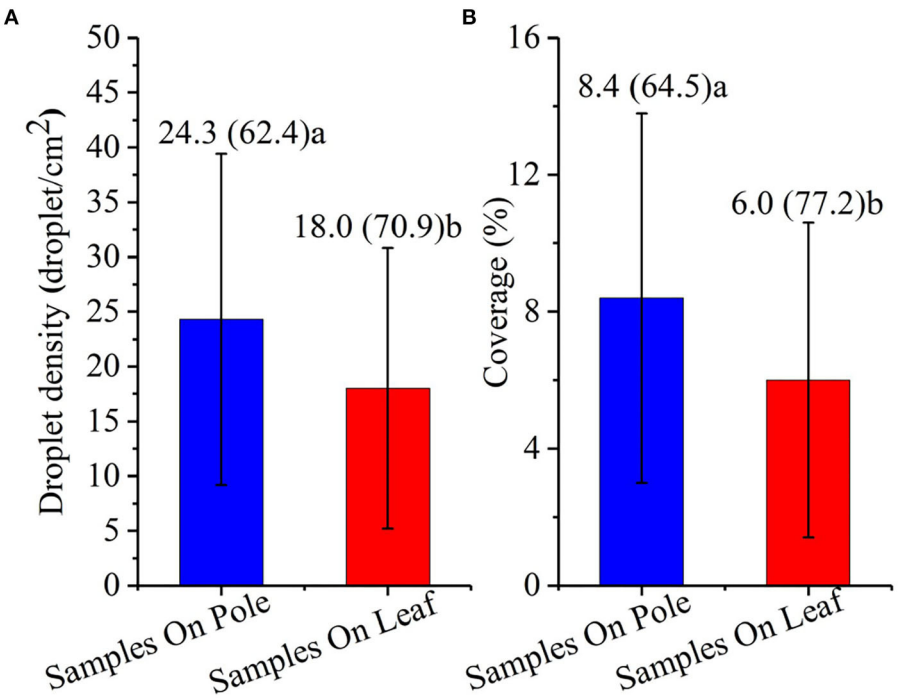

FIGURE 5 | Effects of sampling pole method and sampling leaf method on deposition characteristics of droplet density and coverage. **(A)** Droplet density and **(B)** coverage. The numbers in the figure are the mean value (CV), and the different lowercase letters after the numbers indicate the significant difference, $p < 0.01$.

volume. The coefficients of determination of the droplet density and coverage were 0.89 and 0.92, respectively.

Control Efficacy for Fall Armyworms

Effect of Water Application Volumes on the Control Efficacy

The control efficacy under different water application volumes achieved by the UASS sprayer on FAW is indicated in **Figure 7**. From the live insect investigation results, the control efficacy significantly increased as the water application volume increased ($p < 0.01$). At 7 days after treatment (DAT), the best control efficacy was achieved at 30.0 L/ha using the UASS sprayer. However, the control efficacy of the water application volume of 30.0 and 22.5 L/ha did not differ significantly. Meanwhile, it can also be seen that the control effect of the same water application volume varies with different application days. The

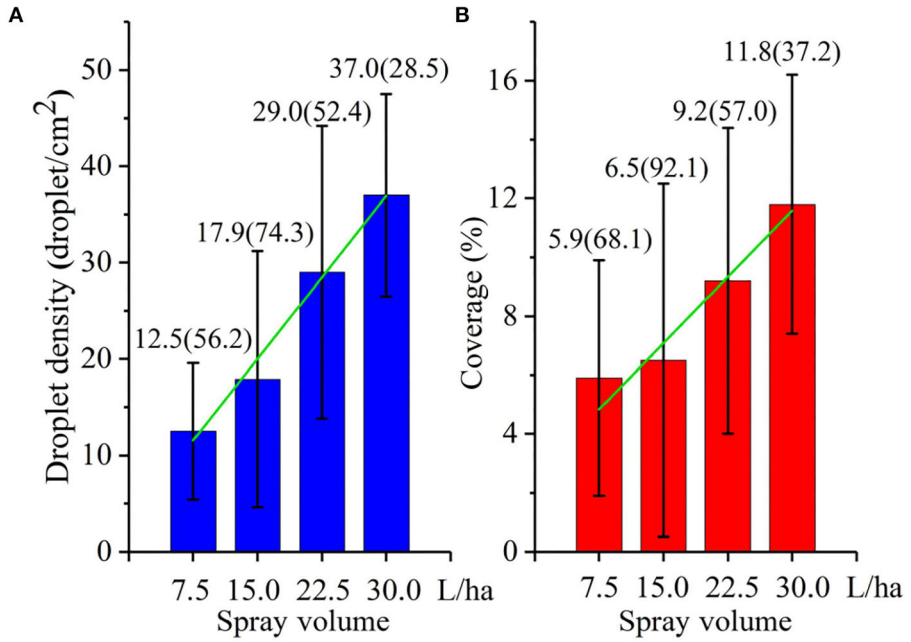

FIGURE 6 | Droplet deposition at different water application volumes for various treatments. **(A)** Droplet density and **(B)** coverage. The numbers in the figure represent the mean value (CV). The green line is a fitted curve for the droplet density/coverage and water application volume.

control efficacy gradually increased from 1 to 7 DAT and decreased from 7 to 14 DAT. The peak of the control efficacy appeared at 7 DAT. This changing trend was the same under different water application volumes.

Effect of Water Application Volumes on the Damage Index

The damage index of FAW for corn when employing the UASS sprayers and a blank control at 0, 1, 3, 7, and 14 DAT is indicated in **Figure 8**. Before application, the damage index of each treatment area was approximately the same, which indicated that the original insect population of each treatment was similar. The trough of the damage index appeared at 7 DAT, after which the damage index began to increase, which corresponds to the results of the insect control efficacy. At 14 DAT, the blank control displayed the largest difference in the damage index compared with the treatment, which was 61.7% higher than the worst control efficacy treatment of the UASS.

DISCUSSION

The experimental results of this study show that there are significant differences between the two sampling methods used for droplet deposition. The results of this experiment were related to the angle of the Kromekote® card arrangement. The Kromekote® card arrangement affects the sampling efficiency of the droplet to some extent. Capri et al. (2005) measured the off-target deposition of chlorpyrifos in two fields: one field was flat and the other field was sloped. It was indicated that the flat field deposition was higher than that of the sloped field. Besides, the Kromekote® cards arranged on the sampling leaves were affected by the shielding of the leaves. Various crops have different canopy sizes, canopy shapes, foliage densities, and planting arrangements, all of which affect the droplet density and coverage (Heidary et al., 2014; Pan et al., 2016; Badules et al., 2017; Hong et al., 2017, 2018). Mostly, the upper layer of the plant canopy displays higher deposition than that of the lower layers. In a study on cotton defoliant spraying, the droplet density and coverage of the upper layer increased by 61.9 and 150.0%, respectively, compared with the lower layers (Xiao et al., 2019). The reason for this was that the upper leaves of the cotton canopy were complex and overlapping, which affected the deposition of the lower droplet. Lefrancq et al. (2013) used 51 glass Petri dishes to successfully collect the sample deposition of kresoxim-methyl in a vineyard catchment, for which the change in the deposition values was caused by the droplet being intercepted by the vine plant canopy. Of course, various sampling methods have different advantages. In this study, the sampling pole method can avoid the influence of the canopy structure and arrangement angle on droplet deposition and collect droplet deposition without bias, which will help in comparing the results obtained from different research. The sampling pole method should be used for physical characterization studies. For example, the performance of different UASS and the effects of operating parameters on droplet deposition characteristics were studied. However, it cannot replace the deposition of droplets on the leaves. The method of arranging the Kromekote® cards directly on the leaves could directly obtain the deposition of the droplets on specific leaves at different growth stages of the plant, which helped build a relationship between the droplet deposition and

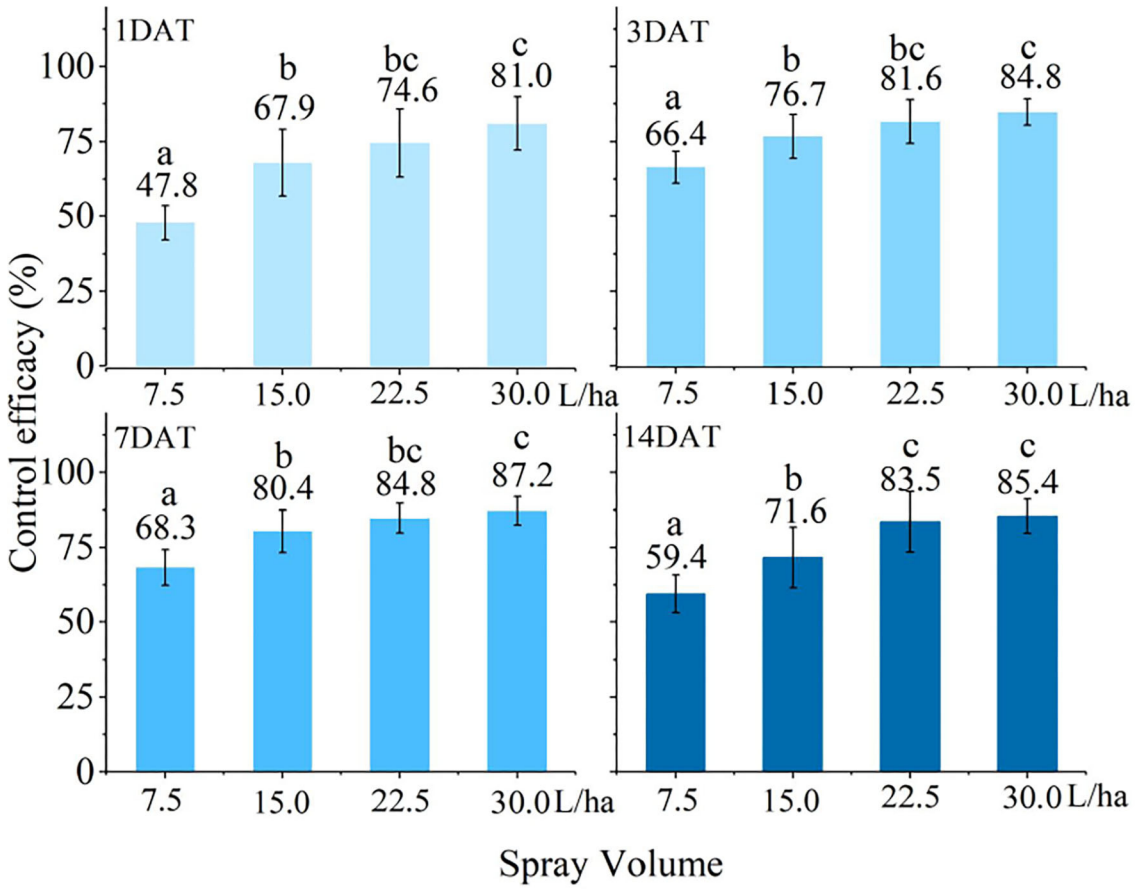

FIGURE 7 | Control efficacy (%) of fall armyworm (FAW) was evaluated at 1, 3, 7, and 14 days after treatment (DAT) resulting from field-treated 25% Spinetoram water-dispersible granule (Delegate®) with an unmanned aerial spray system sprayer at four spray volumes (the different lowercase letters indicate significant results, $p < 0.01$).

control efficacy. The sampling leaf method needs to include a more natural target configuration to be representative of the target structure. For example, the control effect of pests and the penetration research test of droplets.

Control efficacy experiments on corn FAW were performed with different water application volumes using UASS sprayers. The experimental results of this study show that the control efficacy gradually increased with the water application volume increased. Wang et al. (2019a) used UASS to study the control experiments of three different water application volumes (9.0, 16.8, and 28.1 L/ha) on wheat aphids. Their results were consistent with this experimental research results. However, their control efficacy results were better than this experimental result, which may be related to the operating parameters of the UASS and the droplet size. Qin et al. (2016) compared the control efficacy of low-volume spraying technology for rice planthoppers (*N. lugens*). By optimizing the spraying parameters of the UASS, the control efficacy was improved. Chen et al. (2020) used three nozzles with different droplet sizes to study the effects of different droplet sizes on the rice planthopper control efficacy. The results show that the selection of nozzles with smaller atomizing particle sizes for UASS can improve the control efficacy of rice planthoppers (*N. lugens*). In addition, different results were found by other researchers. Roehrig et al. (2018) tested spray volumes between 40 and 160 L/ha and verified that the 130 L/ha was higher than the others for soybean yield, being statistically similar to the 160 L/ha. Sánchez-Hermosilla et al. (2011) reduced application volumes from 1,000 to 500 L/ha and improved crop control product application in tomatoes by altering the spray gun (900 and 1,800 L/ha) on the vertical spray boom. Berger-Neto et al. (2017) compared two spray volumes of 100 and 200 L/ha, and concluded that spray volume did not affect the control of white mold in soybean. Garcerá et al. (2014) also found that spray application volumes (11.74, 17.65, and 32.21 L/ha) did not affect two of the organophosphate insecticides controlling California red scale infestation. Their results were not consistent with our research results. This may be caused by excessive spray volume. Wang et al. (2019a) conducted experiments on wheat with different sprayers, and the results proved that high-volume (225 and 450 L/ha) spraying easily leads to run-off and lower

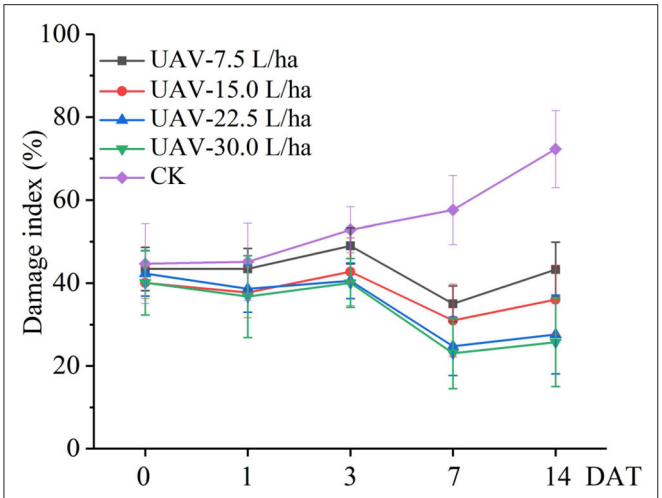

FIGURE 8 | The damage index changed with the application time.

deposition, thereby reducing the control efficacy of high-volume. Thus, it is not necessary to use high-volume spraying, as a certain number of spray volumes achieve good efficacy.

In this study, the number of live insects decreased significantly by 1 DAT, but the damage index did not change much. This may be because the investigation method of the damage index has hysteresis compared with the investigation method of the insect control efficacy. The control effect was best on the 7DAT. At 14 DAT, the control efficacy was reduced, indicating that the insecticides had a shelf life of fewer than 14 days, increasing the number of live insects. The control efficacy of the water application volume of 30.0 and 22.5 L/ha did not differ significantly. Considering work efficiency, a water application volume of 22.5 L/ha is recommended for field operation. The control efficacy (84.8%) of the UASS sprayer meets basic field control requirements, but the UASS has the advantage of a high efficiency in comparison with the large-capacity spray, which has an important role in the rapid control of explosive pests. Of course, further work will be to continuously improve the control efficacy of the UASS by adding spraying adjuvants or optimizing the spraying system.

CONCLUSIONS

In this study, four different water application volumes were used for pesticide application in the cornfield. The droplet deposition characteristics of different sampling methods and the control efficacy for corn FAW using different water application volumes were compared in this research. The conclusions are as follows:

1) The droplet density and coverage were affected by the sampling method;
2) There was a good linear relationship between the droplet deposition (droplet density or coverage) and water application volumes;
3) The control efficacy increased and the damage index decreased with the increase of water application volumes. When using plant protection UASS in the field, it is recommended to use 22.5 L/ha of water application volume.

The experiments demonstrated the feasibility of UASS sprayers in controlling corn FAW fields. However, the control efficacy of UASS needs to be further improved. Due to the poor deposition uniformity, effective measures, such as adding an adjuvant in the tank or optimizing the spraying system, which can improve the deposition uniformity, will be needed in the future.

DATA AVAILABILITY STATEMENT

The original contributions presented in the study are included in the article/**Supplementary Material**, further inquiries can be directed to the corresponding authors.

AUTHOR CONTRIBUTIONS

CSh designed the experiments and wrote the manuscript. JWu, SC, CSo, and JWa carried out the experiments. CSo and HW collected material data and analyzed experimental results. GW and YL supervised and revised the manuscript. All authors contributed to the article and approved the submitted version.

FUNDING

This study was supported by Top Talents Program for One Case One Discussion of Shandong Province, Academy of Ecological Unmanned Farm (Grant No. 2019ZBXC200), Shandong Province Natural Science Foundation (Grant No. ZR2021QC154), and Young Innovative Talents Project of Regular Institutions of Higher Education of Guangdong Province (Grant No. 2018KQNCX020).

ACKNOWLEDGMENTS

We deeply thank Corteva Yunnan Research Center for providing UASS and corresponding materials, and also thank reviewers and editors for giving relevant revision advice to improve the paper.

SUPPLEMENTARY MATERIAL

The Supplementary Material for this article can be found online at: https://www.frontiersin.org/articles/10.3389/fpls.2022.900939/full#supplementary-material

REFERENCES

American Society of Agricultural Engineers (1995). *Calibration and Distribution Pattern Testing of Agricultural Aerial Application Equipment*. State of Michigan: American Society of Agricultural Engineers. p. 229–232.

Badules, J., Vidal, M., Bon,é, A., Llop, J., Salcedo, R., Gil, E., et al. (2017). Comparative study of CFD models of the air flow produced by an air-assisted sprayer adapted to the crop geometry. *Comp. Electron. Agric*. 149, 166–174. doi: 10.1016/j.compag.2017.09.026

Berger-Neto, A., Jaccoud-Filho, D. D. S., Wutzki, C. R., Tullio, H. E., Pierre, M. L. C., Manfron, F., et al. (2017). Effect of spray droplet size, spray volume and fungicide on the control of white mold in soybeans. *Crop Prot*. 92, 190–197. doi: 10.1016/j.cropro.2016.10.016

Berner, B., and Chojnacki, J. (2017). "Use of drones in crop protection. "Farm Machinery and Processes Management in Sustainable Agriculture"," in *Proceedings of IX International Scientific Symposium, Lublin, Poland*.

Brain, R. A., Perine, J., Cooke, C., Ellis, C. B., Harrington, P., Lane, A., et al. (2017). Evaluating the effects of herbicide drift on nontarget terrestrial plants: a case study with mesotrione. *Environ. Toxicol. Chem*. 36, 2465–2475. doi: 10.1002/etc.3786

Capri, E., Balderacchi, M., Yon, D., and Reeves, G. H. (2005). Deposition and dissipation of Chlorpyrifos in surface water following vineyard applications in Northern Italy. *Environ. Toxicol. Chem*. 24, 852–860. doi: 10.1897/04-151R.1

Casmuz, A., Juárez, M. L., Socías, M. G., Prieto, S., Medina, S., Willink, E., et al. (2010). Revisión de los hospederos del gusano cogollero del maíz, *Spodoptera frugiperda* (Lepidoptera: Noctuidae). *Revista de la Sociedad Entomológica Argentina*. 69, 209–231. Available online at: https://www.redalyc.org/articulo.oa?id=322028487010

Chen, P. C., Lan, Y. B., Huang, X. Y., Qi, H. X., Wang, G. B., Wang, J., et al. (2020). Droplet deposition and control of planthoppers of different nozzles in two-stage rice with a quadrotor unmanned aerial vehicle. *Agronomy* 10, 303. doi: 10.3390/agronomy10020303

Cui, L., Rui, C. H., Li, Y. P., Wang, Q. G., Yang, D. B., Yan, X. J., et al. (2019). Research and application of chemical control technology against *Spodoptera frugiperda* (Lepidoptera:Noctuidae) in foreign countries. *Plant Prot*. 45, 7–13.

Davis, F. M., Ng, S. S., and Williams, W. P. (1992). Visual rating scales for screening whorl-stage corn for resistance to fall armyworm. *Tech. Bull. Mississippi Agric. Forest. Exp. Station*. 186, 1–9.

Ebert, T. A., Taylor, R. A., Downer, R. A., and Hall, F. R. (1999). Deposit structure and efficacy of pesticide application. 1: Interactions between deposit size, toxicant concentration and deposit number. *Pest. Sci*. 55, 783–792. doi: 10.1002/(SICI)1096-9063(199908)55:8<783::AID-PS973>3.0.CO;2-D

Faiçal, B. S., Costa, F. G., Pessin, G., Ueyama, J., Freitas, H., Colombo, A., et al. (2014). The use of unmanned aerial vehicles and wireless sensor networks for spraying pesticides. *J. Syst. Arch*. 60, 393–404. doi: 10.1016/j.sysarc.2014.01.004

Faiçal, B. S., Freitas, H., Gomes, P. H., Mano, L. Y., Pessin, G., Carvalho, A., et al. (2017). An adaptive approach for UAV-based pesticide spraying in dynamic environments. *Comp. Electron. Agric*. 138, 210–223. doi: 10.1016/j.compag.2017.04.011

Ferreira Filho, J. B., Alves, L. R. A., Gottardo, L. C. B., and Georgino, M. (2010). "Dimensionamento do custo economico representado por Spodoptera frugiperda na cultura do milho no Brasil," in *48 Congresso Sociedade Brasileira de Economia. Administracao e Sociologia Rural*.

Garcerá, C., Moltó, E., and Chueca, P. (2014). Factors influencing the efficacy of two organophosphate insecticides in controlling California red scale, *Aonidiella aurantii* (Maskell). A basis for reducing spray application volume in Mediterranean conditions. *Pest Manage. Sci*. 70, 28–38. doi: 10.1002/ps.3515

Goergen, G., Kumar, P. L., Sankung, S. B., Togola, A., and Tamò, M. (2016). First report of outbreaks of the fall armyworm *Spodoptera frugiperda* (J E Smith) (Lepidoptera, Noctuidae), a new alien invasive pest in west and central Africa. *PLoS ONE* 11, e0165632. doi: 10.1371/journal.pone.0165632

Guo, H., Zhou, J., Liu, F., He, Y., Huang, H., and Wang, H. Y. (2020). Application of machine learning method to quantitatively evaluate the droplet size and deposition distribution of the UAV spray nozzle. *Appl. Sci*. 10, 1759. doi: 10.3390/app10051759

Harrison, R. D., Thierfelder, C., Baudron, F., Chinwada, P., Midega, C., Schaffner, U., et al. (2019). Agro-ecological options for fall armyworm (*Spodoptera frugiperda JE Smith*) management: providing low-cost, small holder friendly solutions to an invasive pest. *J. Environ. Manage*. 243, 318–330. doi: 10.1016/j.jenvman.2019.05.011

He, L., Wang, G. B., Hu, T., Meng, Y. H., Yan, X. J., and Yuan, H. Z. (2017). Influences of spray adjuvants and spray volume on the droplet deposition distribution with unmanned aerial vehicle (UAV) spraying on rice. *J. Plant Prot*. 44, 1046–1052. (In Chinese). doi: 10.13802/j.cnki.zwbhxb.2017.2016147

Heidary, M. A., Douzals, J. P., Sinfort, C., and Vallet, A. (2014). Influence of spray characteristics on potential spray drift of field crop sprayers: a literature review. *Crop Prot*. 63, 120–130. doi: 10.1016/j.cropro.2014.05.006

Hong, S. W., Zhao, L., and Zhu, H. (2017). CFD simulation of airflow inside tree canopies discharged from air-assisted sprayers. *Comp. Electron. Agric*. 149, 121–132. doi: 10.1016/j.compag.2017.07.011

Hong, S. W., Zhao, L. Y., and Zhu, H. P. (2018). SAAS, a computer program for estimating pesticide spray efficiency and drift of air-assisted pesticide applications. *Comp. Electron. Agric*. 155, 58–68. doi: 10.1016/j.compag.2018.09.031

Hruska, A., and Gould, F. (1997). Fall armyworm (Lepidoptera: Noctuidae) and *Diatraea lineolata* (Lepidoptera:Pyralidae): impact of larval population level and temporal occurrence on maize yield in nicaragua. *J. Econ. Entomol*. 90, 611–622. doi: 10.1093/jee/90.2.611

Huang, Y. B., Thomson, S. J., Hoffmann, W. C., Lan, Y. B., and Fritz, B. K. (2013). Development and prospect of unmanned aerial vehicle technologies for agricultural production management. *Int. J. Agric. Biol. Eng*. 6, 1–10. doi: 10.3965/j.ijabe.20130603.001

Jeon, H. Y., and Tian, L. (2010). Machine vision instrument to measure spray droplet sizes. *J. Biosyst. Eng*. 35, 443–449. doi: 10.5307/JBE.2010.35.6.443

Jing, D., Guo, J., Jiang, Y., Zhao, J., Sethi, A., He, K., et al. (2019). Initial detections and spread of invasive *Spodoptera frugiperda* in China and comparisons with other noctuid larvae in cornfield using molecular techniques. *Insect Sci*. 27, 780–790. doi: 10.1111/1744-7917.12700

Johnson, J. S. (1987). Migration and the life history strategy of the fall armyworm, *Spodoptera frugiperda* in the western hemisphere. *Int. J. Trop. Insect Sci*. 8, 543–549. doi: 10.1017/S1742758400022591

Kharim, M. N. A., Wayayok, A., Shariff, A. R. M., Abdullah, A. F., and Husin, E. M. (2019). Droplet deposition density of organic liquid fertilizer at low altitude UAV aerial spraying in rice cultivation. *Comp. Electron. Agric*. 167, 105045. doi: 10.1016/j.compag.2019.105045

Lan, Y. B., and Chen, S. D. (2018). Current status and trends of plant protection UAV and its spraying technology in China. *Int. J. Precis. Agric. Aviat*. 1, 1–9. doi: 10.33440/j.ijpaa.20180101.0002

Lefrancq, M., Imfeld, G., Payraudeau, S., and Millet, M. (2013). Kresoxim methyl deposition, drift and runoff in a vineyard catchment. *Sci. Total Environ*. 442, 503–508. doi: 10.1016/j.scitotenv.2012.09.082

Lu, H., Li, F., Zhu, X. M., Tang, J. H., Lyu, Q. B., and Wu, S. Y. (2021). Preliminary study on the effect of using unmanned aerial vehicles (UAVs) to control *Spodoptera frugiperda*. *Entomol. Res*. 51, 453–461. doi: 10.1111/1748-5967.12538

Meng, Y. H., Han, Y. X., Liang, Z., Su, J., and Lan, Y. B. (2019). Harvest-aid application strategy in different cotton planting densities using UAV: effects of dosage and application frequency on defoliation efficacy, boll opening rate, fiber quality, and lint cotton yield. *Int. J. Precis. Agric. Aviat*. 2, 31–41. doi: 10.33440/j.ijpaa.20190201.0027

Mitchell, E. R. (1979). Fall armyworm symposium: preface. *Fla. Entomol*. 62, 81. doi: 10.2307/3494085

Montezano, D., Specht, A., Sosa-G'omez, D., Roque-Specht, V., Sousa-Silva, J., PaulaMoraes, S., et al. (2018). Host plants of spodoptera frugiperda (Lepidoptera: Noctuidae) in the Americas. *Afr. Entomol*. 26, 286–300. doi: 10.4001/003.026.0286

Pachuta, A., Boguslawa, B., and Chojnacki, J. (2018). "Evaluation of liquid transverse distribution under a twin spray jet installed on a drone," in *MendelNet Conference Bron 2018, Brno, Czech Republic*.

Pan, Z., Lie, D., Qiang, L., He, S. L., Yi, S., Liu, Y. D., et al. (2016). Effects of citrus tree-shape and spraying height of small unmanned aerial vehicle on droplet distribution. *Int. J. Agric. Biol. Eng*. 9, 45–52. doi: 10.3965/j.ijabe.20160904.2178

Phani, K. K., Mohan, V. K., Kamakshi, N., Dakshina, M. K., and Mohan, R. K. (2021). Field efficacy of selected insecticides against invasive pest, fall

armyworm *Spodoptera frugiperda* (j. E. Smith) on maize crop. *Pharma Innovat. J.* 10, 884–889. doi: 10.1653/024.103.0211

Qin, W. C., Qiu, B. J., Xue, X. Y., Chen, C. C., Xu, Z. F., and Zhou, Q. Q. (2016). Droplet deposition and control effect of insecticides sprayed with an unmanned aerial vehicle against plant hoppers. *Crop Prot.* 85, 79–88. doi: 10.1016/j.cropro.2016.03.018

Qin, W. C., Xue, X. Y., Zhou, Q. Q., Cai, C., Wang, G., and Jin, Y. (2018). Use of RhB and BSF as fluorescent tracers for determining pesticide spray distribution. *Anal. Methods UK* 10, 4073–4078. doi: 10.1039/C8AY01198B

Roehrig, R., Boller, W., Forcelini, C. A., and Chechi, A. (2018). Use of surfactant with different volumes of fungicide applications in soybean culture. *Engenharia Agrícola* 38, 577–589. doi: 10.1590/1809-4430-eng.agric.v38n4p577-589/2018

Sánchez-Hermosilla, J., Rincón, V. J., Páez, F., Agüera, F., and Carvajal, F. (2011). Field evaluation of a self-propelled sprayer and effects of the application rate on spray deposition and losses to the ground in greenhouse tomato crops. *Pest Manag. Sci.* 67, 942–947. doi: 10.1002/ps.2135

Wang, G. B., Lan, Y. B., Qi, H. X., Chen, P. C., Hewitt, A., and Han, Y. X. (2019a). Field evaluation of an unmanned aerial vehicle (UAV) sprayer: effect of spray volume on deposition and the control of pests and disease in wheat. *Pest Manag. Sci.* 75, 1546–1555. doi: 10.1002/ps.5321

Wang, G. B., Lan, Y. B., Yuan, H. Z., Qi, H. X., Chen, P. C., Ouyang, F., et al. (2019b). Comparison of spray deposition, control efficacy on wheat aphids and working efficiency in the wheat field of the unmanned aerial vehicle with boom sprayer and two conventional knapsack sprayers. *Appl. Sci.* 9, 218. doi: 10.3390/app9020218

Westbrook, J. K., Nagoshi, R. N., Meagher, R. L., Fleischer, S. J., and Jairam, S. (2015). Modeling seasonal migration of fall armyworm moths. *Int. J. Biometeorol.* 60, 255–267. doi: 10.1007/s00484-015-1022-x

Xiao, Q. G., Xin, F., Lou, Z. X., Zhou, T. T., Wang, G. B., Han, X. Q., et al. (2019). Effect of aviation spray adjuvants on defoliant droplet deposition and cotton defoliation efficacy sprayed by unmanned aerial vehicles. *Agronomy* 9, 217. doi: 10.3390/agronomy9050217

Xin, F., Zhao, J., Zhou, Y. T., Wang, G. B., Han, X. Q., Fu, W., et al. (2018). Effects of dosage and spraying volume on cotton defoliants efficacy: a case study based on application of unmanned aerial vehicles. *Agronomy* 8, 85. doi: 10.3390/agronomy8060085

Yan, X. J., Yuan, H. Z., Chen, Y. X., Shi, X., Liu, X. H., Wang, Z. Y., et al. (2021). Broadcasting of tiny granules by drone to mimic liquid spraying for the control of fall armyworm (*Spodoptera frugiperda*). *Pest Manag. Sci.* 78, 43–51. doi: 10.1002/ps.6604

Zhang, D. Y., Chen, L. P., Zhang, R. R., Hoffmann, W. C., Xu, G., Lan, Y. B., et al. (2015). Evaluating effective swath width and droplet distribution of aerial spraying systems on M-18B and thrush 510G airplanes. *Int. J. Agric. Biol. Eng.* 8, 21–30. doi: 10.3965/j.ijabe.20150802.1493

Zhang, P., Wang, K. J., Lyu, Q., He, S. L., Yi, S. L., Xie, R. J., et al. (2017). Droplet distribution and control against citrus leafminer with UAV spraying. *Int. Conf. Robot. Autom.* 32, 299–307. doi: 10.2316/Journal.206.2017.3.206-4980

Conflict of Interest: JWu and HW were employed by Corteva Agroscience Technology (Shanghai) Co., Ltd.

The remaining authors declare that the research was conducted in the absence of any commercial or financial relationships that could be construed as a potential conflict of interest.

Publisher's Note: All claims expressed in this article are solely those of the authors and do not necessarily represent those of their affiliated organizations, or those of the publisher, the editors and the reviewers. Any product that may be evaluated in this article, or claim that may be made by its manufacturer, is not guaranteed or endorsed by the publisher.

frontiers | Frontiers in Plant Science

TYPE Original Research
PUBLISHED 16 September 2022
DOI 10.3389/fpls.2022.907916

OPEN ACCESS

EDITED BY
Wei Qiu,
Nanjing Agricultural University, China

REVIEWED BY
Yang Li,
Shihezi University, China
Fiaz Ahmad,
Bahauddin Zakariya University, Pakistan

*CORRESPONDENCE
Giovanni Pau
giovanni.pau@unibo.it
Zhen-ping Qiang
qzp@swfu.edu.cn

SPECIALTY SECTION
This article was submitted to Sustainable and Intelligent Phytoprotection, a section of the journal Frontiers in Plant Science

RECEIVED 30 March 2022
ACCEPTED 22 July 2022
PUBLISHED 16 September 2022

CITATION
Lin H, Tse R, Tang S-K, Qiang Z-p and Pau G (2022) Few-shot learning approach with multi-scale feature fusion and attention for plant disease recognition.
Front. Plant Sci. 13:907916.
doi: 10.3389/fpls.2022.907916

Few-shot learning approach with multi-scale feature fusion and attention for plant disease recognition

Hong Lin[1], Rita Tse[1,2], Su-Kit Tang[1,2], Zhen-ping Qiang[3]* and Giovanni Pau[1,4,5]*

[1]Faculty of Applied Sciences, Macao Polytechnic University, Macau, Macao SAR, China, [2]Engineering Research Centre of Applied Technology on Machine Translation and Artificial Intelligence of Ministry of Education, Macao Polytechnic University, Macau, Macao SAR, China, [3]College of Big Data and Intelligent Engineering, Southwest Forestry University, Kunming, China, [4]Department of Computer Science and Engineering, University of Bologna, Bologna, Italy, [5]Samueli Computer Science Department, University of California, Los Angeles, Los Angeles, CA, United States

Image-based deep learning method for plant disease diagnosing is promising but relies on large-scale dataset. Currently, the shortage of data has become an obstacle to leverage deep learning methods. Few-shot learning can generalize to new categories with the supports of few samples, which is very helpful for those plant disease categories where only few samples are available. However, two challenging problems are existing in few-shot learning: (1) the feature extracted from few shots is very limited; (2) generalizing to new categories, especially to another domain is very tough. In response to the two issues, we propose a network based on the Meta-Baseline few-shot learning method, and combine cascaded multi-scale features and channel attention. The network takes advantage of multi-scale features to rich the feature representation, uses channel attention as a compensation module efficiently to learn more from the significant channels of the fused features. Meanwhile, we propose a group of training strategies from data configuration perspective to match various generalization requirements. Through extensive experiments, it is verified that the combination of multi-scale feature fusion and channel attention can alleviate the problem of limited features caused by few shots. To imitate different generalization scenarios, we set different data settings and suggest the optimal training strategies for intra-domain case and cross-domain case, respectively. The effects of important factors in few-shot learning paradigm are analyzed. With the optimal configuration, the accuracy of 1-shot task and 5-shot task achieve at 61.24% and 77.43% respectively in the task targeting to single-plant, and achieve at 82.52% and 92.83% in the task targeting to multi-plants. Our results outperform the existing related works. It demonstrates that the few-shot learning is a feasible potential solution for plant disease recognition in the future application.

KEYWORDS

few-shot learning, meta-learning, multi-scale feature fusion, attention, plant disease recognition, cross-domain, training strategy, sub-class classification

1. Introduction

Plant disease has always been a significant concern in agriculture since it results in reduction of crop quality and production (Campbell and Madden, 1990; Oerke and Dehne, 2004; Strange and Scott, 2005). Image-based auto-diagnosing method is very accessible and economical for farmers. It is especially friendly to those farmers who are in remote areas or on a small scale. In recent years, deep learning methods are widely used in image-based recognition (Lin et al., 2021). Many networks have achieved excellent performance when trained with relevant large-scale datasets. As we know, the performance of deep learning network relies on data. As the network gets deeper, the number of trainable parameters becomes larger and the demand for data increases. Insufficient data can easily lead to overfitting (Simonyan and Zisserman, 2014; Dong et al., 2021). In plant disease recognition, the existing data resources are limited. Meanwhile, creating a large-scale plant disease dataset is difficult due to: (1) the number of species and diseases are very huge; (2) disease identification and annotation requires expert involvement; (3) some diseases are too rare to collect sufficient samples. The long-tailed distribution of data is common in nature and it is difficult to be used to train a balanced model. In brief, creating large-scale dataset of plant disease is a time-consuming and exhausting work (Deng et al., 2009; Singh et al., 2020). Severe shortage of data has become a barrier to take advantage of deep learning methods.

Generally, there are three ways to alleviate the problems caused by data shortages. Data augmentation, as the most common solution, augments instances by image scaling, rotation, affine transformation, etc. Transfer learning method delivers prior knowledge from source domain to target domain and adapts to the target domain by a small amount of data. But the two solutions cannot generalize to new categories in test, which means that the classes in test must have been learned in training. In addition to these two solutions, meta-learning, an approach that mimics human learning mechanisms, has been proposed in recent years. The objective of this solution is not to learn knowledge, but to learn to learn. Different from the conventional classification methods, few-shot learning (FSL) is a kind of meta-learning method which can quickly generalize to unseen categories with the supports of few samples.

One branch of FSL is metric-based method (Wang et al., 2020). The principle is that the features of samples belonging to the same category are close to each other, while the features of samples belonging to different categories are far from each other. The earliest representative work is Siamese Network, which is trained with positive or negative sample pairs (Koch et al., 2015). Vinyals et al. (2016) proposed the Matching Networks, and they borrowed the concept "seq2seq+attention" to train an end-to-end nearest neighbor classifier. Snell et al. (2017) proposed Prototypical Network, which learns to match the proto center of class in semantic space through few samples. Sung et al. (2018) proposed Relation Network, which concatenates the feature vectors of the support samples and the query samples to discover the relationship of classes. Li et al. (2019) proposed CoveMNet based on the covariance presentation and covariance metric of the consistency of distribution. The network extracts the second order statistic information of each category by an embedding local covariance to measure the consistency of the query samples with the novel classes. Chen et al. (2020) proposed Meta-Baseline method, which achieves good performance on some FSL benchmarks. The accuracy achieves at 83.74% with *5-way, 5-shot* task of Tiered-ImageNet, and 90.95% with *1-way, 5-shot* task of Mini-ImageNet.

Recently, FSL has started to be used in research on plant disease identification. Argüeso et al. (2020) used Siamese Network on the dataset PlantVillage (PV). Jadon (2020) proposed SSM-Net that uses the Siamese framework and combines two features from a Conv and a VGG16. Zhong et al. (2020) proposed a novel generative model for zero-shot and few-shot recognition of citrus aurantium L. diseases by using conditional adversarial auto-encoders. Afifi et al. (2021) compared Triplet network, Baseline, Baseline++, and DAML on PV and coffee leaf datasets. The results show that the Baseline has the best performance. Li and Chao (2021b) proposed a semi-supervised FSL method and tested it with PV. Nuthalapati and Tunga (2021) introduced transformer into plant disease recognition. Chen et al. (2021) used meta-learning on Mini-plant-disease dataset and PV. Li and Yang (2021) used Matching Network and tested cross-domain performance by mixing pest data. These methods have been tried from various perspective and have made important progresses. Nevertheless, FSL still has two common challenging issues: (1) limited features extracted from few samples are less representative for a class (Wang et al., 2020); (2) the generalization requirements are very high and various. In this work, we tackle the two issues by using multi-scale feature fusion (MSFF) and improving training strategies.

CNN is widely used in image-based deep learning methods. In a CNN architecture, the local features with more details and small perceptive fields are extracted from low-level layers, while the global features with rich semantic information and large perceptive fields are extracted from high-level layers (Goodfellow et al., 2016). MSFF is the technology using multi-scale features which are extracted from different layers of CNN (Dogra et al., 2017). In object detection and semantic segmentation, many excellent networks are proposed by using MSFF, such as Feature Pyramid Network (Lin et al., 2017), U-net (Ronneberger et al., 2015), Fully Convolutional Network (Long et al., 2015) etc. MSFF is also used in image restoration, image dehazing and image super resolution etc. (Li et al., 2018; Zhang and Patel, 2018; Zhang et al., 2018; Lan et al., 2020). These methods fuse features by using dense connection, feature concatenation or weighted element-wise summation (Dong et al., 2020). In common, the mentioned methods

have encoder-decoder framework. The multi-scale features extracted from encoder are reused in decoder to enhance feature representation. However, in conventional classification task, MSFF is seldom used because the network does not have decoder. Generally, only the top semantic features are fed into classifier, but other scale features are abandoned. But in fact, the high-level features and the low-level features are not subordination relationship. The local features including rich fine-grained features can be an effective compensation to formulate a richer feature representation of sample (Lim and Kang, 2019). In the data-limitation condition, it requires to extract as many features as possible from a limited amount of data. Therefore, in this work, we propose to leverage the MSFF to enhance feature representation. Multi-scale features can be fused in different ways. In our work, we use cascaded multi-scale feature fusion (CMSFF).

The channels of feature maps increase after feature fusion. But it does not mean that all channels are the same significance. The contribution of each channel is different. Some channels should be emphasized and some should be suppressed. Attention can help to focus on the meaningful channels. Attention mechanism plays important role in human perception to selectively focus on salient parts in order to capture visual structure better (Guo et al., 2021). It has been leaded into some areas of machine learning such as computer vision, natural language processing etc. and has significance to improve performance (Hu, 2019; Hafiz et al., 2021). It not only tells where to focus, but also improves the representation of interests. Recently, some light-weight attention modules have been proposed. Wang et al. (2017) proposed Residual Attention Network that uses encoder-decoder style attention module. Hu et al. (2018) introduced a compact module to exploit the inter-channel relationship, which was named as Squeeze-and-excitation module. Woo et al. (2018) proposed Convolutional Block Attention Module that includes channel attention (CA) and spatial attention. These light-weight attention modules can be easily embedded into deep learning networks as plug-ins. In this work, we use the CA to weight the accumulated channels obtained from CMSFF. The CMSFF and CA is an effective combination to enhance the representation of category under few-shot condition.

As the definition of FSL, it is asked to generalize to novel categories or novel domains. Generalizing to new categories within the same domain of training is defined as intra-domain classification, while generalizing to novel domain is defined as cross-domain classification. Long-tail distribution of data is common in plant disease datasets. To identify the part of categories with few samples, the model can be trained with the part of diseases that have more samples. This generalization happens in the same domain. Cross-domain happens when a set of categories with few shots is required to be identified but does not belong to any dataset. Cross-domain adaption happens between different datasets, which is more difficult than intra-domain adaption. However, researchers found that it is frequently encountered situation and inescapable for boosting FSL to practical application. Guo et al. (2020) established a new broader study of cross-domain few-shot learning benchmark and pointed out that all meta-learning methods underperform in relation to simple fine-tuning methods, which indicates that the difficulty of the cross-domain issue. Adler et al. (2020) proposed a method of representation fusion by an ensemble of Hebbian learners acting on different layers of a deep neural network, which is from feature representation perspective. Li W.-H. et al. (2022) proposed a task-specific adapters for cross-domain problem from the perspective of network architecture. Qi et al. (2022) proposed a meta-based adversarial training framework for this problem, which is also from the perspective of network architecture. As we know, there is no research that has been done from a training strategy perspective. These efforts are the kind of general explorations of using general benchmarks (e.g., ImageNet, CIFAR etc.) and rarely discuss specific domains. In fact, different domain has its own characteristics and resources to utilize when crossing domains. Hence, in this work, we propose a set of training strategies to match various cases of generalization using the available data resources.

The contributions of this work are summarized as: (1) we propose a Meta-Baseline (MB) based FSL approach merging with CMSFF and CA for plant disease recognition; (2) we propose a group of training strategies to meet different generalization requirements; (3) through extensive comparative experiments and ablation experiments, we validate the superiority of our method and analyze various factors of FSL. Comparing with the existing related works under the same data conditions, our method has achieved at the best accuracy.

2. Materials and methods

2.1. Materials

In this research, three public datasets are used in our experiments. Mini-ImageNet is a subset of the ImageNet, which includes 100 classes and 600 images per class. We select 64 classes in our experiments. The second is PV (Hughes and Salathé, 2015) released in 2015 by Pennsylvania State University. It is the most frequently used and comprehensive dataset in academic research up to now in plant disease recognition. Totally, it includes 50,403 images which crosses over 14 crop species and covers 38 classes, as shown in Table 1. Because the number of samples in PV is unbalanced, we use the data after augmentation and select 1,000 images per class to keep balance. The third is the dataset of apple foliar disease (AFD), which was published in FGVC8 Plant Pathology 2021 Competition. All images of AFD were taken in wild with complicated backgrounds, as shown in Figure 1A. We perform pre-processing to reduce the complexity of the surroundings

TABLE 1 The 14 species and 38 categories in PV.

Species	Class number	Class name
Apple	4	Apple scab, black rot, cedar apple rust, healthy
Blueberry	1	Healthy
Cherry	2	Healthy, powdery mildew
Corn	4	Gray leaf spot, common rust, healthy, northern leaf blight
Grape	4	Black rot, black measles, healthy, leaf blight
Orange	1	Haunglongbing
Peach	2	Bacterial spot, healthy
Pepper	2	Bacterial spot, healthy
Potato	3	Early blight, healthy, late blight
Raspberry	1	Healthy
Soybean	1	Healthy
Squash	1	Powdery mildew
Strawberry	2	Healthy
Tomato	10	Bacterial spot, early blight, healthy, late blight, leaf mold, septoria leaf spot, spider mites, target, mosaic virus, yellow leaf curl virus

TABLE 2 The algorithm of meta-learning.

Algorithm of meta-learning

***Input*:** data_loader,n_way,n_shot,n_query,task_per_batch
***Output*:** avg_acc, avg_loss
for i in epoch:
  train :
  for j in batch:
    $task = task(data\_loader, n\_way, n\_shot, n\_query, task\_per\_batch)$
    $x_0 \cdots x_n = f_\theta(task.x\_shot)$
    $x = mean(x_0 \cdots x_n)$
    $y = f_\theta(task.x\_query)$
    $logits = classifier(distance(x, y))$
    $loss = cross\_entropy(logits, task.label)$
    $acc = compute\_acc(logits, task.label)$
    $loss.backwardpropagation \,\&\, optimize$
  end for
  validation : *val*
  compute : *avg_acc*, *avg_loss*
end for
***return*:** avg_acc, avg_loss

by removing background other than leaves. YOLO-v3 (Redmon and Farhadi, 2018) is adopted to detect leaves in images which is shown in Figure 1B. After segmentation and resizing, the images with a single leaf in each image are used in this work, as shown in Figure 1C.

The hardware configurations are: Graphics: Tesla V100-DGXS-32GB; Video Memory: $32G \times 4$; Processor: Intel(R) Xeon(R) CPU E5-2698 v4 @ 2.20GHz; Operating System: Ubuntu 18.04.6 LTS.

2.2. Problem formulation

In FSL paradigm, given two labeled sets with categories C_{train} and C_{novel}, C_{train} is used in training and C_{novel} is used in test. The two sets are exclusive, $C_{train} \cap C_{novel} = \varnothing$, which means that categories used in test are not seen during training. Data is formulated to tasks and each task T is made up of a *support set* S and a *query set* Q. The sample of S is denoted by (x_s, y_s) which is a $(image, label)$ pair and the sample of Q is denoted by (x_q, y_q). In training, the label y_q is used for calculating loss, which is supervised learning.

An *N-way, K-shot* task indicates that the S contains N categories with K samples in each category, and the Q contains the same N categories with W samples in each category. The goal is to classify the $N \times W$ unlabeled samples of Q into N categories. For evaluation, the average accuracy is computed from many tasks sampled from C_{novel}, $N \in C_{novel}$.

2.3. Architecture

2.3.1. Meta-Baseline framework

Like classical classification structure, our framework contains two components: an encoder and a classifier, which is illustrated in Figure 2A. The encoder noted as f_θ is a CNN-based network merging with CMSFF and CA. It is trained in two stages: base-training and meta-learning.

In base-training, the network contains f_θ and base-training classifier, which is trained with image-wise data. The goal in this stage is to learn the general features as prior knowledge. Some large-scale general datasets with more classes and diverse data, such as ImageNet, Mini-ImageNet etc. are good choices for learning prior knowledge. The classifier can be linear classifier, fully connected layer, SVM, or other classifiers. The cross-entropy loss is calculated to update the parameters of f_θ during back propagation. After base-training is completed, the classifier is removed and the trained model is delivered to the meta-learning stage.

In meta-learning, f_θ is initialized by the trained model from base-training. Meta-learning is a concept of learning to learn. So, the purpose is not to learn the knowledge of the training classes, but to learn how to differentiate between classes. Aiming at the objective, the classifier in meta-learning is replaced by a distance measurement module. The classification result is decided by the distances from the support samples to the query sample. Meta-learning is a task-driven paradigm where training data is formulated as *N-way, K-shot* tasks. Based on a simple machine learning principle: test and training conditions must

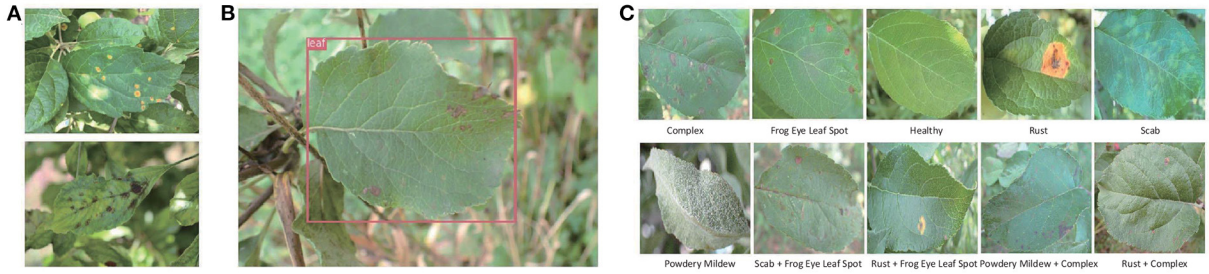

FIGURE 1
(A) The original samples of AFD. **(B)** The leaf detection result by YOLO-v3. **(C)** The samples of 10 classes after segmentation and resizing.

match (Vinyals et al., 2016), the data of C_{novel} is also formatted into tasks in test.

Given an *N-way, K-shot* task, K samples of a category c in S are embedded into feature space by f_θ and become K feature vectors. A mean vector of the K vectors are calculated as the centroid of c, which is consider as the representative of category c:

$$\omega_c = \frac{1}{|S_c|} \sum_{x_s \in S_c} f_\theta(x_s) \tag{1}$$

where, S_c denotes the samples of class c in S, $|S_c| = K$, x_s denotes each sample of class c. The query sample x_q in an *N-way, K-shot* task is also embedded by f_θ. The probability that sample x_q belongs to class c is calculated as:

$$p(y = c|x_q) = \frac{exp(\gamma . < f_\theta(x_q), \omega_c >)}{\sum_{c'} exp(\gamma . < f_\theta(x_q), \omega_{c'} >)} \tag{2}$$

where, $< ., . >$ denotes the distance of two vectors, c' denotes all the classes in S, $\omega_{c'}$ denotes all the centroids of S, γ is a learnable parameter to scale the distance. In training, we use cross-entropy loss to update the parameters of the network. The algorithm of meta-learning is shown in Table 2.

2.3.2. Distance measurement

After embedding, the 2D color image has been a high dimensional vector in semantic space. The distance of query sample to the class centroid is calculated by a distance metric. Distance metric uses distance function which provides a relationship metric between each element in the dataset. In many machine learning algorithms, distance metric is used to know the input data pattern in order to make any data-based decision. The most common used measures to calculate the distance between two vectors are cosine similarity, dot product and Euclidean distance.

Cosine similarity is a measure of similarity between two non-zero vectors of an inner product space. It is measured by the cosine of the angle between two vectors and determines whether two vectors are pointing in roughly the same direction. It is the same as the inner product after normalization (Han et al., 2012). In Euclidean geometry, the dot product of the Cartesian coordinates of two vectors is widely used. It is often called as inner product or projection product of Euclidean space. The length of projection represents the distance of two vectors. In mathematics, the Euclidean distance between two high-dimensional vectors is the square root of the sum of the squares of the distances in each dimension.

2.3.3. MSFF

Basically, the structure of MSFF includes two categories: parallel multi-scale feature fusion (PMSFF) and cascaded multi-scale feature fusion (CMSFF). The two fusion methods are illustrated in Figure 2B. The PMSFF concatenates the features from different layers of CNN simultaneously. The different resolutions of feature maps are uniformed before concatenation. Comparatively, the CMSFF fuses the different resolution feature maps step by step. Taking Resnet12 as backbone network, four convolutional blocks are linked. A group of feature maps of double times of channels and half resolution is generated after each block forwarding. In the backward fusion, small size feature maps are two times up-sampled and concatenated with the feature maps of previous block. After a series of up-sampling and concatenation, all channels are fused together to be the fused full-scale feature, noted as F. The CMSFF is used in this work.

2.3.4. CA

The CA is used to exploit the inter-channel relationship of features by learning the weights of channels (Woo et al., 2018). The structure of CA module is shown in Figure 2B. Each channel of F is considered as a feature detector. The spatial dimension of input feature map is aggregated by pooling operation. In this module, average-pooling and max-pooling are conducted simultaneously and two spatial context descriptors: F_{avg} and

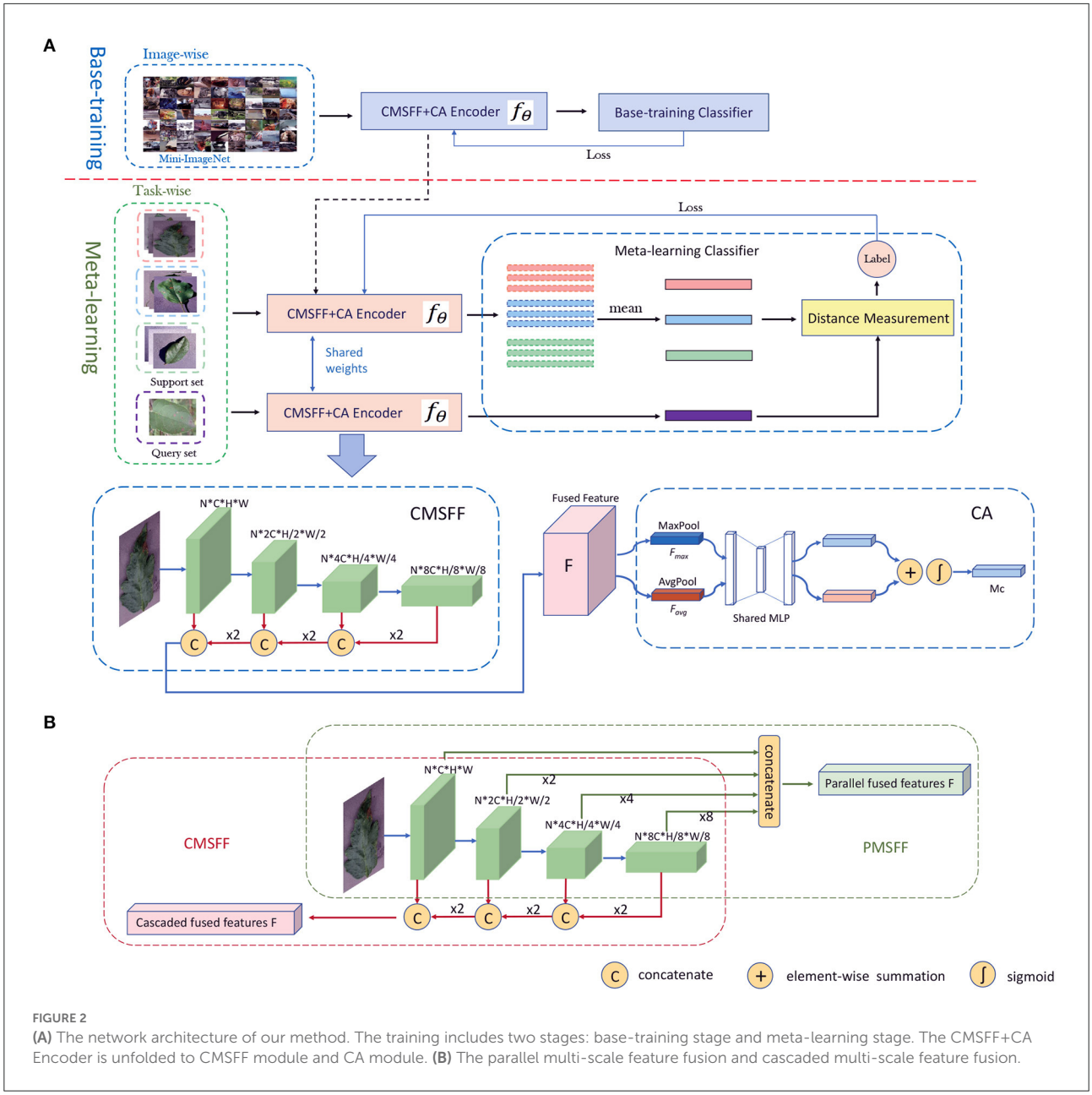

FIGURE 2
(A) The network architecture of our method. The training includes two stages: base-training stage and meta-learning stage. The CMSFF+CA Encoder is unfolded to CMSFF module and CA module. **(B)** The parallel multi-scale feature fusion and cascaded multi-scale feature fusion.

F_{max}, are generated, respectively. Then they are forwarded to a shared network which is composed of multi-layer perceptron (MLP) with one hidden layer. The element-wise summation of the two outputs from MLP goes through a sigmoid. Then the channel attention map $M_c \in \mathbb{R}^{C\times1\times1}$ is produced.

3. Results

We carried out 43 groups of comparison experiments and ablation experiments to illustrate our method, training strategies, and the effects of various factors. The details of experiments and results are illustrated and analyzed as below. The bold values listed in tables indicate the highest results for each group under the same conditions.

3.1. Data settings

The PV is separated into three parts for training, validation, and test, respectively. According to the requirement of FSL: the testing categories are novel, the classes of the three parts do not intersect, $C_{train} \cap C_{val} \cap C_{test} = \varnothing$. In this work,

TABLE 3 Three data settings of PV used in our experiments.

ID	Training	Validation	Test
PV-Setting-1 (22-6-10)	(PV-1-22): apple-3,blueberry-1,cherry-2,corn-3,grape-3,orange-1,peach-2,pepper-1,potato-2,raspberry-1,soybean-1,squash-1,strawberry-1	Apple-1,corn-1,grape-1,pepper-1,potato-1,strawberry-1	(PV-1-10T): tomato-10
PV-Setting-2 (22-6-10)	(PV-2-22): apple-2,blueberry-1,cherry-1,corn-2,grape-2,orange-1,peach-1,pepper-1,potato-1,raspberry-1,soybean-1,squash-1,strawberry-1,tomato-6	Apple-1,corn-1,grape-1,potato-1,tomato-2	(PV-2-10): apple-1,cherry-1,corn-1,grape-1,peach-1,pepper-1,potato-1,strawberry-1,tomato-2
PV-Setting-3 (10-6-22)	(PV-3-10): apple-1,cherry-1,corn-1,grape-1,peach-1,pepper-1,potato-1,strawberry-1,tomato-2	Apple-1,corn-1,grape-1,potato-1,tomato-2	(PV-3-22): apple-2,blueberry-1,cherry-1,corn-2,grape-2,orange-1,peach-1,pepper-1,potato-1,raspberry-1,soybean-1,squash-1,strawberry-1,tomato-6

The total 38 classes are separated into three parts for training, validation and test, respectively. "Apple-1" means a class of apple species.

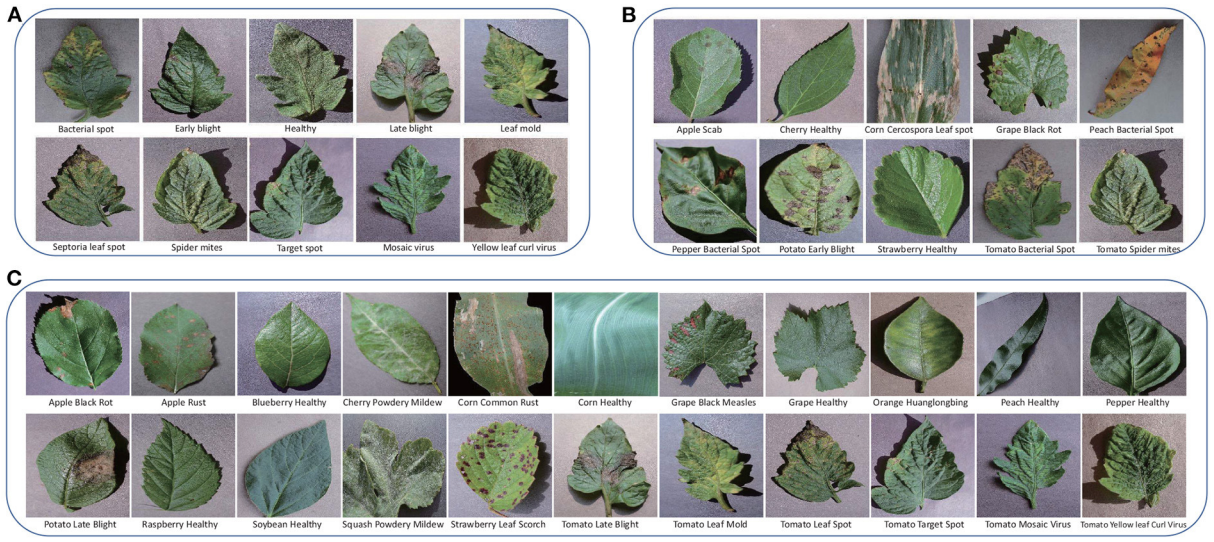

FIGURE 3
(A) The testing classes of PV-Setting-1. **(B)** The testing classes of PV-Setting-2. **(C)** The testing classes of PV-Setting-3.

PV is split to three settings as shown in Table 3. PV-Setting-1 is with 22 classes for training, 6 classes for validation, and 10 classes covered by tomato for test. The samples are shown in Figure 3A, which are very similar with each other. PV-Setting-2 is with 22 classes for training, six classes for validation, and 10 classes belonging to nine different species for test. The samples of this setting are shown in Figure 3B. PV-Setting-3 exchanges the training set and testing set of PV-Setting-1 and keeps the same validation set as PV-Setting-1, using 10 classes for training and 22 classes for test. The samples are shown in Figure 3C. The three settings represent "sub-class" task, "train more, test less" task and "train less, test more" task, respectively. In addition, 10 classes of AFD and 200 samples per class are used in this work for cross-domain testing purpose. Since all classes belong to the same super-class: apple leaf, it is also a sub-class classification task.

3.2. Training strategy

The domain of training is noted as source domain (SD), and the domain of test is noted as target domain (TD). Data from different domains can be used in the three stages: base-training, meta-learning, and test. It is special that there are two training stages of our method, and the datasets used in the two stages could be different. We just consider the domain of meta-learning stage as SD. When SD is the same as TD, it is intra-domain adaption, otherwise, it is cross-domain adaption.

In order to mimic different adaption situations, we design different data configurations. Five adaption configurations using Mini-ImageNet, three PV settings, and AFD are proposed. As shown in Figure 4, *S*1 uses a general dataset (e.g., Mini-ImageNet) in base-training and meta-learning, then uses target dataset (e.g., PV) in test, which is the adaptation from one

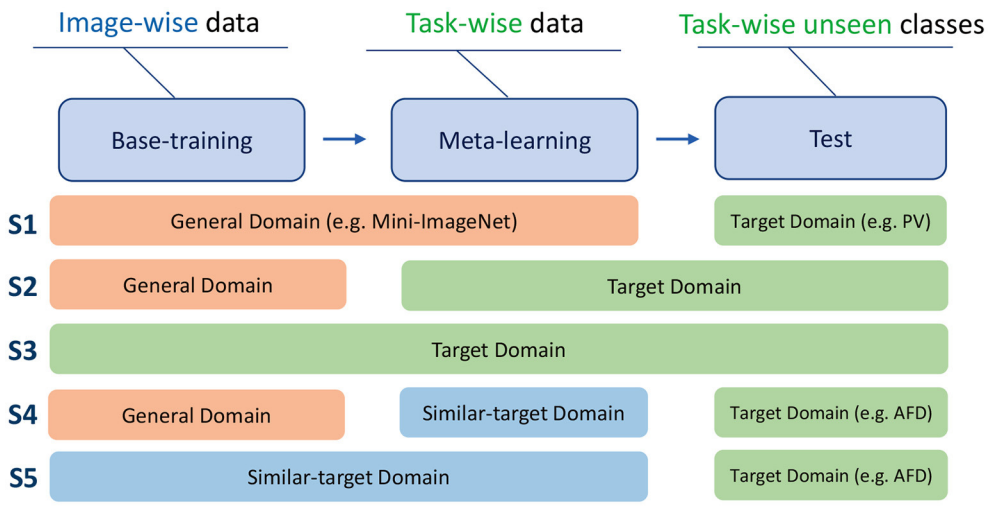

FIGURE 4
The data formats used in base-training, meta-learning, and test. The five training strategies.

domain to another, denoted in Formula 3. *S*2 uses a general dataset in base-training, target dataset in meta-learning and test, which is denoted in Formula 4. *S*3 uses target dataset in three stages, which is denoted in Formula 5. *S*4 uses general dataset in base-training, similar-target dataset (e.g., PV) in meta-learning, and target dataset (e.g., AFD) in test, which is denoted in Formula 6. When AFD is used in test, PV is considered as a similar domain as the target domain, because they are both associated with leaf diseases of the plants. *S*5 uses the similar-target dataset in base-training and meta-learning, and target domain dataset in test, which is denoted in Formula 7. *S*1, *S*4, *S*5 are cross-domain, and *S*2, *S*3 are intra-domain.

$$S1: G \rightarrow G \rightarrow T \tag{3}$$

$$S2: G \rightarrow T \rightarrow T \tag{4}$$

$$S3: T \rightarrow T \rightarrow T \tag{5}$$

$$S4: G \rightarrow S \rightarrow T \tag{6}$$

$$S5: S \rightarrow S \rightarrow T \tag{7}$$

where, *G* denotes the general domain, T denotes the target domain, *S* denotes the similar-target domain.

As shown in Table 4, e1, e2, and e3 are conducted with Mini-ImageNet and PV-Setting-1 by using *S*1, *S*2, *S*3. e4, e5, e6 are conducted with Mini-ImageNet and PV-Setting-2 by using *S*1, *S*2, *S*3. e7, e8, e9 are conducted with Mini-ImageNet and PV-Setting-3 by using *S*1, *S*2, *S*3. e10, e11, and e12 are conducted with Mini-ImageNet, PV-Setting-2, and AFD by using *S*1, *S*4, *S*5. For the 12 experiments, the training epoch is 100, and the learning rate is 0.1 and decayed to 0.01 after 90 epochs in base-training. In meta-learning, the training epoch is 50, and the learning rate is 0.001. The validation task is 5-*way*, 1-*shot*, 15-*query*. The backbone network is Resnet12. The distance metric is cosine similarity.

3.2.1. Intra-domain

According to the definitions of SD and TD, e2, e3, e5, e6, e8, e9 are intra-domain experiments, because the data used in meta-learning and test is from the same dataset. The results are shown in Table 4 and Figure 5A. In PV-Split-2, the accuracy of e5 is better than e4 and e6. In PV-Split-3, the accuracy of e8 is better than e7 and e9. What the two settings have in common is that the disease classes belong to different plants. To the diverse species cases, *S*2 is better than *S*1 and *S*3. Especially when the number of species is bigger, the superiority of *S*2 is more obvious. As listed, e6 gets close to e5, but e8 is much better than e9, which means that the general dataset is better supported when the testing data is more diverse. A broad prior knowledge is very useful for adapting to diverse target. However, in PV-Split-1, e3 is the best one by using *S*3 because the testing data belongs to the same plant. So, the features of testing data are intensive and the general date in base-training is not helpful. Oppositely, the data belonging to the same dataset is easier for adaption. In short, to the intra-domain cases, if the testing classes are of super-classes, *S*2 is

TABLE 4 The group of experiments with different training strategies and different data settings.

ID	Method	TS	Base-training	Meta-learning	Test	1-shot	5-shot	10-shot	20-shot	30-shot	40-shot	50-shot
PV-Setting-1												
e1	MB	S1	Mini	Mini	PV-1-10T	41.08	60.59	66.27	69.87	71.26	71.86	72.30
e2	MB	S2	Mini	PV-1-22	PV-1-10T	56.07	72.90	76.62	78.87	79.74	79.81	80.11
e3	MB	S3	PV-1-22	PV-1-22	PV-1-10T	**57.85**	**75.04**	**79.08**	**81.51**	**82.47**	**82.83**	**83.08**
PV-Setting-2												
e4	MB	S1	Mini	Mini	PV-2-10	60.23	83.08	87.02	88.97	89.61	89.76	90.12
e5	MB	S2	Mini	PV-2-22	PV-2-10	80.88	**91.75**	**93.44**	**94.27**	**94.53**	**94.70**	**94.84**
e6	MB	S3	PV-2-22	PV-2-22	PV-2-10	**81.05**	91.47	93.14	94.00	94.29	94.41	94.53
PV-Setting-3												
e7	MB	S1	Mini	Mini	PV-3-22	65.46	85.37	88.81	90.54	91.09	91.33	91.45
e8	MB	S2	Mini	PV-3-10	PV-3-22	**78.74**	**88.96**	**90.58**	**91.52**	**91.97**	**92.05**	**92.17**
e9	MB	S3	PV-3-10	PV-3-10	PV-3-22	74.58	84.77	86.82	87.82	88.29	88.43	88.57
AFD												
e10	MB	S1	Mini	Minit	AFD-10	28.26	39.12	44.20	47.83	49.02	50.31	51.32
e11	MB	S4	Mini	PV-2-22	AFD-10	**38.41**	**51.71**	**55.58**	**58.08**	**58.84**	**59.70**	**60.09**
e12	MB	S5	PV-2-22	PV-2-22	AFD-10	36.19	49,16	54.05	57.13	58.47	59.25	59.46

(Task in meta-learning: 5-way, 1-shot, 15-query; backbone network: Resnet12; batchsize: 128; Lr: 0.1 in base-training, 0.001 in meta-learning; distance metric: cosine similarity; Mini, Mini-ImageNet; TS, training strategy).

the best strategy. If the testing classes are sub-classes, *S*3 is the best strategy.

3.2.2. Cross-domain

Experiments e1, e4, e7, e10, e11, e12 are cross-domain cases. e1, e4, e7, e10 are the experiments with the worst results in their respective data settings by using *S*1, due to the big gap between the general domain and target domain.

Comparing e10, e11 and e12, e11 has the highest accuracy by using *S*4, which are shown in Table 4 and Figure 5B. e12 is not as good as e11 because too intensive features extracted from monotonous samples leads to weaker adaptation. *S*4 is the best training strategy for cross-domain cases, which uses general dataset in base-training to learn the prior knowledge in a wide range, and uses similar-target dataset in meta-learning for adapting to new domain smoothly.

3.3. CMSFF and CA

Ablation experiments e13–e22 are conducted to show the positive effects of CMSFF module and CA module, respectively. The results are listed in Table 5. Under four data configurations: PV-Setting-1, PV-Setting-2, PV-Setting-3, and AFD, we execute 8 experiments. The training settings are listed: Mini-ImageNet is used in base-training; backbone network is Resnet12; distance metric is cosine similarity; training strategy is *S*2 and *S*4. Taking e2, e5, e8, e11 as the baseline, the CMSFF module is added and the results of e13, e15, e19, e21 show the improvement of CMSFF. e14, e18, e20, and e22 indicate that CA has further improved the performances on the basis of CMSFF. e15 and e17 are used to compare the PMSFF module with the CMSFF module, and the results show that CMSFF outperforms PMSFF.

3.4. Sub-class classification

Sub-class is defined as the classes belong to the same entry class. The PV-Setting-1 and AFD are sub-class classification examples. Sub-class classification is also named as fine-grained vision categorization which aims to distinguish subordinate categories within entry level categories. Because the samples belonging to the same super-class are similar with each other, sub-class classification is a challenging problem.

In Table 4, the PV-setting-1 is the lowest accuracy group among the three PV-settings, as the samples all belong to tomato and are indistinguishable. The results of AFD group are worse than PV-Setting-1, which is not only because of Sub-class reason, also due to cross-domain and in-wild setting of images. Even if the images of AFD are already pre-processed, the backgrounds of images are still different from PV. Also, the illumination condition, resolution, photography devices are all different. Intuitively, the gap of features from SD to TD causes the accuracy declining.

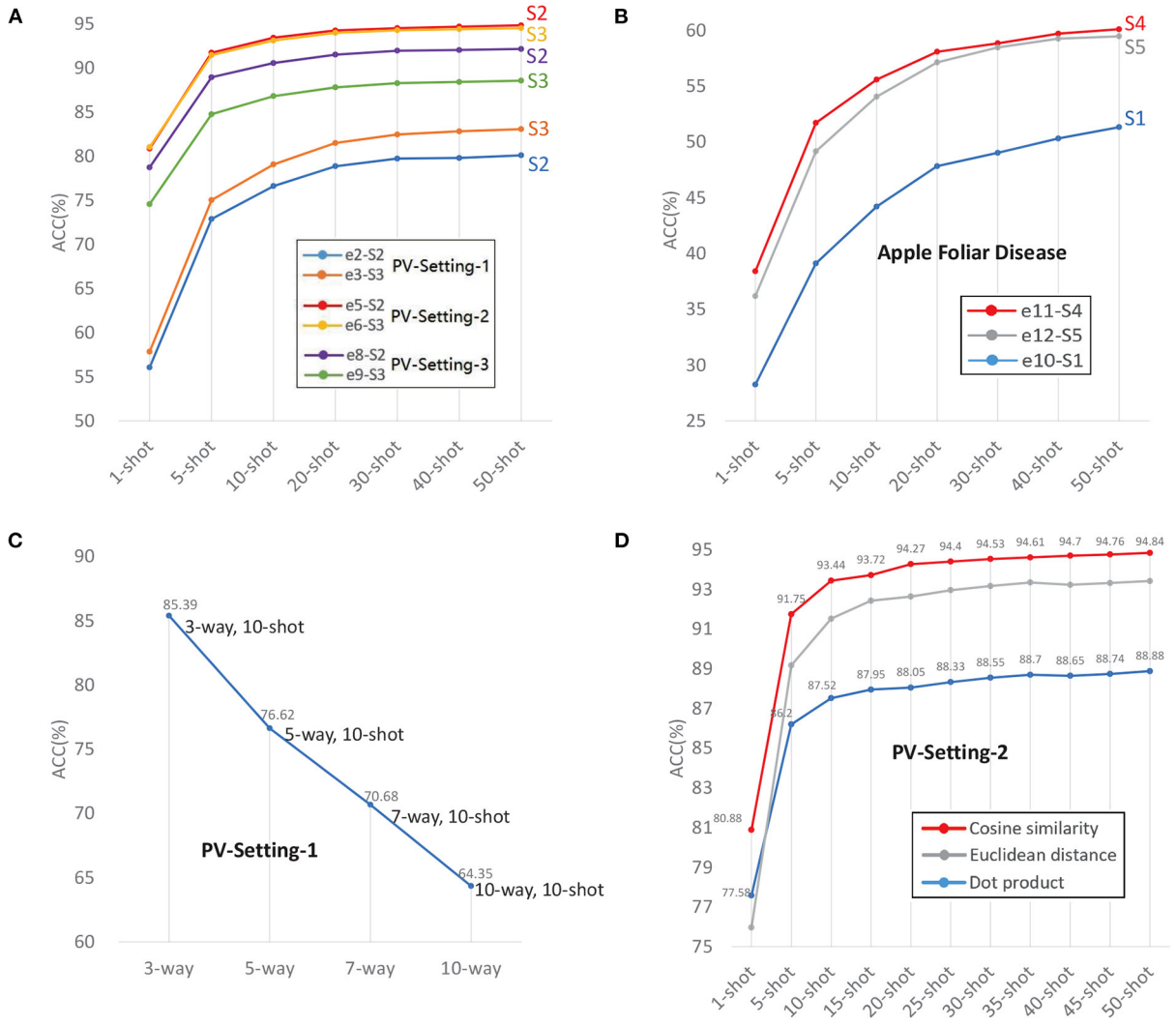

FIGURE 5
(A) Intra-domain experiments with three data settings. **(B)** Cross-domain experiments with AFD. **(C)** The accuracy decreases as Way increases. **(D)** Distance metrics.

3.5. Way and shot

N-way and *K-shot* are the configurations of the task that indicate the difficulty of the task. Given a fixed *K*, the accuracy decreases as *N* increases. The result of PV-split-1 with *N-way, 10-shot* is shown in Figure 5C. The accuracy drops down from 85.39% to 64.35% as *N-way* increases from 3 to 10.

All experimental results listed in Table 4 are executed with fixed *5-way*, which indicates that regardless of the data configurations, all experiments follow the common trend: accuracy increases with the number of shots. The accuracy sharply increases as the *Shot* increases from *1-shot* to *5-shot*, and tends to be stable when the *Shot* is larger than 10. After the *shot* is larger than 20, the growth is not significant. From *1-shot* to *50-shot*, the increase of accuracy ranges from at least 10% to a maximum of 32%.

The results show that the accuracy increases with the number of *shot* and decreases with the number of *way*. More *ways* means higher complexity, and more *shots* means more supporting information. In existing researches, the *N—way* is set to 5 generally. In application scenarios, the *N* is determined by the number of target categories and should not be limited to 5. For example, a plant may have more than five diseases, then the *ways* should the same as the number of diseases that may occur in the specific scenario. *N-way* and *K-shot* are a pair with trade-off relationship. When expanding novel classes, we can increase the number of shots as compensation to maintain accuracy. For a new class to be identified, it is acceptable to collect 10 to 50

TABLE 5 The ablation experiment results of MB, MB+CMSFF, and MB+CMSFF+CA.

ID	Method	TS	1-shot	5-shot	10-shot	20-shot	30-shot	40-shot	50-shot
PV-Setting-1									
e2	MB	S2	56.07	72.90	76.62	78.87	79.74	79.81	80.11
e13	MB+CMSFF	S2	61.20	77.09	80.92	83.03	84.05	84.34	84.56
e14	MB+CMSFF+CA	S2	**61.24**	**77.43**	**81.28**	**83.59**	**84.46**	**84.70**	**84.86**
PV-Setting-2									
e5	MB	S2	81.05	91.47	93.14	94.00	94.29	94.41	94.53
e15	MB+PMSFF	S2	81.46	91.86	93.51	94.57	94.81	94.88	95.03
e16	MB+CMSFF	S2	82.21	92.32	93.87	94.71	95.03	95.15	95.31
e17	MB+PMSFF+CA	S2	81.87	92.39	93.93	94.86	95.29	95.31	95.50
e18	MB+CMSFF+CA	S2	**82.52**	**92.83**	**94.39**	**95.29**	**95.65**	**95.73**	**95.74**
PV-Setting-3									
e8	MB	S2	74.58	84.77	86.82	87.82	88.29	88.43	88.57
e19	MB+CMSFF	S2	76.61	88.45	90.17	91.32	91.78	91.86	92.14
e20	MB+CMSFF+CA	S2	**78.15**	**89.57**	**91.24**	**92.46**	**92.67**	**93.02**	**93.07**
AFD									
e11	MB	S4	38.41	51.71	55.58	58.08	58.84	59.70	60.09
e21	MB+CMSFF	S4	40.77	54.14	57.68	60.13	61.30	62.03	62.69
e22	MB+CMSFF+CA	S4	**43.94**	**56.93**	**60.64**	**63.66**	**64.50**	**65.55**	**66.18**

(Base-training: Mini-ImageNet; backbone network: Resnet12; distance metric: cosine similarity; TS, training strategy).

samples as its support set. However, the positive relationship of shots and accuracy is not linear. The increase of accuracy as *K-shot* has ceiling. When the *K* is larger than 30, the accuracy is still growing but very slowly.

3.6. The diversity of meta-learning data

The number of classes in meta-learning is noted as N_{train}, and noted as N_{test} in test. Comparing e5 with e8, they are both trained with Mini-ImageNet in base-training. e5 uses 28 classes in meta-learning and 10 classes in test, which is the case $N_{train} > N_{test}$. The training set and testing set of e5 are exchanged in e8, which is the case $N_{train} < N_{test}$.

The training tasks and testing tasks are all formulated as *5-way*, which means that five classes are sampled in each task. The *N-way* of task is the same in e5 and e8. However, the accuracy of e5 is at least 2% higher than e8. It indicates that the size of data used in meta-learning is a factor effects the performance. Using more classes in meta-learning leads to positive results, providing more diverse features and improving the robustness of the model.

3.7. Distance metric

In this work, we compared three distance metrics: dot product, cosine similarity, and Euclidean distance. The same distance measurement module is used in meta-learning and test. This is because even if there is no parameter to be trained in this module, the losses calculated from the distance measurement still affect the parameter updates in the iterations.

An appropriate distance metric significantly helps in improving the performance of classification, clustering process etc. Cosine similarity hits the best performance, as shown in Table 6 and in Figure 5D. The reason is that the vectors obtained from encoder are high dimensional vectors. The cosine similarity has often been used to counteract the problem of Euclidean distance in high dimensional space. The normalization in cosine similarity also has positive effect.

3.8. Backbone networks

In this work, we compared different backbone networks: Convnet4 (Snell et al., 2017), AlexNet (Krizhevsky et al., 2012), Resnet12, Resnet18, Resnet50, Resnet101 (He et al., 2016), DenseNet (Huang et al., 2017), MobileNet-V2 (Sandler et al., 2018). The Convnet4 is the classical architecture used in FSL which stacks four blocks of convolutional calculation. Different networks include different sizes of trainable parameters. The trainable parameters are more in base-training than in meta-learning because the base-training classifier is removed in meta-learning. The size of trainable parameters, learning rate (Lr), training time, and epochs in the two training stages are listed in Table 7. e25–e31 are conducted with the configuration:

TABLE 6 The results of different distance metrics.

ID	Metric	1-shot	5-shot	10-shot	20-shot	30-shot	40-shot	50-shot
e23	Dot product	77.58	86.2	87.52	88.05	88.55	88.65	88.88
e5	Cosine similarity	**80.88**	**91.75**	**93.44**	**94.27**	**94.53**	**94.70**	**94.84**
e24	Euclidean distance	75.96	89.17	91.52	92.64	93.17	93.23	93.42

(Method: MB; backbone network: Resnet12; batchsize: 128; Lr: 0.1 in base-training, 0.001 in meta-learning).

TABLE 7 The experiment efficiencies of different backbone networks.

		Base-training				Meta-learning			
ID	Backbone network	Size	Lr	Training time	Epoch	Size	Lr	Training time	Epoch
e25	Convnet4	215.6 K	0.01	40 m	100	113.1 K	0.001	31 m	50
e26	AlexNet	3.8 M	0.01	40 m	100	3.7 M	0.001	17 m	50
e5	Resnet12	8.0 M	0.1	1.2 h	100	8.0 M	0.001	18 m	20
e27	Resnet18	11.2 M	0.1	1.4 h	100	11.2 M	0.001	40 m	50
e28	Resnet50	23.6 M	0.1	2.3 h	100	23.5 M	0.001	38 m	30
e29	Resnet101	42.6 M	0.01	3.3 h	100	42.5 M	0.001	35 m	20
e30	DenseNet	791.1 K	0.1	3.8 h	100	769.2 K	0.001	1.9 h	50
e31	MobileNet-v2	3.6 M	0.1	2.2 h	100	3.5 M	0.001	1.0 h	50

(Bae-training: Mini-imageNet; meta-learning: PV-2-22; distance metric: cosine similarity).

TABLE 8 The results of different backbone networks.

ID	Backbone networks	1-shot	5-shot	10-shot	20-shot	30-shot	40-shot	50-shot
e25	Convnet4	69.06	85.91	89.91	91.88	92.35	92.79	93.11
e26	AlexNet	68.35	83.12	85.73	87.00	87.27	87.44	87.92
e5	Resnet12	80.88	**91.75**	**93.44**	**94.27**	**94.53**	**94.70**	**94.84**
e27	Resnet18	78.58	89.16	91.36	91.96	92.26	92.44	92.78
e28	Resnet50	**80.89**	90.91	92.56	93.86	94.08	94.15	94.33
e29	Resnet101	74.93	85.59	87.63	89.12	89.67	89.91	89.91
e30	DenseNet	79.39	89.21	90.82	91.84	92.21	92.10	92.50
e31	MobileNet-V2	78.17	89.21	91.48	92.42	92.83	93.02	93.41

(Method: MB; backbone network: resnet12; batchsize: 128; Lr: 0.1 in base-training, 0.001 in meta-learning; Data: Mini-imageNet in base-training, PV-setting-2 in meta-learning and test).

Mini-ImageNet is used in base-training (100 epochs) and PV-2-22 is used in meta-learning. The different number of iterations is due to the different convergence speed in meta-learning. The performances of the backbone networks are listed in Table 8. Resnet12 and Resnet50 outperform the other networks, with Resnet12 being more efficient.

In base-training and meta-learning, we use the validation data to test the accuracy of *5-way, 1-shot* tasks which is shown in Figure 6. The black numbers on the black lines are the best accuracy in base-training, and the black numbers on the red lines are the best accuracy in meta-learning. The lifting ranges of accuracy in meta-learning are marked in red numbers. It is shown that the model trained in base-training stage already has the identification ability with few shots to some extent, even without training with tasks in meta-learning. However, in base-training, the model is already convergent by training with image-wise data, and the accuracy of task testing no longer increases. In fact, the model still has space to improve. Based on this, in meta-learning, by using task-wise data, the accuracy has been further promoted around 20% to 30%.

In recent years, the architectures of networks go deeper and deeper. Some researchers proposed a question that do we really need so deep networks? Our results show that a medium-sized network outperforms other networks in this task. We summarized two reasons: (1) In CNNs, the simpler and more basic features are learnt in shallower layers, the more abstract and complex features are learnt from deeper layers. From shallower layers to deeper layers, the features transition from

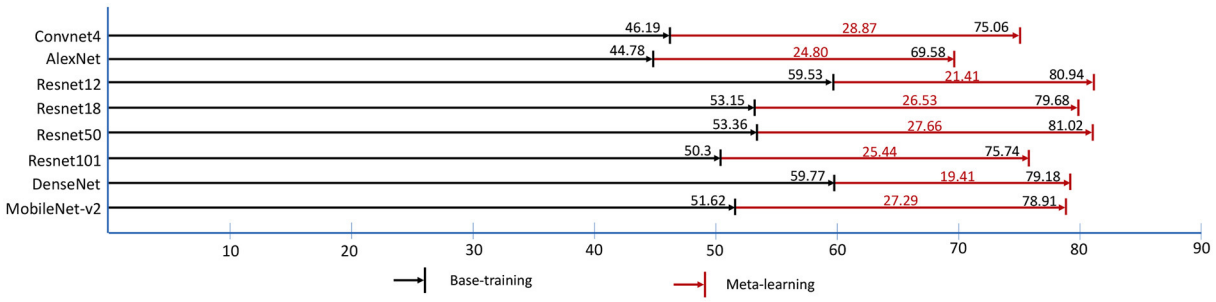

FIGURE 6
The best validation accuracy (%) of "1-shot, 5-way" task in base-training and meta-learning. The red digits represent the accuracy lifting ranges (%) of meta-learning.

edges, lines, and colors, to textures and patterns, to complex graphics, even to specific objects. For our specific task, even humans (e.g. plant experts) rely more on color, shape, and texture for disease identification. Hence, the too deep networks may be not critical meaningful. (2) FSL is the kind of learning task with limited data-scale. For a deeper network, it always has large number of parameters needed to be updated. In the data-limitation condition, too deep network could meet insufficient updating of parameters in backpropagation due to the too long backpropagation path. In parameter updating, shallower networks are more flexible, while the deeper networks look bulky. In short, it does not mean that deeper networks always outperform shallower networks. The size of network should match the specific task and data resources.

3.9. Compare with related works

In order to show the superiority of our method, we conducted several experiments to compare with some recent related researches. Argüeso et al. (2020) used Siamese Network, Triplet Network, and PV as their experimental material. They set a different data splitting: 32 classes are used for training and the rest six classes (apple four classes, blueberry healthy, cherry healthy) for testing. They listed results of three methods: transfer learning, Siamese Network, and Triplet Network. Their backbone network is Inception-V3. In order to be comparable, we executed the experiments with the same data setting as their work. Mini-ImageNet is used in base-training, 32 classes of PV are used in meta-learning, and the rest 6 classes are used in test. The results of e32–e34 are shown in Table 9.

We also compared with Li and Chao (2021b). They proposed a Semi-supervised (SS) FSL approach. The baseline is a typical fine-tuning model. The Single SS adds Semi-supervised step on the top of baseline. The Iterative SS adds one more Semi-supervised step on the top of Single SS. PV was also used as their experimental material and set to three splits. Each split has 28 classes for training and the rest 10 classes for testing. They compared with Argüeso et al. (2020) too. We also conducted experiments by our methods with the same data settings as Li and Chao (2021b). The results of e35–e43 are shown in Table 9. All the comparison results are shown in Figure 7.

The data settings of the two references are different from our data settings. The results indicate that our method outperforms the existing works with all data settings, which means that our method is superior and robust.

4. Discussion

4.1. Motivation and contribution

The method learning from few samples is very promising in plant disease recognition, which has wide range of potential application scenarios for its saving of cost on data. When expanding the range of application, a well-established model of FSL can easily generalize to novel species or diseases without retraining and providing large-scale training data. However, some existing limitations of the FSL itself and the specific applied areas are needed to be considered. Our main contributions in this work are two-folds: (1) we propose to merge the CMSFF in the backbone network to enhance the feature representation, and combine the CA to focus on the informative channels; (2) we propose a group of training strategies to match the different generalization scenarios.

4.2. Limitation and future work

The theoretical research of FSL is in the stage of rapid development at present. Although FSL is very suitable for plant disease recognition, the applications of smart agriculture have just begun (Yang et al., 2022). In this research direction,

TABLE 9 The results compared with related works.

ID	Method	1-shot	5-shot	10-shot	20-shot
			Data setting in Argüeso et al. (2020)		
	Finetuning (Argüeso et al., 2020)	18.2	25.4	30.3	41.1
	Siamese contrastive (Argüeso et al., 2020)	50.2	64.2	70.2	74.1
	Siamese triplet (Argüeso et al., 2020)	65.2	72.3	76.8	81.8
	Single SS (Li and Chao, 2021b)	74.5	89.7	92.6	93.9
	Iterative SS (Li and Chao, 2021b)	75.1	90.0	92.7	93.9
e32	**Ours MB**	76.4	91.0	93.2	94.2
e33	**Ours MB+CMSFF**	80.0	91.9	93.7	**94.3**
e34	**Ours MB+CMSFF+CA**	**80.4**	**92.8**	**94.1**	**94.3**
			Data Split-1 of Li and Chao (2021b)		
	Baseline (Li and Chao, 2021b)	32.8	46.7	64	73.2
	Single SS (Li and Chao, 2021b)	33.7	50.9	66.7	74.7
	Iterative SS (Li and Chao, 2021b)	34	53.1	68.8	75.6
e35	**Ours MB**	55.7	72.8	76.7	79.5
e36	**Ours MB+CMSFF**	60.6	**78.4**	**82.4**	84.3
e37	**Ours MB+CMSFF+CA**	**60.7**	78.1	82.2	**84.5**
			Data Split-2 of Li and Chao (2021b)		
	Baseline (Li and Chao, 2021b)	43.9	68.5	78.7	89.1
	Single SS (Li and Chao, 2021b)	44.7	74.7	85.7	89.7
	Iterative SS (Li and Chao, 2021b)	46.4	76.9	89.2	91.9
e38	**Ours MB**	77.1	91.1	92.9	93.8
e39	**Ours MB+CMSFF**	78.8	91.6	93.5	94.6
e40	**Ours MB+CMSFF+CA**	**79.1**	**92.2**	**94.0**	**95.1**
			Data Split-3 of Li and Chao (2021b)		
	Baseline (Li and Chao, 2021b)	50.7	63.1	77.2	89.3
	Single SS (Li and Chao, 2021b)	52.3	67.6	79.9	90.1
	Iterative SS (Li and Chao, 2021b)	55.2	69.3	80.8	91.5
e41	**Ours MB**	78.1	89.4	91.4	92.6
e42	**Ours MB+CMSFF**	80.6	90.8	92.4	93.3
e43	**Ours MB+CMSFF+CA**	**81.5**	**91.1**	**92.8**	**93.4**

(Ours: backbone network: Resnet12; distance metric: cosine similarity; base-training: Mini-ImageNet).

there are still huge potential space needed to explore. In here, we discuss the limitations of this work and some future works.

1. Multi-disease. The PV and AFD used in this work as target data which have a common characteristic that only single disease is included in per image. In fact, once a plant is infected by the first disease, it is easily infected by other diseases because the immune system is attacked and becomes weak (Barbedo, 2016). Multiple diseases occur in a plant is more common in the real field condition. But the combinations of different diseases are too many to collect sufficient samples for each category from classification perspective (e.g., three diseases of a species generate 7 categories). The current researches prefer to solve this problem by semantic segmentation. We do not cover this challenging problem due to limitations of data resources in this work.

2. Formulation of meta-learning data. The samples of PV were taken under controlled condition (lab-settings), which have a clean board as the unified background, the illumination is under controlled, only single leaf in per image, only single disease occurs in per leaf. The settings are simple and very different from the in-wild conditions. That is the reason many researches already achieved high accuracy by using deep learning CNNs on PV (Hasan et al., 2020). But the samples of AFD were taken under in-wild condition, which have complex surroundings. When testing with AFD, we use PV in meta-learning, mainly considering that both datasets are about plant diseases. Since we did not find any other appropriate dataset, the

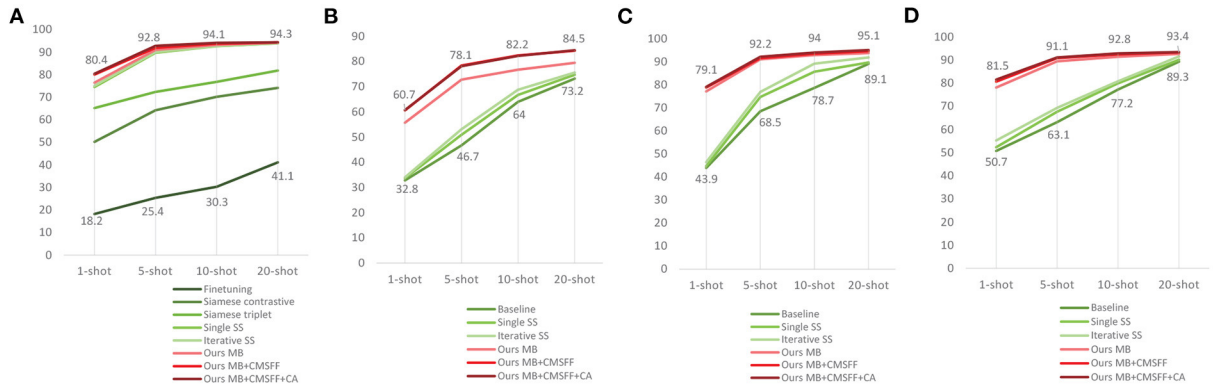

FIGURE 7
The results compared with related works. **(A)** Our work compares with (Argüeso et al., 2020) and (Li and Chao, 2021b). **(B)** Our work compares with Li and Chao (2021b) using the data split-1. **(C)** Our work compares with Li and Chao (2021b) using the data split-1. **(D)** Our work compares with Li and Chao (2021b) using the data split-1.

degree of similarity of the data used in training and test was not taken in account.

According to our hypothesis, the degree of similarity of data used in meta-learning and test is higher, the adapting is easier, and the result would be better. It is demonstrated that the selection of meta-learning data is critical in this pipeline. The data used in meta-learning stage should be determined by the target. When the application scenarios cannot be predicted, how to formulate an appropriate meta-learning dataset is worthy to study. Inspired by Nuthalapati and Tunga (2021) and Li and Yang (2021), the effectiveness of a mixed dataset for meta-learning will be considered.

3. Sub-class classification. For the application of plant disease recognition, it is more meaningful to distinguish the diseases belonging to the same species. What farmers need more than anything else is a diagnostic assistant that can identify similar diseases belonging to the same plant. Although sub-class classification is difficult (Liu and Wang, 2021), it is an inescapable work in plant disease recognition and the performance is needed to be improved urgently. Fine-grained features of the lesions being the distinguishable features to solve this issue. In this direction, lesion detection and segmentation, fine-grained visual classification are involved.

4. The quality and quantity of training data. Most of the current researches of FSL deal with the configuration of data used in test, but very little work has concerned the data used in training. The common sense is that deep learning networks rely on large-scale data. However, a new direction is discussing the quality and quantity of training data recently (Li and Chao, 2021a,c; Li et al., 2021; Li Y. et al., 2022). These works indicate that part of data can achieve at the same performance as full data. Date quality can be assessed, which can guide to establish a dataset with enough diversity data while without redundant samples. The networks of appropriate depth using good data can achieve optimal results in many traditional CNN classification tasks.

In this work, we use large-scale data in base-training and meta-learning. The quantity of data follows the conventional settings for comparison purposes. The data quality assessment work is not involved in this work. For the specific topic of plant disease, the data quality is very important. We know that at different stages of development of plants and diseases, the symptom appearances are very different. How to construct a comprehensive set without redundant data to represent a disease is a valuable work in the future (Barbedo, 2018).

5. Cross-domain. The significance of cross-domain has been introduced in prior sections. We emphasize cross-domain again because it is common when we cannot predict the species, surroundings, and photo conditions in test. In this work, we consider it from training strategies. There are many aspects to explore in future work, such as network architecture, feature distribution calibration etc.

5. Conclusion

In response to the two problems when using FSL for plant disease recognition, we propose a network based on the MB approach that merges CMSFF and CA to obtain a richer feature representation. From experiments, we found that the CMSFF is effective to obtain richer feature representation, especially under the few-shot condition. The CA is an important compensation to the CMSFF, which helps to focus on these meaningful channels. Our method outperforms the existing related works, which indicates that our method is highly robust. The CMSFF+CA is an appropriate combination that fits for any algorithm that needs enhance the feature representation. In addition, a group of training strategies is proposed to meet requirements of different generalization situations. Many factors are discussed

in this work, such as backbone networks, distance metrics etc. The limitations of this work and some new related research directions are discussed.

Data availability statement

The dataset Mini-Imagenet for this study can be found in Kaggle, https://www.kaggle.com/datasets/whitemoon/miniimagenet; The dataset PlantVillage for this study can be found in Kaggle, https://www.kaggle.com/datasets/abdallahalidev/plantvillage-dataset; The dataset Apple Foliar Diseases for this study can be found in Kaggle, https://www.kaggle.com/c/plant-pathology-2021-fgvc8/data.

Author contributions

HL, GP, RT, and S-KT: conceptualization. HL: methodology, experiment, and writing—original draft and editing. GP, RT, and S-KT: writing—review. Z-pQ: experiment and writing—review. All authors contributed to the article and approved the submitted version.

Funding

This research was funded by the projects of Natural Science Foundation of China (Grant No. 12163004), the Yunnan Fundamental Research Projects (Grant No. 202101BD070001-053), and the Fundamental Research Projects of Yunnan Provincial Department of Education (Grant No. 2022J0496). This work was also supported in part by the Macao Polytechnic University—Edge Sensing and Computing: Enabling Human-centric (Sustainable) Smart Cities (RP/ESCA-01/2020).

Conflict of interest

The authors declare that the research was conducted in the absence of any commercial or financial relationships that could be construed as a potential conflict of interest.

Publisher's note

All claims expressed in this article are solely those of the authors and do not necessarily represent those of their affiliated organizations, or those of the publisher, the editors and the reviewers. Any product that may be evaluated in this article, or claim that may be made by its manufacturer, is not guaranteed or endorsed by the publisher.

References

Adler, T., Brandstetter, J., Widrich, M., Mayr, A., Kreil, D., Kopp, M., et al. (2020). Cross-domain few-shot learning by representation fusion. *arXiv preprint arXiv:2010.06498*. doi: 10.48550/arXiv.2010.06498

Afifi, A., Alhumam, A., and Abdelwahab, A. (2021). Convolutional neural network for automatic identification of plant diseases with limited data. *Plants* 10:28. doi: 10.3390/plants10010028

Argüeso, D., Picon, A., Irusta, U., Medela, A., San-Emeterio, M. G., Bereciartua, A., et al. (2020). Few-shot learning approach for plant disease classification using images taken in the field. *Comput. Electron. Agric.* 175:105542. doi: 10.1016/j.compag.2020.105542

Barbedo, J. G. A. (2016). A review on the main challenges in automatic plant disease identification based on visible range images. *Biosyst. Eng.* 144, 52–60. doi: 10.1016/j.biosystemseng.2016.01.017

Barbedo, J. G. A. (2018). Impact of dataset size and variety on the effectiveness of deep learning and transfer learning for plant disease classification. *Comput. Electron. Agric.* 153, 46–53. doi: 10.1016/j.compag.2018.08.013

Campbell, C. L., and Madden, L. V. (1990). *Introduction to Plant Disease Epidemiology*. New York, NY: John Wiley & Sons.

Chen, L., Cui, X., and Li, W. (2021). Meta-learning for few-shot plant disease detection. *Foods* 10:2441. doi: 10.3390/foods10102441

Chen, Y., Wang, X., Liu, Z., Xu, H., and Darrell, T. (2020). A new meta-baseline for few-shot learning. *arXiv preprint arXiv:2003.04390*. doi: 10.48550/arXiv.2003.04390

Deng, J., Dong, W., Socher, R., Li, L.-J., Li, K., and Fei-Fei, L. (2009). "Imagenet: a large-scale hierarchical image database," in *2009 IEEE Conference on Computer Vision and Pattern Recognition* (Miami, FL), 248–255. doi: 10.1109/CVPR.2009.5206848

Dogra, A., Goyal, B., and Agrawal, S. (2017). From multi-scale decomposition to non-multi-scale decomposition methods: a comprehensive survey of image fusion techniques and its applications. *IEEE Access* 5, 16040–16067. doi: 10.1109/ACCESS.2017.2735865

Dong, H., Pan, J., Xiang, L., Hu, Z., Zhang, X., Wang, F., et al. (2020). "Multi-scale boosted dehazing network with dense feature fusion," in *Proceedings of the IEEE/CVF Conference on Computer Vision and Pattern Recognition* (Seattle, WA), 2157–2167. doi: 10.1109/CVPR42600.2020.00223

Dong, S., Wang, P., and Abbas, K. (2021). A survey on deep learning and its applications. *Comput. Sci. Rev.* 40:100379. doi: 10.1016/j.cosrev.2021.100379

Goodfellow, I., Bengio, Y., and Courville, A. (2016). *Deep Learning*. Cambridge, MA: MIT Press.

Guo, M.-H., Xu, T.-X., Liu, J.-J., Liu, Z.-N., Jiang, P.-T., Mu, T.-J., et al. (2021). Attention mechanisms in computer vision: a survey. *arXiv preprint arXiv:2111.07624*. doi: 10.1007/s41095-022-0271-y

Guo, Y., Codella, N. C., Karlinsky, L., Codella, J. V., Smith, J. R., Saenko, K., et al. (2020). "A broader study of cross-domain few-shot learning," in *European Conference on Computer Vision* (Glasgow: Springer), 124–141. doi: 10.1007/978-3-030-58583-9_8

Hafiz, A. M., Parah, S. A., and Bhat, R. U. A. (2021). Attention mechanisms and deep learning for machine vision: a survey of the state of the art. *arXiv preprint arXiv:2106.07550*. doi: 10.48550/arXiv.2106.07550

Han, J., Kamber, M., and Pei, J. (2012). "Chapter 2: Getting to know your data," in *Data Mining, 3rd Edn, The Morgan Kaufmann Series in Data Management*

Systems, eds D. Cerra, and H. Severson (Boston, MA: Morgan Kaufmann), 39–82. doi: 10.1016/B978-0-12-381479-1.00002-2

Hasan, R. I., Yusuf, S. M., and Alzubaidi, L. (2020). Review of the state of the art of deep learning for plant diseases: a broad analysis and discussion. *Plants* 9:1302. doi: 10.3390/plants9101302

He, K., Zhang, X., Ren, S., and Sun, J. (2016). "Deep residual learning for image recognition," in *Proceedings of the IEEE Conference on Computer Vision and Pattern Recognition* (Las Vegas, NV), 770–778. doi: 10.1109/CVPR.2016.90

Hu, D. (2019). "An introductory survey on attention mechanisms in NLP problems," in *Proceedings of SAI Intelligent Systems Conference* (London, UK: Springer), 432–448.

Hu, J., Shen, L., and Sun, G. (2018). "Squeeze-and-excitation networks," in *Proceedings of the IEEE Conference on Computer Vision and Pattern Recognition* (Salt Lake City, UT), 7132–7141. doi: 10.1109/CVPR.2018.00745

Huang, G., Liu, Z., Van Der Maaten, L., and Weinberger, K. Q. (2017). "Densely connected convolutional networks," in *Proceedings of the IEEE Conference on Computer Vision and Pattern Recognition* (Honolulu, HI), 4700–4708. doi: 10.1109/CVPR.2017.243

Hughes, D., and Salathé, M. (2015). An open access repository of images on plant health to enable the development of mobile disease diagnostics. *arXiv preprint arXiv:1511.08060*. doi: 10.48550/arXiv.1511.08060

Jadon, S. (2020). "SSM-net for plants disease identification in low data regime," in *2020 IEEE/ITU International Conference on Artificial Intelligence for Good (AI4G)* (Geneva), 158–163. doi: 10.1109/AI4G50087.2020.9311073

Koch, G., Zemel, R., and Salakhutdinov, R. (2015). "Siamese neural networks for one-shot image recognition," in *ICML Deep Learning Workshop, Vol. 2* (Lille).

Krizhevsky, A., Sutskever, I., and Hinton, G. E. (2012). "Imagenet classification with deep convolutional neural networks," in *Advances in Neural Information Processing Systems* (Lake Tahoe, NV), 25.

Lan, R., Sun, L., Liu, Z., Lu, H., Pang, C., and Luo, X. (2020). MADNet: a fast and lightweight network for single-image super resolution. *IEEE Trans. Cybern.* 51, 1443–1453. doi: 10.1109/TCYB.2020.2970104

Li, J., Fang, F., Mei, K., and Zhang, G. (2018). "Multi-scale residual network for image super-resolution," in *Proceedings of the European Conference on Computer Vision (ECCV)* (Munich), 517–532. doi: 10.1007/978-3-030-01237-3_32

Li, W., Xu, J., Huo, J., Wang, L., Gao, Y., and Luo, J. (2019). "Distribution consistency based covariance metric networks for few-shot learning," in *Proceedings of the AAAI Conference on Artificial Intelligence* (Honolulu, HI), 33, 8642–8649. doi: 10.1609/aaai.v33i01.33018642

Li, W.-H., Liu, X., and Bilen, H. (2022). "Cross-domain few-shot learning with task-specific adapters," in *Proceedings of the IEEE/CVF Conference on Computer Vision and Pattern Recognition*, 7161–7170.

Li, Y., and Chao, X. (2021a). Distance-entropy: an effective indicator for selecting informative data. *Front. Plant Sci.* 12:818895. doi: 10.3389/fpls.2021.818895

Li, Y., and Chao, X. (2021b). Semi-supervised few-shot learning approach for plant diseases recognition. *Plant Methods* 17, 1–10.

Li, Y., and Chao, X. (2021c). Toward sustainability: trade-off between data quality and quantity in crop pest recognition. *Front. Plant Sci.* 12:811241. doi: 10.3389/fpls.2021.811241

Li, Y., Chao, X., and Ercisli, S. (2022). Disturbed-entropy: a simple data quality assessment approach. *ICT Express*. doi: 10.1016/j.icte.2022.01.006

Li, Y., and Yang, J. (2021). Meta-learning baselines and database for few-shot classification in agriculture. *Comput. Electron. Agric.* 182:106055. doi: 10.1016/j.compag.2021.106055

Li, Y., Yang, J., and Wen, J. (2021). Entropy-based redundancy analysis and information screening. *Digit. Commun. Netw*. doi: 10.1016/j.dcan.2021.12.001

Lim, Y.-C., and Kang, M. (2019). "Global and local multi-scale feature fusion for object detection and semantic segmentation," in *2019 IEEE Intelligent Vehicles Symposium (IV)* (Paris), 2557–2562. doi: 10.1109/IVS.2019.8813786

Lin, H., Tse, R., Tang, S.-K., Chen, Y., Ke, W., and Pau, G. (2021). "Near-realtime face mask wearing recognition based on deep learning," in *2021 IEEE 18th Annual Consumer Communications & Networking Conference (CCNC)* (Las Vegas, NV), 1–7. doi: 10.1109/CCNC49032.2021.9369493

Lin, T.-Y., Dollár, P., Girshick, R., He, K., Hariharan, B., and Belongie, S. (2017). "Feature pyramid networks for object detection," in *Proceedings of the IEEE Conference on Computer Vision and Pattern Recognition* (Honolulu, HI), 2117–2125. doi: 10.1109/CVPR.2017.106

Liu, J., and Wang, X. (2021). Plant diseases and pests detection based on deep learning: a review. *Plant Methods* 17, 1–18. doi: 10.1186/s13007-021-00722-9

Long, J., Shelhamer, E., and Darrell, T. (2015). "Fully convolutional networks for semantic segmentation," in *Proceedings of the IEEE Conference on Computer Vision and Pattern Recognition* (Boston, MA), 3431–3440. doi: 10.1109/CVPR.2015.7298965

Nuthalapati, S. V., and Tunga, A. (2021). "Multi-domain few-shot learning and dataset for agricultural applications," in *Proceedings of the IEEE/CVF International Conference on Computer Vision* (Montreal, BC), 1399–1408. doi: 10.1109/ICCVW54120.2021.00161

Oerke, E.-C., and Dehne, H.-W. (2004). Safeguarding production-losses in major crops and the role of crop protection. *Crop Protect.* 23, 275–285. doi: 10.1016/j.cropro.2003.10.001

Qi, J., Zhang, R., Li, C., and Mao, Y. (2022). Cross domain few-shot learning via meta adversarial training. *arXiv preprint arXiv:2202.05713*. doi: 10.48550/arXiv.2202.05713

Redmon, J., and Farhadi, A. (2018). YOLOV3: an incremental improvement. *arXiv preprint arXiv:1804.02767*. doi: 10.48550/arXiv.1804.02767

Ronneberger, O., Fischer, P., and Brox, T. (2015). "U-Net: Convolutional networks for biomedical image segmentation," in *International Conference on Medical Image Computing and Computer-Assisted Intervention* (Munich: Springer), 234–241. doi: 10.1007/978-3-319-24574-4_28

Sandler, M., Howard, A., Zhu, M., Zhmoginov, A., and Chen, L.-C. (2018). "Mobilenetv2: inverted residuals and linear bottlenecks," in *Proceedings of the IEEE Conference on Computer Vision and Pattern Recognition* (Salt Lake City, UT), 4510–4520. doi: 10.1109/CVPR.2018.00474

Simonyan, K., and Zisserman, A. (2014). Very deep convolutional networks for large-scale image recognition. *arXiv preprint arXiv:1409.1556*. doi: 10.48550/arXiv.1409.1556

Singh, D., Jain, N., Jain, P., Kayal, P., Kumawat, S., and Batra, N. (2020). "Plantdoc: a dataset for visual plant disease detection," in *Proceedings of the 7th ACM IKDD CoDS and 25th COMAD* (Hyderabad), 249–253. doi: 10.1145/3371158.3371196

Snell, J., Swersky, K., and Zemel, R. S. (2017). Prototypical networks for few-shot learning. *arXiv preprint arXiv:1703.05175*. doi: 10.48550/arXiv.1703.05175

Strange, R. N., and Scott, P. R. (2005). Plant disease: a threat to global food security. *Annu. Rev. Phytopathol.* 43, 83–116. doi: 10.1146/annurev.phyto.43.113004.133839

Sung, F., Yang, Y., Zhang, L., Xiang, T., Torr, P. H., and Hospedales, T. M. (2018). "Learning to compare: relation network for few-shot learning," in *Proceedings of the IEEE Conference on Computer Vision and Pattern Recognition* (Salt Lake City, UT), 1199–1208. doi: 10.1109/CVPR.2018.00131

Vinyals, O., Blundell, C., Lillicrap, T., Wierstra, D., and Kavukcuoglu, K. (2016). "Matching networks for one shot learning," in *Advances in Neural Information Processing Systems* (Barcelona), 29, 3630–3638.

Wang, F., Jiang, M., Qian, C., Yang, S., Li, C., Zhang, H., et al. (2017). "Residual attention network for image classification," in *Proceedings of the IEEE Conference on Computer Vision and Pattern Recognition* (Honolulu, HI), 3156–3164. doi: 10.1109/CVPR.2017.683

Wang, Y., Yao, Q., Kwok, J. T., and Ni, L. M. (2020). Generalizing from a few examples: a survey on few-shot learning. *ACM Comput. Surveys* 53, 1–34. doi: 10.48550/arXiv.1904.05046

Woo, S., Park, J., Lee, J.-Y., and Kweon, I. S. (2018). "CBAM: Convolutional block attention module," in *Proceedings of the European Conference on Computer Vision (ECCV)* (Munich), 3–19. doi: 10.1007/978-3-030-01234-2_1

Yang, J., Guo, X., Li, Y., Marinello, F., Ercisli, S., and Zhang, Z. (2022). A survey of few-shot learning in smart agriculture: developments, applications, and challenges. *Plant Methods* 18, 1–12. doi: 10.1186/s13007-022-00866-2

Zhang, H., and Patel, V. M. (2018). "Densely connected pyramid Dehazing network," in *Proceedings of the IEEE Conference on Computer Vision and Pattern Recognition* (Salt Lake City, UT), 3194–3203. doi: 10.1109/CVPR.2018.00337

Zhang, H., Sindagi, V., and Patel, V. M. (2018). "Multi-scale single image Dehazing using perceptual pyramid deep network," in *Proceedings of the IEEE Conference on Computer Vision and Pattern Recognition Workshops* (Salt Lake City, UT), 902–911. doi: 10.1109/CVPRW.2018.00135

Zhong, F., Chen, Z., Zhang, Y., and Xia, F. (2020). Zero-and few-shot learning for diseases recognition of citrus aurantium l. using conditional adversarial autoencoders. *Comput. Electron. Agric.* 179:105828. doi: 10.1016/j.compag.2020.105828

frontiers | Frontiers in Plant Science

TYPE Original Research
PUBLISHED 23 September 2022
DOI 10.3389/fpls.2022.1010540

OPEN ACCESS

EDITED BY
Daobilige Su,
China Agricultural University,
China

REVIEWED BY
Changling Wang,
China Agricultural University,
China
Dong Wang,
Henan University,
China

*CORRESPONDENCE
Liping Chen
chenlp@nercita.org.cn
Changyuan Zhai
zhaicy@nercita.org.cn

SPECIALTY SECTION
This article was submitted to Sustainable and Intelligent Phytoprotection, a section of the journal Frontiers in Plant Science

RECEIVED 03 August 2022
ACCEPTED 29 August 2022
PUBLISHED 23 September 2022

CITATION
Gu C, Zou W, Wang X, Chen L and Zhai C (2022) Wind loss model for the thick canopies of orchard trees based on accurate variable spraying. *Front. Plant Sci.* 13:1010540. doi: 10.3389/fpls.2022.1010540

Wind loss model for the thick canopies of orchard trees based on accurate variable spraying

Chenchen Gu[1,2,3], Wei Zou[1,2,3], Xiu Wang[1,2,3], Liping Chen[3]* and Changyuan Zhai[1,2]*

[1]Intelligent Equipment Research Center, Beijing Academy of Agriculture and Forestry Sciences, Beijing, China, [2]National Engineering Research Center for Intelligent Equipment in Agriculture, Beijing, China, [3]National Engineering Research Center for Information Technology in Agriculture, Beijing, China

Variable application by wind is an efficient application technology recommended by the Food and Agriculture Organization (FAO) of the United Nations that can effectively improve the deposition effect of liquid medicine in a canopy and reduce droplet drift. In view of the difficulty of modelling wind forces in orchard tree canopies and the lack of a wind control model, the wind loss model for a canopy was studied. First, a three-dimensional wind measurement test platform was built for an orchard tree canopy. The orchard tree was located in three-dimensional space, and the inner leaf areas of the orchard tree canopy and the wind force in different areas were measured. Second, light detection and ranging (LiDAR) point cloud data of the orchard tree canopy were obtained by LiDAR scanning. Finally, classic regression, partial least squares regression (PLSR), and back propagation (BP) neural network algorithms were used to build wind loss models in the canopy. The research showed that the BP neural network algorithm can significantly improve the fitting accuracy of the model. Under different fan speeds of 1,381 r/min, 1,502 r/min, and 1,676 r/min, the coefficient of determination (R^2) of the model were 81.78, 72.85, and 69.20%, respectively, which were 19.38, 7.55, and 12.3% higher than those of the PLSR algorithm and 21.48, 22.25, and 24.3% higher than those of multiple regression analysis. The comparison showed that the BP neural network algorithm obtains the highest model accuracy, but because the model is not intuitive, PLSR has the advantages of intuitive and simple models in the three algorithms. In practical applications, the wind loss model based on a BP neural network or PLSR can be selected according to the operational requirements and software and hardware conditions. This study can provide a basis for wind control in precise variable spraying and promote the development of wind control technologies.

KEYWORDS

wind variable application, wind loss, regression algorithm, canopy thickness, leaf area, LiDAR

Introduction

Pesticide spraying can effectively control diseases and pests and improve fruit quality and fruit yield (Eugen et al., 2017; Nuyttens et al., 2017; Gu et al., 2020). At present, continuous and undifferentiated application is widely used for pesticide applications in orchards, which presents a series of economic and ecological problems such as large amounts of pesticide spraying, low utilization rates, excessive pesticide residues in agricultural products, and environmental pollution (Abbas et al., 2020; Manandhar et al., 2020; Song et al., 2020). Accurate variable spraying can be utilized according to information on crop canopy characteristics, realizing pesticide application according to the presence or absence of crops, canopy volume, and density and effectively addressing problems in existing application operations (Zhou et al., 2017; Colaço et al., 2018), which can effectively promote sustainable agricultural economy and ecology.

Variable wind applications can disturb leaves, enhance the ability of droplets to penetrate and deposit in the canopy, and improve spray operation quality (Gu et al., 2014). This approach is an internationally recognized technical means to effectively improve the utilization rate of pesticides (Chen et al., 2017; Li et al., 2017). At present, research on wind regulation is in the primary stages of development, the regulation method is not mature, and there is a lack of effective control models. Whether wind control is appropriate during the application process directly affects the operational effect (Al-Jumaili and Salyani, 2014; Chen et al., 2017; Song et al., 2017). If the wind force is too small, the chemical solution cannot penetrate the surface of the canopy and deposit inside the canopy, resulting in incomplete disease prevention and control, increasing the occurrence of diseases. Excessive wind force will cause the drifting of liquid medicine, polluting the soil and the surrounding environment and endangering humans and livestock. Khot et al. (2012) studied variable spraying under different wind conditions and walking speeds. Their test results showed that a 70% air-assisted spray was more effective than the 100% air-assisted spray, which can effectively reduce droplet drift. Wind regulation methods have mainly focused on wind regulation technologies and sprayer devices, the establishment of distribution methods for wind and fog fields outside a canopy, and so on. There is less research on the distribution of wind fields and wind demand and loss models in orchard tree canopies (Zhai et al., 2018). Accurately regulating the wind force of a spray and studying the influence law of wind force on fog droplets in a canopy is the focus of this current research.

Wind regulation includes wind direction, wind speed, and wind volume. The basis of wind regulation is to control the direction of air supply consistent with the direction of spray (Duga et al., 2015b). Wind speed and wind volume are the main research topics of wind regulation, and the two are coupled relationships. Through the coordinated regulation of the air inlet and outlet of a sprayer fan, wind force regulation can be achieved to provide appropriate wind force for an orchard tree canopy and ensure that the liquid medicine evenly covers the fronts and backs of leaves and the surfaces of orchard tree branches. The distribution of wind power in space and the canopy of an air-delivered sprayer is mainly studied through computational fluid dynamics (CFD) simulation technology. CFD technology can reduce the cost of wind prediction, and it is an important means to study the wind fields of sprayers. Dekeyser et al. (2013) used CFD to simulate a wind field outside the air outlet of a horizontal axis sprayer, distribution sprayer, and independent nozzle air sprayer. Through experimental verification, it was concluded that the CFD simulated wind field can better fit the experimental data. Duga et al. (2015a) studied the influence of external wind force and spray type on spray distribution in different orchards by establishing three-dimensional numerical models of tree crowns for four orchard trees using CFD modeling and orchard test verification methods and improved the quantitative understanding of spray design, wind force, and canopy structure interaction. In the above research, through CFD modeling, the wind field distribution of the sprayer was found to be mostly the wind field outside the canopy. There has been less research on wind fields inside a canopy. Hong et al. (2017) used CDF technology for modeling by using virtual porous media instead of actual trees. It was found that canopy size and canopy density have a great impact on air entering the canopy, and the air velocity will decrease with increasing canopy thickness, tree height, and canopy density. They established a CFD model for the distribution of wind forces in a canopy but did not obtain an effective mathematical model that could directly calculate the wind force in a canopy.

The wind regulation model is the basis of wind regulation. The wind force is affected by the canopy thickness and canopy density during canopy penetration. Most of the existing studies have focused on modern orchards, and the research objects were characterized by small canopy thicknesses, dense branches and leaves, and uniform distribution. The wind loss model can make the wind force regulation reasonable. Through the wind loss model, the wind loss can be calculated through the canopy information, and then the wind speed served by the sprayer can be known. Reasonable wind for spray can improve the uniformity of pesticide deposition and the efficacy. Research on a wind field and wind loss model in a traditional thick canopy has not been carried out. Due to the large changes in canopy thickness and density in different areas of orchard tree canopies, the distribution of wind forces in different areas of a canopy has the characteristics of large differences in change rules and is difficult to measure and quantify, which hinders the establishment of wind control models.

At present, research on variable wind spraying technology has achieved variable spray volume control and wind direction control, and variable spray technology has been preliminarily achieved. However, there is a lack of research on the law of wind change in orchard tree canopies. To study the law of wind loss under different influencing factors in orchard tree canopies, based on previous canopy volume detection (Gu et al., 2021a) and the fitting model of LiDAR point cloud data and the leaf area (Gu et al., 2021a, 2022). By gridding the tree canopy, the wind was

measured outside and inside the canopy. The wind loss model in canopies based on the wind speed at the entrance of the canopies, canopy thickness, and canopy leaf area/LiDAR point cloud data are evaluated in this study. The classic regression, PLSR, and BP neural network algorithms are used to establish the wind loss model in canopies, which provides an effective basis for wind regulation for accurate variable spraying and plays an important role in achieving pesticide reduction and increased efficiency.

Materials and methods

Test platform

We designed a three-dimensional measurement platform of orchard tree canopies, enveloped a whole orchard tree canopy in the platform, and achieved the positioning of canopies in three-dimensional space. Figure 1 shows a schematic diagram of the wind measurement process in a canopy. The sprayer sends air through the air supply system. The sprayer applies the pesticide on one side of the orchard tree when working between rows, and then spray on the other side when the row changed. According to the operation mode of the sprayer, only one side of the orchard tree canopy was studied. In the wind measurement of canopy, the outermost side of the tree is the wind inlet measurement point, and the central line of the tree row is the wind outlet measurement point. The wind force at the canopy inlet (black measurement point) and outlet (red measurement point) is measured by a wind meter, and L is the distance (2 M) from the wind supply center of the sprayer to the position of the orchard tree row during the wind measurement process. A Langshan 3 WGF-300D air-driven orchard applicator is used for air supply. The working pressure of the applicator is 1.2–1.5 MPa, the flow of the medicine pump is 60 l/min, the fan speed is 0–2,800 r/min, the volume of the medicine box is 300 l, and the overall dimension is 2.5 × 1.3 × 1.16 M. Moreover, the spray width is greater than or equal to 20 M, the spray height is greater than or equal to 7 m, and the operation speed is 3–4.2 km/h. The thermal anemometer is used to measure the wind force in the canopy. The model is gm8903, the measurement range is 0–30 m/s, and the resolution is 0.001 m/s. The canopy between the measurement points of the canopy inlet and canopy outlet is the wind measurement canopy area (green area).

According to the distribution of the orchard tree canopy in the grid area, the canopy is divided into different measurement areas by dividing lines. The number of measurement areas is the same as the number of applicator nozzles, and the measurement area is divided into 0.2 × 0.2 M (Figure 2), realizing the positioning of different measurement areas in the canopy area. Marking the positions of wind measurement points at the entrance and exit of the canopy with label paper is conducive to the smooth progress of wind speed measurement in the canopy. In Figure 2, the red point is the measurement position mark point, and the green frame is the measurement division area.

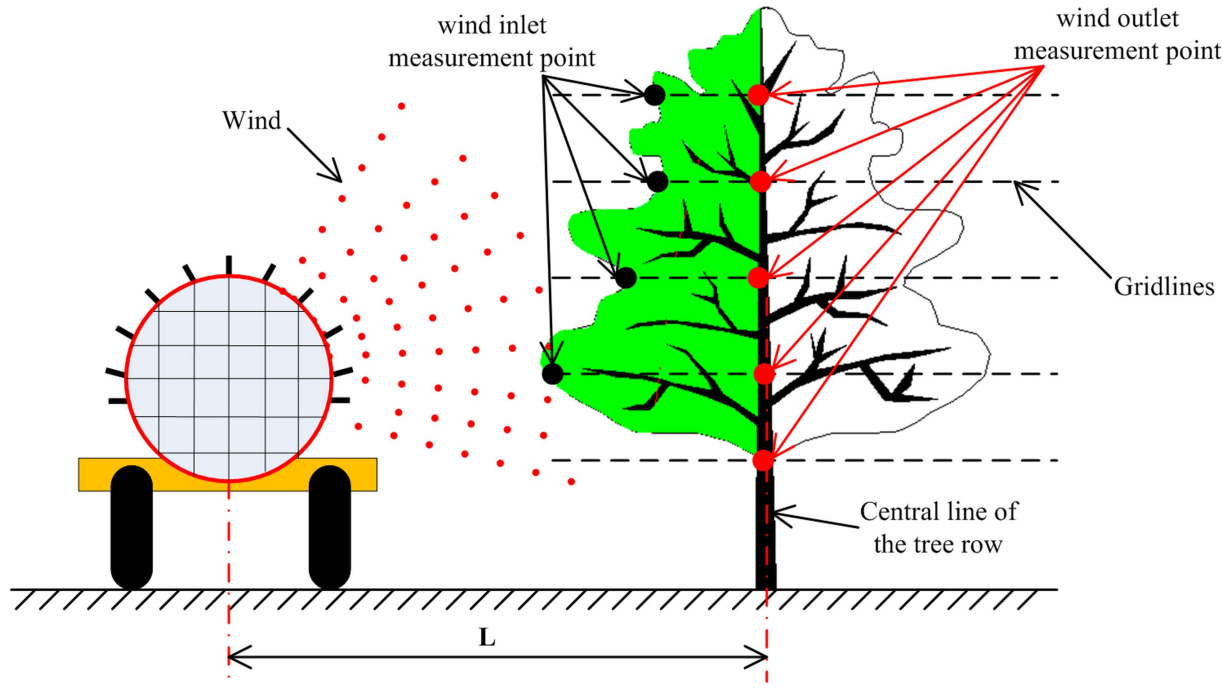

FIGURE 1
Schematic diagram of the canopy wind measurement.

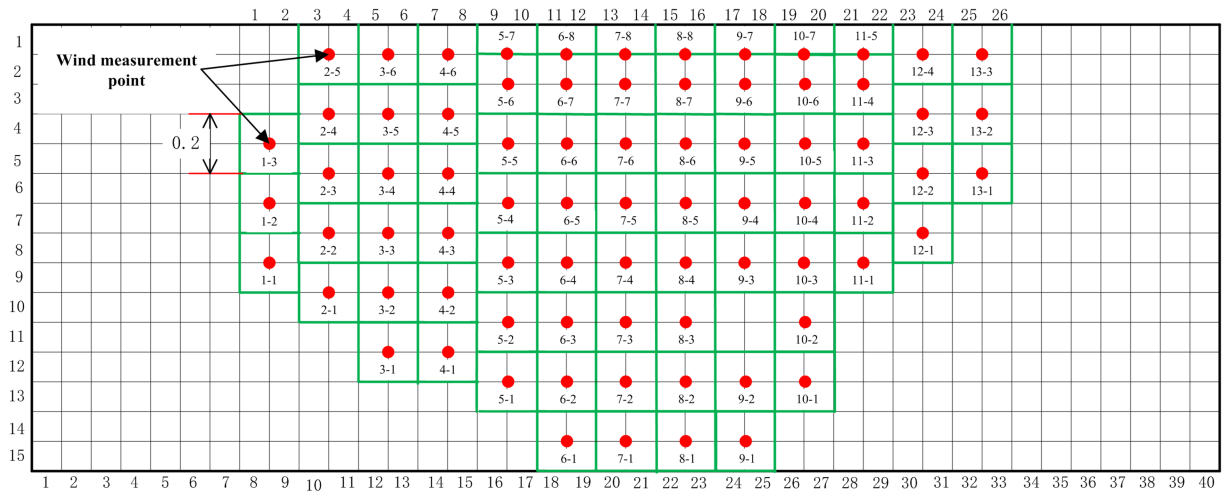

FIGURE 2
Canopy grid division and measurement point marking for the airflow test.

Test orchard tree

The selected orchard tree in the test is shown in Figure 3. The test site is the Xiaotangshan National Precision Agriculture Research Demonstration Base in Changping District, Beijing. The test tree was one Fuji apple tree, and the tree was 5 years old. The tree used in the research is open center tree shape (Gao et al., 2015). It has the advantages of obvious middle trunk, main branch, and natural stratification. During the processes of growth, the tree pruning amount is light, growth and formation are fast, and bearing of fruits early. The height of the tree was 2.3 M, the lower edge of the canopy was 0.8 M from the ground, and the crown was 1.5 M high and 2.5 M wide. The row spacing is 4 M and the plant spacing is 3.5 M. The experimental research time was October 11, 2020. According to the definition of the growth stage of mono- and dicotyledonous plants (Bleiholder et al., 2001), the apple tree is in the final stage of the principal growth stage: maturity of the fruit and seed; fruit ripening for consumption; and fruit achieving typical taste and firmness. At this time, the apples are mature with typical taste and hardness. Apple trees in the orchard have no fallen leaves, and the distribution of the leaf area in the canopy has not changed.

FIGURE 3
Test orchard tree.

Test method of wind in the canopy and natural wind measurement

Before the test, the air supply width of different wind forces of the sprayer was determined, the measurement position was set to 1, 1.5, and 2 M away from the fan outlet, and the air supply width range of the wind force from the sprayer outlet to the measurement position was measured based on a position 1 M away from the horizontal ground in the vertical direction. During the measurement process, different applicator fan speeds were set, the wind speed boundary was measured as 2 m/s, the horizontal displacement between the measurement position and the left and right sides of the air outlet was recorded, and the wind supply width of the sprayer was determined.

The wind measurement points were laid out on a three-dimensional measurement test bench, as shown in Figure 2, and

the wind speed measurement points were marked at the entrance and exit of the canopy with label paper (Figure 4A). The air supply width was determined according to the results. Before the test, the moving distance of the applicator was calibrated. After each measurement, the wind speed at the corresponding canopy position at the air outlet of a group of sprayers moved forward and continued to measure the next test unit, as shown in Figure 4B. During the experiment, the sprayer is in the middle of tree row. The center of sprayer from the center line of tree row is 2 M, and consistent with the distance of the fruit farmers' planting operation.

During the measurement of the wind speed at the wind inlet and outlet at the marked position of the canopy, to detect the wind force at different positions in the canopy and reduce artificial interference, an anemometer measuring probe was fixed on the 1.5 M probe rod (Figure 5), the probe was placed at the measuring point in the canopy through the probe rod, the wind speed was measured, and the wind value at each measuring position was read 3 times.

When the orchard experiment was conducted, the nature wind speed was measured. We set up a WindSonic portable weather station which was used to measure natural wind speed in the orchard. The data was obtained once per minute.

Data processing method of the wind measurement test in the canopy

During the test, the fan speeds of the sprayer were set to 1,381, 1,502, and 1,676 r/min, and the wind speeds at the inlet and outlet of the wind were obtained to conduct an experimental study on the wind loss in the canopy. The three levels of spray fan speed represent different air-supplied conditions for the diversity of test conditions. The wind loss model is different with different air supply speed. The canopy wind loss rate was calculated using the inlet and outlet wind speeds of the canopy wind, and the calculation formula is:

$$SpeedLoss_{\text{Canopy}} = \left(Speed_{\text{CanopyIN}} - Speed_{\text{CanopyOUT}}\right) / Speed_{\text{CanopyIN}} \quad (1)$$

where,
$SpeedLoss_{Canopy}$ - wind speed loss rate.
$Speed_{CanopyIN}$ - inlet wind speed, m/s.
$Speed_{CanopyOUT}$ - outlet wind speed, m/s.

Due to the influence of the location of air inlets and outlets and the external natural wind, any unreasonable data groups need to be removed in the process of calculating the wind loss. First, according to the wind blowing process, the wind speed at the canopy outlet should be able to continuously disturb the leaves (Dai, 2008), ensure that the liquid medicine is evenly deposited on the fronts and backs of the leaves at the canopy outlet, and remove the measurement points where the wind speed at the canopy wind outlet is zero. Due to the influence of natural wind, the measurement points where the wind speed at the canopy inlet is less than that at the canopy outlet are removed. Due to the small canopy thickness and density of branches and leaves at individual positions of the canopy, the data of measurement points with equal wind speed at the entrance and exit of the canopy are removed. Using the above process, effective data for the study of the wind loss model of the orchard tree canopy are obtained.

Measurement of canopy thickness and leaf area

Before the wind measurement test, the canopy thickness and leaf area of different areas of the orchard tree canopy were measured. The canopy thickness measurement adopted the

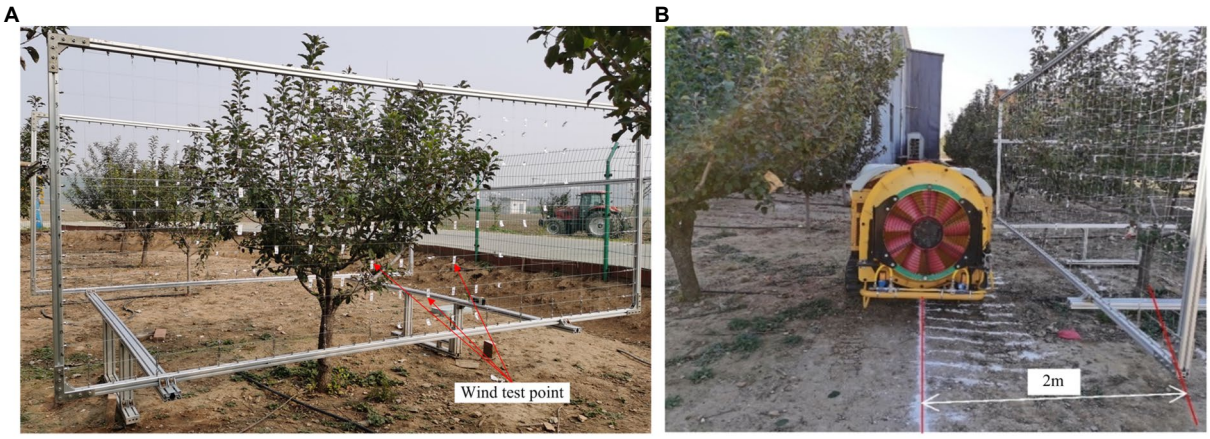

FIGURE 4
Canopy airflow measurement test. **(A)** Layout of canopy airflow test points. **(B)** Canopy airflow measurement test.

canopy volume detection method CMC (canopy meshing profile characterization; Gu et al., 2021b) obtained in previous research to calculate the thickness of different canopy positions.

The measurement method for the canopy leaf area adopts a non-destructive statistical measurement method to calculate the leaf area for different areas in the canopy (Figure 6). To manually measure the leaf area of apple trees in different areas, a three-dimensional measurement grid frame of canopy leaf area is used to divide the apple tree canopy into different areas. It is necessary to count the number of leaves in the three grades of large, medium, and small leaves in the measurement area, multiply the calculated average value of leaf area in each grade by the number of leaves in each grade, and sum the leaf area calculated in each grade to obtain the sum of the leaf area in this area. The leaf area obtained by statistical analysis was compared with the total leaf area measured by the leaf area instrument one by one, and the relative error was 1.8% (Gu et al., 2022). The accuracy is high and is feasible and appropriate for this experimental study.

FIGURE 5
Airflow measurement in the canopy.

Wind loss model

To obtain the wind speed at the entrance of the canopy, the wind stroke in the canopy, the leaf area/LiDAR point cloud data in different areas of the canopy, and the wind loss rate in the canopy under different wind conditions, multiple regression, PLSR, and BP neural network algorithms that can perform regression analysis on multiple dependent variables and multiple independent variables were used.

Classic regression analysis was carried out using Minitab software; the appropriate relationship model was selected, the regression statistics were stored, the residual analysis and confidence interval were tested, and a lack-fit test was carried out. When creating regression equations, the PLSR algorithm considers extracting the principal components of dependent variables and independent variables (principal component analysis: PCA) and extracting the maximum correlation between principal components (canonical correlation analysis: CCA). This is the product of three basic algorithms, PCA, CCA, and multiple linear regression, which can remove the redundancies among data to the greatest extent. The BP neural network regression algorithm can carry out more accurate regression on multiple influencing factors and obtain an accurate model. 77 sets of data were obtained in the research. To prevent the obtained model from fitting the training set well, the fitting effect of data other than the training data is inconsistent. 70% of the data are used for model establishment, and the remaining 30%

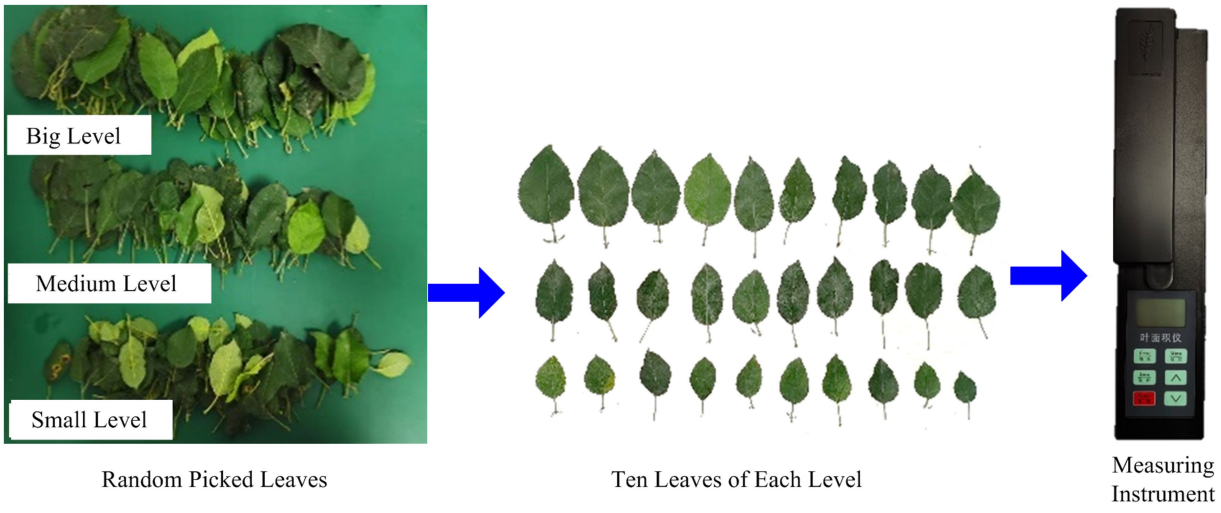

FIGURE 6
Leaf area measurement by statistical analysis.

of the data are used for model verification. The data set was disorganized in the process, and the training and test set was randomly extracted.

Results

In this study, the selected object is orchard trees that are widely planted in Chinese apple orchards and have large canopy thicknesses. During the experiment, the natural wind speed range was 0.2 m/s-0.9 m/s, less than 1 m/s. Since the air-assisted sprayer supplied high-intensity wind, the interior of the tree canopy would not be affected by the natural wind. The concept of canopy zoning is used to study the wind loss model, which meets the actual requirements of orchard pesticide application.

The sprayer ranges of the air delivery width

Table 1 shows that there is a large gap between the first group and the second group at the fan speed range of 490 r/min. The reason is that the natural wind force interferes with the wind force measurement resulting in the wind turbine wind force measurement process. At fan speeds of 1,207 and 1,280 r/min, the measured fan speed range is relatively uniform. The measured values in Table 1 indicate that the air supply range of the sprayer can be set to 0.2 M. This is consistent with the wind grid size of 0.2 × 0.2 M set in this study.

Normality test of the residual of the wind measurement experimental data

Before the multiple regression analysis of the data, a residual normal analysis of the test data is required (Figure 7). The normal probability diagram of the residual is approximately a straight line, indicating that the data are randomly distributed, have good fitting to the random error, and can extract all the predictable data ranges.

Correlation analysis of the research factor interaction items

During the modeling process, in addition to the influencing factors of experimental research, data interaction is key to an accurate model. Table 2 shows a correlation analysis between the two factors of the overall canopy data under different fan speeds. According to Table 2, the correlation between the influencing factors under different fan speeds is generally less than 0.5, which shows that the above factors are independent of each other. During wind loss model research on the data, the interactions between the factors were not considered.

TABLE 1 The measurement range of the air delivery width of the sprayer.

Fan speed (r/min)	Measurement position from wind outlet (m)	Wind supply width (m)	
490	1	0.18	0.1
	1.5	0.32	0.09
	2	0.33	0.078
1,207	1	0.23	0.1
	1.5	0.4	0.1
	2	0.21	0.23
1,280	1	0.25	0.12
	1.5	0.2	0.13
	2	0.11	0.14

Research on wind loss models in canopies based on classic regression algorithms

Based on the canopy leaf area group data and LiDAR point cloud data group, a multiple regression model within the canopy was constructed by using the classic regression method, and the model was evaluated. The canopy inlet wind speed, canopy thickness, canopy leaf area, and canopy wind loss model under different wind conditions were calculated, and the canopy inlet wind speed, canopy thickness, LiDAR point cloud data, and canopy wind loss rate model were evaluated. Formulas 2–7 are the regression models of 1,381 r/min canopy leaf area, 1,381 r/min canopy LiDAR point cloud, 1,502 r/min canopy leaf area, 1,502 r/min canopy LiDAR point cloud, 1,676 r/min canopy leaf area and 1,676 r/min canopy LiDAR point cloud data set in turn:

$$SpeedLoss_{Canopy1} = 0.303 - 1.59 \times 10^{-2} x_1 + 0.403 x_2 - 1.4 \times 10^{-5} x_3 \quad (2)$$

$$SpeedLoss_{Canopy2} = 0.301 - 1.64 \times 10^{-2} x_1 + 0.401 x_2 - 3 \times 10^{-6} x_4 \quad (3)$$

$$SpeedLoss_{Canopy3} = 0.341 + 2.77 \times 10^{-2} x_5 + 0.284 x_2 - 2.4 \times 10^{-5} x_3 \quad (4)$$

$$SpeedLoss_{Canopy4} = 0.335 + 3.16 \times 10^{-2} x_5 + 0.286 x_2 - 1.8 \times 10^{-5} x_4 \quad (5)$$

$$SpeedLoss_{Canopy5} = 0.277 + 1.12 \times 10^{-2} x_6 + 0.283 x_2 - 9 \times 10^{-6} x_3 \quad (6)$$

$$SpeedLoss_{Canopy6} = 0.274 + 1.2 \times 10^{-2} x_6 + 0.285 x_2 - 6 \times 10^{-6} x_4 \quad (7)$$

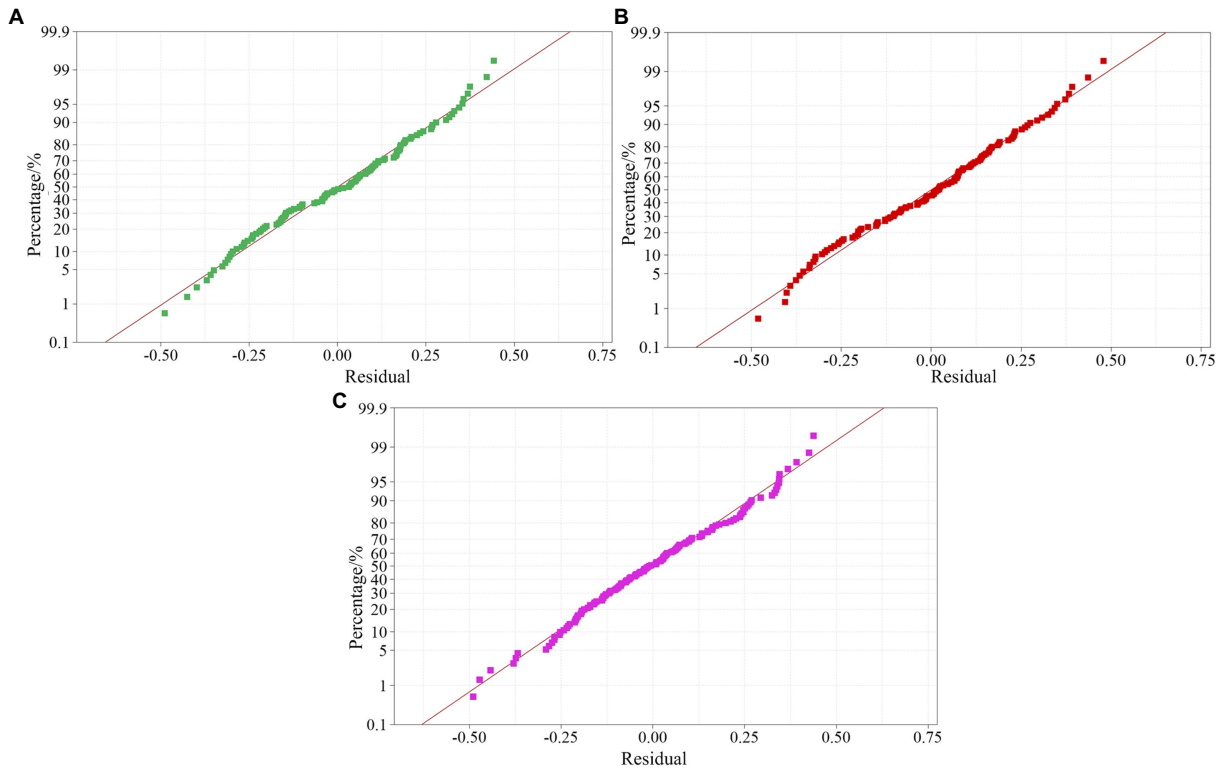

FIGURE 7
Normal distribution of residuals in the canopy leaf area data set at different sprayer fan speeds. **(A)** 1381 r/min data set. **(B)** 1502 r/min data set. **(C)** 1676 r/min data set.

TABLE 2 Correlation analysis of all data before and after the canopy at different speeds.

Fan speed (r/min)	Canopy thickness × inlet wind speed	Canopy thickness × leaf area	Inlet wind speed × leaf area	Canopy thickness × LiDAR point cloud data	Inlet wind speed × LiDAR point cloud data
1,381	0.487	0.416	0.374	0.498	0.490
1,502	0.351	0.400	0.352	0.475	0.541
1,676	0.226	0.412	0.238	0.487	0.404

where:

$SpeedLoss_{Canopy1}$—Wind loss rate based on canopy leaf area at 1381 r/min.

$SpeedLoss_{Canopy2}$—Wind loss rate based on the LiDAR point cloud of the canopy at 1381 r/min.

$SpeedLoss_{Canopy3}$—Wind loss rate based on canopy leaf area at 1502 r/min.

$SpeedLoss_{Canopy4}$—Wind loss rate based on the LiDAR point cloud of the canopy at 1502 r/min.

$SpeedLoss_{Canopy5}$—Wind loss rate based on canopy leaf area at 1676 r/min.

$SpeedLoss_{Canopy6}$—Wind loss rate based on the LiDAR point cloud of the canopy at 1676 r/min.

x_1—wind speed at canopy inlet at 1381 r/min, m/s.

x_2—canopy thickness, m.

x_3—canopy leaf area, cm^2.

x_4—LiDAR point cloud data of canopy, PCs.

x_5—1,502 r/min, wind speed at canopy inlet, m/s.

x_6—1,676 r/min, wind speed at canopy inlet, m/s.

Table 3 shows the R^2 of the above regression model (Formulas 3–8), and it is clear that the R^2 range of the canopy regression model at different speeds is 45–60.4%. The difference between the leaf area and LiDAR point cloud data group in the regression model R^2 is small, which can be ignored in the range of 0 ~ 0.2%, indicating that the leaf area data and LiDAR point cloud data have the same impact on the wind loss model, and they have a strong correlation. Consistent with the research results of Sanz-Cortiella et al. (2011); Zhang et al. (2017) and Gu et al. (2021a) on the relationship between LiDAR point cloud data and canopy leaf

area, when calculating the canopy wind loss model, the leaf area data and LiDAR point cloud data are selected to build the wind loss model. Because LiDAR point cloud data are easier to obtain than the leaf areas of different canopy areas, LiDAR point cloud data are used to replace the canopy leaf area data.

Table 4 analyses the significance of various test factors on the regression process of the model. In the variance calculation process, the *p* value distribution of LiDAR point cloud data and canopy leaf area in the model is 0.281–0.851, which are both greater than 0.1 and indicate that these two factors have no significant impact on the model. Based on previous research on the distribution of wind fields in a canopy (Hong et al., 2017), it is concluded that density is the main factor affecting the distribution of wind fields in a canopy because the research object is modern orchards, which are characterized by thin canopies and dense leaf distributions. The orchard trees selected in this study are traditional thick canopy orchard trees, and the leaves in the canopy are unevenly distributed, which has little impact on the wind loss under the action of wind. Through the above analysis, the canopy leaf area and LiDAR point cloud data are removed, and the wind loss model of canopy inlet wind speed and overall canopy thickness is further studied. The model of the wind loss rate in the canopy under different rotating speeds of 1,381, 1,502, and 1,676 r/min (Formulas 8–10) are calculated.

$$SpeedLoss_{Canopy7} = 0.3 - 1.74 \times 10^{-2} x_1 + 0.4 x_2 \quad (8)$$

$$SpeedLoss_{Canopy8} = 0.335 + 2.53 \times 10^{-2} x_5 + 0.278 x_2 \quad (9)$$

TABLE 3 R^2 values of the regression models under different spray fan speeds.

Project	1,381 r/min		1,502 r/min		1,676 r/min	
	Leaf area	LiDAR	Leaf area	LiDAR	Leaf area	LiDAR
Model	2	3	4	5	6	7
R^2	60.4%	60.3%	51.2%	51.4%	45%	45%

TABLE 4 Significance of the factors of the regression models of the canopy wind loss model under different spray fan speeds.

Fan speed r/min	Model	Significance			
		Inlet wind speed	Canopy thick	Leaf area	LiDAR
1,381	2	0.22	0.000	0.604	
	3	0.231	0.000		0.851
1,502	4	0.022	0.000	0.351	
	5	0.017	0.000		0.281
1,676	6	0.267	0.000	0.726	
	7	0.260	0.000		0.721

$$SpeedLoss_{Canopy9} = 0.274 + 1.07 \times 10^{-2} x_6 + 0.281 x_2 \quad (10)$$

where:

$SpeedLoss_{Canopy7}$—Wind loss rate based on canopy thickness at 1381 r/min.

$SpeedLoss_{Canopy8}$—Wind loss rate based on canopy thickness at 1502 r/min.

$SpeedLoss_{Canopy9}$—Wind loss rate based on canopy thickness at 1676 r/min.

The R^2 values of the obtained model are 60.3, 50.6 and 44.9% at 1381 r/min, 1,502 r/min and 1,676 r/min, respectively. Through the study of different canopy wind loss models, it is concluded that the canopy inlet wind speed and canopy thickness are the main influencing factors of wind loss, among which the canopy thickness is more significant. Hong et al. (2017) also demonstrated that canopy thickness is the main factor affecting the distribution of wind in a canopy.

Through the above analysis, it is concluded that the accuracy of the regression model gradually decreases with increasing fan speed because with increasing fan speed, the wind speed at the entrance of the canopy increases, and after the wind enters the canopy, it is affected by factors such as the density and direction of branches in the canopy, resulting in a decline in the fitting effect of the wind loss model. This is consistent with the research results of Khot et al. (2012), who found that 70% wind assistance achieves a better result than 100% wind assistance.

Research on the wind loss model in a canopy based on the PLSR algorithm

Through classic multiple regression analysis, it is concluded that the correlation coefficient R^2 of the regression model is small, and the interpretation ability of the prediction data is weak. To obtain a better wind loss model based on multiple regression, the PLSR algorithm is used to study the canopy wind loss model based on canopy inlet wind speed and canopy thickness. Formulas 11–13 are the wind loss models obtained under the conditions of fan speeds of 1,381, 1,502, and 1,676 r/min, respectively.

$$SpeedLoss_{Canopy10} = 0.282 - 1.22 \times 10^{-2} x_1 + 0.391 x_2 \quad (11)$$

$$SpeedLoss_{Canopy11} = 0.213 + 3.39 \times 10^{-2} x_5 + 0.319 x_2 \quad (12)$$

$$SpeedLoss_{Canopy12} = 0.22 + 1.03 \times 10^{-2} x_6 + 0.321 x_2 \quad (13)$$

where,

$SpeedLoss_{Canopy10}$—Wind loss rate based on PLSR at 1381 r/min.

$SpeedLoss_{Canopy11}$—Wind loss rate based on PLSR at 1502 r/min.

$SpeedLoss_{Canopy12}$—Wind loss rate based on PLSR at 1676 r/min.

Table 5 shows that the fitting accuracy of the model obtained by PLSR is higher than that of the multiple regression model by 2.1, 14.7, and 12%. With the increase in the fan speed, the obtained canopy wind loss model R^2 gradually decreases. As the fan speed increases, the wind speed at the canopy inlet gradually increases, but as the fan outlet of the sprayer remains unchanged, the increase in the wind speed at the canopy inlet does not increase synchronously with the fan speed. The wind loss rate obtained through the wind inlet and the canopy wind outlet fluctuates greatly, resulting in the fitting effect of the model not increasing with increasing speed. At the same time, it is concluded that the prediction of the model for the verification set is weak, and the prediction ability gradually decreases with increasing speed. The reason for this phenomenon is that the wind loss rate gradually increases with the fluctuation of fan speed, and the extraction of verified data sets has a great impact on the verification results. The root mean square error of the data is less than 0.3, indicating a good degree of data concentration.

Study of the wind loss model in the canopy based on the BP neural network

The fitting accuracy of the regression model obtained by the PLSR algorithm is significantly higher than that of the multiple regression model, but the fitting accuracy of the model is still low, at less than 0.7, which cannot predict the canopy wind loss well. The BP neural network can use the error after output to evaluate the leading error of the output layer, update the error of the previous layer, and gradually calculate the errors of other layers to obtain a more accurate regression model calculation of the data. A BP neural network is used to train the wind loss model of the data group at different speeds through the test data group, and the prediction ability of the model to the data is obtained through analysis.

TABLE 5 R^2 and RMSE of the airflow speed loss rate model under different fan speeds.

Fan speed r/min	Model R^2	Model RMSE	Validation set R^2	Validation set RMSE
1,381	62.4%	0.262	52.8%	0.164
1,502	65.3%	0.216	33.5%	0.216
1,676	56.9%	0.234	10.8%	0.188

N-fold crossover divides the data set for many times, and averages the results of multiple evaluations, so as to eliminate the adverse effects caused by unbalanced data division in a single division. The model with the best generalization ability can be selected from a variety of models. It can effectively solve the over fitting of data, avoid the limitations and particularity of fixed divided data sets, and have more obvious advantages in small-scale data sets. In the study, 3-fold cross validation and 5-fold cross validation were selected according to the number of data sets (77 sets). The BP neural network-n-fold cross validation method is adopted, and the training sets and test sets with different ratios are used for multiple tests, and the results are averaged.

Under the conditions of different fan speeds of 1,381, 1,502 and 1,676 r/min, the R^2 of wind loss model of the BP neural network-3-fold cross validation is 76.55, 63.53 and 60.22%. The R^2 of the BP neural network-5-fold cross validation is 81.78, 72.85 and 69.20%. The models of BP neural network-5-fold cross validation were better than the BP neural network-3-fold cross validation. The accuracy of both the models is higher than that of the model obtained by the PLSR algorithm. The BP neural network-5-fold cross validation are used for the wind loss model. Figure 8 shows the relationship of BP neural network-5-fold cross validation between the predicted value and measured value of wind loss through the trained BP neural network model.

The equation of the two fitting formulas is shown in Formulas 14–16:

$$Y_1 = 0.93T_1 \tag{14}$$

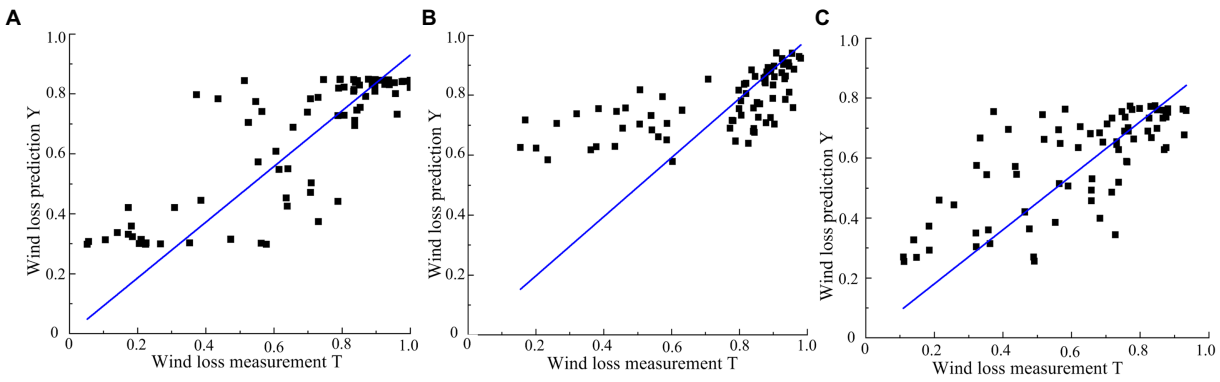

FIGURE 8
BP neural network training model measurement accuracy based on different conditions. (A) 1381 r/min. (B) 1502 r/min. (C) 1671 r/min.

$$Y_2 = 0.99T_2 \quad (15)$$

$$Y_3 = 0.90T_3 \quad (16)$$

where,

Y_1—Prediction value of the wind loss rate of the BP neural network model at 1381 r/min.

Y_2—Prediction value of the wind loss rate of the BP neural network model at 1502 r/min.

Y_3—Prediction value of the wind loss rate of the BP neural network model at 1676 r/min.

T_1—Measured value of wind loss at 1381 r/min.

T_2—Measured value of wind loss at 1502 r/min.

T_3—Measured value of wind loss at 1676 r/min.

The R^2 of the formulas of 1,381, 1,502 and 1,676 r/min is 95.13, 94.74, and 94.25%. The root mean square error is 0.15, 0.18, and 0.15. The standard error is 0.02, 0.03, and 0.03. The smaller the root mean square error and standard error, the models more stable. According to the metrics above, the BP neural network model can better fit the data.

Discussion

In this study, the classic regression algorithm, PLSR algorithm, and BP neural network algorithm are used to obtain a wind loss model. The BP neural network model has the highest accuracy, and the classic regression model has the lowest accuracy.

The process of obtaining functional equations through classic regression depends on the selection of equation types. Whether the selection of equation types is appropriate has a great impact on the accuracy of the model. In the process of data regression using classic regression and the PLSR algorithm, the obtained regression equation is more intuitive. The calculation processes of PLSR and classic regression models are highly dependent on the mathematical knowledge of operators. For functional equations with low regression accuracy, it is necessary to carry out stepwise regression. In the BP neural network training process, to obtain a better model and accuracy, it is necessary to set reasonable parameters and approach the objective function through multiple regression training (Lu, 2014). This algorithm cannot directly calculate the regression equation, and it needs a program to calculate the obtained model by importing software (Xin et al., 2002). The BP neural network cannot directly reflect the relationship between the input and output data but can only draw the relationship model of the input and output by tracing points. The BP neural network can be used for the regression of complex models, especially when the relationship of variables in the model cannot be determined. Through the above analysis, it is concluded that the BP neural network regression algorithm is better than the PLSR algorithm and classic regression algorithm. Because the wind loss model obtained by the BP neural network algorithm is not intuitive, PLSR has the advantages of an intuitive and simple model in the three algorithms, which may cause some wind delivery errors in the spraying process. In the process of variable spraying selection, the wind loss model based on a BP neural network or PLSR can be selected according to the required spraying accuracy and spraying error range.

This research shows that there is a correlation between the inner leaf area of the canopy and LiDAR point cloud data, which is consistent with the research results of Sanz-Cortiella et al. (2011); Sanz et al. (2013) and Zhang et al. (2017). However, because these two factors have no significant impact on wind loss, the obtained wind loss model does not present leaf area and LiDAR point cloud data as independent variables in the model. On the one hand, the canopy leaves of orchard trees are not concentrated in the direction of canopy thickness, which has little impact on wind loss; on the other hand, the wind from the sprayer is strong, and the leaves in the canopy have little impact on its loss.

There are many factors affecting the loss of wind power in and out of the canopy. In addition to the thickness of the canopy and the number of leaves in the canopy, the loss is also affected by the growth direction of the branches in the canopy, the leaf inclination of the leaves, and the distribution form of the leaves in the canopy. Measurement methods are also important factors affecting the loss of wind power. In this study, an anemometer is used for multipoint measurement, and the measurement results are more accurate. However, there are shortcomings of low measurement efficiency, and wind measurements in the same measurement area are not obtained at the same time. In future research, multiple anemometers can be used to measure at the same time to reduce the impact caused by anemometer measurements during the testing process.

Conclusion

In the process of variable wind spraying, the appropriate wind force is determined in real time according to parameters such as canopy size and biomass in the canopy of orchard trees so that the droplets can penetrate the surface of the canopy and deposit into the interior of the canopy for the effective prevention and control of diseases and pests. The influencing factors and models of the wind loss rate in the canopy under different sprayer fan speeds are studied. Through classic regression analysis, the PLSR algorithm, and the BP neural network regression algorithm for data processing and model establishment, the following conclusions are drawn:

Classic regression analysis was used to conduct multiple regression analysis on the relevant factors that were assumed to affect the wind loss rate in the canopy. Under the conditions of different fan speeds of 1,381, 1,502, and 1,676 r/min, the R^2 values of the obtained model are 0.603, 0.506, and 0.449, respectively. With increasing fan speed, the R^2 of the obtained canopy wind loss model gradually decreases. The wind force at the entrance of the canopy and the travel of air flow in the canopy are the main

factors affecting the wind loss rate. Due to the uneven distribution of leaves in the canopy of orchard trees, the influence of the inner leaf area of the canopy and LiDAR point cloud data on the wind loss rate was not significant and was not studied as an influencing factor. However, it was shown that there was a correlation between the inner leaf area of the canopy and LiDAR point cloud data.

Using the PLSR algorithm and BP neural network algorithm to study the regression model of canopy wind loss can further improve the accuracy of the model. Under the above fan speed conditions, the R^2 values obtained by the PLSR algorithm are 0.624, 0.653, and 0.569, which are 0.021, 0.147, and 0.120 higher than those of the multiple regression algorithm, respectively. Compared with the above two methods, the BP neural network regression algorithm can significantly improve the fitting accuracy of the model. Under different fan speeds, the determination coefficients R^2 of the model are 0.783, 0.679, and 0.715, which are 0.18, 0.173, and 0.266 higher than those of the multiple regression analysis.

In this study, combined with the canopy volume and canopy leaf area model, a wind loss rate model under different algorithm conditions is proposed, which provides a reference for the wind control of a sprayer.

Data availability statement

The raw data supporting the conclusions of this article will be made available by the authors, without undue reservation.

Author contributions

CG and CZ: conceptualization, validation, investigation, and methodology. CG: software and visualization. CG, LC, and WZ: formal analysis. CG, CZ, and WZ: data curation. WZ and CZ: resources and supervision. CG and WZ: writing—original draft preparation. CG, CZ, LC, WZ, and XW writing—review and editing and funding acquisition. CZ: project administration. All authors contributed to the article and approved the submitted version.

Funding

This work was financially supported by the Beijing Rural Revitalization Project (grant number: 2022), the National Key Research and Development Plan Project, Robotic Systems for Agriculture (RS-Agri) (grant number: 2019YFE0125200), the Outstanding Scientist Program of Beijing Academy of Agriculture and Forestry Sciences (grant number: jkzx202212), and the Natural Science Foundation of China (grant number: NSFC31971775).

Conflict of interest

The authors declare that the research was conducted in the absence of any commercial or financial relationships that could be construed as a potential conflict of interest.

Publisher's note

All claims expressed in this article are solely those of the authors and do not necessarily represent those of their affiliated organizations, or those of the publisher, the editors and the reviewers. Any product that may be evaluated in this article, or claim that may be made by its manufacturer, is not guaranteed or endorsed by the publisher.

Supplementary material

The Supplementary material for this article can be found online at: https://www.frontiersin.org/articles/10.3389/fpls.2022.1010540/full#supplementary-material

References

Abbas, I., Liu, J. Z., Faheem, M., Noor, R. S., Shaikh, S. A., Solangi, K. A., et al. (2020). Different sensor based intelligent spraying systems in agriculture. *Sens. Actuator A Phys.* 316:112265. doi: 10.1016/j.sna.2020.112265

Al-Jumaili, A., and Salyani, M. (2014). Variation in deposition of an air-assisted sprayer in open field due to wind conditions. *Trans. ASABE* 57, 1297–1305. doi: 10.13031/trans.57.10633

Bleiholder, H., Frau, E., Lancashire, P. D., Feller, C., Buhr, F. L., Hess, M., et al. (2001). *Growth stages of mono-and dicotyledonous plants—BBCH monograph* Uwe Meier Federal Biological Research Centre for Agriculture and Forestry. 52–54.

Chen, J. Z., Song, S. R., Sun, D. Z., Hong, T. S., and Zhang, L. (2017). Test on airflow field and spray characteristics for long-range air-blast sprayer. *Transact. CSAE* 33, 72–79. doi: 10.11975/j.issn.1002-6819.2017.24.010

Colaço, A. F., Molin, J. P., Rosell-Polo, J. R., and Escola, A. (2018). Application of light detection and ranging and ultrasonic sensors to high-throughput phenotyping and precision horticulture: current status and challenges. *Horticulture Res.* 5:35. doi: 10.1038/s41438-018-0043-0

Dai, F. F. (2008). Selection and calculation of the blowing rate of air-assisted sprayers. *Plant Prot.* 34, 124–127.

Dekeyser, D., Duga, A. T., Verboven, P., Endalew, A. M., Hendrickx, N., and Nuyttens, D. (2013). Assessment of orchard sprayers using laboratory experiments and computational fluid dynamics modelling. *Biosyst. Eng.* 114, 157–169. doi: 10.1016/j.biosystemseng.2012.11.013

Duga, A. T., Dekeyser, D., Ruysen, K., Bylemans, D., Nuyttens, D., Nicolai, B. M., et al. (2015a). Numerical analysis of the effects of wind and sprayer type on spray distribution in different orchard training system. *Boundary-layer Mrteorol* 157, 517–535. doi: 10.1007/s10546-015-0064-2

Duga, A. T., Ruysen, K., Dekeyser, D., Nuyttens, D., Bylemans, D., Nicolai, B. M., et al. (2015b). "CFD based analysis of the effect of wind in orchard spraying," in *Frutic Italy 2015: 9th nut and vegetable production engineering symposium*. eds. R. Guidetti, L. Bodria and S. Best (Milano: Aidic Servizi Srl), 289–294.

Eugen, M., Mihai, M., Mihaela, N., and Gabriel, G., (2017). Experimental researches regarding assessment of coverage degree obtained by orchard spraying machine[C]//Adamchuk Valeriy. *16th International Scientific*

Conference: Engineering for Rural Development, 1239–1243. doi: 10.22616/ERDev2017.16.N271

Gao, Z. Q., Li, J., and Ding, G. L. (2015). Discussion on the main characteristics of open center apple trees and the reasons of high quality and high yield. *Fruit Grow. Friend* 5, 39–41.

Gu, J. B., Ding, W. M., Qiu, W., and Sun, C. D. (2014). Current research situation and development trend of equipment and technology for orchard spraying. *J. Fruit Sci.* 31, 1154–1157. doi: 10.13925/j.cnki.gsxb.20130500

Gu, C. C., Wang, X., Wang, X. L., Yang, F. Z., and Zhai, C. Y. (2020). RESEARCH PROGRESS ON VARIABLE-RATE SPRAYING TECHNOLOGY IN ORCHARDS. *Applied R Engineer. Agricul.* 36, 927–942. doi: 10.13031/aea.14201

Gu, C. C., Zhai, C. Y., Chen, L. P., Li, Q., Hu, L. N., and Yang, F. Z. (2021a). Detection model of tree canopy leaf area based on LiDAR technology. *Transact. Chinese Soc. Agricul.l Machin.* 52, 137–145. doi: 10.6041/j.issn.1000-1298.2021.11.030

Gu, C. C., Zhai, C. Y., Wang, X., and Wang, S. L. (2021b). CMPC: an innovative Lidar-based method to estimate tree canopy meshing-profile volumes for orchard target-oriented spray. *Sensors* 21:4252. doi: 10.3390/s21124252

Gu, C. C., Zhao, C. J., Zou, W., Yang, S., Dou, H. J., and Zhai, C. Y. (2022). Innovative leaf area detection models for orchard tree thick canopy based on LiDAR point cloud data. *Agriculture* 12:1241. doi: 10.3390/agriculture12081241

Hong, S. W., Zhao, L., and Zhu, H. (2017). CFD simulation of airflow inside tree canopies discharged from air-assisted sprayers. *Comput. Electron. Agr.* 149, 121–132. doi: 10.1016/j.compag.2017.07.011

Khot, L. R., Ehsani, R., Albrigo, G., Larbi, P. A., Landers, A., Campoy, J., et al. (2012). Air-assisted sprayer adapted for precision horticulture: spray patterns and deposition assessments in small-sized citrus canopies. *Biosyst. Eng.* 113, 76–85. doi: 10.1016/j.biosystemseng.2012.06.008

Li, L. L., He, X. K., Song, J. L., Wang, X. N., Jia, X. M., and Liu, C. H. (2017). Design and experiment of automatic profiling orchard sprayer based on variable air volume and flow rate. *Transac. CSAE* 33, 70–76. doi: 10.11975/j.issn.1002-6819.2017.01.009

Lu, W. Y. (2014). Comparative study on modeling accuracy between BP neural network and regression analysis. *J. Qiqihar Institute Techn.* 8, 68–72.

Manandhar, A., Zhu, H. P., Ozkan, E., and Shah, A. (2020). Techno-economic impacts of using a laser-guided variable-rate spraying system to retrofit conventional constant-rate sprayers. *Precis. Agric.* 21, 1156–1171. doi: 10.1007/s11119-020-09712-8

Nuyttens, D., Zwertuaegher, I. K. A., and Dekeyser, D. (2017). Spray drift assessment of different application techniques using a drift test bench and comparison with other assessment methods. *Biosyst. Eng.* 154, 14–24. doi: 10.1016/j.biosystemseng.2016.09.013

Sanz, R., Rosell, J. R., Llorens, J., Gil, E., and Planas, S. (2013). Relationship between tree row LiDAR-volume and leaf area density for fruit orchards and vineyards obtained with a LiDAR 3D dynamic measurement system. *Agric. For. Meteorol.* 171, 153–162. doi: 10.1016/j.agrformet.2012.11.013

Sanz-Cortiella, R., Llorens-Calveras, J., Escola, A., Arno-Satorra, J., Ribes-Dasi, M., Masip-Vilalta, J., et al. (2011). Innovative LiDAR 3D dynamic measurement system to estimate fruit-tree leaf area. *Sensors* 11, 5769–5791. doi: 10.3390/s110605769

Song, S. R., Chen, J. Z., Hong, T. S., Xue, X. Y., Xia, H. B., and Song, Y. (2017). Variation of droplet diameter in wind field for long-range air-assisted sprayer. *Transac. CSAE* 33, 59–66. doi: 10.11975/j.issn.1002-6819.2017.06.008

Song, L. P., Huang, J. P., Liang, X. W., Yang, S. X., and Tang, D. D. (2020). An intelligent multi-sensor variable spray system with chaotic optimization and adaptive fuzzy control. *Sensors* 20, 2954–2977. doi: 10.3390/s20102954

Xin, D. Y., Wang, C. Y., and Xiao, F. (2002). A study on the BP neural network applied to regression analysis. *J. Xi'an institute Techn.* 22, 129–135. doi: 10.3969/j.issn.1673-9965.2002.02.008

Zhai, C. Y., Zhao, C. J., Wang, N., Long, J., Wang, X., Weckler, P., et al. (2018). Research progress on precision control methods of air-assisted spraying in orchards. *Trans. CSAE* 34, 1–15. doi: 10.11975/j.issn.1002-6819.2018.10.001

Zhang, M. N., Lv, X. L., Qiu, W., Lei, X. H., Yang, Q. S., and Zhang, D. X. (2017). Calculation method of leaf area density based on three-dimensional laser point cloud. *Trans. CSAM* 48, 172–178. doi: 10.6041/j.issn.1000-1298.2013.08.038

Zhou, L. F., Xue, X. Y., Zhou, L. X., Zhang, L., Ding, S. M., Chang, C., et al. (2017). Research situation and progress analysis on orchard variable rate spraying technology. *Transac. CSAE* 33, 80–92. doi: 10.11975/j.issn.1002-6819.2017.23.011

frontiers | Frontiers in Plant Science

TYPE Original Research
PUBLISHED 29 September 2022
DOI 10.3389/fpls.2022.981494

OPEN ACCESS

EDITED BY
Wei Qiu,
Nanjing Agricultural University, China

REVIEWED BY
Fiaz Ahmad,
Bahauddin Zakariya University, Pakistan
Jianli Song,
China Agricultural University, China

*CORRESPONDENCE
Ping Han
hanp@brcast.org.cn
Ruirui Zhang
zhangrr@nercita.org.cn

SPECIALTY SECTION
This article was submitted to Sustainable and Intelligent Phytoprotection, a section of the journal Frontiers in Plant Science

RECEIVED 29 June 2022
ACCEPTED 19 August 2022
PUBLISHED 29 September 2022

CITATION
Li L, Hu Z, Liu Q, Yi T, Han P, Zhang R and Pan L (2022) Effect of flight velocity on droplet deposition and drift of combined pesticides sprayed using an unmanned aerial vehicle sprayer in a peach orchard.
Front. Plant Sci. 13:981494.
doi: 10.3389/fpls.2022.981494

Effect of flight velocity on droplet deposition and drift of combined pesticides sprayed using an unmanned aerial vehicle sprayer in a peach orchard

Longlong Li[1,3,4], Zhihong Hu[1,2], Qingju Liu[1,2], Tongchuan Yi[1,3,4], Ping Han[1,2]*, Ruirui Zhang[1,3,4]* and Ligang Pan[1,2]

[1]Beijing Academy of Agriculture and Forestry Sciences, Beijing, China, [2]Institute of Quality Standard and Testing Technology of Beijing Academy of Agriculture and Forestry Sciences, Beijing, China, [3]Research Center of Intelligent Equipment, Beijing Academy of Agricultural and Forestry Sciences, Beijing, China, [4]National Research Center of Intelligent Equipment for Agriculture, Beijing, China

Extensive research has been conducted on plant protection unmanned aerial vehicle (UAV) chemical application technology in recent years owing to its importance as a means of pest and disease control. UAV spraying in orchards faces the drawback of drift risk and can be hazardous to non-targeted crops, humans, and the environment. A detailed and systematic analysis must be performed to determine the uniformity and drift risk of plant UAV sprays. In this study, a peach orchard is sprayed with a plant-protection UAV at three different flight velocities and we evaluate the combined pesticide deposition performance of the canopy, ground loss, downwind ground drift, and airborne drift. Additionally, the droplet size and coverage rate in the canopy are calculated by using water-sensitive paper. The results demonstrate that there is significant difference in the droplet size at flight velocities of 1–3 m/s. The droplet size in the lower canopy is slightly smaller than those in the middle and upper parts. Increasing the flight velocity helps the pesticide droplets to spread and penetrate the canopy. However, it also causes a non-uniform pesticide deposition, reduced effective coverage ratio and effective density ratio. Among the three pesticides used in the experiment, imidacloprid exhibits the best deposition efficiency. The deposition amount and normalized deposition amount in the canopy were the highest at a flight velocity of 2 m/s, accompanied by a lower ground loss under the canopy. The highest near-field ground drift is observed at a velocity of 1 m/s, and the far-field airborne drift is highest at 3 m/s. Lastly, this study provides a reference for the commercial application of plant-protection UAVs.

KEYWORDS

unmanned aerial vehicle (UAV), spray deposition, spray drift, combined pesticides, canopy, peach orchard

Introduction

Diseases and pests are the primary factors affecting crop production, which includes the yield and quality of grain (Godfray et al., 2010). Statistical data confirm that diseases, pests, and weeds account for 30% of the global crop losses each year (Guo et al., 2019). Therefore, active measures must be taken to reduce the impact of diseases and pests. Currently, the most widely used method for the prevention and control of diseases and pests involves spraying chemical pesticides on crops (Chen et al., 2021; Sparks and Bryant, 2021; Zhang Y.L. et al., 2021). Various methods have been developed to improve the spraying efficiency and control the effect of pesticides, such as ground spraying, aerial spraying, air-assisted spraying, and knapsack spraying (Qin et al., 2016; Pan et al., 2017; Wang et al., 2019b).

Extensive research has been conducted on plant-protection unmanned aerial vehicles (UAVs) in East Asia, China, and other regions in recent years (Li et al., 2019; Chen et al., 2021). In China, plant protection UAVs have been widely implemented for field crops, fruit trees, tea trees, cotton, and several other crops. This method significantly improves the operational efficiency, and reduces the labor and exposure to pesticides when compared to traditional knapsack spraying methods. Additionally, plant protection UAVs can overcome the limitations of traditional ground spraying equipment and can also realize free pesticide application operations in hills, mountains, and paddy fields. Furthermore, the downwash airflow generated by the rotors can overturn the leaves and promote the penetration and attachment of fine droplets inside the canopy (Meng et al., 2019). These advantages have led to the increased application of plant-protection UAVs.

Droplet deposition and spray drift characteristics are important indicators for the evaluation of plant protection equipment. Extensive research has been conducted on the factors affecting droplet deposition in UAV spraying, such as droplet size (Chen et al., 2020), flight velocity (Meng et al., 2020; Zhang S.C. et al., 2021), flight height (Zhang S.C. et al., 2021), tree shape (Pan et al., 2017; Tang et al., 2018; Meng et al., 2020), wind field (Chen et al., 2017), spray volume (Wang et al., 2019a; Li et al., 2021b), aerial spray adjuvants (Meng et al., 2018), UAV type (Wang et al., 2017, 2021), and nozzle type (Wang et al., 2021). In terms of crop types, the existing studies are primarily focused on field crops. The effects of UAV parameters on droplet deposition in wheat (Lou et al., 2018; Shan et al., 2021), cotton (Qin et al., 2018), and rice (Chen et al., 2020), corns (Zheng et al., 2017) were analyzed extensively. The canopy of fruit trees is three-dimensional and the density of branches and leaves is higher when compared to field crops. Overcoming these limitations and improving the droplet deposition uniformity in the canopy is an important research objective for plant-protection UAVs. Chen et al. (2017) and Tang et al. (2018) analyzed the effects of flight velocity, height, and application rate on droplet deposition and distribution in citrus canopies.

The existing studies on spray tests in orchards with UAV sprayers primarily use tracers to simulate pesticides. The droplet deposition on the target and the spread of the tracer solution may not concur with the results of actual pesticide spraying due to the aerosol characteristics. Additionally, a compound pesticide spraying mode is generally adopted during actual application to avoid various diseases and pests, which increases the uncertainty of deposition.

Peach (Prunus persica) is one of the most popular fruits worldwide and presents several health benefits. Peach trees are particularly vulnerable to pests and diseases (e.g., *Myzus persicae*, *Cercospora circumscissa* Sacc.) at different growth stages (Li et al., 2018; Samad et al., 2019). The spraying of pesticides and fungicides can ensure the quality and yield of peaches. In addition to the advantages of UAV spraying techniques mentioned above, the UAV spraying of chemical pesticides can overcome the drawback of a lack of row spacing for Y-shaped peach trees. However, the research on the canopy deposition of pesticides sprayed by plant-protection UAVs remains limited. Therefore, a detailed and systematic analysis of the spray deposition and drift from a UAV sprayer in a peach orchard is crucial.

In this study, spraying tests were conducted in a peach orchard to obtain a better understanding of the canopy deposition and droplet drift characteristics of plant-protection UAV spraying methods. The spray solutions were prepared by using three commonly applied pesticides. The effects of flight velocity on the canopy deposition and drift were analyzed. The deposition distribution characteristics of insecticides and fungicides in the canopy were also analyzed using ultra-high-performance liquid chromatography-tandem triple quadrupole mass spectrometry. This study can provide data support for the selection and optimization of the pesticide application parameters for fruit trees using plant-protection UAVs.

Materials and methods

Experimental plots

The experiments were carried out commercial peach orchard at growth stage BBCH 91 "Shoot growth completed; foliage still fully green" (Meier et al., 1994) located at Dahuashan Town, Pinggu District, Beijing, China. The main peach variety of the orchard is Okubo. The trees were planted at a density of 1,000 trees/ha with a canopy height of 3.5 m, row spacing of 5 m, and between-tree spacing of 2 m.

Plant protection unmanned aerial vehicle

A four-rotor electric plant protection UAV with a spray tank volume of 22 L was used in the experiment (3WYD-4-22A, Wuxi Hanhe Aviation Technology Co., Ltd.), as shown in Figure 1. This UAV is based on a three-blade propeller design which effectively reduces the vibration of the airframe during the spray operation and also improves the flight balance. Additionally, strong downwash airflow can be generated to promote the penetration of droplets into the canopy. A flat-fan nozzle is fixed under each rotor wing. The pesticide application operation mode includes both automatic and manual modes. In the automatic mode, the flight velocity, height, application rate, and route can be set beforehand, and the UAV can implement an autonomous spray operation. Thus, the flight errors caused by manual operation can be effectively avoided. Before conducting the experiment, the effective spray swath of the UAV was determined to be 4.0 m. Table 1 lists the technical parameters of the plant-protection UAV used in this experiment.

TABLE 1 Technical parameters of the plant protection UAV used in this study.

Classification	Parameters
Number of rotors	4
Number of nozzles	4
Nozzle type	Flat-fan, Lu120-015
Flow rate (in L/min)	0–7, adjustable
Tank capacity (in L)	22
Size (in m)	1.235 × 1.235 × 0.647
Rotor diameter (in mm)	838
Flight velocity (in m/s)	1.0–7.0
Effective spray swath (in m)	4
Flight duration (in min)	30
Operation efficiency (in ha/hour)	10–14
Positioning mode	GNSS + RTK
Operation method	Intelligent stability control
Weight (in kg)	23.5

Experimental design

The experiments were conducted in a field with an area of 150 m × 50 m; the plant protection UAV performed the spraying operations along tree rows with a spraying length of 50 m. The UAV performed one-and-a-half rounds of spraying in each test, covering three adjacent rows of fruit trees. The spray-treated area was 50 m × 15 m. The measurements comprised four parameters: droplet deposition in the canopy, ground loss, ground drift, and airborne drift. Water-sensitive paper (WSP, 26 mm × 76 mm, Syngenta Crop Protection AG, Basel, Switzerland) and a Mylar card (MCD, 85 mm × 54 mm, Wuxi Baike Electronic Materials Co., LTD., China) were selected as the droplet collectors. Figure 2 depicts the sample layout of the experimental area.

Canopy deposition

Three typical peach trees were selected as targets in the spray-tested area. The canopy of each peach tree was divided into three layers, i.e., upper, middle, and lower. Each canopy layer was divided into five azimuths based on the UVA flight direction: front, back, left, right, and center positions, corresponding to locations 1, 2, 3, 4, and 5 in Figure 2, respectively. There were 15 sampling points in the target tree. A WPS card was fixed on the leaf using a paper clip at each sampling point to ensure that the sensitive side of the WPS faced

FIGURE 1
Experimental site. **(A)** 3WYD-4-22A plant protection UAV; **(B)** spraying in peach orchard.

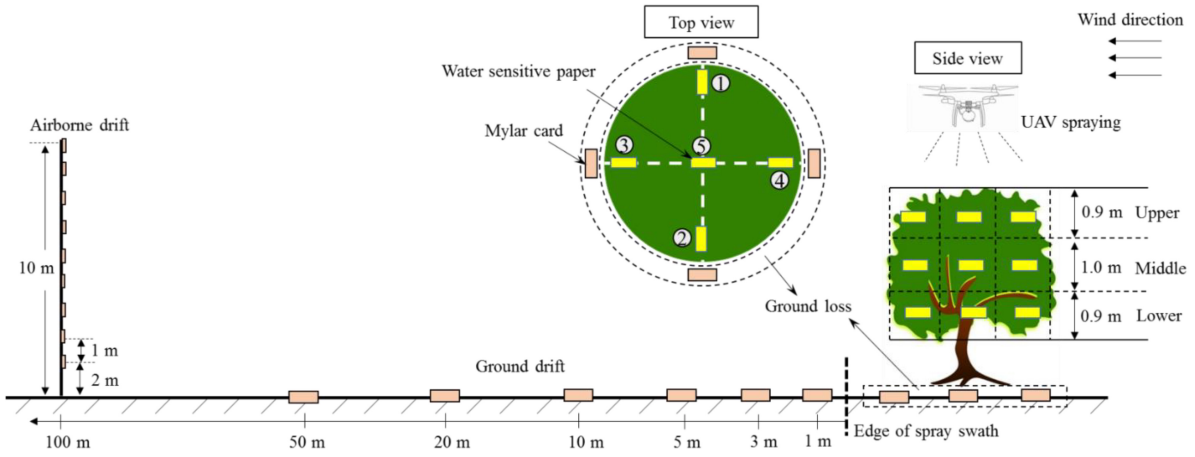

FIGURE 2
Schematic diagram of sample layout in the treated area.

upward, which was used to measure the droplet size, coverage, and density in the canopy. Five complete leaves were collected from each sampling point to determine the pesticide content on the leaf surface (mg/kg).

Ground loss

During the actual chemical applications, the pesticide droplets are not completely deposited in the canopy. Some of the droplets pass through the canopy and are deposited on the ground, causing soil pollution. Five MCDs were arranged on the ground under the three target peach trees to collect the pesticides lost on the ground. MCDs were placed in five directions under the canopy, similar to the arrangement of the WPS in each canopy layer.

Downwind ground drift

The plant-protection UAV adopts the aerial operation mode. The pesticide droplets easily form a downwind drift due to crosswinds, causing pesticide damage to adjacent sensitive crops, along with water pollution, fish and shrimp deaths, and other events. Five MCDs were arranged on the ground in the downwind direction at distances of 1, 3, 5, 10, 20, and 50 m from the edge of the spray swath to measure the drift mass at different distances.

Airborne drift

To further understand the drift potential of UAV spraying, a metal pole was fixed at a distance of 100 m from the edge of the treated area. Nine MCDs were successively fixed from bottom to top at intervals of 1 m at a height of 2–10 m from the ground. The card interface was perpendicular to the wind direction.

The flight velocity of the UAV sprayer was set to 1, 2, and 3 m/s, and the relative height between the UAV sprayer and the top of the canopy was set to 2 m. In this study, the application rate was set as 33 L/ha. Therefore, the nozzle flow rate at 1, 2, and 3 m/s were 0.79, 1.58, and 2.37 L/min, respectively. During the experiment, the mean temperature, mean humidity, and mean wind speed of the environment were 16.8°C, 46.3%, and 1.8 m/s, respectively.

After the spraying is completed, the droplets were allowed to dry on the target surface for 5 min, and all samples were carefully collected and stored in ziplock bags. A desiccant must be placed in the ziplock bag to collect the WPS to prevent them from being contaminated by moisture. The collected peach leaves and MCDs were stored in a small refrigerator for further analysis.

Reagents of combined pesticides

Combined pesticide were prepared by using three widely applied pesticides and fungicides: difenoconazole, azoxystrobin, and imidacloprid. Formulations containing 325 g L^{-1} suspension concentrate of difenoconazole-azoxystrobin (200 g L^{-1} for azoxystrobin and 125 g L^{-1} for difenoconazole) were obtained from Syngenta Nantong Crop Protection Co., Ltd. (Jiangsu, China). This formulation is widely employed to control and prevent peach anthracnose, peach brown spot shot holes, and other diseases. Formulations containing imidacloprid (25%, wettable powder) were obtained from Hebei Kaisite Agrochemical Co., Ltd. (Hebei, China). Imidacloprid wettable powder (WP) is used to control peach aphids, scale insects, and other common pests.

The three analytical standards used in the pesticide deposition detection stage were purchased from Beijing Mindleader Agroscience Co., Ltd. (Beijing, China), with purities of 98.0% for azoxystrobin, 95.0% for difenoconazole, and 97.0% for imidacloprid. Analytical grade NaCl and $MgSO_4$ were obtained from Sinopharm Chemical Reagent Co., Ltd.

(Shanghai, China). Methanol, acetonitrile, and ammonium acetate were purchased from Thermo Fisher Scientific (Waltham, MA, United States). The primary secondary amine (PSA) and graphitized carbon black (GCB) were provided by Shanghai Aladdin Biochemical Technology Co., Ltd. All the solvents used for measuring pesticide deposition were of the LC-MS grade.

Sample processing

The water-sensitive paper samples were scanned into digital grayscale images by using a TSN450 handheld scanner (Tiancai Electronics (Shenzhen) Co., Ltd.) with a resolution of 1200 × 1200, and the blue droplet spots on the WPS surface were analyzed by using the *i*DAS image processing software which was developed by the National Research Center of Intelligent Equipment for Agriculture (Xu et al., 2016). This software can be used to quickly calculate the spray deposition parameters, such as the droplet spectral distribution, coverage, and number of droplets. In this study, the droplet coverage rate (Cov), volume median diameter (VMD), diffusion ratio (RD), and droplet density (Dent) of droplets on a WPS were measured.

The pesticide deposition on the peach leaves was recorded in terms of the mass of active ingredient (a.i.) per leaf (mg a.i. per kg biomass). Pesticide recovery on mylar cards in the ground loss, ground drift, and airborne drift tests was of the mass of the active ingredient (a.i.) per unit area of the maylar card (μg a.i. per cm^2). Based on the application rate, the theoretical deposition of the three pesticides is determined to be 2.00 μg a.i. /cm^2 for azoxystrobin, 1.25 μg a.i. /cm^2 for difenoconazole, and 0.75 μg a.i. /cm^2 for imidacloprid. Ultra-high-performance liquid chromatography-tandem mass spectrometry (UPLC-MS/MS) was used to determine the deposition of the three pesticides from the leaves and droplet collection cards. The deposition amounts of the difenoconazole, azoxystrobin, and imidacloprid agents were represented by DEP_{Dif}, DEP_{Azo}, and DEP_{Imi}, respectively. The UPLC-MS/MS parameters of azoxystrobin, difenoconazole, and imidacloprid were determined before the measurement, and the calibration curves, R^2, LOD, LOQ, recoveries, and RSD of azoxystrobin, difenoconazole, and imidacloprid in the leaves were developed based on the analytical standards.

The uniformity of the droplet distribution is an important index of the pesticide application quality, which is described by the coefficient of variation (*CV*). The smaller the *CV* value, the more uniform the droplet distribution. The calculation formula is given as:

$$\mathrm{CV} = \frac{S}{\overline{X}} \times 100\% \; S = \sqrt{\frac{\sum_{i=1}^{n} \left(Xi - \overline{X}\right)^2}{n = 1}}$$

where *CV* denotes the coefficient of variation (%), S denotes the standard deviation of one group, *X* denotes the average deposition data for one group, *n* denotes the number of samplers, and X_i denotes the deposition from each sampling point.

The droplet size distribution is a parameter which directly reflects the distribution of droplets in the target. When applying pesticides, a relatively uniform droplet size deposit on the leaves achieves better coverage and control. Diffusion ratio, RD, was used to measure the spectral distribution quality of the droplet (Musiu et al., 2019). It represents the uniformity of the droplet size distribution on a WPS. In general, this value exhibits a positive correlation with the uniformity of the droplet size distribution; a larger RD indicates a more uniform droplet spectrum.

$$RD = \frac{NMD}{VMD}$$

Here, NMD, i.e., the number median diameter, denotes the droplet diameter below which the droplet diameter is 50% of the total number of drops (in μm). VMD, i.e., the volume median diameter, denotes the droplet diameter below which smaller droplets constitute 50% of the total volume (μ m).

Droplet deposition penetration in the tree canopy represents the diffusion ability. The penetration efficiency in the vertical direction of the canopy was calculated as follows:

$$PE_V = \frac{DEP_{Low}}{DEP_{Upp\&Mid}} \times 100\%$$

where PE_V denotes the vertical deposition penetration (in %), DEP_{Low} denotes the mean value of the amount of deposition in the lower canopy (mg/kg), and $DEP_{Upp\&Mid}$ denotes the mean value of the deposition amount collected in the upper and middle canopies (mg/kg).

The diffusion efficiency in the horizontal direction of the canopy was calculated as follows:

$$PE_H = \frac{DEP_{int}}{DEP_{ext}} \times 100\%$$

where PE_H denotes the deposition penetration in the horizontal direction (in %), DEP_{int} denotes the mean value of the amount of deposition in the interior zone (mg/kg), and DEP_{ext} denotes the mean value of the deposition in the exterior zone (mg/kg). Samples 1, 2, 3, and 4 at the periphery of the canopy were set as the exterior zones, and sample 5 was set as the interior zone. The deposition in the canopy improves when this value is closer to 1 (Chen et al., 2022).

The minimum droplet density and coverage rate required for canopy deposition in the traditional ground orchard air-assisted spray mode with an application rate of 500–7000 L/ha, are 30/cm^2 (Grella et al., 2022) and 10–15% (Deveau et al., 2021), respectively. However, ultra-low volume (ULV) or very low volume (VLV) applications are adopted for plant protection UAV sprays implemented in orchards with an application rate of 45–150 L/ha. The minimum droplet density threshold required for effective spray swath measurement of the plant protection

UAV is 15 deposits/cm^2 (MH/T 1002.1, 2016). Therefore, we selected the effective coverage ratio (ECR) and effective density ratio (EDR) as the two indicators, according to Wang et al. (2022), to evaluate the deposition performance of the plant-protection UAV. ECR represents the ratio of the sample number with a droplet coverage of more than 1% of the total samples, and EDR represents the ratio of the sample number with a droplet density of more than 15 deposits/cm^2 to the total samples.

The deposition efficiency of the three pesticides could not be compared owing to the difference in the contents of the active ingredients of the three pesticides in the spray tank. Therefore, the measured amount of sediment was normalized to obtain the normalized deposition amounts, $DEP_{Azo-nor}$, $DEPD_{if-nor}$, and $DEP_{Imi-nor}$ (mg·cm^2/kg·μg) based on the previously described content of the active ingredients of the three pesticides (2.00 μg a.i. /cm^2 for azoxystrobin, 1.25 μg a.i. /cm^2 for difenoconazole, and 0.75 μg a.i. /cm^2 for imidacloprid).

An ANOVA test was conducted to evaluate the droplet parameters and deposition data at different canopy locations and three flight velocity settings, at a significance level of 0.05. All the statistical analyses were performed using the IBM SPSS Statistics (Version 17.0) software for Windows.

Results

The effect of flight velocity on droplet size in the canopy

Figure 3 depicts the distribution of the droplet VMD for different combinations of velocity and canopy height. The size of the droplets gradually increases with an increase in the flight velocity from 1 to 3 m/s; this change can be observed by the naked eye, as shown in **Figure 4**. The blue color represents the distribution of the droplets. The flight velocity significantly affected the droplet size in the same canopy layer. For example, in the upper canopy, the corresponding droplet sizes at flight velocities of 1, 2, and 3 m/s were 302, 423, and 496 μm, respectively, and the droplet size at 3 m/s increased by 64.23% when compared to that at 1 m/s. This was mainly attributed to the downwash airflow generated by the UAV rotor. An increase in the flight velocity leads to the formation of wingtip vortices and other airflow structures. These flow structures drive the movement of fine droplets with the airflow, resulting in an increase in the number of larger droplets deposited on the canopy. The canopy height level does not significantly affect the droplet size. However, the lower canopy droplet size (VMD_{Low}) is slightly lower than the upper canopy droplet size (VMD_{Upp}) and the middle canopy droplet size (VMD_{Mid}), as expected. During the droplet deposition on the canopy, the branches and leaves on the upper layer block the large droplets, while the fine droplets easily pass through the pores of the branches and leaves and settle into the canopy. Particularly, smaller droplets may be required to ensure an effective deposition of pesticides in a canopy with high crown density. For UAVs, the downwash airflow may promote the penetration of droplets into the interior of the canopy. On the one hand, the downwash airflow causes disturbance to the canopy, breaking the original branch and leaf distribution structure, and the porosity of the canopy becomes larger; On the other hand, the downwash airflow increases the movement velocity of the droplets and enhances the kinetic energy of the droplets transported to the canopy.

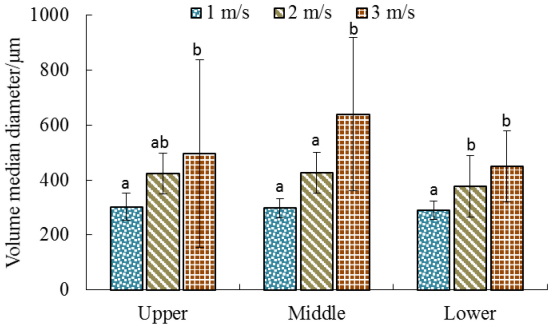

FIGURE 3
Comparison of droplet volume median diameter on WPS at three canopy layers. Letters indicate significant differences between flight velocities (Duncan test, α = 0.05).

The diffusion ratio is a widely used international index to measure the spraying effect of droplets. It can effectively characterize the uniformity of the droplet diameter distribution on the surface of the target. The ideal value of the droplet diffusion ratio is 1; that is, the volume of all the droplets is identical. Generally, the droplet distribution is considered even when the diffusion ratio range lies within 0.67–1 (Chen et al., 2022). **Figure 5** presents the diffusion ratio of the droplets on the surface of the water-sensitive paper at different flight velocities. Unfortunately, the droplet distribution was not ideal for the set experimental conditions and the level of RD > 0.67 was not achieved. The diffusion ratios exhibited significant variation between different velocities at the same canopy height. Overall, the diffusion ratio of the surface of the water-sensitive paper exhibited a gradual decreasing trend with the increase in flight velocity, indicating that an increase in the flight velocity reduces the uniformity of the droplet size distribution. The average diffusion ratios at velocities of 1, 2, and 3 m/s were 0.58, 0.45, and 0.39, respectively, as shown in **Table 2**. The DR values at different canopy heights did not vary significantly at the same velocity. However, Xu et al. (2017) confirmed that when the plant protection drones perform rice application operations, the diffusion ratio in the middle layer of the rice is better than that in the upper and lower layers.

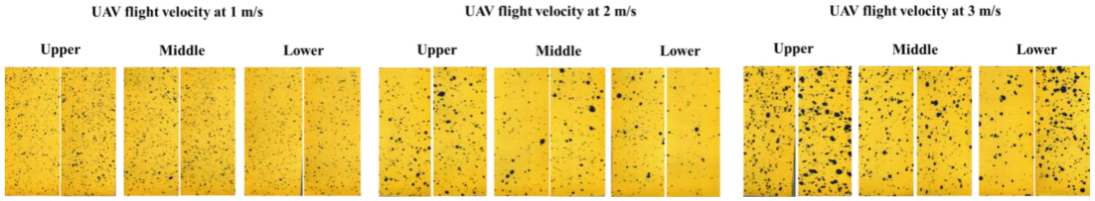

FIGURE 4
Droplet distribution stains on water sensitive paper in canopy layers under different flight velocity of UAV.

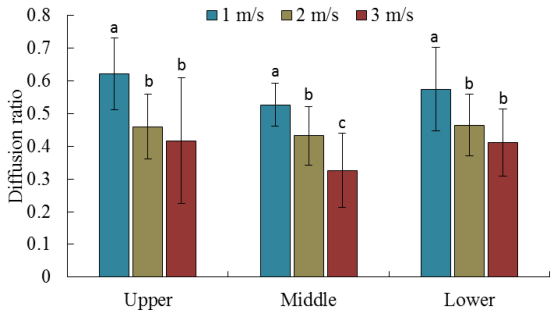

FIGURE 5
Mean diffusion ratio for different canopy locations and flight velocity. Letters indicate significant differences.

The effect of flight velocity on droplet coverage characteristics in canopy

Figure 6 presents the correlation between Cov and Dent under real operating conditions for plant-protection UAVs. Cov and Dent exhibit a good linear correlation, except for a few values with Cov of more than 20% for 3 m/s, which concurs with the findings of Grella et al. (2020). The study reported that a good linear correlation is generally observed between Cov and Dent when the Cov is less than 20% in the measurement of the droplet deposition using water-sensitive paper. This is primarily attributed to the fact that more droplets exhibit overlapping staining when the Cov exceeds 20%. The effect of pest control exhibits a strong correlation with the coverage characteristics of droplets; however, excessive droplet coverage does not indicate high control efficiency (Garcerá et al., 2011). Chen et al. (2013) considered a Cov of more than 30% on water-sensitive paper to indicate excessive spraying. For the conventional orchard air-assisted spraying approach, the effective thresholds of dents for fungicide and insecticide spraying were 70 deposits/cm^2 and 30 deposits/cm^2, respectively (Zhu et al., 2011; Salcedo et al., 2020). However, the plant protection UAV adopts an ultralow-volume spray method (ISO 5681, 2020) with less water consumption and a larger concentration of pesticides. Further research is required to determine the consistency of the droplet density and coverage required for disease and pest control with the conventional spraying methods. However, in China, the minimum value of Dent required for the effective spray amplitude of the current plant protection UAV is observed to be 15 deposits/cm^2 based on a large number of spraying experiments conducted in the early stage; relevant standards have also been formulated for regulation (MH/T 1002.1, 2016; Song et al., 2017). Therefore, droplet densities higher than 15 deposits/cm^2 and coverage rates higher than 1% (Wang et al., 2022) were selected as the effective deposition thresholds. For the three flight velocities, the number of samples that met the requirements was the largest at 1 m/s, followed by the 2 and 3 m/s conditions. The maximum Dent difference does not significantly vary for the three flight velocities, while the Cov varies considerably. For more samples, Cov was below 3% at 1 m/s, below 6% at 2 m/s, and mostly below 15% at 3 m/s. Additionally, although the Cov of some samples reached 30% at a velocity of 3 m/s, the Dent did not increase significantly, primarily due to the large size of the droplets at this velocity.

The effective coverage ratio (ECR) and effective density ratio (EDR) were calculated based on the aforementioned effective droplet deposition requirements (**Table 2**). The ECR at the flight velocities of 1 and 2 m/s were 73.3 and 71.1, respectively; however, it was significantly reduced at 3 m/s, which was 57.8 and 21.14% lower than that at 1 m/s. The EDR gradually decreased with an increase in the flight velocity, and the EDR was 48.90, 33.33, and 28.90% at the velocities of 1, 2, and 3 m/s, respectively. In terms of Cov within the canopy, the upper canopy coverage (Cov_{Upp}), middle canopy coverage (Cov_{Mid}), and lower canopy coverage (Cov_{Low}) all exhibited an increasing trend with an increase in the flight velocity, such that the Cov_{Mid} at 1 m/s was 2.44%, and the Cov_{Mid} at 3 m/s increased to 6.49%. These results indicate that the ECR and EDR of the droplets decrease despite the increase in the flight velocity and the mean coverage (Cov_{Mean}). Overall, an increase in flight velocity reduces the proportion of effective droplet coverage which meets pest control requirements.

The Cov at the three canopy heights did not significantly vary at different velocities. The interior zone coverage (Cov_{Int}) and exterior zone coverage (Cov_{Ext}) of the canopy are relatively similar, primarily due to the divergent canopy pattern of peach trees. Therefore, it is not as difficult to apply pesticide inside the canopy as that of dense fruit trees. Cov_{Int} reached 9.35 at

TABLE 2 Spray coverage characteristics in canopy for the different flight velocities.

Parameters		Treatment		
		1 m/s	2 m/s	3 m/s
Upper canopy coverage	Cov_{Upp} (%)	2.25 ± 1.71a	2.98 ±3 .10a	3.4 ± 4.34a
Middle canopy coverage	Cov_{Mid} (%)	2.44 ± 1.54a	3.67 ± 3.71a	6.49 ± 10.30a
Lower canopy coverage	Cov_{Low} (%)	1.69 ± 1. 51a	2.82 ± 2.30a	4.17 ± 4.38a
Exterior zone coverage	Cov_{Ext} (%)	2.3 ± 1.68a	3.15 ± 3.11a	3.52 ± 6.00a
Interior zone coverage	Cov_{Int} (%)	1.45 ± 0.95a	3.09 ± 4.27a	9.30 ± 8.62b
Mean coverage	Cov_{Mean} (%)	2.13 ± 1.59a	3.14 ± 3.32ab	4.68 ± 6.89b
Coverage distribution uniformity	CV (%)	74.70	105.88	147.49
Effective coverage ratio	ECR (%)	73.30	71.10	57.80
Upper canopy droplet density	Den_{Upp} (deposits/cm^2)	16.27 ± 13.49a	11.41 ± 9.31a	9.08 ± 10.67a
Middle canopy droplet density	Den_{Mid} (deposits/cm^2)	18.84 ± 9.17a	13.93 ± 10.81a	12.66 ± 15.80a
Lower canopy droplet density	Den_{Low} (deposits/cm^2)	13.92 ± 11.81a	11.84 ± 9.82a	13.85 ± 10.38a
Exterior zone droplet density	Den_{Ext} (deposits/cm^2)	17.43 ± 12.26a	12.54 ± 9.56ab	9.57 ± 11.01b
Interior zone droplet density	Den_{Int} (deposits/cm^2)	12.01 ± 6.92a	11.83 ± 11.46a	21.06 ± 14.12a
Mean droplet density	Den_{Mean} (deposits/cm^2)	16.34 ± 11.54a	12.39 ± 9.83a	11.86 ± 12.42a
Effective density ratio	EDR (%)	48.90	33.33	28.90
Upper canopy droplet size	VMD_{Upp} (μm)	302.15 ± 50.17a	423.54 ± 74.33ab	496.92 ± 341.03b
Middle canopy droplet size	VMD_{Mid} (μm)	297.00 ± 35.11a	427.00 ± 74.17a	639.33 ± 278.91b
Lower canopy droplet size	VMD_{Low} (μm)	290.13 ± 33.19a	376.87 ± 113.07b	449.93 ± 129.10b
Mean droplet size	VMD_{Mean} (μm)	301.89 ± 39.58a	420.54 ± 82.35b	512.51 ± 261.30c
Average diffusion ratio	RD	0.58 ± 0.11a	0.45 ± 0.092b	0.39 ± 0.14c

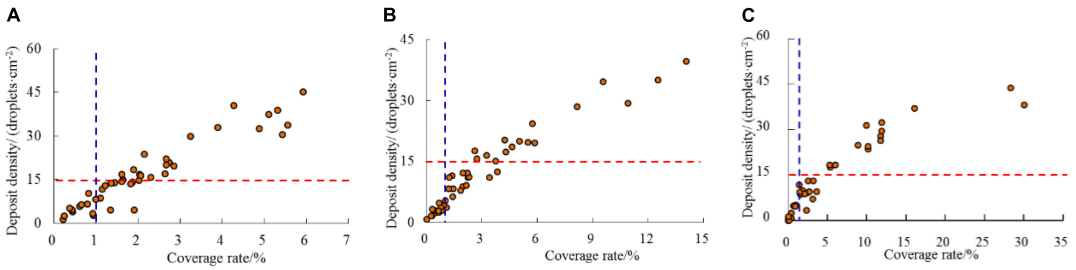

FIGURE 6
Plots of deposit density and spray coverage rate for different flight velocities. The horizontal red dashed line and the vertical blue dashed line represent the minimum droplet density (15 deposits/cm^2, Song et al., 2017) and coverage (1%, Chen et al., 2022) required for plant protection UAV application, respectively. **(A)** 1 m/s. **(B)** 2 m/s. **(C)** 3 m/s.

a flight velocity of 3 m/s, which significantly exceeded the value of others. The individual samples were possibly contaminated during the application process. The Cov_{Mean} values at 1, 2, and 3 m/s were 2.13, 3.14, and 4.68%, respectively. The coverage distribution uniformity (CV) decreased with an increase in the velocity and the CV value increased from 74.7% at 1 m/s to 147.49% at 3 m/s. This is primarily attributed to the fact that the downward speed of the down-wash airflow is decomposed with the increase in flight velocity, and part of the airflow generates a wingtip vortex. Some droplets deviate from their initial motion direction under the action of a complex wind field, which can easily cause a sudden increase or decrease in the deposition in some canopy areas.

Dents exhibited opposite trends at different canopy heights (Table 2). The Dent value exhibited a gradual decreasing trend with the increase of the velocity. For example, the middle canopy droplet density (Den_{Mid}) at 1 m/s decreased from 18.84 deposits/cm^2 to 12.66 deposits/cm^2 at 3 m/s, indicating a decrease of 32.80%. The Cov_{Mean} and mean droplet density (Den_{Mean}) in the middle layer were higher than those in the upper and lower layers, which is related to the special downwash airflow auxiliary spray method of the UAV. The downwash airflow transports droplets to the inside of the canopy, and the upper canopy is most disturbed by the airflow due to the shaking effect of the branches and leaves. Some of the droplets cannot effectively attach themselves, while the lower part is more severely occluded by the middle and upper branches and leaves. The Den_{Mean} values at the three velocities did not exhibit a significant variation.

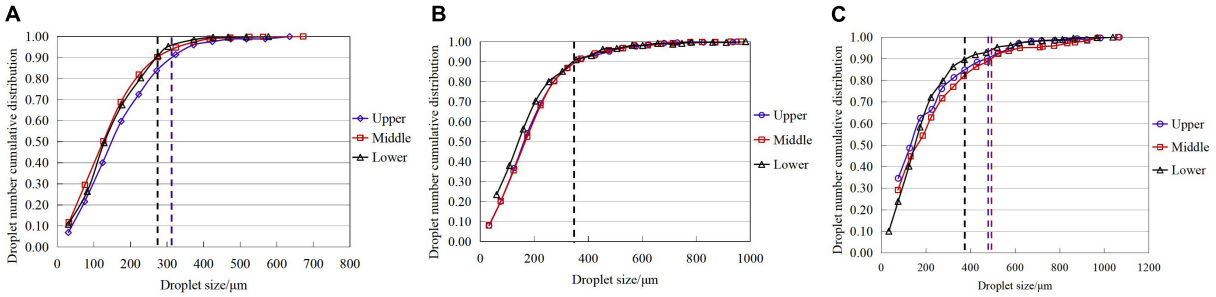

FIGURE 7
Cumulative ratio of droplet number and the corresponding droplet size at various canopy layers under different flight velocity. The vertical dotted lines represent the VMD when the cumulative proportion of droplet points reaches 0.9, where the blue, red, and black dotted lines represent the upper, middle, and lower layer of the canopy, respectively. **(A)** 1 m/s. **(B)** 2 m/s. **(C)** 3 m/s.

The cumulative ratio of the droplet number and the corresponding droplet size were calculated in 20 gradients (0–50 μm, 50–100 μm, 100–150 μm... 950–1000 μm), and the results are presented in Figure 7. The droplet number cumulative ratio curve at various canopy parts exhibits a high similarity at the same flight velocity. The droplet size varied at different flight velocities corresponding to a cumulative ratio equal to 0.9. At 1 m/s, the droplet size corresponding to the cumulative ratio equal to 0.9 in the middle and lower layers, was identical at 273 μm, while that in the upper layer was approximately 315 μm. At 2 m/s, the droplet size at the three canopy heights was consistent at 355 μm. For 3 m/s, the droplet sizes in the upper, middle, and lower layers when the cumulative ratio reached 0.9, were 475, 482, and 370 μm, respectively. In general, the droplet size at an accumulation ratio of 0.9 exhibited an increasing trend with the increase in velocity.

Spray deposition characteristics of combined pesticides in the canopy

The collected leaves were crushed, extracted, and filtered, and the difenoconazole, azoxystrobin, and imidacloprid contents were determined by using UPLC-MS/MS. The proposed method realizes trace detection of pesticide deposition and better reflects the pesticide attachment on the leaf surface when compared to the tracer method. We weighed the leaves at each sampling point due to the difference in the size of the collected leaves, to effectively characterize the amount of deposition on the unit leaves. Subsequently, we obtained the mass of all the leaves and obtained the deposition amount (mg/kg) of the unit mass. Figure 8 presents the experimental results, which demonstrate that the standard deviation of the amount of deposition is relatively large as a whole. This indicates that the deposition of the pesticide is very uneven, which corresponds to the trace detection method of the pesticide. The velocity significantly affected the deposition amount, and the average deposition was the lowest at a velocity of 3 m/s. Furthermore, we calculated the mean deposition of the three pesticides at different velocities (Table 3). The azoxystrobin mean deposition ($DEP_{Azo-Mean}$) was the highest at 27.01, 30.61, and 20.56 mg/kg, followed by the Imidacloprid mean deposition ($DEP_{Imi-Mean}$) and difenoconazole mean deposition ($DEP_{Dif-Mean}$). The deposition amount was normalized owing to the differences in the dosages of the three pesticides during dispensation. The results demonstrated that the imidacloprid normalized deposition ($DEP_{Imi-nor}$) was the highest, followed by azoxystrobin normalized deposition ($DEP_{Azo-nor}$) and difenoconazole normalized deposition ($DEP_{Dif-nor}$), which is mainly attributed to the precipitation of imidacloprid. In terms of dosage forms, azoxystrobin and difenoconazole are used as the suspension agents (SC) and imidacloprid is used as a wettable powder (WP). The pipe connected to the liquid pump is located at the bottom of the spray tank, and the content of the active ingredient of imidacloprid in the liquid can be increased at the bottom of the pipe or at the bottom of the tank even though the spray tank is shaken before the spray test to mix the liquid.

The deposition distribution characteristics of the pesticide solutions were analyzed at different locations in the canopy. The results demonstrated that an increase in the flight velocity improved the penetration efficiency of the pesticide solution. For example, the azoxystrobin vertical penetration efficiencies (PEV_{Azo}) at 1, 2, and 3 m/s were 81.44, 90.19, and 155.97%, respectively, and that at 3 m/s was 91.51% higher than that at 1 m/s. Similarly, the lateral horizontal diffusion efficiency of the canopy also improved. The horizontal diffusion efficiency of azoxystrobin (PEH_{Azo}) increased from 98.32% at 1 m/s to 261.47% at 3 m/s. However, a higher flight velocity increases the coefficient of variation of the droplet deposition distribution, due to which the deposition distribution becomes uneven and the azoxystrobin deposition distribution uniformity (CV_{Azo}) reaches 130% at 3 m/s.

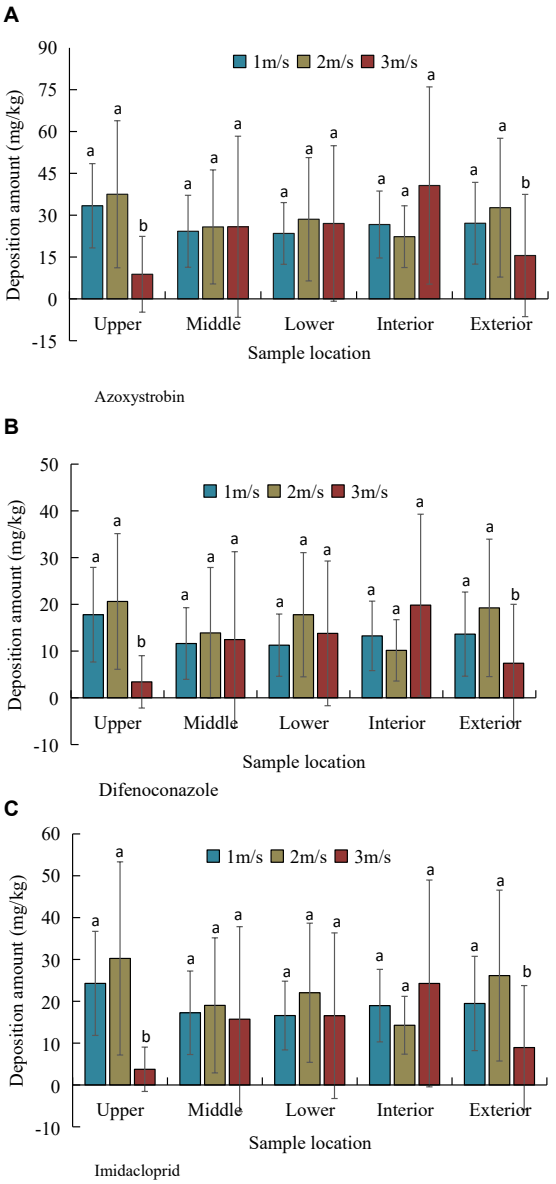

FIGURE 8
Deposition amount of pesticides at different velocities and canopy heights. **(A)** Azoxystrobin, **(B)** Difenoconazole, and **(C)** Imidacloprid.

The effect of flight velocity on ground loss

The effects of different flight velocities on the ground loss of pesticides under tree canopies were analyzed. The ground loss value of the three pesticides was minimum when the flight velocity was 2 m/s, and the deposition loss on the ground was similar at velocities of 1 and 3 m/s, as shown in **Figure 9**. This is because the droplets are driven to move toward the canopy by the downwash flow when the wind velocity is 1 m/s, and some droplets drop from the leaf surface or are directly deposited on the ground through the canopy gap. The downwash airflow velocity decomposed at a flight velocity of 3 m/s, and the fine droplets moved along a zig-zag direction to the ground under the action of the wing tip vortex, resulting in a large pesticide loss.

The effect of flight velocity on spray drift

Figure 10 depicts the pesticide drift curve within 50 m of the drift treatment area. The drift volume exhibits a gradual decreasing trend with an increase in the flight velocity. This concurs well with the existing reports (Chen et al., 2020). The drift percentage can reach 85% at 1 m, and the drift percentage is less than 5% when the distance is 10 m. The drift percentage was less than 0.2% 50 m downwind (**Table 4**).

The pesticides can still be detected 100 m downwind, and the drift percentage goes up to 1%, indicating that the application drift of the plant-protection UAV remains relatively significant. **Figure 11** presents the drift percentages at different heights. Overall, the pesticide drift in the vertical direction was not closely related to the height. However, the vertical distribution of the three pesticides was saddle-shaped at 3 m/s, and the drift volume was highest at 3 and 8 m. The airborne drift was the highest at 3 m/s when compared to the three flight velocities, which was the opposite of the close ground drift (the drift volume was the highest at 1 m/s at the three flight velocities). This is primarily attributed to the increase in the flight velocity, which forms a characteristic airflow structure such as a wingtip vortex. These vortex structures typically exhibit higher energy, and the fine droplets can be transported in the air over a long distance under the joint action of the ambient crosswind. Among the three pesticides, imidacloprid presented the highest drift percentage, followed by azoxystrobin, while difenoconazole presented the lowest drift percentage, which was consistent with canopy normalization deposition.

Discussion

In recent years, the use of plant protection UAVs for pesticide spraying operations has been increasing rapidly in China. The application field has gradually extended from grain crops to commercial crops such as fruit trees, tea trees, and vegetables. This operation method does not consider topographic factors, and thus presents broad development and application potential in hilly areas where it is difficult to operate ground machinery. The plant protection UAV presents the characteristics of low water consumption and high liquid concentration when compared to the traditional spraying method. Multiple pesticides can be simultaneously included in

TABLE 3 Spray deposition distribution characteristics in canopy for the different flight velocities.

Parameters		Treatment		
		1 m/s	2 m/s	3 m/s
Difenoconazole vertical penetration efficiency	PE_{VDif} (%)	76.63	103.03	173.36
Azoxystrobin vertical penetration efficiency	PE_{VAzo} (%)	81.44	90.19	155.97
Imidacloprid vertical penetration efficiency	PE_{VImi} (%)	79.90	89.47	170.01
Difenoconazole horizontal diffusion efficiency	PE_{HDif} (%)	97.24	52.76	267.97
Azoxystrobin horizontal diffusion efficiency	PE_{HAzo} (%)	98.32	68.21	261.47
Imidacloprid horizontal diffusion efficiency	PE_{HImi} (%)	97.36	54.59	271.28
Difenoconazole deposition distribution uniformity	CV_{Dif} (%)	63.70	79.78	150.12
Azoxystrobin deposition distribution uniformity	CV_{Azo} (%)	51.95	75.57	130.00
Imidacloprid deposition distribution uniformity	CV_{Imi} (%)	55.28	80.20	149.91
Difenoconazole mean deposition	$DEP_{Dif-Mean}$ (mg/kg)	13.55 ± 8.63ab	17.42 ± 13.90a	9.88 ± 14.84b
Azoxystrobin mean deposition	$DEP_{Azo-Mean}$ (mg/kg)	27.01 ± 14.04ab	30.61 ± 13.13a	20.56 ± 26.69b
Imidacloprid mean deposition	$DEP_{Imi-Mean}$ (mg/kg)	19.38 ± 10.71a	23.77 ± 19.06a	12.01 ± 18.00b
Difenoconazole normalized deposition	$DEP_{Dif-nor}$ (mg·cm^2/kg·μg)	10.84 ± 6.91ab	13.94 ± 11.12a	7.91 ± 11.88b
Azoxystrobin normalized deposition	$DEP_{Azo-nor}$ (mg·cm^2/kg·μg)	13.52 ± 7.02ab	15.30±11.57a	10.28±13.34b
Imidacloprid normalized deposition	$DEP_{Imi-nor}$ (mg·cm^2/kg·μg)	25.83 ± 14.28a	31.69 ± 25.41a	16.01 ± 24.00b

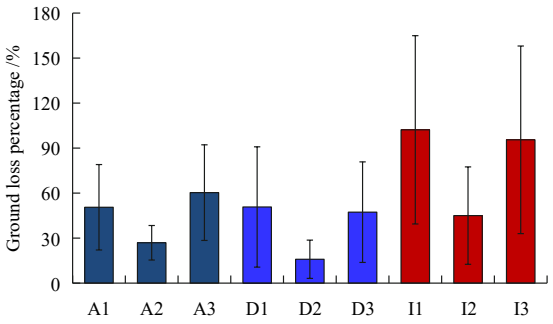

FIGURE 9
Histogram of ground loss percentage of three pesticides at three flight velocities. On the abscissa, the letters A, D, and I denote Azoxystrobin, Difenoconazole, and Imidacloprid, respectively. The numbers 1, 2, and 3 denote the flight velocity of 1, 2, and 3 m/s, respectively.

a single spraying process, which has been widely implemented to avoid various pests and diseases. For example, the application strategy of "one spraying and three defenses" is implemented for wheat when using the plant-protection UAVs in China. A similar strategy was also used for orchards. Therefore, we conducted spray tests of a plant-protection UAV using a combination of three pesticides in a peach orchard. The effect of flight speed on the droplet size, deposition in the canopy, ground loss, ground drift, and airborne drift was analyzed.

Firstly, the effect of flight velocity on the volume median diameter was analyzed (**Figure 4**). The results demonstrate that the flight velocity significantly affects the droplet size. A higher flight velocity increases the droplet size on the target, which is attributed to the down-wash airflow generated by the UAV rotor wing. An increase in the flight velocity contributes to the formation of wingtip vortices and other airflow structures. These vortex structures cause the fine droplets to spread with the airflow, resulting in the deposition of larger droplets on the canopy. It was also observed that the droplet size in the lower canopy was slightly smaller than those in the middle and upper parts.

We also analyzed the diffusion ratio (RD) of the dyed droplets on a water-sensitive paper surface (**Figure 5**), which is typically used to characterize the uniformity of the droplet size distribution. The droplet size distribution was not ideal, and failed to meet the spray requirement of RD > 0.67. Xu et al. (2017) conducted a spray test using a plant-protection UAV in rice, and the obtained RD value did not exceed 0.67. This is mainly attributed to the combined effect of the plant canopy and UAV downwash airflow. The canopy foliage blocks larger droplets from deposition, and the downwash airflow drives smaller droplets away from the initial trajectory. Computer simulation modeling must be employed to further analyze the diffusion law of droplets with different sizes inside the canopy to optimize the nozzle and flight parameters and achieve a uniform distribution of droplet sizes.

The droplet coverage characteristics of the water-sensitive paper were measured. A good linear correlation was observed between the droplet coverage and droplet density since the droplet coverage is lower than 20% (**Figure 6**), which is consistent with the findings of Grella et al. (2022). Wang et al. (2022) selected a droplet density higher than 15 deposits/cm^2 and a coverage rate higher than 1% as the lowest threshold indicators and analyzed the spray coverage parameters. For the

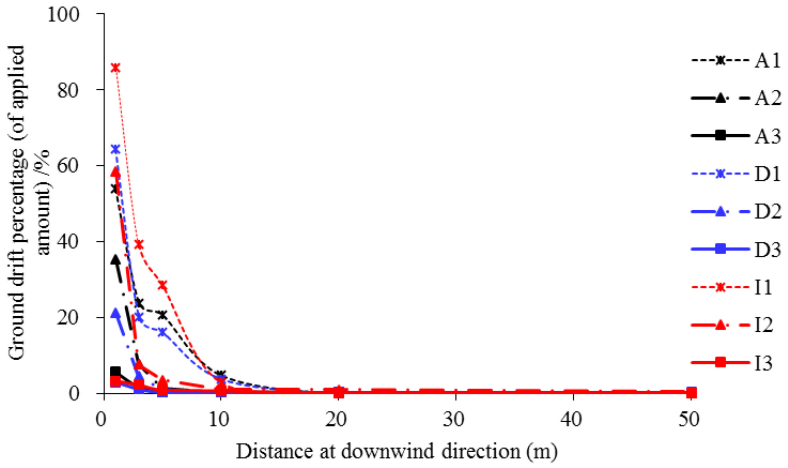

FIGURE 10
The curve of downwind ground drift at the setting distance from the spray treated area. The letters A, D, and I represent Azoxystrobin, Difenoconazole, and Imidacloprid, respectively. The numbers 1, 2, and 3 represent the flight velocity at 1, 2, and 3 m/s, respectively.

TABLE 4 Spray drift percentage (%) for the three pesticides used in the experiments under the setting flight velocity.

Drift percentage (%)		Azoxystrobin			Difenoconazole			Imidacloprid		
		1 m/s	2 m/s	3 m/s	1 m/s	2 m/s	3 m/s	1 m/s	2 m/s	3 m/s
Distance from the spray treated area (in m)	1	53.7930	35.2925	5.5225	64.3002	21.0757	2.9056	85.8106	58.3701	3.2498
	3	23.8631	7.6444	1.5557	20.0874	4.4341	1.0670	39.2380	7.5472	2.1489
	5	20.6228	1.3623	0.3638	16.0613	1.0287	0.2478	28.5091	3.5206	0.8438
	10	4.7109	0.2953	0.2952	3.6673	0.1931	0.2364	2.8036	0.9102	0.6067
	20	0.0094	0.1613	0.2142	0.0384	0.1366	0.1820	0.0236	0.8959	0.0692
	50	0.0081	0.1422	0.1313	0.0145	0.1189	0.1729	0.0024	0.4365	0.0510
	Average	17.1679	7.4830	1.3471	17.3615	4.4978	0.8019	26.0645	11.9467	1.1615
Sampling height at 100 m distance from the spray treated area (in m)	2	0.0019	0.0708	0.4194	0.0072	0.0392	0.1423	0.0073	0.2016	0.9993
	3	0.0022	0.0809	0.5098	0.0186	0.0167	0.2735	0.0112	0.1240	1.0283
	4	0.0019	0.1005	0.4406	0.0068	0.0471	0.1873	0.0012	0.1428	0.7536
	5	0.0000	0.0602	0.2631	0.0076	0.0523	0.0623	0.0099	0.0699	0.3878
	6	0.0043	0.1436	0.3329	0.0262	0.0540	0.0832	0.0006	0.2900	0.6540
	7	0.0011	0.0958	0.3590	0.0043	0.0361	0.1426	0.0015	0.1716	0.5961
	8	0.0011	0.0715	0.6266	0.0051	0.0592	0.2888	0.0015	0.1581	0.9262
	9	0.0048	0.0943	0.4399	0.0071	0.0240	0.1541	0.0519	0.1431	0.6550
	10	0.0023	0.0484	0.0626	0.0146	0.0264	0.0253	0.0016	0.1348	0.1223
	Average	0.0021	0.0851	0.3837	0.1083	0.0394	0.1510	0.0096	0.1595	0.6803

three flight velocities considered in the experiment, the number of samples that met the requirements was largest at a speed of 1 m/s, followed by 2 and 3 m/s. This implies that increasing the flight velocity can reduce the control effect when the application rate is fixed. Consequently, the effective coverage ratio (ECR) and effective density ratio (EDR) were calculated at different speeds (Table 2); they tended to decrease with an increase in the flight velocity. Furthermore, we observed that the average droplet coverage rate gradually increased with the increase in the flight velocity, and the average coverage rates at 1, 2, and 3 m/s were 2.13, 3.14, and 4.68%, respectively, which was not consistent with the expected values. This is mainly attributed to the increase in the droplet size as explained earlier. Blue streaks were observed on the surface when processing the water-sensitive paper, which indicate the "hard landing" of a droplet. That is, the droplets from UAV applications may impact the

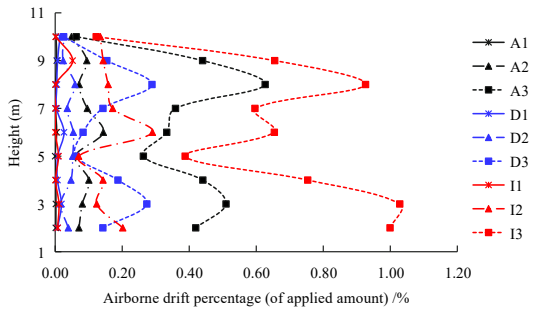

FIGURE 11
Airborne drift profile at 100 m distance from treated area. The letters A, D, and I represent Azoxystrobin, Difenoconazole, and Imidacloprid, respectively. The numbers 1, 2, and 3 represent the flight velocity at 1, 2, and 3 m/s, respectively.

target surface with significant high-speed horizontal motion (Li et al., 2021a). This was mainly attributed to the combined action of forward flight inertia and downwash airflow, which extended the dyed area.

The droplet density gradually decreased with the increase in the flight velocity, contrary to the droplet coverage. This is because the droplet density measurement does not consider the droplet point area in the statistics as long as the dyed droplet point exists individually. Therefore, the number of droplets did not increase at a flight velocity of 3 m/s despite the increase of the droplet coverage rate. In general, the droplet coverage rate and density in the middle canopy were higher than those in the upper and lower canopies, which was primarily attributed to the disturbance of the upper canopy due to airflow and the occlusion of the lower canopy due to branches and leaves.

The droplets on all the water-sensitive paper samples were statistically analyzed. The droplet size was divided into 20 gradients with an interval of 50 μm in the range of 0–1000 μm. The cumulative ratio of the droplet numbers under different operating conditions was calculated (**Figure 7**). The droplet size corresponding to the droplet number cumulative ratio value of 0.9 increases with the increase in the flight velocity. At 2 m/s, the corresponding droplet sizes of the upper, middle, and lower canopies were observed to be identical when the cumulative ratio was 0.9. The droplet sizes for the three canopy heights varied at 3 m/s.

For the pesticide deposition in the canopy, we used UPLC-MS/MS to determine the active ingredient amounts of the three pesticides on the leaves in different parts of the canopy. The flight velocity significantly affects the pesticide deposition. The mean deposition amount was highest at 2 m/s and lowest at 3 m/s. Zhang et al. (2012) reported that the deposition amount negatively correlated with the flight velocity of rice sprayed with an unmanned helicopter. In this study, the flight velocity significantly affects the uniformity of deposition. Therefore, an increase in the flight velocity is detrimental to uniform deposition. The CV reduced from 60% at 1 m/s to 140% at 3 m/s, which is consistent with the findings of Qiu et al. (2013). However, Chen et al. (2016) reported that the flight velocity significantly affects the deposition amount, but does not significantly affect the deposition uniformity. This deviation in the experimental conclusions is primarily attributed to the differences in the target plant and the types of plant protection UAVs used. Among the three pesticides used in this study, the normalized deposition amount of imidacloprid was the highest, indicating that it had the best deposition efficiency, followed by azoxystrobin and difenconazole. This phenomenon may be attributed to the fact that the dosage form of imidacloprid is a wettable powder (WP), which tends to accumulate at the bottom of the tank during operation. It was observed that an increase in the flight velocity improved the vertical penetration efficiency (PEV) and horizontal diffusion efficiency (DEV) while causing an uneven deposition distribution.

The ground loss percentage of the applied amount under the canopy was relatively large in terms of the pesticide loss and spray drift (**Figure 9** and **Table 4**), particularly for the imidacloprid component, which reached a maximum of nearly 100%. For the three flight velocities, the ground loss percentage was the lowest at 2 m/s, and the deposition amount and normalized deposition amount were the highest at this speed, indicating that a better deposition effect was achieved at a 2 m/s flight velocity. The ground loss in vineyards with UAV spraying were studied by Biglia et al. (2022), and found that the ground losses decrease with the increase of the UAV cruise speed. This difference is mainly caused by the canopy morphology, planting pattern of fruit trees and UAV operation mode. The ground drift percentage gradually decreased with the increase in the distance from the spraying-treated area, and the drift percentage was lower than 5% when the distance was 10 m, this is consistent with the results obtained by Wang et al. (2021). The sprayed pesticide could still be detected in the air at 100 m downwind, and the airborne drift percentage of imidacloprid reached 1% at a height of 2 m under 3 m/s. In general, the airborne drift is larger at the heights of 3 and 8 m, which makes the distribution curve appear saddle shaped. At present, the aerial drift of plant protection UAV sprays is mainly measured in the near field within 20 far away from the spray area (Wang Z. C. et al., 2020; Wang et al., 2021). Wang G. B. et al. (2020) tested the airborne drift at 12 m from the sprayed erea, and found that at a height of 1–5 m from the ground, spray drift gradually decreased with the increase of height.

Conclusion

In this study, the effects of flight velocities on the droplet size, deposition distribution in the canopy, ground loss, and spray drift of peach orchards were systematically analyzed to improve the spray effect. The flight velocity significantly affects the droplet size, and an increase in the flight velocity increases the droplet size on the target. The droplet size in

the lower canopy was slightly smaller than those in the middle and upper parts. Unfortunately, the diffusion ratio of the droplets is not ideal and is not greater than 0.67. A higher flight velocity presented a larger droplet coverage rate and a smaller density on the target, which was mainly attributed to the expansion of the dyed area formed by the hard landing of the droplet. The increase in the flight velocity reduced the effective coverage ratio and effective density ratio, while increasing the vertical penetration efficiency and horizontal diffusion efficiency; however, it also reduced the uniformity of the droplet deposition distribution. The ground loss and spray drift were significantly high during the operation of the plant protection UAV, and the maximum airborne drift percentage reached 1% at a distance 100 m away from the spraying treated area.

This study quantified the deposition and drift of pesticides from the plant protection UAVs sprayed at different flight velocities based on the analysis of ultra-high-performance liquid chromatography-tandem triple quadrupole mass spectrometry, which provides a reference for the commercial application of plant-protection UAVs. However, several aspects must be determined to determine the effect of other parameters such as flying height and spraying dosage on the spray effect in order to improve the spray performance of the plant-protection UAVs. The actual performance of peach trees must be evaluated for pest control before the commercialization of the optimized operation strategy when compared to the traditional manual knapsack method. Additionally, the residue and digestion dynamics of pesticides in fruits must be further analyzed after the plant-protection UAV spraying.

Data availability statement

The original contributions presented in this study are included in the article/supplementary material, further inquiries can be directed to the corresponding authors.

Author contributions

LL: conceptualization, methodology, and writing – original draft. ZH: data curation, formal analysis, writing – review and editing, and funding acquisition. QL: software, data curation, and investigation. TY: resources, validation, and investigation. PH: resources, writing – review and editing, and funding acquisition. RZ: methodology, supervision, writing – review and editing, and funding acquisition. LP: methodology. All authors contributed to the article and approved the submitted version.

Funding

This work was sponsored by the National Natural Science Foundation of China (32071907), Special Projects of Construction of Science and Technology Innovation Ability of Beijing Academy of Agriculture and Forestry Sciences (KJCX201910), Outstanding Scientist Cultivation Project of Beijing Academy of Agriculture and Forestry Sciences (JKZX202205), Postdoctoral Research Foundation of Beijing Academy of Agriculture and Forestry (2020-ZZ-016), and Beijing Postdoctoral Research Foundation (2021-ZZ-139).

Acknowledgments

We acknowledged the contributions of specific colleagues, institutions, or agencies that aided the efforts of the authors.

Conflict of interest

The authors declare that the research was conducted in the absence of any commercial or financial relationships that could be construed as a potential conflict of interest.

Publisher's note

References

Biglia, A., Grella, M., Bloise, N., Comba, N., Mozzanini, E., Sopegno, A., et al. (2022). UAV-spray application in vineyards: Flight modes and spray system adjustment effects on canopy deposit, coverage, and off-target losses. *Sci. Total Environ.* 845:157292. doi: 10.1016/j.scitotenv.2022.157292

Chen, C., Li, S. G., Wu, X. Y., Wang, Y. X., and Kang, F. (2022). Analysis of droplet size uniformity and selection of spray parameters based on the biological optimum particle size theory. *Environ. Res.* 204:112076. doi: 10.1016/j.envres.2021.112076

Chen, H., Lan, Y. B. K., Fritz, B., Clint Hoffmann, W., and Liu, S. (2021). Review of agricultural spraying technologies for plant protection using unmanned aerial vehicle (UAV). *Int. J. Agric. Biol. Eng.* 14, 38–49. doi: 10.25165/j.ijabe.20211401.5714

Chen, S. D., Lan, Y. B., Li, J. Y., Zhou, Z. Y., Jin, J., and Liu, A. M. (2016). Effect of spray parameters of small unmanned helicopter on distribution regularity of droplet deposition in hybrid rice canopy. *Trans. Chin. Soc. Agric. Eng.* 32, 40–46. doi: 10.11975/j.issn.1002-6819.2016.17.006

Chen, S. D., Lan, Y. B., Li, J. Y., Zhou, Z. Y., Liu, A. M., and Mao, Y. D. (2017). Effect of wind field below unmanned helicopter on droplet deposition distribution of aerial spraying. *Int. J. Agric. Biol. Eng.* 10, 67–77. doi: 10.3965/j.ijabe.20171003.3078

Chen, S. D., Lan, Y. B., Zhou, Z. Y., Ouyang, F., Wang, G. B., Huang, X. Y., et al. (2020). Effect of droplet size parameters on droplet deposition and drift of aerial spraying by using plant protection UAV. *Agronomy* 10:195. doi: 10.3390/agronomy10020195

Chen, Y., Ozkan, E., Zhu, H., Derksen, R., and Krause, C. (2013). Spray deposition inside tree canopies from a newly developed variable-rate air-assisted sprayer. *Trans. ASABE* 56, 1263–1272. doi: 10.13031/trans.56.9839

Deveau, J., Ledebuhr, M., and Manketelow, D. (2021). *Airblast101—Your guide to effective and efficient spraying, 2nd edn. Sprayer 101, Ontario, Canada*. Available online at: https://platform.innoseta.eu/storage/training_material_files/1610107418_136075_2021_Airblast101-2ndEdition-ProtectedA7.pdf

Garcerá, C., Moltó, E., and Chueca, P. (2011). Effect of spray volume of two organophosphate pesticides on coverage and on mortality of California Red scale Aonidiella aurantii (Maskell). *Crop Prot.* 30, 693–697. doi: 10.1016/j.cropro.2011.02.019

Godfray, H. C. J., Beddington, J. R., Crute, I. R., Haddad, L., Lawrence, D., Muir, J. F., et al. (2010). Food security: The challenge of feeding 9 billion people. *Science* 327, 812–818. doi: 10.1126/science.1185383

Grella, M., Gioelli, F., Marucco, P., Zwertvaegher, I., Mozzanini, E., Mylonas, N., et al. (2022). Field assessment of a pulse width modulation (PWM) spray system applying different spray volumes: Duty cycle and forward speed effects on vines spray coverage. *Precis. Agric.* 23, 219–252. doi: 10.1007/s11119-021-09835-6

Grella, M., Miranda-Fuentes, A., Marucco, P., and Balsari, P. (2020). Field assessment of a newly-designed pneumatic spout to contain spray drift in vineyards: Evaluation of canopy distribution and off-target losses. *Pest Manag. Sci.* 76, 4173–4191. doi: 10.1002/ps.5975

Guo, S., Li, J. Y., Yao, W. X., Zhan, Y. L., Li, Y. F., and Shi, Y. Y. (2019). Distribution characteristics on droplet deposition of wind field vortex formed by multi-rotor UAV. *PLoS One* 14:e0220024. doi: 10.1371/journal.pone.0220024

ISO 5681 (2020). *IS0 5681 Equipment for Crop Protection-Vocabulary*. Geneva: ISO Int Stand.

Li, J. Y., Shi, Y. Y., Lan, Y. B., and Guo, S. (2019). Vertical distribution and vortex structure of rotor wind field under the influence of rice canopy. *Comput. Electron. Agric.* 159, 140–146. doi: 10.1016/j.compag.2019.02.027

Li, X., Giles, D. K., Andaloro, J. T., Long, R., Lang, E. B., Watson, L. J., et al. (2021a). Comparison of UAV and fixed-wing aerial application for alfalfa insect pest control: Evaluating efficacy, residues, and spray quality. *Pest Manag. Sci.* 77, 4980–4992. doi: 10.1002/ps.6540

Li, X., Giles, D. K., Niederholzer, F. J., Andaloro, J. T., Lang, E. B., and Watson, L. J. (2021b). Evaluation of an unmanned aerial vehicle as a new method of pesticide application for almond crop protection. *Pest Manag. Sci.* 77, 527–537. doi: 10.1002/ps.6052

Li, Z. X., Nie, J. Y., Yan, Z., Cheng, Y., Lan, F., Huang, Y. N., et al. (2018). A monitoring survey and dietary risk assessment for pesticide residues on peaches in China. *Regul. Toxicol. Pharmacol.* 97, 152–162. doi: 10.1016/j.yrtph.2018.06.007

Lou, Z., Xin, F., Han, X., Lan, Y., Duan, T., and Fu, W. (2018). Effect of unmanned aerial vehicle flight height on droplet distribution, drift and control of cotton aphids and spider mites. *Agronomy* 8:187. doi: 10.3390/agronomy8090187

Meier, U. H., Graf, H., Hack, M., Hess, W., Kennel, R., Klose, D., et al. (1994). Phänologische Entwick-lungsstadien des Kernobstes (Malus domestica Borkh. und Pyruscommunis L.), des Steinobstes (Prunus-Arten), der Johannisbeere (Ribes-Arten) undder Erdbeere (Fragaria x ananassa Duch.). *Nachrichtenbl. Deut. Pflanzenschutzd* 46, 141–153.

Meng, Y. H., Lan, Y. B., Mei, G. Y., Guo, Y. W., Song, J. L., and Wang, Z. G. (2018). Effect of aerial spray adjuvant applying on the efficiency of small unmanned aerial vehicle for wheat aphids control. *Int. J. Agric. Biol. Eng.* 11, 46–53. doi: 10.25165/j.ijabe.20181105.4298

Meng, Y. H., Song, J. L., Lan, Y. B., Mei, G. Y., Liang, Z., and Han, Y. X. (2019). Harvest aids efficacy applied by unmanned aerial vehicles on cotton crop. *Ind. Crops Prod.* 140:111645. doi: 10.1016/j.indcrop.2019.111645

Meng, Y. H., Su, J. Y., Song, J. L., Chen, W. H., and Lan, Y. B. (2020). Experimental evaluation of UAV spraying for peach trees of different shapes: Effects of operational parameters on droplet distribution. *Comput. Electron. Agric.* 170:105282. doi: 10.1016/j.compag.2020.105282

MH/T 1002.1, (2016). Quality Indexes of Agricultural Aviation Operation part1: Spraying Operation. (2016). Civ. Aviat. Ind. Stand Peoples Repub. China. Available online at: http://www.caac.gov.cn/XXGK/XXGK/BZGF/HYBZ/201708/t20170803_45750.html

Musiu, E. M., Qi, L. J., and Wu, Y. L. (2019). Evaluation of droplets size distribution and velocity pattern using computational fluid dynamics modelling.. *Comput. Electron. Agric.* 164:104886. doi: 10.1016/j.compag.2019.104886

Pan, Z., Kejian, W., Qiang, L., Shaolan, H., Shilai, Y., Rangjin, X., et al. (2017). Droplet distribution and control against citrus leafminer with UAV spraying. *Int. J. Robot. Autom.* 32, 299–307. doi: 10.2316/Journal.206.2017.3.206-4980

Qin, W. C., Qiu, B. J., Xue, X. Y., Chen, C., Xu, Z. F., and Zhou, Q. Q. (2016). Droplet deposition and control effect of insecticides sprayed with an unmanned aerial vehicle against plant hoppers. *Crop Prot.* 85, 79–88. doi: 10.1016/j.cropro.2016.03.018

Qin, W. C., Xue, X. Y., Zhang, S. M., Gu, W., and Wang, B. K. (2018). Droplet deposition and efficiency of fungicides sprayed with small uav against wheat powdery mildew. *Int. J. Agric. Biol. Eng.* 11, 27–32. doi: 10.25165/j.ijabe.20181102.3157

Qiu, B. J., Wang, L. W., Cai, D. L., Wu, J. H., Ding, G. R., and Guan, X. P. (2013). Effects of flight altitude and speed of unmanned helicopter on spray deposition uniformity. *Trans. Chin. Soc. Agric. Eng.* 29, 25–32. doi: 10.3969/j.issn.1002-6819.2013.24.004

Salcedo, R., Zhu, H., Zhang, Z., Wei, Z., Chen, L., Ozkan, E., et al. (2020). Foliar deposition and coverage on young apple trees with PWM-controlled spray systems. *Comput. Electron. Agric.* 178:105794. doi: 10.1016/j.compag.2020.105794

Samad, A., Akhtar, S., Shahid, M. M., and Ahad, K. (2019). Determination of pesticide residues in peaches by using gas chromatography and mass spectrometric detection. *Int. J. Environ. Anal. Chem.* 99, 1446–1458. doi: 10.1080/03067319.2019.1622699

Shan, C. F., Wang, G. B., Wang, H. H., Xie, Y. J., Wang, H. Z., Wang, S. L., et al. (2021). Effects of droplet size and spray volume parameters on droplet deposition of wheat herbicide application by using UAV. *Int. J. Agric. Biol. Eng.* 14, 74–81. doi: 10.25165/j.ijabe.20211401.6129

Song, J. L., Liu, Y., Liu, Y. J., He, X. K., Wang, C. L., and Wang, S. (2017). Effective spray swath width determination of aerial spraying using unmanned aerial vehicle. *J. China Agric. Univ.* 22, 126–132. doi: 10.11841/j.issn.1007-4333.2017.10.15

Sparks, T. C., and Bryant, R. J. (2021). Crop protection compounds – trends and perspective. *Pest Manag. Sci.* 77, 3608–3616. doi: 10.1002/ps.6293

Tang, Y., Hou, C. J., Luo, S. M., Lin, J. T., Yang, Z., and Huang, W. F. (2018). Effects of operation height and tree shape on droplet deposition in citrus trees using an unmanned aerial vehicle. *Comput. Electron. Agric.* 148, 1–7. doi: 10.1016/j.compag.2018.02.026

Wang, C. L., Herbst, A., Zeng, A. J., Wongsuk, S., Qiao, B. Y., Qi, P., et al. (2021). Assessment of spray deposition, drift and mass balance from unmanned aerial vehicle sprayer using an artificial vineyard. *Sci. Total Environ.* 777:146181. doi: 10.1016/j.scitotenv.2021.146181

Wang, C. L., Liu, Y., Zhang, Z. H., Han, L., Li, Y. F., Zhang, H., et al. (2022). Spray performance evaluation of a six-rotor unmanned aerial vehicle sprayer for pesticide application using an orchard operation mode in apple orchards. *Pest Manag. Sci.* 78, 2449–2466. doi: 10.1002/ps.6875

Wang, G. B., Han, Y. X., Li, X., Andaloro, J., Chen, P. C., Hoffmann, W. C., et al. (2020). Field evaluation of spray drift and environmental impact using an agricultural unmanned aerial vehicle (UAV) sprayer. *Sci. Total Environ.* 737:139793. doi: 10.11975/j.issn.1002-6819.2020.04.007

Wang, G. B., Lan, Y. B., Qi, H. X., Chen, P. C., Hewitt, A., and Han, Y. X. (2019a). Field evaluation of an unmanned aerial vehicle (UAV) sprayer: Effect of spray volume on deposition and the control of pests and disease in wheat. *Pest Manag. Sci.* 75, 1546–1555. doi: 10.1002/ps.5321

Wang, G. B., Lan, Y. B., Yuan, H. Z., Qi, H. X., Chen, P. C., Ouyang, F., et al. (2019b). Comparison of spray deposition, control efficacy on wheat aphids and working efficiency in the wheat field of the unmanned aerial vehicle with boom sprayer and two conventional knapsack sprayers. *Appl. Sci.* 9:218. doi: 10.3390/app9020218

Wang, S. L., Song, J. L., He, X. K., Song, L., Wang, X. N., Wang, C. L., et al. (2017). Performances evaluation of four typical unmanned aerial vehicles used for pesticide application in China. *Int. J. Agric. Biol. Eng.* 10, 22–31. doi: 10.25165/j.ijabe.20171004.3219

Wang, Z. C., Herbst, A., Bonds, J., Zeng, A. J., Zhao, C., and He, X. K. (2020). Stereoscopic test method for low-altitude and low-volume spraying deposition and drift distribution of plant protection UAV. *Trans. Chin. Soc. Agric. Eng.* 36, 54–62. doi: 10.1016/j.scitotenv.2020.139793

Xu, G., Chen, L. P., and Zhang, R. R. (2016). "An image processing system for evaluation of aerial application quality," in *International Conference on Interlligent Information Processing*, (Wuhan), doi: 10.1145/3028842.3028895

Xu, T. Y., Yu, F. H., Cao, L. Y., Du, W., and Ma, M. Y. (2017). Vertical Distribution of Spray Droplet Deposition of Plant Protection Multi Rotor UAV for Japonica Rice. *Trans. Chin. Soc. Agric. Mach.* 48, 101–107. doi: 10.6041/j.issn.1000-1298.2017.10.012

Zhang, J., He, X. K., Song, J. L., Zeng, A. J., Liu, Y. J., and Li, X. F. (2012). Influence of spraying parameters of unmanned aircraft on droplets deposition. *Trans. Chin. Soc. Agric. Mach.* 43, 94–96.

Zhang, S. C., Qiu, B. J., Xue, X. Y., Sun, T., Gu, W., Zhou, F. L., et al. (2021). Effects of crop protection unmanned aerial system flight velocity, height on effective spraying width, droplet deposition and penetration rate, and control effect analysis on wheat aphids, powdery mildew, and head blight. *Appl. Sci.* 11:712. doi: 10.3390/app11020712

Zhang, Y. L., Huang, X. R., Lan, Y. B., Wang, L. L., Lu, X. Y., Yan, K. T., et al. (2021). Development and prospect of UAV-based aerial electrostatic spray technology in China. *Appl. Sci.* 11:4071. doi: 10.3390/app11094071

Zheng, Y. J., Yang, S. H., Zhao, C. J., Chen, L. P., Lan, Y. B., and Tan, Y. (2017). Modelling operation parameters of UAV on spray effects at different growth stages of corns. *Int. J. Agric. Biol. Eng.* 10, 57–66. doi: 10.3965/j.ijabe.20171003.2578

Zhu, H., Salyani, M., and Fox, R. D. (2011). A portable scanning system for evaluation of spray deposit distribution. *Comput. Electron. Agric.* 76, 38–43. doi: 10.1016/j.compag.2011.01.003

frontiers | Frontiers in Plant Science

TYPE Original Research
PUBLISHED 10 October 2022
DOI 10.3389/fpls.2022.1003471

OPEN ACCESS

EDITED BY
Wei Qiu,
Nanjing Agricultural University, China

REVIEWED BY
Wang Jinwu,
Northeast Agricultural University, China
Noman Ali Buttar,
Khwaja Fareed University of Engineering and Information Technology (KFUEIT), Pakistan

*CORRESPONDENCE
Kuan Qin
qinkuan@ahau.edu.cn

SPECIALTY SECTION
This article was submitted to Sustainable and Intelligent Phytoprotection, a section of the journal Frontiers in Plant Science

RECEIVED 26 July 2022
ACCEPTED 22 September 2022
PUBLISHED 10 October 2022

CITATION
Zhang YZ, Tian L, Cao CM, Zhu CL, Qin K and Ge J (2022) Optimization and validation of blade parameters for inter-row weeding wheel in paddy fields.
Front. Plant Sci. 13:1003471.
doi: 10.3389/fpls.2022.1003471

Optimization and validation of blade parameters for inter-row weeding wheel in paddy fields

Yongzheng Zhang[1], Liang Tian[1], Chengmao Cao[1], Chengliang Zhu[2], Kuan Qin[1]* and Jun Ge[1]

[1]School of Engineering, Anhui Agricultural University, Hefei, China, [2]Quality Supervision Department, Anhui Province Agricultural Machinery Test and Appraisal Station, Hefei, China

The performance of existing rice-paddy weeding machines is not optimal. In this study, the influence of the installation angle of the weeding-wheel blade on cutting resistance and soil-slippage ability was analyzed. The optimal blade angle of the weeding wheel (i.e., the angle at which the resistance to the weeding wheel is minimal and the disturbance speed of the soil maximal) was shown to be< 20°; numerical simulation showed the actual optimal value to be 0°. Different weeding depths (30, 40, and 50 mm), rotation speed of weeding wheel (120, 180, and 240 r/min), and weeder forward speeds (0.3, 0.6, and 0.9 m/s) were used as test factors, and the rates of seedling injury and weeding were used as performance-evaluation criteria to optimize the machine in a secondary orthogonal-rotation combination test. Field experiments showed that the weeding wheel can exhibit optimal working performance under the operating conditions of weeding depth of 39 mm, rotation speed of 175 r/min, and forward speed of 0.6 m/s. The seedling injury and weeding rates were 4.4% and 88.2%, respectively, which were consistent with the numerically predicted results and met the agronomic requirements. This study provides a technical reference for the improvement of paddy-field weeding components.

KEYWORDS

paddy field, weeding wheel, blade angle, optimal composition, field test

1 Introduction

Weeds spread easily in the rice-field ecosystem and cause great harm to the growth of rice (Zhang et al., 2015; Zhang et al., 2016; Kaur et al., 2018). Weed control in paddy fields is an important part of yield assurance (Armengot et al., 2013; Pannacci and Tei, 2014). Mechanical weeding has attracted wide attention as a non-chemical weed-control method (Shaner and Beckie, 2014). It has the advantages of low labor intensity, high

work efficiency, and low cost (Fontanelli et al., 2013); it can also disturb the field soil and increase its oxygen content, promoting the growth of crop roots. Different types of weed control machinery for paddy fields have been developed, among them battery-assisted inter-row weeders (Jiao et al, 2022), self-propelled inter-row weeders (Tang et al., 2021a), and vision-based weeding robots (Wang et al., 2018). However, most of these studies focused on the light simplification and intelligent design of the whole machine rather than on the optimization of the characteristics of key components. Only a few studies have been conducted on the relationship between the structure of key weeding components and weeding performance. In actual operation, weeding machines are prone to problems such as excessive working resistance, low weeding rates, and excessive damage to crop seedlings.

In other branches of agriculture, the influence of the parameters of soil-contacting components on the working resistance and effectiveness has been studied. Fang et al. (2016) approached this problem through numerical simulation, using discrete-element methods. Bentaher et al. (2013) used three-dimensional reconstruction and the finite-element method to simulate the interaction between the plow and the soil, obtaining the working angle of the minimum resistance of the plow. These researchers assumed dryland soil, but a similar approach may be applicable to weeding in paddy fields. The soil in rice fields has a strong adhesive force, and the weeding wheel is subject to great resistance during operation. Discovering the optimal installation angle for the blade of the weeding wheel would reduce the operating resistance and improve the weeding performance.

In this study, the weeding-wheel blade-mounting angle and the field-operation parameters are optimized. The relationship between the installation angle of the weeding-wheel blade and the resistance and weeding performance of the weeding wheel is determined through theoretical analysis and simulation, and the optimal combination of parameters for weeding-wheel operation is determined through orthogonal-rotation tests. The operational performance of the weeding wheel is verified by conducting field experiments.

2 Material and methods

2.1 Overall structure of weeder

The team has developed a paddy-field inter-row weeder (Figure 1) that typically contains rake-tooth weeding wheels, a frame, front and rear vehicle wheels, a hoeing-depth-adjustment device, and related accessories (Tian et al., 2022). The most important working part is the inter-row weeding device, installed in front of the driver's seat between the front and rear wheels of the weeding machine.

The weeding device includes a square shaft, weeding wheels, and a gearbox (Figure 2A). Each weeding wheel is composed of a shaft sleeve, blades, blade-mounting seats, and side plates, as shown in Figure 2B. The width of a weeding wheel is 220 mm; its radius is designed to be 125 mm. The six blades have rake teeth; the blade length is 120 mm (Tian et al., 2021).

During operation, the weeding wheel rotates. As it enters the soil, each blade produces a downward pressure on the soil and weeds. Subsequently, when the rake tooth is unearthed, the soil and weeds are thrown back; thus, weeds are removed and the soil is loosened.

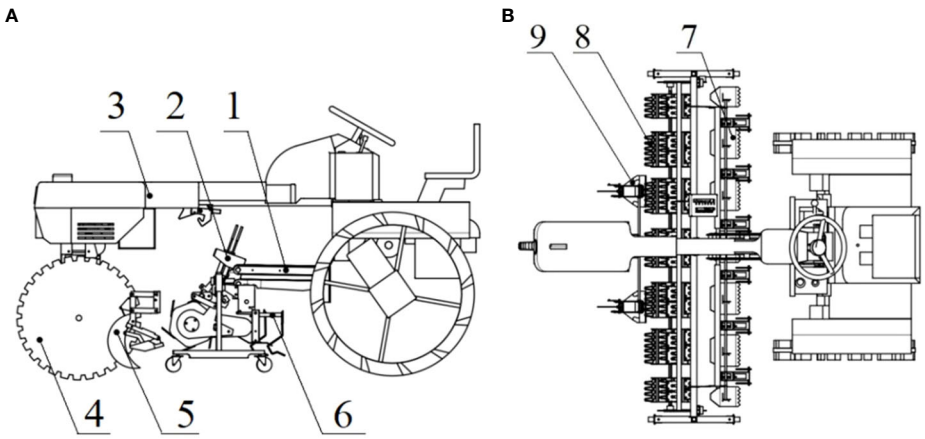

FIGURE 1
Schematic diagram of a paddy field weeding device: **(A)** top view; **(B)** bottom view. (1. Suspension device. 2. Hoeing-depth-adjusting device. 3. Frame. 4. Walking device. 5. Anti-winding knife. 6. Intra-row weeding device. 7. Mud scraper. 8. Inter-row weeding device. 9. Depth-limit plate.).

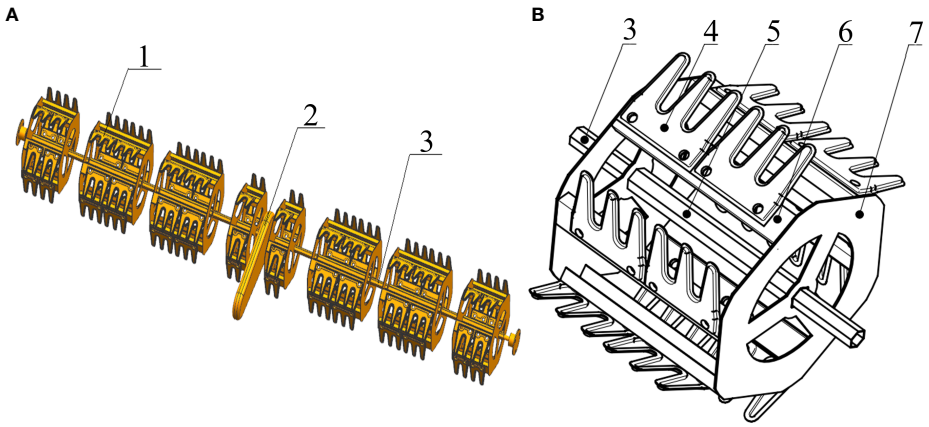

FIGURE 2
Schematic diagram of **(A)** inter-row weeding component and **(B)** individual weeding wheel (1. Weeding wheel. 2. Gear box. 3. Square shaft. 4. Rake tooth. 5. Bearing sleeve. 6. Mounting base. 7. Side plate.).

2.2 Optimization range analysis of blade parameters of weeding wheel

Each blade is installed on the hexagonal wheel at a fixed angle α. As shown in Figure 3A, stands are installed between the blades and the wheel to ensure stability; thus, α is a constant. In actual operation, the existence of the stands means thathe blades cannot be completely buried. The installation angle (α) of the blade will affect the actual penetration length, and thus the resistance to the weeding wheel during operation. Figure 3B reveals that the relationship between α and the actual penetration length of the blade is

$$S_1 = L\cos\alpha\ , \tag{1}$$

$$S = S_{max} - S_1 = S_{max} - L\cos\alpha\ , \tag{2}$$

where S_1 is the length of blade not buried, L is the length of the blade-installation side, S_{max} is the total length of the blade, and all distances are in mm.

In Eq. (2), when the total length of the blade and the installation-side length are fixed, a smaller α corresponds to a smaller S. As per an established formula (Liu et al., 2019) and Eq. (2), the resistance of the weeding wheel to cut the soil can be expressed as

$$P_c = k_c\frac{3Sv_m}{9.55\pi} = (S_{max} - L\cos\alpha)\frac{3k_cv_m}{9.55\pi}\ , \tag{3}$$

where P_c is the resistance of the weeding wheel [N], k_c is the specific energy consumption in cutting [N·m/mm ^{3}], and v_m is the forward speed of the weeding wheel as it cuts the soil [m/s].

In Eq. (3), α is the only variable. It can be seen that P_c decreases when α also decreases; when $\alpha = 0°$, the resistance of the blade to cutting the soil is the smallest.

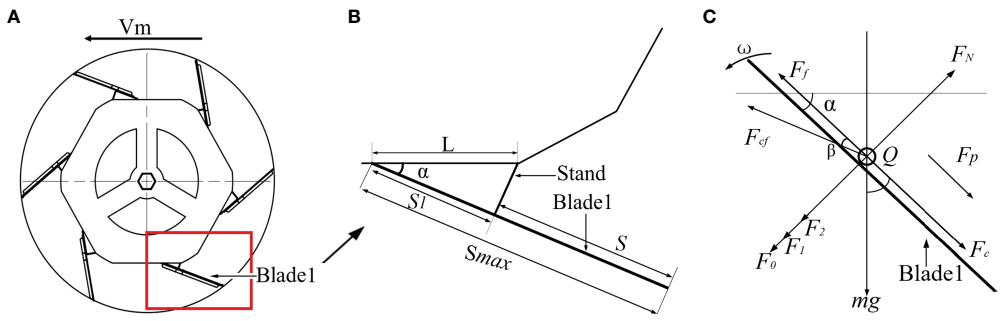

FIGURE 3
Operation of weeding wheel: **(A)** side view of wheel; **(B)** enlarged view of blade-attachment site, showing the installation angle α; **(C)** soil-particle stress-analysis diagram.

When the blade is out of the soil, any soil wrapped with weed roots that has accumulated on it will slip off under the action of gravity. Different angles of α result in different values of the sliding force, which should be maximized for the best soil-desorption effect. To explore the influence of angle on the soil particle sliding force, mechanical analysis was conducted on soil particles on the blade out of the soil, as shown in Figure 3C.

The soil particles are subjected to gravitational force $-mg$, the supporting force of the blade $-F_N$, and sliding friction F_f. (All forces are measured in newtons.) Decompose mg into a component force F_0 perpendicular to the blade downward and a component force parallel to the blade plane reveals that

$$F_0 = F_1 + F_2 = mg \cos\alpha \tag{4}$$

where F_1 is the component that provides centripetal force to the soil, and F_2 is the reaction to F_N. The normal force, F_{nf}, on soil particles can be expressed as

$$F_{nf} = ma_{nv} = F_N - F_2, \tag{5}$$

where a_{nv} is the normal relative acceleration of soil particles [m/s^2]. The normal relative force, F_1, of the soil particles can be decomposed into the centripetal force, F_{cf}, and the tangential component, F_c, of the soil-implicated movement, related by

$$F_{cf} = ma_{ta} = m\omega^2 r_Q = \frac{F_c}{\cos\beta}, \tag{6}$$

where a_{ta} is the soil-implicated acceleration [m/s^2], ω is the angular speed of the weeding wheel [rad/s], r_Q is the distance between the soil particle and the rotation center [mm], and β is the angle between the soil particles and the rotation center line and the blade plane[°]. The tangential force, F_{ta}, of the soil particles parallel to the downward direction of the blade is

$$F_{ta} = ma_{tv} = F_c + mg\sin\alpha - \mu F_N, \tag{7}$$

where a_{tv} is the tangential relative acceleration of the soil particles [m/s^2] and μ is the coefficient of sliding friction between the soil particles and the blade of weeding wheel. According to Eq. (4) – (7), the resultant force F_p of soil particles is

$$\begin{aligned} F_p &= ma_{tv} + \mu ma_{ta} sin\beta \\ &= mg\sin\alpha - \mu mg\cos\alpha + m\omega^2 r_Q \cos\beta + \mu m\omega^2 r_Q \sin\beta \end{aligned} \tag{8}$$

To find the value of α that maximizes F_p, perform the following calculation:

$$\begin{cases} f(\alpha,\beta) = F_p \\ f'_\alpha(\alpha,\beta) = 0 \\ f'_\beta(\alpha,\beta) = 0 \end{cases} \tag{9}$$

It can be drawn by calculating Eq.(9) that when α is 20°, F_p gets the maximum value.

To reduce the cutting resistance as much as possible and ensure the soil removal ability of the blade, the installation angle of the blade should be between 0° (where the resistance is smallest) and 20° (where the soil-removing ability is greatest).

2.3 Simulation test

In order to determine the best installation angle of the blade of the weeding wheel, five weeding wheel models were designed with α = 0°, 5°, 10°, 15°, 20°, and their operation was simulated and analyzed by EDEM discrete-element modeling software. Because weed growth in paddy fields is complex, directly analyzing a blade–water–soil model using simulation software is difficult. Therefore, in this study, α was evaluated from the resistance received by the weeding wheel in the process of operation and from the movement speed of soil particles.

During the weeding of paddy fields, the soil in the tillage layer is saturated with water after irrigation and bubble-field treatment. In this study, two different particle sizes were chosen to represent soil and water in the paddy soil layer. To save simulation time and reduce storage space, the simulation of soil particles was appropriately enlarged. Soil particles with a radius of 5 mm were used to simulate paddy soil, and the shear modulus of water in the simulation experiment was set to 1.0×10^8 Pa. Based on a review of the paddy-soil literature (Yang et al., 2021), Poisson's ratio of the paddy soil was taken to be 0.5, the shear modulus to be 1.0×10^8 Pa, the density to be 1860 kg/m^3, and the surface energy to be 0.15 J/m^2. The weeding wheel was made of steel, with Poisson's ratio 0.3, elastic modulus 7.0×10^{10} Pa, and density 7800 kg/m^3. To meet the requirements of the medium-tillage weeding simulation, a virtual soil tank was established with length × width × height 1000 mm × 450 mm × 100 mm, and a 20-mm-thick water layer was established on the soil tank (Jiang et al., 2020).

Table 1 lists the contact parameters of the simulation model. To ensure the continuity of the simulation process (Zhang et al., 2020), the fixed time step was set to 4.15×10^6 s (20% of the Rayleigh time step). The data storage interval was 0.01 s. After the simulation, the results were exported and analyzed using the EDEM software post-processing tool module.

Figure 4 shows the analyzed comprehensive resistance of the weeding wheels with different blade-installation angles according to the simulation results:

- When α=0°, the resistance fluctuated in the range of 40–130 N, and the average resistance was approximately 61 N.
- When α=5°, the resistance fluctuated in the range of 10–150 N, and the average resistance was approximately 68 N.

TABLE 1 Contact parameter table of simulation model.

Category	Coefficient of restitution	Coefficient of static friction	Coefficient of kinetic friction
Weeding wheel: soil	0.10	0.20	0.20
Weeding wheel: water	0.05	0.05	0.01
Soil: soil	0.05	0.05	0.05
Soil: water	0.70	0.10	0.05
Water: water	0.01	0.01	0.01

- When α=10°, the resistance fluctuated in the range of 20–150 N, and the average resistance was approximately 73 N.
- When α=15°, the resistance fluctuated in the range of 40–150 N, and the average resistance was approximately 82 N.
- When α=20°, the resistance fluctuated in the range of 40–160 N, and the average resistance was approximately 91 N.

Thus, with the increase in α, the resistance of the weeding wheel increases.

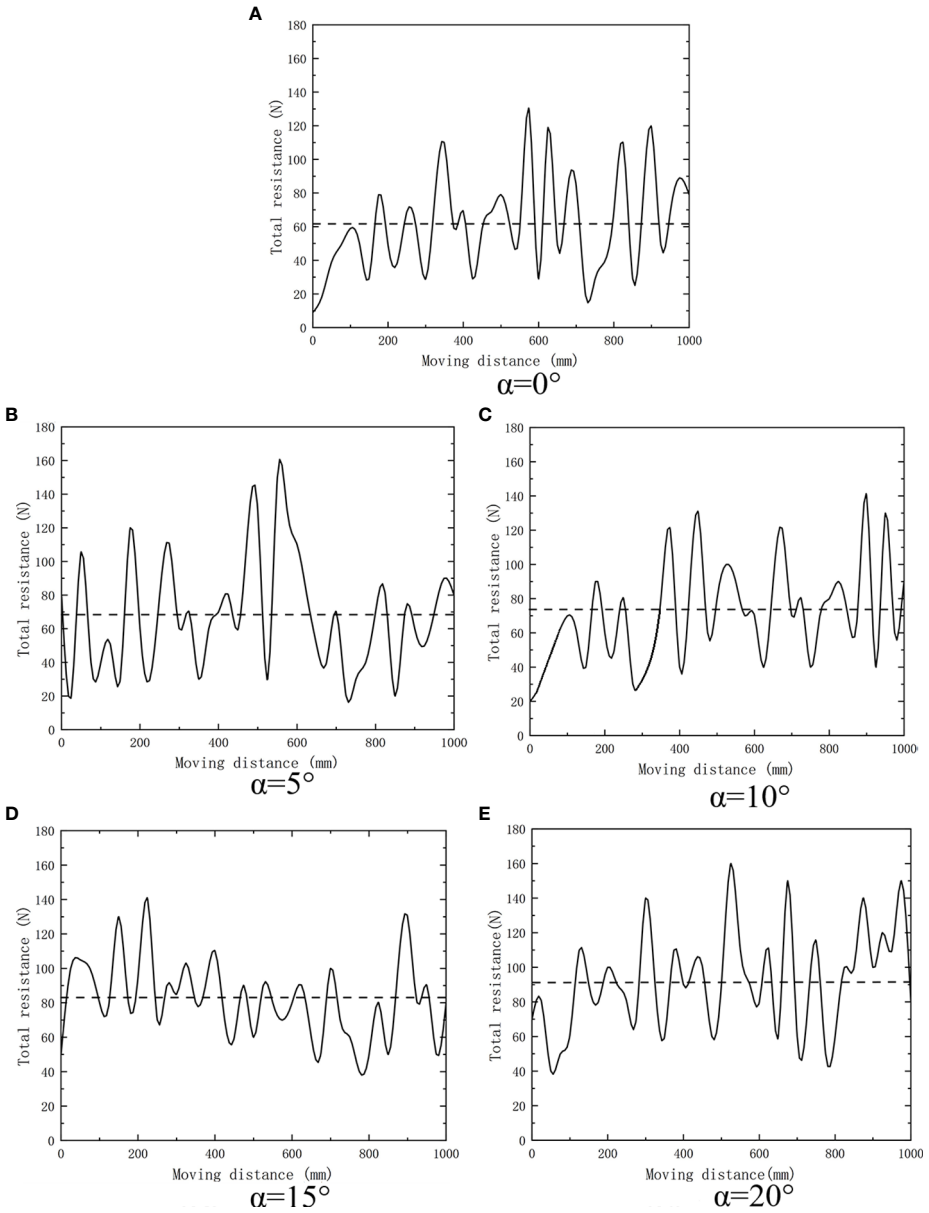

FIGURE 4
Comprehensive resistance diagram of weeding wheel at five installation angles.

Figure 5 shows the relationship between soil particle velocity and blade installation angle of weeding wheel.

During the weeding operation, the disturbance of the weeding wheel on the soil can be expressed by the velocity of the soil-particle movement:

- When α=0°, the maximum value of soil particle velocity was 3.51 m/s, and the average value was 1.81 m/s.
- When α=5°, the maximum value of soil particle velocity was 3.02 m/s, and the average value was 1.35 m/s.
- When α=10°, the maximum velocity of soil particles was 2.7 m/s, and the average velocity was 1.24 m/s.
- When α=15°, the maximum value of soil particle velocity was 2.33 m/s, and the average value was 0.9 m/s.
- When α=20°, the maximum value of soil particle velocity was 2.01 m/s, and the average value was 0.67 m/s.

It can be concluded that with the increase of α, the velocity of soil particles decreased. As α decreased, the resistance of the

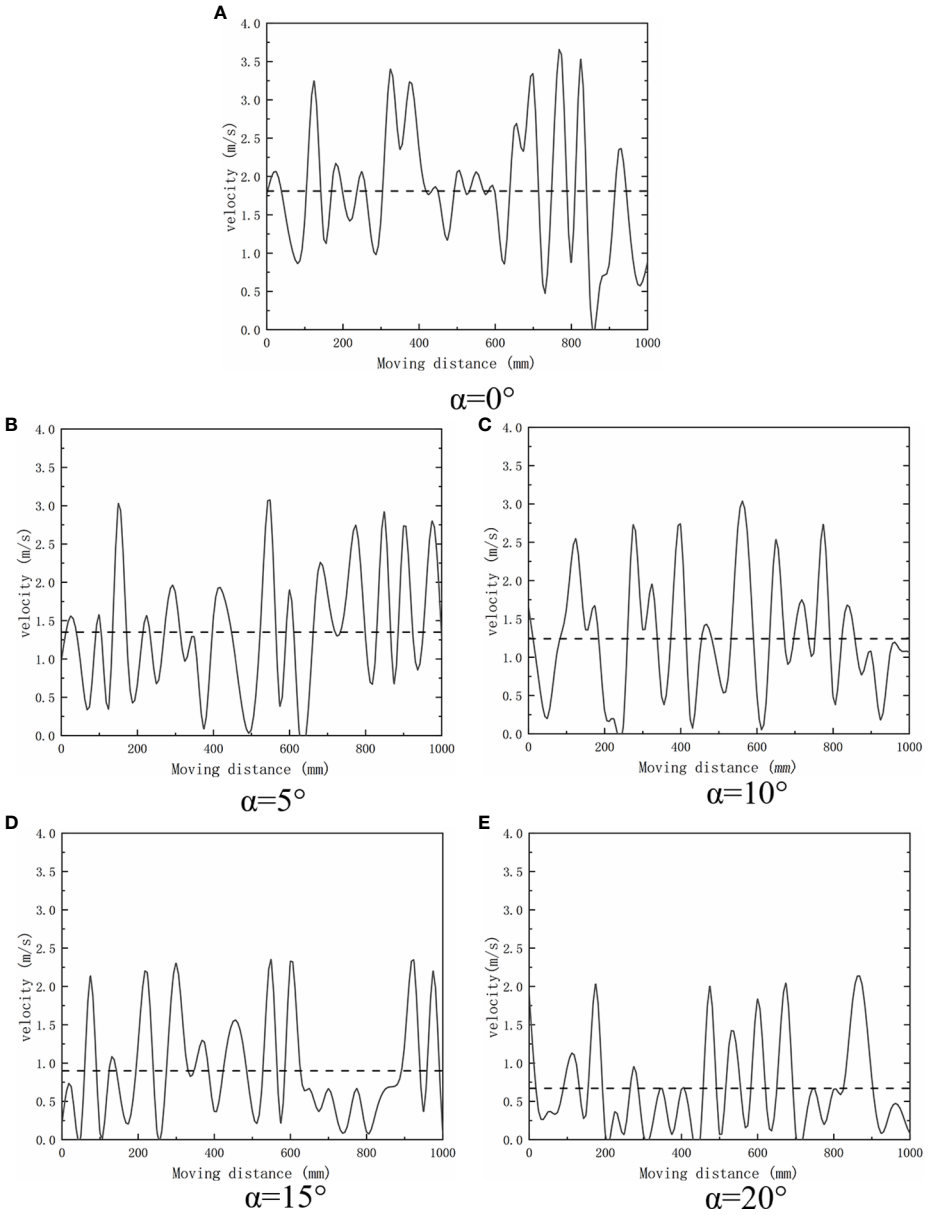

FIGURE 5
Velocity map of soil particles at five installation angles.

weeding wheel also decreased and the moving speed of the soil particles increased. When α=0°, the average resistance of the weeding wheel reached the minimum value of 61 N, and the movement speed of soil particles reached the maximum value of 3.51 m/s, as shown in Figure 6. At this time, the soil disturbance effect was the best. Therefore, the optimal value of α was 0°.

When the weeding wheel acts on the rice field, the disturbance of the soil is less when less of the blade has entered the soil. The smaller the reaction force of the soil on the blade of the weeding wheel results in less resistance of the weeding wheel. The cutting pitch of the weeding wheel also decreases, so less soil is cut in a single time, and better soil-breaking takes place. Therefore, when α=0°, the resistance of the weeding wheel is the smallest (Duan et al, 2015). The installation angle of the blade will affect the penetration angle and penetration point (Tang et al., 2021b), which in turn will affect the movement speed of soil particles. In the actual farming environment, if the penetration angle is too large, the backward movement speed of soil particles is reduced, so that the turning speed is lower than the throwing speed, resulting in backwater. Therefore, when α=0°, the penetration angle of the blade is the smallest and the movement speed of soil particles is the largest (Han et al., 2020).

3 Results and discussion

3.1 Test conditions

To verify the performance of the weeding machine designed in this study, field experiments were conducted in Fenghuang Town, Fengtai County, Huainan City, Anhui Province, China. The experiments were conducted nine days after transplantation, over a test area of ~1.4 hectares. The rice variety cultivated in the experimental field was Nanjing 9108; the average height of seedlings was 255 mm. The rice seedlings grew well, without any obvious diseases or insect pests. No herbicide was applied to the test field. The average height of the weeds was 105 mm; their average root depth was 27 mm. The average density of weeds between rows was approximately 100 plants/m^2, and the average density of weeds between plants was approximately 25 plants/m^2. Figure 7 shows the field-weeding experiment with the paddy-field weeding device.

3.2 Test method

Before weeding, the numbers of weeds and seedlings in the test area were determined. After the weeding test was completed, the numbers of weeds removed and not removed were both counted. Each group of data was collected three times, and an average was taken (Jia et al., 2021).

To verify the weeding performance of the rotary rake-tooth paddy-field weeding components designed in this study, the weeding rate (η_1) and damaged-seedling rate (η_2) were selected as the test indexes for field performance test:

$$\eta_1 = \frac{Z - Z_1}{Z} \times 100\,\%, \tag{10}$$

$$\eta_2 = \frac{M_1}{M} \times 100\,\%, \tag{11}$$

In Eqs. (10) and (11), η_1 is the percent weeding rate of the row-weeding device; Z is the total number of inter-row weeds in rice in the test area; Z_1 is the total number of residual weeds among rice rows after weeding; η_2 is the percent injury rate from weeding between rows; M_1 is the number of damaged seedlings crushed, uprooted, and lodged in the test area after the operation; and M is the total number of seedlings in test area.

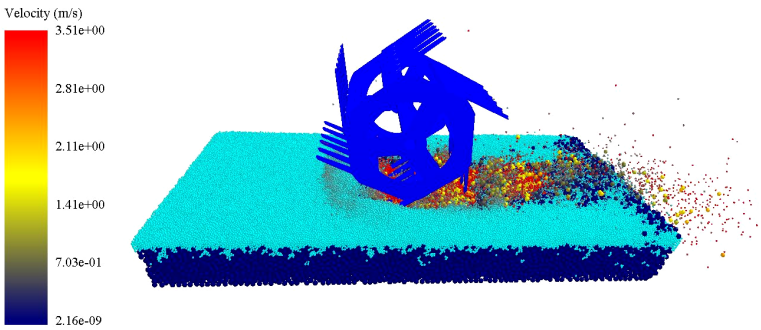

FIGURE 6
Simulation diagram of soil particle velocity at installation angle α = 0°.

FIGURE 7
Field-weeding experiment.

3.3 Experimental design

In the process of weeding, the weeding depth, rotation speed of the weeding wheel, and forward speed also affect the key factors of weeding rate and seedling injury rate. So, weeding depth A [mm], rotation speed B [r/min], and forward speed C [m/s] were used as test factors. Seedling injury rate R_1 and weeding rate R_2 were selected as test indexes. After the test, Design–Expert software was used to process the data, establish the regression equation and the optimization model, and obtain the primary and secondary relationship and the optimal combination of the influence of the test factors on the test indicators. Table 2 is the design-factor-level coding table.

3.4 Multi-factor test results and analysis

The results of the quadratic orthogonal-rotation combination test are shown in Table 3.

TABLE 2 Coding with factors and levels.

Canonical variable	Natural variable		
	Weeding Depth A/mm	Rotation Speed B/r·min^{-1}	Forward Speed C/m·s^{-1}
–Alpha	30	120	0.3
Lower-level/(-1)	34.22	145.32	0.43
Zero-level/(0)	40	180	0.6
Upper-level/(1)	45.78	241.68	0.77
+Alpha	50	240	0.9

3.4.1 Analysis of variance

F-test and variance analysis were conducted for each coefficient in the regression model. The results of variance analysis for the seedling injury rate R_1 and the weeding rate R_2 are shown in Table 4.

The data in Table 4 were subjected to quadratic multiple-regression fitting, and the quadratic-term model was selected to establish the regression model between the seedling injury rate R_1, the weeding rate R_2, and various influencing factors. The following quadratic multiple-regression equations relating R_1 and R_2 to the soil depth A, the rotation speed B of the weeding wheel and the forward speed C are obtained:

$$R_1 = 4.1 + 0.25A + 0.19B + 0.13C + 0.063AB - 0.29AC - 0.012BC + 0.21A^2 + 0.28B^2 + 0.42C^2, \quad (12)$$

$$R_2 = 88.91 + 0.0002A - 0.16B + 0.41C - 0.062AB - 0.54AC - 0.16BC - 0.80A^2 - 1.06B^2 - 0.28C^2 \quad (13)$$

As listed in Table 4, the P-values of the model-misfit terms of the objective functions R_1 and R_2 are 0.0613 and 0.0676, respectively; these are greater than 0.05, indicating no misfit factor. The aforementioned regression equation can be used to replace the real point of the test to analyze the test results.

The analysis of variance in Table 4 shows that the significant P-values of the R_1 and R_2 models are 0.0391 and 0.0221, respectively; these are less than 0.05, indicating that the model is statistically significant. For objective function R_1, factor C^2 is very obvious and factor B^2 is obvious; for objective function R_2, factors A^2 and B^2 are very obvious. The F values in Table 4 indicate the influence of each influencing factor on the test index: larger F values correspond to larger influence. From Table 3, experimental factor A was the factor exerting the most influence on R_1 and

TABLE 3 Protocols and results.

Experimental number	Experimental factor			Experimental index	
	Weeding depth A/mm	Rotation speed B/r min^{-1}	Forward speed C/m s^{-1}	Seedling injury Rate/%	Weeding rate/%
1	45.78	145.32	0.77	5	86.0
2	50.00	180.00	0.60	5.5	87.5
3	40.00	180.00	0.60	4.1	88.3
4	40.00	180.00	0.60	4.1	88.2
5	45.78	145.32	0.43	5.2	87.1
6	40.00	180.00	0.30	5.1	86.7
7	30.00	180.00	0.60	3.5	86.4
8	34.22	145.32	0.77	5.7	87.7
9	45.78	214.68	0.43	5.4	86.5
10	34.22	214.68	0.43	4.7	86.3
11	45.78	241.68	0.77	5.2	85.3
12	34.22	145.32	0.43	4.7	86.1
13	40.00	180	0.60	4.1	89.1
14	34.22	214.68	0.77	5.6	86.7
15	40	240	0.60	5.4	86.1
16	40	180	0.60	4.1	89.7
17	40	180	0.90	5.3	90.2
15	40	120	0.60	4	86.2
19	40	180	0.60	4.1	89.1
20	40	180	0.60	4.1	89.1

TABLE 4 Anova of response surface quadratic model for R_1 and R_2.

Sources of Variance	R_1						R_2					
	Sum of squares	Freedom	Mean square	*F*	*P*	Significant	Sum of squares	Freedom	Mean square	*F*	*P*	Significance
Model	6.42	9	0.71	3.28	0.0391	*	30.10	9	3.34	3.92	0.0221	*
A	0.91	1	0.91	4.17	0.0684		0.00069	1	0.00069	0.00081	0.9993	
B	0.53	1	0.53	2.44	0.1495		0.37	1	0.37	0.43	0.5252	
C	0.24	1	0.24	1.11	0.3168		2.43	1	2.43	2.85	0.1225	
AB	0.031	1	0.031	0.14	0.7125		0.031	1	0.031	0.037	0.8520	
AC	0.66	1	0.66	3.04	0.1117		2.31	1	2.31	2.71	0.1307	
BC	0.0012	1	0.0012	0.0057	0.9410		0.21	1	0.21	0.25	0.6294	
A^2	0.69	1	0.69	3.19	0.1045		9.91	1	9.91	11.63	0.0067	*
B^2	1.2	1	1.2	5.54	0.0405	*	17.70	1	17.70	20.76	0.001	**
C^2	3.01	1	3.01	13.85	0.0040	**	1.29	1	1.29	1.52	0.2465	
Residual	2.17	10	0.22				8.53	10	0.85			
Lack of fiit	2.17	5	0.43		0.0613		6.92	5	6.92	4.30	0.0676	
Pure error	0.02	5	0.03				1.61	5	1.61			
Sum	8.59	19					38.63	19	38.63			

P indicates the level of significance of test/. When P is less than 0.01, the test is highly significant, which can be symbolized with "**"; when P is less than 0.05, the test is highly significant, which can be symbolized with "*".

the least on R_2; factor C exerted the least influence on R_1 and the most on R_2.

The reason that weeding depth has the greatest impact on the rate of seedling injury is related to the characteristics of rice-root growth. Rice is a typical fibrous root plant (Chai et al., 2019). In the field experiment, when the rice roots were at the tillering stage, the lateral expansion was the largest (Lee et al., 2021); the root group was distributed in a flat oval shape in the range of 20 mm (Zheng et al., 2017; Kahriz and Kahriz, 2018), and the root length was generally between 40 and 60 mm. When the weeding depth is greater than 40 mm, the blade on the weeding roller will inevitably disturb and hurt the roots of rice seedlings (Van et al., 2008). With the movement of the roots, the seedlings will also swing towards the weeding-wheel operation area, leading to further damage. When the deepest depth of the weeding wheel increases, the thickness and area of the soil layer stirred by the weeding wheel also increases. While the weeds are buried and removed, some soil blocks are thrown onto the seedlings, so that the injury rate increases.

The reason that the weeder forward speed has the greatest impact on the weeding rate is that when the rotation speed is fixed, a slower forward speed of the machine implies that a longer time is available for the weeding wheel to work on a given length of soil, increasing the cutting frequency of the blade (Wang et al., 2021) and causing greater soil disturbance (Qi et al., 2015); therefore, the weeding effect is better.

3.4.2 Response surface methodology

According to the response surface generated by the Design-Expert software, for the seedling injury rate, the forward speed of the fixed weeding machine is 0.6 m/s; as shown in Figure 8A, when weeding depth A is 34.93 mm and rotation speed B is 170.89 r/min, the seedling injury rate has the minimum value of 3.9%. For the weeding rate, the forward speed of the fixed weeding machine is 0.6 m/s. As shown in Figure 8B, when A is 37.76 mm, B is 174.67 r/min. The maximum weeding rate is 90.2%.

Because the optimal parameter combination of each test factor of the weeding wheel is different under different indicators, it is impossible to evaluate the optimal parameter combination directly; instead, it is necessary to consider the comprehensive impact of various factors on different indicators (Li et al., 2021). The main purpose of weeding between rows in a paddy field is to eliminate young grass between rows and create favorable conditions for crop growth (Shi et al., 2021), the ideal effect of inter-row weeding is to reduce the seeding injury rate as much as possible while ensuring a high weeding rate. Therefore, the weeding rate index should be given priority. Combining literature results (Colbach et al., 2014) with the actual situation of the field experiment, the optimal parameters of the weeding operation were determined to be A = 39 mm, B = 175 r/min, C = 0.6 m/s. According to the results displayed by the Design-Expert software, in this case, the seedling injury rate is 4%, and the weeding rate is 89%.

3.5 Field verification test

On July 5, 2021, a field verification test of the weeding device was conducted in the experimental field described in subsection 3.1, using the optimal parameter combination described in subsection 3.4.2. The seedling injury rate and weeding rate were taken as the test indexes. Five repeated tests were conducted in total, and an average value was taken subsequently. Section 3.2 describes the calculation method for the test structure. Table 5 lists the processed and analyzed results.

Note that in Table 5 that the weeding rate and seedling injury rate obtained from the verification test are 88.2% and

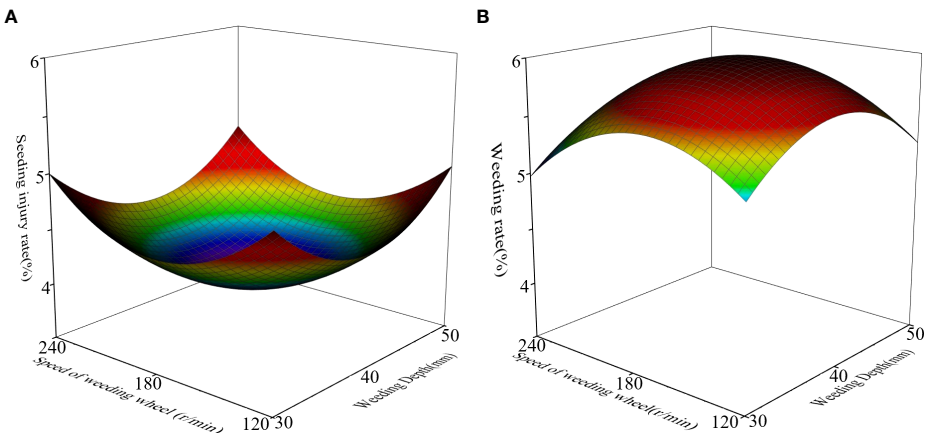

FIGURE 8
Response surfaces for **(A)** injury rate and **(B)** weeding rate.

TABLE 5 Field experiment results.

Test number	Seedling injury rate (%)	Weeding rate (%)
1	3.9	88.5
2	5.3	87.4
3	4.2	89.9
4	5.7	87.7
5	3.0	87.5
Average	4.4	88.2

4.4%, respectively, very close to the software predictions (89% and 4%). This indicates that the software optimization parameters were accurate and feasible. The weeding quality of the machine under the optimal parameter combination was clearly quite good.

4 Conclusion

Existing rice-weeding machines encounter large operating resistances in paddy fields; they have low weeding rates and high seedling-injury rates. To solve these problems, the parameters of the weeding-wheel blades should be optimized. In this study, the key components of mechanical weeding in a paddy field were analyzed. The results showed that when the blade installation angle was 0°, the blade cutting resistance was the smallest; when the blade installation angle was 20°, the blade had the strongest soil-removal ability. Therefore, the range of the installation angle of the weeding-wheel blade should be 0–20°.

EDEM, a discrete-element software, was used to construct a fluid–solid-coupling simulation model of the components and water–soil. The installation angle of the blade of the weeding wheel was taken as the test factor, and the resistance of the weeding wheel and the velocity of soil particles were taken as the test indexes. The test results showed that when the blade installation angle was 0°, the resistance of the weeding roller was the smallest and the velocity of soil particles was the largest. The average resistance was 61 N and the average velocity of soil-particle movement was 1.81 m/s. Therefore, the optimal installation angle of the weeding wheel blade was determined to be 0°.

The combination of machine operation parameters was optimized by conducting a quadratic orthogonal-rotation combination test. The results revealed that the optimal weeding depth was 39 mm, optimal rotation speed was 175 r/min, and optimal forward speed of the machine was 0.6 m/s. The field verification test showed that, for this combination of parameters, the weeding rate was 88.2% and the seedling injury rate was 4.4%, meeting the design requirements of the rice-weeding device.

In this study, the installation angle of the blade of the weeding wheel was optimized, and the effects of the three other key factors (weeding depth, rotation speed, and forward speed) on the weeding and seedling injury rates were studied. However, in actual operation, many other factors (such as the stability of the forward direction of the machine and the cutting effect of the blade on the weed-root system) will affect the weeding rate and the seedling injury rate. Therefore, further research on the effect of the working parameters of key weeding components on weeding-operation quality is needed.

Data availability statement

The original contributions presented in the study are included in the article/supplementary material. Further inquiries can be directed to the corresponding author.

Ethics statement

Written informed consent was obtained from the individual(s) for the publication of any potentially identifiable images or data included in this article.

Author contributions

KQ design the project and performed the literature research. YZ and LT acquired the main data, performed the statistical analysis, and edited the manuscript. CC and JG participated in research and analyzed simulation. CZ participated in research and analyzed the relevant mechanical data and edited the manuscript revision. All authors contributed to the article and approved the submitted version.

Funding

This work supported by the National Natural Science Foundation of China [grant numbers 52105239]; the Open Fund of State Key Laboratory of Tea Plant Biology and Utilization [grant number SKLTOF20210121]. the Anhui Province Science Foundation of China [grant numbers 2008085QE270].The Anhui Agricultural University Graduate Education Teaching Quality Engineering Project[grant number 2021YJSJY06].

Conflict of interest

The authors declare that the research was conducted in the absence of any commercial or financial relationships that could be construed as a potential conflict of interest.

Publisher's note

References

Armengot, L., Jose-Maria, L., Chamorro, L., and Sans, F. (2013). Weed harrowing in organically grown cereal crops avoids yield losses without reducing weed diversity. *Agron. Sustain. Dev.* 33 (2), 405–411. doi: 10.1007/s13593-012-0107-8

Bentaher, H., Ibrahmi, A., Hamza, E., Hamza, E., Hbaieb, M., Kantchev, G., et al. (2013). Finite element simulation of moldboard–soil interaction. *Soil. Till. Res.* 134, 11–16. doi: 10.1016/j.still.2013.07.002

Chai, H. H., Chen, F., Zhang, S. J., Li, Y. D., Liu, Z. S., Kang, ,. Y. J., et al. (2019). Multi-chamber petaloid root-growth chip for the non-destructive study of the development and physiology of the fibrous root system of oryza sativa. *Lab. .Chip* 19 (14), 2383–2393. doi: 10.1039/c9lc00396g

Colbach, N., Biju-Duval, L., Gardarin, ,. A., Granger, S., Guyot, S. H. M., Meziere, ,. D., et al. (2014). The role of models for multicriteria evaluation and multiobjective design of cropping systems for managing weeds. *Weed. Res.* 54 (6), 541–555. doi: 10.1111/wre.12112

Duan, G. Q., Chen, H. T., Li, A., Feng, Y. N., Yang, J. L., and Ji, W. Y. (2015). Effect of rotation direction of knife teeth configuration on clearing straw unit performance for no-tillage and straw mulching precision seeder. *Trans. CSAE.* 31 (12), 48–56. doi: 10.11975/j.issn.1002-6819.2015.12.007

Fang, H. M., Ji, C. ,. Y., Farman, ,. A. C., Guo, J., Zhang, Q. Y., and Chaudhry, A. (2016). Analysis of soil dynamic behavior during rotary tillage based on distinct element method. *Trans. CSAM* 47 (3), 22–28. doi: 10.6041/j.issn.1000-1298.2016.03.004

Fontanelli, M., Raffaelli, M., Martelloni, L., Frasconi, C., Ginanni, M., and Peruzzi, A. (2013). The influence of non-living mulch, mechanical and thermal treatments on weed population and yield of rainfed fresh-market tomato (Solanum lycopersicum l.). *Span. J. Agric. Res.* 11 (3), 593–602. doi: 10.5424/sjar/2013113-3394

Han, B. G, Chang, G. Y, Gao, L. Y., Liu, Q., Sun, S., and Dong, X. W. (2020). Design and experiment of soybean intra-row weeding monomer mechanism and key components. *Trans. CSAM* 51 (06), 112–121. doi: 10.6041/j.issn.1000-1298.2020.06.012

Jia, H. L., Gu, B. L., Ma, Z. Y., Liu, H. L., Wang, G., Li, M. W., et al. (2021). Optimized design and experiment of spiral-type intra-row weeding actuator for maize (Zea mays l.) planting. *Int. J. Agr. Biol. Eng.* 14 (6), 54–60. doi: 10.25165/j.ijabe.20211406.6542

Jiang, M. J., Zhang, A., and Shen, Z. F. (2020). Granular soils: from DEM simulation to constitutive modeling. *Acta Geotech* 15 (7), 1723–1744. doi: 10.1007/s11440-020-00951-7

Jiao, J. K., Wang, Z. M., Luo, H. W., Chen, ,. G. L., Liu, H. L., Guan, J. J., et al. (2022). Development of a mechanical weeder and experiment on the growth, yield and quality of rice. *Int. J. Agr. Biol. Eng.* 15 (3), 92–99. doi: 10.25165/j.ijabe.20221503.6978

Kahriz, M. P., and Kahriz, P. P. (2018). Improving seedling growth and tillering with osmotic priming treatments in rice cv. hamzadere and osmancik 97. *J. Anim. Plant Sci.* 28 (1), 92–99.

Kaur, S., Kaur, R., and Chauhan, B. S. (2018). Understanding crop-weed-fertilizer-water interactions and their implications for weed management in agricultural systems. *Crop Prot* 103, 65–72. doi: 10.1016/j.cropro.2017.09.011

Lee, H. S., Hwang, W. H., Jeong, J. H., Yang, S. Y., Jeong, N. J., and Lee, C. K. (2021). Physiological causes of transplantation shock on rice growth inhibition and delayed heading. *Sci. Rep-UK* 11 (1), 16818. doi: 10.1038/s41598-021-96009-z

Li, W. H., Li, X. G., Deng, J. Z., Wang, Y., and Guo, J. P. (2021). Sentiment based multi-index integrated scoring method to improve the accuracy of recommender system. *Expert. Sys. Appl.* 179, 115105. doi: 10.1016/j.eswa.2021.115105

Liu, D. W., Xie, F. ,. P., Ye, Q., Ren, S. G., Li, X., and Liu, M. Z. (2019). Analysis and experiment on influencing factors on power of ditching parts for 1K-50 orchard ditching. *Trans. CSAE* 35 (18), 19–28. doi: 10.11975/j.issn.1002-6819.2019.18.003

Pannacci, E., and Tei, F. (2014). Effects of mechanical and chemical methods on weed control, weed seed rain and crop yield in maize, sunflower and soyabean. *Crop Prot* 64, 51–59. doi: 10.1016/j.cropro.2014.06.001

Qi, L., Liang, Z. W., Ma, X., Tan, Y. X., and Jiang, L. K. (2015). Validation and analysis of fluid-structure interaction between rotary harrow weeding roll and paddy soil. *Trans. CSAE* 31 (5), 29–37. doi: 10.3969/j.issn.1002-6819.2015.05.005

Shaner, D. L., and Beckie, H. (2014). The future for weed control and technology. *Pest. Manage. Sci.* 70 (9), 1329–1339. doi: 10.1002/ps.3706

Shi, Y. J., Xi, X. B., Gan, H., Shan, X., Zhang, Y. F., Shen, H., et al. (2021). Design and experiment of row-controlled fertilizing-weeding machine for rice cultivation. *Agriculture* 11 (6), 527. doi: 10.3390/agriculture11060527

Tang, H., Jiang, Y. M., Wang, J. W., Guan, R., and Zhou, W. Q. (2021b). Bionic design and parameter optimization of rotating and fixed stem- and leaf-cutting devices for carrot combine harvesters. *Math. Probl. Eng* 2021 (Pt.4), 8873965.1–8873965.14. doi: 10.1155/2021/8873965

Tang, H., Xu, C. S., Wang, Q., Zhou, W., Wang, J., Xu, Y., et al. (2021a). Analysis of the mechanism and performance optimization of burying weeding with a self-propelled inter RowWeeder for paddy field environments. *Appl. Sci.* 11 (21), 9798. doi: 10.3390/app11219798

Tian, ,. L., Cao, C. M., Qin, K., Fang, L. F., and Ge, J. (2021). Design and test of post-seat weeding machine for paddy. *Int. J. Agric. Biol. Eng.* 14 (3), 112–122. doi: 10.25165/j.ijabe.20211403.5936

Tian, ,. L., Cao, C. M., Qin, K., Ge, J., and Fang, L. F. (2022). Design and experiment of self-propelled system for paddy field weeder based on the interaction mechanism of wheel-soil. *Eng. Agr* 42, 1. doi: 10.1590/1809-4430-Eng.Agric.v42n1e20210095/2022

Van, L. S., Mouazen, A. M., Anthonis, J., Ramon, H., and Saeys, W. (2008). Infrared laser sensor for depth measurement to improve depth control in intra-row mechanical weeding. *Biosys. Eng.* 100 (3), 309–320. doi: 10.1016/j.biosystemseng.2008.03.010

Wang, J., Li, X., Ma, X., Zhou, W., and Tang, H. (2018). Small tracked and remote-controlled multifunctional platform for paddy field. *Int. Agric. Eng. J.* 27, 172–182.

Wang, S., Su, D. B., Wang, Z. M., Jiang, Y. Y., Zhang, L. N., and Tan, Y. (2021). Design and experiments of the cam swing rod intra-row weeding device for lettuce farm. *Trans. CSAE* 37 (21), 34–44. doi: 10.11975/j.issn.1002-6819.2021.21.005

Yang, X. L., Liu, G., Li, Y., and Gao, S. H. (2021). Structural optimization of reciprocating seal with magnetic fluid based on orthogonal test design. *J. Magn.* 26 (2), 229–237. doi: 10.4283/JMAG.2021.26.2.229

Zhang, S. Z., Li, Y. H., Kong, C. H., and Xu, X. H. (2016). Interference of allelopathic wheat with different weeds. *Pest. Manage. Sci.* 72 (1), 172–178. doi: 10.1002/ps.3985

Zhang, S., Tekeste, M. Z., Li, Y., Gaul, A., Zhu, D. Q., and Liao, J. (2020). Scaled-up rice grain modelling for DEM calibration and the validation of hopper flow. *Biosys. Eng.* 194, 196–212. doi: 10.1016/j.biosystemseng.2020.03.018

Zhang, J. H., Yao, F. M., Hao, C., and Boken, V. (2015). Impacts of temperature on rice yields of different rice cultivation systems in southern China over the past 40 years. *Phys. Chem. Earth* 87-88, 153–159. doi: 10.1016/j.Pce.2015.08.013

Zheng, L., Luo, X. W., Zeng, S., Wang, Z. M., Liu, C. B., and QI, X. Y. (2017). Shear characteristics of rice root-soil composite. *T. CSAM.* 48(05), 63–71. doi: 10.6041/j.Issn.1000-1298.2017.05.007

frontiers | Frontiers in Plant Science

TYPE Original Research
PUBLISHED 18 October 2022
DOI 10.3389/fpls.2022.1003659

OPEN ACCESS

EDITED BY
Changyuan Zhai,
Beijing Academy of Agricultural and Forestry Sciences, China

REVIEWED BY
Wei Lu,
Nanjing Agricultural University, China
Tomàs Pallejà Cabré,
Universitat de Lleida, Spain

*CORRESPONDENCE
Yongjun Zheng
zyj@cau.edu.cn

SPECIALTY SECTION
This article was submitted to Sustainable and Intelligent Phytoprotection, a section of the journal Frontiers in Plant Science

RECEIVED 26 July 2022
ACCEPTED 30 September 2022
PUBLISHED 18 October 2022

CITATION
Yang S, Li W, Liu X, Wang Z, Zheng Y, Tan Y and Feng H (2022) Synchronous three-dimensional detection method for multiple parameters of wind fields based on vector principle. *Front. Plant Sci.* 13:1003659. doi: 10.3389/fpls.2022.1003659

Synchronous three-dimensional detection method for multiple parameters of wind fields based on vector principle

Shenghui Yang[1,2], Wenwei Li[1,2], Xingxing Liu[1,2], Zimeng Wang[1,2], Yongjun Zheng[1,2]*, Yu Tan[1,2] and Han Feng[1,2]

[1]College of Engineering, China Agricultural University, Beijing, China, [2]The Ministry of Education Engineering Research Center of Modern Agricultural Equipment and Facilities, Beijing, China

In the area of air-assisted spray, conventional detection of speed and direction of the wind fields for spray are separately conducted, and multiple kinds of sensors have to be laid on each coordinate axis during multidimensional detection. It limits the optimization of operation effect of sprayers based on wind-field distribution characteristics. This paper proposes a novel detection method to achieve synchronous measurement of wind speed and direction in three dimensions. Wind flow was considered as vectors and the sensing structure with a regular triangular pyramid shape supported by cantilever pieces was established. Strain gauges were utilized to detect the deformation in each direction by the wind thrust onto a ball before and after wind flow. Moreover, the calculation models of wind speed and direction were developed respectively based on the relationship of 'strains-force-wind pressure-wind velocity' and the principle of space operation of vectors, so multiple parameters of wind fields could be obtained simultaneously. Calibration was conducted based on a wind tunnel and the Testo 405i anemometers. The results showed that: the minimum relative error of wind-speed values was about 0.06%, while the maximum was about 10%. The average relative error of all the directions was less than 5%. Furthermore, the measurement of the wind among artificial tree canopies demonstrated that the proposed method could effectively measure both speed value and direction of the wind among canopies, and it also helped to find the wind distribution characteristics of the fan, SFG4-2R. The results highlighted both the reliability and the practical meaning of the proposed method, which could be a technical solution for measuring and evaluating wind-field characteristics of sprayers.

KEYWORDS

wind, flow fields, vector, multidimensional systems, detection, sensors

1 Introduction

Air-assisted spray, including ground air-assisted spray and Unmanned Aerial Vehicles (UAVs) spray, has been widely used for plant protection. With the help of strong wind fields, droplets are delivered onto targets. At present, droplet deposition in crop canopies is not ideal during spraying, characterizing the issues of uneven distribution, inadequate penetration and significant drift (Pascuzzi et al, 2020; Zheng et al, 2020; Zhang et al, 2020). The fundamental reason is that the attenuation law of the wind field influenced by canopies has not been clearly studied, whose core difficulty is lacking effective detection approaches for the speed and flow direction of the wind in canopies. If there is a breakthrough in the real-time detection method of wind field changes in canopies, it will be of practical significance to help to improve the effect of air-assisted spray based on detection results.

Currently, the speed and direction of wind fields are separately measured by using different types of sensors, and most studies are just about speed quantification. In terms of the measurement of wind-speed values, impeller-type, thermosensitive-type and cup-type anemometers are commonly utilized. The majority of the research was to verify the consistency between Computational Fluid Dynamics (CFD) models and trials or to investigate wind-speed distribution in certain conditions. For impeller-type anemometers, Jiyu and Yubin et al. used them to investigate the downwash wind speed of a UAV, SUMA18 (Li et al, 2015a; Li et al, 2019b), as well as the relationship between wind fields and the distribution of pollen (Li et al, 2017c) or droplets (Chen et al, 2017). The new research of this team was continuous to study the consistency between the distribution of UAV wind fields and that of droplet depositions (Lan et al, 2021; Zhan et al, 2022). All these studies mainly focused on the same type of UAV. Yang et al. (2017) conducted trials to verify the accuracy of downwash CFD models by the Kestrel 4500 anemometer, and Zhang et al. (2019a) and Guo et al. (2020) also did similar works by using Kestrel 4500 or GM8902+. For thermosensitive-type anemometers, Yang et al. (2022a) utilized Testo 405i to examine the transmission of UAV downwash in corn canopies, and Zhang et al. (2019b) also applied this anemometer to observe the conformity between downwash CFD models and the test results. In addition, Wang et al. (2021) developed a kind of thermosensitive anemometer to measure the wind field of a six-rotor UAV, while Cheng et al. (2021) used CTA-type anemometer to measure that of an unmanned helicopter. Cup-type anemometers are generally taken for agricultural meteorological measurement in outdoor conditions (Xing et al, 2015), not for air-assisted spray. Although the wind-speed sensors mentioned above in these studies have a fast response and good stability, they can only detect single-dimensional values. If three-dimensional results are required, such sensors have to be separately laid on each axis. Meanwhile, each sensor takes up space and may be interfered by each other so that the wind field shape may be affected, which will lead to inaccurate results.

In terms of wind direction measurement, wind vane sensors are conventional devices, often adopted for acquiring meteorological and environmental parameters rather than for air-assisted spray. For instance, Li et al. (2021) used wind vanes to measure the wake variation of horizontal axis wind turbine. Sharma et al. (2018) used them to estimate the accuracy of the wind resource of a site. However, wind vanes can only measure an angle from 0 to 360° in a horizontal plane, not suitable for a vertical layout. Therefore, the three-dimensional measurement of wind direction needs another approach.

In order to achieve the synchronous detection of both wind speed and wind direction, several techniques have been developed, typically ultrasonic anemometers and Micro-Electro-Mechanical System (MEMS) anemometers. Ultrasonic anemometers measure by using the frequency difference between the transmitter and the receiver, while MEMS-type ones mainly rely on the change of pressure or thermal fields. Researchers have used ultrasonic ones to measure the downwash of a UAV (Tang et al, 2019) and environmental parameters (Schramm et al, 2019) to control drifts, whilst the MEMS type is generally exploited in non-agricultural areas (Jiang, 2021). Irrespective of the ultrasonic and MEMS types, the measurement results are two-dimensional. Even though a study was related to a three-dimensional wind-field measurement device to observe the wind field of a hovering UAV (Wu et al, 2019), it described the distribution of wind-field intensity rather than wind speed, let alone wind direction. Hence, there is a shortage of the three-dimensional detection method of wind speed and direction.

In fact, if a particular substance in a specific space can be called a "field" in physics, it must consist of vectors in mathematics, and so is the wind field for air-assisted spray. Any vector in a wind field, $\vec{v}$, is composed of three basis vectors ($\vec{v}_x$, $\vec{v}_y$ and $\vec{v}_z$) on the x, y and z axes. If the length (size) and direction of each base vector can be measured, a unique wind-speed vector will be determined, and the angle between the vector and each coordinate axis will also be unique.

This paper proposes a synchronous three-dimensional detection method for multiple parameters of wind fields based on the vector principle. A novel sensing structure and its matching calculation models were developed to tackle the practical difficulty of wind-field detection in the area of air-assisted spray.

2 Materials and methods

2.1 Materials

2.1.1 Hardware

Figure 1 shows the designed system of measurement. The materials contained a smooth hollow plastic ball, three cantilever pieces, three bases, three ball seats and three carbon fiber tubes. The system was a regular triangular pyramid, and the fiber tubes were mutually perpendicular. The radius of the ball, R, was 40 mm, and its mass was only about 40 g. Moreover, Wheatstone Full Bridge was utilized on each cantilever piece to detect and measure strain variations. The strain gauges were resistive type, BFH350-6AA, and NI 9237 combined with NI Compact DAQ 9135 was employed to achieve strain data acquisition and saving. The key specifications of BFH350-6AA, NI 9237 and cantilever pieces are listed in Table 1.

When flowing around a circular sphere, fluid will form a thrust on it in the flow direction (Liu et al, 2017). Therefore, if a force change in this direction can be measured, the thrust will be obtained. Then, the wind speed value can be calculated according to the relations between force, wind pressure and wind speed.

2.1.2 Software

The data acquisition software was developed using LABVIEW 2016 (Figure 2), including real-time data collection, saving and viewing. Three data channels from three Full Bridge could be acquired separately and saved into the same document.

2.2 Measurement method of wind vector

2.2.1 Measurement of wind vector length

As shown in Figure 3, the ball center was taken as the origin, O, to establish the Sensing Coordinate System (SCS, marked by red), O-XYZ, while the center of Triangle ABC was taken as the origin, O_G, to establish the Ground Coordinate System (GCS, marked by blue), O_G-$X_GY_GZ_G$.

In the SCS, the force analysis for the cantilever piece of any direction can be equivalent to a cantilever beam model (Figure 4). Since the solution process of the force in each direction was the same, that in the X direction was taken as an instance for illustration.

In terms of the cantilever pieces, if the elastic modulus is E, the strain without flow around is ϵ_{x_0}, the bending section coefficient is W, and the distance between the two strain gauges on the same side is l, the initial component of the force generated by the gravity of both the ball and the fiber tubes in the X direction, F_{x_0}, should be

$$F_{x_0} = \frac{\epsilon_{x_0} \cdot E \cdot W}{l} \tag{1}$$

When wind flows around the ball, the strain will be changed to ϵ_{x_1}, so the component of the force in this direction, F_{x_1}, will be

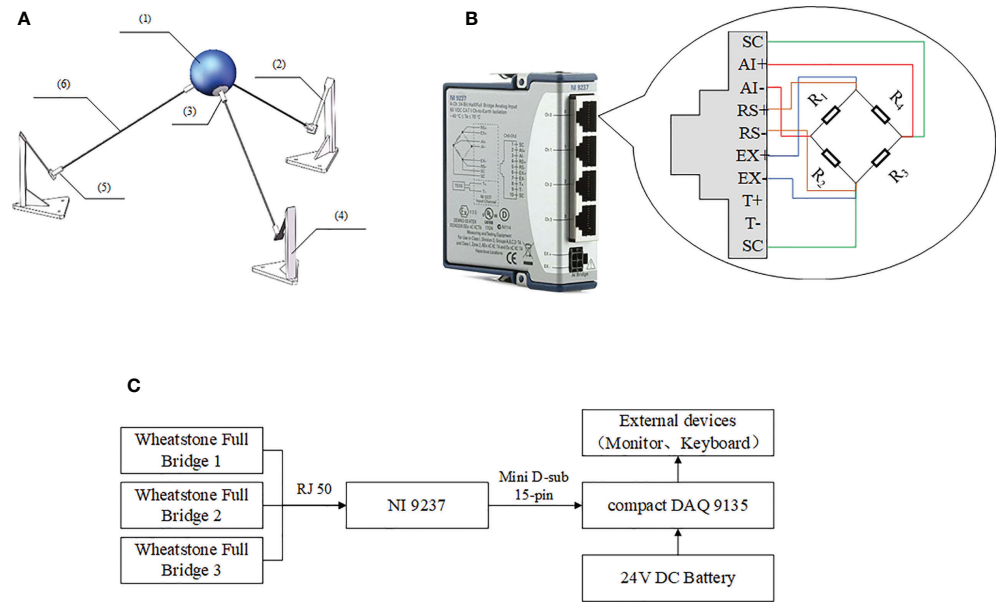

FIGURE 1
The design of the measurement scheme, where **(A)** shows the shape and materials, **(B)** shows the connection between each Wheatstone Full Bridge and NI 9237, and **(C)** shows the combination and connections of each component. (1) a smooth hollow plastic ball, (2) cantilever pieces, (3) ball seats, (4) bases, (5) jacks and (6) carbon fiber tubes.

TABLE 1 The key specifications of BFH350-6AA and NI 9237.

Materials/Device	Parameters	Values with unit	Unit/Remarks
BFH350-6AA	Resistance	350 ± 0.1	Ω
	Base length × base width	10.3×3.9	mm
	Grid length × grid width	6×2.9	mm
	Sensitivity	2.0 ± 1%	—
	Tolerance to nominal values	1000 ± 3	Ω
	Tolerance to means	≤0.5	Ω
NI 9237	Excitation	3.3	V/Four 350 Ω Full Bridges
	Sampling rate	$f_s = \frac{f_M}{256 \cdot n}$	f_M is the principal time base, and n is an integer from 1 to 31
	Accuracy	± 100	ppm·max.value^{-1}
	Excitation noise	100	μV_{rms}
	Conversion accuracy	2.9802	nV·V^{-1}·LSB^{-1}
Cantilever piece	Material	65 Mn	—
	elastic modulus	1.97×10^{11}	Pa
	Width of strain area	7.00	mm
	Thickness	0.50	mm
	Max.length of strain area	55.00	mm

$$F_{x_1} = \frac{\epsilon_{x_1} \cdot E \cdot W}{l} \tag{2}$$

The force difference between these two conditions,

F_{p_x}, is

$$F_{p_x} = F_{x_1} - F_{x_0} = \frac{EW}{l}(\epsilon_{x_1} - \epsilon_{x_0}) \tag{3}$$

In addition, the bending section coefficient, W, can be calculated by

$$W = \frac{bh^2}{6} \tag{4}$$

, where b is the width of the cantilever pieces and h is its thickness.

Thus, the force difference (which is also called the wind thrust),

F_{p_x}, should be

$$F_{p_x} = \frac{Ebh}{6l}(\epsilon_{x_1} - \epsilon_{x_0}) \tag{5}$$

According to Equation (5), the magnitude and direction of the thrust can be calculated by the strain variations.

Moreover, the relationship between force and wind pressure is

$$p_x = \frac{F_{p_x}}{A} \tag{6}$$

, where A is the flow area, equal to the surface area of the ball in this study: $A=4\pi R^2$.

The relation between the wind pressure and wind speed is (Liu et al, 2021):

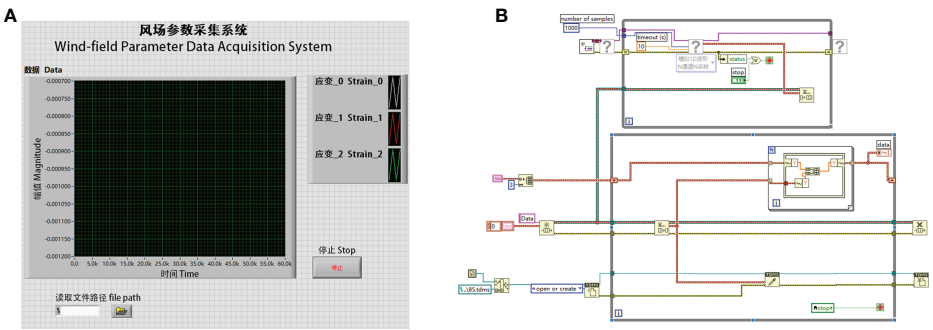

FIGURE 2
The developed software, where **(A)** is the interface of the software and **(B)** is the LABVIEW code of it.

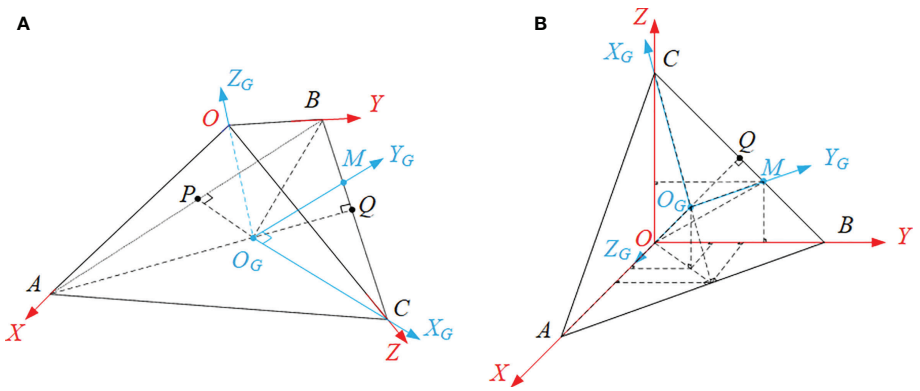

FIGURE 3
The coordinate systems, including the Sensing Coordinate System (marked by red), *O*-*XYZ*, and the Ground Coordinate System (marked by blue), O_G-$X_GY_GZ_G$, where **(A)** is the standard view of the coordinate systems whilst **(B)** is the oblique axonometric drawing for the convenience of calculation.

$$p_x = \frac{v_x^2}{1600} \times 10^3 \tag{7}$$

Hence, based on the Equations from (5) to (7), if $\vec{i} = (1, 0, 0)$ is the unit base vector of the X direction in the SCS, the wind vector of this direction, $\overrightarrow{v_x}$, should be

$$\overrightarrow{v_x} = \sqrt{\frac{200Ebh^2\left|\epsilon_{x_1} - \epsilon_{x_0}\right|}{3\pi lR^2} \times 10^{-3}} \cdot \frac{\epsilon_{x_1} - \epsilon_{x_0}}{\left|\epsilon_{x_1} - \epsilon_{x_0}\right|} \cdot \vec{i}, \text{ or}$$

$$\overrightarrow{v_x} = \begin{cases} \left(\sqrt{\frac{200Ebh^2\left(\epsilon_{x_1} - \epsilon_{x_0}\right)}{3\pi lR^2} \times 10^{-3}}, 0, 0\right), \epsilon_{x_1} > \epsilon_{x_0} \\ \left(-\sqrt{\frac{200Ebh^2\left(\epsilon_{x_0} - \epsilon_{x_1}\right)}{3\pi lR^2} \times 10^{-3}}, 0, 0\right), \epsilon_{x_1} < \epsilon_{x_0} \end{cases}$$

For the same reason, that of the Y and Z directions in the SCS should be

$$\overrightarrow{v_y} = \sqrt{\frac{200Ebh^2\left|\epsilon_{y_1} - \epsilon_{y_0}\right|}{3\pi lR^2} \times 10^{-3}} \cdot \frac{\epsilon_{y_1} - \epsilon_{y_0}}{\left|\epsilon_{y_1} - \epsilon_{y_0}\right|} \cdot \vec{j}, \text{ or}$$

$$\overrightarrow{v_y} = \begin{cases} \left(0, \sqrt{\frac{200Ebh^2\left(\epsilon_{y_1} - \epsilon_{y_0}\right)}{3\pi lR^2} \times 10^{-3}}, 0\right), \epsilon_{y_1} > \epsilon_{y_0} \\ \left(0, -\sqrt{\frac{200Ebh^2\left(\epsilon_{y_0} - \epsilon_{y_1}\right)}{3\pi lR^2} \times 10^{-3}}, 0\right), \epsilon_{y_1} < \epsilon_{y_0} \end{cases} \tag{9}$$

$$\overrightarrow{v_z} = \sqrt{\frac{200Ebh^2\left|\epsilon_{z_1} - \epsilon_{z_0}\right|}{3\pi lR^2} \times 10^{-3}} \cdot \frac{\epsilon_{z_1} - \epsilon_{z_0}}{\left|\epsilon_{z_1} - \epsilon_{z_0}\right|} \cdot \vec{k}, \text{ or}$$

$$\overrightarrow{v_z} = \begin{cases} \left(0, 0, \sqrt{\frac{200Ebh^2\left(\epsilon_{z_1} - \epsilon_{z_0}\right)}{3\pi lR^2} \times 10^{-3}}\right), \epsilon_{z_1} > \epsilon_{z_0} \\ \left(0, 0, -\sqrt{\frac{200Ebh^2\left(\epsilon_{z_0} - \epsilon_{z_1}\right)}{3\pi lR^2} \times 10^{-3}}\right), \epsilon_{z_1} < \epsilon_{z_0} \end{cases} \tag{10}$$

Finally, based on the Equations from (8) to (10), the three-directional wind vector and its length can be calculated by

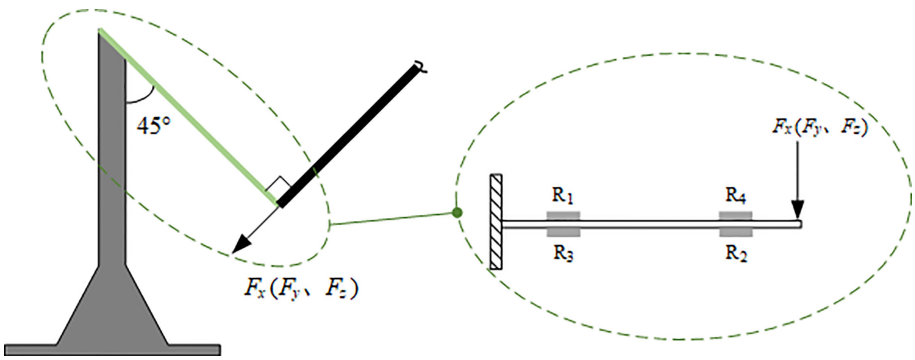

FIGURE 4
The force analysis of the cantilever pieces of the three directions of the Sensing Coordinate System.

Equation (11) and Equation (12):

$$\overrightarrow{v} = \overrightarrow{v_x} + \overrightarrow{v_y} + \overrightarrow{v_z} \tag{11}$$

$$\overrightarrow{|v|} = \sqrt{\frac{200Ebh^2}{3\pi lR^2} \times 10^{-3} \times \left(\left|\epsilon_{x_1} - \epsilon_{x_0}\right| + \left|\epsilon_{y_1} - \epsilon_{y_0}\right| + \left|\epsilon_{z_1} - \epsilon_{z_0}\right|\right)} \tag{12}$$

Equation (12) shows that the measurement result of wind speed is only related to the strains before and after flow when the components of the device are fixed, which means the external conditions have less influence on wind speed measurement.

2.2.2 Measurement of wind vector direction

If the angle between any wind vector and the unit base vectors of the three axes of the GCS can be calculated, the direction of this wind vector will be determined. Therefore, each point in Figure 3 was firstly coordinated in the same coordinate system, the SCS, and then the principle of vector coordinate operation was applied to obtain the results.

If the edge length of the pyramid is κ, the coordinate of Point A, Point B and Point C will be (κ,0,0), (0, κ,0) and (0,0, κ), respectively. According to geometric relations, the coordinate of Point M and Point O_G should be $(0, \frac{2\kappa}{3}, \frac{\kappa}{3})$ and $(\frac{\kappa}{3}, \frac{\kappa}{3}, \frac{\kappa}{3})$, respectively. Hence, the vectors $\overrightarrow{O_GC}$, $\overrightarrow{O_GM}$ and $\overrightarrow{O_GO}$ can be solved and then unitized to be the unit base vectors of the GCS, $\overrightarrow{x_G}$, $\overrightarrow{y_G}$ and $\overrightarrow{z_G}$. Equation (13) are these unit base vectors:

$$\begin{cases} \overrightarrow{x_G} = \dfrac{\overrightarrow{O_GC}}{\left|\overrightarrow{O_GC}\right|} = \left(-\frac{\sqrt{6}}{6}, -\frac{\sqrt{6}}{6}, \frac{\sqrt{6}}{3}\right) \\ \overrightarrow{y_G} = \dfrac{\overrightarrow{O_GM}}{\left|\overrightarrow{O_GM}\right|} = \left(-\frac{\sqrt{2}}{2}, \frac{\sqrt{2}}{2}, 0\right) \\ \overrightarrow{z_G} = \dfrac{\overrightarrow{O_GO}}{\left|\overrightarrow{O_GO}\right|} = \left(-\frac{\sqrt{3}}{3}, -\frac{\sqrt{3}}{3}, -\frac{\sqrt{3}}{3}\right) \end{cases} \tag{13}$$

Finally, based on the Equations from (8) to (13), the direction of the wind vector can be calculated as follows:

$$\begin{cases} \cos\alpha = \dfrac{\overrightarrow{x_G}\cdot\overrightarrow{v}}{\left|\overrightarrow{x_G}\right|\left|\overrightarrow{v}\right|} = -\frac{\sqrt{6}}{6} \cdot \dfrac{\sqrt{\left|\epsilon_{x_1}-\epsilon_{x_0}\right|}\frac{\epsilon_{x_1}-\epsilon_{x_0}}{\left|\epsilon_{x_1}-\epsilon_{x_0}\right|} + \sqrt{\left|\epsilon_{y_1}-\epsilon_{y_0}\right|}\frac{\epsilon_{y_1}-\epsilon_{y_0}}{\left|\epsilon_{y_1}-\epsilon_{y_0}\right|} - 2\sqrt{\left|\epsilon_{z_1}-\epsilon_{z_0}\right|}\frac{\epsilon_{z_1}-\epsilon_{z_0}}{\left|\epsilon_{z_1}-\epsilon_{z_0}\right|}}{\sqrt{\left|\epsilon_{x_1}-\epsilon_{x_0}\right|+\left|\epsilon_{y_1}-\epsilon_{y_0}\right|+\left|\epsilon_{z_1}-\epsilon_{z_0}\right|}} \\ \cos\beta = \dfrac{\overrightarrow{y_G}\cdot\overrightarrow{v}}{\left|\overrightarrow{y_G}\right|\left|\overrightarrow{v}\right|} = -\frac{\sqrt{2}}{2} \cdot \dfrac{\sqrt{\left|\epsilon_{x_1}-\epsilon_{x_0}\right|}\frac{\epsilon_{x_1}-\epsilon_{x_0}}{\left|\epsilon_{x_1}-\epsilon_{x_0}\right|} - \sqrt{\left|\epsilon_{y_1}-\epsilon_{y_0}\right|}\frac{\epsilon_{y_1}-\epsilon_{y_0}}{\left|\epsilon_{y_1}-\epsilon_{y_0}\right|}}{\sqrt{\left|\epsilon_{x_1}-\epsilon_{x_0}\right|+\left|\epsilon_{y_1}-\epsilon_{y_0}\right|+\left|\epsilon_{z_1}-\epsilon_{z_0}\right|}} \\ \cos\varphi = \dfrac{\overrightarrow{z_G}\cdot\overrightarrow{v}}{\left|\overrightarrow{z_G}\right|\left|\overrightarrow{v}\right|} = -\frac{\sqrt{3}}{3} \cdot \dfrac{\sqrt{\left|\epsilon_{x_1}-\epsilon_{x_0}\right|}\frac{\epsilon_{x_1}-\epsilon_{x_0}}{\left|\epsilon_{x_1}-\epsilon_{x_0}\right|} + \sqrt{\left|\epsilon_{y_1}-\epsilon_{y_0}\right|}\frac{\epsilon_{y_1}-\epsilon_{y_0}}{\left|\epsilon_{y_1}-\epsilon_{y_0}\right|} + \sqrt{\left|\epsilon_{z_1}-\epsilon_{z_0}\right|}\frac{\epsilon_{z_1}-\epsilon_{z_0}}{\left|\epsilon_{z_1}-\epsilon_{z_0}\right|}}{\sqrt{\left|\epsilon_{x_1}-\epsilon_{x_0}\right|+\left|\epsilon_{y_1}-\epsilon_{y_0}\right|+\left|\epsilon_{z_1}-\epsilon_{z_0}\right|}} \end{cases} \tag{14}$$

, where α, β and φ are the angles between the wind vector and the X_G, Y_G and Z_G axes of the Ground Coordinate System, respectively.

According to Equation (14), in terms of this determined design, the direction of wind vectors is associated with neither the material characteristics of the cantilever pieces nor the geometric features of the devices, only related to the strains before and after wind flow. Thus, the external influence of direction measurement has been kept to a minimum in theory to reduce errors.

2.3 Experiment schemes

2.3.1 Calibration

Figure 5A shows the wind tunnel used for calibration, which is located on the East Campus of China Agricultural University. The air volume is adjustable at most 60000 $m^3 \cdot h^{-1}$, and the diameter of the air outlet is 555 mm. As shown in Figure 5B, the measurement device was placed about 0.5 m in front of the center of the air outlet to ensure full flow.

Eight-level air volumes were applied, including 1869 $m^3 \cdot h^{-1}$, 2386 $m^3 \cdot h^{-1}$, 3534 $m^3 \cdot h^{-1}$, 4260 $m^3 \cdot h^{-1}$, 5191 $m^3 \cdot h^{-1}$, 6134 $m^3 \cdot h^{-1}$, 7448 $m^3 \cdot h^{-1}$ and 8399 $m^3 \cdot h^{-1}$. The data were collected for more than 1 minute under each air volume condition. The maximum speed from the wind tunnel was approximately 14 $m \cdot s^{-1}$, while that from ground air-assisted sprayers and Unmanned Aerial

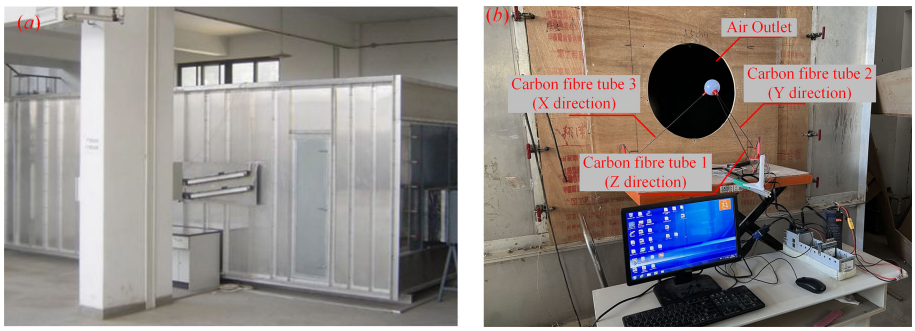

FIGURE 5
The utilized equipment and settings of the calibration tests, where **(A)** shows the used wind tunnel and **(B)** shows the layout of the tests.

Vehicles is generally less than about 12 m·s^{-1} (Yang et al, 2020b). Hence, the range of calibration was sufficient.

Figure 6 shows the process of the tests. Firstly, the measurement device collected the strains of three dimensions. Then, a thermal anemometer, Testo 405i by Testo Germany (Table 2), was used to measure the wind speed along the three fiber tubes, respectively. Finally, the wind speed data were calculated, and the calibration equations by the regression between measurement system results and anemometer ones were established.

After that, the eight-level air volumes were applied again to examine the calibration effect. The regression between the calibrated system results and the anemometer ones was conducted once more to analyze relevance. Meanwhile, the relative errors of the three-directional measurement were indicated, respectively.

2.3.2 Measurement of the wind among tree canopies

After calibration, the system was exploited to measure the wind among tree canopies. The wind was from an axial-flow fan, SFG4-2R, which is commonly used on small Chinese air-assisted ground sprayers. As shown in Figure 7, the ball was placed among the artificial trees, and the distance from the fan to the tree was about 1.20 m. The process was: ①starting the measurement system, ② turning on the fan to reach the rated speed (2800 r·min^{-1}), and ③switching off the fan. Real feature of the wind in canopies was investigated, and the data was collected for about 10 seconds.

2.4 Data processing methods

2.4.1 Data processing for calibration

In stable wind condition, the measured strains and wind speeds significantly fluctuated around a mean. Therefore, Global Average Method (GAM) was applied to process the data from both the wind measurement system and the anemometer, as shown in Equation (15):

$$\overline{v} = \frac{\sum_{i=1}^{n} v_i}{n} \tag{15}$$

Furthermore, the regression and relative errors Equation (16) were calculated using ORIGIN 2018. The data from the anemometer were taken as the standard to make comparisons of accuracy:

$$e = \frac{\left| e_{ane} - e_{sys} \right|}{e_{ane}} \tag{16}$$

, where e is the relative error, e_{ane} is the data from the anemometer and e_{sys} is that from the measurement system.

2.4.2 Data processing for in-canopy wind measurement

Due to wind variation caused by canopies, the measured strains were not fluctuated around a global mean. However, in a certain small period, strains still fluctuated around a local mean. Hence, Local Average Method (LAM) was utilized to process the data.

If the length of the data was U and the grouping interval was u, the local mean was calculated by Equation (17):

$$v_{k+i} = \frac{\sum_{i=1}^{u} x_{i+ku}}{u} \tag{17}$$

, where $k = 0, 1, \ldots, \frac{U}{u} - 1$. Then, the vector components in the GCS were calculated by Equation (18):

$$\begin{cases} \overrightarrow{v_{x_G}} = \overrightarrow{v} \cdot \cos\alpha \\ \overrightarrow{v_{y_G}} = \overrightarrow{v} \cdot \cos\beta \\ \overrightarrow{v_{z_G}} = \overrightarrow{v} \cdot \cos\varphi \end{cases} \tag{18}$$

Finally, the wind vectors were drawn by MATLAB 2019b based on their both starting points and GCS components.

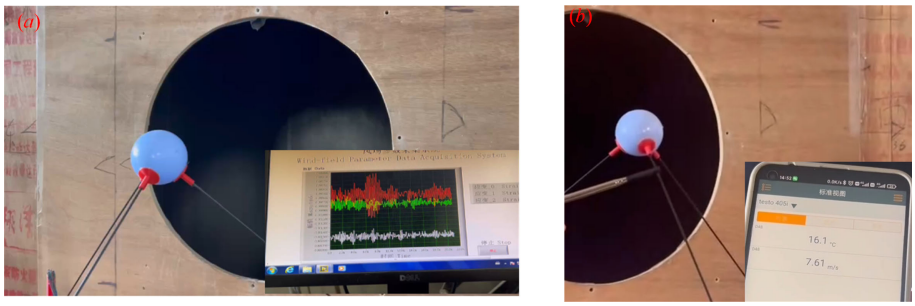

FIGURE 6
The process of the tests, where **(A)** shows the process of the measurement system and **(B)** shows that of the thermal anemometer.

TABLE 2 The key specifications of the thermal anemometer, Testo 405i.

Parameters	Values	Remarks
Measurement Range	0-30 m·s^{-1}	
Sampling Frequency	0.5 Hz	
Resolution	0.01 m·s^{-1}	
Accuracy	±(0.1 m·s^{-1} +5% Measured Value)	0-2 m·s^{-1}
	±(0.3 m·s^{-1} +5% Measured Value)	2-15 m·s^{-1}

3 Results and discussions

3.1 Calibration results

Figure 8, 9 are the collected data from the measurement system and the anemometer, respectively.

Figure 10 shows the regression for calibration. The adjusted R^2 was 0.98678, 0.95953 and 0.96997, respectively, indicating a significant relevance of the results between the thermal anemometer and the measurement system.

According to Figure 10, the calibration equations for each direction of the Sensing Coordinate System were:

$$\begin{cases} Z = 1.00354z + 0.12686 \\ Y = 1.16564y - 0.5876 \\ X = 0.99875x + 0.05868 \end{cases} \quad (19)$$

, where z, y and x are the data from Tube 1, Tube 2 and Tube 3, respectively, while Z, Y and X are that from the thermal anemometer.

Table 3 lists the result comparison between the anemometer and the calibrated measurement system using Equation (19). Three decimal places were kept based on the accuracy of the anemometer.

Figure 11 is the regression between the anemometer and the calibrated measurement results.

According to Table 3 and Figure 11, it can be illustrated that:

(1) the relevance after calibration was greatly improved. The adjusted R^2 was up to 0.99524, 0.99618 and 0.98237 (Figure 11), respectively. Meanwhile, all the slope values were about 1 and the intercepts were lower than 0.07. The calibration was proper.

(2) the proposed synchronous detection method and system could accurately and effectively measure wind speed, as the minimum relative error was about 0.06%, while the maximum error was about 10% (Table 3). The average relative error of all the directions of the SCS was less than 5%. Although the relative errors seemed to vary greatly, the maximum difference was only 1.4 m·s^{-1} in terms of the top wind speed of 14 m·s^{-1}. In other words, the absolute error was still small enough.

(3) compared with the results from the anemometer, the proposed method and system could obtain the direction of wind flow since the calculated positive or negative values obviously indicated it (Table 3). Thus, it is achieved to acquire wind speed and wind direction synchronously.

3.2 Measurement of the wind among tree canopies

Figure 12 demonstrates the results of measurement of in-canopy wind, indicating that:

(1) The system could clearly present the three stages of the trial (①, ② and ③ in Figure 12A) and the variation of wind. In addition, one signal cycle was about 160 ms, so the grouping interval in Equation (17), u, was set as 160 for the LAM processing.

(2) The system could effectively measure both speed value and direction of the wind between canopies (Figure 12B). The wind speed in X direction was the core (about from -2.5 m·s^{-1} to -3.5 m·s^{-1}), while that in the other two directions was approximately equal in absolute value (between 1.0 m·s^{-1} and 1.5 m·s^{-1}). Meanwhile, the wind direction could be known based on the sign of the values. Thus, the wind in the X and Y direction

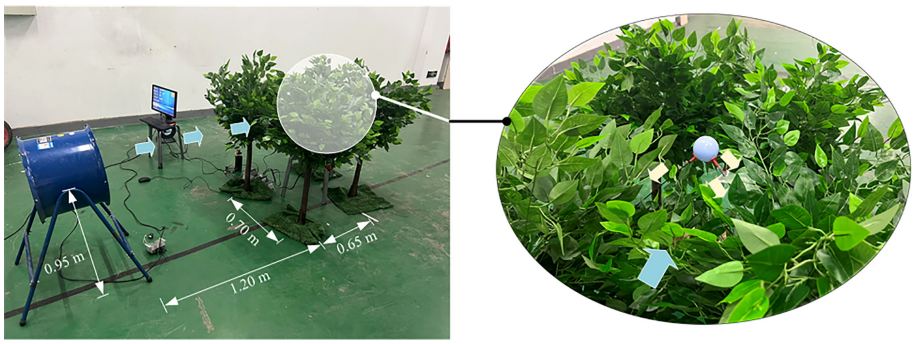

FIGURE 7
The setting of measurement of the wind among canopies.

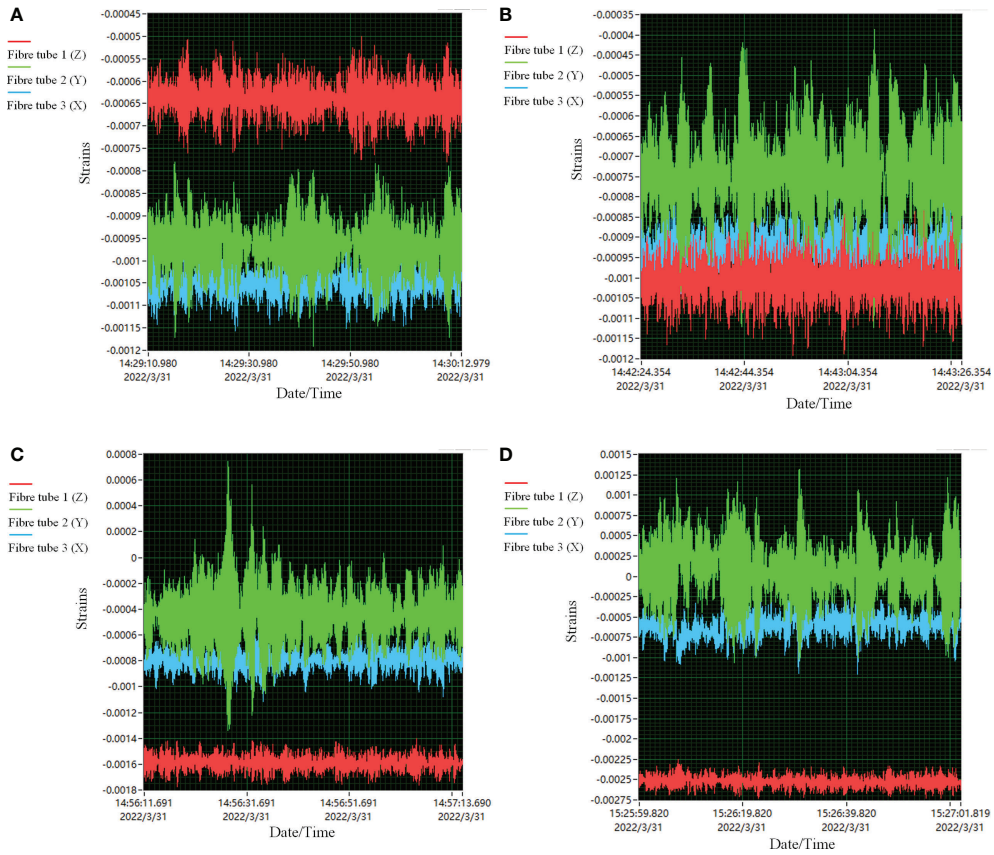

FIGURE 8
Some of the strain data collected by the measurement system, where the air volumes were 2386 $m^3 \cdot h^{-1}$, 4260 $m^3 \cdot h^{-1}$, 6134 $m^3 \cdot h^{-1}$ and 8399 $m^3 \cdot h^{-1}$ from **(A–D)**, respectively.

of the SCS was upward along the tube, while that in the Z direction of the SCS was downward.

(3) The wind field of the fan was not strictly parallel to the ground (Figure 12C). Wind vectors were at an angle with the X, Y and Z direction, which might be caused by canopy obstruction and mechanical accuracy of the fan (such as assembly accuracy and levelling). At the end of data acquisition (after about the 38th data number), the vector pointed in the opposite direction due to the elasticity of the cantilever pieces. Thus, the system could reflect the whole process of the pieces from compression (wind blowing) to recovery (stopping blowing).

(4) The resultant wind speed was about 3 $m \cdot s^{-1}$, within the range from about 2.25 $m \cdot s^{-1}$ to 3.75 $m \cdot s^{-1}$(Figure 12D). The fluctuation might result from the elasticity of the cantilever pieces and the cycle of fan rotation. Combined with Figure 12C, it is identified that the wind between canopies was relatively stable when the fan was working.

Based on the results, if the fan is used to conduct air-assisted spray parallel to the ground, it should get attention to the possibility of excessive droplet depositions and drifts at the upper regions of target tree canopies.

3.3 Discussions

In this paper, a detection method for multiple parameters of wind-field was developed. The idea was inspired by the practice (Yang et al, 2022a) and the literature review (Yang et al, 2019c) by the authors. According to calibrations, the average measurement error of wind-speed values was small (less than 5%), and wind direction could also be synchronously detected. In addition, the real application for measuring the wind between canopies generated by the fan, SFG4-2R, justified that the method could not only directly obtain the speed and direction of wind fields but also help analyze wind-field distributions of specific air-assisted devices. This highlights the practical application value of the proposed method and system. Thus, the method was able to effectively deal with the issue of synchronous three-dimensional measurement of wind speed and direction.

Moreover, it is a common difficulty for not only agricultural but non-agricultural fields to achieve simultaneous detection of wind speed and direction in three dimensions. Combined with a novel structure for wind sensing and its calculation models on

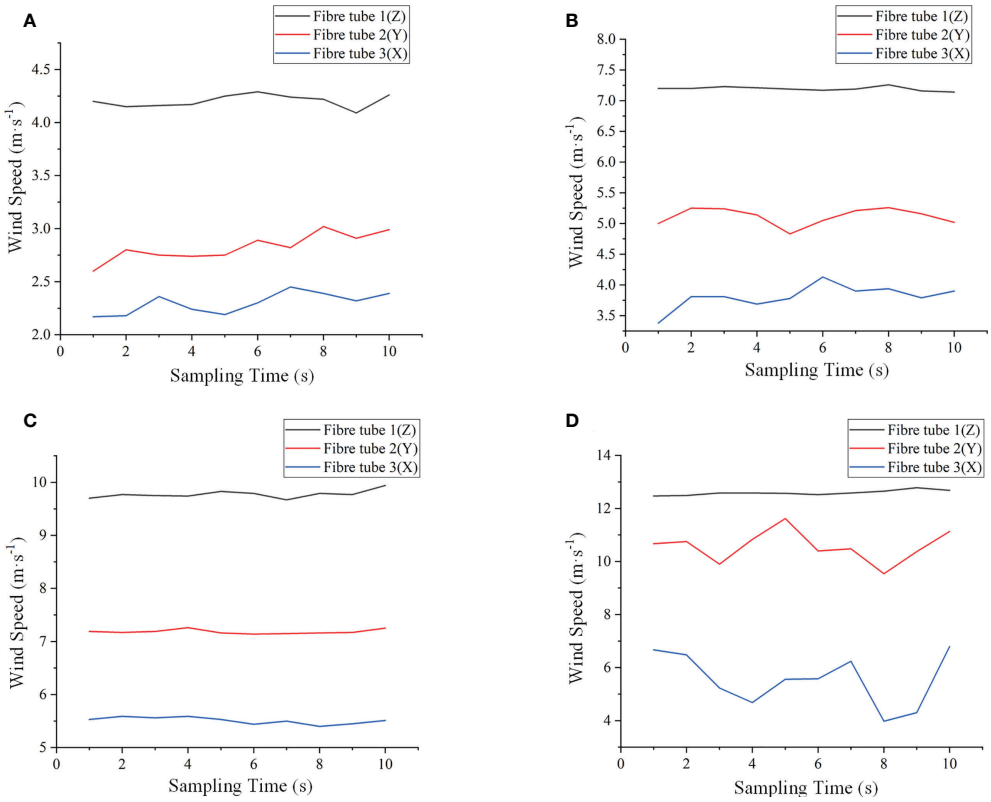

FIGURE 9
Some of the wind speed data from the thermal anemometer, where the air volumes were 2386 $m^3 \cdot h^{-1}$, 4260 $m^3 \cdot h^{-1}$, 6134 $m^3 \cdot h^{-1}$ and 8399 $m^3 \cdot h^{-1}$ from **(A–D)**, respectively.

the basis of the relations between strains and wind speed (from strains to wind thrust to wind pressure to wind speed), stereo wind measurement could be achieved based on the vectors calculated by strains, which means that the method is general and adequate for any wind-field measurement within the sensing range, not only restricted to be used in air-assisted spray conditions. For instance, for the ventilation design of nursery pig houses, the conventional approach for Computational Fluid Dynamics (CFD) verification was just by evaluating wind speed errors (Fang et al, 2022). It might be better to use the proposed method to obtain wind speed and direction at the same time to achieve multi-parameter verifications. In terms of mining, sufficient wind speed can dilute harmful gases to ensure the safety of operators, so it is important to measure accurate wind speed in downhole situations. Compared with the previous contribution (Xue et al, 2022), this proposed method could give 3D results while ensuring accuracy, and then help to predict the potential spatial distribution of gas. If the method

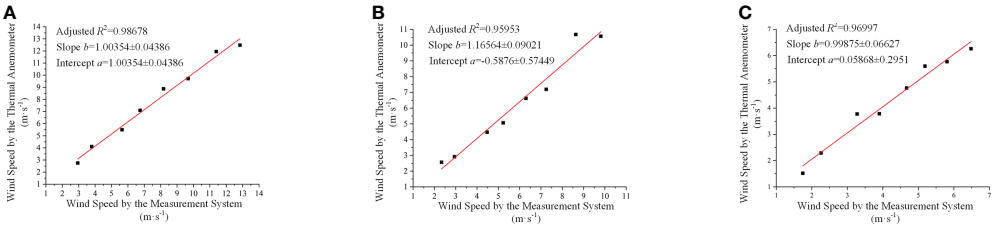

FIGURE 10
The regressions between the thermal anemometer and the measurement system, where **(A–C)** correspond to Carbon Fibre Tube 1, Carbon Fibre Tube 2 and Carbon Fibre Tube 3, respectively.

TABLE 3 The wind speed by the thermal anemometer and the calibrated measurement system.

Air Volume ($m^3 \cdot h^{-1}$)	Wind Speed by the Proposed Measurement System ($m \cdot s^{-1}$)			Wind Speed by the Thermal Anemometer ($m \cdot s^{-1}$)			Relative Error(%)		
	Fibre Tube 1(Z)	Fibre Tube 2(Y)	Fibre Tube 3(X)	Fibre Tube 1(Z)	Fibre Tube 2(Y)	Fibre Tube 3(X)	Fibre Tube 1(Z)	Fibre Tube 2(Y)	Fibre Tube 3(X)
1869	3.075	-1.970	-1.712	2.828	2.150	1.782	8.751	8.370	3.901
2386	3.865	-2.827	-2.181	4.097	2.748	2.285	5.655	2.886	4.547
3534	5.820	-4.532	-3.381	5.963	4.528	3.153	2.405	0.084	7.235
4260	6.852	-5.535	-3.743	6.493	5.502	4.169	5.527	0.606	10.211
5191	8.286	-6.702	-4.720	8.479	6.671	4.826	2.279	0.458	2.203
6134	9.804	-7.789	-5.148	9.775	7.774	5.495	0.298	0.193	6.319
7448	11.419	-9.929	-5.154	11.649	10.324	5.256	1.978	3.829	1.933
8399	12.938	-10.817	-6.416	12.838	10.616	6.412	0.776	1.893	0.062
Average Relative Error (%)							3.458	2.290	4.551

is applied to measure the wind fields with a speed of more than 15 m/s, the materials of cantilever pieces and the calibration range should be changed.

Furthermore, it should be pointed out that an open wind tunnel was exploited for calibration, which was the ONLY resource that can be found during the epidemic, even though a closed one may be more suitable due to low turbulence and uniformed wind. Nonetheless, it was not caused by the limitation of the method itself and can be addressed. For future study, a closed wind tunnel and higher precision anemometers will be taken as standard devices for conducting much more precise calibrations.

In addition, different cantilever piece materials may form different vibration periods because of elasticity, which may influence data processing approaches. In the follow-up study, the effect of cantilever piece materials can be further analyzed. However, irrespective of any materials, the calculation of wind speed and wind direction (the equations from (8) to (14)) will not change. Only the variable values will differ, while the developed method is a general detection technique. Moreover, the impact of the system size could be further analyzed and adjusted based on measurement demand, while this paper mainly focuses on the feasibility and reliability of this new method. Therefore, these two issues were not examined in this paper.

4 Conclusions

This paper proposes a novel synchronous detection method with a regular triangular pyramid shape supported by cantilevers to deal with the difficulty of multi-parameter and multi-dimensional measurement of wind fields. The wind vector principle was utilized to develop the calculation models of values and directions of wind fields, which was related to the relationship of 'strains-force-wind pressure-wind velocity' and that of space operation of vectors, and tests were conducted. The conclusions are:

(1) Thermal anemometers (Testo-405i) and an open wind tunnel were used for calibration. Results showed that the minimum relative error of wind-speed value measurement was

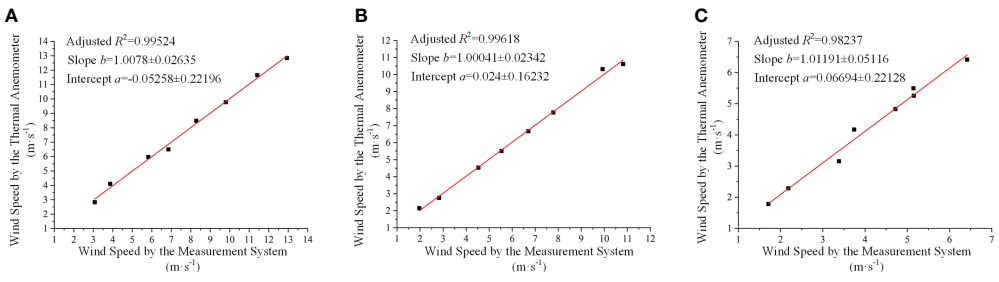

FIGURE 11
The regression between the anemometer and the calibrated measurement results, where **(A–C)** correspond to Carbon Fibre Tube 1, Carbon Fibre Tube 2 and Carbon Fibre Tube 3, respectively.

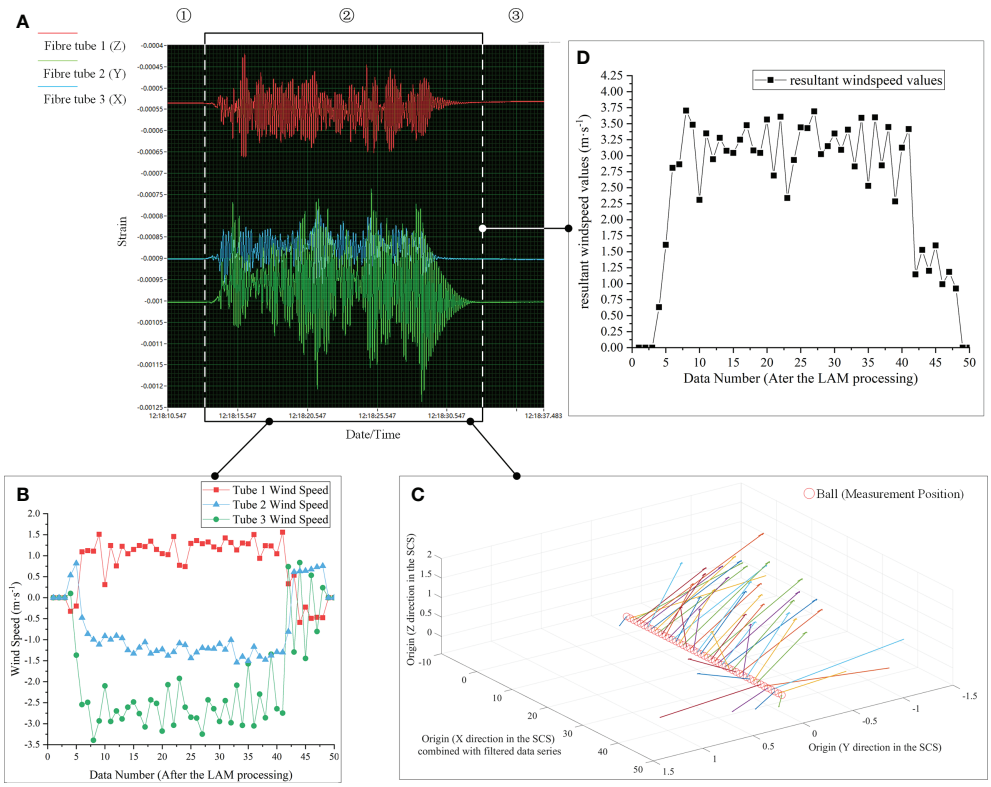

FIGURE 12
The result of measurement of the wind among tree canopies, where **(A)** is the strains measured by the system, **(B)** shows the wind speed of each SCS direction after the LAM processing, **(C)** illustrates the wind vector variations based on the LAM-processed data series, and **(D)** gives the resultant wind speed values based on each direction results shown in **(B)**.

about 0.06%, while the maximum was about 10%. The average relative error of all the directions was less than 5%. It could be illustrated that the proposed method had a good measurement accuracy.

(2) The measurement of the wind among artificial tree canopies demonstrated that the proposed method could effectively measure both speed value and direction of the wind among canopies. Wind vectors could be clearly shown. Moreover, the possibility of bias-to-upper-part depositions and drifts of the fan, SFG4-2R, should be noticed according to the results using the method.

The results highlighted the value of practical application of this approach and showed a technical system solution for evaluating wind-field characteristics of air-assisted sprayers based on three-dimensional simultaneous measurement.

Data availability statement

The original contributions presented in the study are included in the article/supplementary material. Further inquiries can be directed to the corresponding author.

Author contributions

SY: Design, Methodology, Experiments, Data Processing and Manuscript Writing. WL: Design, Coding and Experiments. XL: Design and Discussions. ZW: Scheme and Discussions. YZ: Supervision and Funding. YT: Supervision and Funding. HF: Experiments. All authors contributed to the article and approved the submitted version.

Acknowledgments

This study was funded by the National Natural Science Foundation of China (NSFC, 32171901) and the Research Innovation Fund for Graduate Students of China Agricultural University (2020XYZC38A). The wind tunnel used in the paper was supported by College of Water Resources and Civil Engineering, China Agricultural University. NI 9237 and compact DAQ 9135 used in the paper were supported by the team of Professor Zhenghe SONG and Bin XIE, College of Engineering, China Agricultural University. Meanwhile,

thanks to Doctor Changkai WEN for specific details of the devices.

Conflict of interest

The authors declare that the research was conducted in the absence of any commercial or financial relationships that could be construed as a potential conflict of interest.

Publisher's note

All claims expressed in this article are solely those of the authors and do not necessarily represent those of their affiliated organizations, or those of the publisher, the editors and the reviewers. Any product that may be evaluated in this article, or claim that may be made by its manufacturer, is not guaranteed or endorsed by the publisher.

References

Cheng, S. J., Reza, A. D., Yu, S.-H., Choi, Y., and Lee, J. (2021). Mean and turbulent flow characteristics of downwash air flow generated by a single rotor blade in agricultural drones. *Comput. Electron. Agric.* 190. doi: 10.1016/j.compag.2021.106471

Chen, S. D., Lan, Y. B., Bradley, K. F., Li, J. Y., Liu, A. M., and Mao, Y. D. (2017). Effect of wind field below rotor on distribution of aerial spraying droplet deposition by using multi-rotor UAV. *Trans. Chin. Soc. Agric. Machinery* 48 (08), 105–113. doi: 10.6041/j.issn.1000-1298.2017.08.011

Fang, J. L., Wu, S., Wu, Z. D., and Ba, W. G. (2022). CFD simulation of vertical ventilation and optimal design of wind shield in nursery pig house. *J. Northeast Agric. Univ.* 53 (5), 59–68. doi: 10.19720/j.cnki.issn.1005-9369.2022.05.007

Guo, Q., Zhu, Y., Tang, Y., Hou, C., He, Y., Zhuang, J. J., et al. (2020). CFD simulation and experimental verification of the spatial and temporal distributions of the downwash airflow of a quad-rotor agricultural UAV in hover. *Comput. Electron. Agric.* 172, 105343. doi: 10.1016/j.compag.2020.105343

Jiang, Y. T. (2021). *Research on stability and reliability of MEMS thermal wind sensors. master dissertation* (China: Southeast University), 1–73. Available at: https://kns.cnki.net/KCMS/detail/detail.aspx?dbname=CMFD202201&filename=1022468133.nh.

Lan, Y. B., Qian, S. C., Chen, S. D., Zhao, Y. J., Deng, X. L., Wang, G. B., et al. (2021). Influence of the downwash wind field of plant protection UAV on droplet deposition distribution characteristics at different flight heights. *Biosyst. Eng.* 11 (12), 2399. doi: 10.3390/agronomy11122399

Li, J. Y., Lan, Y. B., Wang, J. W., Chen, S. D., Huang, C., Liu, Q., et al. (2017c). Distribution law of rice pollen in the wind field of small UAV. *Int. J. Agric. Biol. Eng.* 10 (4), 32–40. doi: 10.25165/j.ijabe.20171004.3103

Li, J. Y., Shi, Y. J., Lan, Y. B., and Guo, S. (2019b). Vertical distribution and vortex structure of rotor wind field under the influence of rice canopy. *Comput. Electron. Agric.* 159, 140–146. doi: 10.1016/j.compag.2019.02.027

Liu, Z. J., Zhang, P. Z., Shen, K., and Ni, P. D. (2021). Research on micro meteorological measurement method of power grid based on MEMS. *Electronic Measurement Technol.* 44 (19), 36–390. doi: 10.19651/j.cnki.emt.2107210

Liu, C., Zhao, Z., Du, L. D., and Fang, Z. (2017). Method of measuring two-dimensional wind based on diametrical pressure differences developed by flow around cylinder. *J. Electron. Inf. Technol.* 39 (3), 737–742. doi: 10.11999/JEIT160468

Li, Q., Wang, Y., Kamada, Y., Takao, M., and Cai, C. (2021). Diagonal inflow effect on the wake characteristics of a horizontal axis wind turbine with gaussian model and field measurements. *Energy* 7), 121692. doi: 10.1016/j.energy.2021.121692

Li, J. Y., Zhou, Z. Y., Lan, Y. B., Hu, L., Zang, Y., Liu, A. M., et al. (2015a). Distribution of canopy wind field produced by rotor unmanned aerial vehicle pollination operation. *Trans. Chin. Soc. Agric. Eng. (Transactions CSAE)* 31 (3), 77–86. doi: 10.3969/j.issn.1002-6819.2015.03.011

Pascuzzi, S., Bulgakov, V., Santoro, F., Anifantis, A. S., Ivanovs, S., and Holovach, I. (2020). A study on the drift of spray droplets dipped in airflows with different directions. *Sustainability* . 12 (11), 4644. doi: 10.3390/su12114644

Schramm, M. W., Hanna, H. M., Darr, M. J., Hoff, S. J., and Steward, B. L. (2019). Measuring sub-second wind velocity changes for agricultural drift one meter above the ground. *Am. Soc. Agric. Biol. Engineers (ASABE)* 5). doi: 10.13031/AEA.12264

Sharma, P. K., Warudkar, V., and Ahmed, S. (2018). A comparative analysis of wind resource parameters using WAsP and windPRO. *Int. J. Green Energy* 16 (2), 152–166. doi: 10.1080/15435075.2018.1550783

Tang, Q., Zhang, R., Ding, C., Chen, L., and Deng, W. (2019). Application of ultrasonic anemometer array to field measurements of the downwash flow of an agricultural unmanned helicopter. *Trans. ASABE* 62 (5), 1219–1230. doi: 10.13031/trans.13336

Wang, L., Hou, Q., Wang, J. P., Wang, Z. W., and Wang, S. M. (2021). Influence of inner tilt angle on downwash airflow field of multi-rotor UAV based on wireless wind speed acquisition system. *Int. J. Agric. Biol. Eng.* 14 (6), 19–26. doi: 10.25165/j.ijabe.20211406.6477

Wu, Y., Qi, L., Zhang, H., Musiu, E., Yang, Z. P., and Wang, P. (2019). Design of UAV downwash airflow field detection system based on strain effect principle. *Sensors* 19 (11), 2630. doi: 10.3390/s19112630

Xing, H. Y., Yu, X., Zou, S. P., and Zhao, C. (2015). Analysis and design of the experiment box for the starting wind velocity threshold calibration of cup anemometer. *Chin. J. Sci. Instrument* 36 (9), 1996–2004. doi: 10.19650/j.cnki.cjsi.2015.09.010

Xue, S., Li, P. J., Li, D. L., and Qi, Y. (2022). Ultrasonic downhole wind speed detection method based on time difference method. *Morden Min.* 38 (03), 240–243. doi: 10.3969/j.issn.1674-6082.2022.03.062

Yang, S. H., Tang, Q., Zheng, Y. J., Liu, X. X., Chen, J., and Li, X. L. (2020b). Model migration for CFD and verification of a six-rotor UAV downwash. *Int. J. Agric. Biol. Eng.* 13 (4), 10–18. doi: 10.25165/IJABE.V13I4.5569

Yang, F. B., Xue, X. Y., Zhang, L., and Sun, Z. (2017). Numerical simulation and experimental verification on downwash air flow of six-rotor agricultural unmanned aerial vehicle in hover. *Int. J. Agric. Biol. Eng.* 10 (4), 41–53. doi: 10.25165/j.ijabe.20171004.3077

Yang, S. H., Xu, P. F., Jiang, S. J., and Zheng, Y. J. (2022a). Downwash characteristics and analysis from a six-rotor unmanned aerial vehicle configured for plant protection. *Pest Manage. Sci.* 78 (4), 1707–1720. doi: 10.1002/ps.6790

Yang, S. H., Zheng, Y. J., and Liu, X. X. (2019c). Research status and trends of downwash airflow of spray UAVs in agriculture. *Int. J. Precis. Agric. Aviation* 2 (1), 1–8. doi: 10.33440/j.ijpaa.20190201.0023

Zhan, Y. L., Chen, P. C., Xu, W. C., Chen, S. D., Han, Y. F., Lan, Y. B., et al. (2022). Influence of the downwash airflow distribution characteristics of a plant protection UAV on spray deposit distribution. *Agronomy-Based* 216, 32–45. doi: 10.1016/j.biosystemseng.2022.01.016

Zhang, H. Y., Lan, Y. B., Wen, S., Xu, Y. T., and Yu, F. H. (2020). Research progress in rotor airflow model of plant protection UAV and droplet motion mechanism. *Trans. Chin. Soc. Agric. Eng. (Transactions CSAE)* 36 (22), 1–12. doi: 10.11975/j.issn.1002-6819.2020.22.001

Zhang, H., Qi, L. J., Wu, Y. L., Cheng, Z. Z., Liu, W. W., Elizabeth, M., et al. (2019b). Distribution characteristics of rotor downwash airflow field under spraying on orchard using unmanned aerial vehicle. *Trans. Chin. Soc. Agric. Eng. (Transactions CSAE)* 35 (18), 44–54. doi: 10.11975/j.issn.1002-6819.2019.18.006

Zhang, H., Qi, L. J., Wu, Y. L., Liu, W. W., Cheng, Z. Z., and Musiu, E. (2019a). Spatio-temporal distribution of down-wash airflow for multi-rotor plant protection UAV based on porous model. *Trans. Chin. Soc. Agric. Machinery* 50 112–122 (02). doi: 10.6041/j.issn.1000-1298.2019.02.012

Zheng, Y. J., Chen, B. T., Lyu, H. T., Kang, F., and Jiang, S. J. (2020). Research progress of orchard plant protection mechanization technology and equipment in China. *Trans. Chin. Soc. Agric. Eng. (Transactions CSAE)* 36 (20), 110–124. doi: 10.11975/j.issn.1002-6819.2020.20.014

frontiers | Frontiers in Plant Science

TYPE Original Research
PUBLISHED 03 November 2022
DOI 10.3389/fpls.2022.1019017

OPEN ACCESS

EDITED BY
Wei Qiu,
Nanjing Agricultural University, China

REVIEWED BY
Xavier Frank,
Institut National de recherche pour l'agriculture, l'alimentation et l'environnement (INRAE), France
Manas Ranjan Sahoo,
ICAR-Indian Institute of Horticultural Research, India

*CORRESPONDENCE
Zhang Guozhong
zhanggz@mail.hzau.edu.cn

SPECIALTY SECTION
This article was submitted to Sustainable and Intelligent Phytoprotection, a section of the journal Frontiers in Plant Science

RECEIVED 14 August 2022
ACCEPTED 11 October 2022
PUBLISHED 03 November 2022

CITATION
Wanru L, Guozhong Z, Yong Z, Haopeng L, Nanrui T, Qixin K and Zhuangzhuang Z (2022) Establishment of discrete element flexible model of the tiller taro plant and clamping and pulling experiment.
Front. Plant Sci. 13:1019017.
doi: 10.3389/fpls.2022.1019017

Establishment of discrete element flexible model of the tiller taro plant and clamping and pulling experiment

Liu Wanru[1,2], Zhang Guozhong[1,2]*, Zhou Yong[1,2], Liu Haopeng[1,2], Tang Nanrui[1,2], Kang Qixin[1,2] and Zhao Zhuangzhuang[1,2]

[1]College of Engineering, Huazhong Agricultural University, Wuhan, China, [2]Key Laboratory of Agricultural Equipment in Mid-Lower Yangtze River, Ministry of Agriculture and Rural Affairs, Wuhan, China

The taro harvesting process is affected by a complex system composed of particle mechanics system and multi-body dynamics system. The discrete element method(DEM) can effectively solve the nonlinear problem of the interaction between harvesting components and working materials. Therefore, the discrete element model of taro tiller plants is of great importance for taro harvesting. This paper proposes a simulation method to establish a discrete element flexible plant model and dynamic clamping and pulling process of taro tiller plant. Discrete Element models of taro corm and flexible tiller petiole and leaf were established using DEM method, and the discrete element flexible model of the taro plant was established. Taro clamping and pulling force testing platform was designed and built. The single factor and Plackett-Burman experiments were used to determine the simulation parameters and optimize the taro plant model by taking the correlation coefficient of clamping force and correlation coefficient of pulling force collected from the simulation and the bench experiment as the experiment index. The parameter calibration results of discrete element model of taro plant are as follows: petiole-petiole method/tangential contact stiffness was 8.15×10^{9} N·m^{-3}, and normal/tangential critical stress was 6.65×10^{6} Pa. The contact stiffness of pseudostem- corm method was 1.22×10^{9} N·m^{-3}, the critical stress of normal/tangential was 1.18×10^{5} Pa, and the energy of soil surface was 4.15×10^{6}J·m^{-3}. When the pulling speed is 0.1, 0.2, 0.3, 0.4 and 0.5 m·s^{-1}, the correlation coefficients between the simulation experiment and the bench experiment are 0.812, 0.850, 0.770, 0.697 and 0.652, respectively. The average value of correlation coefficient is 0.756, indicating that the simulated discrete element plant model is close to the real plant model. The discrete element model of taro plant established in this paper has high reliability. The final

purpose of this paper is to provide a model reference for the design and optimization of taro harvester by discrete element method.

KEYWORDS

taro, discrete element flexible model, parameter variation, clamping and pulling force, bench experiment, simulation experiment

1 Introduction

Taro is the most important food crop and cash crop of Araceae, and is the staple food of nearly 70 million people in the world (Andreas and Waqainabete, 2018; Aditika et al., 2022). It has a higher starch content than potatoes, sweet potatoes, cassava, etc. (Singla et al., 2020). Taro is native to India (Wang et al., 2012). By 2020, the harvested area of African taro was about 1.6088 million hectares, accounting for 88.91 percent of the world's planted area. Chinese taro is mainly distributed in the Yangtze River basin, Pearl River Basin and Yellow River basin (Li et al., 2022). Harvesting is an important stage in the process of taro production presently done by digging and clamping. Excavating harvest is a segment-type harvest. First, the thick petiole of the plant is cut off, and then the root and petiole harvester are used to excavate taro corm. This process requires two operations, which is inefficient. Gripper harvesting is combined harvesting, where the belt of the harvester grabs the leaf petiole and pulls the taro out by the roots, then the petiole is cut off by a rotating blade. This way of harvesting can be completed at one time, this way of operation efficiency is high, so the clamping taro harvest is the future harvest taro important way of harvesting (Zhou et al., 2015; Zhu et al., 2022). the research and development cycle of equipment is long, and the cost of processing and trial production is high. Traditional test methods cannot accurately analyze taro plants' force and movement during harvesting. Therefore. It is of great significance for the optimal design of key components of the taro harvester to study the stress and movement of taro plants under the plant-machine-soil interaction in the process of pulling taro by digital simulation method.

The clamping and pulling mechanical system together with taro plants, soil and other microscopic granular materials constitute a complex physical field system with multi-spatial scale coupling. Evaluating the accuracy of clamping resistance and pulling resistance in taro harvesting has an important impact on the design of the taro harvester, optimization of key components and power system of taro harvesting equipment, and evaluation of operation quality and efficiency. The discrete element method can effectively simulate the nonlinear relationship between the interaction between harvesting components and working materials (Ma et al., 2015; Guo et al., 2021). The key to taro clamping and pulling simulation's success is using accurate material parameters and particle contact model (Liu et al., 2022). Compared with rice, wheat and maize, corm crops such as taro and potato are also very important food sources for humans. However, the recent research on corm crops using the discrete element method focuses on corm modeling in potato (Liu et al., 2018) and Cyperus edulis root- corm and soil (HE et al., 2022). Yang et al. (2022) established a discrete meta-model of cassava petiole and applied it to the simulation of pre-cut cassava planter seeding; Chen et al. (2022) established the discrete element model of cassava seed stem and carried out the simulation test of vibration seed dispersing mechanism. Yu Qingxu et al. established the discrete element model of *Panax notoginseng* seeds and carried out the planting test, which proved that *Panax notoginseng* seeds could be used in the discrete element simulation experiment (Yu, 2019; Yu et al., 2020; Yu et al., 2022). Liu (2021) established the discrete element model of sweet potato corm and carried out the simulation of sweet potato transport device.

Due to the lack of discrete element model of corm crops, the development of contact mechanics model between corm crops and agricultural machinery and various agricultural materials is limited, and the in-depth multidimensional research on the internal mechanism of corm crop-soil-machine and tool interaction has been affected. Therefore, this study's key is to construct a discrete element flexible model for the taro plant and explore the dynamic mechanical behavior of taro clamping and pulling under plant-machine-soil interaction. Taro plant has anisotropic, inhomogeneous, and petiole tillering characteristics. When using discrete element method to estabish taro plant model, the simple rules of spherical particles cannot be simulated with the complex shape outline rules such as taro particle collision and friction between features, so the discrete element model of the local petioles and corms cannot meet the needs of taro pulling performance simulation. Currently, there is no literature report on the establishing a discrete element model of the taro plant, and its interaction with soil and machine has also not been solved.

This paper proposed a simulation method to establish a discrete element flexible plant model and dynamic clamping and

pulling process of taro tiller plant. which can reduce the testing cost and shorten the design process in the structural design of the taro harvester. The remainder of the article is organized as follows. Section 2 introduces the discrete element flexible model of taro tiller plant established by EDEM, and the parameters were calibrated by single factor experiment and Plackett-Burman experiment. The practicability of the taro plant model was verified, and the pulling force of the taro plant were explored in Section 3. Finally, conclusion and the future research directions that can be studied in depth is presented in Section 4.

2 Materials and methods

2.1 Establishment of discrete element model of taro tiller plants based on EDEM

2.1.1 Establishment of discrete element model of taro corm

The corms of taro planted by Yanglinggou Taro Cooperative in Hanchuan City, Hubei Province were studied. The geographical location of the area was 113.660221 east longitude and 30.521991 north latitude. Taro corms can be divided into mother corm, sister corms, as shown in Figure 1A. Sixty taro samples without damage and disease were collected, and the vernier caliper with an accuracy of 0.01mm was used to measure the physical dimensions of taro corms, and the average values were calculated. The mean length, width, height of the mother corm was 64.26, 64.46 and 83.01mm, respectively. The mean length, width, height of sister corm was 32.06, 29.01 and 40.85mm, respectively, and the mean length, width, height of sister corm was 27.44, 25.62 and 31.74mm, respectively, the statistical results are shown in Figure 1B.

3D laser scanning technology can accurately obtain the 3D contour of complex plants. As taro corm is irregular particles with complex shapes. A SHINING 3D Einscan-Pro multi-functional handheld scanner was used to conduct 3D scanning and collect the position coordinates of taro corm in 3D space, 3D laser scanning is shown in Figure 1C. Dominik et al. (2021) established an image database of 7 different trees through 3D scanning. Cucinotta et al. (2019) obtained the wear morphology of the plowshare through three-dimensional scanning technology.

Geomagic Warp software is used for reverse engineering processing to obtain the point cloud data of taro corms, as shown in the Figure 2A. The point cloud data is converted into a polygon model to restore the shape contour of taro corms. After trimming the excess surface, deleting the nail, merging, relaxing, smoothing and other operations (Hao et al., 2021), A more

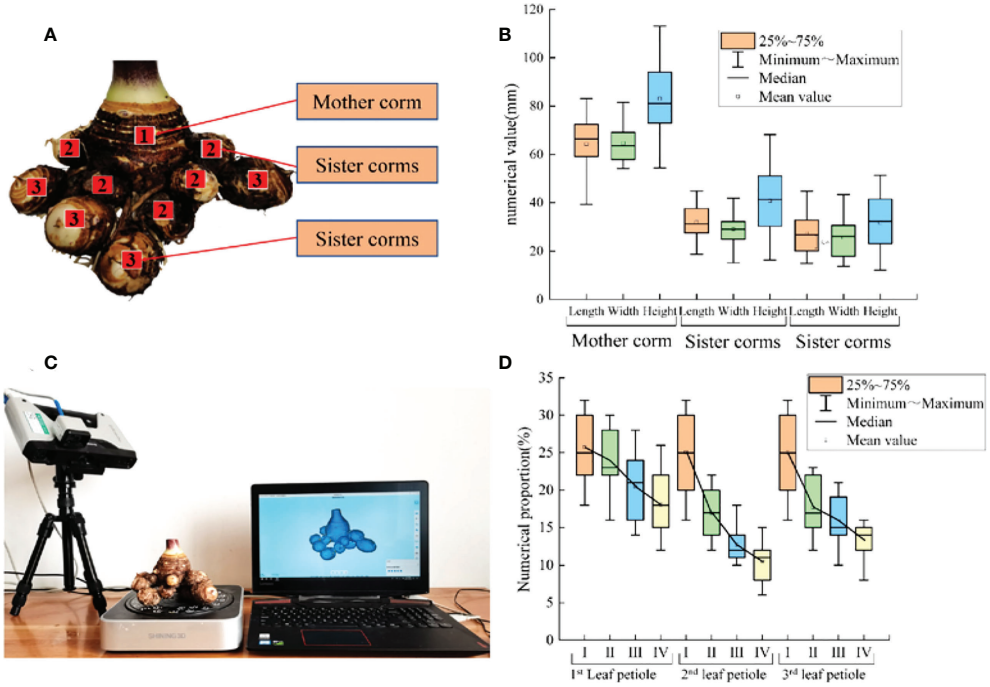

FIGURE 1
Schematic diagram and size statistics of taro corm. **(A)** The growing position of mother corm, and sister corms; **(B)** The length, width and height of mother corm, and sister corms statistics; **(C)** 3D laser scanning experiment of taro corm; **(D)** The length, width and height of 1st leaf petiole, 2nd leaf petiole and 3rd leaf petiole statistics.

FIGURE 2
Discrete element model of taro corm. **(A)** Taro corm 3D scanning point cloud model; **(B)** Taro corm contour model; **(C)** Discrete element model of taro corm.

accurate polygon model of the taro corm was obtained, as shown in the Figure 2B. The discrete element model of the taro corm was established by the fast-filling method of EDEM software, and the number of sphere elements was 58. The discrete element model of taro plant is shown in Figure 2C.

The Hertz-Mindlin (no slip) model with high computational accuracy and simulation speed was used among corm particles, and the contact radius between spherical particles:

$$\delta_i = r_{1i} + r_{2i} - d_i \tag{1}$$

Where δ_i is the contact center distance between two spherical particles, mm; r_{1i} is the radius of the first sphere particle, mm; r_{2i} is the radius of the second sphere particle, mm; d_i is the overlap distance in the direction of the connecting line between the center of two spheres, mm.

2.1.2 Establishment of discrete element flexible model for taro petiole

The taro petiole is in the shape of a tiller, and the inner part of the petiole is mainly composed of axial vascular bundle fibers. The diameters of the 1st side petiole, the 2nd side petiole and the 3rd side petiole at different positions from the ground were measured for 60 plants. I stand for 0-5cm from the ground, II for 5-10cm from the ground, III for 10-15cm from the ground, and IV for 15-20cm from the ground, as shown in the Figure 1D. The average diameter of the petiole gradually increases from the bottom to the top.

Twenty main petioles were cut at a distance of 5-10 cm from the ground, and the TMS-PRO texture analyzer produced by TFC Company in the United States was used to measure the petiole load-deflection curve at an experiment speed of 60 mm·min-1 (Shen et al., 2015), the instrument accuracy is ±1%, the range is 0~1000 N, and the data acquisition frequency is 50 Hz. The petiole was placed on two horizontal metal supports at the testing machine's lower end and aligned the sample's center with the center of the upper clamp; the experiment was started until the petiole was significantly bent, as shown in the Figure 3A. where midpoint A is the elastic limit point, and point B is the biological yield point. as shown in the Figure 3B. The elastic modulus of the petiole is about 16.69MPa after 20 measurements and the average value is obtained by formula (9). The Poisson's ratio ψ of the petiole is 0.4 according to the relevant literature (Shi et al., 2018), and the shear modulus of the petiole is 5.96 MPa obtained by formula (10).

The section of the taro petiole can be approximated as a circle, and the moment of inertia I of the section relative to the neutral axis is:

$$I = \frac{\pi\left[d_1^4 - (d_1 - 2h)^4\right]}{64} \tag{2}$$

Where d_1 is the petiole outer diameter, mm; h is the petiole wall thickness, mm.

petiole elastic modulus E_w:

$$E_W = \frac{FL_1^3}{48SI} \tag{3}$$

Where F is the loading force, N; L_1 is the distance between two supports, mm; S is the Bending deflection at the midpoint of the petiole, mm.

Shear modulus G_1 of the petiole:

$$G_1 = \frac{E}{2(\psi + 1)} \tag{4}$$

The petiole is subjected to clamping load when the taro plant is pulled from the soil. Combined with the deformation and damage characteristics of the petiole after loading, the Hertz-Mindlin with bonding contact model was selected to reflect the anisotropy and agglomeration characteristics of the petiole, as shown in the Figure 3C. the fiber state inside the petiole is characterized by the elastic coefficients K_t, K_n, damping coefficients C_t, C_n and friction coefficient μ between the petiole particles. The model has a total of 5 parameters, the normal bond stiffness S_n and the tangential bond stiffness S_t are iterated continuously at unit step intervals and update the load on the bond. The normal critical stress σ_{max} and the tangential critical stress τ_{max} are the critical threshold for judging whether the cohesive force is broken or not. The cohesive radius is the maximum distance required for the formation of cohesion

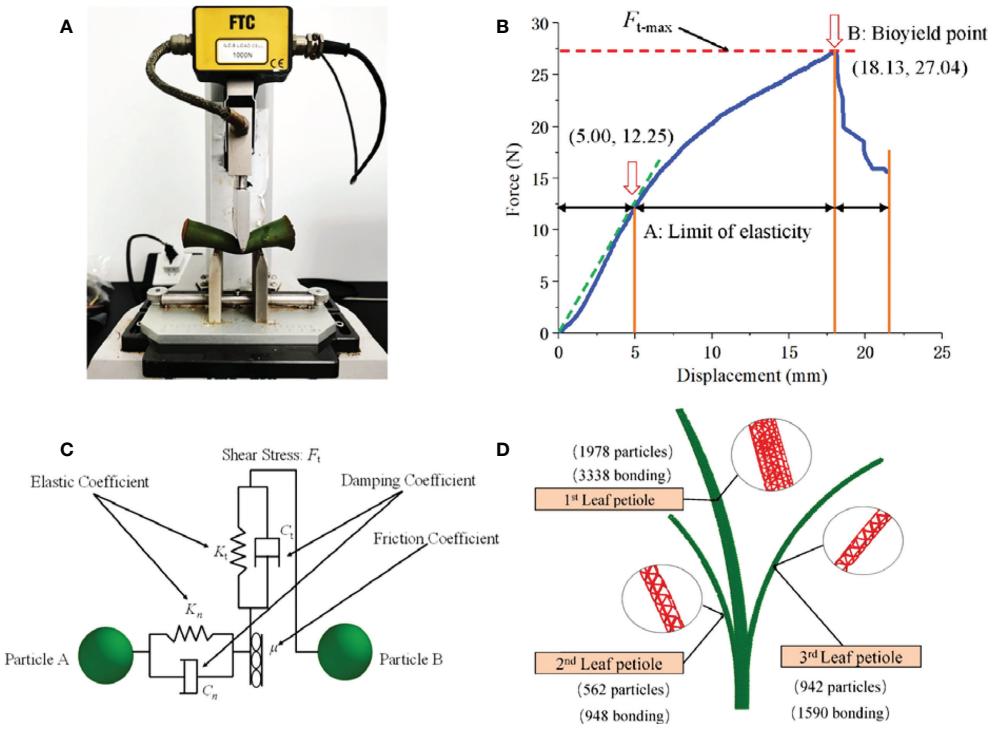

FIGURE 3
Discrete element model of petiole. **(A)** Three point bending experiment of petiole; **(B)** Displacement-Force of petiole obtained by three-point bending test; **(C)** Discrete element model and particle number of petiole; **(D)** Inter-particle force of taro.

between particles. A total of 5876 parallel bonding structures were generated between particles, as shown in the Figure 3D.

The process model of taro petiole particles from cohesion to failure:

$$\begin{cases} \Delta F_\delta = -v_n S_n A_s \Delta t \\ \Delta F_\alpha = -v_t S_t A_s \Delta t \\ \Delta T_n = -w_n S_n J \Delta t \\ \Delta T_t = -w_t S_t J \Delta t \end{cases} \quad (5)$$

Where F_δ is the normal adhesion force, N; $F_\alpha$is the tangential adhesion force, N; T_n is the normal adhesion moment, N·m; T_t is the tangential adhesion moment, N·m; v_n is the particle method Vertical velocity, m·s^{-1}; v_t is the particle tangential velocity, m·s^{-1}; w_n is the normal angular velocity, rad·s^{-1}; w_t is the tangential angular velocity, rad·s^{-1}. S_n is the normal bond stiffness, N·mm^{-1}; S_t is the tangential bond stiffness, N·mm^{-1}; A_s is the contact area, m^2.

The moment of inertia J of the parallel bond and the area of the contact area A_s:

$$J = \frac{1}{2}\pi R_B^4 \quad (6)$$

$$A_S = \pi R_B^2 \quad (7)$$

Where R_B is the bond radius, mm.

Fracture conditions for bond bonds:

$$\begin{cases} \sigma_{max} < \frac{-F_\delta}{A_S} + \frac{2T_t}{J} R_B \\ \tau_{max} < \frac{-F_\alpha}{A_S} + \frac{2T_n}{J} R_B \end{cases} \quad (8)$$

Where σ_{max} is the normal critical stress, Pa; τ_{max} is the tangential critical stress, Pa.

2.1.3 Establishment of discrete element flexible model for the whole taro plant

The taro leaf does not affect the effect of clamping and pulling. Only its gravity affects the clamping posture. To improve the simulation efficiency, the material parameters of the blade part were equivalent to the petiole, and the Hertz-Mindlin (no slip) contact model was used between the particles.

Taking the corm, petiole and leaf as the aggregation unit, according to the actual shape of the taro plant and the coordinate position of each particle cluster unit, the X, Y and Z axis coordinates of the aggregation unit were located, and the Hertz-Mindlin with bonding particle contact model was used to connect the corm to the petiole and the petiole to the leaf. Micro-unit spherical particles characterize the complex stress-strain characteristics of plants under macroscopic load, then

global variables were set, the Fixed Time Step was set to 4.60%, the Cell Size set to 3Rmin, the total number of grids was 3.5×10^6, and the time was set to 10s. The discrete element model of taro plant established is shown in Figure 4.

2.2 Taro clamping and pulling force experiment

2.2.1 Construction of taro clamping and pulling force measuring platform

In order to explore the actual interaction and dynamic mechanical behavior of taro pulling from the soil, a force measuring device for taro clamping and pulling was designed and fabricated, Figure 5A is the 3D model, and Figure 5C is the platform. Working principle: Place the taro plant shown in Figure 5B in the middle of the left and right clamping boards, Under the action of the electric push rod, the taro petioles are clamped at a constant speed. When the clamping plate is in contact with the taro petiole, the pulling platform was driven by the 86 stepper motor to lift at a constant speed until the petiole does contact with the clamping plate, as shown in Figure 5D. Sliding and pulling up the taro plant from the soil, at this time, record the minimum clamping force collected by the clamping platform sensor and the instantaneous pulling resistance collected by the two sensors of the pulling platform.

When the sensor's sensitivity is $0.0105mv{\cdot}V^{-1}$, the dynamic calibration of the sensor is carried out by using weights to eliminate the influence of the vibration of the force measuring platform and the gravity of the bench itself. Finally, complete the process of taro clamping and pulling force measurement

2.2.2 Bench experiment of taro plant clamping and pulling

Use the SDH-1202 fast halogen moisture meter to measure the moisture content of taro corms, petioles and growing soil environment, respectively. Set the drying temperature to 105°C, until the quality no longer changes, and repeat 5 times. The average measured moisture content was 75.42% for corms, 88.34% for petioles, and 21.05% for soil. Take the petiole 5 to 10 cm from the ground as the clamping position, the clamping speed is $12mm{\cdot}s^{-1}$, and the pulling speed is $0.3m{\cdot}s^{-1}$ as the working conditions, and the petiole does not form with the clamping plate during pulling. The minimum clamping force F_C is collected at the moment of slippage, and the instantaneous pulling resistance F_{L1} and F_{L2} collected by the two pull-out sensors are recorded. The sum of F_{L1} and F_{L2} is recorded as F_L. The mean value of F_C and F_L was 300.89N and 201.245N, respectively.

2.3 Simulation experiment of taro clamping and pulling

2.3.1 Experimental procedure

When the discrete element method is used to carry out the simulation research of taro clamping and pulling, the accuracy of the model parameters directly affects the data accuracy of the minimum clamping force and the instantaneous pulling resistance. The intrinsic parameters (density, Poisson's ratio and elastic modulus) are the material's inherent properties. The necessary parameters for the simulation are obtained through physical experiments and literature results, as shown

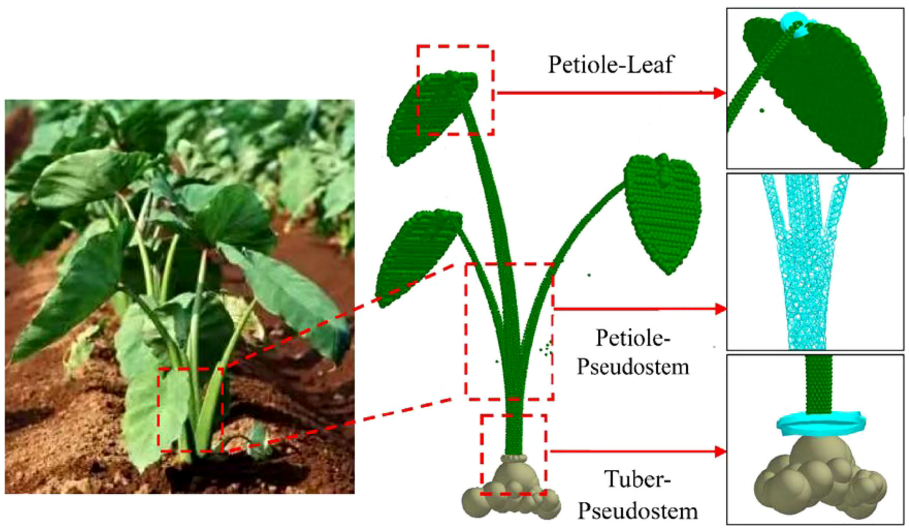

FIGURE 4
Discrete element flexible model of taro plant.

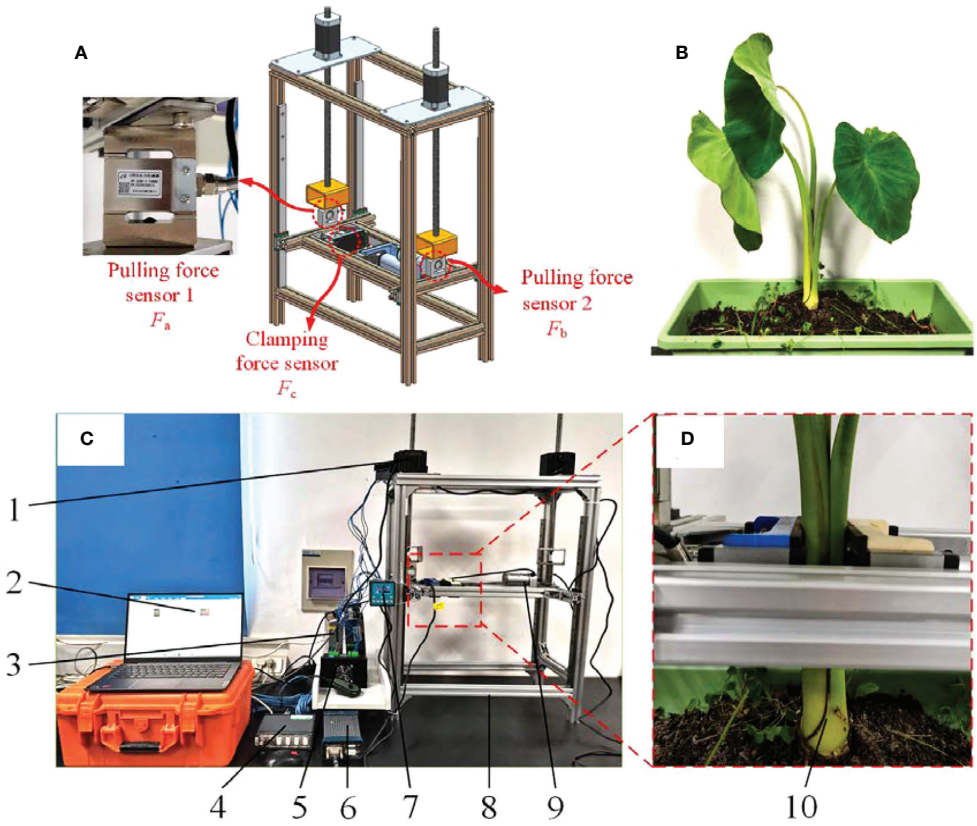

FIGURE 5
Mechanical force measuring platform of clamping and pulling device. **(A)** Sensor installation location; **(B)** Taro plant; **(C)** Mechanical force measuring platform of clamping and pulling device; 1. 86 stepper motor 2. PC test software 3. 48V power supply 4. DH380 controller 5. Motor driver 6. DH3820 collector 7. 86-stepper motor controller 8. Clamping force measuring platform 9. Electric pusher petiole 10. Taro Plant. **(D)** Clamping position of taro petiole.

in Table 1. The contact parameters (coefficient of restitution, coefficient of static friction and coefficient of rolling friction) of taro corm and petiole were obtained through tribometer experiment and high-speed photographic experiment in the early stage. The results are shown in Table 2. The soil in which taro grows is sandy loam, which has the characteristics of granular material. Hertz-Mindlin with JKR is a contact model based on Hertz theory that can characterize the viscoelasticity

TABLE 1 Intrinsic parameters.

Property	Value	Source
Poisson´s ratio of the device	0.3	a, b f
Poisson´s ratio of the corm	0.25	e
Poisson´s ratio of the petiole	0.4	g
Poisson´s ratio of the soil	0.5	c d b
Young's modulus of the device (Pa)	2.78×1011	a, b f
Young's modulus of the corm (Pa)	5.30×106	e
Young's modulus of the petiole (Pa)	1.67×108	Experiment
Young's modulus of the soil (Pa)	7.50×107	c d b
Density of the device (kg·m-3)	7.80×103	a, b f
Density of the corm (kg·m-3)	1540	e
Density of the petiole (kg·m-3)	1.13×103	Experiment
Density of the soil (kg·m-3)	2.60×103	1 2 d

Parameter source: a: (Liu et al., 2018); b: (Ucgul et al., 2017); c: (Wang et al., 2022); d: (Ucgul and Saunders, 2020); e: (Horabik et al., 2019); f: (Su et al., 2020). g: (Shi et al., 2018).

TABLE 2 Contact parameters.

Property	Coefficient of restitution	Coefficient of static friction	Coefficient of rolling friction
Petiole-Steel	0.1487	0.6135	0.3262
Petiole-Soil	0.1128	0.7054	0.4107
Petiole- Petiole	0.3183	0.5583	0.4267
Pseudostem -Corm	0.0891	0.6073	0.4896
Corm-Steel	0.2769	0.2473	0.3404
Corm -Soil	0.2256	0.4457	0.293
Corm - Corm	0.3257	0.7587	0.6187
Soil-Soil	0.1230	0.3853	0.2670

between particles (Horabik and Molenda, 2016). Therefore, the Hertz-Mindlin with JKR model was used for the soil, and the Hertz-Mindlin with bonding was used to reflect the adhesion between the petiole and the soil.

S_n=S_t, σ_{max}=τ_{max} can simplify the parameter calibration, the inter-particle bonding behavior originates from the liquid bridge between particles (Zhu et al., 2020), and the material moisture content is measured by the inter-particle bonding radius.

Assuming that the material moisture is uniformly distributed, and wrapped around the particle to form a uniform water film, the sum of the thickness of the water film and the particle radius represents the bonding radius. Refer to the existing rhizome agricultural material simulation parameters to set its range, as shown in Table 3.

Through the particle filling experiment, the density ρ of the filling particles is obtained by correcting the bulk density of the material, and the formula is:

$$\rho = \frac{3V}{4\pi k R_i^3}\rho_i \tag{9}$$

Where ρ is the density of filling particles, kg·m^{-3}; V is the volume of the container, m^3; K is the number of filling particles, each; R_i is the radius of the filling particles, mm; ρ_i is the bulk density of the material, kg·m^{-3}.

Volume V_s of filled spherical particles:

$$V_S = \frac{4}{3}\pi r^3 \tag{10}$$

Combining (9) and (10) yields:

$$\rho = \frac{V}{kV_S}\rho_i \tag{11}$$

The total volume V_i occupied by the material particles is:

$$V_i = KV_s \tag{12}$$

Therefore, the bulk density ρ_i of the material:

$$\rho_i = \frac{\rho V_i}{V} \tag{13}$$

Then the total weight m_i of material particles is:

$$m_i = \rho_i V_i = \frac{4}{3}\pi R_i^3 \rho_i \tag{14}$$

The total volume of water in the material V_w:

$$V_w = \frac{4}{3}\pi R_B^3 - \frac{4}{3}\pi R_i^3 \tag{15}$$

According to the material moisture content w:

$$w = \frac{\left(\frac{4}{3}\pi R_B^3 - \frac{4}{3}\pi R_i^3\right)\rho_2}{\frac{4}{3}\pi R_i^3 \rho_1} \tag{16}$$

Derivation of formula (13) yields the bonding radius R_B:

$$R_B = \sqrt[3]{\frac{\rho_2 + w\rho_1}{\rho_2}} \tag{17}$$

Where, w is the moisture content of the material, %; R_B is the bonding radius between particles, mm; ρ_i is the bulk density of the material, kg·m^{-3}; ρ_2 is the density of water, kg·m^{-3}; R_i is the filling material particles Radius, mm; V_s is the filling ball particle volume, m^3; V_i is the total volume occupied by material particles, m^3; m_i is the total weight of material particles, kg; m_w is the total moisture weight, kg; V_w is the total volume of water in material, m^3.

The virtual prototype model of the pulling device established by NX.12.0 is saved as stl format and imported into EDEM. In

TABLE 3 Parameter range of particle contact model.

Interparticle contact parameters		Ranges
Petiole - Petiole	Normal/tangential contact stiffness X1/(N·m-3)	1.0×109<1.2×1010
	Normal/tangential critical stress X2/(Pa)	5.0×108<1.5×109
Corm - Soil	Normal/tangential contact stiffness X3/(N·m-3)	5.0×105<1.0×107
	Normal/tangential critical stress X4/(Pa)	1.0×104<1.6×105
Soil - Soil	Surface energy X5/(×105J·m-3)	1.0×105<1.0×107

order to facilitate simulation and calculation, the parts that are not related to contact are removed, and the discrete element model of the taro clamping and pulling device is established. The size of the clamping plate is 100×50mm. The target save interval is set to 0.005s, the total simulation time is 3s, the gravitational acceleration is in the negative direction of the Z axis, and the value is -9.8kg·m^{-3}. The main operation process Includes the following 4 steps:

The actual growth depth of taro in the soil is about 15cm underground, and the surface is exposed to about 1cm of soil. Therefore, according to the actual growth situation, the taro plants are grown in a soil trough with a size of 300 × 300 × 200 mm, and a total of 37875 particles are generated in the soil trough. The position of the clamping experiment platform was adjusted, and the two clamping plates were fixed at the petiole 5<10 cm from the ground, as shown in Figure 6A.

The left and right clamping plates speed were set to 12 mm·s^{-1} in the X-axis to clamp the petiole until the clamping plates on both sides are in contact with the petiole, as shown in Figure 6B.

The clamping plates continue to clamp the petiole, and the left and right clamping plates and the pulling platform are set at a speed of 0.3m·s^{-1} in the Z-axis direction to pull up the plants until the clamping plates do not slip with the petioles. Stop the speed of the clamping plate in the X-axis direction at this time, record the force change of the clamping plate in the X-axis direction, and the clamping force collected at the moment of slip is recorded as the clamping force F_C for pulling out the taro, as shown in Figure 6C.

Continue to pull up the plants in the Z-axis direction until the plants are completely pulled up from the soil and record the pulling platform at the force change in the Z-axis direction, which is recorded as F_L. as shown in Figure 6D.

2.3.2 Experiment index

Bench experiment to measure the holding force of the F_a, pulling force for F_b, simulation experiment of clamping force for the F_C, pulling force for F_L, respectively using Origin data processing software simulation experiment bench experiment and measurement of two curves for data analysis, the correlation coefficient of the two clamping force curve for R_C, the correlation coefficient of the pulling force of two curve for R_L, The larger the correlation coefficient is, the higher the similarity of the two curves is, indicating that the tension measured in the simulation experiment is closer to the tension obtained in the actual experiment. R_C and R_L are calculated according to equations (18) and (19) respectively:

$$R_C = \frac{Cov(F_a, F_C)}{\sigma_{F_a}\sigma_{F_C}} \tag{18}$$

$$R_L = \frac{Cov(F_b, F_L)}{\sigma_{F_b}\sigma_{F_L}} \tag{19}$$

Where, F_a =300.89N; F_b =201.245N.

2.3.3 Single factor simulation experiment

In order to ensure the reliability of the discrete element flexible model of the whole taro plant, the Hertz-Mindlin with bonding model parameters between petiole, corm and soil, and Hertz-Mindlin with JKR model parameters between soils were calibrated. Taking the normal/tangential contact stiffness X_1 between petiole, the normal/tangential critical stress X_2, the normal/tangential contact stiffness X_3 between corm and soil, the normal/tangential critical stress X_4, and the inter-soil surface energy X_5 as for the experimental factors, single-factor simulation experiments were carried out with R_C and R_L as the experimental indicators. The experimental parameter levels are shown in Table 4.

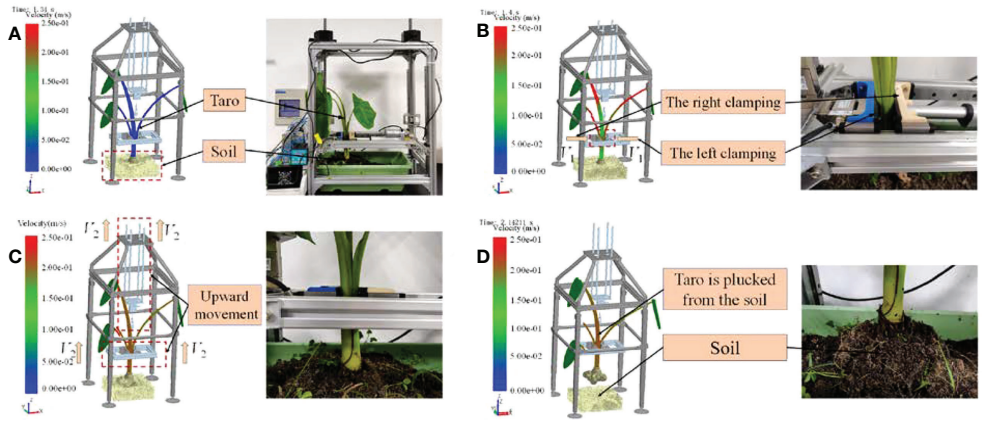

FIGURE 6
DEM simulation process. **(A)** The taro petiole is placed in the middle of the gripper; **(B)** The left and right clamping boards clamp the taro petiole; **(C)** The ascending mechanism lifts the taro plant; **(D)** Taro is completely pulled from the soil.

TABLE 4 Value range of single factor exposure parameters.

Contact parameters		Level	Fixed value
Petiole-Petiole	X1/(N·m-3)	1.0×109, 4.0×109, 6.0×109, 8.0×109, 1.0×1010, 1.2×1010	X2 = 1.1×109, X3 = 6.5×106, X4 = 1.0×105, X5 = 6.0×106
	X2/(Pa)	5.0×108, 7.0×108, 9.0×108, 1.1×109, 1.3×109, 1.5×109	X1 = 0.8×109, X3 = 6.5×106, X4 = 1.0×105, X5 = 6.0×106
Corm - Soil	X3/(N·m-3)	5.0×105, 2.5×106, 4.5×106, 6.5×106, 8.5×106 1.0×107	X1 = 0.8×109, X2 = 1.1×109, X4 = 1.0×105, X5 = 6.0×106
	X4/(Pa)	1.0×104, 4.0×104, 7.0×104, 1.0×105, 1.3×105, 1.6×105	X1 = 0.8×109, X2 = 1.1×109, X3 = 6.5×106, X5 = 6.0×106
Soil-Soil	X5/(×105J·m-3)	1.0×105, 2.0×106, 4.0×106, 6.0×106, 8.0×106, 1.0×107	X1 = 0.8×109, X2 = 1.1×109, X3 = 6.5×106, X4 = 1.0×105,

2.3.4 Plackett-Burman experiment

The Plackett-Burman calibration method is accurate and efficient and has been widely used in discrete element parameter calibration (Xia et al., 2019; Fang et al., 2022). First, based on the single factor experiment results, each factor is increased in equal steps to create each step parameter level and carry out a simulation experiment. Then, the parameters are further reduced through the changing trend of the Correlation coefficient of clamping force R_C and the Correlation coefficient of pulling force R_L, Finally, a multi-factor regression model was established, the maximum optimal solution of R_C and R_L was calculated, and parameter calibration was completed. Single factor simulation experiment parameters with correlation coefficient more than 50% were used as the range of Plackett-Burman experiment parameters, X_1 (6.0×10^9<1.0×10^{10} N·m^{-3}), X_2 (9×10^8<1.5×10^9 Pa), X_3 (4.5×10^6<8.5×10^6 N·m^{-3}), X_4 (7.0×10^4<1.6×10^5 N·m^{-3}), X_5 (2.0×10^6<6.0×10^6 N·m^{-3}).

3 Results and discussion

3.1 Parameter calibration of discrete element model of taro whole plant

3.1.1 Analysis of single factor experiment results

With the increase of X_1 and X_2, both R_C and R_L show a trend of first increasing and then decreasing, as shown in Figures 7A, B, mainly because the cross-section of the petiole is composed of many fiber tubes, and there are a large number of fiber tubes

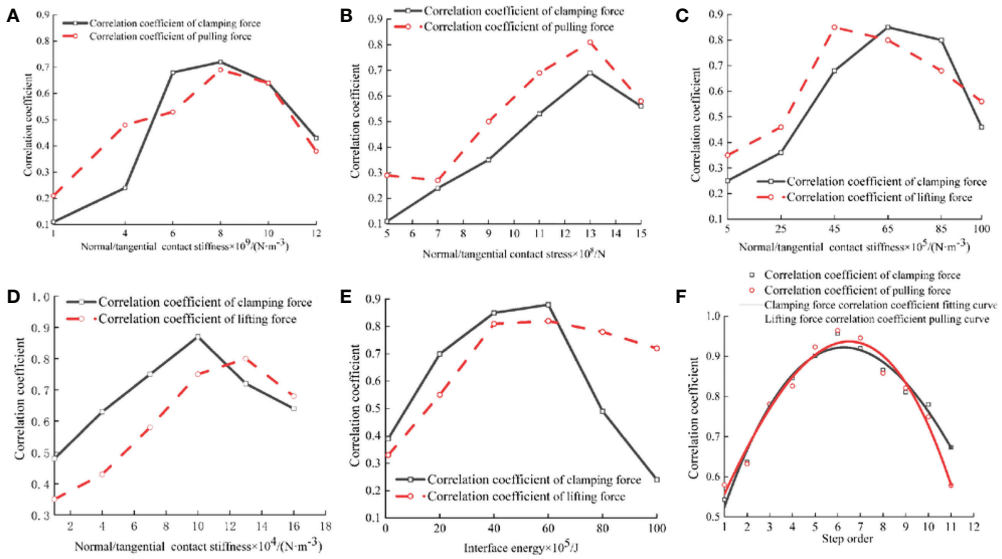

FIGURE 7
Results of Single factor and Plackett-Burman simulation experiments. **(A)** Changes of RC and RL at different X1 levels; **(B)** Changes of RC and RL at different X2 levels; **(C)** Changes of RC and RL at different X3 levels; **(D)** Changes of RC and RL at different X4 levels; **(E)** Changes of RC and RL at different X5 levels; **(F)** Fitting plot of step order and correlation coefficient.

around them. For parenchyma cells, the fibrous tube bundles shrink when they are clamped, and the culm is deformed. When pulling up, friction occurs between the clamping plates on both sides and the epidermis of the culm. Therefore, X_1 and X_2 will affect both R_C and R_L. With the increase of X_3 and X_4, both R_C and R_L showed a trend of first increasing and then decreasing, as shown in Figures 7C, D, With the increase of X_5, both R_C and R_L showed a trend of first increasing and then decreasing, as shown in Figure 7E. The Plackett-Burman experiment was carried out in the range of experimental factor data with correlation coefficient more than 50% in the single factor experiment.

3.1.2 Analysis of Plackett-Burman experiment results

The starting point parameter group of Plackett-Burman experiment climbing was A_1 (the lower limit of the contact parameter to be calibrated), and the end parameter group was A_m (the higher limit of the contact parameter to be calibrated), then each step parameter group can be expressed as:

$$\begin{bmatrix} A_1 \\ A_2 \\ A_3 \\ \cdot \\ \cdot \\ \cdot \\ A_m \end{bmatrix} = \begin{bmatrix} X_{11}\ X_{12} \cdots X_{1n} \\ X_{21}\ X_{22} \cdots X_{2n} \\ X_{31}\ X_{32} \cdots X_{3n} \\ \cdot \\ \cdot \\ \cdot \\ X_{m1}\ X_{m2} \cdots X_{mn} \end{bmatrix} = \begin{bmatrix} A_1 \\ A_1 + A \\ A_1 + 2A \\ \cdot \\ \cdot \\ \cdot \\ A_1 + (m-1)A \end{bmatrix} \quad (20)$$

Where, m is the total number of steps for climbing (that is, the number of calibration experiments), n is the total number of parameters to be calibrated (n=5), and the step size A is:

$$A = \frac{A_m - A_1}{m-1} \quad (21)$$

The value range of step order x is $1 \le x \le m$, and the value corresponding to each contact parameter group:

$$A_x = (x-1)A + A_1 \quad (22)$$

$$E_C = f_C(X_1, X_2, X_3, X_4, X_5) \quad (23)$$

$$E_L = f_L(X_1, X_2, X_3, X_4, X_5) \quad (24)$$

The larger m is, the closer the contact parameters of each group of calibration experiments are, and the clamping force F_C and the pulling resistance F_L will be more accurate with the change of the parameter group, but the number of simulations will increase. Based on the calibration accuracy and workload, this research uses Design Expert software to design 11 groups of experiments including 5 influencing factors and divides the high and low levels of each influencing factor into 10 equally for the steepest climbing experiment. The experimental design is shown in Table 5.

With the increase of step order, both R_C and R_L show a trend of first increasing and then decreasing. The step order and correlation coefficient are fitted, as shown in Figure 7F. The fitting equations:

$$R_C = 3.18 \times 10^{-4}x^3 - 0.02x^2 + 0.20x + 0.35 \quad (25)$$

$$R_L = -5.2 \times 10^{-4}x^3 - 0.005x^2 + 0.14x + 0.43 \quad (26)$$

Among them, the coefficient of determination R_c^2 = 96.65 %, R_L^2 = 95.06 %, the fitting degree of the fitting equation to the simulation experiment value is good.

According to the minimum value of the quadratic fitting parabola, when the step order x_1 = 6.48, x_2 = 6.27, the R_C and R_L values are the maximum. x_1 and x_2 mean x=6.375, at this time R_C=0.865, R_L =0.937. According to formula (22), the final result of the contact parameter group corresponding to the interaction of the taro plant: X_1 (8.15×10^9 N·m^{-3}), X_2 (1.22×10^9 Pa), X_3 (6.65×10^6 N·m^{-3}), X_4 (1.18×10^5 N·m^{-3}), X_5 (4.15×10^6 N·m^{-3}).

TABLE 5 Calibration experiment results.

Step order/x	X1/×109	X2/×108	X3/×106	X4/×104	X5/×106	FC/N	RC	FL/N	RL
1	6.00	9.00	4.50	7.00	2.00	554.23	0.54	347.03	0.58
2	6.40	9.60	4.90	7.90	2.40	472.35	0.64	318.38	0.63
3	6.80	10.20	5.30	8.80	2.80	385.81	0.78	257.68	0.78
4	7.20	10.80	5.70	9.70	3.20	355.91	0.85	243.70	0.83
5	7.60	11.40	6.10	10.60	3.60	333.84	0.90	217.99	0.92
6	8.00	12.00	6.50	11.50	4.00	314.48	0.96	208.67	0.96
7	8.40	12.60	6.90	12.40	4.40	326.98	0.92	212.82	0.95
8	8.80	13.20	7.30	13.30	4.80	347.49	0.87	234.58	0.86
9	9.20	13.80	7.70	14.20	5.20	371.24	0.81	245.09	0.82
10	9.60	14.40	8.10	15.10	5.60	385.76	0.78	268.68	0.75
11	10.00	15.00	8.50	16.00	6.00	447.02	0.67	347.87	0.58

3.2 Validation of the taro tiller plant model

To verify the application of the taro tiller plant model, Substitute X_1, X_2, X_3, X_4, X_5 into the simulation experiment, The clamping speed was set to 12mm·s^{-1}, and the pulling speed was set to 0.3 m·s^{-1}, the clamping plate was set at 5<10 cm from the soil surface at the petiole, and the minimum clamping force F_C and the instantaneous pulling resistance F_L at the critical moment of slippage during the pulling process of the taro are recorded.

The relative velocity of the petiole and the clamping plate in the pulling direction is an important factor to judge whether the two have slipped. Therefore, combined with the post-processing function of EDEM, two local relative velocity monitoring sensors are established at the petiole clamping position. To monitor the movement speed of the holding plate and the taro plant in the pulling direction, as shown in Figure 8, output the speed changes of the petiole and the holding plate in the two monitors at each time step, calculated by formula (27) Obtain the relative motion speed between the petiole and the clamping plate:

$$\eta_i = \frac{V_j}{V_e} \tag{27}$$

where η_i is the relative velocity of the petiole and the clamping plate in the pulling direction at the i moment, m·s^{-1}; V_j is the speed of the clamping plate in the pulling direction, m·s^{-1}; V_e is the taro plant in the pulling direction. The speed in the pulling direction, m·s^{-1}.

When η_i>1, it means that the petiole and the clamping plate have slipped, and the clamping force will continue to be applied at this time; until η_i=1, it means that the petiole and the clamping plate are not affected by the sliding force and record this time. It is the F_C for taro to pull out, and under this clamping force, the F_L of taro is measured synchronously.

3.3 Comparison of bench experiment and simulation experiment

When the clamping force of the simulation experiment and bench experiment set into a fixed value 300 N, respectively, in the speed of 0.1, 0.2, 0.3, 0.4, 0.5 m·s^{-1} under the condition of experiment, we got the data from 10 groups of pulling, the same speed of simulation experiment data and bench data on the same picture, as shown in Figure 9. We know from the experiment data that the pulling variation trend of the simulation experiment and the bench experiment is basically the same, but the pulling value of the bench experiment is larger than that of the simulation experiment, because the environment of the simulation experiment is more ideal than that of the bench experiment. By comparing the result of the same experiment method under the condition of different speed, it is found that with increasing speed, pulling fluctuation frequency is reduced, but the volatility increases, this is because the impact of the speed, the greater the taro plants are bigger, and it also can be faster from the soil, but the petioles is at risk of being destroyed. We successively conducted correlation analysis on different experiments at the same speed and obtained that the correlation coefficients of pulling variation between simulation experiment and bench experiment were 0.812, 0.850, 0.770, 0.697 and 0.652, respectively. The average value of correlation coefficients was 0.756, which indicated that the discrete element

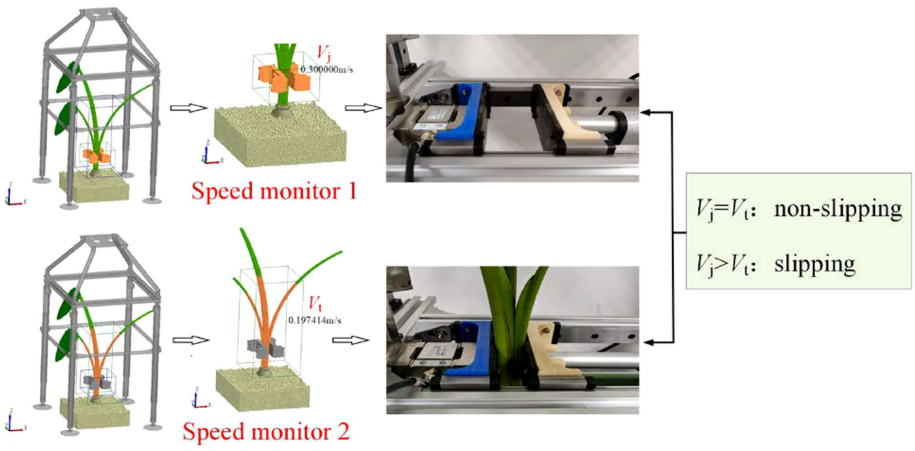

FIGURE 8
The speed monitor established by the simulation experiment.

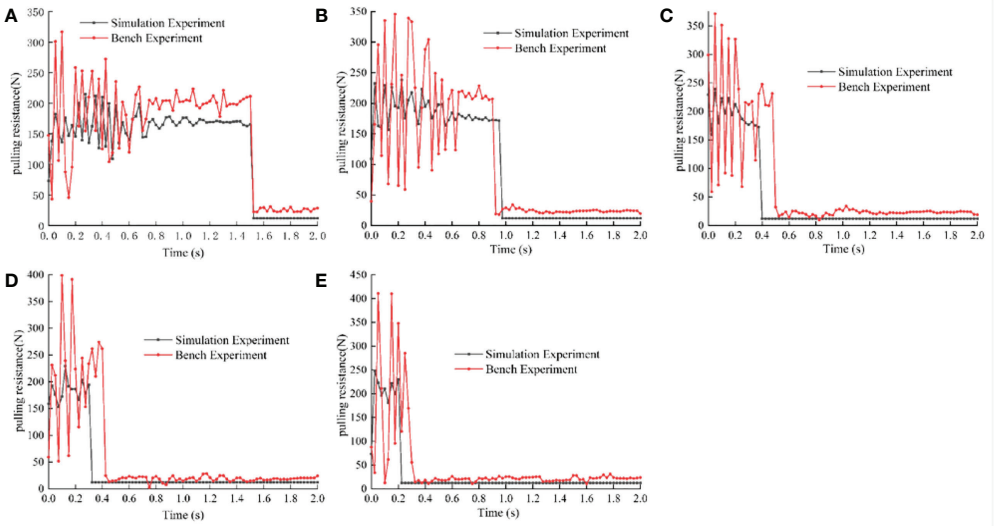

FIGURE 9
Comparison of bench experiment and simulation experiment. **(A)** Comparison between the bench and simulation when the pulling speed is 0.1m·s-1; **(B)** Comparison between the bench and simulation when the pulling speed is 0.2m·s-1; **(C)** Comparison between the bench and simulation when the pulling speed is 0.3m·s-1; **(D)** Comparison between the bench and simulation when the pulling speed is 0.4m·s-1; **(E)** Comparison between the bench and simulation when the pulling speed is 0.5m·s-1.

plant model established by simulation was close to the real plant. The discrete element model of taro plant established in this paper has high reliability.

4 Conclusion

The discrete element flexible model of taro plant was established by using EDEM software, and a method to test the clamping and pulling resistance of taro in the harvesting process was proposed, which provided a theoretical basis and model reference for the research and development of taro harvesting machinery. The parameter calibration results of discrete element model of taro plant are as follows: petiole-petiole method/tangential contact stiffness was 8.15×10^{9} N·m^{-3}, and normal/tangential critical stress was 6.65×10^{6} Pa. The contact stiffness of pseudostem- corm method was 1.22×10^{9} N·m^{-3}, the critical stress of normal/tangential was 1.18×10^{5} Pa, and the energy of soil surface was 4.15×10^{6}J·m^{-3}.

When the pulling speed is 0.1, 0.2, 0.3, 0.4 and 0.5 m·s^{-1}, the correlation coefficients between the simulation experiment and the bench experiment are 0.812, 0.850, 0.770, 0.697 and 0.652, respectively. The average value of correlation coefficient is 0.756, indicating that the simulated discrete element plant model is close to the real plant model. The discrete element model of taro plant established in this paper has high reliability.

In the future, the discrete element flexible model of taro plants can be applied to many aspects - studying the reaction force of taro corms and soil slip process when the tractor walking tire compacts the soil; carrying out the simulation experiment of the cutting process of petiole, which is used for the structural design of the cutting blade and the determination of important parameters such as the cutting angle. It can also provide a basis for the structural design of the excavating shovel based on discrete element and multi-body dynamics methods, and at the same time provide an important theoretical model for the in-depth study of corm excavation damage.

Data availability statement

The original contributions presented in the study are included in the article/supplementary material. Further inquiries can be directed to the corresponding author.

Author contributions

LW, ZG and ZY designed and performed the experiments and analyzed the data. LW, LH and TN wrote the manuscript.

KQ and ZZ made the pictures. All authors contributed to the article and approved the submitted version.

Funding

This study was supported by the National Characteristic Vegetable Industry Technology System Special Project, Project, No. CARS-24-D-02.

Acknowledgments

We thank the Engineering Training Center of Huazhong Agricultural University for providing the test site.

Conflict of interest

The authors declare that the research was conducted in the absence of any commercial or financial relationships that could be construed as a potential conflict of interest.

Publisher's note

All claims expressed in this article are solely those of the authors and do not necessarily represent those of their affiliated organizations, or those of the publisher, the editors and the reviewers. Any product that may be evaluated in this article, or claim that may be made by its manufacturer, is not guaranteed or endorsed by the publisher.

References

Aditika, S., Kapoor, B., Singh, S., and Kumar, P. (2022). Taro (Colocasia esculenta): Zero wastage orphan food crop for food and nutritional security. *South Afr. J. Bot.* 145, 157–169. doi: 10.1016/j.sajb.2021.08.014

Andreas, E., and Waqainabete, L. M. (2018). Conserving and sharing taro genetic resources for the benefit of global taro cultivation: A core contribution of the centre for pacific crops and trees. *Biopreserv Biobank* 16, 361–367. doi: 10.1089/bio.2018.0017

Chen, L. T., Mou, X. W., Xue, J. X., Peng, Z. J., and Liu, W. J. (2022). Research status and prospect of cassava mechanized planting and harvesting equipment at home and abroad. *Agric. Eng.* 12 (02), 10–16. doi: 10.19998/j.cnki.2095-1795.2022.02.002

Chen, L. T., Xue, J. X., Mou, X. W., and Xiang, J. S. (2022). Design and experiments of the stepped vibration seed dispersal mechanism for pre-cut cassava planters. *Trans. Chin. Soc. Agric. Eng.* 38, 27–37. doi: 10.11975/j.issn.1002-6819.2022.08.004

Cucinotta, F., Scappaticci, L., Sfravara, F., Morelli, F., Mariani, F., Varani, M., et al. (2019). On the morphology of the abrasive wear on ploughshares by means of 3D scanning. *Biosyst. Eng.* 179, 117–125. doi: 10.1016/j.biosystemseng.2019.01.006

Dominik, D., Peter, A., Anton, T., Edward, S. Q., Jan-Henrik, T., Jonas, G., et al. (2021). Predicting tree species from 3D laser scanning point clouds using deep learning. *Front. Plant Sci.* 12. doi: 10.3389/fpls.2021.635440

Fang, M., Yu, Z. H., Zhang, W. J., Cao, J., and Liu, W. H. (2022). Friction coefficient calibration of corn petiole particle mixtures using plackett-burman design and response surface methodology. *Powder Technol.* 396, 731–742. doi: 10.1016/j.powtec.2021.10.040

Guo, J., Karkee, M., Yang, Z., Fu, H., Li, J., Jiang, T. T., et al. (2021). Discrete element modeling and physical experiment research on the biomechanical properties of banana bunch petiole for postharvest machine development. *Comput. Electron. Agric.* 188, 106308. doi: 10.1016/j.compag.2021.106308

Hao, J. J., Wei, W. B., Huang, P. C., Qin, J. H., and Zhao, J. G. (2021). Calibration and experimental verification of discrete element parameters of oil sunflower seeds. *Trans. Chin. Soc. Agric. Eng. (Transactions CSAE)* 37, 36–44. doi: 10.11975/j.issn.1002-6819.2021.12.005

He, X. N., Zhang, X. J., Zhao, Z., Shang, S. Q., Wang, D. W., and Yang, S. (2022). Design and optimization tests of reverse spin-throwing cyperus edulis starting device. *Trans. Chin. Soc. Agric. Machinery* 53, 34–43. doi: 10.6041/j.issn.1000-1298.2022.05.004

Horabik, J., and Molenda, M. (2016). Parameters and contact models for DEM simulations of agricultural granular materials: A review. *Biosyst. Eng.* 147, 206–225. doi: 10.1016/j.biosystemseng.2016.02.017

Horabik, J., Wiącek, J., Parafiniuk, P., Stasiak, M., Bańda, M., and Molenda, M. (2019). Tensile strength of pressure-agglomerated potato starch determined *via* diametral compression test: Discrete element method simulations and experiments. *Biosyst. Eng.* 183, 95–109. doi: 10.1016/j.biosystemseng.2019.04.019

Liu, C. L. (2021). Study on the design and damage rule of sweet potato combined harvesting, conveying and separating device. *Shandong Agric. Univ.* doi: 10.27277/d.cnki.gsdnu.2021.001044

Liu, W. Z., He, J., Li, H. W., Li, X. Q., Zheng, K., and Wei, Z. C. (2018). Calibration of simulation parameters for potato mini petiole based on EDEM. *Trans. Chin. Soc. Agric. Machinery* 49, 125–135. doi: 10.6041/j.issn.1000-1298.2018.05.014

Liu, F. Y., Zhang, J., and Chen, J. (2018). Modeling of flexible wheat straw by discrete element method and its parameter calibration. *Int. J. Agr. Biol. Eng.* 11, 42–46. doi: 10.25165/j.ijabe.20181103.3381

Liu, Y. G., Zhao, J. G., Yin, B. Z., Ma, Z. K., Hao, J. J., Yang, X., et al. (2022). Discrete element modelling of the yam root–soil complex and its verification. *Biosyst. Eng.* 220, 55–72. doi: 10.1016/j.biosystemseng.2022.05.002

Li, B. W., Zong, Y. X., and Wu, M. (2022). World taro production and trade situation analysis. *China Vegetables* 6, 1–6. doi: 10.19928/j.cnki.1000-6346.2022.5020

Ma, Z., Li, Y., and Xu, L. (2015). Discrete-element method simulation of agricultural particles' motion in variable-amplitude screen box. *Comput. Electron. Agric.* 118, 92–99. doi: 10.1016/j.compag.2015.08.030

Sharma, S., Jan, R., Kaur, R., and Riar, C. S. (2020). "Taro (Colocasia esculenta)," in *Antioxidants in vegetables and nuts - properties and health benefits*. Eds. G. A. Nayik and A. Gull (Singapore: Springer). doi: 10.1007/978-981-15-7470-2_18

Shen, C., Li, X. W., Tian, K. P., Zhang, B., Huang, J. C., and Chen, Q. M. (2015). Experimental analysis on mechanical model of ramie petiole. *Trans. Chin. Soc. Agric. Eng. (Transactions CSAE)* 31, 26–33. doi: 10.11975/j.issn.1002-6819.2015.20.004

Shi, L. R., Sun, W., Zhao, W. Y., Yang, X. P., and Feng, B. (2018). Parameter determination and validation of discrete element model of seed potato mechanical seeding. *Trans. Chin. Soc. Agric. Eng. (Transactions CSAE)* 34, 35–42. doi: 10.11975/j.issn.1002-6819.2018.06.004

Singla, D., Singh, A., Dhull, S. B., Kumar, P., Malik, T., and Kumar, P. (2020). Taro starch: Isolation, morphology, modification and novel applications concern - a review. *Int. J. Biol. Macromol.* 163, 1283–1290. doi: 10.1016/j.ijbiomac.2020.07.093

Su, Z., Li, Y. M., Dong, Y. H., Tang, Z., and Liang, Z. W. (2020). Simulation of rice threshing performance with concentric and non-concentric threshing gaps. *Biosyst. Eng.* 197, 270–284. doi: 10.1016/j.biosystemseng.2020.05.020

Ucgul, M., and Saunders, C. (2020). Simulation of tillage forces and furrow profile during soil-mouldboard plough interaction using discrete element modelling. *Biosyst. Eng.* 190, 58–70. doi: 10.1016/j.biosystemseng.2019.11.022

Ucgul, M., Saunders, C., and Fielke, J. M. (2017). Discrete element modelling of top soil burial using a full scale mouldboard plough under field conditions. *Biosyst. Eng.* 160, 140–153. doi: 10.1016/j.biosystemseng.2017.06.008

Wang, B., Zhai, G. H., Jiang, L., and Shao, Y. C. (2012). Characteristic export vegetable – high quality and high yield cultivation technology of taro. *J. Changjiang Vegetables* 10, 51–52. doi: 10.3865/j.issn.1001-3547.2012.10.020

Wang, X. Z., Zhang, Q. K., Huang, Y. X., and Ji, J. G. (2022). An efficient method for determining DEM parameters of a loose cohesive soil modelled using hysteretic spring and linear cohesion contact models. *Biosyst. Eng.* 215, 283–294. doi: 10.1016/j.biosystemseng.2022.01.015

Xia, R., Li, B., Wang, X. W., Li, T. J., and Yang, Z. J. (2019). Measurement and calibration of the discrete element parameters of wet bulk coal. *Measurement* 142, 84–95. doi: 10.1016/j.measurement.2019.04.069

Yang, J. M., Yang, W., and Yang, J. (2022). Measurement of cassava seed stem parameters and calibration of EDEM simulation parameters. *J. Agric. Mechanization Res.* 44 (01), 197–202+207. doi: 10.13427/j.cnki.njyi.2022.01.033

Yu, Q. X. (2019). Design and test of air suction hole wheel type notoginseng precision seed arrangement device. *Kunming Univ. Sci. Technol.* doi: 10.27200/d.cnki.gkmlu.2019.000162

Yu, Q. X., Cao, G. Q., Chen, B., Yan., L., Gong, Y., and Chen, X. B. (2022). Application and research status of harvesting mechanization of rhizome Chinese medicinal materials. *Chin. J. Agric. Mechanization* 43 (08), 15–21. doi: 10.13733/j.jcam.issn.2095-5553.2022.08.003

Yu, Q. X., Liu, Y., Chen, X. B., Sun, K., and Lai, Q. H. (2020). Calibration and experiment of simulation parameters for panax notoginseng seeds based on DEM. *Trans. Soc. Agric. Machinery* 51 (02), 123–132. doi: 10.6041/j.issn.1000-1298.2020.02.014

Zhou, K., Jensen, A. L., Bochtis, D. D., and Sørensen, C. G. (2015). Simulation model for the sequential in-field machinery operations in a potato production system. *Comput. Electron. Agric.* 116, 173–186. doi: 10.1016/j.compag.2015.06.018

Zhu, Q. L., Li, B. C., Liu, X. Y., Shan, N., Sun, J. Y., Zhang, H. Y., et al. (2022). Uncovering the mechanism preliminarily of formation and development of taro corm *in vitro* by morphological physiology and transcriptomic analysis. *Scientia Horticulturae* 291, 291. doi: 10.1016/j.scienta.2021.110575

Zhu, Y. H., Xia, J. F., Zeng, R., Zheng, K., and Liu, Z. Y. (2020). Prediction model of rotary tillage power consumption in paddy stubble field based on discrete element method. *Trans. Chin. Soc. Agric. Machinery* 51, 42–50. doi: 10.6041/j.issn.1000-1298.2020.10.006

frontiers | Frontiers in Plant Science

TYPE Original Research
PUBLISHED 08 November 2022
DOI 10.3389/fpls.2022.1026503

OPEN ACCESS

EDITED BY
Claus Zebitz,
University of Hohenheim, Germany

REVIEWED BY
Christopher Menzel,
Department of Agriculture and Fisheries, Australia
Rajkishan Arikapudi,
University of California, Davis, United States

*CORRESPONDENCE
Wei Qiu
qiuwei@njau.edu.cn

SPECIALTY SECTION
This article was submitted to Sustainable and Intelligent Phytoprotection, a section of the journal Frontiers in Plant Science

RECEIVED 24 August 2022
ACCEPTED 14 October 2022
PUBLISHED 08 November 2022

CITATION
Zhang F, Sun H, Qiu W, Lv X, Chen Y and Zhao G (2022) Model construction and validation of airflow velocity attenuation through pear tree canopies.
Front. Plant Sci. 13:1026503.
doi: 10.3389/fpls.2022.1026503

Model construction and validation of airflow velocity attenuation through pear tree canopies

Fubin Zhang[1], Hao Sun[1], Wei Qiu[1]*, Xiaolan Lv[2], Yunfu Chen[1] and Guozhu Zhao[1]

[1]College of Engineering/Key Laboratory of Intelligent Equipment for Agriculture of Jiangsu Province, Nanjing Agricultural University, Nanjing, China, [2]Institute of Agricultural Facilities and Equipment, Jiangsu Academy of Agricultural Sciences, Nanjing, China

To investigate the airflow velocity attenuation inside pear tree canopies and the factors that influence its effect on air-assisted spraying, the relationship between the resistance of the canopies to airflow and airflow velocity inside the canopies was determined. At the same time, the theoretical model of airflow velocity attenuation in the canopy was constructed, in which the velocity attenuation factor k and the incoming velocity were the model input values, and the airflow velocity in the canopy was the model output value. Then, experimental verification of the theoretical model was completed. The determination test of airflow velocity inside canopies with three leaf area densities revealed that the error range between the established theoretical model and the experimental airflow velocity inside the pear tree canopy was 0.11–1.25 m/s, and the mean size of the model accuracy was 83.4% under various working conditions. The results revealed that the region from a depth of 0 m to 0.3 m inside the canopy was the rapid attenuation area of the airflow and that from 0.3 m to 0.9 m was the low attenuation area. Furthermore, they revealed that high-speed airflow could strongly disturb the outer branches and leaves, greatly changing the windward area of the canopy blades and thus affecting the accuracy of the model. By introducing a dynamic parameter of the canopy leaf windward area for model correction, the R^2 of the model was above 0.9. Finally, validation of the model was performed in an air-assisted spraying operation in an orchard. This study can provide a theoretical basis for the regulation of airflow parameters of air-assisted spraying of pear trees.

KEYWORDS

orchard, pear canopy, air-assisted spraying, airflow, resistance, modeling

1 Introduction

As the third largest cultivated fruit tree in China, the pear tree can generate large economic benefits for China every year; however, it is prone to pests and diseases during the growth process. As they prevent the yield loss caused by pests and diseases, pesticides are an indispensable preventive measure in the process of pear tree cultivation (Pan et al., 2019; Li et al., 2022). However, frequent chemical application will cause problems such as pesticide residues and serious pollution.

Air-assisted spraying technology delivers atomized liquid to a canopy with the help of high-speed airflow, which helps to achieve a more homogeneous distribution and significantly improves the deposition of droplets and is, therefore, one of the most important technical measures for increasing the efficiency and reducing the application of pesticides in orchards (Planas et al., 2002; Panneton et al., 2005). Presently, researchers have conducted several studies on air-assisted application technology, mostly focusing on changing the type of fan or related parameters to investigate the movement of airflow in the air (Mion et al., 2011; Chao et al., 2019; Qiu et al., 2020). However, the presence of canopy branches and leaves in fruit trees inevitably makes airflow movement in the canopy different from that in the air. Therefore, researchers pay more and more attention to the study of canopy airflow attenuation. Some scholars have established artificial canopy (Musiu et al., 2019) and computational fluid dynamics (CFD) porous-medium canopy models (Endalew et al., 2008; Salcedo et al., 2017; Hong et al., 2018) to explore the relationship between canopy airflow attenuation and canopy density. Although the above method can reflect the energy change of the airflow passing though the canopy to a certain extent, and has a certain enlightening effect on the study of airflow attenuation in the fruit trees canopy, the actual fruit-tree canopy structure is relatively complex, and there are certain limitations in establishing artificial canopy and CFD models.

The above research shows that scholars have transitioned from focusing on the characteristics of sprayer to the stage of mechanical integration focusing on the characteristics of the canopy, and have paid attention to the influence of the canopy on airflow attenuation. However, there are still some limitations in the study of airflow attenuation in the canopy, mainly because the energy changes of airflow through the canopy are complex, and the characteristics of the canopy will significantly affect the airflow resistance and attenuation in the canopy (Walklate, 1992). Currently, Fruit trees still face "excessive deposition of droplets on the outside of the canopy and insufficient deposition of droplets in the inner chamber and the back of the leaves, the pest-prone areas" (Gil Sierra et al., 2006; Javier Garcia-Ramos et al., 2012; Dekeyser et al., 2014). Therefore, it is important to consider the airflow through a canopy and clarify its attenuation pattern to further improve the application effect and reduce the amount of liquid spray.

For that reason, this study took the crown pear as the research object and constructed a relational quantitative model for the attenuation of intra-canopy airflow velocity and based on the results of previous research on intra-canopy airflow velocity; then, a three-dimensional air-assisted resistance experimental platform was built to measure the relevant parameters using the pear tree canopy as the experimental sample. Furthermore, the experimental values of intra-canopy airflow velocity were obtained and compared with the theoretical values to verify the accuracy of the model. The model errors were then analysed and corrected for accuracy. Finally, the applicability of the model in air-assisted spraying operation was verified in a real orchard. This study aims to clarify the attenuation pattern of airflow velocity inside a canopy and its influencing factors in the air-assisted spraying operation and provide a new basis for the machinery and parameter setting of air-assisted application in orchards.

2 Materials and methods

2.1 Airflow velocity attenuation model

2.1.1 Theoretical model

The air flow is gradually weakened by the obstructive effect of branches and leaves as it flows inside the canopy. According to Кайгородов (Fu, 1963),

$$dv = -kvdy\,. \tag{1}$$

The variation in Eq. (1) is integrated in $v{:}v_*\rightarrow v(y)$; $y{:}0\rightarrow y$:

$$\int_{v_*}^{v(y)} \frac{1}{v}\,dv = \int_0^y -k\,dy\,. \tag{2}$$

Thus,

$$v(y) = v_* e^{-ky}, \tag{3}$$

$v(y)$: the velocity of the airflow at different depths inside the canopy [m/s];v_*: the velocity of the airflow when it reaches the surface of the canopy, i.e., the incoming velocity [m/s];k: the velocity attenuation factor; y: the depth from the canopy surface [m].

2.1.2 Determination of the velocity attenuation factor *k*

Among them, the velocity attenuation factor k is influenced by the canopy structure and other factors. Thus, this study analyzed the causes of airflow attenuation in the canopy, clarified the factors that lead to the change in k values, constructed a correlation model between the k values and canopy structure parameters, and finally obtained a theoretical model of airflow attenuation in the canopy that can guide pesticide application.

The fundamental reason for the attenuation of airflow velocity inside the canopy is that when airflow passes inside

the canopy, the airflow collides with the branches and leaves of the canopy and is obstructed by the branches and leaves, i.e., the drag effect, which generates the attenuation of airflow velocity inside the canopy. Thus, to obtain the relationship between the velocity attenuation factor and the canopy structure, it is necessary to investigate the resistance of the canopy to the airflow so that k values can be analyzed by substitution to clarify the variation pattern of the velocity attenuation factor and the mechanism of action leading to the velocity change.

According to the Burr effort equation, when an impermeable object is placed at a flow field with hydrostatic pressure of P_0, air density of ρ, and flow velocity of v, and when the flow velocity at the leeward edge of the object drops to 0 and the static pressure becomes P, there is a dynamic pressure of

$$P - P_0 = \frac{1}{2}\rho v^2 . \tag{4}$$

The resistance of the canopy to the airflow is calculated by the air resistance equation based on the relationship between the dynamic pressure and drag:

$$F = \frac{1}{2} C_d \rho v^2 S_0 . \tag{5}$$

F: the canopy resistance to airflow [N]; C_d: the air resistance coefficient; ρ: the air density [kg/m^3]; v: the airflow velocity [m/s]; S_0: the windward area [m^2].

At any point inside the canopy (x, y, z) where the velocity of the airflow is $v(x, y, z)$, take a volume element dV and let the windward area per unit volume of the canopy be T, it is a plane perpendicular to the airflow, so the air resistance coefficient C_d is 1.0 (Wu and Qian, 2017). Then, the windward area of the leaves in the volume dV is TdV. Therefore, the resistance to the airflow in the volume dV is

$$dF = \frac{1}{2}\rho[v(x,y,z)]^2 TdV, \tag{6}$$

$$dV = dxdydz, \tag{7}$$

T: the windward area per unit volume of the canopy [m^2]; $v(x, y, z)$: the velocity at any point within the canopy [m/s]; V: the volume of the canopy [m^3].

For this experiment, the experimental range is in the circular air-assisted area when the air blown from the fan reaches the canopy surface. The radius of the air-assisted area is R, and the canopy thickness is D. Therefore, the area size is

$$x: -R \to R; \quad y: 0 \to D; \quad z: -\sqrt{R^2 - x^2} \to \sqrt{R^2 - x^2} .$$

The resistance to airflow created by the canopy in the air-assisted area is

$$F = \int_{-R}^{R} \int_{0}^{D} \int_{-\sqrt{R^2-x^2}}^{\sqrt{R^2-x^2}} \frac{1}{2}\rho[v(x,y,z)]^2 TdV . \tag{8}$$

In the above equation, as the airflow is generated by a fan, the airflow velocity in the direction perpendicular to the horizontal depth is small; therefore, only the airflow velocity along the y direction is retained:

$$v(x, y, z) = v(y), \tag{9}$$

And

$$F = \frac{\pi R^2 T \rho v*^2}{4k}\left(1 - e^{-2kD}\right) . \tag{10}$$

The above equation constructs an expression for the airflow resistance when the airflow passes through the canopy of pear trees. The windward area per unit volume of the canopy in the equation cannot be obtained directly and needs to be further transformed.

In this study, image processing (Figure 1) was used to obtain the ratio of the canopy leaf windward area to its projected area in the air-assisted area. Then, the windward area per unit volume of the canopy was obtained by Eq. (11).

$$T = \frac{s}{\pi R^2 D}, \tag{11}$$

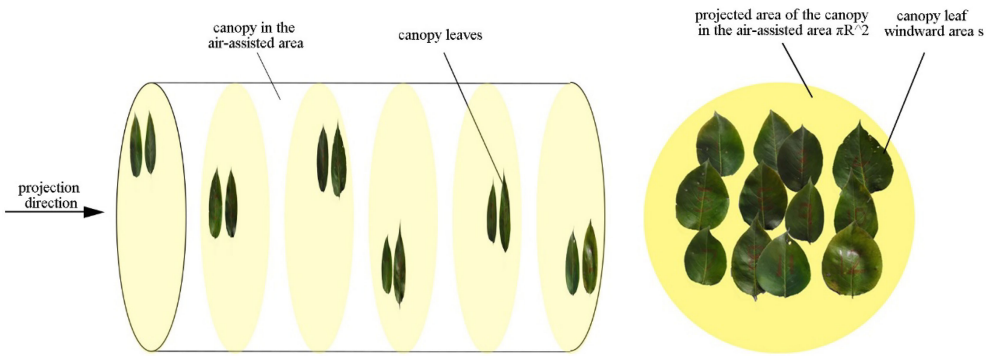

FIGURE 1
Schematic of the canopy projection.

πR^2 : the projected area of the canopy in the air-assisted area [m^2]; D' : the thickness of a section of canopy branches and leaves [m], s: the windward area of the canopy leaves [m^2].

Substituting the windward area per unit volume of the canopy, i.e., Eq. (13) into Eq. (12), we obtain

$$F = \frac{s\rho v*^2}{4kD'}\left(1 - e^{-2kD}\right). \quad (12)$$

The parameters such as flow resistance and windward area of the leaves in the above equation can be determined experimentally; therefore, the velocity attenuation factor k can be determined from Eq. (12), and the theoretical model of airflow velocity attenuation inside the canopy can be obtained after substituting Eq. (12) into Eq. (3).

2.2 Measurement of airflow velocity attenuation model parameters

When measuring the canopy aerodynamic resistance and other related parameters, it is difficult and time-consuming to use the whole pear tree for experimental measurement. In order to ensure the accuracy of the test results, pear tree branches and leaves with different leaf area densities were used for the test. For minimizing the influence of external airflow on the test results, the test was carried out in the laboratory without wind. In September 2021, fresh samples of pear tree branches and leaves were collected from the family farm of Sisi Yu in Pukou District, Nanjing, China for the canopy simulation test in a laboratory environment. Seven-year-old Crown pear trees with an average tree height of 2.1 m, average canopy width of 1.2 m, and average stem height of 0.7 m were tested. The leaf area density of the pear canopy in the orchard ranged from 3.94 –5.72 m^2/m^3, the leaves of the main branches were kept in their natural form, and the time between sampling and conducting the experiment was controlled to be within 6 hours.

2.2.1 Test platform

The experimental system consisted of two main components: the air-assisted platform and the measurement system (Figure 2). The air-assisted platform consisted of a variable frequency mixed-flow duct fan (diameter: 260 mm; air flow: 1080 m^3 h^{-1}; rated speed: 3200 r min^{-1}), mobile working platform (at the fixed walking speed of 1 m/s), and fan position adjustment system (0–1 m range in the walking direction; 0–1 m range in the air delivery direction; 0–1.2 m range in the vertical direction). The fan speed was controlled by a frequency converter. The measurement system consisted of an TSI 9565 anemometer(TSI Inc., Minnesota, USA, measurement error of ± 0.025 m/s), USB HD camera s(shooting speed: 110 fps); data storage device, portable computer and push-pull gauge (ELECALL, China, Zhejiang, the maximum load value was 10 N, the load division was 0.001 N, and the indication error was ± 0.5%).

2.2.2 Measurement of airflow velocity, leaf windward area and airflow resistance in canopy

The test is shown in Figure 3. For the measurement of airflow velocity, the airflow velocity reaching the canopy surface and the airflow velocity at different depths in the canopy were measured by the TSI 9565 anemometer.

For the canopy leaf windward area: a high-speed camera was used to take pictures of the canopy in the direction of the airflow, with a white cloth as the background to avoid the influence of other debris. In the windless condition, the size of the air-assisted area on the canopy was marked with a marker as a

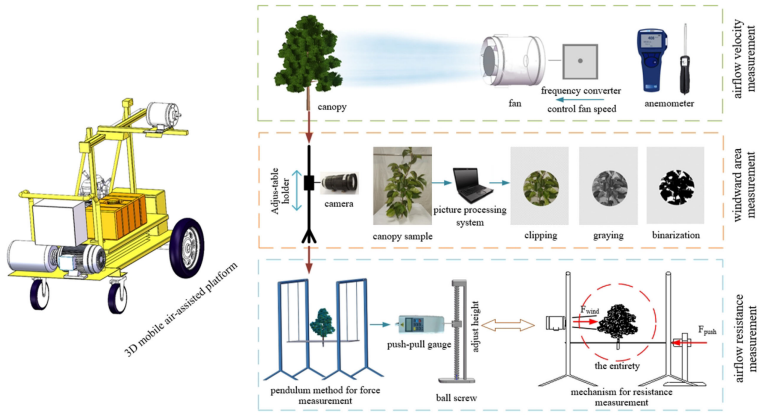

FIGURE 2
Experimental system.

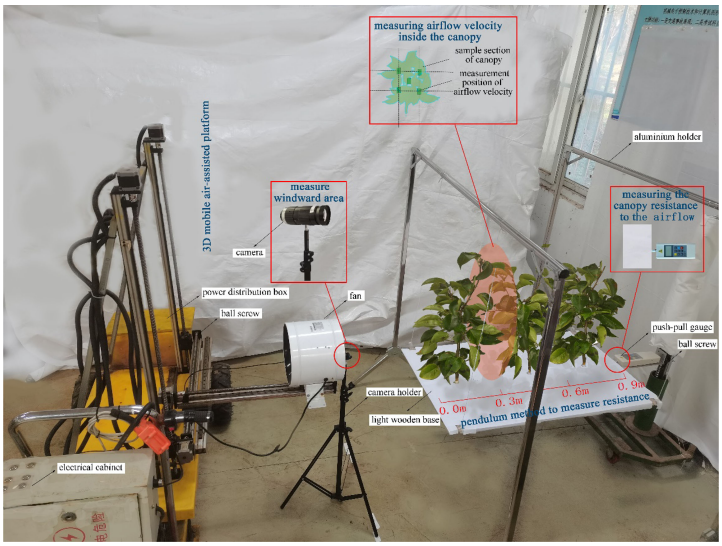

FIGURE 3
Experiment set-up.

selection range for the image processing later. Canopy photos of each leaf area density were taken to calculate the windward area of the canopy leaves in the air-assisted area. Combined with the volume of the canopy in the air-assisted area, the windward area per unit volume of the canopy was obtained for the canopies of different leaf area density.

For the canopy resistance to the airflow: the 3D mobile air-assisted platform was adjusted by turning the ball screw to move the fan to a position at the height of the middle of the canopy, with the air outlet position being 0.5 m from the canopy surface. We found that the airflow blown by the duct fan made a circle of radius 0.16 m after reaching the air-assisted area of the canopy surface. The height of the force measurement platform was adjusted to make the force gauge level with the base plate, bringing it against the base plate and setting the pressure to zero before the experiment started. The fan was started, and the fan wind speed knob was adjusted to control the airflow velocity of reaching the canopy surface. The push-pull gauge was then used to measure the canopy resistance to the airflow.

2.3 Verification of airflow velocity attenuation model

According to previous studies (Guan, 1998), the windward area per unit volume of the canopy is proportional to the leaf area density; therefore, this study set up three different leaf area densities of pear canopies to carry out the experiments: a sparse canopy with a leaf area density of 4.15 m^2/m^3, medium canopy with a leaf area density of 4.79 m^2/m^3, and compact canopy with a leaf area density of 5.65 m^2/m^3.

The canopy of 0.9 m-depth was selected for verification test., The experimental values of the airflow velocity within the canopy at heights of 0.15 m, 0.30 m, 0.45 m, 0.60 m, 0.75 m, and 0.90 m for incoming flow velocities of 4 m/s, 8 m/s, and 12 m/s were detected. At the same time, the leaf windward area of pear canopy and the canopy resistance under different airflow velocity were measured, and the theoretical value of canopy airflow velocity was calculated by formulas (12) and (3).

The theoretical values of the airflow velocity in the canopy were compared with the experimental values for analysis to verify the accuracy of the model and the correction model. The errors and model accuracy were calculated as follows.

$$v_w = |v_2 - v_1| \tag{13}$$

$$I = \left(1 - \frac{|v_2 - v_1|}{v_1}\right) \times 100\,\% \tag{14}$$

v_w: the error between the experimental and theoretical values of airflow velocity [m/s]; v_2: the experimental value of airflow velocity [m/s]; v_1: the theoretical value of airflow velocity [m/s]; I: the model accuracy.

2.4 Field test

To further verify the applicability of the intra-canopy airflow velocity attenuation model in the field environment, A field test

was conducted in the crown pear orchard in the Yu Sisi Family Farm (118.42°E, 32.98°N) in Nanjing in June 2022(average external temperature: 28°; average airflow velocity: 0.3 m/s). Three pear trees with leaf area densities similar to those used in the laboratory test were selected: pear tree A with a leaf area density of 4.08 m^2/m^3; pear tree B with a leaf area density of 4.72 m^2/m^3; and pear tree C with leaf area density of 5.58 m^2/m^3. Two sets of intra-canopy airflow velocity measurements were conducted in this orchard experiment, and the data acquisition method is shown in Figure 4: (1) the fan speed knob was turned to ensure the inflow velocity was 8 m/s and 12 m/s when the inflow reached the surface of the pear tree canopy [the optimum airflow parameter in the field is 9-11 m/s (Dai, 2008)], and the moving speed of the experimental platform was set to 0 m/s to measure the airflow velocity at the positions of 0.30 m, 0.60 m and 0.90 m inside the pear tree canopy with three different leaf area densities; (2) the fan speed knob was turned to ensure the inflow velocity was 8 m/s and 12 m/s when the inflow reached the surface of the pear tree canopy, and the moving speed of the experimental platform was set to 1 m/s to measure the airflow velocity at the positions of 0.30 m, 0.60 m and 0.90 m inside the pear tree canopy for three different leaf area densities.

3 Results

3.1 Calculation of the velocity attenuation factor k

In this study, the canopy airflow resistance and canopy leaf windward area were measured in a laboratory setting for three different leaf area densities at incoming velocities of 4 m/s, 8 m/s and 12 m/s, as shown in Table 1.

The data in Table 1 can be collated and calculated by Eq. (14) to obtain the velocity attenuation factor k for canopies of different leaf area densities at different incoming flow velocities, as shown in Table 2.

3.2 Validation of the airflow velocity attenuation model

The experimental and theoretical airflow velocities at positions 0.15 m, 0.30 m, 0.45 m, 0.60 m, 0.75 m, and 0.90 m in the canopy for three different leaf area densities are given in Figure 5. The processed data reveal that the error values

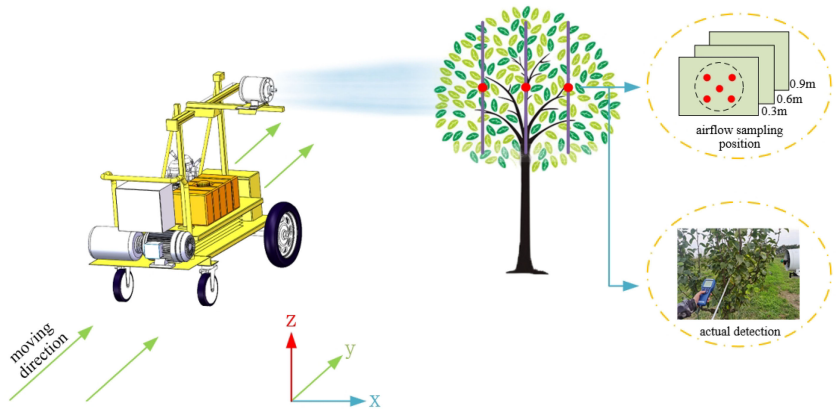

FIGURE 4
Airflow velocity measurements inside the canopy of pear trees in an orchard.

TABLE 1 Canopy leaf windward area values and canopy resistance to airflow values.

Leaf area density (m^2 /m^3)	Windward area of canopy Leaves in air-assisted area s (m^2)	Windward area per unit Volume of the canopy T (m^2 /m^3)	Resistance F (N)		
			Incoming Flow speed v_* (4 m/s)	Incoming Flow speed v_* (8 m/s)	Incoming Flow speed v_* (12 m/s)
4.15	0.057	2.353	0.97	2.96	4.98
4.79	0.060	2.480	0.94	2.63	4.49
5.65	0.065	2.673	0.88	2.35	4.11

v_* is the velocity of the airflow when it reaches the surface of the canopy.

TABLE 2 Velocity attenuation factor at different operating conditions.

Incoming flow velocity v_* (m/s)	Speed attenuation factor k		
	Sparse canopy(Lr = 4.15 m^2/m^3)	Medium canopy(Lr = 4.79 m^2/m^3)	Compact canopy(Lr = 5.65 m^2/m^3)
4	0.746	0.874	1.087
8	1.159	1.457	1.824
12	1.682	2.014	2.401

v_* is the velocity of the airflow when it reaches the surface of the canopy.

of the theoretical and experimental airflow velocities at different positions in the canopy for the three different leaf area densities at each incoming velocity range from 0.11 to 1.25 m/s, while the mean theoretical model accuracy is 83.4% for all the tested operating conditions. Among them, at an incoming flow velocity of 4 m/s, for the pear canopy with leaf area densities of 4.15 m^2/m^3, 4.79 m^2/m^3 and 5.65 m^2/m^3, the mean model accuracies of the attenuation of airflow velocity in the canopy are 82.8%, 78.5%, 72.7%, respectively; at the incoming flow velocity of 12 m/s, for leaf area densities of 4.15 m^2/m^3, 4.79 m^2/m^3 and 5.65 m^2/m^3, the mean accuracies of the intra-canopy airflow velocity attenuation model are 86.7%, 87.3%, and 85.3%,respectively, for the pear canopy. The model accuracies lie in between the values above at the incoming velocity of 8 m/s. In summary, with an increase in airflow velocity, the mean value of model accuracy increases. At smaller incoming velocities, although the accuracy (relative difference) is lower, the absolute difference is in the range of 0.11–0.84 m/s, which meets the requirements of model accuracy.

3.3 Error analysis and correction of the airflow velocity attenuation model

An analysis of the results in Figure 5 reveals that the theoretical values of the airflow velocity in the canopy obtained using the model in this paper are larger than the experimental values, and the error range is between 0.11–1.25 m/s. This is because the model calculates the theoretical airflow velocity using the windward area of the canopy leaves measured in the windless state, yet the leaf windward area of 0–0.3 m in the canopy in the experiment greatly varies with an increase in the incoming flow velocity, resulting in large errors between the theoretical and experimental airflow velocities, as shown in Figure 6

To investigate the specific causes of such errors and the variation law, the dynamic leaf windward area and canopy resistance to airflow for a 0.3 m-thick canopy at an incoming velocity of 6–15 m/s were measured by the method of determining the canopy aerodynamic parameters in Section 2.2. The variation in the leaf windward area, canopy resistance to airflow, and velocity attenuation factor for a 0.3 m-thick canopy at different incoming velocities were clarified. The relationship is shown in Figure 7. It can be seen that the incoming airflow velocity is negatively correlated with the canopy leaf windward area (Figure 7A), positively correlated with the resistance (Figure 7B) and positively correlated with the velocity attenuation factor (Figure 7C). When the incoming velocity increases, the leaves at 0–0.3 m in the canopy are converged by the airflow, the windward area of the canopy leaves reduces, and the velocity attenuation increases. The experimental airflow velocity is smaller than the theoretical airflow velocity calculated using the static canopy leaf windward area, and with an increase in the incoming flow velocity in a certain range, the error values between the two expand. When the incoming velocity increases to a certain degree (Lr = 4.15 m^2/m^3 corresponds to 14 m/s; Lr = 4.79 m^2/m^3 corresponds to 12 m/s; and Lr = 5.65 m^2/m^3 corresponds to 11 m/s), the elastic deformation of the canopy leaves reaches its maximum value, and the canopy leaf windward area and velocity attenuation factor stabilize (Molina-Aiz et al., 2006). The increase in the error between the experimental and theoretical values of the airflow velocity also stabilizes.

In summary, in order to improve the model accuracy, the dynamic changes in the canopy leaf windward area based on different incoming flow velocities were used to modify the 0–0.3 m canopy airflow resistance model. The modified model is shown in Eq. (15). The corresponding canopy leaf windward area and canopy resistance to airflow at different incoming flow velocities in Figure 7 were substituted into the model, and the theoretical values of airflow velocity in the 0.3 m canopy were calculated and compared with the experimental values of airflow velocity to verify the accuracy of the revised model.

$$\begin{cases} F = \frac{s^0 \rho v_*^2}{4kD'}\left(1 - e^{-2kD}\right) & (D > 0.3m) \\ F = \frac{s^\star \rho v_*^2}{4kD'}\left(1 - e^{-2kD}\right) & (0m \le D \le 0.3m) \end{cases} \quad (15)$$

s^0: the windward area of the canopy leaves in the windless condition [m^2]; $s^\star$: the dynamic canopy leaf windward area at different incoming flow velocities [m^2].

The experimental and theoretical airflow velocities at the 0.3 m canopy at an incoming flow velocity of 6–15 m/s were

10.3389/fpls.2022.1026503

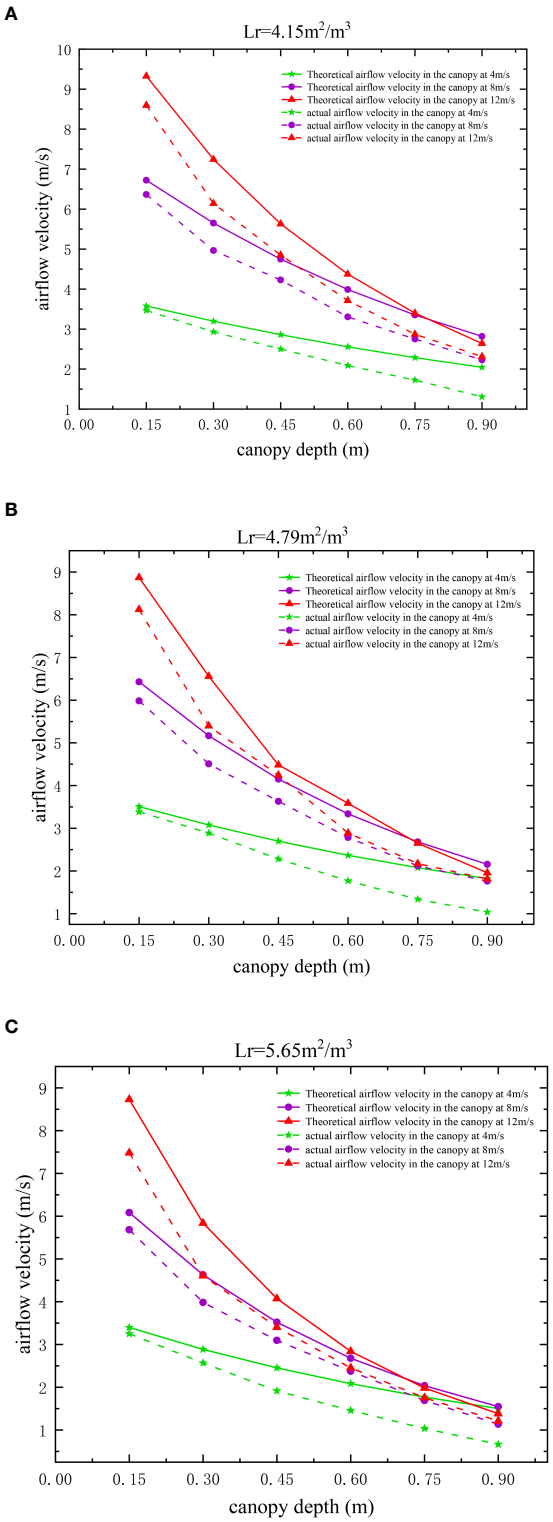

FIGURE 5
Variation in the intra-canopy airflow velocity with canopy depth for different leaf area densities. **(A–C)**.

FIGURE 6
Variation in the windward area of the canopy leaves for different incoming flow velocities.

calculated and perform a linear regression analysis, as shown in Figure 8. The processed data in the figure reveal that, for the three different leaf area densities in this study, the R^2 of the theoretical and experimental airflow velocity at the depth of 0.3 m in the canopy is above 0.9 even when the incoming flow velocity is large, as shown in (Figure 8A–C). This indicates that the theoretical airflow velocity is in good agreement with the actual airflow velocity. It can be seen that the modified model, which considers the coupling effect between the airflow and canopy and calculates the dynamic values of canopy leaf windward area has largely solved the problem of large errors between theoretical and experimental values of airflow velocity in the outer layer of the canopy when the incoming flow velocity is large.

3.4 Analysis of field test results

In this study, two sets of experiments were designed to determine the airflow velocity inside the pear canopy in an orchard environment, where the incoming flow velocities are 8 m/s and 12 m/s, respectively, and the vehicle speeds are 0 m/s and 1 m/s. The results were compared and analyzed with the modified theoretical airflow velocities inside the canopy, as shown in Figure 9.

(1) The effect of the vehicle speed on the magnitude of intra-canopy airflow velocity was investigated by setting the vehicle speeds to 0 m/s and 1 m/s. When the incoming flow velocity was 8 m/s, the mean relative errors at the positions of 0.3 m, 0.6 m and 0.9 m in the canopy were 3.2%, 5.8% and 11.4%, respectively; when the incoming flow velocity was 12 m/s, the mean relative errors at the positions of 0.3 m, 0.6 m and 0.9 m were 2.9%, 7.3%, and 17.9%, respectively. For the three different leaf area densities, the errors of the experimental values of the airflow velocity at any position in the canopy were within 0.4 m/s at incoming flow velocities of 8 m/s and 12 m/s.

Affected by the vehicle speed, the central region of the airflow is slightly off the measurement point of the canopy when the machine reaches the measurement location, resulting in a mildly smaller experimental airflow velocity as the vehicle moves. The difference increases slightly with the depth of the canopy, but remains small in general.

(2) Regarding the applicability of intra-canopy airflow velocity attenuation model in an orchard environment, a comparison between the theoretical and experimental values of the intra-canopy airflow velocities of the pear trees at a vehicle speed of 1 m/s was conducted. It was found that the average model accuracies at the positions of 0.3 m, 0.6 m and 0.9 m were 94.4%, 85.4% and 72.3%, respectively, when the incoming flow velocity was 8 m/s. When the incoming flow velocity was 12 m/s, the average accuracy at the position of 0.3 m, 0.6 m and 0.9 m were 97.2%, 89.3% and 75.1%, respectively. The errors between the theoretical and experimental values of the airflow velocity at any position within the canopies of the three different leaf area densities at the incoming flow velocities of 8 m/s and 12 m/s were within the range of 0.7 m/s.

Only the attenuation effect of the canopy on the airflow was considered when using the model for the theoretical airflow velocity solution; however, the experimental results revealed that the airflow was also obstructed by the air (The deeper the canopy, the stronger the cumulative influence of the air). Therefore, the accuracy of the model was between 70–80% at the canopy position of 0.9 m, but the absolute difference was only between 0.4 and 0.7 m/s. In summary, the attenuation model of intra-canopy airflow velocity constructed in this study is equally applicable in air-assisted spraying in orchards.

10.3389/fpls.2022.1026503

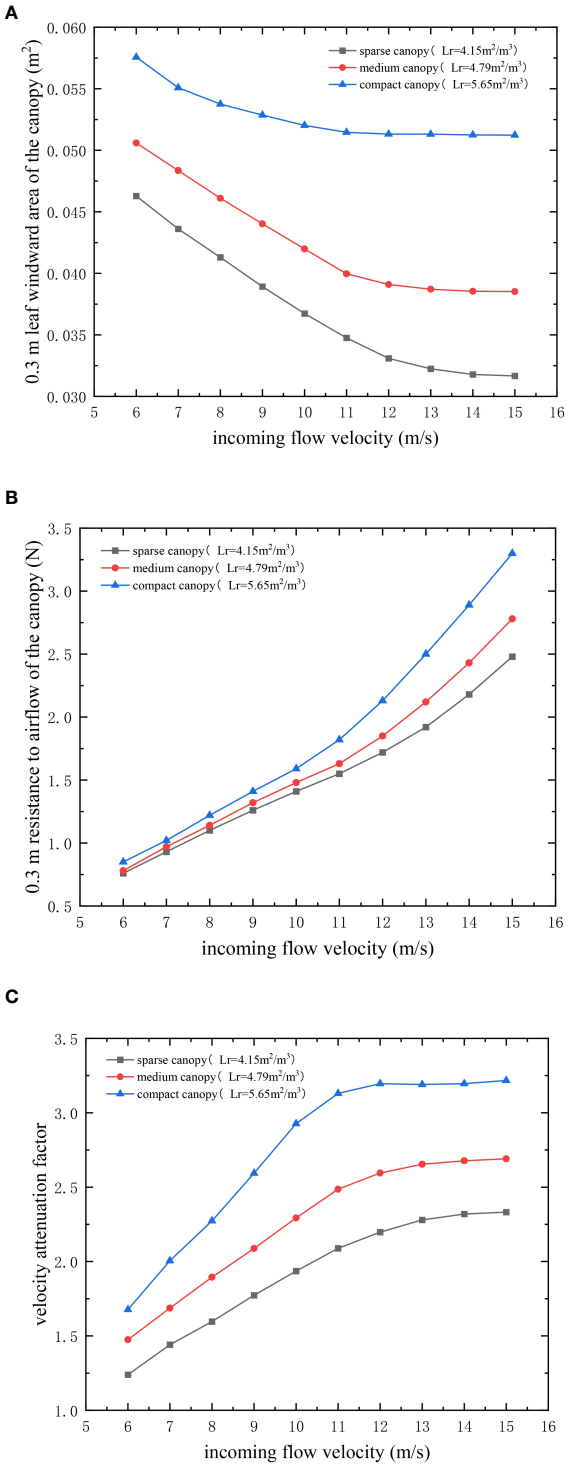

FIGURE 7
Leaf windward area of the canopies and velocity attenuation factor versus the incoming flow velocity. **(A–C)**.

10.3389/fpls.2022.1026503

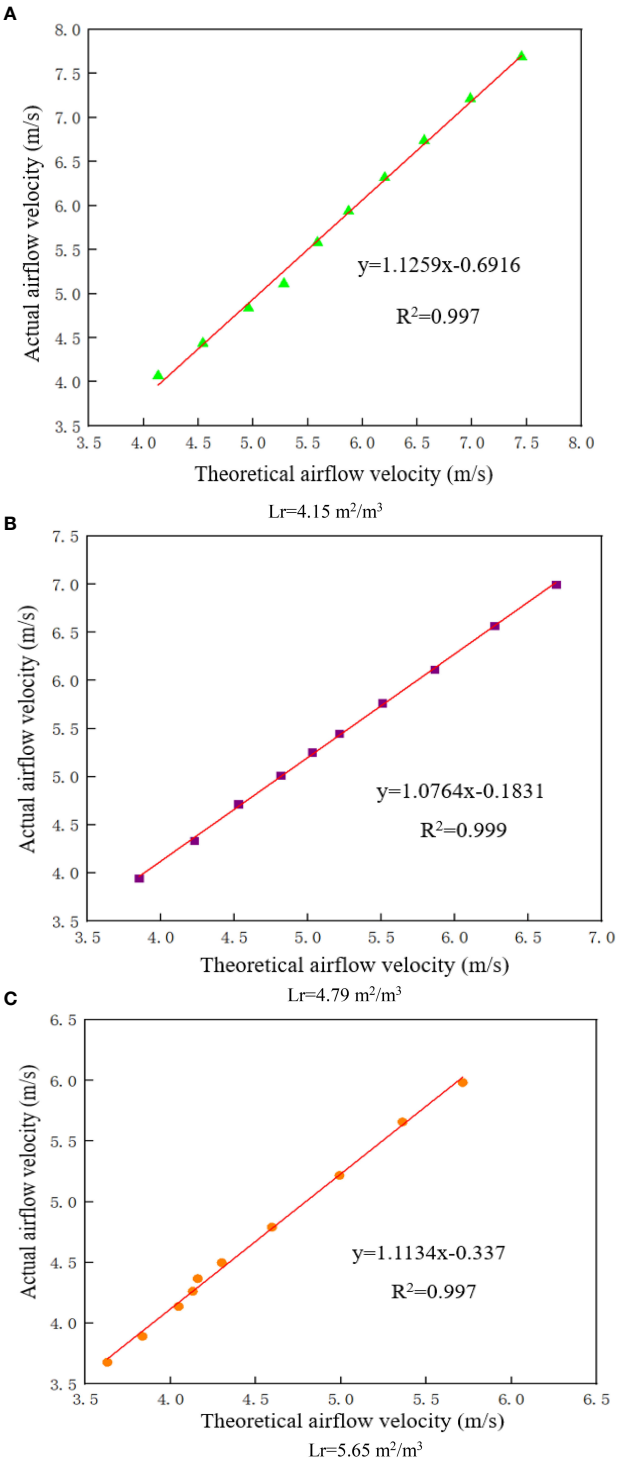

FIGURE 8
Airflow velocity at a depth of 0.3 m in the canopy **(A)** Lr=4.15 m2/m3 **(B)** Lr=4.79 m2/m3 **(C)** Lr=5.65 m2/m3.

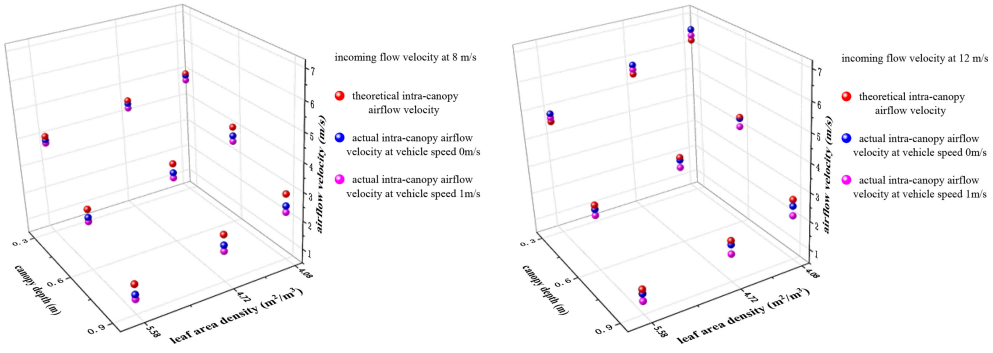

FIGURE 9
Airflow velocities in the pear canopy at different working conditions.

4 Discussion

The superiority of air sprayers in orchard plant protection operations and their control effects have been discussed for decades (Delele et al., 2007). Airflow is one of the most essential parameters of air-spray technology. Therefore, clarifying the attenuation of airflow in a canopy is key to achieving the regulation of airflow parameters of wind-delivered spraying in orchards, and promoting the effect of pest control.

Previous studies on airflow attenuation have reported that the canopy of fruit trees exerts resistance to the flow of air through the passage and captures kinetic energy to reduce the flow rate (Endalew et al., 2008; Endalew et al., 2009). Hence, CFD simulation models were constructed based on resistance coefficients, leaf area density, and other parameters to analyse canopy airflow (Yue et al., 2007; Zhan et al., 2017). However, it is difficult to theoretically reveal the airflow attenuation in the canopy and its influencing factors this way. Based on previous research, the paper constructs a airflow velocity attenuation model in the canopy. The experimental results in this study can reveal the effects of the three variables of leaf area density, canopy depth and incoming velocity on the attenuation of airflow velocity in the canopy respectively: (1) For the canopy with a large leaf area density, the attenuation effect of the canopy on airflow velocity is stronger owing to the denser branches and leaves, and stronger obstruction effect in the canopy; (2) with an increase in the canopy depth, the attenuation degree of airflow velocity gradually decreases, with a rapid attenuation zone at a height of 0–0.3 m and a slow attenuation zone at a height of 0.3–0.9 m. It can be found that the attenuation of airflow in the canopy mainly occurs in the outermost layer of the canopy, thus more attention should be paid to the study of the attenuation of airflow in the outer layer of the canopy. The branches and leaves at a height of 0–0.3 m in the canopy can be pruned appropriately to increase the airflow velocity reaching the canopy and increase the disturbance to the inner canopy to improve the application effect, and to improve the light transmission and air permeability inside the canopy to some extent (Li et al., 2003; McDonald et al., 2013); (3) with an increase in the incoming flow velocity, the attenuation of airflow velocity inside the canopy is greater; therefore, the effect of enhancing the disturbance to the branches and leaves inside the canopy by increasing the incoming flow velocity will decrease with an increase in canopy depth; (4) there is a significant difference between the theoretical and experimental values of the airflow velocity of the outer canopy on the windward side when the flow velocity is larger. This is because the airflow affects the windward area of the outer canopy and subsequently reacts to the airflow, thereby forming an interactive coupling effect.

This study solves the issue of unclear airflow attenuation in the canopy, but certain limitations are still present. (1) only the pear canopy at the same growth period was selected as the research object to verify the accuracy of the model; the leaf area density canopy of the limit working conditions was not verified on other fruit trees. (2) because of the inconvenience in measuring the aerodynamic resistance parameters of the canopy, the canopy foliage was selected instead of the entire canopy. (3) although the influencing factors of the velocity decay factor k and the previously unknown state were sorted, resistance F is still an unassailable parameter, and the quantitative relationship between F and some easily measured parameters of the canopy needs to be further studied. (4) for different types of the canopy was not considered, the current study could not apply directly to commercial orchards based on different planting systems (open-vase, trellis, high-density, etc.).

Although the study has certain limitations, it theoretically reveals the attenuation law of the canopy airflow and its influencing factors. Future studies will track k-values at different growth stages of several representative pear trees;

seek the relationship between k-values, canopy types, and growth periods; and establish a k-value database for pear trees. At the same time, different fruit tree varieties (such as apple trees, peach trees) and different planting systems (open-vase, trellis, high-density, etc.) will be selected to evaluate the applicability of the model. In addition, the optimal intra-canopy airflow velocity can be constructed according to the characteristics of the canopy structure, and the fan speed can be regulated in combination with the wind flow velocity attenuation model in the canopy.

5 Conclusions

This paper clarifies that the intra-canopy airflow velocity attenuation factor k in air-assisted spraying process for pear trees is related to the resistance F, the canopy leaf windward area s and the incoming flow velocity v_*, and constructs the model of airflow velocity attenuation. The model validation results reveal that the average accuracy of the model is around 80% under various working conditions.

As the incoming flow velocity changes the windward area of canopy leaves in the 0–0.3 m region, the greatest difference between the experimental and theoretical values of intra-canopy airflow occurs in this region. In this study, the 0.3 m-thick canopy was used as the research object to modify the model. For the different leaf area density canopy, the R^2 of the theoretical airflow velocity and the actual airflow velocity is above 0.9.

The field experiment results show that the error between the theoretical airflow velocity and actual airflow velocity at any position in the canopy is within 0.7 m/s when the incoming velocity is 8m/s and 12m/s. This indicates that the airflow velocity attenuation model has good applicability in the orchards.

Data availability statement

The original contributions presented in the study are included in the article/supplementary material. Further inquiries can be directed to the corresponding author.

Author contributions

FZ and HS designed the study, performed the experiments. FZ and WQ wrote the manuscript and analyzed the data. XL and WQ suggested changes to the article. YC and GZ contributed to the concept of the study. All authors contributed to the article and approved the submitted version.

Funding

This work was co-financed by the National Natural Science Foundation of China (Grant No. 32171905), the Fundamental Research Funds for the Central Universities (KYCYXT2022016), Jiangsu Agricultural Science and Technology Innovation Fund (CX203172), and the 'Qinglan Project' of Jiangsu Province (QLGC).

Acknowledgments

Appreciations are given to the editor and reviewers of the Journal.

Conflict of interest

The authors declare that the research was conducted in the absence of any commercial or financial relationships that could be construed as a potential conflict of interest.

Publisher's note

References

Chao, X., Chen, S., Qiu, W., Lv, X., Li, H., Han, C., et al. (2019). Simulation and validation of the air flow generated by a multi-channel air-assisted sprayer. *IEEE Access* 7, 94848–94857. doi: 10.1109/access.2019.2927377

Dai, F. F. (2008). Selection and calculation of air volume of air-driven sprayers. *Plant Prot.* 34 (6), 124–127.

Dekeyser, D., Foque, D., Duga, A. T., Verboven, P., Hendrickx, N., and Nuyttens, D. (2014). Spray deposition assessment using different application techniques in artificial orchard trees. *Crop Prot.* 64, 187–197. doi: 10.1016/j.cropro.2014.06.008

Delele, M. A., Jaeken, P., Debaer, C., Baetens, K., Endalew, A. M., Ramon, H., et al. (2007). CFD prototyping of an air-assisted orchard sprayer aimed at drift reduction. *Comput. Electron. Agric.* 55 (1), 16–27. doi: 10.1016/j.compag.2006.11.002

Endalew, A. M., Hertog, M., Delele, M. A., Baetens, K., Ramon, H., Nicolai, B. M., et al. (2008). "Modelling the effect of wind speed and direction on airflow from an air-assisted orchard sprayer through 3D orchard canopy architecture," in *8th International Symposium on Modelling in Fruit Research and Orchard Management.* (Einsiedeln: Acta Horticultu, International Society for Horticultural Science) 97–103.

Endalew, A. M., Hertog, M., Gebrehiwot, M. G., Baelmans, M., Ramon, H., Nicolai, B. M., et al. (2009). Modelling airflow within model plant canopies using an integrated approach. *Comput. Electron. Agric.* 66 (1), 9–24. doi: 10.1016/j.compag.2008.11.002

Fu, B. P. (1963). On forest belt structure and protection efficiency. *J. Nanjing Univ.(Z1)* 9, 109–120.

Gil Sierra, J., Ortiz-Canavate, J., and Riquelme Sanhueza, J. (2006). Short communication. performance of pneumatic spraying with an over-the-row sprayer in high density apple tree orchards. *Spanish J. Agric. Res.* 4 (1), 26–30. doi: 10.5424/sjar/2006041-181

Guan, D. X. (1998). Aerodynamic effect of farmland shelterbelt system. graduate school of Chinese academy of sciences shenyang institute of applied ecology.

Hong, S. W., Zhao, L., and Zhu, H. P. (2018). CFD simulation of airflow inside tree canopies discharged from air-assisted sprayers. *Comput. Electron. Agric.* 149, 121–132. doi: 10.1016/j.compag.2017.07.011

Javier Garcia-Ramos, F., Vidal, M., Bone, A., Malon, H., and Aguirre, J. (2012). Analysis of the air flow generated by an air-assisted sprayer equipped with two axial fans using a 3D sonic anemometer. *Sensors* 12 (6), 7598–7613. doi: 10.3390/s120607598

Li, K. T., Lakso, A. N., Piccioni, R., and Robinson, T. (2003). Summer pruning reduces whole-canopy carbon fixation and transpiration in apple trees. *J. Hortic. Sci. Biotechnol.* 78 (6), 749–754. doi: 10.1080/14620316.2003.11511694

Li, T., Qi, P., Wang, Z. C., Xu, S. Q., Huang, Z., Han, L., et al. (2022). Evaluation of the effects of airflow distribution patterns on deposit coverage and spray penetration in multi-unit air-assisted sprayer. *Agronomy-Basel* 12 (4), 944. doi: 10.3390/agronomy12040944

McDonald, M. R., Gossen, B. D., Kora, C., Parker, M., and Boland, G. (2013). Using crop canopy modification to manage plant diseases. *Eur. J. Plant Pathol.* 135 (3), 581–593. doi: 10.1007/s10658-012-0133-z

Mion, R. L., Sombra, W. A., Duarte, J., Nascimento, E. M. S., Viliotti, C. A., Lucas, F. C. B., et al. (2011). THE USE OF a VERTICAL PATTERNATOR AS PARAMETER FOR ADJUSTMENTS OF AIR ASSITED SPRAYER. *Engenharia Agricola* 31 (2), 352–358. doi: 10.1590/s0100-69162011000200015

Molina-Aiz, F. D., Valera, D. L., Alvarez, A. J., and Madueno, A. (2006). A wind tunnel study of airflow through horticultural crops: Determination of the drag coefficient. *Biosyst. Eng.* 93 (4), 447–457. doi: 10.1016/j.biosystemseng.2006.01.016

Musiu, E. M., Qi, L., and Wu, Y. (2019). Spray deposition and distribution on the targets and losses to the ground as affected by application volume rate, airflow rate and target position. *Crop Prot.* 116, 170–180. doi: 10.1016/j.cropro.2018.10.019

Pan, X. L., Dong, F. S., Wu, X. H., Xu, J., Liu, X. G., and Zheng, Y. (2019). Progress of the discovery, application, and control technologies of chemical pesticides in China. *J. Integr. Agric.* 18 (4), 840–853. doi: 10.1016/s2095-3119(18)61929-x

Panneton, B., Lacasse, B., and Piche, M. (2005). Effect of air-jet configuration on spray coverage in vineyards. *Biosyst. Eng.* 90 (2), 173–184. doi: 10.1016/j.biosystemseng.2004.11.001

Planas, S., Solanelles, F., and Fillat, A. (2002). Assessment of recycling tunnel sprayers in Mediterranean vineyards and apple orchards. *Biosyst. Eng.* 82 (1), 45–52. doi: 10.1006/bioe.2001.0055

Qiu, W., Li, X., Li, C., Ding, W., Lv, X., and Liu, Y. (2020). Design and test of a novel crawler-type multi-channel air-assisted orchard sprayer. *Int. J. Agric. Biol. Eng.* 13 (6), 60–67. doi: 10.25165/j.ijabe.20201306.5362

Salcedo, R., Vallet, A., Granell, R., Garcera, C., Molto, E., and Chueca, P. (2017). Eulerian-Lagrangian model of the behaviour of droplets produced by an air-assisted sprayer in a citrus orchard. *Biosyst. Eng.* 154, 76–91. doi: 10.1016/j.biosystemseng.2016.09.001

Walklate, P. J. (1992). A simulation study of pesticide drift from an air-assisted orchard sprayer. *J. Agric. Eng. Res.* 51 (4), 263–283. doi: 10.1016/0021-8634(92)80042-q

Wu, Q. C., and Qian, Y. D. (2017). The causes and quantitative analysis of air resistance on moving objects are studied by air resistance coefficient tester. *Univ. Phys.* 36 (5), 27–32. doi: 10.16854/j.cnki.1000-0712.2017.05.008

Yue, W., Meneveau, C., Parlange, M. B., Zhu, W., van Hout, R., and Katz, J. (2007). A comparative quadrant analysis of turbulence in a plant canopy. *Water Resour. Res.* 43 (5), W05422. doi: 10.1029/2006wr005583

Zhan, K., Liu, S., Yang, Z., Fang, E., Zhou, L., and Huang, N. (2017). Effects of sand-fixing and windbreak forests on wind flow: a synthesis of results from field experiments and numerical simulations. *J. Arid Land* 9 (1), 1–12. doi: 10.1007/s40333-016-0058-z

frontiers | Frontiers in Plant Science

TYPE Original Research
PUBLISHED 09 November 2022
DOI 10.3389/fpls.2022.962301

OPEN ACCESS

EDITED BY
Paul Weckler,
Oklahoma State University,
United States

REVIEWED BY
Linchun Shi,
Institute of Medicinal Plant Development, Chinese Academy of Medical Sciences and Peking Union Medical College, China
Saeed Hamood Alsamhi,
Ibb University, Yemen

*CORRESPONDENCE
Li Fu
fuli@hdu.edu.cn
Qing Liu
liuqing@cib.ac.cn

SPECIALTY SECTION
This article was submitted to Sustainable and Intelligent Phytoprotection, a section of the journal Frontiers in Plant Science

RECEIVED 06 June 2022
ACCEPTED 24 October 2022
PUBLISHED 09 November 2022

CITATION
Hu J, Shen Y, Zheng Y, Zhou W, Karimi-maleh H, Liu Q and Fu L (2022) Electrochemical fingerprinting sensor for plant phylogenetic investigation: A case of sclerophyllous oak. *Front. Plant Sci.* 13:962301. doi: 10.3389/fpls.2022.962301

Electrochemical fingerprinting sensor for plant phylogenetic investigation: A case of sclerophyllous oak

Jun Hu[1,2], Yin Shen[3], Yuhong Zheng[4], Wei Zhou[4], Hassan Karimi-maleh[5,6,7], Qing Liu[1]* and Li Fu[3]*

[1]CAS Key Laboratory of Mountain Ecological Restoration and Bioresource Utilization & Ecological Restoration and Biodiversity Conservation Key Laboratory of Sichuan Province, Chengdu Institute of Biology, Chinese Academy of Sciences, Chengdu, China, [2]University of Chinese Academy of Sciences, Beijing, China, [3]Key Laboratory of Novel Materials for Sensor of Zhejiang Province, College of Materials and Environmental Engineering, Hangzhou Dianzi University, Hangzhou, China, [4]Institute of Botany, Jiangsu Province and Chinese Academy of Sciences (Nanjing Botanical Garden, Memorial Sun Yat-Sen), Nanjing, China, [5]School of Resources and Environment, University of Electronic Science and Technology of China, Chengdu, China, [6]Department of Chemical Engineering and Energy, Laboratory of Nanotechnology, Quchan University of Technology, Quchan, Iran, [7]Department of Chemical Sciences, University of Johannesburg, Doornfontein Campus, Johannesburg, South Africa

Electrochemical fingerprinting can collect the electrochemical behavior of electrochemically active molecules in plant tissues, so it is regarded as a new plant analysis technology. Because the signal of electrochemical fingerprinting is positively correlated with the amount and type of electrochemically active molecules in plant tissues, it can also be used to reflect genetic differences between different species. Previous electrochemical fingerprinting techniques have been frequently used in phylogenetic studies of herbaceous plants. In this work, 19 *Quercus* species (17 evergreen or semi evergreen species and 2 deciduous species) were selected for investigation. The results indicated the electrochemical fingerprint of some species share similar features but can be distinguished after changing the recording condition (extraction solvent and electrolyte). The two sets of electrochemical fingerprint data can be used to construct different pattern recognition technology, which further speeds up the recognition efficiency. These electrochemical fingerprints were further used in phylogenetic investigations. The phylogenetic results deduced from electrochemical fingerprinting were divided mainly into three clusters. These can provide evidence for some of these arguments as well as new results.

KEYWORDS

electrochemical fingerprint, phytochemistry, electrochemical sensor, pattern recognition, phylogenetics

Introduction

Electrochemical fingerprinting is a new analytical technique, which can be used to collect the information of electrochemically active molecules in plant tissues (Xu et al., 2020; Zhou et al., 2020; Fan et al., 2021; Fu et al., 2021; Wang et al., 2021; Zheng et al., 2021b; Fu et al., 2022). The fingerprint can be used not only for plant identification and growth monitoring, but also for phylogenetic investigation in recent years. These applications are due to the fact that the type and amount of electrochemically active substances in plant tissues can reflect their differences at the genetic level (Karimi-Maleh et al., 2021b; Karimi-Maleh et al., 2021a). Thus, this new analytical technique is beginning to serve as a complementary methodology for phytochemical studies and plant phylogeny. Today, research on electrochemical fingerprinting is mainly focused on herbaceous and lianas. This is because the active substances in these plant tissues can be easily extracted and can contribute a distinct electrical signal. In contrast, there have been few reports on woody plants based on electrochemical fingerprinting. This is because woody plants have more cellulose and lignin in their tissues, which reduces the accuracy of electrochemical fingerprinting.

Quercus is a family of trees under Fagaceae. It is widely distributed in Asia, Africa, Europe and America and other regions, there are about 500 species. *Quercus* are mainly distributed in tropical (subtropical) and temperate regions of the Northern Hemisphere, and are important species of broad-leaved forests. It occupies a large share in the forest area of the northern hemisphere and is of great significance to the local environment beautification and ecological restoration. Abrams believes that *Quercus* has developed root system and thick leaves, which can keep high water potential of these plants in the case of drought and prevent wilting (Abrams, 1990). In addition, *Quercus* can maintain a higher photosynthetic rate under low water potential compared with other groups in the same domain, which is conducive to obtaining competitive advantages in the environment. Cavende-bares et al. (Cavender-Bares et al., 2004b; Cavender-Bares et al., 2004a) found that the life history characteristics of *Quercus* were also influenced and restricted by their living environment. For example, *Quercus* adapted to post-fire habitat are generally shrub type, with strong redifferentiation ability of rhizomes. *Quercus* that grow in humid environment are generally tall trees. *Quercus* distributed in arid environment have resistance mechanism to xylem catheter embolization, which leads to the small amount of water passing through, which is a response of plants to drought stress. *Quercus* grow in humid environments and are free to absorb large amounts of water.

The name *Quercus* was first suggested by the Swedish naturalist Linnaeus. In 1867, Swedish botanist Oersted (Ørsted, 1867) distinguished *Cyclobalanopsis* Oerst from other plants in the genus based on the conformation of shell bracts into concentric circles, and became an independent species of *Cyclobalanopsis* Oerst. In 1924 Trelease (Trelease, 1924) divided *Quercus* into six subgenus groups, including *Cyclobalanopsis*, *Cerris*, *Erythrobalanus*, *Protobalanus* and other subgenera. Camus (Chevalier and Camus, 1954) divided *Quercus* into two subgenera, subgen. *Euquercus* and Subgen. *Cyclobalanopsis*. In 1993, Nixon (Nixon, 1993) adjusted some species of *Quercus* and divided *Quercus* into subgenera Subgen. *Quercus* and subgen. *Cyclobalanopsis*. Japanese scholar Shimaji thought that *Quercus* could be divided into three subgenera after analyzing the anatomical characteristics. It includes subgen. *Erythrobalanus*, subgen. *Lepidobalanus* and subgen. *Cyclobalanopsis*, respectively (Shimaji, 1962). Molecular evidence suggests that there are six large groups of present-day *Quercus*, namely group *Lobatae* (Red Oaks), group *Protobalanus* (Intermediate Oaks), group *Ilex*, group *Cerris*, group *Quercus* (White Oaks) and group *Cyclobalanopsis* (now a separate genus) (Manos et al., 1999; Manos and Stanford, 2001; Denk and Grimm, 2010). In China, botanists have divided *Quercus* into five groups according to the phylogeny and quantitative classification (Peng et al., 2007). They are sect. *Engleriana*, sect. *Brachylepids*, sect. *Quercus*, sect. *Echinolepides* and sect. *Aegilops*. Among them, sect. *Quercus* and sect. *Aegilops* usually deciduous broad-leaved plants, others are evergreen or semi-evergreen broad-leaved plants. Most of evergreen species are called sclerophylla oak because their leaves are leathery, hard and spiny (Chaudhri et al., 2022; Farooq et al., 2022; Ismail et al., 2022). There has been a great controversy about the relationship between species within the sclerophylla oak. In this work, 19 species of Quercus (17 evergreen or semi evergreen species and 2 deciduous species) and 2 species of Cyclobalanopsis were investigated using electrochemical fingerprinting. Electrochemical fingerprinting of all plant tissues was collected under two conditions. The collected results were used not only for plant identification, but also for phylogenetic investigation.

Materials and method

Sample collection

Leaves of *Quercus rehderiana*, *Q. monimotricha, Q. gilliana, Q. variabilis, Q. pseudosemecarpofolia, Q. guajavifolia, Q. longispica, Q. spinosa, Q. engleriana, Q. fimbriata, Q. franchetii, Q. senescens, Q. baronii, Q. dolicholepis, Q. cocciferoides, Q. oxyphylla* and *Q. aquifolioides* were collected during field investigation, *Q. aliena, Q. phillyraeoides, Cyclobalanopsos myrsinifolia* and *Cyclobalanopsis glauca* were collected from Chengdu City Park and Nanjing Botanical Garden Men. Sun Yat-Sen (Table 1). The voucher specimens are deposited in the herbarium of Chengdu Institute of biology (CDBI), Chinese Academy of Sciences and the herbarium of Nanjing Botanical

TABLE 1 Leaves for electrochemical analysis.

NO	species	Collector	Voucher	Location
1	Q. monimotricha	Jun Hu, et all	CDhujun20210713P01S01	Meigu, Sichuan
2	Q. guajavifolia	Jun Hu, et all	CDhujun20210714P02S02	Meigu, Sichuan
3	Q. aquifolioides	Jun Hu, et all	CDhujun20210804P02S01	Meigu, Sichuan
4	Q. senescens	Jun Hu, et all	CDhujun20210717P02S01	Xichang, Sichuan
5	Q. rehderiana	Jun Hu, et all	CDhujun20210724P01S01	Yongsheng, Yunnan
6	Q. longispica	Jun Hu, et all	CDhujun20210721P01S01	Huaping, Yunnan
7	Q. pseudosemecarpifolia	Jun Hu, et all	hujun20210718-B02	Ninglang, Yunnan
8	Q. cocciferoides	Jun Hu, et all	CDhujun20210727P02S01	Muli, Sichuan
9	Q. fimbriata	Jun Hu, et all	CDhujun20210808P02S01	Kangding, Sichuan
10	Q. variabilis	Jun Hu, et all	CDhujun20210809P01S08	Mianning, Sichuan
11	Q. spinosa	Jun Hu, et all	CDluoyao20210914S002	Lixian, Sichuan
12	Q. dolicholepis	Jun Hu, et all	CDluoyao20210914S003	Lixian, Sichuan
13	Q. baronii	Jun Hu, et all	CDluoyao20210914S001	Lixian, Sichuan
14	Q. engleriana	Sirong Yi	yisirong20210911B01	Zunyi, Guizhou
15	Q. oxyphylla	Sirong Yi	yisirong20210905B01	Shizhu, Chongqing
16	Q. franchetii	Jun Hu, et all	hujunCX001	Huili, Sichuan
17	Q. aliena	Yao Luo	None	Chengdu city park, cultivated plants
18	Q. gilliana	Jun Hu, et all	CDhujun20210809P01S01	Mianning, Sichuan
19	Q. phillyraeoides	Yuhong Zheng	NAS00590201	Nanjing Botanical Garden Men.Sun Yat-Sen, cultivated plants
20	Cyclobalanopsis glauca	Yuhong Zheng	None	Nanjing Botanical Garden Men.Sun Yat-Sen, cultivated plants
21	C. myrsinifolia	Yuhong Zheng	None	Nanjing Botanical Garden Men.Sun Yat-Sen, cultivated plants

Garden Men.Sun Yat-Sen (NAS). Only mature and healthy leaves were harvested. All samples were kept frozen (-20°C) before analysis.

Extraction preparation

All extraction process was conducted under room temperature. Water and ethanol were used as the solvents in the extraction procedure. Specifically, 0.3 g leaves were cut and added to 5 mL of solvent. The mixture was supplemented with four grinding beads. The tube was put in a tissue grinding device (Meibi-96, Zhejiang, China) for 2 min extraction. After waiting for precipitation, the supernatant was collected for electrochemical fingerprint collection.

Electrochemical fingerprints collection

Phosphate buffer solution (PBS, 0.1 M) and acetic acid buffer (ABS, 0.1 M) were used as electrolytes to support electrochemical fingerprint collection. Electrochemical fingerprinting was determined using a traditional three-electrode system. A glassy carbon electrode, a platinum wire and an Ag/AgCl electrode were used as working electrode, counter electrode and reference electrode, respectively. All electrochemical experiments were conducted under a CHI 760E working station at room temperature. a differential pulse voltammetry (DPV) was recorded from -0.1 to 1.3 V. The experimental data was then normalized for further analysis.

Results and discussion

The information of electrochemically active molecules in plant tissues was collected by electrochemical fingerprinting. The anodic scanning representing the electrochemical oxidation behavior of molecules. As shown in Figure 1 (collected under PBS after extraction with water), in the range of 0-1.3V, *Q. monimotricha, Q. engleriana, Q. aquifolioides, Q. rehderiana, Q. spinosa, Q. gilliana* and *Q. pseudosemecarpifolia* all showed electrochemical oxidation behavior. In addition, these species show similar electrochemical oxidation trend, with an obvious electrochemical oxidation peak near 0.4 V. This similarity in electrochemical behavior is common among plants of the same genus. This is because species within the genus have relatively similar genes, and therefore have a high degree of similarity in the species of electrochemically active molecules in tissues (Ye et al., 2021). However, beyond the obvious large oxidation peak of about 0.4 V, different species showed different electrochemical behaviors. For example, *Q. aquifolioides* has a half-overlapped oxidation peak near 0.4 V. *Q. rehderiana* has a wide oxidation peak at about 0.6 V, representing a range of substances oxidized in this window. On the other hand, there are some species that

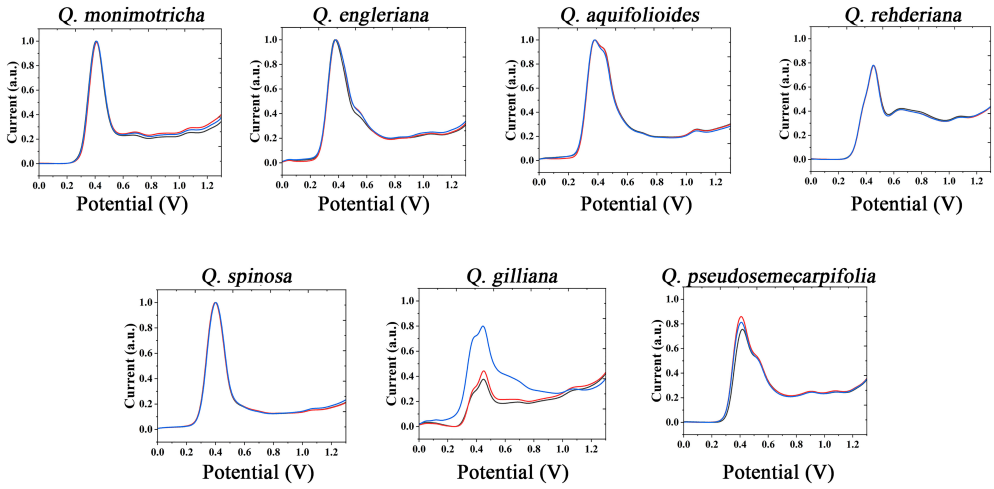

FIGURE 1
Electrochemical fingerprint of *Q. monimotricha, Q. engleriana, Q. aquifolioides, Q. rehderiana, Q. spinosa, Q. gilliana* and *Q. pseudosemecarpifolia* after water extraction and recorded under PBS condition with three repetitive tests.

are very similar in their electrochemical behavior, such as *Q. engleriana and Q. pseudosemecarpifolia*.

Figures S1 and S2 show the electrochemical behavior of the remaining species collected under PBS after water extraction. All species exhibit essentially the electrochemical behavior described above. Some of these species exhibit similar electrochemical behavior, such as *Q. oxyphylla* and *Q. variabilis*. Three electrochemical fingerprints were taken for each sample. It can be seen that most of the samples have very good repeatability. However, the DPV curves of some samples do not coincide completely. However, the different fingerprints have a very consistent behavior, representing the same molecules involved in electrochemical oxidation (Zheng et al., 2021a). Some fingerprints had a higher current intensity than others, indicating a higher concentration of one type of electrochemically active molecule in the sample. This is very common in plant samples. Even among plants in the same area, different environmental factors will lead to changes in the content of molecules in tissues (Łaska et al., 2019; Ousaaid et al., 2021).

The use of the same solvent for plant tissue extraction and the use of the same electrolyte to support electrochemical fingerprinting can cause different species to exhibit relatively similar electrochemical behavior. Therefore, we also extracted the plant tissues with ethanol and collected the electrochemical fingerprints in ABS environment. Figure 2 shows DPV profiles of *Q. monimotricha, Q. engleriana, Q. aquifolioides, Q. rehderiana, Q. spinosa, Q. gilliana and Q. pseudosemecarpifolia* after ethanol extraction under ABS. It can be seen that all species exhibit very different electrochemical behavior under these conditions than in Figure 1. There are two factors that account for the difference in electrochemical behavior. First, different solvents extract different electrochemically active molecules from plant tissues (Moro et al., 2020). Therefore, there are different kinds of molecules involved in the process of electrochemical fingerprinting. On the other hand, ABS has an acidic pH, so the same electrochemically active molecule behaves differently in neutral and acidic environments (Fu et al., 2020). As can be seen from the figure, the electrochemical fingerprints similar in Figure 1, such as *Q. engleriana* and *Q. pseudosemecarpifolia*, show very large differences in Figure 2. Therefore, if the fingerprint of both conditions is combined, the species can be clearly identified. We further conducted MANOVA tests for our data. The p values of the DPVs recorded within species all larger than 0.05, indicating no significant differences. However, when comparing different species, the p-value is between $3.2e^{-07}$ to $6.9e^{-07}$. This result suggesting the significantly different. Therefore, the differences of electrochemical fingerprints between species are much larger than the same species. We believe the environmental factors such as habitat and fertilization certainly affect the content of many chemical constitutions (including electro-active compounds) and consequently change signal intensity. Many GC-MS based works also report the content variation of extracted compounds (Jin, 2009; Berkov et al., 2012). These works suggest the environmental factors can only slightly affect the ratio of compounds without changing compound types. Therefore, main pattern of voltammograms collected from different species will be largely unaffected.

Figures S2 and S3 show the electrochemical behavior of the remaining species collected under ABS after ethanol extraction. The trends of these electrochemical fingerprints are very similar to those in Figures S1 and S2. Different species showed electrochemical oxidation behavior in the scanning window,

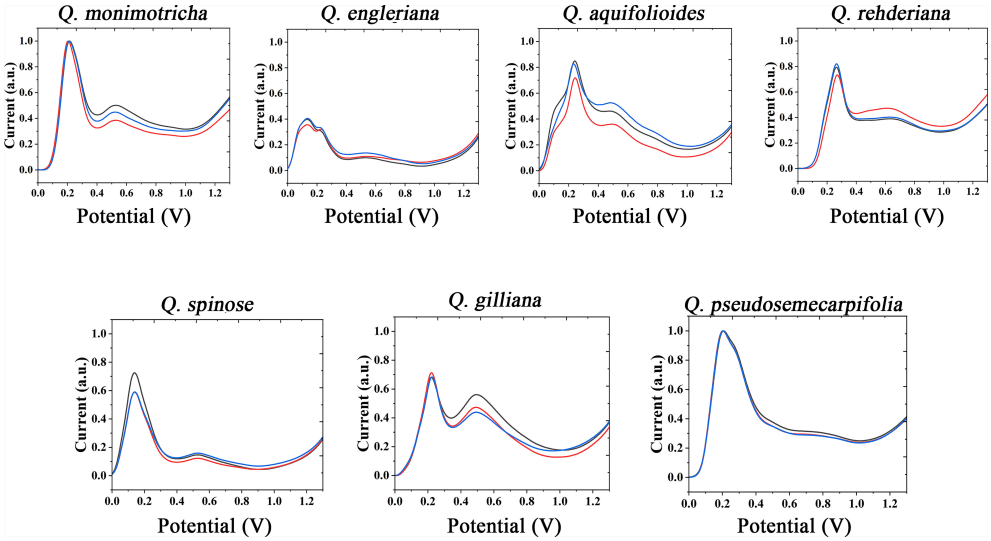

FIGURE 2
Electrochemical fingerprint of *Q. monimotricha, Q. engleriana, Q. aquifolioides, Q. rehderiana, Q. spinosa, Q. gilliana* and *Q. pseudosemecarpifolia* after ethanol extraction and recorded under ABS condition with three repetitive tests.

indicating that chemically active molecules were involved in the reaction. Different species exhibit different behaviors, representing differences in the composition and amount of electrochemically active molecules in their tissues. These differences can be used not only for rapid identification of species, but also to reflect genetic differences.

It is not a fast method to use DPV curve to identify species, especially when some species have similar profiles. Therefore, it is a scientific way to construct the pattern using electrochemical fingerprint. Figure 3 shows the scatter plots of *Q. monimotricha, Q. engleriana, Q. aquifolioides, Q. rehderiana, Q. spinosa, Q. gilliana and Q. pseudosemecarpifolia* constructed by

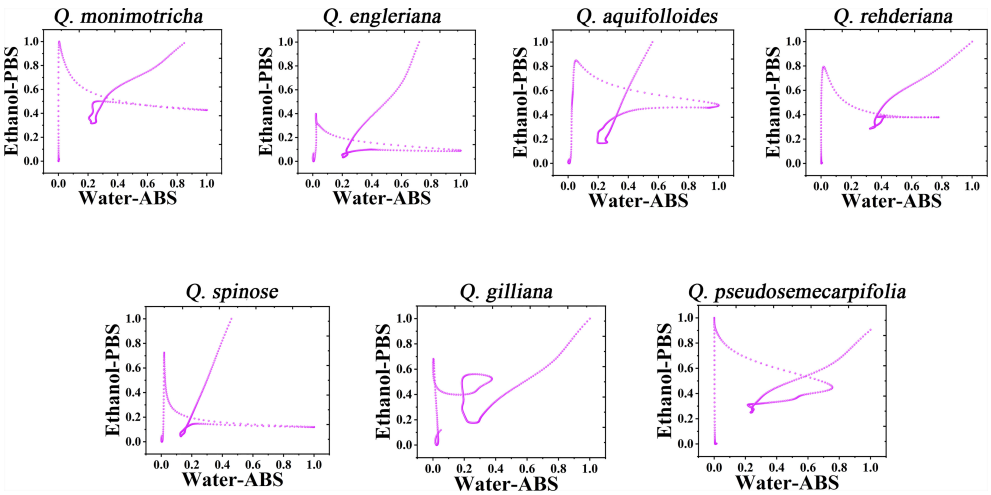

FIGURE 3
Scatter plots of *Q. monimotricha, Q. engleriana, Q. aquifolioides, Q. rehderiana, Q. spinosa, Q. gilliana* and *Q. pseudosemecarpifolia* combining the signals collected under ABS for the water extracts and under PBS for the ethanol extracts.

electrochemical fingerprints collected under two conditions. The data on the X-axis is the current value of the electrochemical fingerprint collected under PBS after water extraction of different species tissues, while the data on the Y-axis is the current value collected under ABS after ethanol extraction of these species. As you can see, when the two sets of fingerprint data are combined, different species present different scatter plots. Scatter plots of the remaining species are provided in Figures S5 and S6. It can be seen that the difference of scatter plots of different species is greater than the direct DPV profile. This is because the superposition of multidimensional data increases the abundance of data and thus improves the resolution (Dexter et al., 2018; Nonato and Aupetit, 2018). Species identification can be achieved by dividing the scatter map and counting the number of points in the region.

Further consideration of the distance between points in the scatter plots can obtain a two-dimensional density diagram. In this mode, areas with multiple points appear bright, while areas with fewer points appear dark. Figure 4 shows the 3D density plots of *Q. monimotricha, Q. engieriana, Q. aquifolioides, Q. rehderiana, Q. spinosa*, *Q. gilliana and Q. pseudosemecarpifolia* constructed by electrochemical fingerprints collected under two conditions. In this model, differences between species can be identified by targeting the highlighted area directly. For example, the similar *Q. engieriana* and *Q. pseudosemecarpifolia* in Figure 1 are not the same in the highlighted area here. More specifically, *Q. engleriana* was highlighted in (0.20, 0.03) while *Q. pseudosemecarpifolia* in (0.22, 0.31). 2D density plots of the remaining species are provided in Figures S7 and S8. The similar profiles of *Q. engleriana* and *Q. pseudosemecarpifolia* in Figure S1 are not the same in the highlighted area here as well. *Q. oxyphylla* was highlighted in (0.38, 0.21) while *Q. variabilis* in (0.25, 0.18).

From the 2D density plots, it was found that the highlights of most species were around 0.2 on the X-axis and 0.4 on the Y-axis. Considering the error of electrochemical fingerprint, this pattern recognition method has a certain probability of misjudgment in theory. However, it was not particularly convenient to determine the unhighlighted areas of the 2D density plots, so we further constructed the heat map using electrochemical fingerprinting. Figure 5 shows the heatmap of *Q. monimotricha, Q. engieriana, Q. aquifolioides, Q. rehderiana, Q. spinosa*, *Q. gilliana and Q. pseudosemecarpifolia* constructed by electrochemical fingerprints collected under two conditions. Heat maps can be graded according to the density of data points. Moreover, it divides the whole region equally, which is good for statistical purposes (Hervella et al., 2020). According to the scoring method of different grades, heat maps are more suitable for the identification of different species.

In addition to species identification, another potential application of electrochemical fingerprinting is to use fingerprint differences to investigate phylogenetic position of species. This is because although electrochemical fingerprinting cannot be used for qualitative and quantitative analysis of active molecules in plant tissues, its current value is proportional to their amount. At the same time, the amount and types of electrochemically active substances in plant tissues are regulated by genes. Therefore, differences in electrochemical fingerprints can be used to reflect genetic differences between different species (Fu et al., 2019; Lu et al., 2020; Sun et al., 2021). The electrochemical fingerprint data under different conditions

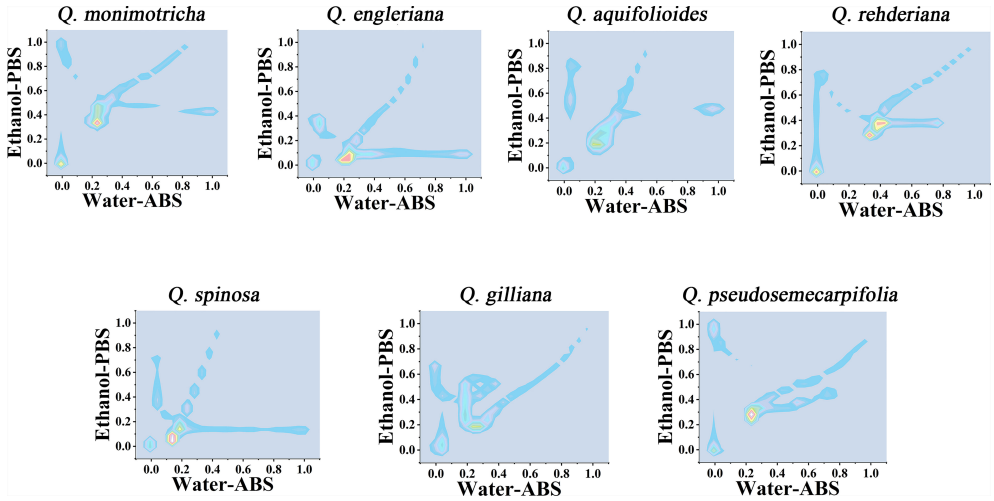

FIGURE 4
Two-dimensional density map of *Q. monimotricha, Q. engleriana, Q. aquifolioides, Q. rehderiana, Q. spinosa, Q. gilliana* and *Q. pseudosemecarpifolia* combining the signals collected under ABS for the water extracts and under PBS for the ethanol extracts.

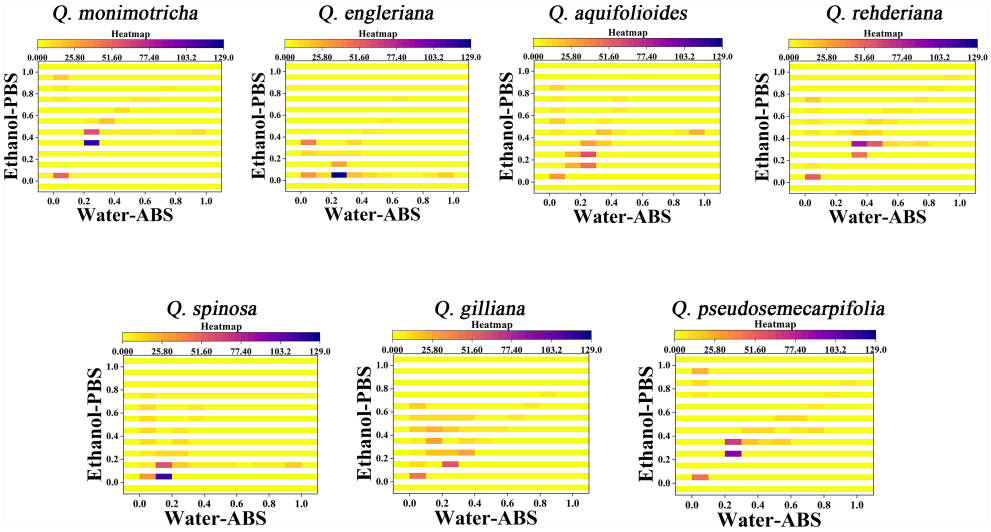

FIGURE 5
Heatmap of *Q. monimotricha, Q. engieriana, Q. aquifolioides, Q. rehderiana, Q. spinosa, Q. gilliana* and *Q. pseudosemecarpifolia* combining the signals collected under ABS for the water extracts and under PBS for the ethanol extracts.

can be used for cluster analysis after the same processing. The collection of electrochemical fingerprinting for more than one condition can increase the abundance of data and provide a more complete picture of electrochemically active molecules in plant tissues. Figure 6 shows the clustering analysis graph constructed by using the electrochemical fingerprints collected under the two conditions. It can be seen from the figure that the whole system tree can be divided into five clusters. *Cyclobalanopsis myrsinifolia* and *Cyclobalanopsis glauca* were grouped together as outgroups. This is because they belong to a different genus than other species. However, *Q. oxyphylla* was also grouped together. We did not find previous reports on *Q. oxyphylla* in related phylogenetic studies, so we could not compare this result with previous investigations. This result deduced from

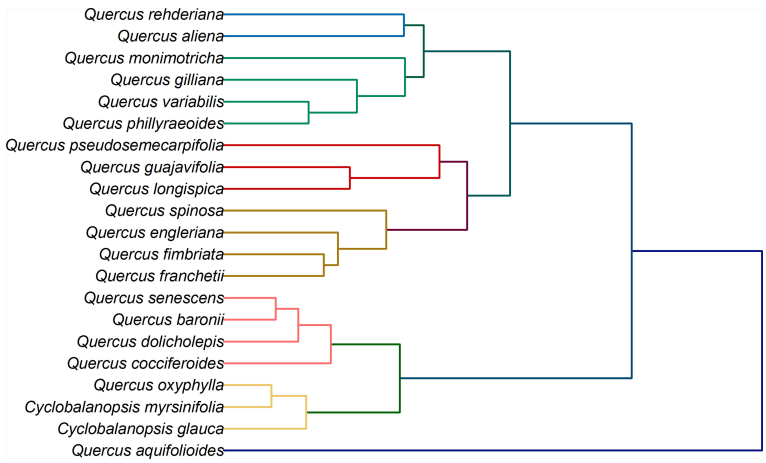

FIGURE 6
Dendrogram of *Q. rehderiana, Q. aliena, Q. monimotricha, Q. gilliana, Q. variabilis, Q. phillyraroides, Q. pseudosemecarpofolia, Q. guajavifolia, Q. longispica, Q. spinosa, Q. engleriana, Q. fimbriata, Q. franchetii, Q. senescens, Q. baronii, Q. dolicholepis, Q. cocciferoides, Q. oxyphylla, Q. aquifolioides, Cyclobalanopsos myrsinifolia* and *Cyclobalanopsis glauca* based on electrochemical fingerprints.

electrochemical fingerprinting potentially provides a report for future research. Curiously, *Q. aquifolioides* did not cluster with any other species. In recent years, several molecular markers have been used to study the evolutionary history and population dynamics of *Q. aquifolioides*, and to reveal the influence of past climate and geological history on the intraspectic radiation evolution of this species (Du et al., 2017). Based on chloroplast fragments (cpDNA), ITS sequences, and microsatellite markers (nSSR), Feng et al. (2016) investigated the evolutionary history and population dynamics of *Quercus pseudosemecarpifolia*, *Quercus aquifolioides*, and *Quercus rehderiana* distributed in the Eastern Himalaya-Hengduan Mountains and their adjacent areas. They reveal the effects of the uplift of the Tibetan Plateau and the quaternary ice age upheaval on the distribution pattern of genetic variation of quercus sclerotiorum species in the region. However, due to the limited number of selected molecular markers and the limitations of selected sample materials, the current studies cannot fully explain their genetic evolution. Unfortunately, the results of electrochemical fingerprinting do not provide further evidence. The remaining species are divided mainly into three clusters. The first cluster is the largest cluster, which contains *Q. rehderiana, Q. aliena, Q. monimotricha, Q. gilliana, Q. variabilis* and *Q. phillyraeoides*. Previously, *Q. rehderiana*, *Q. pseudosemecarpifolia* and *Q. gilliana* were merged into a species based on AFLP markers (Zhou et al., 2003). Our results here support the merge of *Q. rehderiana* and *Q. gilliana*, but *Q. pseudosemecarpifolia* is in another cluster. The second cluster includes *Q. pseudosemecarpifolia, Q. guajavifolia, Q. longispica, Q. spinosa, Q. engleriana, Q. fimbriata* and *Q. franchetii*. Ju et al. (2019) reported in recent work that *Q. pseudosemecarpifolia* and *Q. longispica* can be clustered together. They also reported that *Q. guajavifolia* and *Q. spinosa* could be clustered together. The two species *Q. engleriana* and *Q. franchetii* are rarely studied and no taxonomic results have been reported. The third cluster includes *Q. senescens*, *Q. baronii*, *Q. dolicholepis* and *Q. cocciferoides*. This result is partly confirmed by the AFLP analysis (Shuxia et al., 2003; Shuxia et al., 2005). Although many taxonomists have studied *Quercus*, it is difficult to grasp the taxonomic characters of *Quercus* because of its large number of species and wide distribution. Many of these species have great morphological variation in different habitats. At the same time, the phenomenon of interspecific hybridization is common in natural environment, which brings some difficulties to phylogenetic study. Our phylogenetic results here, based on electrochemical fingerprinting, provide evidence for some of these arguments as well as new results. This provides a direction for future phylogenetic studies of *Quercus*.

Conclusion

The electrochemical fingerprints of *Q. rehderiana, Q. aliena, Q. monimotricha, Q. gilliana, Q. variabilis, Q. phillyraroides, Q. pseudosemecarpofolia, Q. guajavifolia, Q. longispica, Q. spinosa, Q. engleriana, Q. fimbriata, Q. franchetii, Q. senescens, Q. baronii, Q. dolicholepis, Q. cocciferoides, Q. oxyphylla, Q. aquifolioides, Cyclobalanopsos myrsinifolia* and *Cyclobalanopsis glauca* were recorded by their leaf extract under electrolytes. Water and ethanol were selected as extraction solvents while the PBS and ABS were used as supporting electrolyte. The electrochemical fingerprints showed that all *Quercus* showed similar electrochemical oxidation trends, but each species still had its own unique characteristics. Species identification can be achieved by analyzing electrochemical fingerprints. The electrochemical fingerprints collected under the two conditions can be used to form different pattern recognition, which is faster and more effective than DPV profile. Electrochemical fingerprinting is used to construct phylogenetic trees because it can reflect the differences at the genetic level of different species. Our phylogenetic results here, based on electrochemical fingerprinting, provide evidence for some of these arguments as well as new results. This provides a direction for future phylogenetic studies of *Quercus*.

Data availability statement

The original contributions presented in the study are included in the article/Supplementary Material. Further inquiries can be directed to the corresponding authors.

Author contributions

LF, QL, and HK contributed conception and design of the study. JH, YS, YZ, and WZ conducted electrochemical experiments. JH, YS, and HK performed the statistical analysis. JH, YZ and QL wrote the manuscript. All authors contributed to the article and approved the submitted version.

Funding

This research was funded by the Second Tibetan Plateau Scientific Expedition and Research Program (STEP) (Grant no. 2019QZKK0301) and Major Program for Basic Research Project of Yunnan Province (202101BC070002).

Conflict of interest

The authors declare that the research was conducted in the absence of any commercial or financial relationships that could be construed as a potential conflict of interest.

Publisher's note

All claims expressed in this article are solely those of the authors and do not necessarily represent those of their affiliated organizations, or those of the publisher, the editors and the reviewers. Any product that may be evaluated in this article, or claim that may be made by its manufacturer, is not guaranteed or endorsed by the publisher.

Supplementary material

The Supplementary Material for this article can be found online at: https://www.frontiersin.org/articles/10.3389/fpls.2022.962301/full#supplementary-material

References

Ørsted, A. S. (1867). *Bidrag til egeslægtens systematik*. éditeur non identifié. *Vidensk Meded Nat For Kjobenhavn*, 18, 11–96

Abrams, M. D. (1990). Adaptations and responses to drought in quercus species of north America. *Tree Physiol.* 7, 227–238. doi: 10.1093/treephys/7.1-2-3-4.227

Berkov, S., Viladomat, F., Codina, C., Suárez, S., Ravelo, A., and Bastida, J. (2012). GC-MS of amaryllidaceous galanthamine-type alkaloids. *J. Mass Spectrom.* 47, 1065–1073. doi: 10.1002/jms.3059

Cavender-Bares, J., Ackerly, D. D., Baum, D., and Bazzaz, F. (2004a). Phylogenetic overdispersion in Floridian oak communities. *Am. Nat.* 163, 823–843. doi: 10.1086/386375

Cavender-Bares, J., Kitajima, K., and Bazzaz, F. (2004b). Multiple trait associations in relation to habitat differentiation among 17 Floridian oak species. *Ecol. Monogr.* 74, 635–662. doi: 10.1890/03-4007

Chaudhri, S. N., Rajput, N. S., Alsamhi, S. H., Shvetsov, A. V., and Almalki, F. A. (2022). Zero-padding and spatial augmentation-based gas sensor node optimization approach in resource-constrained 6G-IoT paradigm. *Sensors* 22, 3039. doi: 10.3390/s22083039

Chevalier, A., and Camus, A. (1954). L'Œuvre de e. poilane en indochine de 1918 à 1942. *J. Agric. Tradit. Bot. Appliquée* 1, 385–406.

Denk, T., and Grimm, G. W. (2010). The oaks of western Eurasia: traditional classifications and evidence from two nuclear markers. *Taxon* 59, 351–366. doi: 10.1002/tax.592002

Dexter, E., Rollwagen-Bollens, G., and Bollens, S. M. (2018). The trouble with stress: A flexible method for the evaluation of nonmetric multidimensional scaling. *Limnol. Oceanogr. Methods* 16, 434–443. doi: 10.1002/lom3.10257

Du, F. K., Hou, M., Wang, W., Mao, K., and Hampe, A. (2017). Phylogeography of quercus aquifolioides provides novel insights into the neogene history of a major global hotspot of plant diversity in south-west China. *J. Biogeogr.* 44, 294–307. doi: 10.1111/jbi.12836

Fan, B., Wang, Q., Wu, W., Zhou, Q., Li, D., Xu, Z., et al. (2021). Electrochemical fingerprint biosensor for natural indigo dye yielding plants analysis. *Biosensors* 11, 155. doi: 10.3390/bios11050155

Farooq, M. U., Wang, X., Hawbani, A., Khan, A., Ahmed, A., Alsamhi, S., et al. (2022). POWER: probabilistic weight-based energy-efficient cluster routing for large-scale wireless sensor networks. *J. Supercomput.* 78, 12765–12791. doi: 10.1007/s11227-022-04372-z

Feng, L., Zheng, Q.-J., Qian, Z.-Q., Yang, J., Zhang, Y.-P., Li, Z.-H., et al. (2016). Genetic structure and evolutionary history of three alpine sclerophyllous oaks in East himalaya-hengduan mountains and adjacent regions. *Front. Plant Sci.* 7, 1688. doi: 10.3389/fpls.2016.01688

Fu, L., Wu, M., Zheng, Y., Zhang, P., Ye, C., Zhang, H., et al. (2019). Lycoris species identification and infrageneric relationship investigation *via* graphene enhanced electrochemical fingerprinting of pollen. *Sens. Actuators B Chem.* 298, 126836. doi: 10.1016/j.snb.2019.126836

Fu, L., Zhang, X., Ding, S., Chen, F., Lv, Y., Zhang, H., et al. (2022). Recent developments in the electrochemical determination of sulfonamides. *Curr. Pharm. Anal.* 18, 4–13. doi: 10.2174/1573412917999201006195229

Fu, L., Zheng, Y., Wang, A., Zhang, P., Ding, S., Wu, W., et al. (2021). Identification of medicinal herbs in asteraceae and polygonaceae using an electrochemical fingerprint recorded using screen-printed electrode. *J. Herb. Med.* 30, 100512. doi: 10.1016/j.hermed.2021.100512

Fu, L., Zheng, Y., Zhang, P., Zhang, H., Xu, Y., Zhou, J., et al. (2020). Development of an electrochemical biosensor for phylogenetic analysis of amaryllidaceae based on the enhanced electrochemical fingerprint recorded from plant tissue. *Biosens. Bioelectron.* 159, 112212. doi: 10.1016/j.bios.2020.112212

Hervella, Á.S., Rouco, J., Novo, J., Penedo, M. G., and Ortega, M. (2020). Deep multi-instance heatmap regression for the detection of retinal vessel crossings and bifurcations in eye fundus images. *Comput. Methods Programs Biomed.* 186, 105201. doi: 10.1016/j.cmpb.2019.105201

Ismail, A. S., Wang, X., Hawbani, A., Alsamhi, S., and Abdel Aziz, S. (2022). Routing protocols classification for underwater wireless sensor networks based on localization and mobility. *Wirel. Netw.* 28, 797–826. doi: 10.1007/s11276-021-02880-z

Jin, Z. (2009). Amaryllidaceae and sceletium alkaloids. *Nat. Prod. Rep.* 26, 363–381. doi: 10.1039/b718044f

Ju, M.-M., Feng, L., Yang, J., Yang, Y.-C., Chen, X.-D., and Zhao, G.-F. (2019). Evaluating population genetic structure and demographic history of quercus spinosa (Fagaceae) based on specific length amplified fragment sequencing. *Front. Genet.* 965. doi: 10.3389/fgene.2019.00965

Karimi-Maleh, H., Khataee, A., Karimi, F., Baghayeri, M., Fu, L., Rouhi, J., et al. (2021a). A green and sensitive guanine-based DNA biosensor for idarubicin anticancer monitoring in biological samples: A simple and fast strategy for control of health quality in chemotherapy procedure confirmed by docking investigation. *Chemosphere* 291, 132928. doi: 10.1016/j.chemosphere.2021.132928

Karimi-Maleh, H., Orooji, Y., Karimi, F., Alizadeh, M., Baghayeri, M., Rouhi, J., et al. (2021b). A critical review on the use of potentiometric based biosensors for biomarkers detection. *Biosens. Bioelectron.* 184, 113252. doi: 10.1016/j.bios.2021.113252

Łaska, G., Sieniawska, E., Świątek, Ł., Zjawiony, J., Khan, S., Boguszewska, A., et al. (2019). Phytochemistry and biological activities of polemonium caeruleum l. *Phytochem. Lett.* 30, 314–323. doi: 10.1016/j.phytol.2019.02.017

Lu, Y., Xu, Y., Shi, H., Zhang, P. Z. H., and Fu, L. (2020). Feasibility of electrochemical fingerprinting for plant phylogeography study: A case of chimonanthus praecox. *Int. J. Electrochem Sci.* 15, 758–764. doi: 10.20964/2020.01.64

Manos, P. S., Doyle, J. J., and Nixon, K. C. (1999). Phylogeny, biogeography, and processes of molecular differentiation in quercus subgenus quercus (Fagaceae). *Mol. Phylogenet. Evol.* 12, 333–349. doi: 10.1006/mpev.1999.0614

Manos, P. S., and Stanford, A. M. (2001). The historical biogeography of fagaceae: tracking the tertiary history of temperate and subtropical forests of the northern hemisphere. *Int. J. Plant Sci.* 162, S77–S93. doi: 10.1086/323280

Moro, G., Barich, H., Driesen, K., Felipe Montiel, N., Neven, L., Domingues Mendonça, C., et al. (2020). Unlocking the full power of electrochemical fingerprinting for on-site sensing applications. *Anal. Bioanal. Chem.* 412, 5955–5968. doi: 10.1007/s00216-020-02584-x

Nixon, K. C. (1993). Infrageneric classification of quercus (Fagaceae) and typification of sectional names. *Annales des Sciences Forestieres*, 50 (Suppl.1), 25s–34s. doi: 10.1051/forest:19930701

Nonato, L. G., and Aupetit, M. (2018). Multidimensional projection for visual analytics: Linking techniques with distortions, tasks, and layout enrichment. *IEEE Trans. Vis. Comput. Graph.* 25, 2650–2673. doi: 10.1109/TVCG.2018.2846735

Ousaaid, D., Mechchate, H., Laaroussi, H., Hano, C., Bakour, M., El Ghouizi, A., et al. (2021). Fruits vinegar: Quality characteristics, phytochemistry, and functionality. *Molecules* 27, 222. doi: 10.3390/molecules27010222

Peng, Y.-S., Chen, L., and Li, J.-Q. (2007). Study on numerical taxonomy of quercus L.(Fagaceae) in China. *J. Wuhan Bot. Res.* 25, 149–157. doi: 10.3969/j.issn.2095-0837.2007.02.008

Shimaji, K. (1962). Anatomical studies on the phylogenetic interrelationship of the genera in the fagaceae. *Bull. Tokyo Univ For* 57, 1–60.

Wang, S., Hu, Y., and Zhou, Z. (2003). AFLP analysis of genetic variation and structure of natural populations of Quercus senescens. *Plant Divers.* 25, 1. doi: CNKI:SUN:YOKE.0.2005-01-007

Wang, S., Hu, Y., and Zhou, Z. (2005). AFLP analysis of genetic variation and structure of natural populations of Quercus senescen. *Acta Bot. Yunnanica* 27, 49–58. doi: 10.3969/j.issn.2095-0845.2005.01.006

Sun, Y., Gong, D., and Sun, G. (2021). Quality monitoring and evaluation of powdered poppy capsule extractive by multiple wavelengths matching average fusion chromatographic fingerprint combined with electrochemical fingerprint. *Microchem. J.* 169, 106516. doi: 10.1016/j.microc.2021.106516

Trelease, W. L. (1924). *The american oaks*. Memoirs of the National Academy of Sciences (US Government Printing Office). 20, 1–255.

Wang, D., Li, D., Fu, L., Zheng, Y., Gu, Y., Chen, F., et al. (2021). Can electrochemical sensors be used for identification and phylogenetic studies in lamiaceae? *Sensors* 21, 8216. doi: 10.3390/s21248216

Xu, Y., Lu, Y., Zhang, P., Wang, Y., Zheng, Y., Fu, L., et al. (2020). Infrageneric phylogenetics investigation of chimonanthus based on electroactive compound profiles. *Bioelectrochemistry* 133, 107455. doi: 10.1016/j.bioelechem.2020.107455

Ye, W., Zheng, Y., Zhang, P., Fan, B., Li, Y., and Fu, L. (2021). Identification of species in lycoris spp. from stigmatic exudate using electrochemical fingerprints. *Int. J. Electrochem Sci.* 16, 211041. doi: 10.20964/2021.10.56

Zheng, Y., Li, X., Han, F., Fu, L., and Sun, J. (2021a). Identification of foliage plants heuchera based on electrochemical profile of active molecules. *Int. J. Electrochem Sci.* 16, 211136. doi: 10.20964/2021.11.44

Zheng, Y., Wang, D., Li, X., Wang, Z., Zhou, Q., Fu, L., et al. (2021b). Biometric identification of taxodium spp. and their hybrid progenies by electrochemical fingerprints. *Biosensors* 11, 403. doi: 10.3390/bios11100403

Zhou, Z., Pu, C., and Chen, W. (2003). Relationships between the distributions of quercus sect heterobalanus (Fagaceae) and uplift of Himalayas. *Adv. Earth Sci.* 18, 884–890. doi: 10.11867/j.issn.1001-8166.2003.06.0884

Zhou, J., Zheng, Y., Zhang, J., Karimi-Maleh, H., Xu, Y., Zhou, Q., et al. (2020). Characterization of the electrochemical profiles of lycoris seeds for species identification and infrageneric relationships. *Anal. Lett.* 53, 2517–2528. doi: 10.1080/00032719.2020.1746327

Frontiers in
Plant Science

Cultivates the science of plant biology and its applications

The most cited plant science journal, which advances our understanding of plant biology for sustainable food security, functional ecosystems and human health.

Discover the latest Research Topics

See more →

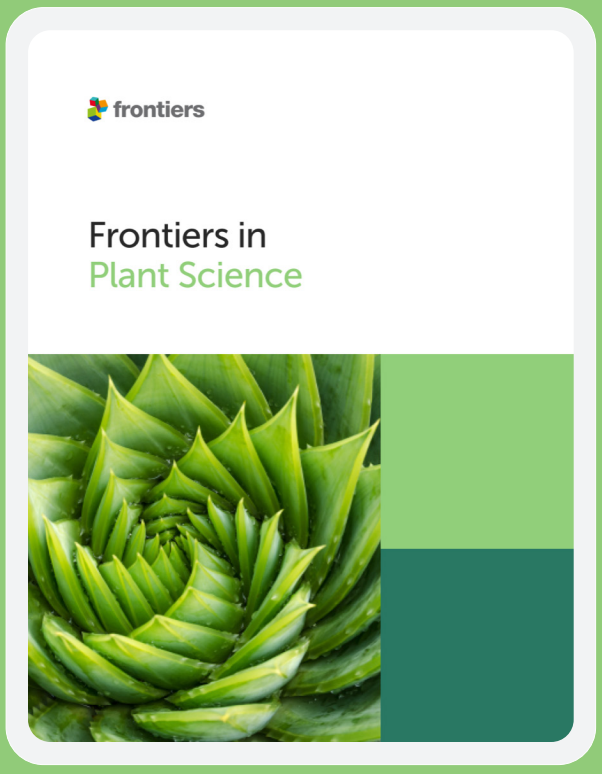

Frontiers

Avenue du Tribunal-Fédéral 34
1005 Lausanne, Switzerland
frontiersin.org

Contact us

+41 (0)21 510 17 00
frontiersin.org/about/contact